University of Massachusetts Dartmouth

Department of Electrical and Computer Engineering

Spectral Projection Model for Electromagnetic Scattering and Radiation

A Dissertation in

Electrical Engineering

by

Anthony Fascia

Submitted in Partial Fulfillment of the

Requirements for the Degree of

Doctor of Philosophy

May 2023

We approve the dissertation of Anthony Fascia

Date of Signature

Dayalan P. Kasilingam
Professor and Chairperson, Department of Electrical and Computer Engineering
Dissertation Advisor

Karen L. Payton
Professor Emerita, Department of Electrical and Computer Engineering (Retired)
Dissertation Committee

Paul J. Gendron
Associate Professor, Department of Electrical and Computer Engineering
Dissertation Committee

Gaurav Khanna Department of Physics
Professor, Department of Physics, University of Rhode Island, Kingston R.I.
Dissertation Committee

Sadasiva M. Rao
Scientist, NP4, Radar Division, Naval Research Laboratory, Washington D.C.
Dissertation Committee

Liudong Xing
Graduate Program Director, Department of Electrical Engineering

Jean VanderGheynst
Dean, College of Engineering

Tesfay Meressi
Associate Provost for Graduate Studies

Abstract

Spectral Projection Model of Electromagnetic Scattering and Radiation

by Anthony Fascia

This dissertation presents two new methods for analyzing electromagnetic scattering from perfect electrically conducting surfaces. The Spectral Projection Model and Direct Spectral Projection Model are spectral techniques for analyzing the scattering patterns from two-dimensional objects. The methods evolved from prior work done on analyzing scattering from perfect electrical conducting surfaces in two-dimensions in the sinusoidal spatial frequency domain using the Spatial Frequency Technique. By employing the addition theorem for Hankel and Bessel functions, the Spectral Projection Model represents the incident and scattered electric fields in the electric field integral equation and magnetic field integral equation as projections of spectral signatures. Using the addition theorem, the incident fields and the scattered fields are decomposed into the product of two matrices whose columns and rows are the spectral signatures of current sources that are projected onto the spectral signatures of the observation points. The Direct Spectral Projection Model, which evolved from Spectral Projection Model, identifies a set of virtual sources that are the eigenfunctions of the scattering problem. The currents induced on the surface are calculated by decomposing the spectral signature of the incident fields in terms of the spectral signatures of these virtual sources.

The first analyses using the Spectral Projection Model were on infinitely long circular cylinders and produced results that agreed well with established techniques like the Method of Moments for transverse magnetic incident waves. Both the Spectral Projection Model and Direct Spectral Projection Model techniques were then applied to elliptical cylinders of different axial ratios for both transverse magnetic and transverse electric incident waveforms. The techniques produced good agreement with Method of Moments techniques but only for small axial ratios. The addition theorem failed to converge for ellipses with large axial ratios.

In this dissertation, it is shown that the spectral signature of a point in space, which is represented by a vector, is equivalent to the convolution of the spectral signatures of two vectors,

which when combined result in the original vector. In order to calculate the scattered fields from elliptical cylinders of larger axial ratios, it was necessary to use the addition theorem as a convolution sum for both the source and observation points. To accomplish this, elliptical patterns were generated by summing two constant magnitude vectors rotating in opposite directions. Known as the Two Vector Sum approach, a variety of two-dimensional surfaces may be generated using two constant amplitude vectors rotating at different rates. Elliptical surfaces are generated using two vectors rotating at the same rate in opposite directions. The Spectral Projection Model was extended to scattering from ellipses with large axial ratios by using the Two Vector Sum approach to describe the model as a convolution of spectral signatures. Calculation of the convolution operation was performed using Hadamard products in the Fourier domain.

Far-field patterns calculated using the Spectral Projection Model are compared with those using the Method of Moments to validate the accuracy of the method for elliptical cylinders of both large major axis and large axial ratio. Computation of the current distribution on elliptical cylinders of large major axis and large axial ratio using the Direct Spectral Projection Model also indicate that Direct Spectral Projection Model and Method of Moments results closely match. Both methods are also used with a few different two-dimensional perfect electrical conducting cylinders other than elliptical cylinders to show the versatility of the two models.

The primary motivation for developing these models was the projection process clearly shows the physics of the scattering process by separating the spectral signatures of the incident sources from those of the induced currents. This allows this model to be used as a tool for surface or target synthesis. The Spectral Projection Model and Direct Spectral Projection Model formulation also has the potential for speeding up the computation by using the well-established properties of the convolution operation and the Fast Fourier Transform algorithm. The computational aspects of this model will be investigated as a follow-up to this dissertation. In the future, the models may also be extended to dielectric objects and three-dimensional objects.

Acknowledgments

I would like to thank my Lord and Savior Jesus Christ for giving me the privilege of attending University of Massachusetts Dartmouth and undertaking my Doctor of Philosophy in Electrical Engineering studies. He is my strength and my all. I would also like to thank my wife Diane, the love of my life, sisters Jean and Jane, cousin Paul, friends Bill McKenna, Bob Burns, Sawako Sugimura, Nichole Hersey, and Tony DelToro for their unwavering support throughout the years. I would also like to thank my committee members, Dr. Sadasiva Rao, Dr. Gaurav Khanna, Dr. Karen Payton, and Dr. Paul Gendron, for generously giving up their time for me, giving me constructive feedback, and meeting with me as part of my committee.

Nineteen years ago, I entered the university as a graduate student under Professor Branislov Notaros. Two years later Dr. Notaros left the university, and God gave me a wonderful gift, the best advisor anyone could ever hope to ask for, Professor Dayalan Kasilingam. It was Dr. Kasilingam's brilliant ideas, knowledge of physics, constant coaching, and unselfish support that made Spectral Projection Model theory and this research blossom, and enabled me to write this dissertation and present the theory in its current form. I am fortunate to have had his guidance and direction throughout the years. I enjoyed working with him, and will always be grateful to him for all he has done for me.

Table of Contents

List of Figures

List of Tables

Nomenclature

1D	One-dimensional
2D	Two-dimensional
3D	Three-dimensional
CG	Conjugate Gradient
CGFFT	Conjugate Gradient Fast Fourier Transform
DFT	Discrete Fourier Transform
DTFT	Discrete Time Fourier Transform
DSPM	Direct Spectral Projection Model
EFIE	Electric Field Integral Equation
EM	Electromagnetic
FDTD	Finite Difference Time Domain
FEM	Finite Element Method
FMM	Fast Multipole Method
FVDM	Finite Volume Discretization Methods
MFIE	Magnetic Field Integral Equation
MOM	Method of Moments
PEC	Perfect Electric Conductor
RWG	Rao-Wilton-Glisson
SPM	Spectral Projection Model
$\hat{\imath}_{ss,inc,Ie}$	Spectral signature of incident electric line source current
$\hat{\imath}_{inc,Ie}$	Incident electric current
$\hat{\imath}_{SS,ind}$	Spectral signature of induced electric current
$\hat{\imath}_{ind}$	Induced electric current
$\hat{\imath}_{ss,inc,Im}$	Spectral signature of incident magnetic line source current
$\hat{\imath}_{inc,Im}$	Incident magnetic current
h_n	**H**-spectral signature of a single virtual current source
e_n	**J**-spectral signature of a single induced current source

$\hat{\imath}_{vir,sum}$	Weighting factors of the virtual current sources
$\hat{\imath}_{vir,sum}$	Sum of the **H**-spectral signatures of the virtual current sources
$i_{ss,vir,sum}^{ff}$	**H**-Spectral signature of electric field wave equivalent produced by virtual sources
h_n	**H**-spectral signature of a single virtual current source
e_n	**J**-spectral signature of a single induced current source
$\hat{\imath}_{ind,sum}$	Vector magnitude and phase of sum of the induced currents
$\hat{\imath}_{SS,ind,sum}$	**J**-spectral signature of sum of the induced currents
$\cdot$	Vector and matrix multiplication
$\times$	Vector cross product
$\otimes$	Convolution
$\odot$	Hadamard product

Chapter 1: Introduction

1.1 Overview of Computational Electromagnetic Techniques

The focus of this dissertation is a new mathematical technique for solving electromagnetic field problems called the Spectral Projection Model (SPM). Other computational techniques such as the Method of Moments (MOM), Finite Element Method (FEM), Finite Difference Time Domain Method (FDTD), Spatial Frequency Technique (SFT), and the Fast Multipole Method (FMM) have all been used successfully to solve different classes of electromagnetic problems. This dissertation presents the theoretical and mathematical basis for the development of the new SPM technique and its offspring the Direct Spectral Projection Model (DSPM), and describes how the proposed techniques are related to these existing methods. The dissertation also provides the rationale for the development of this new technique and its benefits and advantages over existing methods.

The solution of electromagnetic (EM) field problems has evolved from the employment of empirical methods and analytical techniques to a computational science that harnesses the power of microprocessors in less than 200 years. But the basic equations governing the physics of electromagnetic theory have remained largely the same. They were summarized by James Clerk Maxwell (1831-1879) in 1862 in his *Treatise on Electromagnetics* [1]. All electromagnetic fields must satisfy the four Maxwell's equations given in equations $(1-1)$ to $(1-4)$. Faraday's law, Ampere's law, Gauss' law for electric flux, and Gauss' law for magnetic flux are listed in order.

$$\nabla \times E = -\frac{\partial B}{\partial t} \tag{1-1}$$

$$\nabla \times H = J + \frac{\partial D}{\partial t} \tag{1-2}$$

$$\nabla \cdot E = \rho_v \tag{1-3}$$

$$\nabla \cdot B = 0 \tag{1-4}$$

Maxwell's equations are the foundation for solving all electromagnetic field problems. The mathematics necessary for the writing and solution of these equations was developed over centuries by many mathematicians and physicists, most notably the inventors of calculus, Isaac

Newton and Gottfried Wilhelm Leibniz [2]. The analytical solution to Maxwell's equations for different problems was found by numerous mathematicians and physicists. Most analytical solutions to electromagnetic problems made use of symmetry. Unfortunately, many problems with asymmetrical geometry were intractable because analytical solutions could not be derived for these problems.

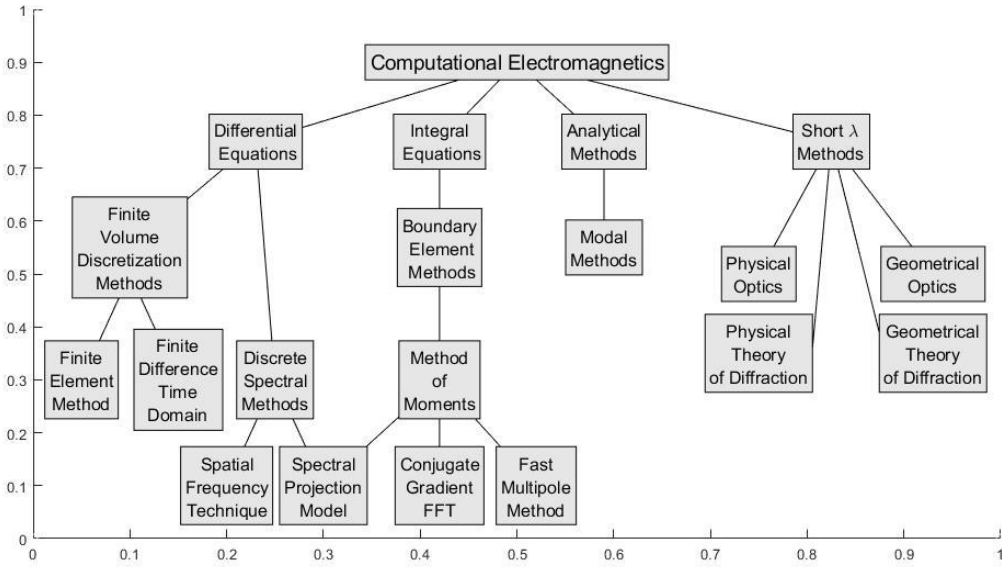

Figure 1-1: Branch chart of methods in computational electromagnetics.

Computational methods involving large matrices were not possible until the 20th century with the invention of electronic computers [3-5]. Numerical techniques are the only way to solve many electromagnetic problems that do not have an analytical solution. In these computational methods, analytical techniques are combined with linear algebra and discretization methods to solve for scattered and radiated electromagnetic fields. The three most important methods are finite volume discretization methods (FVDM), boundary element methods (BEM), and spectral methods (SM). FVDM includes the finite element method (FEM) and the finite difference time domain (FDTD) analysis [6,7]. The most important BEM is the Method of Moments (MOM) first described by Harrington in his classic paper [8]. For large structures, the fast multipole method (FMM) is an alternative boundary element method [9] technique. Spectral methods such

as the spatial frequency technique (SFT) and conjugate gradient FFT (CGFFT) are two types of BEM's that solve the problems either fully or partially in the spatial frequency domain [10,11].

1.2 Finite Volume Discretization Methods

Finite volume discretization methods are useful in applications where the volume of the object is well defined, and the electromagnetic fields inside the object needs to be calculated. FEM is a variational technique that minimizes the electromagnetic energy of a functional F to arrive at a solution [12,13]. A functional maps elements *u, w,* and *g* of the function space *U* into the scalar space of real numbers in range *R*. The element *u* is a basis function, *w* is a testing function, and *g* is the source function. One begins with the homogeneous Helmholtz equation $(1-5)$,

$$\nabla^2 u + k^2 u = g \tag{1-5}$$

where $u, w, g \in U$ and k is a constant. The functional for the Helmholtz equation is formed by setting $f = g - \nabla^2 u - k^2 u$, and then multiplying f by the testing function w. Next f is integrated over an element of volume *V*, and Green's first identity, the divergence theorem $(1-6)$, and the vector theorem in $(1-7)$ are used to simplify the expression.

$$\int_V w\nabla^2 u dV - \int_V u\nabla^2 w dV = \int_{\Gamma_D} w\frac{\partial u}{\partial n} dS - \int_{\Gamma_N} u\frac{\partial w}{\partial n} dS \tag{1-6}$$

$$\int_V w\nabla^2 u dV + \int_V \nabla u \nabla w dV = \int_{\Gamma_D} w\frac{\partial u}{\partial n} dS \tag{1-7}$$

For the Galerkin case when *w* = *u*, and integration over the Dirichlet boundary $\int_{\Gamma_D} w\frac{\partial u}{\partial n} dS = 0$, the functional F is shown in equation $(1-8)$.

$$F = \iiint_V [(\nabla u)^2 - k^2 u^2 + gu] dV \tag{1-8}$$

If one sets $u \to u + \Delta u$, the minimum of the functional *F* occurs when $\Delta u = 0$. The illustrations in Figure 1-2 show two objects divided into triangular basis functions. The nodes are indicated by dots on the vertices of the triangles. Electric and magnetic fields are calculated at these points. Basis functions are generally simple linear functions defined over local elements.

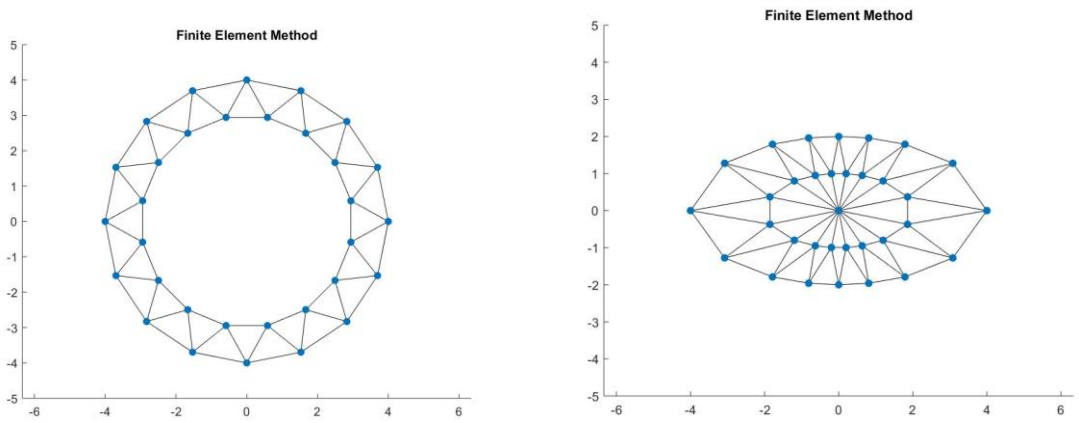

a) b)

Figure 1-2: Finite Element Method grids for (a) annular ring and (b) ellipse.

The finite difference time domain method (FDTD) is a time domain method for solving electromagnetic field problems. It is a grid-based method that approximates spatial and time derivatives using central difference formulas [14,15]. The method calculates first the electric field and then the magnetic field at given time steps and spatial intervals over the grid. See Figure 1-3 for an illustration of an object on a two- dimensional grid subject to an incident electromagnetic field.

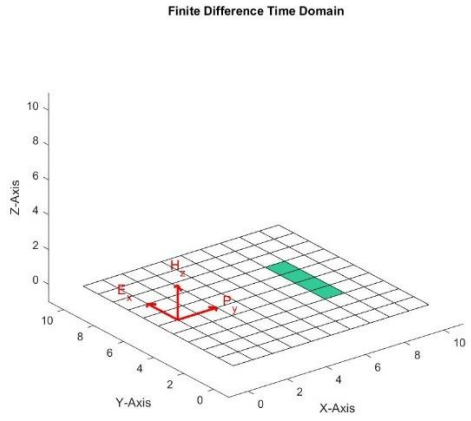

Figure 1-3: Two- dimensional grid subject to an incident electromagnetic field for FDTD analysis. Object is colored green.

Derivation of the FDTD begins with two of Maxwell's equations in differential form, Faraday's law and Ampere's law. See Table 1-1.

Table 1-1: Faraday's Law and Ampere's Law in Differential Form.

Faraday's Law	Ampere's Law
$\frac{\partial H_x}{\partial t} = -\frac{1}{\mu}\left(\frac{\partial E_z}{\partial y} - \frac{\partial E_y}{\partial z}\right)$	$\frac{\partial E_x}{\partial t} = \frac{1}{\varepsilon}\left(\frac{\partial H_z}{\partial y} - \frac{\partial H_y}{\partial z} - \sigma E_x\right)$
$\frac{\partial H_y}{\partial t} = -\frac{1}{\mu}\left(\frac{\partial E_x}{\partial z} - \frac{\partial E_z}{\partial x}\right)$	$\frac{\partial E_y}{\partial t} = \frac{1}{\varepsilon}\left(\frac{\partial H_x}{\partial z} - \frac{\partial HE_z}{\partial x} - \sigma E_y\right)$
$\frac{\partial H_z}{\partial t} = -\frac{1}{\mu}\left(\frac{\partial E_y}{\partial x} - \frac{\partial E_x}{\partial y}\right)$	$\frac{\partial E_z}{\partial t} = \frac{1}{\varepsilon}\left(\frac{\partial H_y}{\partial x} - \frac{\partial H_x}{\partial y} - \sigma E_z\right)$

An illustration of two grid cells for calculating TM^z and TE^z travelling waves impinging on an object is shown in Figure 1-4.

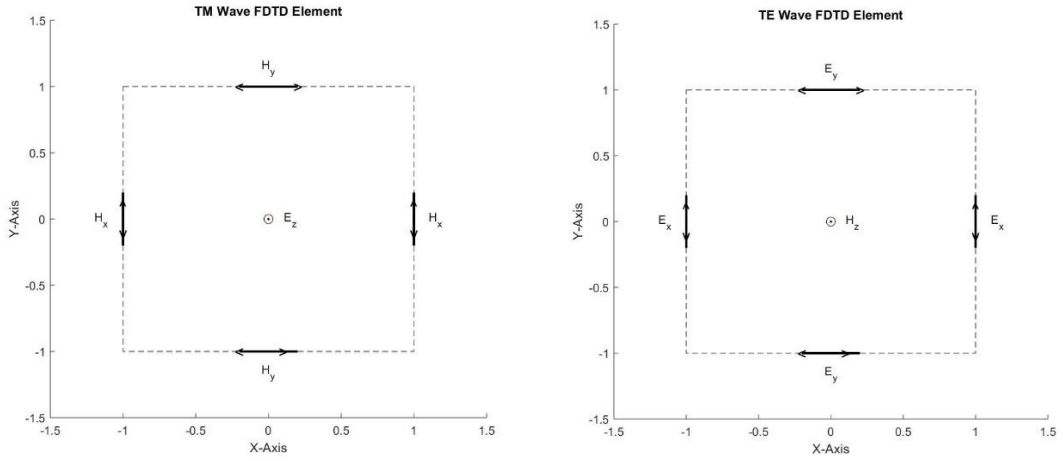

a) b)

Figure 1-4: Finite Difference Time Domain grid elements for infinitely long cylinders. a) TM wave FDTD element. b) TE wave FDTD element.

In transverse magnetic wave analysis case, i.e. TM^z waves, boundary conditions are given in equation $(1-9a)$. The central difference formulas are applied to equations $(1-9b)$ to $(1-9d)$.

$$E_x = 0 \qquad E_y = 0 \qquad H_z = 0 \qquad \frac{\partial}{\partial z} = 0 \tag{1-9a}$$

$$\frac{\partial H_x}{\partial t} = -\frac{1}{\mu}\frac{\partial E_z}{\partial y}$$

$$H_x^{n+\frac{1}{2}}(i,j,k) = H_x^{n-\frac{1}{2}}(i,j,k) + \frac{\Delta t}{\mu(i,j,k)}\left[-\frac{E_z^n(i,j+1,k) - E_z^n(i,j,k)}{\Delta y}\right] \tag{1-9b}$$

$$\frac{\partial H_y}{\partial t} = \frac{1}{\mu}\frac{\partial E_z}{\partial x}$$

$$H_y^{n+\frac{1}{2}}(i,j,k) = H_y^{n-\frac{1}{2}}(i,j,k) + \frac{\Delta t}{\mu(i,j,k)}\left[\frac{E_z^n(i+1,j,k) - E_z^n(i,j,k)}{\Delta x}\right] \tag{1-9c}$$

$$\frac{\partial E_z}{\partial t} = \frac{1}{\varepsilon}\left(\frac{\partial H_y}{\partial x} - \frac{\partial H_x}{\partial y}\right)$$

$$E_z^{n+1}(i,j,k) =$$

$$E_z^n(i,j,k) + \frac{\Delta t}{\varepsilon(i,j,k)}\left[\frac{H_y^{n+\frac{1}{2}}(i,j,k) - H_y^{n+\frac{1}{2}}(i-1,j,k)}{\Delta x} - \frac{H_x^{n+\frac{1}{2}}(i,j,k) - H_x^{n+\frac{1}{2}}(i,j-1,k)}{\Delta y}\right] \tag{1-9d}$$

A full list of the 3D equations and applications of the Finite Difference Time Domain method may be found in the references [7].

A benefit of the FDTD method is that the algorithm does not require the formulation of integral equations, and relatively complex scattering problems can be solved without inverting large matrices. Because it is grid based, each element may have different values of permittivity and permeability. So, it may be used for solving problems involving linear and non-linear materials. Also, derivatives are approximated by the central difference formula, and successive grid points are calculated from previous ones. This makes it excellent for calculating the time response of electromagnetic field problems, and for displaying waveform propagation through animation.

A drawback of this approach is that the grid size can grow very large depending on the problem domain, and the code must satisfy time restraint conditions, i.e. the Courant-Friedrichs-Lewy (CFL) stability criterion [16].

1.3 Boundary Element Methods

Boundary element methods are useful in calculating the electromagnetic fields around an object and the approximate calculation of fields and currents on the boundary. Once the current distribution on the surface of the object is calculated, the far-field radiation pattern may be found.

Most boundary element methods solve integral equations using a mathematical technique called the method of weighted residuals. The most popular BEM is the Method of Moments [17-22]. Objects subjected to radiation and scatterers are first discretized into elements. Examples of one-dimensional discretized objects typically solved using the MOM are shown in Figure 1-5.

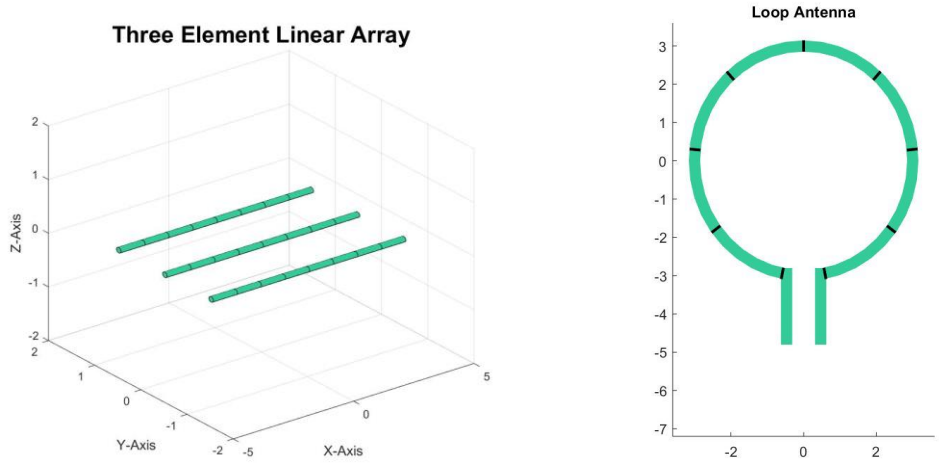

a) b)

Figure 1-5: a) Discretized linear array using Method of Moments. b) Discretized circular loop using Method of Moments.

Solving problems using the Method of Moments often begins with the Helmholtz vector wave equation $(1-10)$ for the vector form of the magnetic vector potential ***A(r)*** and its integral Green's function solution $(1-11)$. See Figure 1-6.

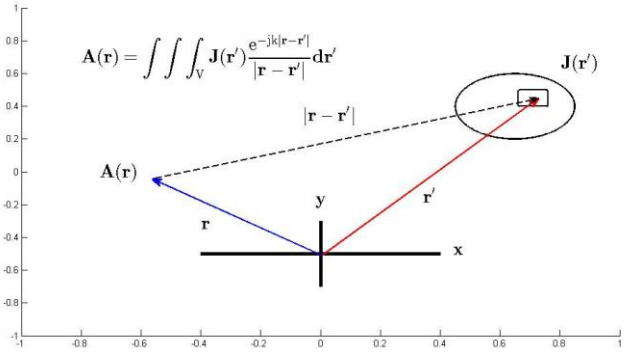

Figure 1-6: Magnetic vector potential and its 3D Green's function integral representation.

$$\nabla^2 \boldsymbol{A} + k_0^2 \boldsymbol{A} = \boldsymbol{J_V} \qquad (1-10)$$

$$\boldsymbol{A}(\boldsymbol{r}) = \frac{\mu}{4\pi} \iiint_V \boldsymbol{J_V}(\boldsymbol{r}')\, G(|\boldsymbol{r} - \boldsymbol{r}'|) dV' \qquad (1-11)$$

After the object is discretized over its entire domain, basis functions representing local current amplitudes and phases may be solved using matrix algebra. Source and observation points are coincident, and calculation of current values requires the inversion of a matrix. The matrix is diagonally dominant because of the existence of a singularity in the Green's function. Different techniques have been developed to assist in inverting these diagonally dominant matrices [23,24].

1.4 Spectral Methods

Another way to calculate the electromagnetic fields on an object is by spectral methods. They use continuous or "smooth" whole domain basis functions. If the basis functions are sinusoidal, they take advantage of the speed of the FFT to reduce calculation time. These methods begin with the differential or integral equations describing the EM fields and transform them into the spatial frequency domain [25-28]. For the vector wave equation $(1-10)$, its spatial frequency representation is the scalar differential equation $(1-12)$.

$$k^2 A(k) + k_0^2 A(k) = J_V(k) \qquad (1-12)$$

The variable k is the spatial frequency, and k_0 is the wavenumber.

For the integral equation $(1-11)$, the integration can be viewed as a convolution operation in the spatial domain. This simplifies the matrix algebra because convolution in the spatial domain is performed as multiplication in the spatial frequency domain. To transform the problem into the spatial frequency domain, one can often use the discrete Fourier transform. Using the FFT algorithm speeds up the solution to the problem. After transformation into the spatial frequency domain, equation $(1-11)$ may be written as equation $(1-13)$.

$$A(k) = \frac{\mu}{4\pi} G(k) J(k) \qquad (1-13)$$

Next the Green's function matrix inverse is taken, and the result is transformed back into the spatial domain to calculate the current distribution.

Even though spectral techniques are accurate due to their use of continuous functions, they are limited as to the geometries they can handle. In order to take advantage of the speed of the FFT, the algorithm requires a uniform grid. The FFT grid for one-dimensional problems must have equal length segments. In two dimensions, the 2D FFT grid must be divided into equal sized rectangles. Figure 1-7 shows illustrations of a rectangular and triangular object whose sampling points fall on a square grid, and an elliptical object whose sampling points do not. The conductor region is in green and the sampling points are the dots. The FFT algorithm may be used to calculate the discrete Fourier transform of the rectangular and triangular objects. In the case of the ellipse, the discrete Fourier transform must be calculated directly for points on the object, slowing down the analysis time considerably.

Because the spectral method uses the discrete Fourier transform, the object is assumed to be periodic in space. Thus, sampling must satisfy the Nyquist criterion. The last illustration shows a square object and its periodicity in space. The green region is the conductor space, and the gray region is called the complementary space. For 2D problems, the complementary space is analogous to adding zeros for the 1D case.

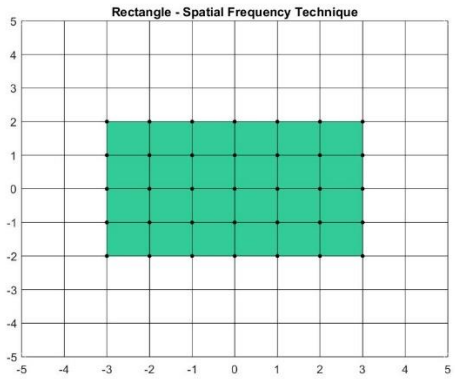

a)

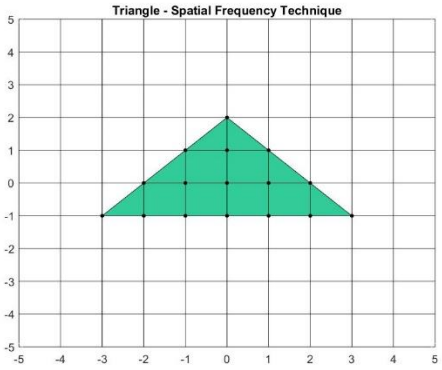

b)

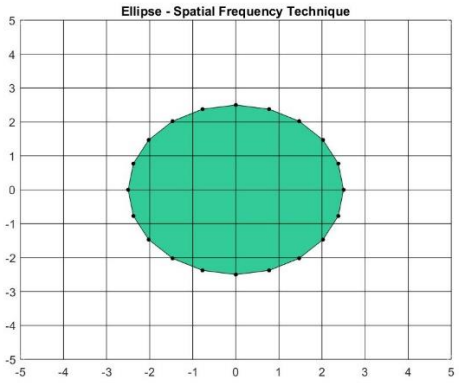

c)

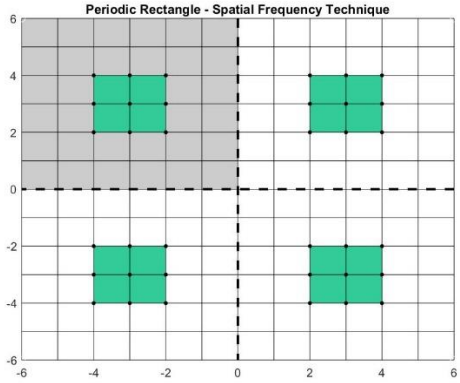

d)

Figure 1-7: Two dimensional spatial grids for a) rectangular b) triangular, and c) elliptical object. d) A periodic rectangular object is the fourth illustration. Dots are the sampling points on each object.

1.5 Spatial Frequency Technique vs. FDTD and FEM

The Spatial Frequency Technique begins with the differential form of Maxwell's equations to develop a set of equations similar to the Finite Difference Time Domain method and the Finite Element Method, but that is where the similarity ends. The FDTD uses approximations to derivatives to solve for the time domain response of electromagnetic systems, and the Finite Element Method uses a variation technique to minimize a functional written from the differential equations.

The SFT applies the discrete Fourier transform to a discretized object with fields characterized by spatial frequencies k. For example, the electric field $E(k)$ shown in equation $(1-14)$ can be written in the spatial frequency domain, reducing the solution of the system for $J(k)$ to an algebraic expression. The wavenumber is k_0.

$$E(k) = \frac{\eta}{k_0}(-k^2 + k_0^2)G(k)J(k) \qquad (1-14)$$

$$J(k) = \frac{k_0}{\eta}[(-k^2 + k_0^2)G(k)]^{-1}E(k) \qquad (1-15)$$

In addition, the power of the FFT can be used to improve the speed of the calculations as long as objects are considered periodic and properties of circulant matrices are exploited. Combining spatial frequency analysis with the conjugate gradient method (CGFFT) has shown to produce even faster results. This technique was investigated and different iterative methods were implemented to improve the calculation of the surface currents. These will be discussed in Chapter 4, was well as the limitations of these iterative methods for SFT analysis.

1.6 Boundary Element Method Adapted to Large Systems of Equations

The Fast Multipole Method is an extension of the Method of Moments in that it expedites the calculation of the off-diagonal terms in the impedance matrix [29,30]. This is useful for problems with many source/observation points that generate large matrices. The method is based on a form of the Hankel Addition Theorem given below in equation $(1-16)$.

$$H_0^{(2)}(\beta|\boldsymbol{\rho} - \boldsymbol{\rho}'|) = \sum_{n=-\infty}^{\infty} J_n(\beta\rho)H_n^{(2)}(\beta\rho')e^{jn(\phi-\phi')} \qquad \rho < \rho' \qquad (1-16)$$

As seen in Figure 1-8 below, the singularity in the Hankel function causes diagonal terms to take on very large values. These terms are calculated using the Method of Moments. The other terms are calculated using an expanded form of the Hankel Addition Theorem. The illustration in Figure 1-8 shows the singularity in yellow along the main diagonal of the impedance matrix. The off-diagonal terms are much smaller and calculated using the Fast Multipole Method.

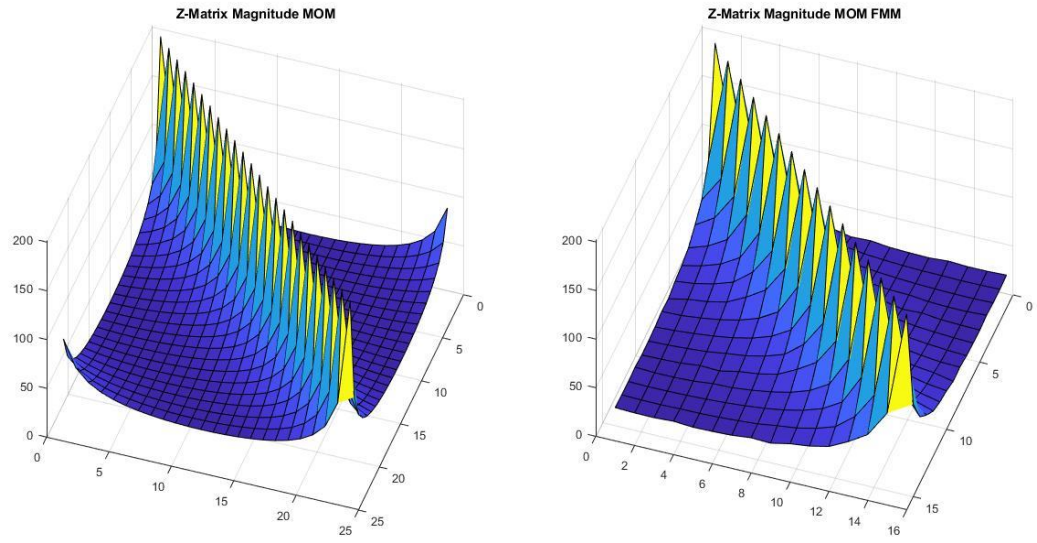

a) b)

Figure 1-8: Surface plot of impedance matrix comparing the a) Method of Moments and b) Fast Multipole Method.

The Fast Multipole Method groups terms around the object being analyzed. This is all done by expanding the summation on the right side of the addition theorem equation (1-13) into three parts. The three parts are formed as matrices called Aggregation, Translation, and Disaggregation (ATD). See equation $(1-17)$.

$$\sum_{n=1}^{N} Z_{m,n} J_n =$$

$$\sum_{q \in B_p} \sum_{n \in G_q} Z_{m,n} J_n + \frac{k_0 Z_0}{8\pi} \sum_{r=1}^{R} t_{m,p}(\alpha_r) \sum_{q \notin G_p} A_{p,q}(\alpha_r) \sum_{n \in G_q} f_{q,n}(\alpha_r) J_n \qquad (1-17)$$

D T A

The illustration in Figure 1-9 shows how source points in Group 1 are aggregated to q=1 and then translated to the other five group centers p = 2 to p = 6. Figure 1-10 illustrates how sources in Group 1 are aggregated to the center of Group 1, translated to the center of Group 5, and then disaggregated to observation points in Group 5.

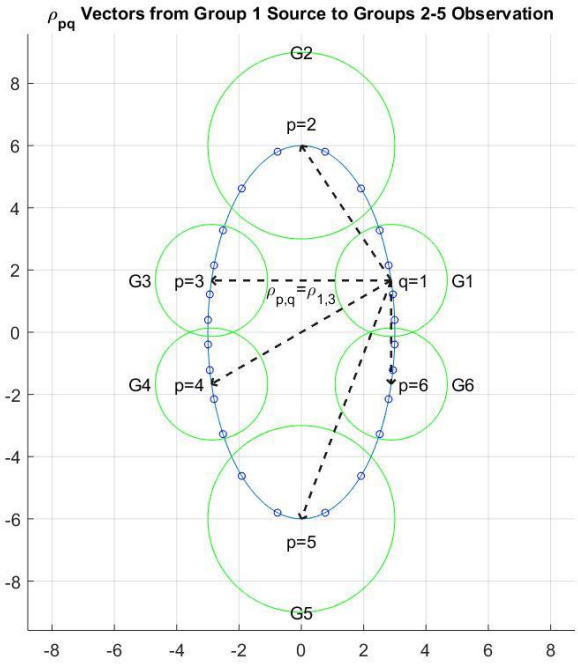

Figure 1-9: Grouping of source and observation points on an elliptical surface using the Fast Multipole Method.

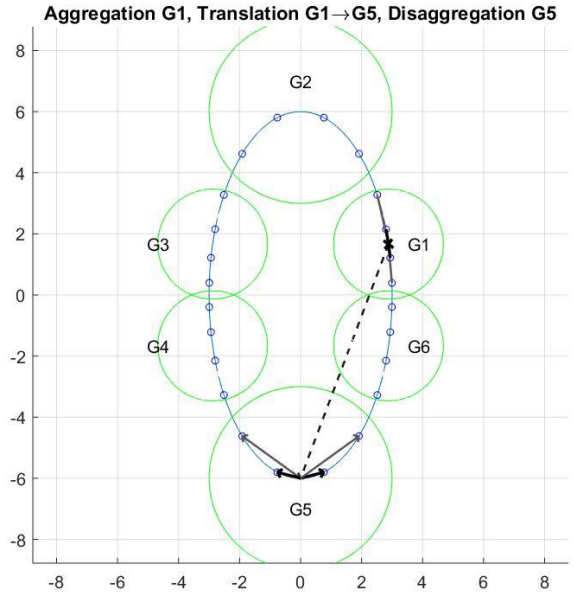

Figure 1-10: Example of aggregation group G1, translation from group G1 to G5, and disaggregation group G5 using the Fast Multipole Method.

1.7 Spectral Projection Method Model and Direct Spectral Projection Model

This dissertation investigates new hybrid BEM/SM computational techniques called the Spectral Projection Model [30] and Direct Spectral Projection Model. The Spectral Projection Model (SPM) has its foundation in the Hankel form of the addition theorem as shown in equation $(1-16)$, and its antecedent known as Graf's addition theorem [31,32]. The addition theorem is a method for calculating a Bessel or Hankel function as an infinite sum of Bessel and Hankel functions.

The addition theorem for Bessel functions has been used by different authors to solve electromagnetic scattering problems. Mittra and Wilton used the addition theorem to solve for surface currents on both circular and elliptical infinitely long 2D PEC and dielectric surfaces of using modal methods [33,34]. Harrington explained how to use modal methods to solve for the currents induced on the surfaces of 2D PEC circular cylinders in his classic text [35], and Balanis detailed modal solutions to the EFIE and MFIE for TM^z and TE^z fields incident on PEC circular cylinders [36]. Examples of modal equations for incident and scattered electric fields for the electric field on a circular cylinder are given in equations $(1-18)$ and $(1-19)$.

$$E_z^i = E_0 \sum_{k=-\infty}^{\infty} j^{-k} J_k(\beta|\boldsymbol{\rho}|) e^{jk(\phi-\phi_i)} \qquad (1-18)$$

$$E_z^s = -E_0 \sum_{k=-\infty}^{\infty} j^{-k} \frac{J_k(\beta|\boldsymbol{a}|)}{H_k^{(2)}(\beta|\boldsymbol{a}|)} H_k^{(2)}(\beta|\boldsymbol{\rho}|) e^{jk(\phi-\phi')} \qquad (1-19)$$

The modal methods implemented by Wilton worked well for elliptical cylinders of small axial ratio, but unlike SPM and DSPM failed for larger axial ratios. Wilton delved into the limits of the addition theorem used as a convolution product, but SPM and DSPM exploit Graf's addition theorem to solve 2D surfaces of large axial ratio that still achieve good convergence.

In the Spectral Projection Model, the addition theorem equation is not written as a sum, but instead as a projection of the spectral signature of source points onto the spectral signature of observation points along the surface of the object. For the incident fields, the **H**-spectral signature of source points are projected onto the **J**-spectral signature of observation points along the surface of the object. For the induced fields, the **J**-spectral signature of source points are projected onto the **H**-spectral signature of observation points along the surface of the object. Equations $(1-20)$ to $(1-22)$ define these new terms for the induced fields described above.

$$H_0^{(2)}(\beta|\boldsymbol{\rho}-\boldsymbol{\rho}'|) = \sum_{k=-K}^{K} J_k(\beta\rho')H_k^{(2)}(\beta\rho)e^{jk(\phi-\phi')} = e_{om}^T e_{sn} \qquad \rho > \rho' \qquad (1-20)$$

where the two vectors,

$$e_{sn} = \left[J_K(\beta\rho')e^{-jK\phi'} \ldots\ J_k(\beta\rho')e^{jk\phi'} \ldots\ J_{-K}(\beta\rho')e^{jK\phi'}\right]^T \qquad (1-21)$$

and

$$e_{om} = \left[H_{-K}^{(2)}(\beta\rho)e^{-jK\phi} \ldots\ H_k^{(2)}(\beta\rho)e^{jk\phi} \ldots\ H_K^{(2)}(\beta\rho)e^{jK\phi}\right]^T \qquad (1-22)$$

The vector e_{sn} is called the **J**-spectral signature of the induced current source point at (ρ', ϕ') and the e_{om} vector is called the **H**-spectral signature of the surface observation point at (ρ, ϕ). The condition $\rho \geq \rho'$ must be satisfied to ensure convergence of equation $(1-19)$. The addition theorem may also be written as the projection of the **H**-spectral signature of the external source points (ρ', ϕ') onto the **J**-spectral signature of the surface observation points (ρ, ϕ) for incident fields, as long as the condition $(\rho' > \rho)$ is satisfied.

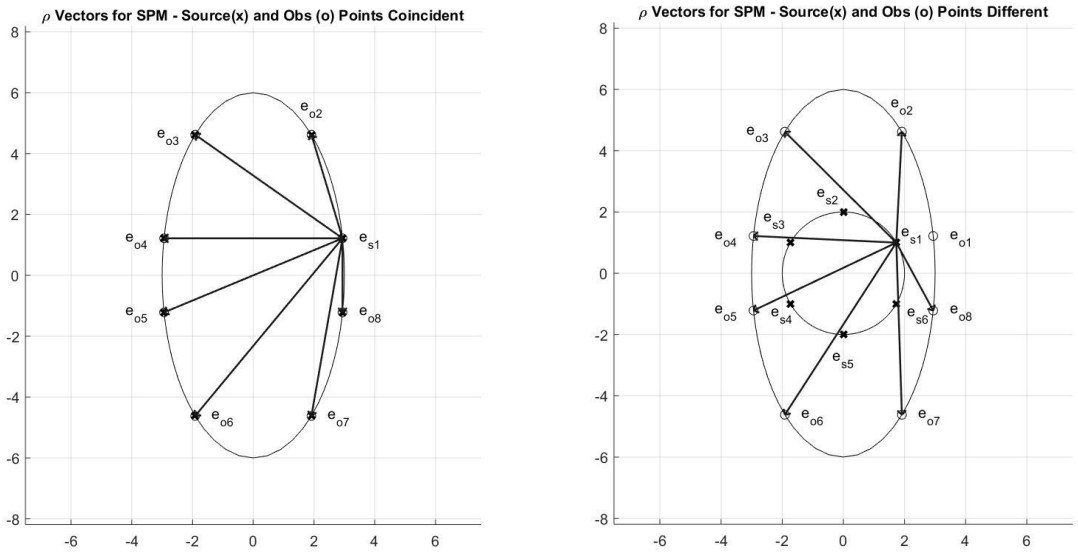

a) b)

Figure 1-11: Examples of source and observation points for two different 2D infinitely long elliptical cylinders using the Spectral Projection Model. a) coincident points b) different points

The observation and source points in $(1-20)$ may or may not be coincident so long as the condition $\rho' \leq \rho$ for the addition theorem is satisfied. See Figures 1-11a and 1-11b.

In the Spectral Projection Model, the projection of the **J**-spectral signature e_{sn} of all source points $\rho_n{}'$ onto the **H**-spectral signature e_{om} of all observation points ρ_m are expressed as a matrix product. For scattering from PEC conductors in EFIE problems, the incident electric field is related to the matrix $\begin{bmatrix} \cdots & \cdots & \cdots \\ \cdots & H_0^{(2)}(\beta|\boldsymbol{\rho}-\boldsymbol{\rho}'|) & \cdots \\ \cdots & \cdots & \cdots \end{bmatrix}$, as is the induced electric field and surface current density coefficients $\begin{bmatrix} \cdots \\ J(\rho_n{}') \\ \cdots \end{bmatrix}$ on the object $(1-23)$.

$$\begin{bmatrix} \vdots \\ E^i(\rho_m) \\ \vdots \end{bmatrix} = \frac{\omega\mu}{4} \begin{bmatrix} \cdots & \cdots & \cdots \\ \cdots & H_0^{(2)}(\beta|\boldsymbol{\rho_m}-\boldsymbol{\rho_n}'|) & \cdots \\ \cdots & \cdots & \cdots \end{bmatrix} \begin{bmatrix} \vdots \\ J(\rho_n{}') \\ \vdots \end{bmatrix} \qquad (1-23)$$

The term $\begin{bmatrix} \cdots & \cdots & \cdots \\ \cdots & H_0^{(2)}(\beta|\boldsymbol{\rho_m}-\boldsymbol{\rho_n}'|) & \cdots \\ \cdots & \cdots & \cdots \end{bmatrix}$ is the Green's function matrix which relates the electric fields to the currents. The incident and scattered electric fields can be written in terms of the **J**-spectral signature of the induced surface current. The **J**-spectral signature of the induced surface current is a linear transformation on the actual surface currents $\begin{bmatrix} \vdots \\ J(\rho_n{}') \\ \vdots \end{bmatrix}$, and the far-field pattern of the scattering problem may be solved directly by calculating the spectral signature, without need for calculating the surface current.

A more versatile technique which originated from the SPM is the Direct Spectral Projection Model (DSPM) described in Chapter 6. It is summarized in the equation $(1-24)$ below:

$$\begin{bmatrix} \vdots \\ i^{ff}_{ss,vir,sum} \\ \vdots \end{bmatrix} = \begin{bmatrix} | & | & | \\ | & H_k^{(2)}(\beta|\boldsymbol{\rho_n}'|) & | \\ | & | & | \end{bmatrix} \begin{bmatrix} \vdots \\ \hat{\imath}_{ind,sum} \\ \vdots \end{bmatrix} \qquad (1-24)$$

This technique directly calculates the induced currents on the surface of an object by setting the weighted sum of the **H**-spectral signature of the virtual currents equal to the spectral signature of the equivalent electric field generated either by an incident plane wave or a set of infinite line sources. The DSPM may be used for arbitrarily shaped objects and fields generated by convolving multiple vectors in opposite directions.

The SPM and DSPM are new hybrid spectral/BEM approaches that differ from ordinary boundary element methods, and are simpler to solve than Fourier spectral methods like the SFT and the CGFFT. They are different from other BEMs like the MOM and FMM in that the source

and observation points do not need to coincide. Consequently, when calculating the Hankel function, the singularity at $\rho = 0$ may be avoided. For SPM there is no need to calculate the surface current. The far-field scattered and radiated fields outside the object can be found directly from the **J**-spectral signature of the source current. The SPM is a spectral method because the spectral signature of the surface currents defined by $J_n(\beta\rho')e^{-jn\phi'}$ are analogs to the complex exponentials found in the Fourier series. But these functions have the advantage that the two-dimensional spectrum is defined by one set of modal terms, at $\rho' e^{-jn\phi'}$, and not two sets of spatial frequency terms k_x and k_y. Also, source and observation points do not have to lie on a uniform spatial grid as required by the FFT. Moreover, the number of source and observation points may differ.

The DSPM offers advantages over the SPM in simplicity, and it facilitates direct calculation of the surface currents for arbitrary geometries as an alternative to other boundary element methods. It also offers the potential to solve antenna and electromagnetic field synthesis problems.

The first three computational techniques explained in this dissertation are the Method of Moments, the Fast Multipole Method, and the Spatial Frequency Technique. Their importance and relevance are discussed next with respect to the development and implementation of the Spectral Projection Model and Direct Spectral Projection Model.

Chapter 2: Method of Moments

2.1 Foundational Mathematics of Computational Electromagnetics

There are three classes of electromagnetic field problems: propagation, scattering and radiation. In this dissertation only electromagnetic scattering from objects that are perfect electric conductors (PEC) are considered. To determine the electromagnetic fields around a conducting object, one must apply Maxwell's equations to the region of interest with appropriate boundary conditions. Depending upon the problem, the region may or may not contain sources.

A fundamental equation of mathematics used to solve many electromagnetic field problems is the Fredholm integral equation [37]. Equation $(2-1)$ is the inhomogeneous Fredholm equation of the first kind.

$$f(t) = \int_a^b K(t,t')J(t')dt' \qquad (2-1)$$

Here $K(t,t')$ is a continuous function called the kernel, the function $f(t)$ is a known excitation, and the term $J(t')$ is a function to be determined. The kernel is usually a Green's function, which carries special properties. The unknown function $J(t')$ is usually the current density on the surface of the object.

2.2 Differential Form of Electric and Magnetic Field Equations

By applying Maxwell's equations, the electromagnetic fields around a perfect electric conductor are generally characterized by a partial differential equation. BEM next transform this equation into an integral equation. The conductor space is then discretized, and the integral equation is solved by numerical methods for parameters such as the electric field, magnetic field, or current density distribution.

The partial differential equations describing electric field intensity $\boldsymbol{E_A}$ and magnetic field intensity $\boldsymbol{H_F}$ are commonly given in equations $(2-2)$ and $(2-3)$.

$$\boldsymbol{E_A} = -j\omega\mu\boldsymbol{A} + \frac{1}{j\omega\varepsilon}\nabla(\nabla\cdot\boldsymbol{A}) \qquad (2-2)$$

$$\boldsymbol{H_F} = -j\omega\boldsymbol{F} + \frac{1}{j\omega\varepsilon}\nabla(\nabla\cdot\boldsymbol{F}) \qquad (2-3)$$

In these two equations, A is the magnetic vector potential, and F is the electric vector potential. E_A is the electric field given as a function of the magnetic vector potential, and H_F is the magnetic field as a function of the electric vector potential.

The Helmholtz wave equations for vector potential plane waves are as follows:

$$\nabla^2 \boldsymbol{A} + \beta^2 \boldsymbol{A} = \mu \boldsymbol{J} \qquad Magnetic\ Vector\ Potential \qquad (2-4)$$

$$\nabla^2 \boldsymbol{F} + \beta^2 \boldsymbol{F} = -\varepsilon \boldsymbol{M} \qquad Electric\ Vector\ Potential \qquad (2-5)$$

The Green's function solution to Helmholtz equation $(2-4)$ is the integral product of magnetic vector potential A and current density$J(r')$ seen in equation $(2-6)$. The Green's function $G(r, r')$ may also written $G(r-r')$.

$$\boldsymbol{A}(\boldsymbol{r}) = \frac{\mu}{4\pi} \iiint_V \boldsymbol{J}(\boldsymbol{r}')\, G\big(|\boldsymbol{r}-\boldsymbol{r}'|\big) dV' \qquad (2-6)$$

The 3D Green's function for a point source is given in $(2-7)$,

$$G\big(|\boldsymbol{r}-\boldsymbol{r}'|\big) = \frac{e^{-jk|\boldsymbol{r}-\boldsymbol{r}'|}}{|\boldsymbol{r}-\boldsymbol{r}'|} \qquad (2-7)$$

This can be written as the zeroth order spherical Hankel function of the second kind $(2-8)$.

$$h_0^{(2)}\big(\beta|\boldsymbol{r}-\boldsymbol{r}'|\big) = \frac{e^{-j\beta|\boldsymbol{r}-\boldsymbol{r}'|}}{|\boldsymbol{r}-\boldsymbol{r}'|} \qquad (2-8)$$

The Green's function $G(r-r')$ solution to the Helmholtz equation $(2-5)$ in terms of electric vector potential F is shown in equation $(2-9)$.

$$\boldsymbol{F}(\boldsymbol{r}) = \frac{\mu}{4\pi} \iiint_V \boldsymbol{M}(\boldsymbol{r}')\, G\big(|\boldsymbol{r}-\boldsymbol{r}'|\big) dV' \qquad (2-9)$$

So, equations $(2-6)$ and $(2-9)$ are the Green's function integral solutions for each of the differential electromagnetic field equations.

Table 2-1: Vector Potentials and Helmholtz Equation.

Vector Potential	Symbol	Helmholtz Equation
Magnetic	$\boldsymbol{A}(\boldsymbol{r})$	$\nabla^2 \boldsymbol{A} + \beta^2 \boldsymbol{A} = \mu \boldsymbol{J}$
Electric	$\boldsymbol{F}(\boldsymbol{r})$	$\nabla^2 \boldsymbol{F} + \beta^2 \boldsymbol{F} = -\varepsilon \boldsymbol{M}$

2.3 Electric and Magnetic Field Integral Equations

As mentioned earlier, the Method of Moments is a BEM that solves partial differential equations describing the behavior of electromagnetic problems as integral equations [18,20,21,36,38]. The two most common integral equations used to calculate scattering of fields from conducting bodies are called the Electric Field Integral Equation (EFIE) and the Magnetic Field Integral Equation (MFIE). The EFIE and MFIE will now be discussed.

The three-dimensional EFIE [36] for point sources scattering from a surface is given in equation $(2-10)$.

$$\boldsymbol{E_t^i}(r = r_s) = \frac{\eta}{\beta}\left[\beta^2 \iint_S \boldsymbol{J_S}(\boldsymbol{r'}) G(\boldsymbol{r_s}, \boldsymbol{r'}) ds' + \boldsymbol{\nabla} \iint_S \boldsymbol{\nabla'} \cdot \boldsymbol{J_S}(\boldsymbol{r'}) G(\boldsymbol{r_s}, \boldsymbol{r'}) ds'\right] \qquad (2-10)$$

The three- dimensional MFIE [36] for point sources scattering from a closed surface is given in equation $(2-11)$.

$$\hat{\boldsymbol{n}} \times \boldsymbol{H^i}(r = r') = \boldsymbol{J_S}(\boldsymbol{r'}) - \lim_{r \to S}\left[\hat{\boldsymbol{n}} \times \iint_S \boldsymbol{J_S}(\boldsymbol{r'}) \times \{\boldsymbol{\nabla'} G(\boldsymbol{r}, \boldsymbol{r'})\} ds'\right] \qquad (2-11)$$

The Method of Moments is a BEM useful in calculating the current distribution on a variety of structures. Once the current distribution is calculated, the far-field pattern may then be calculated from the current distribution. Starting with the 3D EFIE, the MOM analysis of a finite length discretized dipole antenna [39] is shown in Figures 2-1 and Figure 2-2. The dipole depicted in Figure 2-1a is a half wavelength dipole aligned with the Z-axis. It is subdivided into eight segments, and is excited by a voltage across the gap shown in Figure 2-1b.

As shown in Figure 2-2b for the case of the half wavelength dipole antenna, the far-field radiation pattern is symmetrical around the axis of the dipole structure. If the dipole antenna is

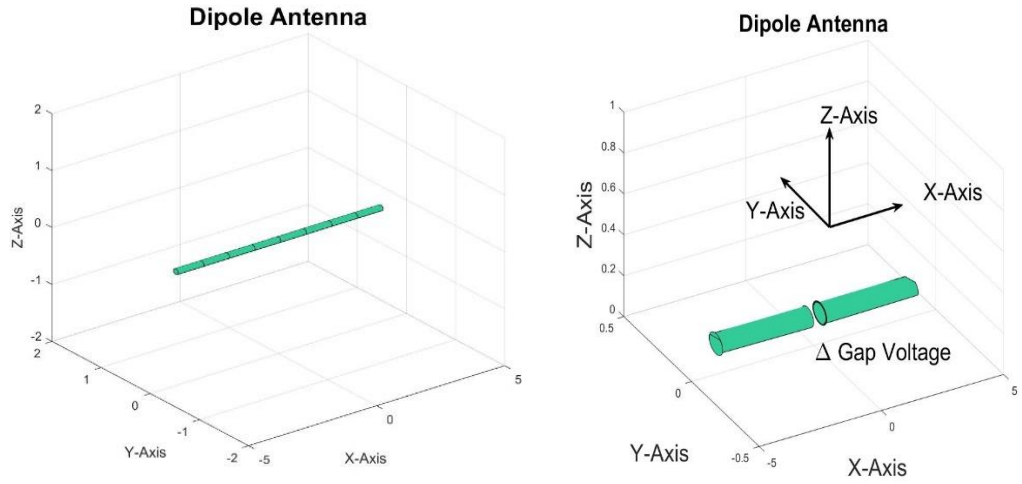

a) b)

Figure 2-1: a) Dipole antenna discretized into 8 segments. b) Illustration of dipole antenna shown with gap where voltage source is placed.

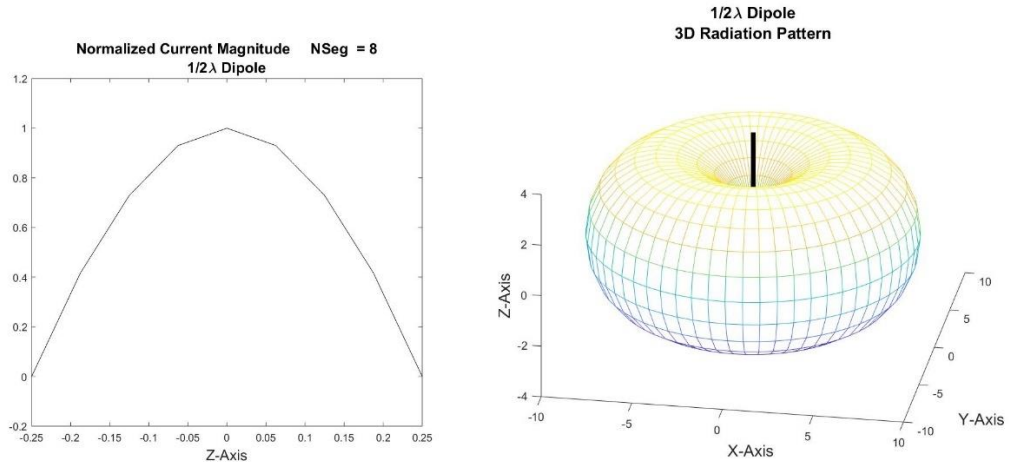

a) b)

Figure 2-2: a) Current distribution along a dipole antenna discretized into 8 segments. b) Three-dimensional radiation pattern of dipole antenna.

acting as a passive receiver of an incident electric field polarized in the Z-direction, the induced current on the antenna would be the same as in Figure 2-2a. When an electromagnetic structure

absorbs radiation and emits an electric field due to induced currents, it is referred to as electromagnetic scattering.

2.4 Scattering on Infinitely Long Structures by TM^z and TE^z Waves

Two-dimensional electromagnetic scattering problems for infinitely long structures are often divided into two classes by the polarization of the incident electric and magnetic fields. Transverse magnetic waves TM are those in which the magnetic field is oriented in the plane of incidence (across the structure) and the electric field is parallel to the radial axis of the structure. Transverse electric field waves TE are those in which the electric field lies in the plane of incidence and the magnetic field is parallel radially to the structure. See Figure 2-3 for examples.

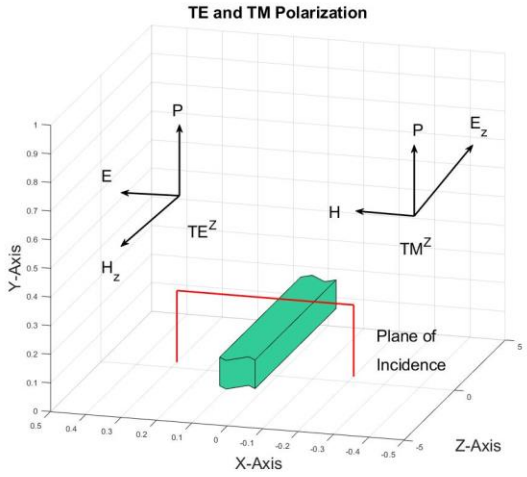

Figure 2-3: Vector representation of TM^z and TE^z waves on an infinitely long rectangular cylinder travelling in the +Y direction. The plane of incidence is normal to the E-field for TM^z waves, and is normal to the H-field for TE^z waves.

A TM^z plane wave incident on an infinitely long perfectly conducting cylinder is illustrated in Figure 2-4. The wave is illustrated passing by the cylinder with the electric field in the cylinder's radial direction.

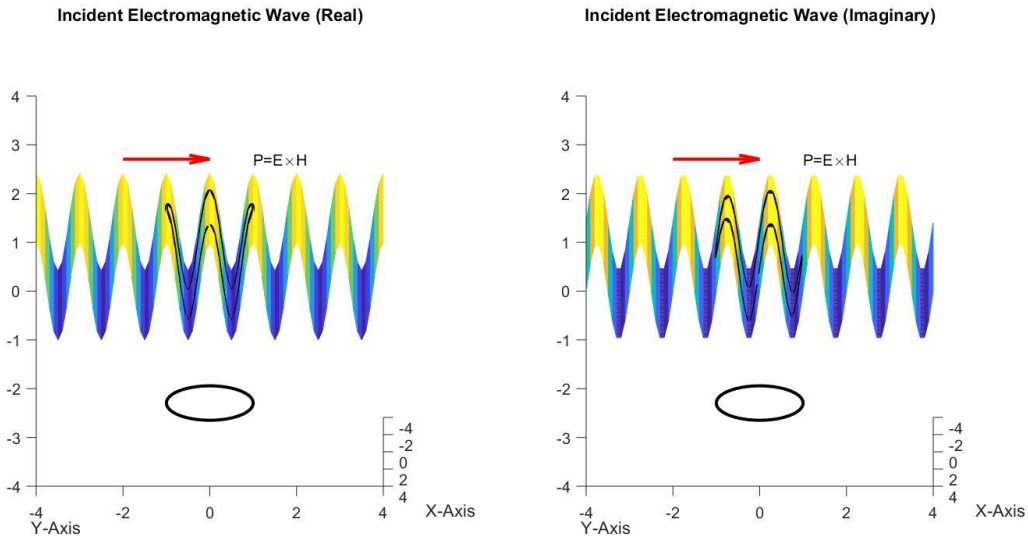

a) b)

Figure 2-4: a) Incident plane wave travelling in the y-direction incident upon an infinitely long conducting elliptical cylinder. b) The wave is travelling in the direction of the major axis, and the cross section is shown below the wave and traced on the waveform.

The two-dimensional EFIE for scattering of TM^z polarized waves from infinitely long cylindrical structures is derived from the three-dimensional EFIE and given in equation $(2-12)$. Note for 3D problems, the spherical Hankel function $h_0^{(2)}(R)$ is used as the Green's function.

$$A_z(\rho) = \frac{\mu}{4\pi}\iint_S J_z(\rho')h_0^{(2)}(R)dS' \qquad (2-12)$$

R for the 3D case is defined in equation $(2-13)$.

$$R = \sqrt{|\rho-\rho'|^2+(z-z')^2} \qquad (2-13)$$

Substituting the term R from $(2-13)$ into equation $(2-12)$, one may integrate with respect to z in equation $(2-12)$ and expand equation $(2-12)$

$$A_z(\rho) = \frac{\mu}{4\pi}\int_L J_z(\rho')\int_{-\infty}^{\infty}\left[\frac{e^{-j\beta\sqrt{|\rho-\rho'|^2+(z-z')^2}}}{\sqrt{|\rho-\rho'|^2+(z-z')^2}}dz'\right]d\rho' \qquad (2-14)$$

to find a simplified expression $(2-15)$ for the electric field by substituting $A_z(\rho)$ into equation $(2-2)$ and applying boundary conditions.

$$E^i(\rho) = \frac{\omega\mu}{4} \oint_{C'} J_z(\rho') H_0^{(2)}(\beta|\rho - \rho'|) dc' \qquad (2-15)$$

For a more detailed explanation, see Appendix B. Here *C'* is the radial cross section of the scattering antenna, ρ_m is an observation point, and ρ' is the source point variable.

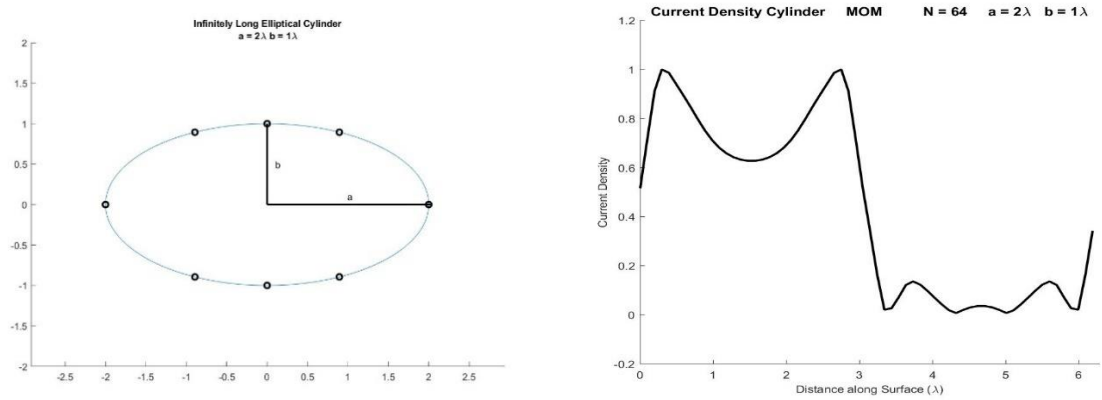

a) b)

Figure 2-5: a) Elliptical cylinder cross section with major axis $a = 2\lambda$, minor axis $b = 1\lambda$. The elliptical cylinder on the left shows 8 source/observation points. The source/observation points are indicated by o's, and are spaced at equal angles. b) Current distribution along an infinitely long elliptical cylinder discretized into 64 segments.

Shown in Figure 2-6 is an incident electromagnetic plane wave in the +Y direction passing through an infinitely long elliptical cylinder. The real and imaginary parts are shown separately to emphasize its oscillatory nature. Below the wave is a sketch of the elliptical cylinder cross section.

An electric field around a PEC object can be written as the sum of two waves, the incident electric field E^i and the scattered electric field E^s. Shown in Figure 2-7a is a surface plot of the magnitude of the electric field pattern of a TM^z plane wave incident on a conducting circular cylinder of infinite length, whose cross section is indicated by the dashed circle. The scattered near-field pattern of the radiated electric field is shown in Figure 2-7b. In Figure 2-7c calculation of the sum of the incident E^i and scattered E^S electric fields inside the cylinder.

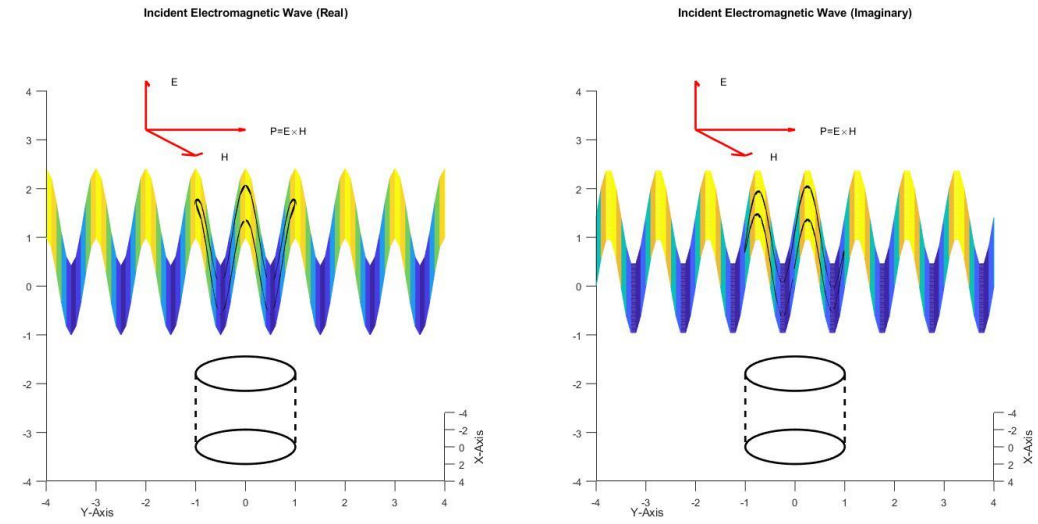

a) b)

Figure 2-6: a) Real part of a plane wave incident upon an infinitely long elliptical conducting cylinder. b) Imaginary part of an incident plane wave upon the same infinitely long elliptical conducting cylinder.

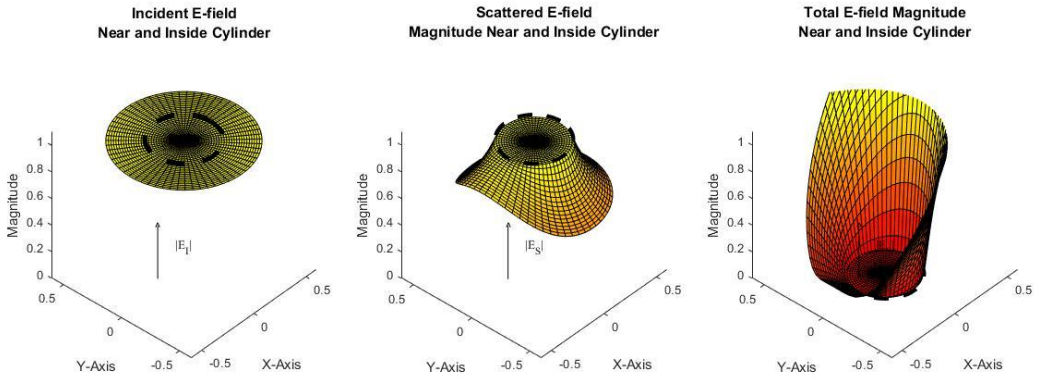

a) b) c)

Figure 2-7: a) Incident electric field near and inside a circular conducting cylinder. b) Scattered electric field due to induced current near and inside a circular conducting cylinder. c) Zero electric field predicted by the extinction principle.

As shown in Figure 2-7a, the magnitude of the calculated total electric field E_T inside the cylinder equals zero, i.e. $|E^T| = |E^i + E^s|$, where E^s is the scattered field due to the induced current and E^i is the incident electric field plane wave. This calculation is consistent with the extinction principle, i.e. the total electric field inside the cylinder must equal zero, shown in Figure 2-7b.

Illustrations of an infinitely long strip and infinitely long cylindrical structure subjected to a TM^z polarized wave are shown in Figure 2-8.

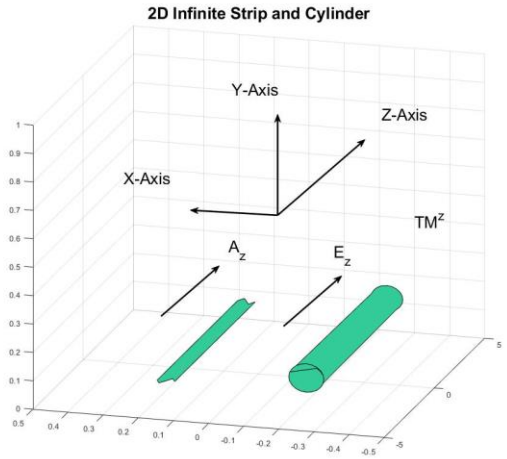

Figure 2-8: Infinitely long strip and infinitely long circular cylinder excited by TM^z incident wave.

The two-dimensional EFIE [36] for scattering of TM^z polarized waves from an infinitely long strip with normalized electric field, $E_0 = 1$, is given in equation $(2-16)$.

$$e^{j\beta x_m cos(\phi_i)} = \frac{\eta\beta}{4}\int_0^w J_z(x')H_0^{(2)}(\beta|x_m - x'|)dx' \qquad (2-16)$$

See Figure 2-9a for an illustration of incident angle and observation points on a strip from a TM^z polarized wave incident at angle ϕ_i. The strip is width w. The current distribution on a strip of width $w = .5\lambda$ is shown in Figure 2-10.

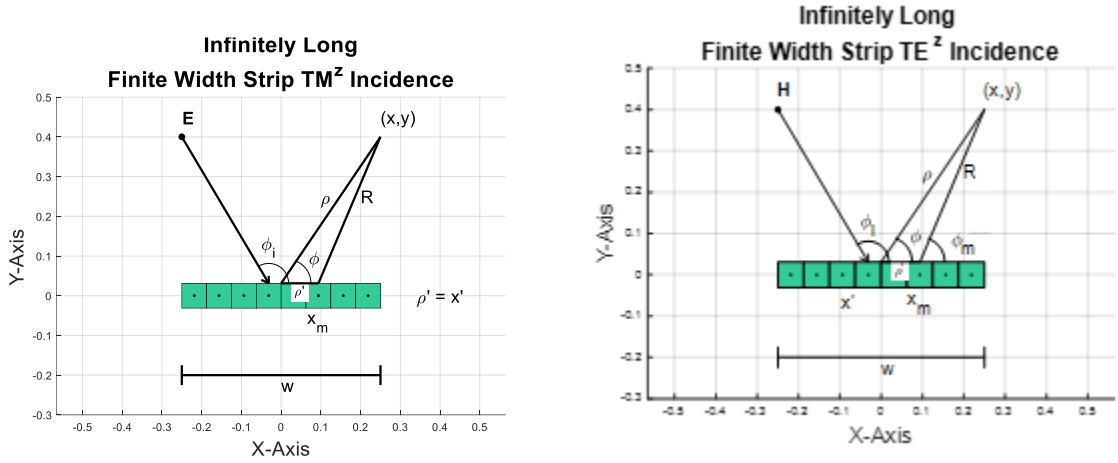

Figure 2-9: Finite width strips with incident a) TM^z polarized wave and b) TE^z polarized wave [36].

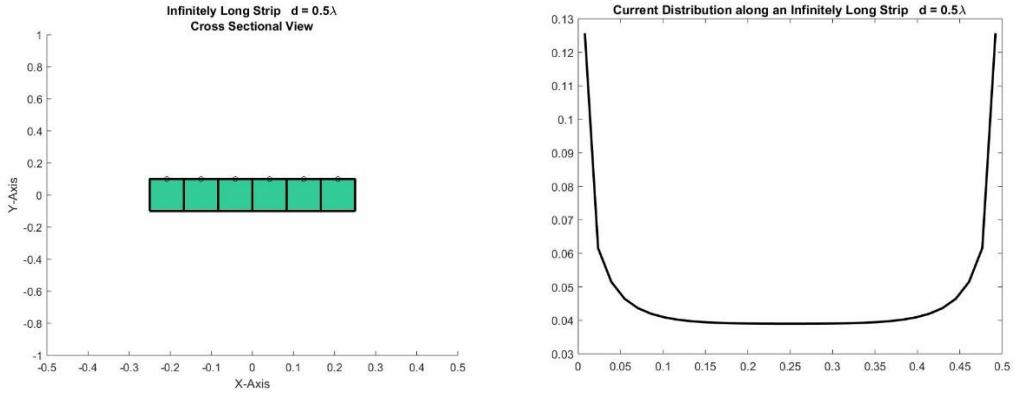

a) b)

Figure 2-10: a) An infinitely long strip divided into 6 segments with observation points on the top surface. b) Current distribution along the width of an infinitely long strip .5λ wide excited by TM^z wave.

The two-dimensional EFIE for scattering from infinitely long structures by TE^z polarized waves are sometimes derived from the three-dimensional EFIE [36]. The equation and its associated Green's function are given in equations $(2-17)$ and $(2-18)$.

$$-\boldsymbol{E}_C^i(\boldsymbol{\rho_m}) = \frac{\eta}{4\beta}\left[\beta^2 \iint_C \boldsymbol{J_C}(\boldsymbol{\rho}')[\hat{\boldsymbol{c}}_{\boldsymbol{m}} \cdot \hat{\boldsymbol{c}} G(|\boldsymbol{\rho_m}, \boldsymbol{\rho}'|)]dC' + \frac{d}{dC}\iint_C \boldsymbol{\nabla} \cdot \boldsymbol{J_C}(\boldsymbol{\rho}')\hat{\boldsymbol{c}}' G(|\boldsymbol{\rho_m}, \boldsymbol{\rho}'|)dC'\right]$$

$$(2-17)$$

$$G(|\boldsymbol{\rho_m}, \boldsymbol{\rho'}|) = H_0^{(2)}(\beta|\boldsymbol{\rho_m} - \boldsymbol{\rho'}|) \quad (2-18)$$

For the specific case of TE^z scattering from the surface of an infinitely long strip [36], the solution to equation $(2-17)$ is given in equation $(2-19)$.

$$sin(\phi_i)e^{j\beta x_m cos(\phi_i)} = \frac{\eta\beta}{8}\left[\int_0^w J_x(x')\left\{H_0^{(2)}(\beta|\rho_m - \rho'|) + H_2^{(2)}(\beta|\rho_m - \rho'|)cos(\phi_m)\right\}dx'\right] \quad (2-19)$$

The angles and points associated with equation $(2-19)$ is shown in Figure 2-9b. An example of a current distribution along an infinitely long conducting strip subject to an incident TE^z polarized wave is plotted in Figure 2-11.

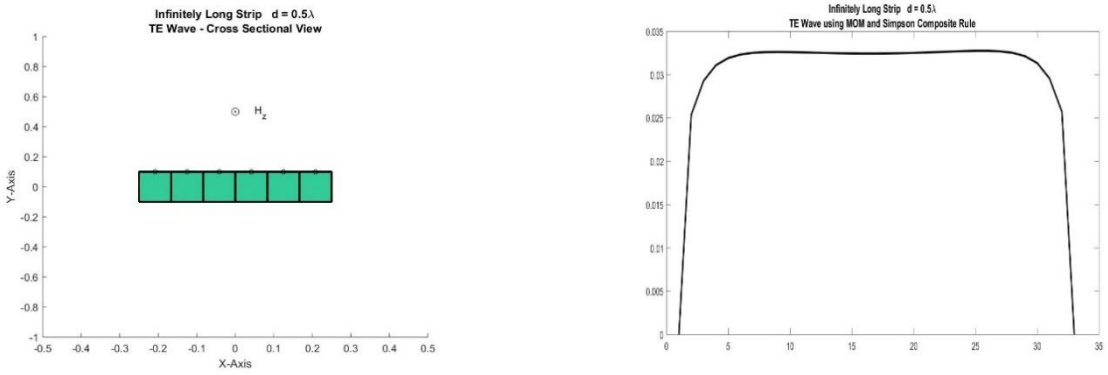

a) b)

Figure 2-11: a) Infinitely long strip divided into 6 segments with observation points on the top surface. b) Current distribution along an infinitely long strip .5λ wide excited by TE^z wave.

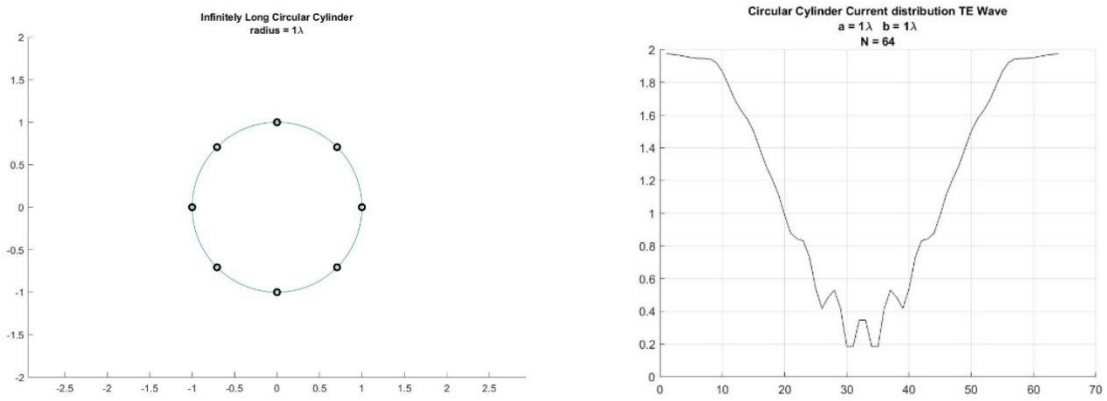

a) b)

Figure 2-12: a) Circular cylinder cross section with radius 1λ. The circular cylinder on the left shows 8 source/observation points. b) TE^z wave current distribution along an infinitely long circular cylinder discretized into 64 segments.

The two-dimensional MFIE for infinitely long cylindrical structures subject to plane waves with TE^z polarization is derived from the three-dimensional MFIE. It is shown in equation $(2-20)$. Integration is performed around a cross section of the surface along contour *C*.

$$-H_z^i(\rho)\Big|_C = J_C(\rho)\Big|_C + \frac{j\beta}{4}\lim_{\rho \to C}\int_C J_C(\rho')cos(\gamma)H_1^{(2)}(\beta|\rho_m - \rho'|)dc' \qquad (2-20)$$

The solution of the two-dimensional MFIE for TE^z scattering from the surface of an infinitely long cylinder along contour *C* is given in equation $(2-21)$.

$$-H_z^i(\rho) = \frac{J_C(\rho_m)}{2} + \frac{j\beta}{4}\int_{C-\Delta C} J_C(\rho')cos(\gamma)H_1^{(2)}(\beta|\rho_m - \rho'|)dc' \qquad (2-21)$$

Illustrations of a cylinder subject to an incident TE^z polarized wave and its current distribution is shown in Figure 2-12. The MFIE and is derivation are presented at the end of tis chapter.

2.5 Discretization of Objects into Elements and Coupling of Elements

In the procedure for MOM analysis, an infinite strip or cylinder is first divided into segments, inner products are taken, boundary conditions are applied, and finally induced fields are calculated from each segment element to itself (self-impedance term) and every other

element. An example of an infinite strip divided into 6 segments is shown below in Figure 2-13. Arrows between different elements represent coupling of fields between segments, the circle above a single element represents a self-coupling term. When the impedance matrix is formed, coupling between different elements results in mutual impedances, and the self-coupling term results in a self-impedance term.

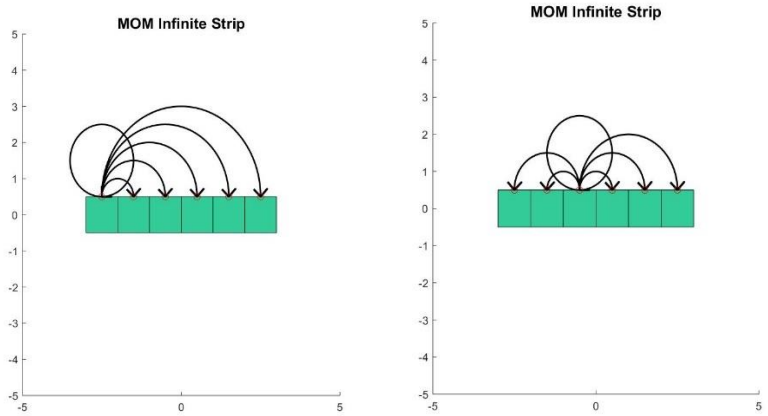

a) b)

Figure 2-13: Mutual coupling on an infinitely long conducting strip divided into six elements using the Method of Moments. a) Source is located at element one on the left. b) Source is located at element three near the center.

2.6 Subdomain Basis Functions

Once discretization is complete, the fields are calculated by representing the current sources on each segment by a subdomain basis function with amplitude α_n over domain D. The subdomain function is usually a real valued waveform over the segment, and zero over the rest of the object's domain.

$$J = \sum_{n=1}^{N-1} \alpha_n J_n \qquad (2-22)$$

The subdomain basis functions $J_m(x)$ and $J_n(x)$ are orthogonal in the following inner product space over the problem domain D. See equations $(2-23a)$ and $(2-23b)$.

$$\langle J_m(x), J_n(x) \rangle = \int_D J_m(x) J_n(x)\, dx \qquad if\ m = n \qquad (2-23a)$$

$$\langle J_m(x), J_n(x) \rangle = 0 \qquad if\ m \neq n \qquad (2-23b)$$

Shown in Figure 2-14 is an example of pulse basis functions over the domain D. Domain D is the interval [-.5,.5]. Note these basis functions are orthogonal and cover the entire domain. Subdomain basis functions are not necessarily orthogonal.

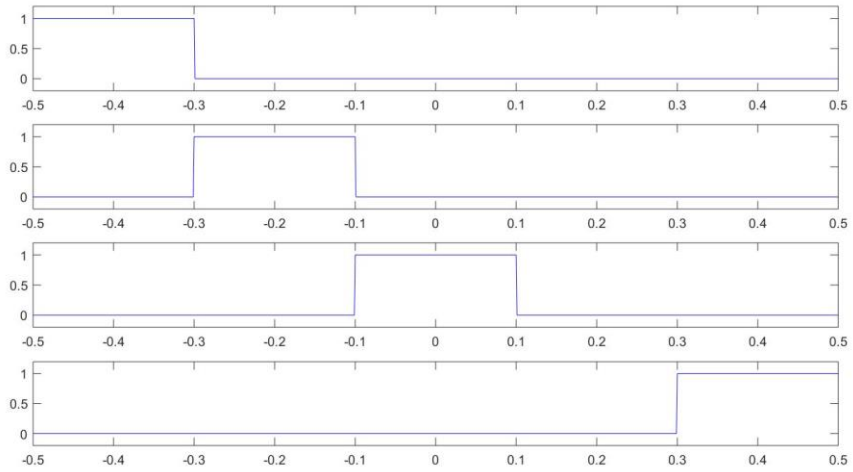

Figure 2-14: Pulse subdomain basis functions over domain D for a linear object subdivided into five segments.

Other types of basis functions are shown in Figure 2-15. These include the delta basis function (used for point matching at specific sets of coordinates), pulse basis function, sine basis functions, and triangle basis functions. Green's functions typically have a singularity that must be integrated in any MOM formulation. Various approaches have been used to calculate these values for different basis functions, including a commonly used approximation calculated by Harrington [8].

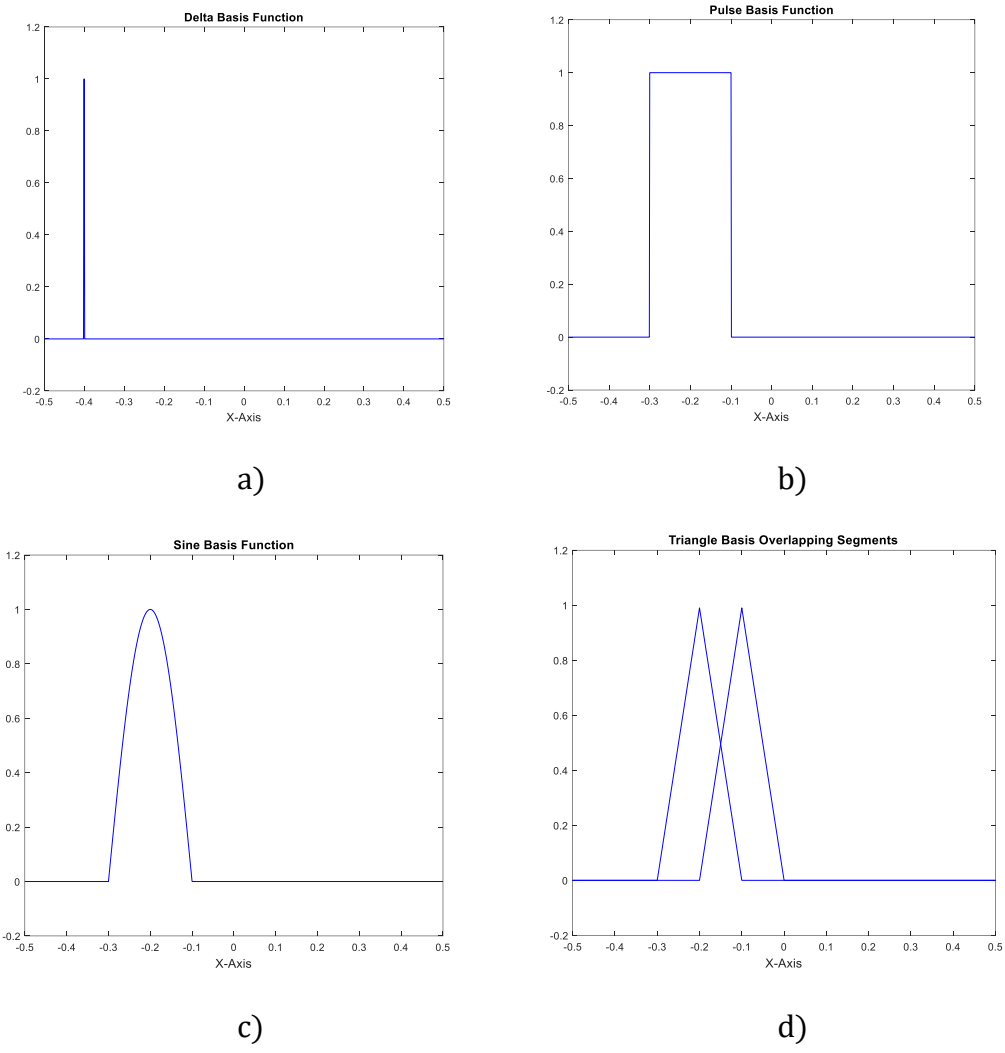

Figure 2-15: a) Delta basis function, b) pulse basis function, c) sine basis functions, and d) triangle basis functions.

2.7 Assembling the Impedance Matrix using Inner Products

The general method for solving an electromagnetic scattering problem is to define the linear operator, L, below in equation $(2-24)$.

$$LJ = \int_V GJdV \qquad (2-24)$$

In equation $(2-21)$, J is the current density, and G is the Green's function. One may also consider this operation as an inner product shown in equation $(2-25)$.

$$\langle G, J\rangle = \int_V GJdV \tag{2-25}$$

The linear integral operator may be applied to a set of subdomain basis functions, i.e. equation $(2-26)$,

$$J = \sum_{n=1}^{N} \alpha_n J_n \tag{2-26}$$

to obtain the expression in equation $(2-27)$. Equation $(2-27)$ is a general solution to an electromagnetic scattering problem using the MOM technique.

$$LJ = \sum_{n=1}^{N} \alpha_n LJ_n \cong E \tag{2-27}$$

To enforce the boundary conditions at the testing or observation points (or the testing intervals), $j \in \{1,2,\dots,N\}$, one takes the inner product of both sides of equation $(2-27)$ with weighting functions. For one-dimensional problems, these weighting functions are often are delta functions $w_j = \delta(x - x_j)$ for measurements made at specific points on the object, or pulse basis functions over intervals of the object $w_j = p(x_{j,j+1})$.

$$\sum_{i=1}^{N} \alpha_i < LJ_i, w_j >= < E, w_j > \tag{2-28}$$

The inner product of each integral operator L over a subdomain with the weighting function w_j, and the inner product of each weighting function w_j with the electric field E_j is entered into a matrix.

$$\begin{bmatrix} < LJ_1, w_1 > & < LJ_2, w_1 > & \cdots & \cdots & < LJ_N, w_1 > \\ < LJ_1, w_2 > & < LJ_2, w_2 > & \cdots & \cdots & \cdots \\ \cdots & \cdots & < LJ_i, w_j > & \cdots & \cdots \\ \cdots & \cdots & \cdots & \cdots & \cdots \\ < LJ_1, w_N > & \cdots & \cdots & \cdots & < LJ_N, w_N > \end{bmatrix} \begin{bmatrix} \alpha_1 \\ \alpha_2 \\ \vdots \\ \vdots \\ \alpha_N \end{bmatrix} = \begin{bmatrix} < E_1, w_1 > \\ < E_2, w_2 > \\ < E_j, w_j > \\ \vdots \\ < E_n, w_N > \end{bmatrix} \tag{2-29}$$

The next step is calculating the terms of the square impedance matrix with the number of elements in each row corresponding to the impedance of each self-impedance term $Z_{m,m}$ and induced-impedance term $Z_{m,n}$.

$$\begin{bmatrix} Z_{11} & Z_{12} & \cdots & \cdots & Z_{1n} \\ Z_{21} & Z_{22} & \cdots & \cdots & \cdots \\ \cdots & \cdots & Z_{mn} & \cdots & \cdots \\ \cdots & \cdots & \cdots & \cdots & \cdots \\ Z_{n1} & \cdots & \cdots & \cdots & Z_{NN} \end{bmatrix} \begin{bmatrix} \alpha_1 \\ \alpha_2 \\ \vdots \\ \vdots \\ \alpha_N \end{bmatrix} = \begin{bmatrix} e_1 \\ e_2 \\ \vdots \\ \vdots \\ e_N \end{bmatrix} \qquad (2-30)$$

Figure 2-16 shows the relationship between coupling terms and elements using MOM analysis.

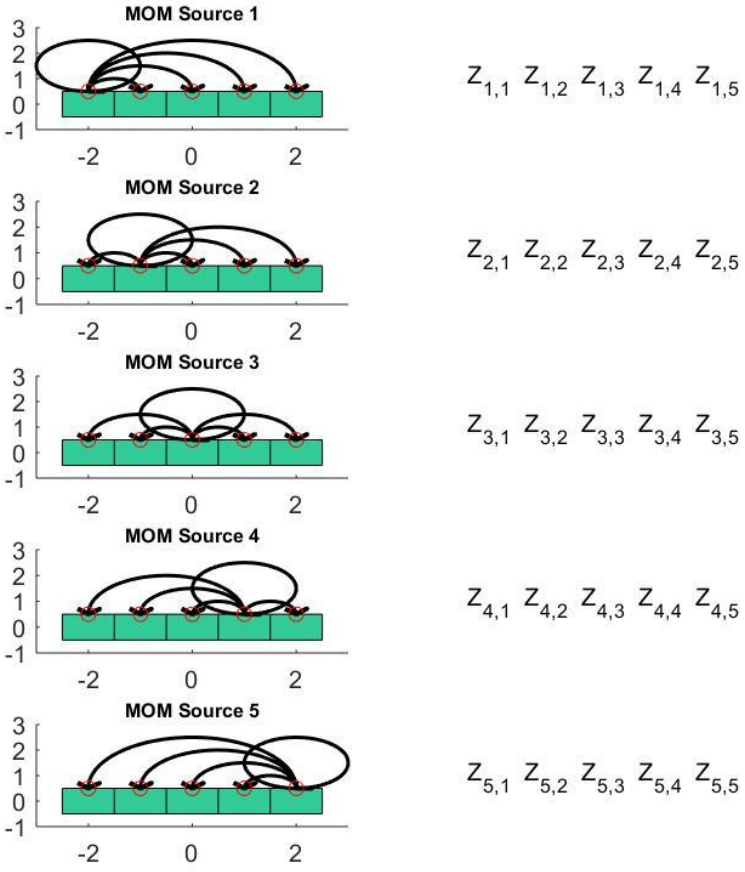

Figure 2-16: Mutual coupling between elements using the Method of Moments and their corresponding impedances.

The complete integral equation for a single source (s'), to observation point (s), on a surface S' is given in equation $(2-31)$. The source or basis function are $b_n(s')$, the testing or observation function are $t_m(s)$, and the Green's function is $G(\beta|s-s'|)$.

$$Z_{m,n} = \frac{\beta Z_0}{4} \int_S t_m(s) \int_{S'} G(\beta|s-s'|)\, b_n(s') dS' dS \qquad (2-31)$$

Note that the testing functions are projected onto electric field and onto the subspace of inner products of the Green's function and basis functions.

2.8 Whole Domain Basis Functions

Basis functions need not always be subdomain, but may also be whole domain. See Figure 2-17. A common type of whole domain function is the sinusoid.

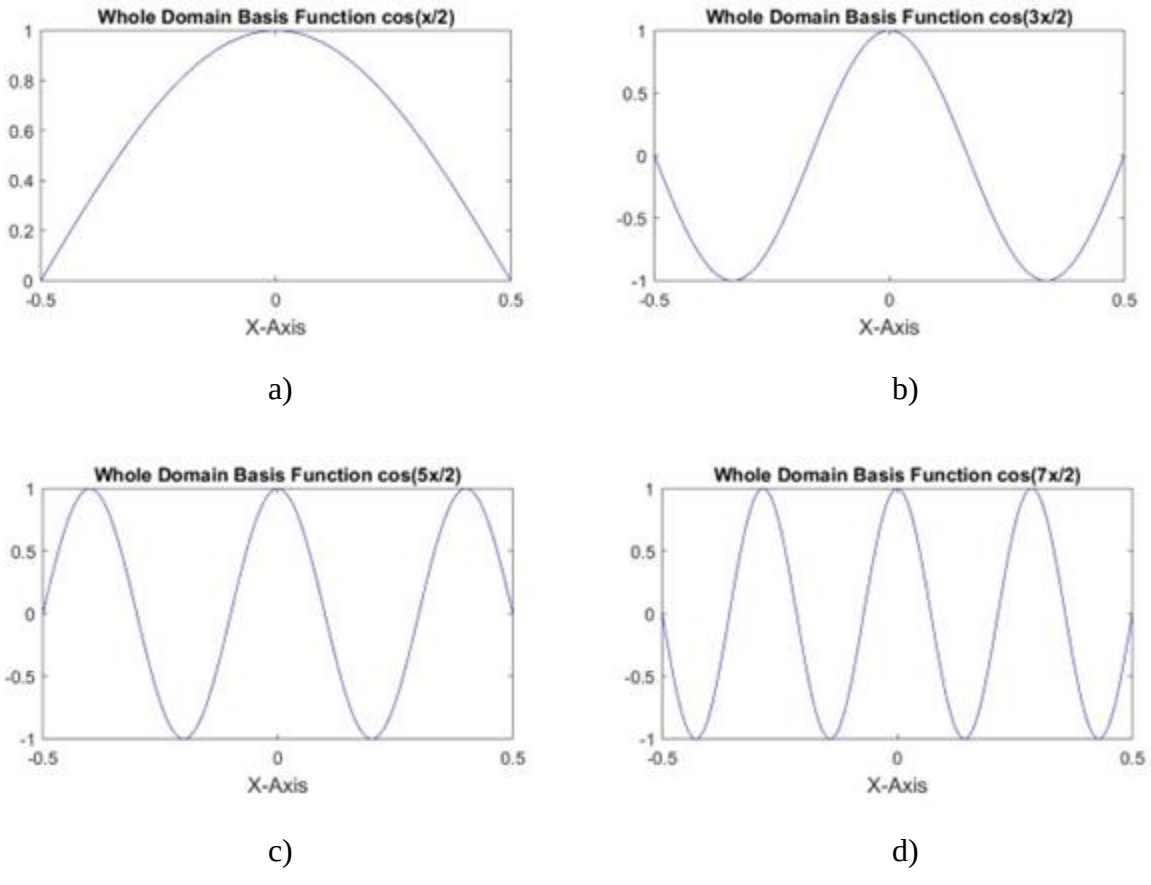

Figure 2-17: Examples of four types of whole domain basis functions: a) cos(x/2), b) cos(3x/2), c) cos(5x/2), and d) cos(7x/2).

The sum of the basis functions approximates the current distribution. The current distribution of the object is usually calculated by inverting the impedance matrix, and the far-field pattern can be calculated from the current distribution [40]. Iterative methods have also been developed to solve for the current distribution without inverting the matrix. One of these techniques, the conjugate gradient method (CG), has gained importance in this field. See Appendix G on the conjugate gradient.

2.9 Two-Dimensional Solutions for Flat Objects

The Method of Moments is not restricted to one-dimensional objects and infinitely long two-dimensional objects. More general shapes of two and three-dimensional objects may also be analyzed. An example of a finite length two-dimensional object is shown in Figure 2-17, a conductive plate.

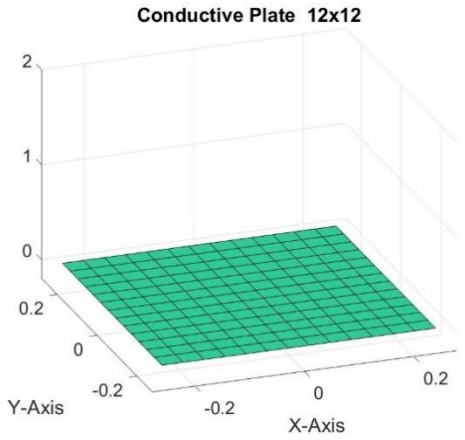

Figure 2-18: Illustration of a discretized $1\lambda \times 1\lambda$ conductive plate *12x12* square segments.

To solve the two-dimensional conductive plate problem, the MOM implemented basis functions such as 2D pulse and rooftop functions initially. RWG basis functions are triangular in shape and are much more versatile for calculating electromagnetic scattering from asymmetrical and three-dimensional objects. They are used extensively to model EM scattering from aircraft and ships because the triangular shape adapts well to three-dimensional geometries [41].

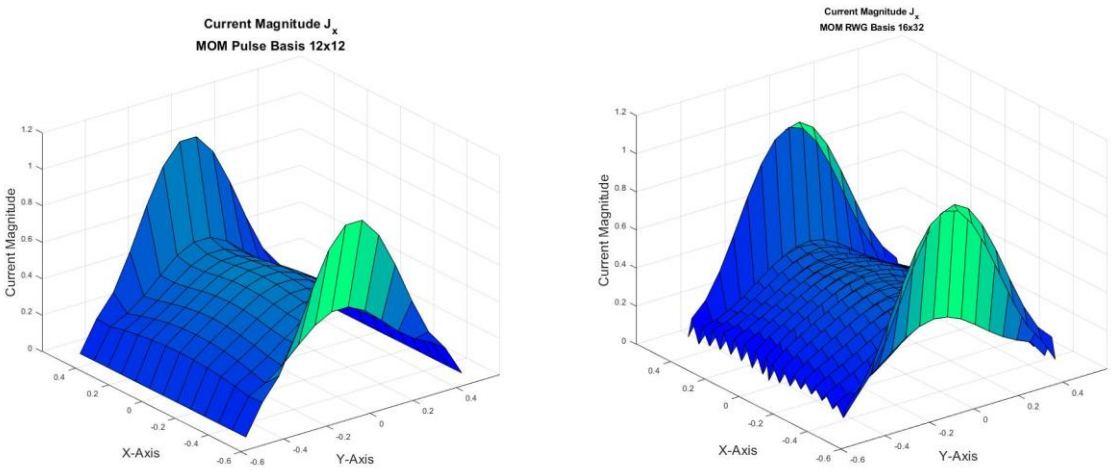

b) c)

Figure 2-19: a) Current distribution J_x on the conductive plate using the Method of Moments pulse basis functions. b) Current distribution J_x on the conductive plate using the Method of Moments RWG basis functions.

2.10 TM^z Incidence on Infinitely Long Cylinders using the EFIE

To calculate the current distribution on infinitely long PEC cylinders, one begins with equations in the spatial domain. Starting with the magnetic vector potential, $A_z(\rho)$, and the spherical Hankel function $h_0^{(2)}(R) = \frac{e^{-j\beta R}}{R}$, one utilizes the symmetry to evaluate the integrand over its infinite limits in the Z-direction of polarization [36]. Beginning with equation $(2-32)$ and integrating along the Z-direction in equation $(2-34)$, the new integral equation and Green's function are shown in equations $(2-35)$ and $(2-36)$.

$$A_z(\rho) = \frac{\mu}{4\pi}\iint_S J_z(\rho')h_0^{(2)}(\beta R)dS' \qquad (2-32)$$

$$R = \sqrt{|\rho-\rho'|^2 + (z-z')^2} \qquad (2-33)$$

$$A_z(\rho) = \frac{\mu}{4\pi}\int_L J_z(\rho')\int_{-\infty}^{\infty}\left[\frac{e^{-j\beta\sqrt{|\rho-\rho'|^2+(z-z')^2}}}{\sqrt{|\rho-\rho'|^2+(z-z')^2}}dz'\right]d\rho' \qquad (2-34)$$

$$A_z(\rho) = -j\frac{\mu}{4}\iint_S J_z(\rho')'H_0{}^{(2)}\left(\beta|\rho-\rho'|\right)d\rho' \qquad (2-35)$$

$$G(\rho,\rho') = H_0^{(2)}\left(\beta\left|\rho-\rho'\right|\right) \qquad (2-36)$$

2.11 TE^z Incidence on Infinitely Long Cylinders using the MFIE

In this section the Magnetic Field Integral Equation (MFIE) is derived by subjecting a PEC object to a TE^z wave. When the PEC object is subjected to an external stimulus like a TE^z wave, currents are induced on the surface of the conductor. Let vectors $\boldsymbol{H^i}$ and $\boldsymbol{H^s}$ be incident and scattered magnetic field intensities, respectively. At the surface of the cylinder, the induced current density, $\boldsymbol{J_s}$, is equal to the discontinuity in the tangential component of the magnetic field.

$$\boldsymbol{J_S} = \hat{\boldsymbol{n}} \times (\boldsymbol{H^i} + \boldsymbol{H^s}) \qquad at\ boundary \qquad (2-37)$$

Boundary conditions for a transverse magnetic TE^z wave are shown in Figure 5-8. The incident magnetic field, $\boldsymbol{H^i} = H_z^i\hat{\boldsymbol{z}}$, is parallel to the cylinder axis for TE^z plane waves, as is the scattered magnetic field $\boldsymbol{H^s} = H_z^s\hat{\boldsymbol{z}}$.

To calculate the scattered magnetic field for TE^z incidence [21], one begins with a differential magnetic vector potential at an observation point (x, y, z) from a current element source oriented in the $\boldsymbol{l}$ direction at source location (x', y', z') is given in equation $(2-38)$.

$$\boldsymbol{dA} = h_0^{(2)}(\beta|\boldsymbol{R}|)I\boldsymbol{dl} \qquad (2-38)$$

$$R = \sqrt{(x-x') + (y-y') + (z-z')} \qquad (2-39)$$

For an induced differential current element of length $\boldsymbol{dl}$ on the surface of an infinitely long cylinder excited by an incident TE wave, the appropriate Green's function is $H_0^{(2)}(\beta|\boldsymbol{R}|)$. The magnetic vector potential may be written as $(2-40)$. See Figure 2-20.

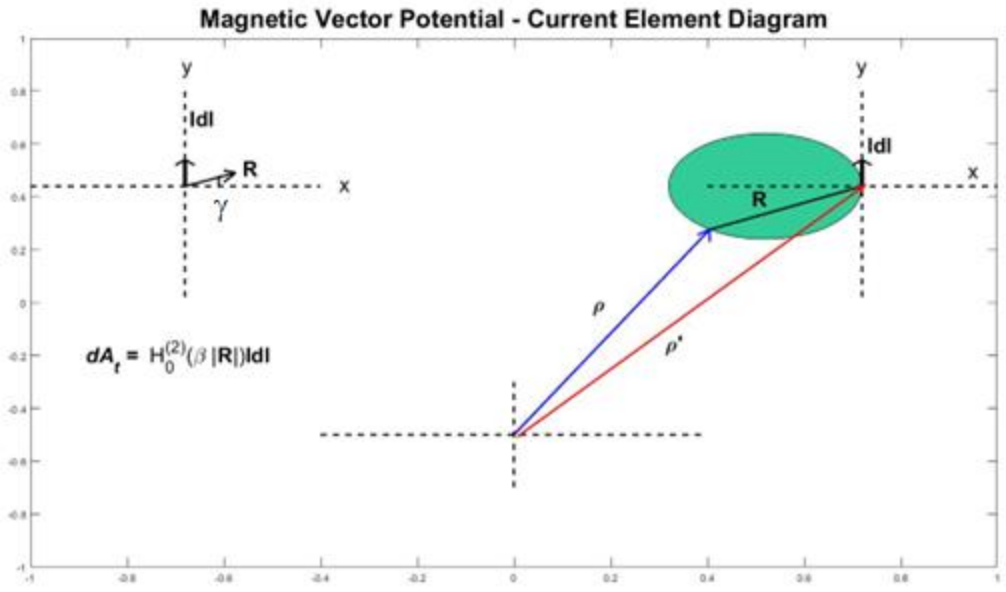

Figure 2-20: Illustration of magnetic vector potential with an incremental current contribution along an incremental length [21].

$$\boldsymbol{dA_t} = H_0{}^{(2)}(\beta|\boldsymbol{R}|)I\boldsymbol{dl} \qquad (2-40)$$

In this case, the differential current element $I\boldsymbol{dl}$ and resulting magnetic vector potential $\boldsymbol{dA_t}$ are both in the Y-direction, and tangent to the cylinder surface. The normal vector to the surface is in the X-direction. For this illustration of an incident TE^z plane wave, the plane of incidence is the X-Y plane, and the resulting magnetic field may be calculated using the relation given in equation given in $(2-41)$.

$$\boldsymbol{H_z} = \frac{1}{\mu}\nabla \times \boldsymbol{A_t} \qquad (2-41)$$

The term $\boldsymbol{H_z}$ is the Z-component of the magnetic field, calculated from the tangential component of the magnetic vector potential.

The differential magnetic field may be written as equation $(2-42)$. See reference [21].

$$\boldsymbol{dH_z} = \frac{1}{\mu}\nabla \times \boldsymbol{dA_t} \qquad (2-42)$$

Expanding using the curl operator in rectangular coordinates,

$$\nabla \times \boldsymbol{A} = \hat{\boldsymbol{x}}\left(\frac{\partial A_z}{\partial y} - \frac{\partial A_y}{\partial z}\right) + \hat{\boldsymbol{y}}\left(\frac{\partial A_x}{\partial z} - \frac{\partial A_z}{\partial x}\right) + \hat{\boldsymbol{z}}\left(\frac{\partial A_y}{\partial x} - \frac{\partial A_x}{\partial y}\right) \qquad (2-43)$$

and defining

$$\boldsymbol{dA_t} = dA_x\hat{\boldsymbol{x}} + dA_y\hat{\boldsymbol{y}} \qquad (2-44)$$

equation $(2-42)$ may be expanded into equation $(2-45)$.

$$dH_z = \frac{1}{\mu}\left(\frac{\partial A_y}{\partial x} - \frac{\partial A_x}{\partial y}\right) \qquad (2-45)$$

If the differential current element is aligned with the Y-axis and the normal vector with the X-axis, then $dA_x = 0$, and

$$dA_y = \frac{\mu}{4j}H_0^{(2)}(\beta|\boldsymbol{R}|)Idl \qquad (2-46)$$

with the variable R now in two dimensions.

$$R = \sqrt{(x-x') + (y-y')} \qquad (2-47)$$

Applying differentiation, equation $(2-45)$ may be written as $(2-48)$.

$$dH_z = \frac{1}{4j}H_0^{(2)\prime}(\beta|\boldsymbol{R}|)Idl \qquad (2-48)$$

where the prime indicates the partial derivative with respect to x.

After taking the partial derivative, equation $(2-48)$ is then written as

$$dH_z = \frac{\beta Idl}{4j}H_1^{(2)}(\beta|\boldsymbol{R}|)\frac{dR}{dx} \qquad (2-49)$$

with

$$\frac{dR}{dx} = \frac{x}{R} \qquad (2-50)$$

$$\frac{dR}{dx} = cos(\gamma) \qquad (2-51)$$

This results in the differential expression given in equation $(2-52)$,

$$dH_z = \frac{\beta Idl}{4j}H_1^{(2)}(\beta|\boldsymbol{R}|)cos(\gamma) \qquad (2-52)$$

and angle γ is the angle between normal vector $\hat{\boldsymbol{n}}$ and the $\boldsymbol{R}$ vector. The normal vector $\hat{\boldsymbol{n}}$ is aligned with the X-axis in Figure 2-20.

Now one can change to cylindrical coordinates, with $\boldsymbol{\rho}$ being the observation point vector and $\boldsymbol{\rho}'$ being the source point vector,

$$\boldsymbol{R} = \boldsymbol{\rho} - \boldsymbol{\rho}' \qquad (2-53)$$

For an observation point ρ_m, and current element dc' along contour C (instead of dl), one can integrate and find the scattered magnetic field along the contour of the cylinder.

$$H_z^s(\rho_m) = \frac{j\beta}{4}\int_C J_C(\rho')cos(\gamma)H_1^{(2)}(\beta|\boldsymbol{\rho_m} - \boldsymbol{\rho'}|)dc' \qquad (2-54)$$

Thus, substituting into equation $(2-54)$, the MFIE for TE^z waves at observation point ρ_m can now be written as $(2-55)$. See Chapter 5 and Appendix B for illustrations of angles.

$$H_z^i(\rho_m) = \frac{J_C(\rho_m)}{2} + \frac{j\beta}{4}\int_{C-\Delta C} J_C(\rho')cos(\gamma)H_1^{(2)}(\beta|\boldsymbol{\rho_m} - \boldsymbol{\rho'}|)dc' \qquad (2-55)$$

Table 2-2: EFIE and MFIE for TM^z and TE^z Waves [36].

Transverse Magnetic Waves (TM^z) for 2D Scattering	
$E_z^i(\rho) = \frac{\beta\eta}{4}\oint_C J_z(\rho')H_0^{(2)}(\beta R)dc$	$EFIE$
$H_C^i(\rho)\Big\|_C = J_z(\rho)\Big\|_C + \frac{j\beta}{4}\lim_{\rho\to C}\left(\int_{C-\Delta C} J_z(\rho')cos(\gamma)H_1^{(2)}(\beta R)dc'\right)$	$MFIE$
Transverse Electric Waves (TE^z) for 2D Scattering	
$-E_c^i(\rho) = \frac{\eta}{4\beta}\left\{\beta^2\oint_C J_c(\rho')\left[\hat{c}\cdot\hat{c}'H_0^{(2)}(\beta R)\right]dc' + \frac{d}{dc}\left[\nabla\cdot\oint_C J_c(\rho')\left[\hat{c}H_0^{(2)}(\beta R)\right]dc'\right]\right\}$	$EFIE$
$-H_z^i(\rho) = H_z^i(\rho_m) = \frac{J_C(\rho_m)}{2} + \frac{j\beta}{4}\int_{C-\Delta C} J_C(\rho')cos(\gamma)H_1^{(2)}(\beta\|\rho_m - \rho'\|)dc'$	$MFIE$

Chapter 3: Fast Multipole Method

3.1 Comparison of the Method of Moments and Fast Multipole Method

The fast multipole method (FMM) is a hybrid approach used in computational electromagnetics based on the Method of Moments and the addition theorem [27]. It's main advantage over the MOM is that it speeds up populating the terms of the impedance matrix for large systems. The Method of Moments approach requires each current element of the scattering object to act as a source upon itself and every other current element. The current elements of the scattering object that act as a source upon themselves are called the self-impedance terms $Z_{m,m}$, and those that act on other elements are called mutual-impedance terms $Z_{m,n}$. See the Figure 2-12. The self-impedance terms occur along the main diagonal of the impedance matrix, and the mutual impedance terms are the off-diagonal elements.

For an infinitely long cylinder, the regions over which the source (basis) functions and testing (observation) functions are defined are P′ and P, respectively. For the surface shown in Figure 3-1, the source and testing function regions are defined along the same contour, P = P'.

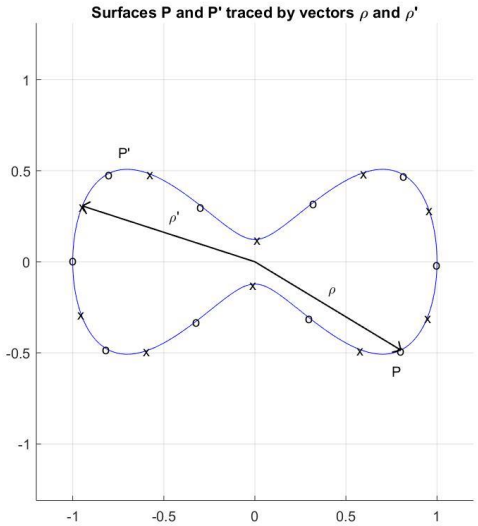

Figure 3-1: Cross-sectional view of a symmetrically shaped infinitely long cylinder with source points *x* and observation points *o*. A single source vector, ρ', and observation vector, ρ, are illustrated.

The impedance matrix for FMM analysis shares many similarities to MOM. For electric field incidence, the EFIE is used to calculate the terms of the impedance matrix (Chapter 2). For an infinitely long perfectly conducting cylinder, the FMM terms of the impedance matrix are given as equation $(3-1)$. The basis and testing functions are $b_n(\rho')$ and $t_m(\rho)$, respectively [27].

$$Z_{m,n} = \frac{\beta Z_0}{4} \int_{\mathrm{P}} t_m(\rho) \int_{\mathrm{P}'} H_0^{(2)}(\beta|\boldsymbol{\rho} - \boldsymbol{\rho}'|)\, b_n(\rho')\mathrm{dP}'\mathrm{dP} \qquad (3-1)$$

Except for the self-impedance term, point matching is used for both the basis functions and testing functions and are delta functions, i.e. $b_n(\rho') = \delta(\rho' - \rho_n{}')$ and $t_m(\rho) = \delta(\rho' - \rho_m{}')$.

$$Z_{m,n} = \frac{\beta Z_0 \Delta s}{4} H_0^{(2)}(\beta|\boldsymbol{\rho} - \boldsymbol{\rho}'|) \qquad (3-2)$$

For the self-impedance term, $n = m$ in which $\rho - p' = 0$, the integral expression in equation $(3-1)$ must be evaluated. The well-known approximation given by Harrington [17] is employed.

$$Z_{m,m} = \frac{\beta Z_0 \Delta s}{4}\left[1 - \frac{2j}{\pi}\left(\frac{\beta\gamma'\Delta s}{4e}\right)\right] \qquad (3-3)$$

The term $\gamma' = 2.7183$ is Euler's constant, and Δs is the arc length.

3.2 Fast Multipole Method and the Addition Theorem

The Fast Multipole Method is a computational electromagnetic technique that groups discrete points on the surface of an object and their basis functions to calculate the radiated fields of an object. Basis functions for source points are first grouped together and their collective contributions are calculated at the center of their group. This aggregate contribution is used to represent a radiated wave from the center of the group to the center of an observation group that is not a nearby neighbor. The field at the center of the observation group is then distributed to the points in the observation group.

The Fast Multipole Method decomposes the impedance integral using the addition theorem, or sometimes called the summation theorem. Then the impedance matrix is calculated as groups of sources and groups of test points. To understand the addition theorem, begin with

the law of cosines given in equation$(3-4)$ and the scalene triangle shown below in Figure 3-2 [29].

$$R = \sqrt{\rho^2 + (\rho')^2 - 2\rho\rho' cos(\phi_R)} \qquad (3-4)$$

The sides and angles of the scalene triangle in Figure 3-2 can be associated with the arguments R, ρ, and ρ' of the summation theorem for Bessel functions [27]. The angles $\phi_\rho, \phi_{\rho'}$ and ϕ_R correspond to the phase term arguments of the summation theorem.

$$e^{jm\phi_R} H_m(\beta R) = \sum_{k=-\infty}^{\infty} J_k(\beta\rho') H_{m+k}(\beta\rho) e^{jk\phi_R} \qquad (3-5)$$

The arguments $\rho, \rho',\ \phi_R$ have conditions given in $(3-6)$ and $(3-7)$.

$$\rho > \rho' \qquad (3-6)$$

$$0 < \phi_R < \frac{\pi}{2} \ \ and \ \ e^{2j\phi_R} = \frac{\rho - \rho' e^{-j\phi_R}}{\rho - \rho' e^{j\phi_R}} \qquad (3-7)$$

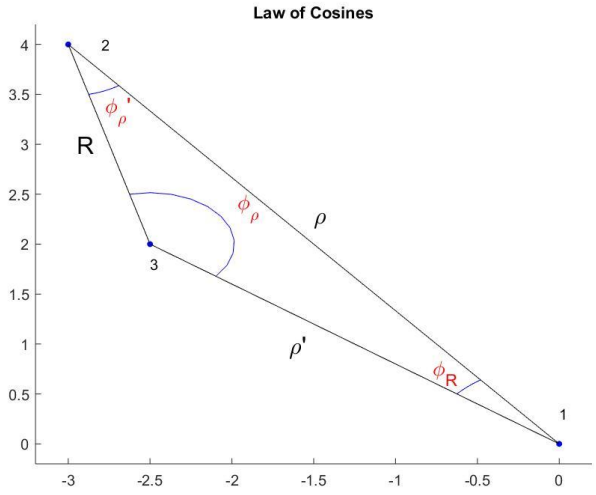

Figure 3-2: Scalene triangle and sides associated with the addition theorem.

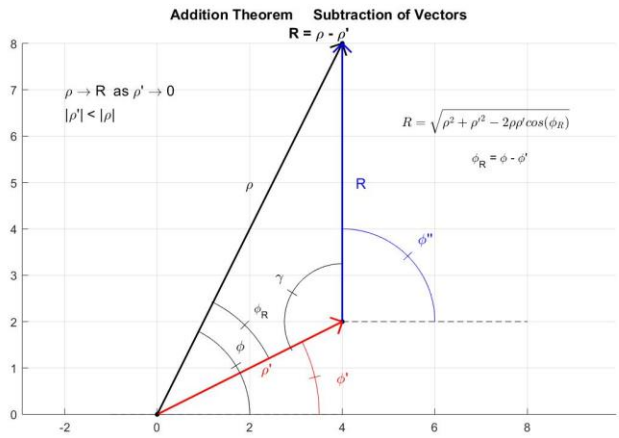

Figure 3-3: Addition theorem expansion for Hankel function $H_0^{(2)}(\beta|\boldsymbol{\rho}-\boldsymbol{\rho}'|)$.

If the addition theorem equation is written for the zeroth order Hankel function of the second kind, $m = 0$, it takes two forms shown in equations $(3-8)$ and $(3-9)$.

$$H_0^{(2)}(\beta|\boldsymbol{\rho}-\boldsymbol{\rho}'|) = \sum_{k=-\infty}^{\infty} J_k(\beta\rho)H_k^{(2)}(\beta\rho')e^{jk(\phi-\phi')} \qquad \rho < \rho' \qquad (3-8)$$

$$H_0^{(2)}(\beta|\boldsymbol{\rho}-\boldsymbol{\rho}'|) = \sum_{n=-\infty}^{\infty} J_k(\beta\rho')H_k^{(2)}(\beta\rho)e^{jk(\phi'-\phi)} \qquad \rho' < \rho \qquad (3-9)$$

Figure 3-3 illustrates the addition theorem vectors and corresponding angles $\rho,\ \rho', \phi,$ and ϕ' for $H_0^{(2)}(\beta|\boldsymbol{\rho}-\boldsymbol{\rho}'|)$ given in equations $(3-8)$ and $(3-9)$.

3.3 Fast Multipole Method Grouping of Sources and Observation Points

The best way to explain the FMM is through an example. Start with an infinitely long PEC cylinder with 24 source/observations points. For the circular cylinder illustrated in Figure 3-4, the sources and observation points are grouped together in sets of four. See Table 3-1.

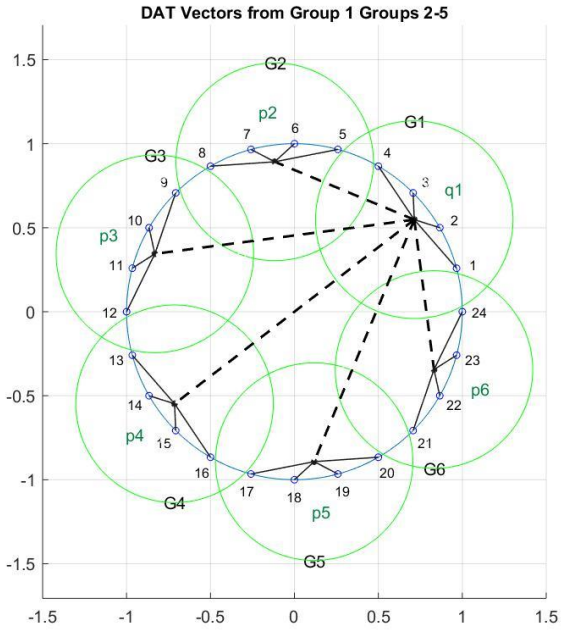

Figure 3-4: Example of infinitely long circular cylinder with 24 source/observation points with groupings of 4 points.

In this FMM example, groups G1 through G6 are rotated as the source groups one at a time acting on the remaining groups which become observation point groups. Points in the source groups are *q's* and observation groups *p's*.

Table 3-1: Groupings of Sources and Observation Points on Figure 3-4.

Group	Points
G1	1,2,3,4
G2	5,6,7,8
G3	9,10,11,12
G4	13,14,15,16
G5	17,18,19,20
G6	21,22,23,24

In Figure 3-4, G1 is the source group and G2 to G6 are the observation groups. The center of the source group is designated q1, and the centers of the observation groups are p2 to p6. Points 1-4 along the circle are the location of the source elements, and points 5 – 24 are the location of the testing or observation points.

3.4 Governing Equations for Fast Multipole Method

The FMM process is often referred to as Aggregation, Translation, and Disaggregation, or ATD for short. It calculates the fields by starting from a group of vectors aggregated to a common center q (Aggregation Matrix), then translated to a new center point distant from the aggregation center p (Translation Matrix), and then disaggregated from the new center to a new group of current elements (Disaggregation Matrix). Once again refer to Figure 3-4. The source vectors in group G1 are aggregated to the center q1 of group G1, then translated from q1 to centers of the target groups G2 to G6, and lastly the vectors are disaggregated from the centers of groups G2 through G6 to the observation points of these target groups.

The Hankel function is written as a sum using the addition theorem and is shown in equation $(3-10)$. This equals equation $(3-9)$, with (ρ', ϕ') replaced by $(de^{j\pi}, \phi_d)$.

$$H_0^{(2)}(\beta|\boldsymbol{\rho}+\boldsymbol{d}|) = \frac{1}{2\pi}\sum_{k=-\infty}^{\infty} J_k(\beta d)H_k^{(2)}(\beta\rho)\, e^{jk(\phi-\phi_d-\pi)} \qquad |\boldsymbol{\rho}| > |\boldsymbol{d}| \qquad (3-10)$$

Bessel's definition of $J_k(\rho)$ is given in equation $(3-11)$.

$$J_k(\rho) = \frac{1}{2\pi}\int_0^{2\pi} cos(k\theta - \rho sin\theta)d\theta \qquad (3-11)$$

Using the appropriate trigonometric identities, equation $(3-11)$ can be transformed into equation $(3-12)$. See the Appendix E Fast Multipole Method for detailed derivation. Equation $(3-12)$ is in the form of a Fourier transform.

$$J_k(\beta d)e^{-jk(\phi_d+\pi)} = \frac{1}{2\pi}\int_0^{2\pi} e^{-j\boldsymbol{\beta}\cdot\mathbf{d}-jk(\alpha+\pi/2)}\, d\alpha \qquad (3-12)$$

Substituting equation $(3-12)$into equation $(3-10)$, a new expression for the Hankel function $H_0^{(2)}(\beta|\boldsymbol{\rho}+\boldsymbol{d}|)$ is given below:

$$H_0^{(2)}(\beta|\boldsymbol{\rho}+\boldsymbol{d}|) = \frac{1}{2\pi}\sum_{k=-\infty}^{\infty} H_k^{(2)}(\beta\rho)\, e^{jk\phi}\int_0^{2\pi} e^{-j\boldsymbol{\beta}\cdot\mathbf{d}-jk(\alpha+\pi/2)}\, d\alpha \qquad \rho > d \qquad (3-13)$$

with the corresponding vectors defined by equations $(3-14)$ to $(3-18)$

$$\boldsymbol{\beta} = \beta\left(\hat{\boldsymbol{x}}cos(\alpha) + \hat{\boldsymbol{y}}sin(\alpha)\right) \quad (3-14)$$

$$\mathbf{d} = \left(\boldsymbol{\rho} - \boldsymbol{\rho_p}\right) + \left(\boldsymbol{\rho_q} - \boldsymbol{\rho}'\right) \quad (3-15)$$

$$\boldsymbol{\rho} - \boldsymbol{\rho}' = \left(\boldsymbol{\rho} - \boldsymbol{\rho_p}\right) + \boldsymbol{\rho_{pq}} + \left(\boldsymbol{\rho_q} - \boldsymbol{\rho}'\right) \quad (3-16)$$

$$\boldsymbol{\rho} - \boldsymbol{\rho_p} = \left|\boldsymbol{\rho} - \boldsymbol{\rho_p}\right|\angle\phi_{p,m} \quad (3-17)$$

$$\boldsymbol{\rho_q} - \boldsymbol{\rho}' = \left|\boldsymbol{\rho_q} - \boldsymbol{\rho}'\right|\angle\phi_{n,q} \quad (3-18)$$

For the example started above, with source group G1 and observation group G3, Figures 3-5a and Figure 3-5b illustrate the angles and vectors used in solving the example FMM problem.

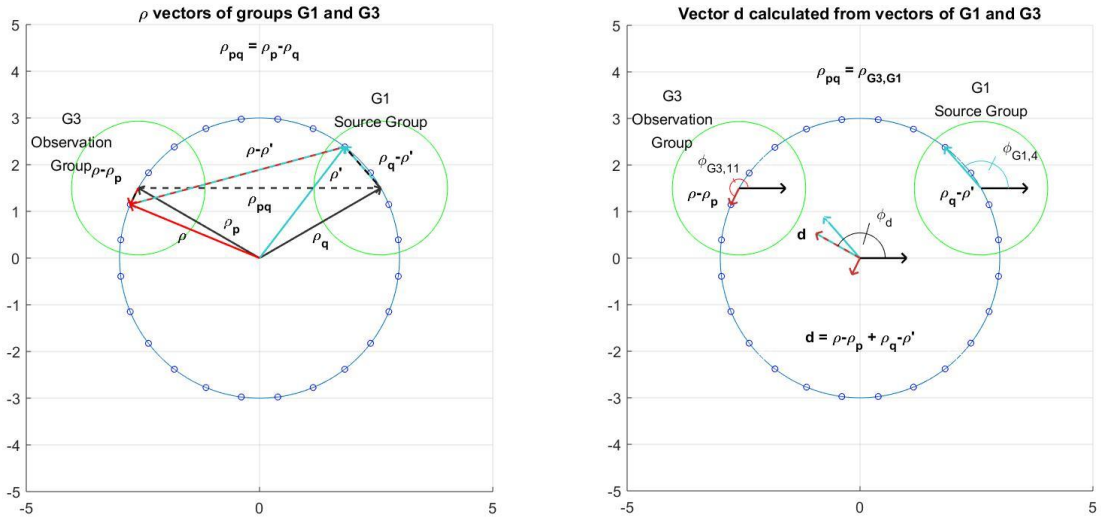

a) b)

Figure 3-5: a) Elements in source group G1 excite observation elements in group G3. b) Illustration of the vector sums and angles in equations $(3-14)$ to $(3-18)$.

Equation $(3-13)$ can be rewritten after substituting for $\boldsymbol{\rho} - \boldsymbol{\rho}'$ from equation $(3-16)$ under the conditions set in equations $(3-14)$ to $(3-18)$, $|\boldsymbol{\rho}| > |\boldsymbol{d}|$, yielding the new equation $(3-19)$.

$$H_0^{(2)}(\beta|\boldsymbol{\rho} - \boldsymbol{\rho}'|) = \frac{1}{2\pi}\int_0^{2\pi} e^{-j\boldsymbol{\beta}\cdot(\boldsymbol{\rho}-\boldsymbol{p_p})} A_{p,q}(\alpha) e^{-j\boldsymbol{\beta}\cdot(\boldsymbol{p_q}-\boldsymbol{\rho'})} d\alpha \quad (3-19)$$

with the condition in equation $(3-20)$

$$|\rho_{p,q}| > |(\rho - \rho_p)| + |\rho_q - \rho'| \tag{3-20}$$

and with the aggregate term, $A_{p,q}(\alpha)$, defined in equation $(3-21)$.

$$A_{p,q}(\alpha) \approx \sum_{l=-L}^{L} H_l^{(2)}\left(\beta\rho_{p,q}\right) e^{jl\left(\phi_{p,q}-\alpha-\frac{\pi}{2}\right)} \tag{3-21}$$

The impedance matrix for the Fast Multipole Matrix can be calculated using equation $(3-22)$, by first integrating with respect to the testing functions $t_m(\rho)$ and source basis functions $b_n(\rho')$ over the range of α values from 0 to 2π.

$$Z_{m,n} = \frac{\beta Z_0}{8\pi}\int_0^{2\pi} \int_{\mathrm{P}} t_m(\rho) e^{-j\beta\cdot(\rho-p_p)} d\mathrm{P}\, A_{p,q}(\alpha) \int_{P'} b_n(\rho') e^{-j\beta\cdot(p_q-\rho')} d\mathrm{P}'\, d\alpha \tag{3-22}$$

Equation $(3-22)$ can be broken up into three different integral expressions given in equations $(3-23)$ to $(3-25)$,

$$Z_{m,n} = \frac{\beta Z_0}{8\pi}\int_0^{2\pi} t_{m,p}(\alpha)\, A(\alpha) f_{q,n}(\alpha) d\alpha \tag{3-23}$$

$$t_{m,p}(\alpha) = \frac{\beta Z_0}{8\pi}\int_{\mathrm{P}} t_m(\rho)\, e^{-j\beta\cdot(\rho-p_p)} dP \tag{3-24}$$

$$f_{q,n}(\alpha) = \frac{\beta Z_0}{8\pi}\int_{\mathrm{P}'} f_n(\rho')\, e^{-j\beta\cdot(p_q-\rho')} dP' \tag{3-25}$$

The expression for impedance can be further simplified with equation $(3-26)$. In this equation, the impedance block $Z_{m,n}$ is defined as a combination of MOM and FMM terms.

$$\sum_{n=1}^{N} Z_{m,n}J_n = \sum_{q\in G_p}\sum_{n\in G_q} Z_{m,n}J_n + \frac{\beta Z_0}{8\pi}\int_0^{2\pi} t_{m,p}(\rho) \sum_{q\notin G_p} A_{p,q}(\alpha) \sum_{n\in G_q} f_{q,n}(\alpha) J_n d\alpha \tag{3-26}$$

The first term in the summations $\sum_{q\in B_p}\sum_{n\in G_q} Z_{m,n}J_n$ for the right side of equation $(3-26)$ is the MOM term, and the second summation is the FMM term. Here G_q is a source group and G_p is an observation group. The integral in equation $(3-26)$ can be replaced by a summation, and the final expression is equation $(3-27)$.

$$\sum_{n=1}^{N} Z_{m,n}J_n = \sum_{q\in B_p}\sum_{n\in G_q} Z_{m,n}J_n + \frac{\beta Z_0}{8\pi}\sum_{r=1}^{R} t_{m,p}(\alpha_r) \sum_{q\notin G_p} A_{p,q}(\alpha_r) \sum_{n\in G_q} f_{q,n}(\alpha_r) J_n \tag{3-27}$$

$$\sum_{q\in B_p}\sum_{n\in G_q} Z_{m,n}J_n \qquad \frac{\beta Z_0}{8\pi}\sum_{r=1}^{R} t_{m,p}(\alpha_r) \qquad \sum_{q\notin G_p} A_{p,q}(\alpha_r) \qquad \sum_{n\in G_q} f_{q,n}(\alpha_r)J_n$$

MOM Disaggregation Translation Aggregation

3.5 Aggregation, Translation, and Disaggregation Matrices

The FMM term in equation $(3-27)$ can be expressed in matrix notation using three matrices called the aggregation, translation, and disaggregation matrices (ATD), all shown in equation $(3-28)$.

$$\begin{bmatrix} \vdots & \vdots & \vdots \\ \cdots & Disaggregation & \cdots \\ \vdots & \vdots & \vdots \end{bmatrix} \cdot \begin{bmatrix} \vdots & \vdots & \vdots \\ \cdots & Translation & \cdots \\ \vdots & \vdots & \vdots \end{bmatrix} \cdot \begin{bmatrix} \vdots & \vdots & \vdots \\ \cdots & Aggregation & \cdots \\ \vdots & \vdots & \vdots \end{bmatrix} \begin{bmatrix} \vdots \\ J \\ \vdots \end{bmatrix} \qquad (3-28)$$

Equation $(3-29)$ shows the actual ATD matrices for numerical calculation of FMM [29].

$$\begin{bmatrix} e^{-j\beta\cdot\rho_{1,p}cos(\alpha_1-\phi_{1,p})} & e^{-j\beta\cdot\rho_{1,p}cos(\alpha_2-\phi_{1,p})} & \vdots & e^{-j\beta\cdot\rho_{1,p}cos(\alpha_r-\phi_{1,p})} \\ e^{-j\beta\cdot\rho_{2,p}cos(\alpha_1-\phi_{2,p})} & e^{-j\beta\cdot\rho_{2,p}cos(\alpha_2-\phi_{2,p})} & \vdots & e^{-j\beta\cdot\rho_{2,p}cos(\alpha_r-\phi_{2,p})} \\ \vdots & \vdots & & \vdots \\ e^{-j\beta\cdot\rho_{m,p}cos(\alpha_1-\phi_{m,p})} & e^{-j\beta\cdot\rho_{m,p}cos(\alpha_2-\phi_{m,p})} & \vdots & e^{-j\beta\cdot\rho_{m,p}cos(\alpha_r-\phi_{m,p})} \end{bmatrix}.$$

$$\begin{bmatrix} A_{p,q}(\alpha_1) & 0 & 0 & 0 \\ 0 & A_{p,q}(\alpha_2) & 0 & 0 \\ 0 & 0 & \ddots & 0 \\ 0 & 0 & 0 & A_{p,q}(\alpha_r) \end{bmatrix}.$$

$$\begin{bmatrix} e^{-j\beta\cdot\rho_{q,1}cos(\alpha_1-\phi_{q,1})} & e^{-j\beta\cdot\rho_{q,2}cos(\alpha_1-\phi_{q,2})} & \vdots & e^{-j\beta\cdot\rho_{q,n}cos(\alpha_1-\phi_{q,n})} \\ e^{-j\beta\cdot\rho_{q,1}cos(\alpha_2-\phi_{q,1})} & e^{-j\beta\cdot\rho_{q,2}cos(\alpha_2-\phi_{q,2})} & \vdots & e^{-j\beta\cdot\rho_{q,n}cos(\alpha_2-\phi_{q,n})} \\ \vdots & \vdots & & \vdots \\ e^{-j\beta\cdot\rho_{q,1}cos(\alpha_r-\phi_{q,1})} & e^{-j\beta\cdot\rho_{q,2}cos(\alpha_r-\phi_{q,2})} & \vdots & e^{-j\beta\cdot\rho_{q,n}cos(\alpha_r-\phi_{q,n})} \end{bmatrix} \begin{bmatrix} J_1 \\ J_2 \\ \vdots \\ J_N \end{bmatrix} \qquad (3-29)$$

Each matrix block for the FMM matrix is calculated and substituted into the impedance matrix. The FMM procedure is used to fill in blocks of the impedance matrix. Self-impedance terms are denoted $M_{MOM\text{-}n,n}$ and lie along the main diagonal of the matrix. Off diagonal blocks are calculated using the Fast Multipole Method. These FMM blocks calculated using matrix equation $(3-27)$ to $(3-29)$ are designated $M_{FMM\text{-}m,n}$. For symmetric bodies, the same

impedance blocks may be calculated once and then substituted into the impedance matrix multiple times. Figure 3-6 depicts the block matrix formulation of a MOM/FMM impedance matrix for an infinitely long PEC cylinder divided into the same 6 groups shown in the previous illustrations.

$MOM_{p,q}$ and $FMM_{p,q}$ Block Matrices

$M_{MOM-1,1}$	$M_{FMM-1,2}$	$M_{FMM-1,3}$	$M_{FMM-1,4}$	$M_{FMM-1,5}$	$M_{FMM-1,6}$
$M_{FMM-2,1}$	$M_{MOM-2,2}$	$M_{FMM-2,3}$	$M_{FMM-2,4}$	$M_{FMM-2,5}$	$M_{FMM-2,6}$
$M_{FMM-3,1}$	$M_{FMM-3,2}$	$M_{MOM-3,3}$	$M_{FMM-3,4}$	$M_{FMM-3,5}$	$M_{FMM-3,6}$
$M_{FMM-4,1}$	$M_{FMM-4,2}$	$M_{FMM-4,3}$	$M_{MOM-4,4}$	$M_{FMM-4,5}$	$M_{FMM-4,6}$
$M_{FMM-5,1}$	$M_{FMM-5,2}$	$M_{FMM-5,3}$	$M_{FMM-5,4}$	$M_{MOM-5,5}$	$M_{FMM-5,6}$
$M_{FMM-6,1}$	$M_{FMM-6,2}$	$M_{FMM-6,3}$	$M_{FMM-6,4}$	$M_{FMM-6,5}$	$M_{MOM-6,6}$

Figure 3-6: Fast Multipole Method matrix structure. The main diagonal is calculated using the Method of Moments.

TM wave analysis was performed on infinitely long elliptical cylinder using FMM and MOM. Figure 3-7 shows the FMM grouping of elements in an ellipse with a major axis of 2λ, and a minor axis of λ for specific groups. The ATD matrices for Groups 1 and 3 depicted in Figures (3-7) are shown in the matrix equation (3-30) below when $G_p = G_3$ for $m \in \{9,10,11,12\}$ in G_3, $G_q = G_1$, and $n \in \{1,2,3,4\}$ in G_1.

$$\begin{bmatrix} t_{9,3(\alpha_1)} & t_{9,3(\alpha_2)} & t_{9,3(\alpha_3)} & t_{9,3(\alpha_4)} \\ t_{10,3(\alpha_1)} & t_{10,3(\alpha_2)} & t_{10,3(\alpha_1)} & t_{10,3(\alpha_4)} \\ t_{11,3(\alpha_1)} & t_{11,3(\alpha_2)} & t_{11,3(\alpha_3)} & t_{11,3(\alpha_4)} \\ t_{12,3(\alpha_1)} & t_{12,3(\alpha_2)} & t_{12,3(\alpha_3)} & t_{12,3(\alpha_4)} \end{bmatrix} \begin{bmatrix} A_{3,1(\alpha_1)} & 0 & 0 & 0 \\ 0 & A_{3,1(\alpha_2)} & 0 & 0 \\ 0 & 0 & A_{3,1(\alpha_3)} & 0 \\ 0 & 0 & 0 & A_{3,1(\alpha_4)} \end{bmatrix}.$$

$$\begin{bmatrix} f_{1,1(\alpha_1)} & f_{1,2(\alpha_1)} & f_{1,3(\alpha_1)} & f_{1,4(\alpha_1)} \\ f_{1,1(\alpha_2)} & f_{1,2(\alpha_2)} & f_{1,3(\alpha_2)} & f_{1,4(\alpha_2)} \\ f_{1,1(\alpha_3)} & f_{1,2(\alpha_3)} & f_{1,3(\alpha_3)} & f_{1,4(\alpha_3)} \\ f_{1,1(\alpha_4)} & f_{1,2(\alpha_4)} & f_{1,3(\alpha_4)} & f_{1,4(\alpha_4)} \end{bmatrix} \qquad (3-30)$$

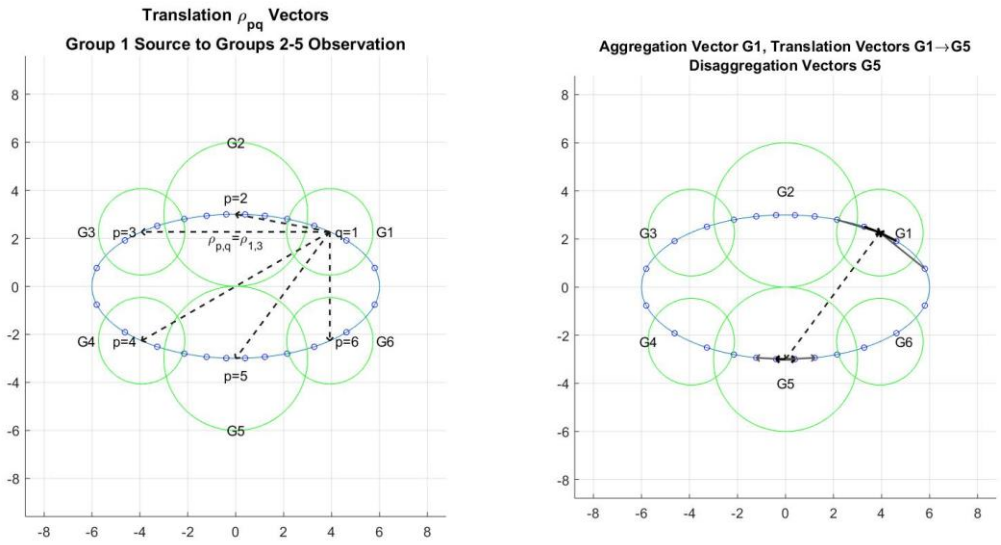

a) b)

Figure 3-7: Infinitely long elliptical cylinder with major axis $a = 2\lambda$, and minor axis $b = 1\lambda$. a) Translation vectors for a 24 element ellipse with groups of four. b) Aggregation, translation, and disaggregation (ATD) vectors from source group G1 to observation group G5.

3.6 FMM vs. MOM Results

As can be seen from Figure (3-8), the MOM and FMM analyses agree perfectly. In the FMM analysis, the main diagonal elements were calculated using the MOM. Off diagonal elements were calculated using the FMM technique outlined in this chapter. Equations $(3-27)$ to $(3-29)$ were employed and assembled as a DAT matrix. Delta basis functions were used for point matching the source to observation points.

The FMM formulation provided the motivation for the spectral projection model. The addition theorem was utilized extensively in modal analysis by Wilton, Harrington and Balanis [34-36]. Like the FMM formulation the Spectral Projection Model rewrites the addition theorem in a form that takes advantage of its ability to translate vectors from source points to observation

points. In SPM, the addition theorem is used to match the boundary conditions by writing spectral signatures as projections of sources onto the spectral signature of the observation points. Different forms of the addition theorem are used to decompose vectors into vector sums to solve a large variety of EM scattering problems.

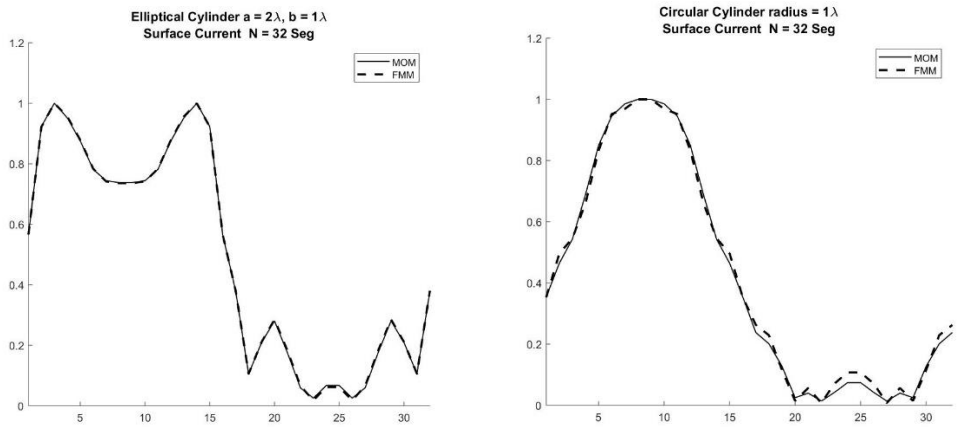

a) b)

Figure 3-8: a) MOM vs. FMM analysis of TM wave excitation on an infinitely long elliptical cylinder with major axis $a = 2\lambda$, and minor axis $b = 1\lambda$. b) MOM vs. FMM analysis of TM wave excitation on an infinitely long circular cylinder with radius = 1λ.

Chapter 4: Spatial Frequency Technique

4.1 Method of Moments vs. Spatial Frequency Technique

The Spatial Frequency Technique was developed in 1971 by N.N. Bojarski as a method of solving large integral equations iteratively [10,25,26]. The technique was intended to increase the convergence rate and size of the domain over other techniques and previous problem formulations. For N data points on an object, the SFT made the following in memory and speed over the MOM. See Table 4-1.

Table 4-1: Comparison between MOM and SFT of Memory and Computer Operations needed for Processing.

Computer Resource	SFT	MOM
Memory Locations	N	N^2
Multiplication Addition Operations	$N \log_2 N$	N^3

The Method of Moments normally formulates its impedance matrix in the form of a Toeplitz matrix. Some spectral methods have been developed to invert Toeplitz matrices using the FFT. Circulant matrices are special types of Toeplitz matrices [42,43]. See Figure 4-1a and Figure 4-1b for examples. In a Toeplitz matrix each diagonal is from left to right and is a constant. In a circulant matrix, each row has the same elements but rotated by one element each row down.

The SFT technique differs from the Method of Moments in that it requires the Green's function be expressed in circulant matrix form, G_C, so that its matrix representation can be calculated using the FFT and its eigenvalues [40,44]. The eigenvalues are in a diagonal matrix form D_{eval}.

$$G_C = F^{-1} D_{eval} F \qquad (4-1)$$

This technique was investigated in this research along with other attempts at improving the convergence rate of integral equation problems.

a	b	c	d	e
f	a	b	c	d
g	f	a	b	c
h	g	f	a	b
i	h	g	f	a

a)

a	b	c	d	e
e	a	b	c	d
d	e	a	b	c
c	d	e	a	b
b	c	d	e	a

b)

Figure 4-1: a) Example of Toeplitz matrix. b) Example of circulant matrix.

4.2 Continuous Fourier Transforms

For the case of an aperiodic function the continuous spatial Fourier transform in one and two dimensions is given below in equations $(4-2)$ and $(4-3)$, respectively.

$$G_F(k) = \int_{-\infty}^{\infty} G(x)\, e^{-jkx} dx \qquad (4-2)$$

$$G_F(k_x, k_y) = \int_{-\infty}^{\infty} \int_{-\infty}^{\infty} G(x,y)\, e^{-jk_x x} e^{-jk_y y} dxdy \qquad (4-3)$$

If the continuous function is periodic with a spatial period of λ_T, one may calculate the Fourier series representation of the function. The Fourier series coefficients c_n are related to the Fourier transform, and the frequency spacing of the coefficients are $\Delta k = 2\pi/\lambda_T$. These Fourier series coefficients can be calculated directly by sampling the Fourier transform in spatial frequency. The continuous domain and discrete spatial frequency domain are linked by the fact that the coefficients of the Fourier series of a continuous periodic object are equal to the coefficients of the discrete Fourier transform [45,46].

The spatial frequency technique requires treating a continuous object in space as a function and then taking the discrete Fourier transform of the function. Figure 4-2 is an illustration of this process. In this illustration a continuous pulse *f(x)* is transformed from the spatial domain to the spatial frequency domain by the discrete time Fourier transform (DTFT), (a) and (b). Discretization of a continuous function *f(x)* into the sequence *f(n)* is accomplished by multiplying the function *f(x)* by a delta pulse train in space, i.e. sampling it with a delta pulse train (c) and (d). The Fourier transform of a delta pulse train in space is another delta pulse train in the spatial frequency domain (e). Convolution of the spatial frequency delta pulse train with

the spatial Fourier transform of the function *f(x)* generates a periodic representation of the spatial Fourier transform (f). This is the discrete time Fourier transform (DTFT) of the pulse. This modulated waveform resembles a repeated spatial Fourier transform passed through an ideal lowpass filter with passbands from $-\pi/\Delta\lambda$ to $\pi/\Delta\lambda$.

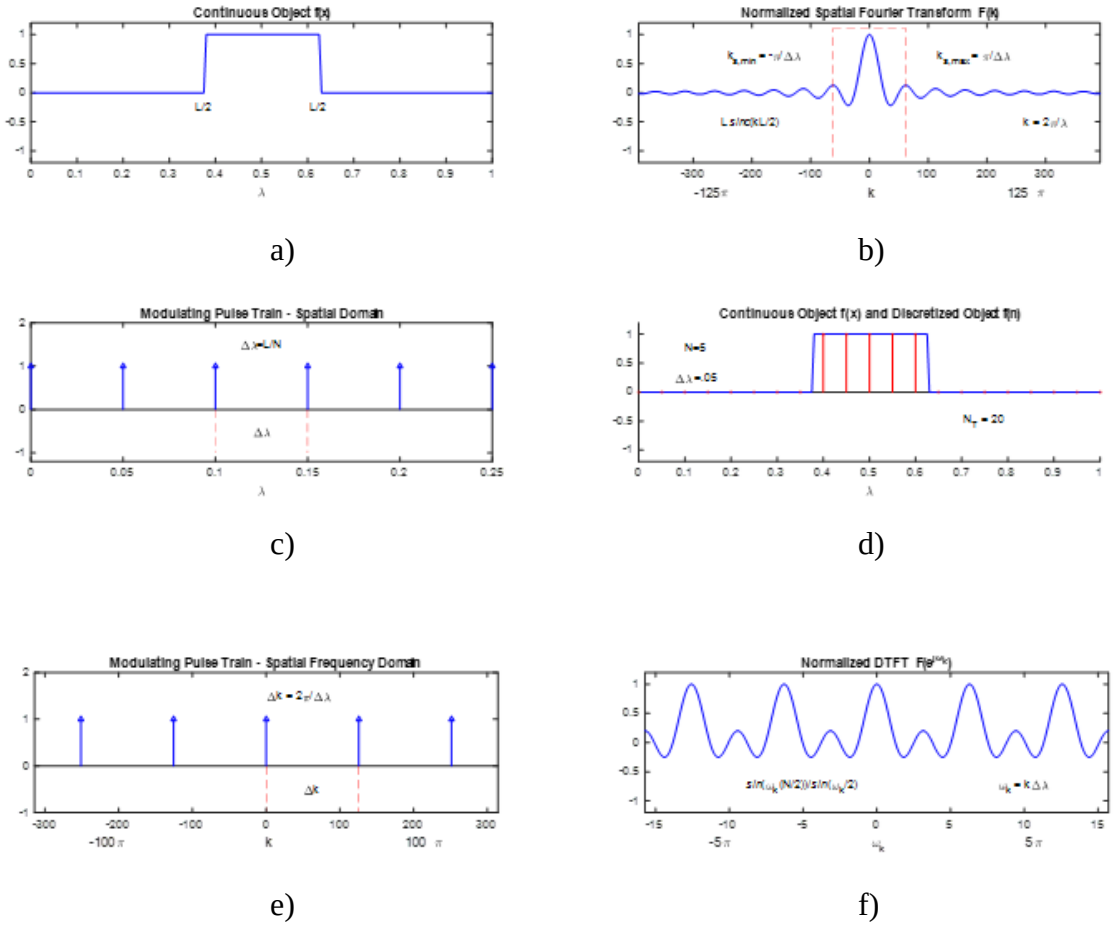

Figure 4-2: a) Continuous pulse function. b) Continuous pulse function normalized spatial Fourier transform. c) Pulse train in the spatial domain. d) Product of the pulse train and the continuous pulse function. e) Corresponding pulse train in the spatial frequency domain. f) Normalized discrete time Fourier transform.

4.3 Discrete Sequences and Fourier Transforms

Note in Figure (4-2) the spatial sampling rate is $\Delta\lambda$, Δk is the spacing in the spatial frequency domain of the modulating pulse train, and ω_k is the spatial frequency normalized to a

period of 2π. The Fourier transform and discrete Fourier transform functions of a continuous pulse are shown on the diagram as well.

The Fourier transform equation of a one-dimensional sequence is shown in equation $(4-3)$ below.

$$X\left(e^{j\omega_k}\right) = \sum_{n=-\infty}^{\infty} x[n]e^{-j\omega_k n} \qquad (4-3)$$

Its inverse is given in equation $(4-4)$.

$$x[n] = \int_{-\pi}^{\pi} X\left(e^{j\omega_k}\right)e^{j\omega_k}d\omega_k \qquad (4-4)$$

For a one-dimensional continuous time-sampled signal in the spatial domain, the spatial frequency normalized to 2π becomes ω_k,

$$\omega_k = k\Delta\lambda \qquad (4-5)$$

The letter k is the continuous time spatial frequency and $\Delta\lambda$ is the spatial domain spacing of the modulating pulse train in wavelengths.

Substituting for ω_k and making note that the waveform multiplied by the pulse train is now discrete, the expression for the DTFT of a pulse train is given in equation $(4-6)$.

$$X\left(e^{j\omega}\right) = \frac{1}{\Delta\lambda}\sum_{n=-\infty}^{\infty} F\left(j\left(\frac{\omega}{\Delta\lambda} - \frac{2\pi k}{\Delta\lambda}\right)\right) \qquad (4-6)$$

The discrete Fourier series and discrete Fourier transform (DFT) are the most effective ways of dealing with discrete waveforms. The DFT is a sampled version of the DTFT. The spatial frequency technique employs the DFT specifically to analyze continuous objects. The DFT transformation can be applied to discretized objects the same way the Fourier transform is applied to continuous waveforms. In the spatial frequency domain, these discretized objects can be thought of as frequency sampled discrete waveforms in space.

Shown in Figure 4-3 is an example of a discretized object, a periodic discretized object, five spatial frequency period of its DTFT, and five spatial frequency periods of its discrete Fourier transform (DFT).

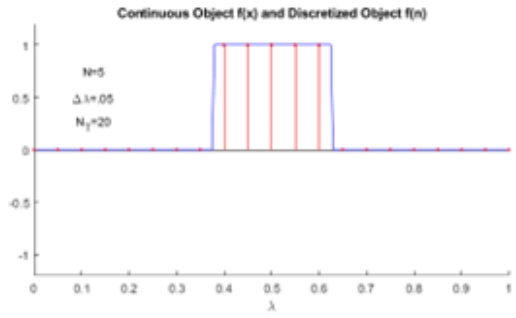

a)

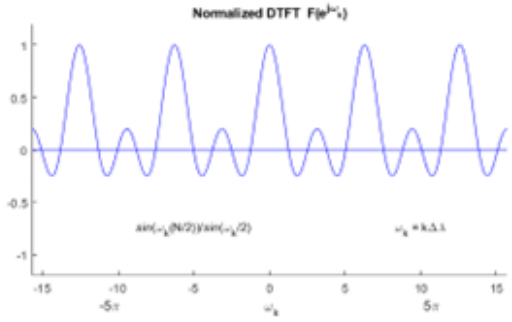

b)

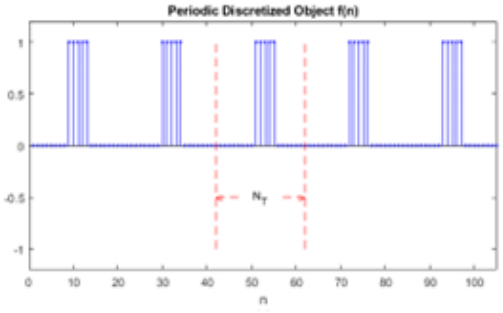

c)

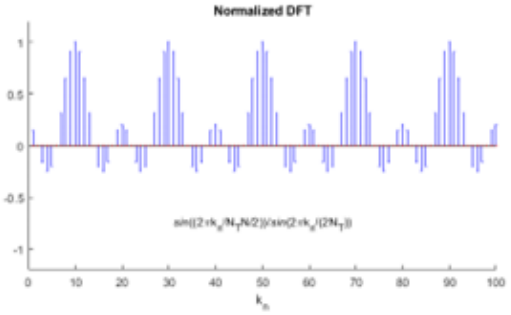

d)

Figure 4-3: a) Discretized pulse function. b) Normalized discrete time Fourier transform of pulse function. c) Periodic discretized pulse function. d) Normalized discrete Fourier transform.

As mentioned above, the discrete Fourier transform (DFT) is a version of the continuous Fourier transform for sequences and sampled waveforms $g(n)$. These waveforms must meet the Nyquist criteria to accurately represent the waveform being represented. The DFT for one and two dimensions can be calculated using equations $(4-7)$ and $(4-8)$ below, respectively.

$$G_{DFT}(k_x) = \frac{1}{N}\sum_{n=0}^{N-1} g(n)e^{-jk_x n/N} \qquad (4-7)$$

$$G_{DFT}(k_x, k_y) = \frac{1}{NM}\sum_{n=0}^{N-1}\sum_{m=0}^{M-1} g(n,m)\left(e^{-\frac{jk_x n}{N}}\right)\left(e^{-\frac{jk_y m}{M}}\right) \qquad (4-8)$$

4.4 Continuous Fourier Transforms and the Spatial Frequency Technique

The Spatial Frequency Technique can be applied to electromagnetic problems in two different ways. One way is that it may be used to transform a partial differential equation in spatial coordinates to the spatial frequency domain, i.e. complex exponential representation. For example, it can be used to solve the Helmholtz equation $(4-9)$. The integral solution to equation $(4-9)$ is given in equation $(4-10)$. The wavenumber symbol for this section is k_0.

$$\nabla^2 A(r) + k_0^2 A(r) = -\mu J(r) \qquad (4-9)$$

$$A(r) = \frac{\mu}{4\pi} \iiint_V J(r')\, G(r-r') dV' \qquad (4-10)$$

Firstly, one takes the spatial Fourier transform of both sides of equation $(4-10)$. Next, one takes the Fourier transform of the convolution expression between the current $J(r')$ and the Green's function $G(r-r')$. Through the DFT, convolution in the spatial domain is performed as multiplication in the spatial frequency k domain. See equation $(4-12)$.

$$-k^2 A(k) + k_0^2 A(k) = -\mu J(k) \qquad (4-11)$$

$$A(k) = \frac{\mu}{4\pi} J(k) G(k) \qquad (4-12)$$

Then one substitutes the spatial Fourier transform of $A(r)$ into equation $(4-11)$ to solve for $J(k)$. The resulting spatial frequency current distribution is finally transformed back into the spatial domain, and the far-field pattern is calculated from the spatial current distribution.

Another method begins with the electric field differential equation $(2-2)$. Once again, the Fourier transform of each side of the equation is taken, and one arrives at equation $(4-13)$.

$$E(k) = \frac{\eta}{k_0}(-k^2 + k_0^2) G(k) J(k) \qquad (4-13)$$

Then $(4-13)$ is solved for $J(k)$. The result is again transformed back into the spatial domain, and the far-field pattern can once again be calculated from the spatial current distribution.

4.5 Discrete Fourier Transforms and the Spatial Frequency Technique

When employing the Spatial Frequency Technique, objects are first discretized and so considered as periodic in spatial frequency. The DFT requires the object be periodic in space

because it is discrete in frequency. An example problem solved using the SFT is the periodic finite length strip shown below in Figure 4-4.

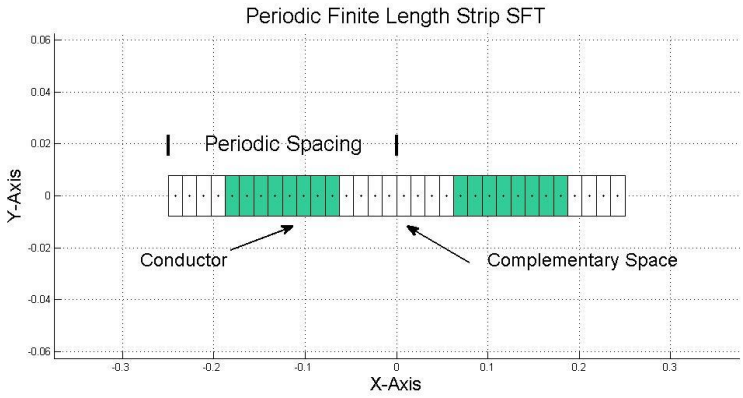

Figure 4-4: Periodic representation of an infinitely long strip in spatial domain.

The periodic structure domain is both conductor and free space. The domain is divided into a conductor subspace and a complementary subspace. The complementary subspace is a sequence of zeros equal in length or greater to the sequence specifying the object. This is necessary to satisfy the Nyquist criterion. It can be lengthened by padding the sequence of data with additional zeros. By zero padding, although the amount of information on the object is not increased, it enables one to use the FFT algorithm to calculate the DFT because the FFT algorithm uses data length equal to 2^n. Also, zero padding the DFT allows interpolation between the points of the sequence, but the additional zeros unfortunately alter the phase of the result. So, resulting curves generally look smoother, but at a cost.

For objects whose surface does not lie on grid points, such as the ellipse shown in Figure 4-5, the Fourier domain convolution property must be used. The discrete Fourier transform of the ellipse is first calculated, then the FFT is used to transform the Green's function matrix to the frequency domain. Then two Fourier transforms can be multiplied in the frequency domain and convolution in the spatial domain is avoided. Next inversion of the matrix product follows by transformation into the spatial frequency domain to calculate the current distribution.

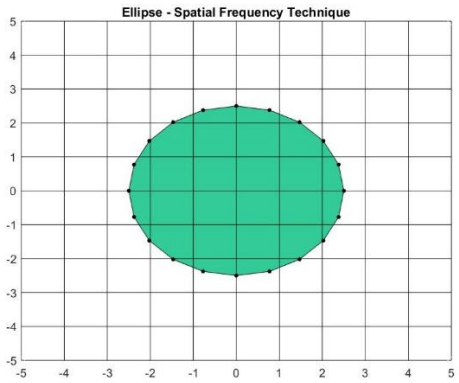

Figure 4-5: Elliptical object in the spatial domain.

4.6 Scattering with TM^z Waves and the Spatial Frequency Technique Theory

Shown in Figure 4-5 are illustrations of several different infinitely long conducting objects in X,Y,Z coordinates along with the orientation of TM^z and TE^z polarized waves. The plane of incidence is also indicated on the diagram.

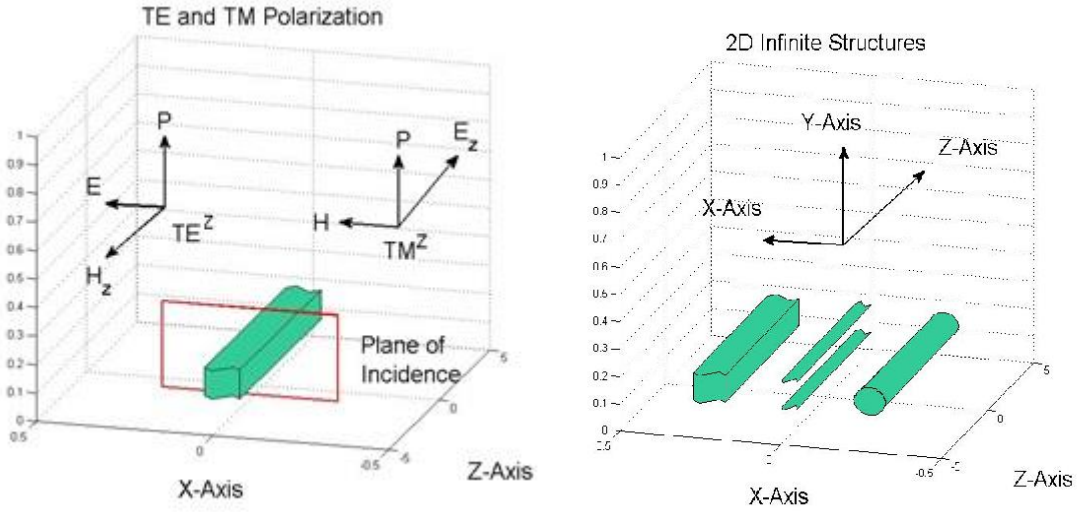

a) b)

Figure 4-6: a) Polarization of TM^z and TE^z waves. b) Infinitely long conducting structures: rectangular box, parallel plates, and circular cylinder.

As mentioned earlier, for TM^z wave incidence on infinitely long cylindrically symmetric conducting bodies, the appropriate Green's function is the zeroth order Hankel function of the

second kind $H_0^{(2)}(x)$. For the structures analyzed in Figure 4-6b, the electric field is polarized in the Z-direction. See also Figure 4-6a.

To calculate the current distribution on the objects in Figure 4-5b, the Spatial Frequency Technique begins with equations in the spatial domain. Starting with the magnetic vector potential, $A_z(\rho)$, and the spherical Hankel function $h_0^{(2)}(R) = \frac{e^{-jk_0R}}{R}$, one utilizes the symmetry to evaluate the integrand over its infinite limits in the Z-direction of polarization. As shown in Chapter 2 for the MOM, application of the SFT begins with equation $(4-14)$.

$$A_z(\rho) = -j\frac{\mu}{4}\iint_S J_z(\rho')' H_0{}^{(2)}\left(k_0\left|\rho-\rho'\right|\right)d\rho' \qquad (4-14)$$

$$G(\rho,\rho') = H_0{}^{(2)}\left(k_0\left|\rho-\rho'\right|\right) \qquad (4-15)$$

The Fourier transform of the zeroth order Hankel function of the second kind for two-dimensional problems is shown below in equation $(4-16)$.

$$G_F(K_x) = \int_{-\infty}^{\infty} H_0^{(2)}\left(k_0\sqrt{x^2+y^2}\right)e^{-jK_xx}dx \qquad (4-16)$$

Equation $(4-16)$ can be simplified into equation $(4-17)$,

$$G_F(K_x) = 2\int_0^{\infty} H_0^{(2)}\left(k_0\sqrt{x^2+y^2}\right)cos(K_xx)dx \qquad (4-17)$$

and integrated to find the Fourier transforms given in equations $(4-18)$ and $(4-19)$.

$$G_F(K_x) = \frac{2e^{-j|y|\sqrt{k_0^2-K_x^2}}}{\sqrt{k_0^2-K_x^2}} \qquad k_0 > K_x \qquad (4-18)$$

$$G_F(K_x) = \frac{2e^{-j|y|\sqrt{K_x^2-k_0^2}}}{\sqrt{K_x^2-k_0^2}} \qquad k_0 < K_x \qquad (4-19)$$

4.7 Scattering with TM^z Waves and the Spatial Frequency Technique Results

In this investigation, although formulas $(4-18)$ and $(4-19)$ were available, instead of using the Fourier transform of the Hankel function of the second kind, $H_0^{(2)}(k_0\sqrt{x^2+y^2})$, the Fourier transform for infinitely long conducting bodies was calculated by first generating a matrix containing the integral of the Green's function over the conductor and complementary subspaces. The complementary space is required to ensure that the Nyquist criterion is met for

analyzing periodic structures. Then using the FFT algorithm, the discrete Fourier transform of the entire problem space is calculated.

The conductor region and the complementary space region are both subspaces of a vector space that defines the whole problem. The complementary space region, which is a zero-padded region, is orthogonal to the conductor subspace. See Figure 4-7 for examples of the complementary spaces of a two-dimensional and a one-dimensional object.

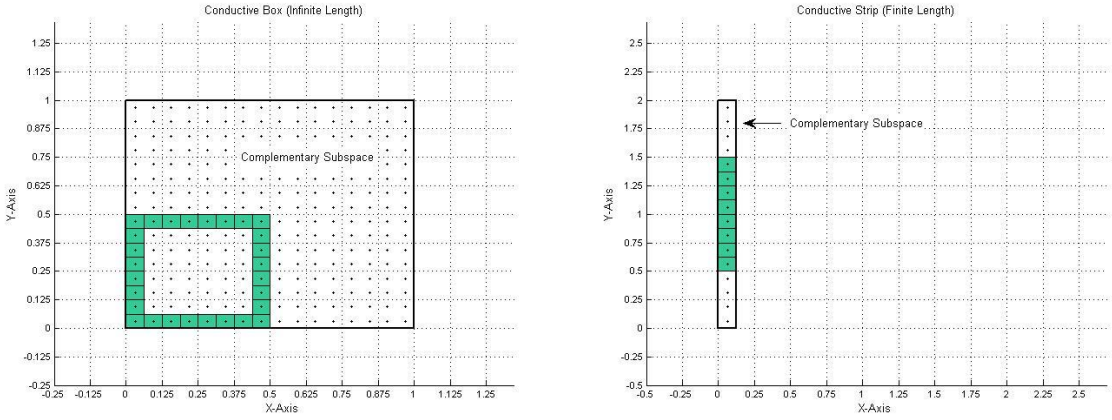

a) b)

Figure 4-7: Conductor (shaded) and complementary space for a) infinite length rectangular cylinder and b) finite length strip.

Calculated results of the current density distribution for TM^z polarization are shown below for the following infinitely long cylindrical objects: parallel strips, rectangular cylinder, and circular cylinder [47]. See Figures 4-8, 4-9, and 4-10.

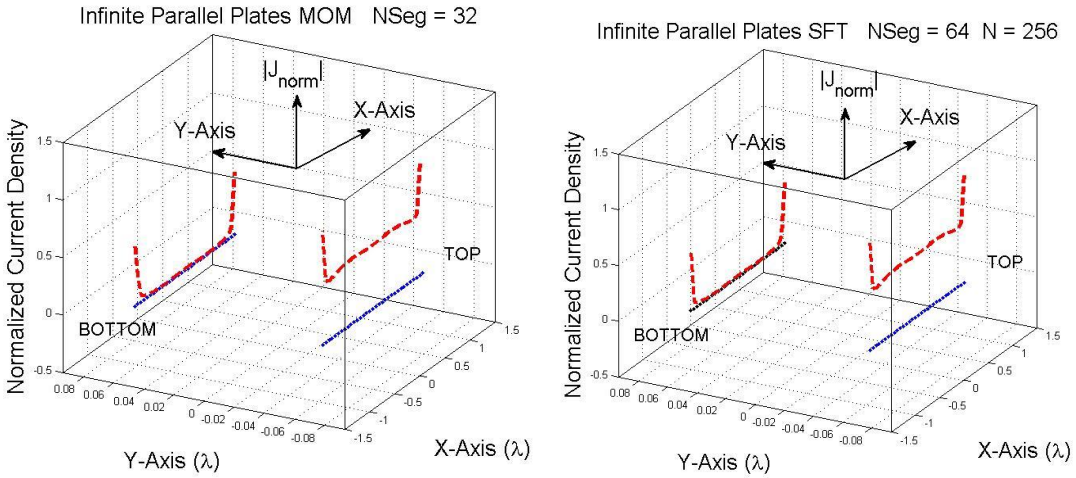

a) b)

Figure 4-8: 3D Current density along infinite parallel plates using a) MOM and b) SFT [47].

The SFT and MOM techniques produced the identical results for two infinite parallel strips and an infinite rectangular cylinder placed on evenly separated spatial gridlines produced.

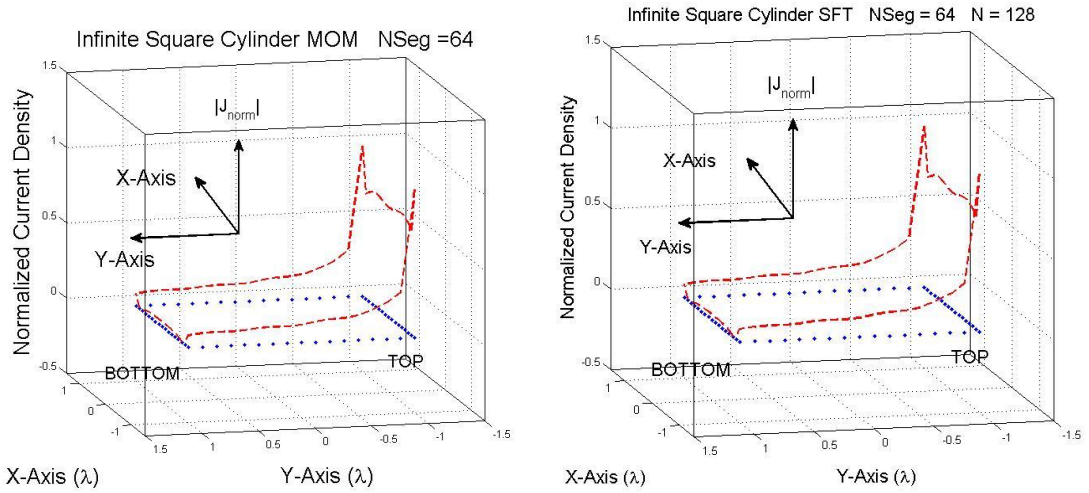

a) b)

Figure 4-9: 3D Current density along infinite rectangular cylinder a) MOM and b) SFT [47].

For points on an infinitely long cylinder that did not lie on grid points, the FFT could not be utilized. Instead, the discrete Fourier transform was used to perform frequency domain calculations. In this other approach for using the Spatial Frequency Technique, the DFT was

applied directly to points of the calculated Green's function that lay on the perimeter of the cylinder. Points on the circular conductor were separated by the same arc length, similar to the way points on the rectangular grid were evenly spaced for the other geometries. This approach was necessary for an infinitely long conducting cylinder since no off-grid techniques for the SFT have been developed as yet. Preconditioning techniques have been developed for electrostatic problems, but not time harmonic problems as yet [48]. Figure 4-8 shows plots of the current distribution calculated using the MOM technique and the SFT. Both the conjugate gradient method and direct matrix inversion were used to solve for the current distribution. All three calculations produced identical results.

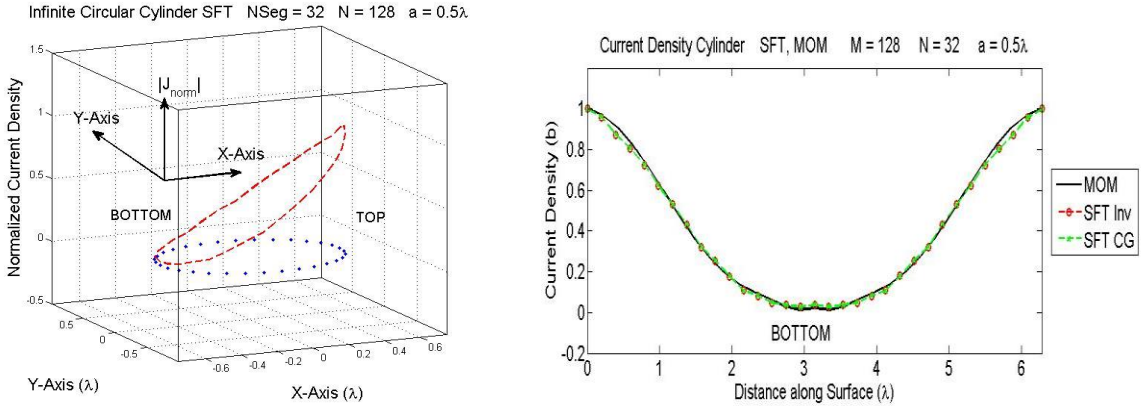

a) b)

Figure 4-10: a) 3D Current density along infinitely long circular cylinder d = .5 λ using SFT method 3D view. b) Linear plot of current density along the circumference of the cylinder [47].

When calculating the DFT in two-dimensions, careful attention must be paid in keeping track of each column of angular spatial frequency variables $k_{x,m}$ and $k_{y,n}$ to ensure their agreement with matrix calculations throughout the solution. Sub-matrices were generated within the DFT operator for angular spatial frequencies and *(x,y)* coordinates shown below in Figure 4-11.

$$\begin{bmatrix} \begin{bmatrix} k_{x,0}, k_{y,0}, x_0, y_0 \\ \vdots \\ k_{x,M-1}, k_{y,0}, x_0, y_0 \end{bmatrix} & \begin{bmatrix} k_{x,0}, k_{y,0}, x_1, y_0 \\ \vdots \\ k_{x,M-1}, k_{y,0}, x_1, y_0 \end{bmatrix} & \dots & \begin{bmatrix} k_{x,0}, k_{y,0}, x_{M-1}, y_0 \\ \vdots \\ k_{x,M-1}, k_{y,0}, x_{M-1}, y_0 \end{bmatrix} \\ \begin{bmatrix} k_{x,0}, k_{y,1}, x_0, y_1 \\ \vdots \\ k_{x,M-1}, k_{y,1}, x_0, y_1 \end{bmatrix} & \begin{bmatrix} k_{x,0}, k_{y,1}, x_1, y_1 \\ \vdots \\ k_{x,M-1}, k_{y,1}, x_1, y_1 \end{bmatrix} & \dots & \\ \begin{bmatrix} k_{x,0}, k_{y,2}, x_0, y_2 \\ \vdots \\ k_{x,M-1}, k_{y,2}, x_0, y_2 \end{bmatrix} & \vdots & \dots & \\ \vdots & \vdots & & \\ \begin{bmatrix} k_{x,0}, k_{y,N-1}, x_0, y_{N-1} \\ \vdots \\ k_{x,M-1}, k_{y,N-1}, x_0, y_{N-1} \end{bmatrix} & \dots & \begin{bmatrix} k_{x,0}, k_{y,N-1}, x_{M-1}, y_{N-1} \\ \vdots \\ k_{x,M-1}, k_{y,N-1}, x_{M-1}, y_{N-1} \end{bmatrix} & \end{bmatrix}$$

Figure 4-11: Two-dimensional discrete Fourier transform matrix representation.

4.8 Fast Algorithms for the Spatial Frequency Technique

The aim of the research on the SFT was to develop fast algorithms implementing iterative techniques to calculate current distributions using the Spatial Frequency Technique. Illustrated in Figure 4-12 is an infinite length strip shown with its axes and complementary space region. In a conference paper, a fast algorithm for calculating the current distribution on a 2D infinitely long conducting strip was shown to have significant speed improvement over former methods [49,50]. Figure 4-13 shows plots comparing the rate of convergence of the SFT using the conjugate gradient algorithm [51] versus the new fast iterative method known as the Fast-SFT algorithm. See the Appendix G on the conjugate gradient method for more information.

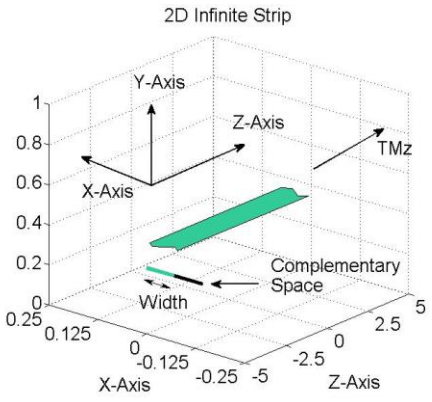

Figure 4-12: Two-dimensional infinite length strip with incident TM^z electromagnetic wave.

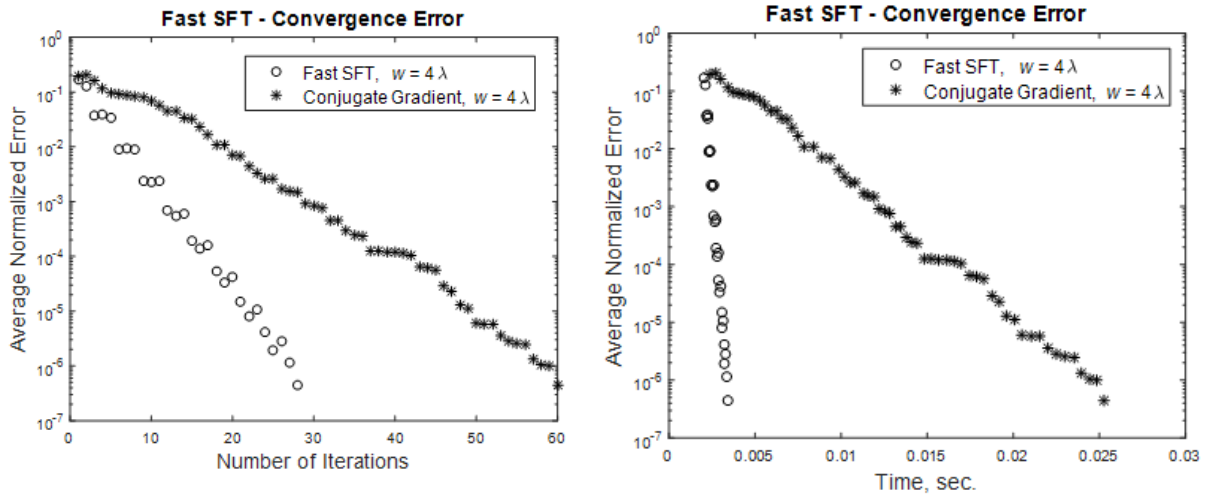

a) b)

Figure 4-13: a) Average normalized error versus number of iterations when calculating the current distribution of an infinitely conducting strip with the SFT method using the fast convergence algorithm and conjugate gradient approach. b) Convergence time [49,50].

The governing equation for the infinite length strip using the SFT is written below. Note the change in notation, $F_{e(x)} = F_1$ and $F_{\Delta e(x)} = F_2$.

$$\hat{J}(x) = F' H_D F_1 e(x) + F' H_D F_2 F_2{}' L_F G_D F \hat{J}(x) \qquad (4-20)$$

$$\hat{J}_{n+1} = \hat{J}_0 + F' H_D F_2 F_2{}' L_F G_D F \hat{J}_n \qquad (4-21)$$

$$G_D = H_0^{(2)}(k_0 R) \qquad (4-22)$$

$$H_D = G_D^{-1} \quad (4-23)$$

The iterative routine in the paper [50] is shown below.

Start

$$\hat{J}_0 = F' H_D F_1 e(x) \quad (4-24)$$

Repeat until $\Delta\hat{J} <$ tolerance

$$\hat{J}_{n+1} = \hat{J}_0 + F_1'\left[H_D \times (F_2 \times F_2')L_F G_D \times F_1'\hat{J}_n\right] \quad (4-25)$$

$$\Delta\hat{J} = \left|\hat{J}_{n+1} - \hat{J}_n\right| \quad (4-26)$$

End

The Fast-SFT algorithm takes the same form as a basic iterative method for solving a matrix equation $(4-27)$.

$$A\hat{x} = \hat{b} \quad (4-27)$$

Given an initial vector x_0 one can generate a sequence with variable x_m that can converges to the solution.

$$A^{-1}\hat{b} = \hat{x} \quad (4-28)$$

The value of x_{m+1} is fast and efficient to compute. The convergence criteria depend on the operator norm$\| R\|_0$ of the iterative equation below,

$$\hat{x}_{m+1} = R\hat{x}_m + \hat{c} \quad (4-29)$$

that is defined below in terms of the vector space norms $\| \|$ [52],

$$\| R\|_0 = max_{x\neq 0}\frac{\| R\hat{x}\|}{\| \hat{x}\|} \quad (4-30)$$

Besides another aim of this method was to investigate further the relationship between the convergence criteria and the spectral radius of R, defined as $\rho(R)$ below,

$$\rho(R) = max|\lambda| \quad (4-31)$$

which is the absolute value of the maximum value of the eigenvalues of R.

Although the Fast-SFT worked well for the infinite strip problem, it did not work well for 2D and 3D problems. The geometric series implemented in the algorithm shown in equation $(4-29)$ did not converge for the 2D and 3D geometries. The application of the Fast-SFT algorithm to 2D and 3D structures resulted in eigenvalues that were greater than one, which caused the recursive algorithm to fail to converge. Without the introduction of some form of

preconditioning or lowpass filtering by the introduction of basis functions, this method proved to be limited to 1D structures.

4.9 Numerical Electromagnetic Analysis in this Dissertation

This dissertation presents a new method of analyzing electromagnetic structures and their scattering properties called the Spectral Projection Model. The first chapter presents an overview of different electromagnetic methods and their differences. Some techniques are best for finding the electromagnetic fields confined within an object or region. Others are suitable for calculating electromagnetic fields induced by currents on the surface of objects. Still others are developed to calculate the electromagnetic fields absorbed and reflected off boundaries. The finite element method is used often for calculating the electromagnetic fields within closed regions containing different media, for example magnetic and dielectric materials. The finite difference time domain method is a technique used to calculate the propagation of fields within an object or region as it varies in time and space. The method of moments is a boundary element method used to calculate the scattering and radiative properties of different electromagnetic structures. For large objects, the fast multipole method speeds up the process of populating the impedance matrix of BEM problems by grouping sources and observation points together.

The Spectral Projection Model and its successor Direct Spectral Projection Model originated from using the method of moments and point matching to compute the Green's function for source and observation points. By avoiding numerical integration of different shaped basis functions, the simplicity of calculating the impedance matrix is greatly improved. The fast multipole method is similar to the method of moments in that it is a boundary element method, and uses MOM techniques for calculating the Green's function of near-field sources and observation points. But for points farther away, it employs the addition theorem to aggregate source points to a central points, then translate them to another central point, and fnally disaggregate their effects to observation points, thereby speed up populating the impedance matrix.

The Spectral Projection Model is a spectral method that applies a linear transformation to source and observation points and in order to represent them as Bessel and Hankel function spectral signatures. It uses the addition theorem to calculate the Green's function by projecting

the source spectral signatures onto the observation point spectral signatures. It also uses the translation property to circumvent the restrictions that the addition theorem places on the source and observation point vectors in polar coordinates.

Research on spectral methods began with the Spatial Frequency Technique which uses complex exponentials and discrete Fourier transform methods to solve integral equation electromagnetic field problems. This technique used the DFT in the spatial domain, and the basis functions were complex exponentials in the X-direction and the Y-direction. The FFT was widely used to make gains in the speed of calculating results. By using iterative methods to invert matrices, some results were seen to converge faster for certain classes of problems. These improvements were not applicable to a more a general class of problems, which was the aim of the research.

Investigation into this spectral technique was then modified by representing source and observation points in polar coordinates with the family of Bessel functions through the addition theorem. This new spectral approach is named the Spectral Projection Model, and it enables one to analyze different object shapes without the restriction of uniform grid spacing in two dimensions imposed by FFT algorithms. Far-field patterns can be calculated directly from the **J**-spectral signature of the current distribution. SPM also applies to a broader spectrum of problems than traditional modal methods by using rotating vectors and the convolution property of the addition theorem to generate incident fields for a variety of object geometries.

SPM spawned a simpler technique called the DSPM which calculates the current distribution on a wide variety of PEC objects. This has the advantage of still using the projection of the modal spectral signatures in polar coordinates and avoiding integration of basis functions. DSPM also offers promise as a synthesis technique because by using a set of rotating vectors, any incident waveform and object geometry can be specified.

Chapter 5: Spectral Projection Model

5.1 Genesis of the Spectral Projection Model

The Spectral Projection Model (SPM) is a new technique for solving problems in electromagnetic scattering and radiation. The analysis is different from the Method of Moments (MOM), spatial frequency technique (SFT), and hybrid techniques like the Fast Multipole Method (FMM), but incorporates many of the same principles. The previous three methods set up integral equations with appropriate Green's functions and then discretize the surface of the scattering object. Once discretized, inner products are taken with basis functions to set up an impedance matrix. The impedance matrix is then solved to calculate the current distribution on the surface of the object. Once the surface current is calculated, other useful parameters such as the far-field radiation pattern, directivity of the radiation pattern, radar cross-section, etc. are determined from the current distribution.

In two-dimensions, the Spectral Projection Model is based on the addition theorem for Bessel and Hankel functions and can be applied to electromagnetic scattering and radiation from infinitely long, two-dimensional PEC objects. An addition theorem is the expansion of a Bessel or Hankel function into an infinite sum of Bessel and Hankel functions. Equations $(5-1)$ and $(5-2)$ are two forms of Graf's addition theorem. By changing the direction of the vector $\boldsymbol{\rho}'$ and its rotation around the origin, the two forms are interchangeable. Various other forms of the addition theorem are explained in detail in Appendix A: SPM and Graf's Equation.

Considering the vectors $\boldsymbol{\rho}$ and $\boldsymbol{\rho}'$, Figure 5-1 and Figure 5-2 illustrate the subtraction $|\boldsymbol{\rho}-\boldsymbol{\rho}'|$ and the addition $|\boldsymbol{\rho}+\boldsymbol{\rho}'|$ and these factors, respectively. For the particular Green's function, $H_0^{(2)}(\beta|\boldsymbol{\rho}+\boldsymbol{\rho}'|)$, the sum can be approximated by truncating the addition theorem to *2K+1* terms, as shown in equation $(5-1)$.

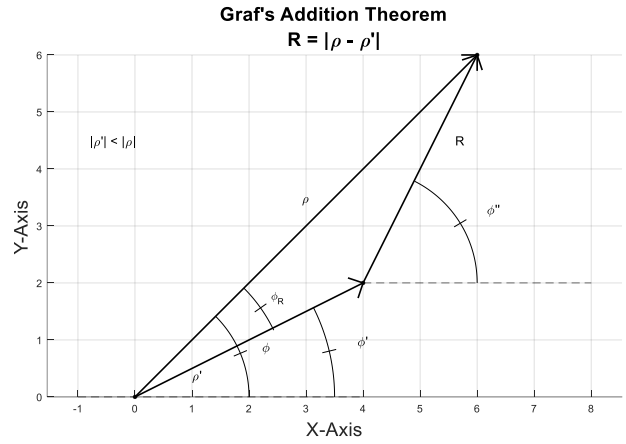

Figure 5-1: Graf's addition theorem for $|\boldsymbol{\rho} - \boldsymbol{\rho}'|$.

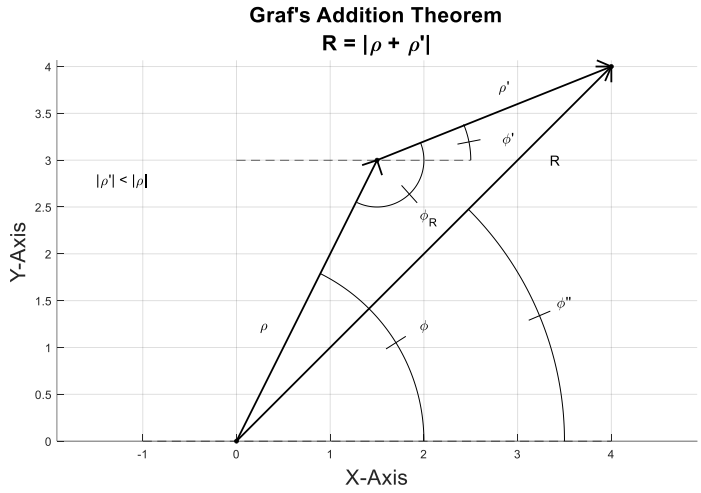

Figure 5-2: Graf's addition theorem for $|\boldsymbol{\rho} + \boldsymbol{\rho}'|$.

Equation $(5-1)$ is a form of Graf's addition theorem may be viewed as a correlation operation due to the *m+k* order on the Hankel function sum.

$$H_m^{(2)}(\beta|\boldsymbol{\rho} - \boldsymbol{\rho}'|)e^{jm\phi''} = \sum_{k=-\infty}^{\infty} H_{m+k}^{(2)}(\beta|\boldsymbol{\rho}|)J_k(\beta|\boldsymbol{\rho}'|)e^{j[(m+k)\phi - k\phi']} \qquad \rho > \rho' \qquad (5-1)$$

Equation $(5-2)$ is another form of Graf's addition theorem. This version may be viewed as a convolution operation because of the *m-k* order on the Hankel function sum.

$$H_m^{(2)}(\beta|\boldsymbol{\rho} + \boldsymbol{\rho}'|)e^{jm\phi''} = \sum_{k=-\infty}^{\infty} H_{m-k}^{(2)}(\beta|\boldsymbol{\rho}|)J_k(\beta|\boldsymbol{\rho}'|)e^{j[(m-k)\phi - k\phi']} \qquad \rho > \rho' \qquad (5-2)$$

For computational purposes, the particular Green's function, $H_0^{(2)}(\beta|\boldsymbol{\rho}-\boldsymbol{\rho}'|)$ can be approximated by truncating it to *2K+1* terms.

$$H_0^{(2)}(\beta|\boldsymbol{\rho}-\boldsymbol{\rho}'|) = \sum_{k=-K}^{K} J_k(\beta|\boldsymbol{\rho}'|)H_k^{(2)}(\beta|\boldsymbol{\rho}|)e^{jk(\phi-\phi')} \qquad \rho > \rho' \qquad (5-3)$$

This summation in equation $(5-3)$ can be written in vector form as a projection or inner product.

The Spectral Projection Model uses the truncated form of the addition theorem to represent the Green's function as the projection of the **H** or **J**-spectral signatures of the source points (ρ', ϕ') onto the **H** or **J**-spectral signatures of the observation points (ρ, ϕ). Illustrated in Figure 5-3a is a depiction of the **J**-spectral signature of source point (ρ', ϕ') projected onto the **H**-spectral signature of observation point (ρ, ϕ) using the addition theorem in equation $(5-3)$. Note that the inner product (or projection) is not the dot product shown in Figure 5-3b. The inner product using SPM is the projection of one spectral signature vector onto another, and it obeys the law of cosines. This is explained in further detail in Appendix A: SPM and Graf's Equation.

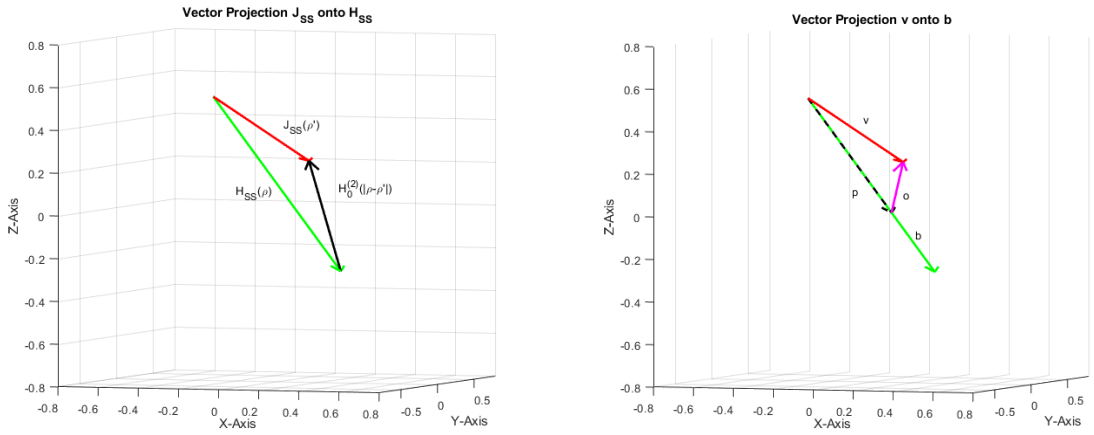

a) b)

Figure 5-3: a) Projection **p** of vector **v** onto **b** using dot product. b) Projection of $J_n(\beta|\boldsymbol{\rho}'|)$ onto $H_n^{(2)}(\beta|\boldsymbol{\rho}|)$ to yield $H_0^{(2)}(\beta|\boldsymbol{\rho}-\boldsymbol{\rho}'|)$. The value of $|\boldsymbol{R}| = |\boldsymbol{\rho}-\boldsymbol{\rho}'|$ is calculated using the law of cosines, i.e. $R = \sqrt{\rho^2 + \rho'^2 - 2\rho\rho' cos(\gamma)}$.

The method is called the Spectral Projection Model because the incident fields and the scattered fields are related to the incident and induced currents as projections of spectral signatures.

For scattering analysis in two-dimensions, the spectral signatures may be viewed as the spectral description of the fields and currents in a cylindrical coordinate system. The Spectral Projection Model enables one to calculate the far-field pattern without calculating the impedance matrix or electric current distribution on the conductor. Instead, the model requires calculation of the spectral signatures of the surface currents. The far-field pattern can be calculated from the spectral signature of the surface currents directly by a linear transformation.

These spectral signatures in SPM are analogous to spatial frequency representations using Fourier analysis when solving problems in the spatial frequency domain. However, in Fourier analysis, once the Fourier transform of current is calculated, the spatial domain equivalent must be found using the inverse Fourier transform in order to calculate the far-field pattern.

The Spectral Projection Model approach in electromagnetics may be used to solve for electromagnetic fields scattered from cylindrical objects of various axial ratios. In this dissertation, the first objects to be considered are infinitely long perfectly conducting cylinders with axial ratios $\frac{a}{b} \approx 1$. See Figure 5-4 for an illustration of several cylinders with different axial ratios.

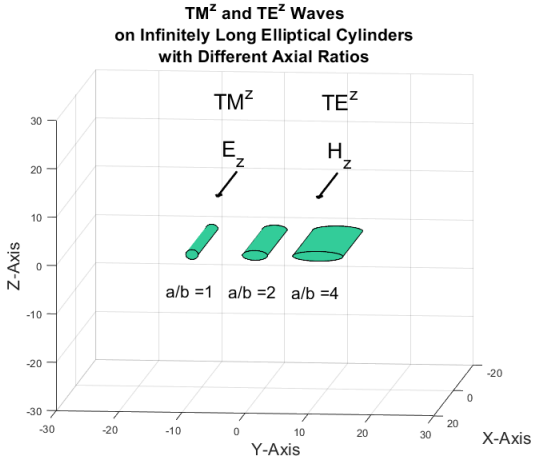

Figure 5-4: Elliptical cylinders with various axial ratios. Axial ratio $\frac{a}{b} = 1$ is a circular cylinder.

For the purpose of clarity, scattering from objects with axial ratios $\frac{a}{b} = 1$, i.e. circular cylinders, which are excited by electric line sources and TM^z electromagnetic waves are analyzed first. Then scattering from circular cylinders by magnetic line sources and TE^z waves

are discussed next. An illustration of a TM^z wave with the electric field in the axial Z-direction, the transverse magnetic field in the Y-direction, and propagation in the X-direction, is shown in Figure 5-5a. An illustration of a TE^z wave with the magnetic field in the axial Z-direction, the transverse electric field in the Y-direction, and propagation in the X-direction, is shown in Figure 5-5b.

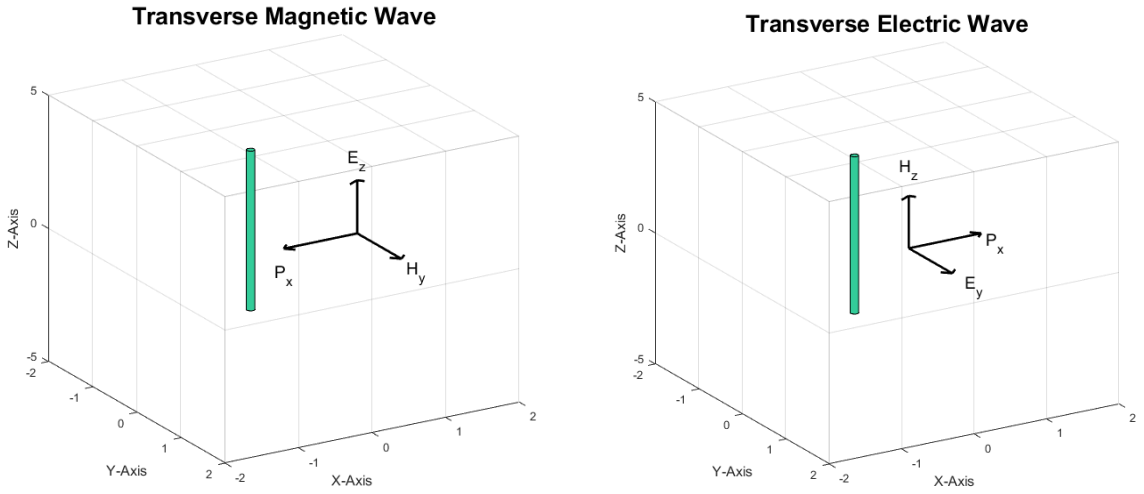

a) b)

Figure 5-5: a) Transverse magnetic wave TM^z propagating in the X-direction impingent on an infinitely long PEC cylinder. b) Transverse electric wave TE^z propagating in the X-direction impingent on an infinitely long PEC cylinder.

After the introductory remarks, a short exposition on electric/magnetic line currents is given, followed by application of the SPM to electromagnetic boundary conditions. The chapter continues with a discussion of the relationship between the far-field spectral signature of a plane wave and discrete Fourier transform. SPM results for axial ratios $\frac{a}{b} = 1$ are validated by comparing them with modal analysis of circular cylinders illuminated by a plane wave. Next, limitations of SPM and methods for dealing with these limitations are discussed, including a method for translating the origin of the problem to analyze structures with large axial ratios. Lastly, results for elliptical cylinders with large axial ratios excited by TM^z and TE^z incident waves are presented.

5.2 Spectral Projection Model Applied to Line Currents

In 2D analysis, the Spectral Projection Model postulates that all incident electromagnetic fields are generated by infinitely long line current sources. Shown below in Figure 5-6 are three independent line sources and their radiated fields.

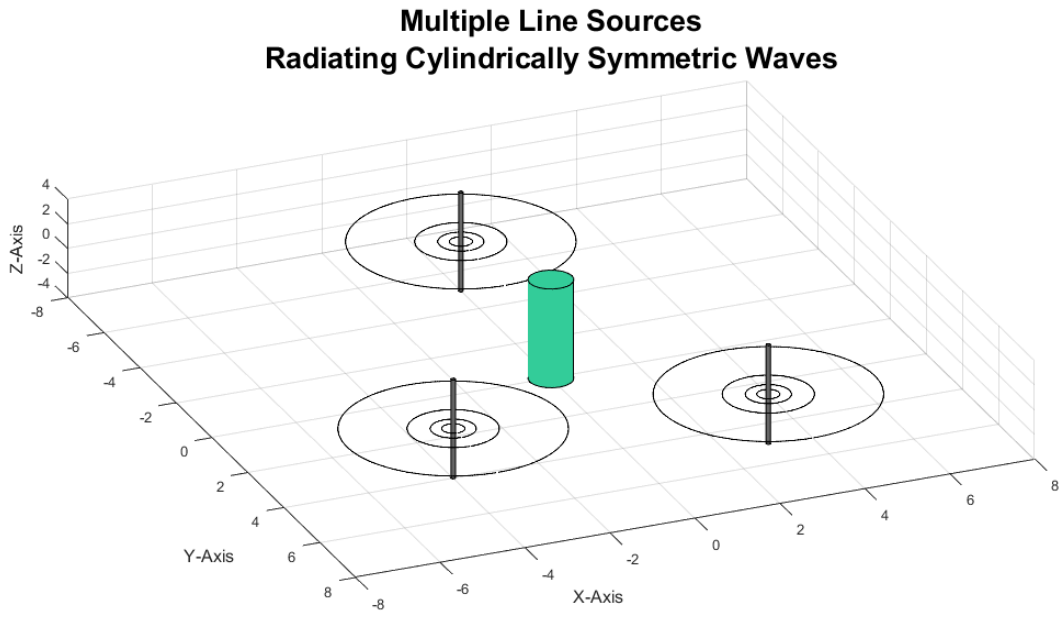

Figure 5-6: Three infinitely long line sources and their radiated fields with an elliptical cylindrical cylinder centered at the origin.

These impressed current line sources produce incident electric and magnetic fields that scatter off PEC objects either in the near-field or far-field depending on the problem statement. The waves are cylindrically symmetric and so can be described by Bessel and Hankel functions. Bessel and Hankel functions are frequently used to represent electromagnetic waves propagating through space they satisfy Maxwell's equations in 2D problems. As $\rho \to \infty$, Hankel functions are used to represent planar wavefronts.

The impressed currents do not change in the presence or absence of the scattering object, and are independent of the total electromagnetic field. The top-view of an infinite line source and its radiated fields is shown in Figure 5-6.

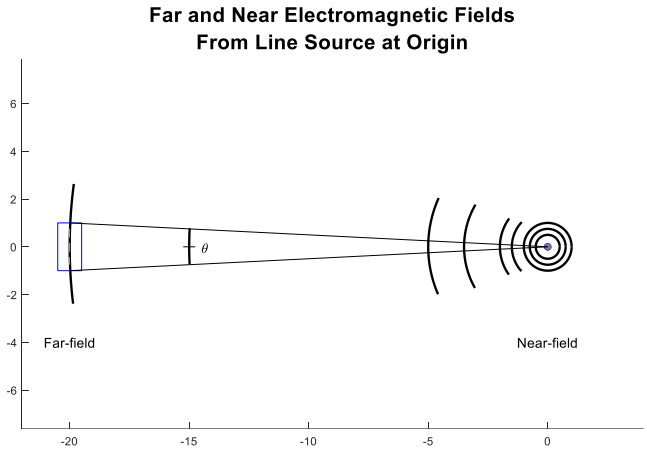

Figure 5-7: Far-field and near-field electromagnetic waves produced by an infinitely long line source. Near-fields radiate as cylindrical waves, far-fields are approximated as plane waves. The far-field plane wave approximation is indicated by the dotted line in the boxed region subtended by the angle θ.

Electric and magnetic line current sources generate electric and magnetic fields that are aligned with the axis of the line source. In order to calculate the electric and magnetic fields scattered by the PEC cylinders, boundary conditions must be applied to the fields at the surface of the PEC cylinders in the presence of these line sources. This process lends itself to application of the addition theorem for solving scattering problems. It will be shown that the addition theorem in equation $(5-3)$ is useful for representing the incident and induced electromagnetic fields.

5.2.1 Representation of Electric and Magnetic Fields using the Spectral Projection Model

For a single electric current line source of current magnitude I_e aligned in the Z-direction, the radiated electric field is given in equation $(5-4)$ from [36].

$$E_z(\beta|\boldsymbol{\rho}-\boldsymbol{\rho}'|) = -\frac{\beta^2 I_e}{4\omega\varepsilon} H_0^{(2)}(\beta|\boldsymbol{\rho}-\boldsymbol{\rho}'|)e^{j\beta(\phi-\phi')} \qquad (5-4)$$

The spatial parameters of equation $(5-4)$ are defined below:

$\boldsymbol{\rho}'$ - vector from the reference origin to the line source at coordinates (ρ', ϕ')

$\boldsymbol{\rho}$ - vector from the reference origin to an observation point at coordinates (ρ, ϕ)

The zeroth order Hankel function of the second kind $H_0^{(2)}(\beta|\boldsymbol{\rho}|)$ is a cylindrically symmetric function. In the near-field, the radiated electric field E_z can be approximated as a cylindrical wave front. See Figure 5-8. The E_ρ, E_ϕ, and H_z components of the electric and magnetic field equal zero for an electric current line source.

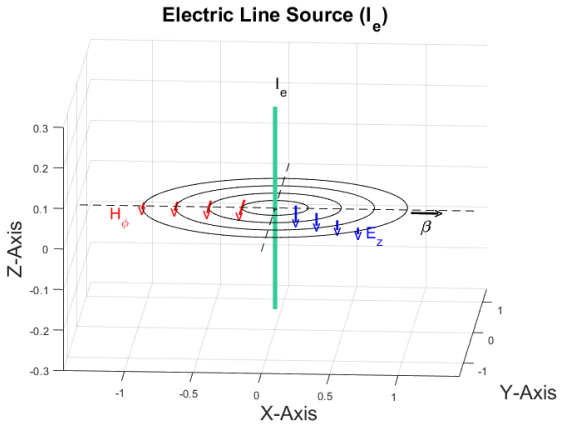

Figure 5-8: Illustration of an electric current line source with electric field, $E_z\hat{\boldsymbol{z}}$, magnetic field, $H_\phi\hat{\boldsymbol{\phi}}$, and direction of propagation $\boldsymbol{\beta} = \hat{\boldsymbol{\rho}}$ positioned at the origin.

In the far-field, the radiated electric field E_z is a plane wave, as illustrated before in Figure 5-6.

Using the principle of duality with substitutions given in equation $(5-5)$,

$$\varepsilon \to \mu \qquad E_z^i \to H_z^i \qquad I_e \to I_m \tag{5-5}$$

from equation $(5-4)$ one can find the magnetic field produced by an equivalent magnetic current line source. The magnetic near-field radiated by a magnetic current line source aligned in the Z-direction is given in equation $(5-6)$.

$$H_z\ (\beta|\boldsymbol{\rho}-\boldsymbol{\rho}'|) = -\frac{\beta^2 I_m}{4\omega\mu} H_0^{(2)}(\beta|\boldsymbol{\rho}-\boldsymbol{\rho}'|)e^{j\beta(\phi-\phi')} \tag{5-6}$$

The components of the electric and magnetic field of the magnetic current line source that equal zero are H_ρ, H_ϕ, and E_z. An illustration of a magnetic current line source is shown in Figure 5-8.

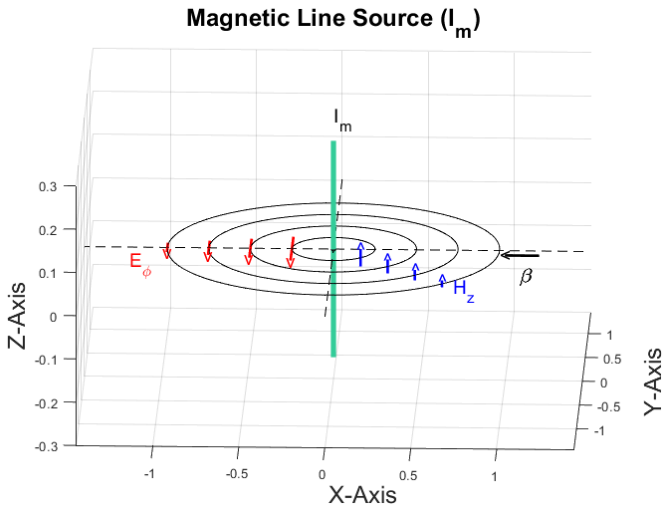

Figure 5-9: Illustration of a magnetic current line source with magnetic field, $H_z\hat{\boldsymbol{z}}$, magnetic field, $E_\phi\hat{\boldsymbol{\phi}}$, and direction of propagation $\boldsymbol{\beta} = \hat{\boldsymbol{\rho}}$.

The addition theorem applied to $H_0^{(2)}(\beta|\boldsymbol{\rho} - \boldsymbol{\rho}'|)$ may be viewed as a projection of one infinitely long vector onto another infinitely long vector. For computational purposes when implementing SPM, the two vectors are truncated at some finite number of *2K+1* modes. This limits the number of modes in the summation expansion, and is adjusted dependent on the size of the object being analyzed. Two forms of a truncated addition theorem are given in equations $(5-7)$ and $(5-8)$.

$$H_0^{(2)}(\beta|\boldsymbol{\rho} - \boldsymbol{\rho}'|) \approx \sum_{k=-K}^{K} H_k^{(2)}(\beta|\boldsymbol{\rho}|)J_k(\beta|\boldsymbol{\rho}'|)e^{jk(\phi-\phi')} \qquad \rho > \rho' \qquad (5-7)$$

$$H_0^{(2)}(\beta|\boldsymbol{\rho} - \boldsymbol{\rho}'|) \approx \sum_{k=-K}^{K} H_k^{(2)}(\beta|\boldsymbol{\rho}'|)J_k(\beta|\boldsymbol{\rho}|)e^{jk(\phi-\phi')} \qquad \rho' > \rho \qquad (5-8)$$

The addition theorem for a single source location (ρ', ϕ') and single observation location (ρ, ϕ) with $\rho' > \rho$ is an inner product. See equation $(5-9)$.

$$H_0^{(2)}(\beta|\boldsymbol{\rho}-\boldsymbol{\rho}'|) \approx$$

$$\left[J_{-K}(\beta|\boldsymbol{\rho}|)e^{-jK\phi} \quad .. \quad J_k\,(\beta|\boldsymbol{\rho}|)e^{jk\phi} \quad ... \quad J_K\,(\beta|\boldsymbol{\rho}|)e^{jK\phi}\right]\begin{bmatrix} H_{-K}^{(2)}(\beta|\boldsymbol{\rho}'|)e^{jK\phi'} \\ .. \\ H_k^{(2)}(\beta|\boldsymbol{\rho}'|)e^{jk\phi'} \\ .. \\ H_K^{(2)}(\beta|\boldsymbol{\rho}'|)e^{-jK\phi'} \end{bmatrix} \qquad (5-9)$$

This inner product is the projection of two vectors, the **H**-spectral signature (or Hankel spectral signature) of a source point, (ρ', ϕ'),

$$e_{sn} = \left[H_{-K}^{(2)}(\beta|\boldsymbol{\rho}'|)e^{jK\phi'} \quad .. \quad H_k^{(2)}(\beta|\boldsymbol{\rho}'|)e^{jk\phi'} \quad ... \quad H_K^{(2)}(\beta|\boldsymbol{\rho}'|)e^{-jK\phi'}\right]^T \qquad (5-10)$$

onto the **J**-spectral signature (or Bessel spectral signature) of an observation point, (ρ, ϕ).

$$e_{om} = [J_{-K}(\beta|\boldsymbol{\rho}|)e^{-jK\phi} \quad .. \quad J_k(\beta|\boldsymbol{\rho}|) \quad ... \quad J_K(\beta|\boldsymbol{\rho}|)e^{jK\phi}]^T \qquad (5-11)$$

The Green's function $H_0^{(2)}(\beta|\boldsymbol{\rho}-\boldsymbol{\rho}'|)$ may now be written as equation $(5-12)$.

$$H_0^{(2)}(\beta|\boldsymbol{\rho}-\boldsymbol{\rho}'|) = e_{om}^T e_{sn} \qquad \rho' > \rho \qquad (5-12)$$

In general, when $\rho' > \rho$ the electric or magnetic field radiated by a line source can be calculated by projecting the **H**-spectral signature of the line source at (ρ', ϕ') onto the **J**-spectral signature of the observation point (ρ, ϕ).

5.2.2 Fields due to Electric Line Sources

This section discusses the derivation of the electromagnetic fields produced by infinitely long electric line sources. Electric line sources radiate cylindrical waves in the near-field and TM^z plane waves in the far-field. For two-dimensional TM-wave scattering, the electric field may be described by a Green's function, the zeroth order Hankel function of the second kind, $H_0^{(2)}(\beta|\boldsymbol{\rho}-\boldsymbol{\rho}'|)$. The magnitude variable $|\boldsymbol{\rho}-\boldsymbol{\rho}'|$of $H_0^{(2)}(\beta|\boldsymbol{\rho}-\boldsymbol{\rho}'|)$ is the distance between the line current source $\boldsymbol{\rho}'$ and the observation point $\boldsymbol{\rho}$ where the fields are calculated. The distance $R = |\boldsymbol{\rho}-\boldsymbol{\rho}'|$ is also defined by the law of cosines discussed later in this chapter.

The radiated electric near-field of an electric current line source was given in equation $(5-4)$, and for a specific line source location (ρ_0', ϕ_0') and observation point (ρ_m, ϕ_m),

$$E_z(\beta|\boldsymbol{\rho_m}-\boldsymbol{\rho_0}'|) = -\frac{\beta^2 I_e}{4\omega\varepsilon}H_0^{(2)}(\beta|\boldsymbol{\rho_m}-\boldsymbol{\rho_0}'|)e^{j\beta(\phi-\phi_0')} \qquad (5-13)$$

and using the addition theorem, the electric field can be expressed as the projection below:

$$E_z(\beta|\boldsymbol{\rho_m} - \boldsymbol{\rho_0}'|) = -\frac{\beta^2 I_e}{4\omega\varepsilon} e_{om}^T e_{sn} \qquad \rho' > \rho \qquad (5-14)$$

According to equation $(5-14)$, the electric field at the m^{th} observation point is the projection of the electric line current source at $n = 0$, i.e. $(\rho_0', \phi_0{}')$ onto the m^{th} observation point. The **H**-spectral signature of the source point e_{sn} and **J**-spectral signature of the observation point e_{om} are defined by the equations below:

$$e_{sn} = \left[H_{-K}^{(2)}(\beta|\boldsymbol{\rho_0}'|)e^{jK\phi_0'} \quad .. \quad H_k^{(2)}(\beta|\boldsymbol{\rho_0}'|)e^{jk\phi_0'} \quad ... \quad H_K^{(2)}(\beta|\boldsymbol{\rho_0}'|)e^{-jK\phi_0'}\right]^T \qquad (5-15)$$

and

$$e_{om} = [J_{-K}(\beta|\boldsymbol{\rho_m}|)e^{-jK\phi_m} \quad .. \quad J_k(\beta|\boldsymbol{\rho_m}|)e^{jk\phi_m} \quad ... \quad J_K(\beta|\boldsymbol{\rho_m}|)e^{jK\phi_m}]^T \qquad (5-16)$$

The radial and azimuthal components of the radiated magnetic fields, H_ρ and H_ϕ, due to the electric line source can be calculated using Faraday's law.

$$\boldsymbol{\nabla \times E} = -\frac{\boldsymbol{\partial B}}{\boldsymbol{\partial t}} \qquad (5-17)$$

Using cylindrical coordinates and rearranging, one can find the $\widehat{\boldsymbol{\rho}}$ and $\widehat{\boldsymbol{\phi}}$ components of the outward magnetic field.

$$\boldsymbol{H} = \frac{-1}{j\omega\mu}\boldsymbol{\nabla \times E_z} \qquad (5-18)$$

$$\boldsymbol{H} = \frac{-1}{j\omega\mu}\left(\widehat{\boldsymbol{\rho}}\frac{1}{\rho}\frac{\partial E_z}{\partial \phi} - \widehat{\boldsymbol{\phi}}\frac{\partial E_z}{\partial \rho}\right) \qquad (5-19)$$

$$H_\rho = -\frac{1}{j\omega\mu\rho}\frac{\partial E_z}{\partial \phi} \qquad (5-20)$$

The Hankel function $H_0^{(2)\prime}(\beta|\boldsymbol{\rho}|)$ is cylindrically symmetric and does not have azimuthal dependence, so $\frac{\partial E_z}{\partial \phi} = 0$. Thus, the ρ component of the magnetic field must be zero.

$$H_\rho = 0 \qquad (5-21)$$

To calculate the ϕ component of the magnetic field, H_ϕ, one uses equation $(5-22)$.

$$H_\phi = \frac{1}{j\omega\mu}\frac{\partial E_z}{\partial \rho} \qquad (5-22)$$

$$H_\phi = \frac{j\beta I_e}{4} H_0^{(2)\prime}(\beta|\boldsymbol{\rho} - \boldsymbol{\rho}'|) \qquad (5-23)$$

where $\frac{j\beta I_e}{4} H_0^{(2)\prime}(\beta|\boldsymbol{\rho}-\boldsymbol{\rho}'|)$ is the derivative of the zeroth order Hankel function of the second kind with respect to the variable ρ.

The azimuthal field, H_ϕ, may be written as a projection of the **H**-spectral signature of the source vector e_{sn} onto the **J**-spectral signature of the observation vector e'_{om}.

$$e_{sn} = \left[H_{-K}^{(2)}(\beta|\boldsymbol{\rho_0}'|)e^{jK\phi_0} \quad .. \quad H_k^{(2)}(\beta|\boldsymbol{\rho_0}'|)e^{jk\phi_0} \quad ... \quad H_K^{(2)}(\beta|\boldsymbol{\rho_0}'|)e^{-jK\phi_0}\right]^T \qquad (5-24)$$

$$e'_{om} = [J_{-K}{}'(\beta|\boldsymbol{\rho_m}|)e^{-jK\phi_m} \quad .. \quad J_k{}'(\beta|\boldsymbol{\rho_m}|)e^{jk\phi_m} \quad ... \quad J_K{}'(\beta|\boldsymbol{\rho_m}|)e^{jK\phi_m}]^T \qquad (5-25)$$

Similar to the electric field, the azimuthal magnetic field at the m^{th} observation point will be the contribution of the magnetic line current source at $(\rho_0', \phi_0{}')$ onto the m^{th} observation point.

$$H_\phi(\rho_m, \rho_0) = \frac{j\beta I_e}{4} e'^T_{om} e_{sn} \qquad (5-26)$$

5.2.3 Hankel Prime Function

One can rewrite the derivative in the expression for H_ϕ using the relation in equation $(5-27)$,

$$H_0^{(2)\prime}(\beta|\boldsymbol{\rho}-\boldsymbol{\rho}'|) = -H_1^{(2)}(\beta|\boldsymbol{\rho}-\boldsymbol{\rho}'|) \qquad (5-27)$$

The expression in $(5-28)$ is of importance in solving MFIE problems using SPM.

$$H_0^{(2)\prime}(\beta|\boldsymbol{\rho}-\boldsymbol{\rho}'|)\cos(\gamma) = -H_1^{(2)}(\beta|\boldsymbol{\rho}-\boldsymbol{\rho}'|)\cos(\gamma) \qquad (5-28)$$

The angle γ is defined in Figure 5-10. The function $H_0^{(2)\prime}(\beta|\boldsymbol{\rho}-\boldsymbol{\rho}'|)$ will be referred to as the zeroth order Hankel Prime function of the second kind. The addition theorem for derivative $H_0^{(2)\prime}(\beta|\boldsymbol{\rho}-\boldsymbol{\rho}'|)$ can be written as

$$H_0^{(2)\prime}(\beta|\boldsymbol{\rho}-\boldsymbol{\rho}'|)\cos(\gamma) = \sum_{k=-\infty}^{\infty} H_k^{(2)}(\beta|\boldsymbol{\rho}'|)J_k{}'(\beta|\boldsymbol{\rho}|)e^{j\beta(\phi-\phi')} \qquad \rho' > \rho \qquad (5-29)$$

and

$$H_0^{(2)\prime}(\beta|\boldsymbol{\rho}-\boldsymbol{\rho}'|)\cos(\gamma) = \sum_{k=-\infty}^{\infty} H_k^{(2)\prime}(\beta|\boldsymbol{\rho}|)J_k(\beta|\boldsymbol{\rho}'|)e^{j\beta(\phi-\phi')} \qquad \rho > \rho' \qquad (5-30)$$

The Hankel Prime function $H_0^{(2)\prime}(\beta|\boldsymbol{\rho}-\boldsymbol{\rho}'|)$ is of major importance to the Spectral Projection Model, especially in the application of the MFIE. This Green's function relates the *Z*-directed electric currents to transverse magnetic fields in TM^z waves. It also relates the Z-

directed magnetic currents to transverse electric fields in TE^z waves. The Spectral Projection Model is founded on the addition theorem representations of the Green's functions $H_0^{(2)}(\beta|\boldsymbol{\rho}-\boldsymbol{\rho}'|)$ and $H_0^{(2)\prime}(\beta|\boldsymbol{\rho}-\boldsymbol{\rho}'|)\cos(\gamma)$. In this chapter, the addition theorem relation for $H_1^{(2)}(\beta|\boldsymbol{\rho}-\boldsymbol{\rho}'|)\cos(\gamma)$ is used in developing the SPM expression for TE^z waves from the MFIE. Figure 5-10 illustrates the important vectors and angle γ for the SPM Green's function. The vector $\boldsymbol{R}=\boldsymbol{\rho}-\boldsymbol{\rho}'$.

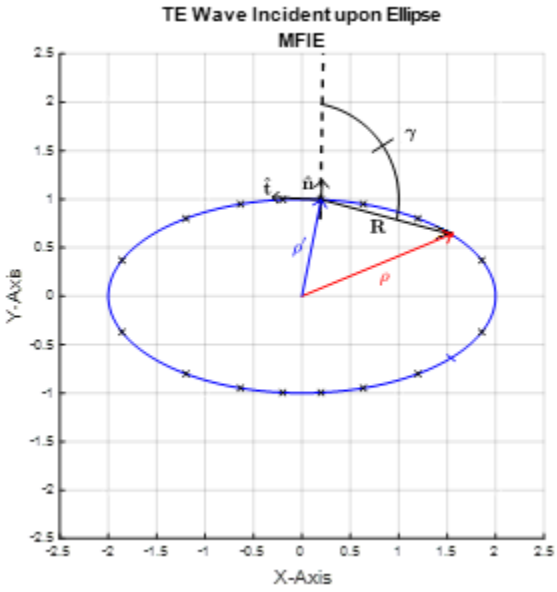

Figure 5-10: Diagram of vectors on an ellipse for MFIE equation.

5.2.4 Fields due to Magnetic Line Sources

The Z-component of the magnetic field of a magnetic line source aligned with the Z-axis is described by equation $(5-31)$,

$$H_z(\beta|\boldsymbol{\rho_m}-\boldsymbol{\rho_0}'|)=-\frac{\beta^2 I_m}{4\omega\mu}H_0^{(2)}(\beta|\boldsymbol{\rho_m}-\boldsymbol{\rho_0}'|)e^{j\beta(\phi-\phi_{0'})} \qquad (5-31)$$

It can be expressed as the projection e_{sn} onto e_{om} below for a line source location at $n=0$, i.e. $(\rho_{0,}\phi_0)$, and observation point $(\rho_{m,}\phi_m)$.

$$H_z(\beta|\boldsymbol{\rho_m}-\boldsymbol{\rho_0}'|)=-\frac{\beta^2 I_m}{4\omega\mu}e_{om}^T e_{sn} \qquad \rho'>\rho \qquad (5-32)$$

The vectors e_{sn} and e_{om} are defined the same as in equations $(5-15)$ and $(5-16)$.

The $\boldsymbol{H_z}$ component may be used to solve for the radial and azimuthal components of the radiated electric field. Using Ampere's law one can find the $\widehat{\boldsymbol{\rho}}$ and $\widehat{\boldsymbol{\phi}}$ components of the outward electric field.

$$\boldsymbol{E} = \frac{1}{j\omega\varepsilon}\boldsymbol{\nabla} \times \boldsymbol{H_z} \tag{5-33}$$

$$\boldsymbol{E} = \frac{1}{j\omega\varepsilon}\left(\widehat{\boldsymbol{\rho}}\frac{1}{\rho}\frac{\partial H_z}{\partial \phi} - \widehat{\boldsymbol{\phi}}\frac{\partial H_z}{\partial \rho}\right) \tag{5-34}$$

$$E_\rho = \frac{1}{j\omega\varepsilon\rho}\frac{\partial H_z}{\partial \phi} \tag{5-35}$$

$$E_\rho = 0 \qquad \frac{\partial H_z}{\partial \phi} = 0 \tag{5-36}$$

and the azimuthal component of the radiated electric field is given in equation $(5-37)$.

$$E_\phi = -\frac{1}{j\omega\varepsilon}\frac{\partial H_z}{\partial \rho} \tag{5-37}$$

$$E_\phi = \frac{j\beta I_m}{4} H_0^{(2)\prime}(\beta|\boldsymbol{\rho} - \boldsymbol{\rho}'|) \tag{5-38}$$

The expression for E_ϕ includes the derivative of the zeroth order Hankel function of the second kind as did the magnetic field H_ϕ for the electric line source. Using the same relation for $H_0^{(2)\prime}(\beta|\boldsymbol{\rho} - \boldsymbol{\rho}'|)$, and the addition theorem for derivatives of $H_0^{(2)\prime}(\beta|\boldsymbol{\rho} - \boldsymbol{\rho}'|)$, the azimuthal electric field for a magnetic line source is given by the projection of e_{sn} onto e'_{om} in equation $(5-39)$,

$$E_\phi = \frac{j\beta I_m}{4} e'^{\,T}_{om} e_{sn} \tag{5-39}$$

with the vector e_{sn} being the spectral signature of the magnetic line current source at $(\rho_{0,}{}'\phi_0{}')$ and e'_{om} the spectral signature of the m^{th} observation point. The two spectral signatures were defined previously in equations $(5-25)$ and $(5-26)$.

5.3 Boundary Conditions Described as Spectral Projections

In this section boundary conditions for SPM will be discussed. A summary of electric field and magnetic field boundary conditions at the surface of a PEC are given in Table 5-1

below. Both transverse magnetic TM^z and transverse electric TE^z plane waves travelling toward an infinitely long cylinder are considered. See Figure 5-11 for illustrations of both.

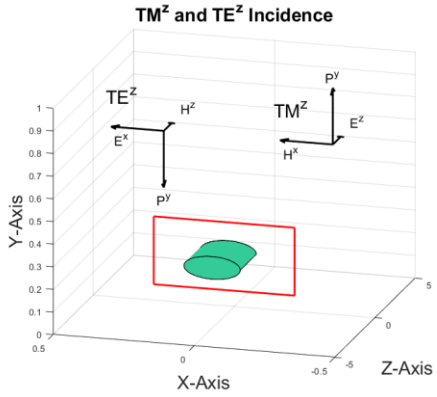

Figure 5-11: TM^z and TE^z incident waves on an infinitely long PEC cylinder of elliptical shape. The direction of propagation is the same as $\mathbf{P_y}$, the Poynting vector. The rectangular box shown around the cross section is the plane of incidence.

Table 5-1: Boundary Conditions for PEC's.

Boundary	Field Equations		Field Conditions
Tangential Electric Field E_{tan}	$E_{tan} = 0$	$n \times E = 0$	Continuous Electric Field
Tangential Magnetic Field H_{tan}	$H_{tan} = J_S$	$n \times H = J_S$	Discontinuity in Magnetic Field equals Surface Current Density J_S
Normal Electric Flux Density D_{norm}	$D_{norm} = \rho_S$	$n \cdot D = \rho_S$	Discontinuity in Electric Flux Density equals Surface Charge Density ρ_S
Normal Magnetic Flux Density B_{norm}	$B_{norm} = 0$	$n \cdot B = 0$	Continuous Magnetic Flux Density

5.3.1 Electric Field Integral Equation for TM^z Incidence on PEC Cylinders

For a TM^z wave, the angle of incidence ϕ_i and the scattering angle ϕ_s are both defined with respect to the positive horizontal axis, as shown in Figure 5-12. TM plane waves are E-polarized because the electric field is perpendicular to the plane of incidence and the magnetic field is transverse or parallel to the plane of incidence. The electric field is aligned with the Z-axis for TM^z waves.

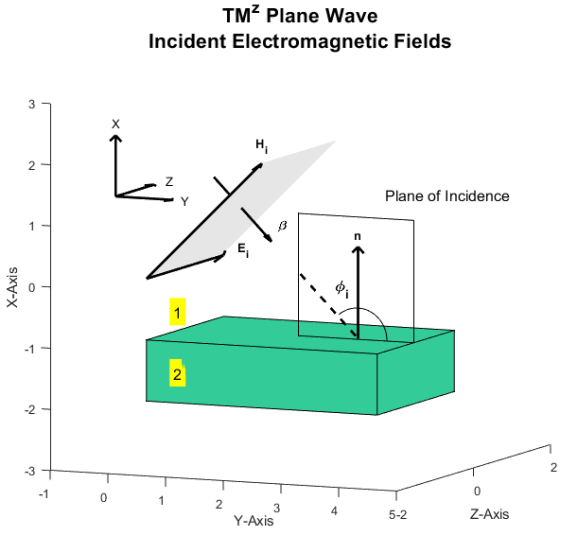

Figure 5-12: Illustration of incident TM^z wave.

Consider an infinitely long PEC cylinder with $\sigma \to \infty$ in free space being excited by a TM^z plane wave. An incident Z-polarized electric field $\boldsymbol{E^i} = \hat{\boldsymbol{z}}E_z$, is parallel to the cylinder axis. The scattered electric field is designated $\boldsymbol{E^s}$. From the above discussion, the electric field inside the perfect electric conductor (medium 2) is $\boldsymbol{E}^{\boldsymbol{PEC}}$, and this electric field $\boldsymbol{E}^{\boldsymbol{PEC}} = \boldsymbol{0}$ inside the conductor and at the boundary.

The boundary condition for the electric field at the surface of a PEC conductor requires that the total tangential electric field must equal zero, i.e. $E_{tan} = 0$. The vector relation is given in equation $(5-40)$.

$$\hat{\boldsymbol{n}} \times (\boldsymbol{E^i} + \boldsymbol{E^s}) = 0 \qquad (5-40)$$

For TM^z waves, the incident electric field $E_z^i\hat{\boldsymbol{z}}$ is polarized only in the Z-direction. The boundary condition for the E_z component at every surface point (ρ, ϕ) is given in equation $(5-41)$. Refer back to Chapter 2 on the Method of Moments for details.

$$E_z^i + E_z^s = 0 \qquad (5-41)$$

The scattered electric field, which was derived in Chapter 2, is related to induced currents and given in equation $(5-42)$.

$$E_z^s(\rho) = -\frac{\omega\mu}{4}\oint_{C'} J_z(|\boldsymbol{\rho}'|)H_0^{(2)}(\beta|\boldsymbol{\rho}-\boldsymbol{\rho}'|)dc' \qquad (5-42)$$

Substituting into equation $(5-42)$ for the boundary conditions, one arrives at the electric field integral equation, EFIE, for TM^z waves.

$$E_z^i(\rho) = \frac{\omega\mu}{4}\oint_{C'} J_z(|\boldsymbol{\rho}'|)H_0^{(2)}(\beta|\boldsymbol{\rho}-\boldsymbol{\rho}'|)dc' \qquad (2-15)$$

The boundary conditions for the EFIE equation are given in matrix equation $(5-43)$. The discretized form of the boundary condition can be written as

$$\begin{bmatrix} \cdots \\ E_{inc} \\ \cdots \end{bmatrix} = -\begin{bmatrix} \cdots \\ E_{ind} \\ \cdots \end{bmatrix} \qquad (5-43)$$

5.3.2 Magnetic Field Integral Equation for TE^z Incidence on PEC Cylinders

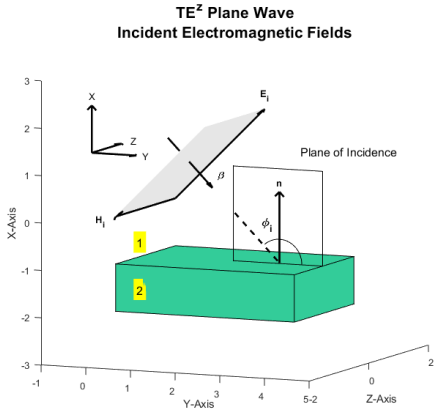

Figure 5-13: Illustration of incident TE^z wave.

An incident TE^z polarized plane wave is illustrated in Figure 5-13. It is oriented with H-polarization because the magnetic field is perpendicular to the plane of incidence and the electric field is transverse or parallel to the plane of incidence.

In this section, the magnetic field integral equation (MFIE) is derived by subjecting a PEC object to a TE^z wave. When the PEC object is subjected to an external stimulus like a TE^z wave, currents are induced on the surface of the conductor. Let vectors $\boldsymbol{H^i}$ and $\boldsymbol{H^s}$ be incident and scattered magnetic field intensities, respectively. At the surface of the cylinder, the induced current density, $\boldsymbol{J_s}$, is equal to the discontinuity in the tangential component of the magnetic field. The surface current is illustrated in Figure 5-14.

$$\boldsymbol{J_S} = \hat{\boldsymbol{n}} \times (\boldsymbol{H^i} + \boldsymbol{H^s}) \qquad (5-44)$$

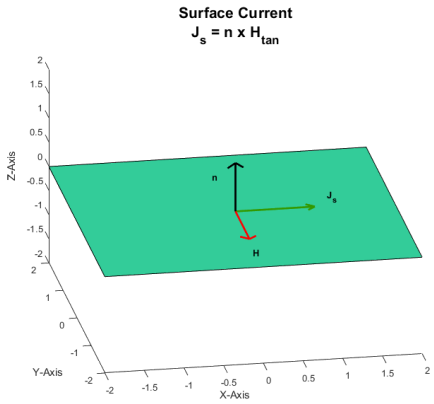

Figure 5-14: Illustration of Surface Current $\boldsymbol{J_s = n \times H_{tan}}$.

For a Z-directed transverse electric TE^z wave, the incident magnetic field, $\boldsymbol{H^i} = H_z^i \hat{\boldsymbol{z}}$, is parallel to the cylinder axis for TE^z plane waves, as is the scattered magnetic field $\boldsymbol{H^s} = H_z^s \hat{\boldsymbol{z}}$.

For an observation point (ρ_m, ϕ_m), and current element dc' along contour C, one can integrate and find the scattered magnetic field along the contour of the cylinder. See Chapter 2 on the Method of Moments for the derivation of the MFIE.

$$H_z^s(\rho_m) = \frac{j\beta}{4} \int_{C-\Delta C} J_C(|\boldsymbol{\rho}'|) cos(\gamma) H_1^{(2)}(\beta|\boldsymbol{\rho_m} - \boldsymbol{\rho}'|) dc' \qquad (5-45)$$

Then, substituting into equation $(5-45)$, the MFIE for TE^z waves at observation point ρ_m can now be written as equation $(2-20)$,

$$H_z^i(\rho_m) = \frac{J_C(\rho_m)}{2} + \frac{j\beta}{4} \int_{C-\Delta C} J_C(|\boldsymbol{\rho}'|) cos(\gamma) H_1^{(2)}(\beta|\boldsymbol{\rho_m} - \boldsymbol{\rho}'|) dc' \qquad (2-20)$$

where the incident field at observation point (ρ_m, ϕ_m) is $H_z^i(\rho_m)$.

The term J_C is the current along the contour *C*. For the self-term $\rho_m = \rho_n{}'$, the integral goes to zero because $\gamma = 90^o$. The current at the self -term is calculated using the Kronecker delta function, and because of this the surface current term can be expressed as in equation $(5-46)$.

$$J_C(\rho_m = \rho_n{}') = \frac{\delta_{mn\prime}}{2} \qquad (5-46)$$

The term, $J_C(\rho_m = \rho_n{}') = 0.5$, is the coefficient of the basis function for the surface current at the self-term, and $\boldsymbol{J_s}$ equals the integral when $m \neq n$ and $\gamma \neq 90^o$. This integral term thus includes the coefficients $J_{C\ m,n}$ for all $m \neq n$, and the self-term for the case $\rho_m = \rho_n{}'$. Thus, upon discretization, integral terms can be represented by a single matrix when coding as long as the Green's function is set to 0.5 at $m = n$, i.e. Kronecker delta function. This matrix relation is given in the matrix equation $(5-48)$, where $\begin{bmatrix} \cdots \\ H_{inc} \\ \cdots \end{bmatrix}$ and $\begin{bmatrix} \cdots \\ H_{ind} \\ \cdots \end{bmatrix}$ are $M \times 1$ vectors.

$$\begin{bmatrix} \cdots \\ H_{inc} \\ \cdots \end{bmatrix} = -\begin{bmatrix} \cdots \\ H_{ind} + J_C(\rho_m = \rho_n{}') \\ \cdots \end{bmatrix} \qquad (5-47)$$

5.3.3 Summary Table of EFIE and MFIE for TM^z and TE^z Waves

The Electric Field Integral Equation (EFIE) and Magnetic Field Integral Equation (MFIE) may both be used to solve TM and TE wave problems. An EFIE may be written by enforcing the electric field boundary conditions at the surface of the conductor, and a MFIE may be written from enforcing the magnetic field boundary conditions just inside the surface of the conductor. The four equations are given in Table 5-2.

From Table 5-2, application of the EFIE* is the most direct way to solve TM^z wave problems, and the MFIE* is usually the best way to solve TE^z wave scattering problems through enforcement of the boundary conditions.

Table 5-2: EFIE and MFIE for TM^z and TE^z Waves.

Transverse Magnetic Waves (TM^z)	
$E_z^i(\rho) = \frac{\omega\mu}{4}\oint_C J_z(\rho')H_0^{(2)}(\beta R)dc$	$EFIE^*$
$H_C^i(\rho)\Big\|_C = J_z(\rho)\Big\|_C + \frac{j\beta}{4}\lim_{\rho\to C}\left(\int_{C-\Delta C} J_z(\rho')cos(\gamma)H_1^{(2)}(\beta R)dc'\right)$	$MFIE$
Transverse Electric Waves (TE^z)	
$-E_c^i(\rho) = \frac{\eta}{4\beta}\left\{\beta^2\oint_C J_c(\rho')\left[\hat{c}\cdot\hat{c}'H_0^{(2)}(\beta R)\right]dc' + \frac{d}{dc}\left[\nabla\cdot\oint_C J_c(\rho')\left[\hat{c}H_0^{(2)}(\beta R)\right]dc'\right]\right\}$	$EFIE$
$-H_z^i(\rho) = H_z^i(\rho_m) = \frac{J_C(\rho_m)}{2} + \frac{j\beta}{4}\int_{C-\Delta C} J_C(\rho')cos(\gamma)H_1^{(2)}(\beta\|\rho_m - \rho'\|)dc'$	$MFIE^*$

5.3.4 Spectral Projection Model Applied to the Electric Field Integral Equation

The boundary condition for EFIE using $(2-15)$ is that the incident electric field, E_{inc}, at each point on the PEC boundary surface must equal negative the scattered or induced wave E_{ind}. From equation $(5-40)$, for *N* external source points and *N* induced source points, this is given in matrix equation $(5-43)$, where $\begin{bmatrix}\cdots\\ E_{inc}\\ \cdots\end{bmatrix}$ and $\begin{bmatrix}\cdots\\ E_{ind}\\ \cdots\end{bmatrix}$ are $N\times 1$ vectors.

$$\begin{bmatrix}\cdots\\ E_{inc}\\ \cdots\end{bmatrix} = -\begin{bmatrix}\cdots\\ E_{ind}\\ \cdots\end{bmatrix} \qquad (5-48)$$

The incident or external electric field on the surface of the conductor may be illuminated by a nearby external electric line current source or plane wave from the far-field.

As stated earlier for infinitely long conducting structures, the Green's function for TM^z waves is $H_0^{(2)}(\beta|\boldsymbol{\rho}-\boldsymbol{\rho}'|)$. The Spectral Projection Model applies the addition theorem to decompose this Green's function into the sum of products of Bessel and Hankel functions. The relative positions of ρ and ρ' determine whether the addition theorem for the induced or the addition theorem for the incident fields must be employed. Both equations are shown below.

$$H_0^{(2)}(\beta|\boldsymbol{\rho}-\boldsymbol{\rho}'|)=\sum_{k=-\infty}^{\infty}J_k(\beta|\boldsymbol{\rho}'|)H_k^{(2)}(\beta|\boldsymbol{\rho}|)e^{jk(\phi-\phi')} \qquad \rho>\rho' \qquad (5-49)$$

Induced Fields

$$H_0^{(2)}(\beta|\boldsymbol{\rho}-\boldsymbol{\rho}'|)=\sum_{k=-\infty}^{\infty}J_k(\beta|\boldsymbol{\rho}|)H_k^{(2)}(\beta|\boldsymbol{\rho}'|)e^{jk(\phi-\phi')} \qquad \rho<\rho' \qquad (5-50)$$

Incident Fields

5.3.4.1 Scattered Electric Field and Spectral Signature of Induced Electric Currents from the EFIE using the Spectral Projection Model

The scattered or induced electric field can be calculated by applying the boundary conditions in this EFIE. The induced electric field at the surface of the conductor as the projection of the **J**-spectral signature of the source points (ρ',ϕ') onto the **H**-spectral signature of the observation points (ρ,ϕ). The amplitude and phase of the induced currents at the surface of the conductor are contained in the vector $\begin{bmatrix}\cdots\\ \hat{\imath}_{ind}\\ \cdots\end{bmatrix}$.

$$\begin{bmatrix}\cdots\\ E_{ind}\\ \cdots\end{bmatrix}=\frac{\omega\mu}{4}\begin{bmatrix}\cdots & \cdots & \cdots\\ \cdots & H_k^{(2)}(\beta|\boldsymbol{\rho}|)e^{jk\phi} & \cdots\\ \cdots & \cdots & \cdots\end{bmatrix}^T\begin{bmatrix}\cdots & \cdots & \cdots\\ \cdots & J_k\,(\beta|\boldsymbol{\rho}'|)e^{-jk\phi'} & \cdots\\ \cdots & \cdots & \cdots\end{bmatrix}\begin{bmatrix}\cdots\\ \hat{\imath}_{ind}\\ \cdots\end{bmatrix}$$

$$\rho>\rho' \qquad (5-51)$$

In equation $(5-52)$, the columns of $\begin{bmatrix}\cdots & \cdots & \cdots\\ \cdots & J_k\,(\beta|\boldsymbol{\rho}'|)e^{-jk\phi'} & \cdots\\ \cdots & \cdots & \cdots\end{bmatrix}$ are the **J**-spectral signature of the source points,

$$\begin{bmatrix}| & | & |\\ | & J_k\,(\beta|\boldsymbol{\rho}'|)e^{-jk\phi} & |\\ | & | & |\end{bmatrix}=$$

$$\begin{bmatrix}J_{-K}(\beta|\boldsymbol{\rho_0}'|)e^{jK\phi_0} & : & : & : & J_{-K}\left(\beta\left|\boldsymbol{\rho_{N_O-1'}}\right|\right)e^{jK\phi_{N_O-1}}\\ : & : & : & : & :\\ : & : & : & : & :\\ : & : & : & : & :\\ J_K\,(\beta|\boldsymbol{\rho_0}'|)e^{-jK\phi_{0'}} & : & : & : & J_K\left(\beta\left|\boldsymbol{\rho_{N_O-1}}'\right|\right)e^{-jK\phi_{N_O-1'}}\end{bmatrix} \qquad (5-52)$$

The left side of equation $(5-52)$ illustrates this concept of columnar spectral signature in a descriptive matrix with the | vertical bar symbol.

The rows of the matrix transpose $\begin{bmatrix} \cdots & \cdots & \cdots \\ \cdots & H_k^{(2)}(\beta|\boldsymbol{\rho}|)e^{jk\phi} & \cdots \\ \cdots & \cdots & \cdots \end{bmatrix}^T$ are the **H**-spectral signature of the observation points.

$$\begin{bmatrix} - & - & - \\ - & H_k\ (\beta|\boldsymbol{\rho}|)e^{jk\phi} & - \\ - & - & - \end{bmatrix}^T =$$

$$\begin{bmatrix} H_{-K}^{(2)}(\beta|\boldsymbol{\rho_0}|)e^{-jK\phi_0} & \cdots & \cdots & \cdots & H_K^{(2)}(\beta|\boldsymbol{\rho_0}|)e^{jK\phi_0} \\ \cdots & \cdots & \cdots & \cdots & \cdots \\ \cdots & \cdots & \cdots & \cdots & \cdots \\ \cdots & \cdots & \cdots & \cdots & \cdots \\ H_{-K}^{(2)}\left(\beta\left|\boldsymbol{\rho_{N_S-1}}\right|\right)e^{-jK\phi_{N_S-1}} & \cdots & \cdots & \cdots & H_K^{(2)}\left(\beta\left|\boldsymbol{\rho_{N_S-1}}\right|\right)e^{jK\phi_{N_S-1}} \end{bmatrix} \qquad (5-53)$$

The **H**-spectral signature subspace is organized in rows as shown with the – slash symbol. Equation $(5-51)$ may now be written with the descriptive matrices below:

$$\begin{bmatrix} \cdots \\ E_{ind} \\ \cdots \end{bmatrix} = \frac{\omega\mu}{4}\begin{bmatrix} - & - & - \\ - & H_k\ (\beta|\boldsymbol{\rho}|)e^{jk\phi} & - \\ - & - & - \end{bmatrix}^T \begin{bmatrix} | & | & | \\ | & J_k\ (\beta|\boldsymbol{\rho'}|)e^{-jk\phi} & | \\ | & | & | \end{bmatrix}\begin{bmatrix} | \\ \hat{\imath}_{ind} \\ | \end{bmatrix}$$

$$\rho > \rho' \qquad (5-54)$$

In most numerical electromagnetic methods, the scattering problems are solved for the induced surface current $\begin{bmatrix} \cdots \\ \hat{\imath}_{ind} \\ \cdot\cdot \end{bmatrix}$. In the Spectral Projection Model, it is only necessary to solve for the spectral signature of the induced surface current.

The **J**-spectral signature of the induced current $\begin{bmatrix} \cdots \\ \hat{\imath}_{iss,ind} \\ \cdot\cdot \end{bmatrix}$ on the surface of the conductor is found from equation $(5-54)$ by applying the linear transformation and shown in equation $(5-55)$.

$$\begin{bmatrix} \cdots \\ \hat{\imath}_{iss,ind} \\ \cdot\cdot \end{bmatrix} = \frac{\omega\mu}{4}\begin{bmatrix} \vdots & \vdots & \vdots \\ \vdots & J_k\ (\beta|\boldsymbol{\rho'}|)e^{-jk\phi'} & \vdots \\ \vdots & \vdots & \vdots \end{bmatrix}\begin{bmatrix} \cdots \\ \hat{\imath}_{ind} \\ \cdot\cdot \end{bmatrix} \qquad \rho > \rho' \qquad (5-55)$$

The induced electric field is equal to the **J**-spectral signature of the induced surface current $\begin{bmatrix} \cdots \\ \hat{\imath}_{iss,ind} \\ \cdot\cdot \end{bmatrix}$ projected onto the **H**-spectral signature subspace $\begin{bmatrix} \cdots & \cdots & \cdots \\ \cdots & H_k\ (\beta|\boldsymbol{\rho}|)e^{jk\phi} & \cdots \\ \cdots & \cdots & \cdots \end{bmatrix}^T$ of the observation points at (ρ_m, ϕ_m).

Thus equation $(5-55)$ may be written as $(5-56)$.

$$\begin{bmatrix} \cdots \\ E_{ind} \\ \cdots \end{bmatrix} = \begin{bmatrix} \cdots & \cdots & \cdots \\ \cdots & H_k\ (\beta|\boldsymbol{\rho}|)e^{jk\phi} & \cdots \\ \cdots & \cdots & \cdots \end{bmatrix}^T \begin{bmatrix} \cdots \\ \hat{\imath}_{iss,ind} \\ \cdots \end{bmatrix} \qquad \rho > \rho' \qquad (5-56)$$

Equation $(5-56)$ describes the scattered electric fields as a projection of the **J**-spectral signature of the current onto the **H**-spectral signature of each observation point where the field is to be evaluated.

5.3.4.2 Incident Electric Field and Spectral Signature of Incident Electric Currents from the EFIE using the Spectral Projection Model

A Z-directed electric line source I_e generates an electric field $E = E_z\hat{\boldsymbol{z}}$ in the near field, and a TM^z plane wave if placed in the far-field. See Figure 5-15a and 5-15b.

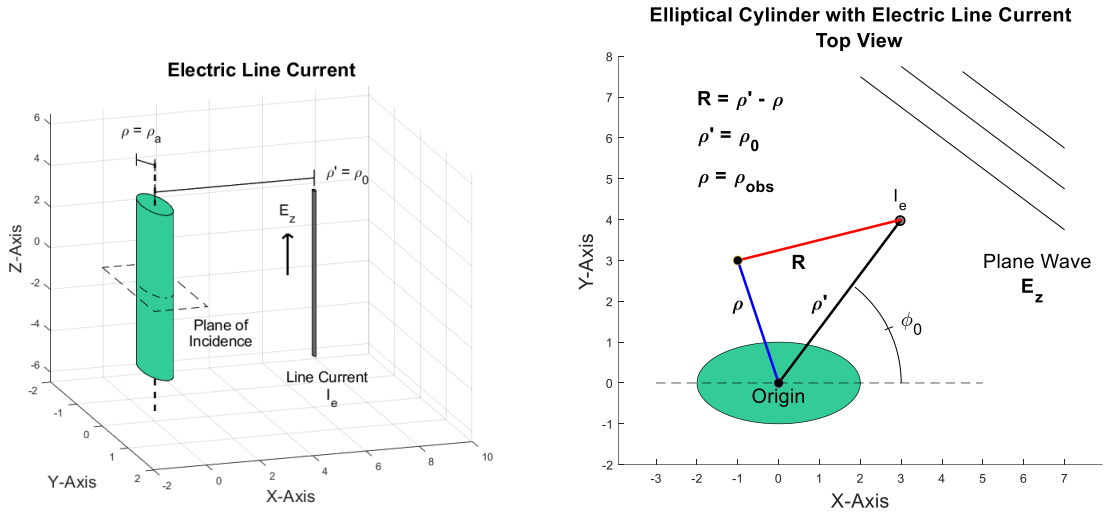

a) b)

Figure 5-15: a) Illustration of electric line current and elliptical cylinder. b) Top view of electric line source near a PEC elliptical cylinder and a TM^z plane wave impingent on the cylinder.

Shown in Figure 5-15 are two views of an elliptical cylinder excited by two external sources, a line source and a TM^z plane wave. In Figure 5-15a the surface of the cylinder radius is a function of the azimuthal angle ϕ, $\rho = f(\phi)$, and the dotted square around the cross section of the cylinder is the plane of incidence. In Figure 5-15b is a top view of the cylinder showing vectors ρ, ρ', and , R. The distance from the origin to the line source $\rho' = \rho_0$ is illustrated, as

well as its angle of incidence, ϕ_0. The angle of incidence of the E_z plane wave is also shown as ϕ_0.

The **H**-spectral signature of the line source at (ρ_0', ϕ_0') shown above is given in equation $(5-57)$,

$$e_{sn} = \left[H_{-K}^{(2)}(\beta|\boldsymbol{\rho_0}'|)e^{jK\phi_0'} \quad .. \quad H_k^{(2)}(\beta|\boldsymbol{\rho_0}'|)e^{jk\phi_0'} \quad ... \quad H_K^{(2)}(\beta|\boldsymbol{\rho_0}'|)e^{-jK\phi_0'}\right]^T \qquad (5-57)$$

and the **J**-spectral signature of an observation point $(\rho_{m,}\phi_m)$ on the surface of the cylinder is given in equation $(5-58)$.

$$e_{om} = [J_{-K}(\beta|\boldsymbol{\rho_m}|)e^{-jK\phi_m} \quad .. \quad J_k(\beta|\boldsymbol{\rho_m}|)e^{jk\phi_m} \quad ... \quad J_K(\beta|\boldsymbol{\rho_m}|)e^{jK\phi_m}]^T \qquad (5-58)$$

For a single electric current line source at (ρ_0', ϕ_0') and single observation point at $(\rho_{m,}\phi_m)$, the incident electric field was shown to be the projection given in equation $(5-14)$.

$$E_z(\beta|\boldsymbol{\rho_m} - \boldsymbol{\rho_0}'|) = -\frac{\beta^2 I_e}{4\omega\varepsilon} e_{om}^T e_{sn} \qquad \rho' > \rho \qquad (5-14)$$

This vector product is the made up of two vectors, the **H**-spectral signature (or Hankel spectral signature) of the source point projected onto the **J**-spectral signature (or Bessel spectral signature) of the observation point.

The Spectral Projection Model applies the addition theorem to represent the incident electric field at the surface of the conductor as the projection of the **H**-spectral signature of all the source points (ρ', ϕ') onto the **J**-spectral signature of all the observation points (ρ, ϕ). For external sources, this relationship can be expressed in matrix form as equation $(5-59)$.

$$\begin{bmatrix} \cdots \\ E_{inc} \\ \cdots \end{bmatrix} = \begin{bmatrix} \cdots & \cdots & \cdots \\ \cdots & J_k(\beta|\boldsymbol{\rho}|)e^{jk\phi} & \cdots \\ \cdots & \cdots & \cdots \end{bmatrix}^T \begin{bmatrix} \cdots & \cdots & \cdots \\ \cdots & H_k\,(\beta|\boldsymbol{\rho}'|)e^{-jk\phi'} & \cdots \\ \cdots & \cdots & \cdots \end{bmatrix} \begin{bmatrix} \cdots \\ \hat{\imath}_{inc,Ie} \\ .. \end{bmatrix} \qquad \rho < \rho' \qquad (5-59)$$

The vector $\begin{bmatrix} \cdots \\ \hat{\imath}_{inc,Ie} \\ .. \end{bmatrix}$ is the incident line electric current source vector. The matrix $\begin{bmatrix} \cdots & \cdots & \cdots \\ \cdots & H_k^{(2)}(\beta|\boldsymbol{\rho}'|)e^{-jk\phi'} & \cdots \\ \cdots & \cdots & \cdots \end{bmatrix}$ in equation $(5-60)$ is the matrix representation of the **H**-spectral signatures of the N_S source points and $2K+1$ modes. The size of the **H**-spectral signature matrix is $(2K+1) \times N_S$.

$$\begin{bmatrix} | & | & | \\ | & H_k^{(2)}(\beta|\boldsymbol{\rho}'|)e^{-jk\phi'} & | \\ | & | & | \end{bmatrix} =$$

$$\begin{bmatrix} H_{-K}^{(2)}(\beta|\boldsymbol{\rho_0}'|)e^{jK\phi_0'} & : & : & : & H_{-K}^{(2)}\left(\beta\left|\boldsymbol{\rho_{N_S-1}}'\right|\right)e^{jK\phi_{N_S-1}'} \\ : & : & : & : & : \\ : & : & H_k\ (\beta|\boldsymbol{\rho}'|)e^{-jk\phi'} & : & : \\ : & : & : & : & : \\ H_K^{(2)}(\beta|\boldsymbol{\rho_0}'|)e^{-jK\phi_0'} & : & : & : & H_K^{(2)}\left(\beta\left|\boldsymbol{\rho_{N_S-1}}'\right|\right)e^{-jK\phi_{N_S-1}'} \end{bmatrix} \qquad (5-60)$$

Each column vector is the **H**-spectral signature of a single source at (ρ_n', ϕ_n'), as indicated by the | symbol in the matrix.

From equation $(5-59)$, one can calculate the **H**-spectral signature of the incident current on the surface of the conductor using the relation as shown in equation $(5-61)$.

$$\begin{bmatrix} \cdots \\ \hat{\imath}_{ss,inc,Ie} \\ \cdot\cdot \end{bmatrix} = \begin{bmatrix} \cdots & \cdots & \cdots \\ \cdots & H_k^{(2)}(\beta|\boldsymbol{\rho}'|)e^{-jk\phi'} & \cdots \\ \cdots & \cdots & \cdots \end{bmatrix} \begin{bmatrix} \cdots \\ \hat{\imath}_{inc,Ie} \\ \cdot\cdot \end{bmatrix} \qquad \rho < \rho' \qquad (5-61)$$

given

$$\begin{bmatrix} \cdots \\ E_{inc} \\ \cdots \end{bmatrix} = \begin{bmatrix} \cdots & \cdots & \cdots \\ \cdots & J_k(\beta|\boldsymbol{\rho}|)e^{jk\phi} & \cdots \\ \cdots & \cdots & \cdots \end{bmatrix}^T \begin{bmatrix} \cdots \\ \hat{\imath}_{ss,inc,Ie} \\ \cdot\cdot \end{bmatrix} \qquad \rho < \rho' \qquad (5-62)$$

The matrix $\begin{bmatrix} \cdots & \cdots & \cdots \\ \cdots & J_k(\beta|\boldsymbol{\rho}|)e^{jk\phi} & \cdots \\ \cdots & \cdots & \cdots \end{bmatrix}^T$ in equation $(5-62)$ is the matrix representation of the corresponding **J**-spectral signature subspace for M_O observation points. This is given in equation $(5-63)$. The size of the **J**-spectral signature matrix is $(2K+1) \times M_O$.

$$\begin{bmatrix} - & - & - \\ - & J_k(\beta|\boldsymbol{\rho}|)e^{jk\phi} & - \\ - & - & - \end{bmatrix}^T =$$

$$\begin{bmatrix} J_{-K}(\beta|\boldsymbol{\rho_0}|)e^{-jK\phi_0} & \cdots & \cdots & \cdots & J_K(\beta|\boldsymbol{\rho_0}|)e^{jK\phi_0} \\ \cdots & \cdots & \cdots & \cdots & \cdots \\ \cdots & \cdots & J_k(\beta|\boldsymbol{\rho}|)e^{jk\phi} & \cdots & \cdots \\ \cdots & \cdots & \cdots & \cdots & \cdots \\ J_{-K}\left(\beta\left|\boldsymbol{\rho_{M_O-1}}\right|\right)e^{-jK\phi_{M_O-1}} & \cdots & \cdots & \cdots & J_K\left(\beta\left|\boldsymbol{\rho_{M_O-1}}\right|\right)e^{jK\phi_{M_O-1}} \end{bmatrix} \qquad (5-63)$$

Each row vector is the **J**-spectral signature of a single observation point (ρ_m, ϕ_m). So, one can rewrite equation $(5-59)$ in terms of column and row spectral signatures in $(5-64)$,

$$\begin{bmatrix} \cdots \\ E_{inc} \\ \cdots \end{bmatrix} = \begin{bmatrix} - & - & - \\ - & J_k(\beta|\boldsymbol{\rho}|)e^{jk\phi} & - \\ - & - & - \end{bmatrix}^T \begin{bmatrix} | & | & | \\ | & H_k^{(2)}(\beta|\boldsymbol{\rho}'|)e^{-jk\phi'} & | \\ | & | & | \end{bmatrix} \begin{bmatrix} | \\ \hat{\imath}_{inc,Ie} \\ | \end{bmatrix}$$

$$\rho < \rho' \qquad (5-64)$$

or in terms of the spectral signature of incident currents,

$$\begin{bmatrix} \cdots \\ E_{inc} \\ \cdots \end{bmatrix} = \begin{bmatrix} - & - & - \\ - & J_k(\beta|\boldsymbol{\rho}|)e^{jk\phi} & - \\ - & - & - \end{bmatrix}^T \begin{bmatrix} | \\ \hat{\imath}_{ss,inc,Ie} \\ | \end{bmatrix} \qquad \rho < \rho' \qquad (5-65)$$

Equation $(5-65)$ describes the incident electric fields as the projection of the **H**-spectral signatures of the sources onto the **J**-spectral signatures of the observation points where the fields are to be evaluated.

For the external electric fields, $\rho < \rho'$, the observation points are on the surface of the cylinder, and the sources ${\rho_n}'$ for $n \in \{0,1, \ldots, N-1\}$ are outside the target cylinder. Returning to a single electric current line source, the external electric field E_{inc} for this line source may also be written as the projection of the **H**-spectral signature of the incident current $\begin{bmatrix} \cdots \\ \hat{\imath}_{ss,inc,Ie} \\ \cdot\cdot \end{bmatrix}$ from line source location at $({\rho_0}', {\phi_0}')$ onto the **J**-spectral signature of all the observation points.

$$\begin{bmatrix} \cdots \\ E_{inc} \\ \cdots \end{bmatrix} = \begin{bmatrix} \cdots & \cdots & \cdots \\ \cdots & J_k(\beta|\boldsymbol{\rho}|)e^{jk\phi} & \cdots \\ \cdots & \cdots & \cdots \end{bmatrix}^T \begin{bmatrix} \cdots \\ \hat{\imath}_{ss,inc,Ie} \\ \cdot\cdot \end{bmatrix} \qquad \rho < \rho' \qquad (5-66)$$

Now one can write equation $(5-67)$ from $(5-64)$ for the incident current spectral signature.

$$\begin{bmatrix} \cdots \\ \hat{\imath}_{ss,inc,Ie} \\ \cdot\cdot \end{bmatrix} = \begin{bmatrix} \cdots & \cdots & \cdots \\ \cdots & H_k^{(2)}(\beta|\boldsymbol{\rho}'|)e^{-jk\phi\prime} & \cdots \\ \cdots & \cdots & \cdots \end{bmatrix} \begin{bmatrix} \cdots \\ \hat{\imath}_{inc,Ie} \\ \cdot\cdot \end{bmatrix} \qquad \rho < \rho' \qquad (5-67)$$

For a single electric line source, the vector $\begin{bmatrix} \cdots \\ \hat{\imath}_{inc,Ie} \\ \cdot\cdot \end{bmatrix}$ contains all zeros except for the row corresponding to angle ${\phi_0}'$. This non-zero row of the vector $\begin{bmatrix} \cdots \\ \hat{\imath}_{inc,Ie} \\ \cdot\cdot \end{bmatrix}$ will correspond to the column of the $\begin{bmatrix} \cdots & \cdots & \cdots \\ \cdots & H_k\ (\beta|\boldsymbol{\rho}'|)e^{-jk\phi\prime} & \cdots \\ \cdots & \cdots & \cdots \end{bmatrix}$ matrix with the source $({\rho_0}', {\phi_0}')$ coordinates.

For the example, below in equation $(5-68)$, the source coordinates are in the first row of $\begin{bmatrix} \cdots \\ \hat{\imath}_{inc,Ie} \\ \cdot\cdot \end{bmatrix}$.

$$\begin{bmatrix} \cdots \\ \hat{\imath}_{ss,inc,Ie} \\ \cdot\cdot \end{bmatrix} = \begin{bmatrix} H_{-K}^{(2)}(\beta|\boldsymbol{\rho_0}'|)e^{jK\phi_0\prime} & \cdots & \cdots & \cdots & H_{-K}^{(2)}\left(\beta\left|\boldsymbol{\rho_{N_S-1}}'\right|\right)e^{jK\phi_{N_S-1}\prime} \\ \vdots & \vdots & \vdots & \vdots & \vdots \\ \vdots & \vdots & \vdots & \vdots & \vdots \\ \vdots & \vdots & \vdots & \vdots & \vdots \\ H_K^{(2)}(\beta|\boldsymbol{\rho_0}'|)e^{-jK\phi_0\prime} & \cdots & \cdots & \cdots & H_K^{(2)}\left(\beta\left|\boldsymbol{\rho_{N_S-1}}'\right|\right)e^{-jK\phi_{N_S-1}\prime} \end{bmatrix} \begin{bmatrix} -\dfrac{\beta^2 I_e}{4\omega\varepsilon} \\ 0 \\ \vdots \\ \vdots \\ 0 \end{bmatrix} \qquad (5-68)$$

Simplifying the matrix product $(5-68)$, the vector $\begin{bmatrix} \cdots \\ \hat{\imath}_{ss,inc,Ie} \\ \cdot\cdot \end{bmatrix}$ for a line source is given in equation $(5-69)$.

$$\begin{bmatrix} \cdots \\ \hat{\imath}_{ss,inc,Ie} \\ \cdot\cdot \end{bmatrix} = -\frac{\beta^2 I_e}{4\omega\varepsilon} \begin{bmatrix} H_{-K}^{(2)}(\beta|\boldsymbol{\rho_0}'|)e^{jK\phi_0'} \\ \vdots \\ H_k^{(2)}(\beta|\boldsymbol{\rho_0}'|)e^{-jk\phi_0'} \\ \vdots \\ H_K^{(2)}(\beta|\boldsymbol{\rho_0}'|)e^{-jK\phi_0'} \end{bmatrix} \tag{5-69}$$

This vector $\begin{bmatrix} \cdots \\ \hat{\imath}_{ss,inc,Ie} \\ \cdot\cdot \end{bmatrix}$ represents the **H**-spectral signature of a single line source located at (ρ_0', ϕ_0').

For an external electric line source at infinity $\rho_0' \to \infty$, the resulting electric field is a plane wave. The large argument approximation for a Hankel function is given in equation $(5-70)$.

$$H_k^{(2)}(\beta|\boldsymbol{\rho_0}'|)|_{\rho_0'\to\infty} \Rightarrow e^{-jk\left(\phi_0'-\frac{\pi}{2}\right)} \tag{5-70}$$

In order to represent a plane wave incident from an angle ϕ_0' in terms of its spectral signature, one substitutes the large argument approximation in equation $(5-70)$ for $\begin{bmatrix} \vdots \\ H_k^{(2)}(\beta|\boldsymbol{\rho_0}'|)e^{-jk\phi_0'} \\ \vdots \end{bmatrix}$. The **H**-spectral signature of the incident electric field may be calculated using equation $(5-71)$.

$$\begin{bmatrix} \vdots \\ i_{ss,inc,Ie}^{ff} \\ \vdots \end{bmatrix} = E_0 \begin{bmatrix} e^{-jK\left(\phi_0'-\frac{\pi}{2}\right)} & \cdots & e^{-jK\left(\phi_{N_S-1}'-\frac{\pi}{2}\right)} \\ \vdots & \cdots & \vdots \\ \vdots & \cdots & \vdots \\ \vdots & \cdots & \vdots \\ e^{jK\left(\phi_0'-\frac{\pi}{2}\right)} & \cdots & e^{jK\left(\phi_{N_S-1}'-\frac{\pi}{2}\right)} \end{bmatrix} \begin{bmatrix} 1 \\ 0 \\ \vdots \\ \vdots \\ 0 \end{bmatrix} \tag{5-71}$$

or

$$\begin{bmatrix} \vdots \\ i_{ss,inc,Ie}^{ff} \\ \vdots \end{bmatrix} = E_0 \begin{bmatrix} e^{-jK\left(\phi_0'-\frac{\pi}{2}\right)} \\ \vdots \\ e^{jk\left(\phi_0'-\frac{\pi}{2}\right)} \\ \vdots \\ e^{jK\left(\phi_0'-\frac{\pi}{2}\right)} \end{bmatrix} \tag{5-72}$$

This represents the **H**-spectral signature of a TM^z electric field plane wave source in the direction ϕ_0.

5.3.5 Spectral Projection Model Applied to the Magnetic Field Integral Equation

For the Spectral Projection Model, the general form of the boundary condition for the MFIE is that the incident magnetic field, H_{inc}, at each point on the PEC boundary surface must equal negative the scattered or induced magnetic field H_{ind}. This is given in the matrix equation $(5-47)$, where $\begin{bmatrix} \cdots \\ H_{inc} \\ \cdots \end{bmatrix}$ and $\begin{bmatrix} \cdots \\ H_{ind} \\ \cdots \end{bmatrix}$ are $M \times 1$ vectors.

$$\begin{bmatrix} \vdots \\ H_{inc} \\ \vdots \end{bmatrix} = -\begin{bmatrix} \vdots \\ H_{ind} + J_C(\rho_m = \rho_n{}') \\ \vdots \end{bmatrix} \qquad (5-47)$$

As was the case for MOM analysis, for SPM the electric current term J_C is absorbed into the $\begin{bmatrix} \vdots \\ H_{ind} \\ \vdots \end{bmatrix}$ vector.

For infinitely long conducting structures, the Green's function for incident TE^z waves is $H_0^{(2)}(\beta|\boldsymbol{\rho}-\boldsymbol{\rho}'|)$. Once again, the Spectral Projection Model applies the addition theorem to decompose this Green's function into the sum of products of Bessel and Hankel functions. For induced fields, the derivative of the Green's function is the proper function $H_0^{(2)\prime}(\beta|\boldsymbol{\rho}-\boldsymbol{\rho}'|)$ due to the physics. Recall equation $(5-30)$. The relative positions of ρ and ρ' determine whether the addition theorem for induced or incident fields must be employed.

$$H_0^{(2)\prime}(\beta|\boldsymbol{\rho}-\boldsymbol{\rho}'|)\cos\psi' = \sum_{k=-\infty}^{\infty} H_k^{(2)\prime}(\beta|\boldsymbol{\rho}|)J_k(\beta|\boldsymbol{\rho}'|)e^{j\beta(\phi-\phi')} \qquad \rho > \rho' \qquad (5-73)$$

Induced Fields

$$H_0^{(2)}(\beta|\boldsymbol{\rho}-\boldsymbol{\rho}'|) = \sum_{k=-\infty}^{\infty} J_k(\beta|\boldsymbol{\rho}|)H_k^{(2)}(\beta|\boldsymbol{\rho}'|)e^{jk(\phi-\phi')} \qquad \rho < \rho' \qquad (5-74)$$

Incident Fields

5.3.5.1 Induced Magnetic Field and Spectral Signature of Induced Electric Currents from the MFIE using the Spectral Projection Model

As stated earlier for the MFIE and TE^z waves, the induced surface currents may be calculated using the Green's function $H_1^{(2)}(\beta|\boldsymbol{\rho}-\boldsymbol{\rho}'|) = H_0^{(2)\prime}(\beta|\boldsymbol{\rho}-\boldsymbol{\rho}'|)$. The Spectral Projection Model applies the addition theorem and decomposes this Green's function into the sum of products of Bessel and Hankel functions also. The addition theorem is used to represent the induced magnetic fields on the surface of the conductor as the projection of the **J**-spectral signature of the source points (ρ', ϕ') onto the **H**-spectral signature of the observation points (ρ, ϕ).

To calculate the scattered (induced) magnetic field $\begin{bmatrix} \cdots \\ H_{ind} \\ \cdots \end{bmatrix}$ due to induced currents, one refers back to the MFIE equation. This may now be rewritten as equation $(5-75)$.

$$\begin{bmatrix} \cdots \\ H_{ind} \\ \cdots \end{bmatrix} = \frac{j\beta}{4}\left(\begin{bmatrix} \cdots & \cdots & \cdots \\ \cdots & \cos(\gamma) & \cdots \\ \cdots & \cdots & \cdots \end{bmatrix}\begin{bmatrix} \cdots & \cdots & \cdots \\ \cdots & H_k^{(2)\prime}(\beta|\boldsymbol{\rho}|)e^{jk\phi} & \cdots \\ \cdots & \cdots & \cdots \end{bmatrix}\right)^T \begin{bmatrix} \cdots & \cdots & \cdots \\ \cdots & J_k\,(\beta|\boldsymbol{\rho}'|)e^{-jk\phi\prime} & \cdots \\ \cdots & \cdots & \cdots \end{bmatrix}\begin{bmatrix} \cdots \\ \hat{\imath}_{ind} \\ \cdots \end{bmatrix} \qquad \rho > \rho' \qquad (5-75)$$

In equation $(5-75)$ the vector $\begin{bmatrix} \cdots \\ \hat{\imath}_{ind} \\ \cdots \end{bmatrix}$ is the induced electric current vector. It represents the amplitudes and phases of the induced current on the surface of the conductor due to the incident magnetic field.

From equation $(5-75)$, the spectral signature of the induced electric current vector $\begin{bmatrix} \cdots \\ \hat{\imath}_{iss,ind} \\ \cdots \end{bmatrix}$ is derived as the projection of $\begin{bmatrix} \cdots \\ \hat{\imath}_{ind} \\ \cdots \end{bmatrix}$ onto the **J**-spectral signature of the source points, and written as $(5-76)$.

$$\begin{bmatrix} \cdots \\ \hat{\imath}_{iss,ind} \\ \cdots \end{bmatrix} = \frac{j\beta}{4}\begin{bmatrix} \cdots & \cdots & \cdots \\ \cdots & J_k\beta|\boldsymbol{\rho}'|)e^{-jk\phi\prime} & \cdots \\ \cdots & \cdots & \cdots \end{bmatrix}\begin{bmatrix} \cdots \\ \hat{\imath}_{ind} \\ \cdots \end{bmatrix} \qquad \rho > \rho' \qquad (5-76)$$

Each column of $\begin{bmatrix} \cdots & \cdots & \cdots \\ \cdots & J_k\beta|\boldsymbol{\rho}'|)e^{-jk\phi\prime} & \cdots \\ \cdots & \cdots & \cdots \end{bmatrix}$ is the **J**-spectral signature of an electric current source point.

The projection of the **J**-spectral signature of the induced current sources at source points (ρ', ϕ') onto the **H**-*prime*-spectral signature of the observation points (ρ, ϕ) can be expressed in matrix form as equation $(5-77)$.

$$\begin{bmatrix} \cdots \\ H_{ind} \\ \cdots \end{bmatrix} = \left(\begin{bmatrix} \cdots & \cdots & \cdots \\ \cdots & \cos(\gamma) & \cdots \\ \cdots & \cdots & \cdots \end{bmatrix} \begin{bmatrix} \cdots & \cdots & \cdots \\ \cdots & H_k^{(2)\prime}(\beta|\boldsymbol{\rho}|)e^{jk\phi} & \cdots \\ \cdots & \cdots & \cdots \end{bmatrix} \right)^T \begin{bmatrix} \cdots \\ \hat{\imath}_{iss,ind} \\ \cdots \end{bmatrix} \qquad \rho > \rho' \qquad (5-77)$$

Each row of $\begin{bmatrix} \cdots & \cdots & \cdots \\ \cdots & H_k^{(2)\prime}(\beta|\boldsymbol{\rho}|)e^{jk\phi} & \cdots \\ \cdots & \cdots & \cdots \end{bmatrix}$ is the **H**-*prime* spectral signature of an observation point at (ρ, ϕ).

5.3.5.2 Incident Magnetic Field and Spectral Signature of Incident Magnetic Currents from the MFIE using the Spectral Projection Model

The incident or external magnetic field on the surface of the conductor may be generated by a nearby external magnetic line current source or magnetic plane wave from the far-field. As stated earlier for infinitely long line currents sources at $\rho' > \rho$, the Green's function for TE^z waves is $H_0^{(2)}(\beta|\boldsymbol{\rho} - \boldsymbol{\rho}'|)$. The Spectral Projection Models applies the addition theorem to decompose this Green's function into the sum of products of Bessel and Hankel functions. The addition theorem is used to represent the incident magnetic fields on the surface of the conductor as the projection of the **H**-spectral signature of the source points (ρ_n', ϕ_n') onto the **J**-spectral signature of the observation points $(\rho_{m,}\phi_m)$.

The incident magnetic field from a magnetic line source H_z^i from angle ϕ_0' was previously written as equation $(5-31)$.

$$H_z(\beta|\boldsymbol{\rho_m} - \boldsymbol{\rho_0}'|) = -\frac{\beta^2 I_m}{4\omega\mu} H_0^{(2)}(\beta|\boldsymbol{\rho_m} - \boldsymbol{\rho_0}'|)e^{j\beta(\phi_m - \phi_0')} \qquad (5-31)$$

The **H**-spectral signature (or Hankel spectral signature) of the source point, (ρ_n', ϕ_n'), and the **J**-spectral signature (or Bessel spectral signature) of the observation point, $(\rho_{m,}\phi_m)$, for the incident magnetic field are given in equations $(5-78)$ and $(5-79)$.

$$e_{sn} = \left[H_{-K}^{(2)}(\beta|\boldsymbol{\rho_n}'|)e^{jK\phi_{n'}} \quad .. \quad H_0^{(2)}(\beta|\boldsymbol{\rho_n}'|)e^{jk\phi_{n'}} \quad ... \quad H_K^{(2)}(\beta|\boldsymbol{\rho_n}'|)e^{-jK\phi_{n'}}\right]^T \qquad (5-78)$$

$$e_{om} = [J_{-K}(\beta|\boldsymbol{\rho_m}|)e^{-jK\phi_m} \quad .. \quad J_k(\beta|\boldsymbol{\rho_m}|)e^{jk\phi_m} \quad ... \quad J_K(\beta|\boldsymbol{\rho_m}|)e^{jK\phi_m}]^T \qquad (5-79)$$

A single Z-directed magnetic line source I_m generates a magnetic field $H = H_z\hat{\boldsymbol{z}}$ in the near field, and a TE^z wave if the line source is placed in the far-field. See Figure 5-16a and 5-16b.

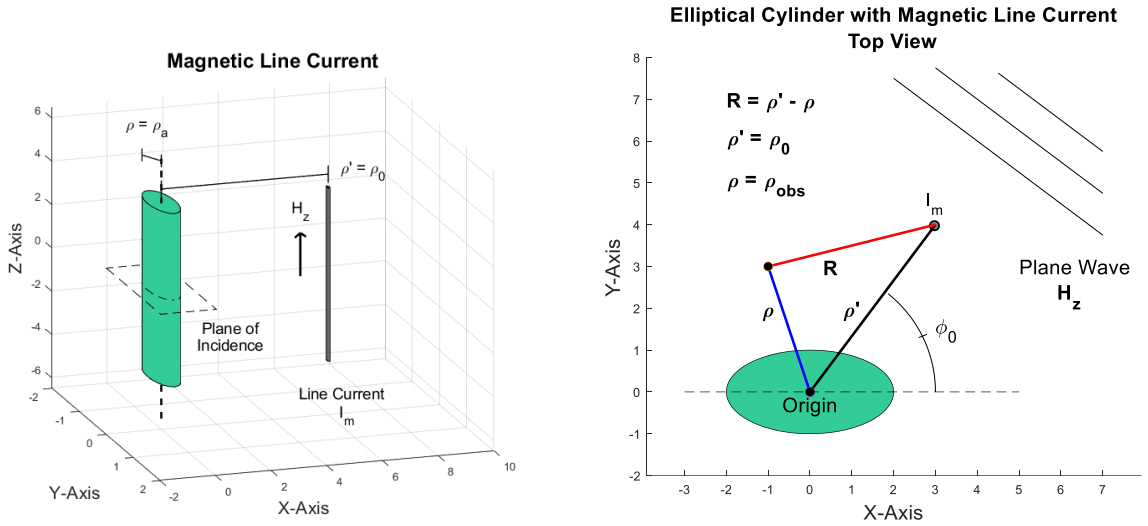

a) b)

Figure 5-16: a) Illustration of magnetic line current and elliptical cylinder. The dotted square around the cross section of the cylinder is the plane of incidence. The surface of the cylinder is at radius $\rho(\phi)$. b) Magnetic line source near an elliptical cylinder and a TE^z plane wave impingent on an elliptical cylindrical conductor (top view). A cross-sectional view of the elliptical cylinder with vectors ρ, ρ', R is also illustrated. The angle of incidence is ϕ_0.

For external sources impingent upon a target, this relationship can be expressed in matrix form as equation $(5-80)$.

$$\begin{bmatrix} \cdots \\ H_{inc} \\ \cdots \end{bmatrix} = \begin{bmatrix} \cdots & \cdots & \cdots \\ \cdots & J_k(\beta|\boldsymbol{\rho}|)e^{jk\phi} & \cdots \\ \cdots & \cdots & \cdots \end{bmatrix}^T \begin{bmatrix} \cdots & \cdots & \cdots \\ \cdots & H_k^{(2)}(\beta|\boldsymbol{\rho'}|)e^{-jk\phi'} & \cdots \\ \cdots & \cdots & \cdots \end{bmatrix} \begin{bmatrix} \cdots \\ \hat{\imath}_{inc,Im} \\ .. \end{bmatrix} \quad \rho < \rho' \qquad (5-80)$$

In equation $(5-80)$ the vector $\begin{bmatrix} \cdots \\ \hat{\imath}_{inc,Im} \\ .. \end{bmatrix}$ is the incident magnetic current vector due to a magnetic current line source. The columns of $\begin{bmatrix} \cdots & \cdots & \cdots \\ \cdots & H_k^{(2)}(\beta|\boldsymbol{\rho'}|)e^{-jk\phi'} & \cdots \\ \cdots & \cdots & \cdots \end{bmatrix}$ are the **H**-spectral

signature of all the source points, and rows of the matrix transpose $\begin{bmatrix} \cdots & \cdots & \cdots \\ \cdots & J_k(\beta|\boldsymbol{\rho}|)e^{jk\phi} & \cdots \\ \cdots & \cdots & \cdots \end{bmatrix}^T$ are the **J**-spectral signature of the observation points as shown descriptively in equation $(5-79)$.

$$\begin{bmatrix} \cdots \\ H_{inc} \\ \cdots \end{bmatrix} = \begin{bmatrix} - & - & - & - & - & - \\ - & - & J_k(\beta|\boldsymbol{\rho}|)e^{jk\phi} & - & - \\ - & - & - & - & - \end{bmatrix}^T \begin{bmatrix} | & & | & | \\ | & H_k\ (\beta|\boldsymbol{\rho}'|)e^{-jk\phi'} & | & | \\ | & & | & | \end{bmatrix} \begin{bmatrix} & | & \\ \hat{\imath}_{inc,Im} & & \\ & | & \end{bmatrix}$$

$$\rho < \rho' \qquad (5-81)$$

Equation $(5-81)$ may also be written as the projection of the spectral signature of incident magnetic currents onto the **J**-spectral signature of the observation points,

$$\begin{bmatrix} \cdots \\ H_{inc} \\ \cdots \end{bmatrix} = \begin{bmatrix} - & - & - & - & - & - \\ - & - & J_k(\beta|\boldsymbol{\rho}|)e^{jk\phi} & - & - \\ - & - & - & - & - \end{bmatrix}^T \begin{bmatrix} & | & \\ \hat{\imath}_{ss,inc,Im} & & \\ & | & \end{bmatrix} \qquad \rho < \rho' \qquad (5-82)$$

In equation $(5-82)$, the incident magnetic field is described as the projection of the **H**-spectral signatures of the incident fields onto the **J**-spectral signatures of the observation points.

The spectral signature of the incident magnetic currents $\begin{bmatrix} \cdots \\ \hat{\imath}_{iss,inc,Im} \\ \cdot\ \cdot \end{bmatrix}$ equals the projection of the incident magnetic current source amplitudes and phases $\begin{bmatrix} \cdots \\ \hat{\imath}_{inc,Im} \\ \cdot\ \cdot \end{bmatrix}$ onto the **H**-spectral signature of the source points.

$$\begin{bmatrix} \cdots \\ \hat{\imath}_{iss,inc,Im} \\ \cdot\ \cdot \end{bmatrix} = \begin{bmatrix} \cdots & \cdots & \cdots \\ \cdots & H_k^{(2)}(\beta|\boldsymbol{\rho}'|)e^{-jk\phi} & \cdots \\ \cdots & \cdots & \cdots \end{bmatrix} \begin{bmatrix} \cdots \\ \hat{\imath}_{inc,Im} \\ \cdot\ \cdot \end{bmatrix} \qquad \rho < \rho' \qquad (5-83)$$

The incident magnetic field is then the projection of the spectral signature of the incident magnetic currents $\begin{bmatrix} \cdots \\ \hat{\imath}_{iss,inc,Im} \\ \cdot\ \cdot \end{bmatrix}$ onto the **J**-spectral signature subspace $\begin{bmatrix} \cdots & \cdots & \cdots \\ \cdots & J_k\ (\beta|\boldsymbol{\rho}|)e^{jk\phi} & \cdots \\ \cdots & \cdots & \cdots \end{bmatrix}^T$ of the observation points.

$$\begin{bmatrix} \cdots \\ H_{inc} \\ \cdots \end{bmatrix} = \begin{bmatrix} \cdots & \cdots & \cdots \\ \cdots & J_k(\beta|\boldsymbol{\rho}|)e^{jk\phi} & \cdots \\ \cdots & \cdots & \cdots \end{bmatrix}^T \begin{bmatrix} \cdots \\ \hat{\imath}_{iss,inc,Im} \\ \cdot\ \cdot \end{bmatrix} \qquad \rho < \rho' \qquad (5-84)$$

If the external stimulus is a single incident magnetic field from a nearby magnetic current line source, recalling section 5.2, the radiated magnetic field, H_z^i, from a single magnetic line I_m

source at polar coordinates (ρ_1, ϕ_1) projected onto an observation point $(\rho_{m,}\phi_m)$ is given in equation $(5-32)$.

$$H_z^i(\rho_m, \rho_1) = -\frac{\beta^2 I_m}{4\omega\mu} e_{om}^T e_{sn} \qquad (5-32)$$

The external field H_{inc} for this magnetic line source may be written as the projection of the **H**-spectral signature of the incident magnetic currents onto the **J**-spectral signature of all the observation points.

$$\begin{bmatrix} \cdots \\ H_{inc} \\ \cdots \end{bmatrix} = \begin{bmatrix} \cdots & \cdots & \cdots \\ \cdots & J_k(\beta|\boldsymbol{\rho}|)e^{jk\phi} & \cdots \\ \cdots & \cdots & \cdots \end{bmatrix}^T \begin{bmatrix} \cdots \\ \hat{\imath}_{ss,inc,Im} \\ \cdot\cdot \end{bmatrix} \qquad \rho < \rho_1 \qquad (5-85)$$

For the case of the MFIE and a line source at (ρ_1', ϕ_1'), one may write the incident magnetic current spectral signature as shown in equation $(5-86)$.

$$\begin{bmatrix} \cdots \\ \hat{\imath}_{ss,inc,Im} \\ \cdot\cdot \end{bmatrix} = \begin{bmatrix} \cdots & \cdots & \cdots \\ \cdots & H_k^{(2)}(\beta|\boldsymbol{\rho}'|)e^{-jk\phi'} & \cdots \\ \cdots & \cdots & \cdots \end{bmatrix} \begin{bmatrix} \cdots \\ \hat{\imath}_{inc,Im} \\ \cdot\cdot \end{bmatrix} \qquad \rho < \rho' \qquad (5-86)$$

As an example, for a single magnetic line source at (ρ_1', ϕ_1'), vector $\begin{bmatrix} \cdots \\ \hat{\imath}_{inc,Im} \\ \cdot\cdot \end{bmatrix}$ is all zeros except for the row with the phase term ϕ_1'. The row of the vector $\begin{bmatrix} \cdots \\ \hat{\imath}_{inc,Im} \\ \cdot\cdot \end{bmatrix}$ must correspond to the column of the $\begin{bmatrix} \cdots & \cdots & \cdots \\ \cdots & H_k^{(2)}(\beta|\boldsymbol{\rho}'|)e^{-jk\phi'} & \cdots \\ \cdots & \cdots & \cdots \end{bmatrix}$ matrix with the source (ρ_1', ϕ_1') coordinates. Equations $(5-87)$ and $(5-88)$ illustrate this concept.

$$\begin{bmatrix} \cdots \\ \hat{\imath}_{ss,inc,Im} \\ \cdot\cdot \end{bmatrix} = \begin{bmatrix} H_{-K}^{(2)}(\beta|\boldsymbol{\rho_0}'|)e^{jK\phi_0'} & \cdots & \cdots & \cdots & H_{-K}^{(2)}(\beta|\boldsymbol{\rho_{N_S-1}}'|)e^{jK\phi_{N_S-1}'} \\ \vdots & \vdots & \vdots & \vdots & \vdots \\ \vdots & \vdots & \vdots & \vdots & \vdots \\ \vdots & \vdots & \vdots & \vdots & \vdots \\ H_K^{(2)}(\beta|\boldsymbol{\rho_0}'|)e^{-jK\phi_0'} & \cdots & \cdots & \cdots & H_K^{(2)}(\beta|\boldsymbol{\rho_{N_S-1}}'|)e^{-jK\phi_{N_S-1}'} \end{bmatrix} \begin{bmatrix} 0 \\ -\frac{\beta^2 I_m}{4\omega\mu} \\ 0 \\ \vdots \\ 0 \end{bmatrix} \qquad (5-87)$$

The vector $\begin{bmatrix} \cdots \\ \hat{\imath}_{ss,inc,Im} \\ \cdot\cdot \end{bmatrix}$ is now defined for a magnetic line source in equation $(5-88)$.

$$\begin{bmatrix} \cdots \\ \hat{\imath}_{ss,inc,Im} \\ \cdot\cdot \end{bmatrix} = -\frac{\beta^2 I_m}{4\omega\varepsilon} \begin{bmatrix} H_{-K}^{(2)}(\beta|\boldsymbol{\rho_1}|)e^{jK\phi_1} \\ \vdots \\ H_k^{(2)}(\beta|\boldsymbol{\rho_1}|)e^{-jk\phi_1} \\ \vdots \\ H_K^{(2)}(\beta|\boldsymbol{\rho_1}|)e^{-jK\phi_1} \end{bmatrix} \tag{5-88}$$

This is the near-field **H**-spectral signature of a single line source located at (ρ_1, ϕ_1).

For an external line source at infinity $\rho_1{}' \to \infty$, the resulting magnetic field is a plane wave. The large argument approximation for a Hankel function is given in equation $(5-89)$.

$$H_k^{(2)}(\beta|\boldsymbol{\rho_1}'|)|_{\rho_1'\to\infty} \Rightarrow e^{-jk\left(\phi_1'-\frac{\pi}{2}\right)} \tag{5-89}$$

For a plane wave incident from an angle $\phi_1{}'$, using the large argument approximation for $\begin{bmatrix} \vdots \\ H_k^{(2)}(\beta|\boldsymbol{\rho_1}'|)e^{-jk\phi_1'} \\ \vdots \end{bmatrix}$, the spectral signature of the incident magnetic far-field is calculated using equation $(5-90)$.

$$\begin{bmatrix} \vdots \\ i_{ss,inc,Im}^{ff} \\ \vdots \end{bmatrix} = H_0 \begin{bmatrix} e^{-jK\left(\phi_0'-\frac{\pi}{2}\right)} & \vdots & \vdots & \vdots & e^{-jK\left(\phi_{N_S-1}'-\frac{\pi}{2}\right)} \\ \vdots & \vdots & \vdots & \vdots & \vdots \\ \vdots & \vdots & \vdots & \vdots & \vdots \\ \vdots & \vdots & \vdots & \vdots & \vdots \\ e^{jK\left(\phi_0'-\frac{\pi}{2}\right)} & \vdots & \vdots & \vdots & e^{jK\left(\phi_{N_S-1}'-\frac{\pi}{2}\right)} \end{bmatrix} \begin{bmatrix} 0 \\ 1 \\ 0 \\ \vdots \\ 0 \end{bmatrix} \tag{5-90}$$

or

$$\begin{bmatrix} \vdots \\ i_{ss,inc,Im}^{ff} \\ \vdots \end{bmatrix} = H_0 \begin{bmatrix} e^{-jK\left(\phi_1'-\frac{\pi}{2}\right)} \\ \vdots \\ e^{jk\left(\phi_1'-\frac{\pi}{2}\right)} \\ \vdots \\ e^{jK\left(\phi_1'-\frac{\pi}{2}\right)} \end{bmatrix} \tag{5-91}$$

This is the **H**-spectral signature of a plane wave from the direction $\phi_1{}'$.

5.3.6 General Solution to Spectral Projection Model using the EFIE and MFIE

In this section a general matrix equation for solving electromagnetic scattering problems from surfaces using the Spectral Projection Model is given. The first set of equations is for the EFIE. The second set of equations applies to the MFIE.

5.3.6.1 General Solution to Spectral Projection Model using the EFIE

To solve the EFIE, begin by defining two matrices in order to represent the spectral signatures as row vectors instead of column vectors. The matrices are written below descriptively to show their composition as row and column vectors.

$$\begin{bmatrix} - & - & - \\ - & H_k^{(2)}(\beta|\boldsymbol{\rho_{ob}}|) & - \\ - & - & - \end{bmatrix} = \begin{bmatrix} | & | & | \\ | & H_k^{(2)}(\beta|\boldsymbol{\rho_m}|) & | \\ | & | & | \end{bmatrix}^T \quad (5-92)$$

$$\begin{bmatrix} - & - & - \\ - & J_k(\beta|\boldsymbol{\rho_{ob}}|) & - \\ - & - & - \end{bmatrix} = \begin{bmatrix} | & | & | \\ | & J_k(\beta|\boldsymbol{\rho_m}|) & | \\ | & | & | \end{bmatrix}^T \quad (5-93)$$

Next apply the boundary condition for the EFIE.

$$\begin{bmatrix} \cdots \\ E_{inc} \\ \cdot\cdot \end{bmatrix} = -\begin{bmatrix} \cdots \\ E_{ind} \\ \cdot\cdot \end{bmatrix} \quad (5-43)$$

Using the matrices $\begin{bmatrix} \cdots & \cdots & \cdots \\ \cdots & H_k^{(2)}(\beta|\boldsymbol{\rho_{ob}}|) & \cdots \\ \cdots & \cdots & \cdots \end{bmatrix}$ and $\begin{bmatrix} \cdots & \cdots & \cdots \\ \cdots & J_k(\beta|\boldsymbol{\rho_{ob}}|) & \cdots \\ \cdots & \cdots & \cdots \end{bmatrix}$, equation$(5-43)$, $(5-56)$ and $(5-62)$, one may write equations $(5-94)$ to $(5-96)$.

$$\begin{bmatrix} \cdots \\ E_{inc} \\ \cdot\cdot \end{bmatrix} = \begin{bmatrix} \cdots & \cdots & \cdots \\ \cdots & J_k(\beta|\boldsymbol{\rho_{ob}}|) & \cdots \\ \cdots & \cdots & \cdots \end{bmatrix} \begin{bmatrix} \cdots \\ \hat{\imath}_{SS,inc,Ie} \\ \cdot\cdot \end{bmatrix} \quad (5-94)$$

$$\begin{bmatrix} \cdots \\ E_{ind} \\ \cdot\cdot \end{bmatrix} = \begin{bmatrix} \cdots & \cdots & \cdots \\ \cdots & H_k^{(2)}(\beta|\boldsymbol{\rho_{ob}}|) & \cdots \\ \cdots & \cdots & \cdots \end{bmatrix} \begin{bmatrix} \cdots \\ \hat{\imath}_{SS,ind} \\ \cdot\cdot \end{bmatrix} \quad (5-95)$$

$$\begin{bmatrix} \cdots & \cdots & \cdots \\ \cdots & J_k(\beta|\boldsymbol{\rho_{ob}}|) & \cdots \\ \cdots & \cdots & \cdots \end{bmatrix} \begin{bmatrix} \cdots \\ \hat{\imath}_{SS,inc,Ie} \\ \cdot\cdot \end{bmatrix} = -\begin{bmatrix} \cdots & \cdots & \cdots \\ \cdots & H_k^{(2)}(\beta|\boldsymbol{\rho_{ob}}|) & \cdots \\ \cdots & \cdots & \cdots \end{bmatrix} \begin{bmatrix} \cdots \\ \hat{\imath}_{SS,ind} \\ \cdot\cdot \end{bmatrix} \quad (5-96)$$

5.3.6.2 General Solution to Spectral Projection Model using the MFIE

To solve the MFIE, once again one begins by defining two matrices in order to represent the spectral signatures as row vectors instead of column vectors. The matrices are written descriptively, and note that the Hankel Prime spectral signature subspace matrix is used instead of the Hankel spectral signature subspace matrix.

$$\begin{bmatrix} - & - & - \\ - & H_k^{(2)}(\beta|\boldsymbol{\rho_{ob}}|) & - \\ - & - & - \end{bmatrix} = \begin{bmatrix} | & | & | \\ | & H_k^{(2)}(\beta|\boldsymbol{\rho_m}|) & | \\ | & | & | \end{bmatrix}^T \quad (5-97)$$

$$\begin{bmatrix} - & - & - \\ - & H_k^{(2)\prime}(\beta|\boldsymbol{\rho_{ob}}|) & - \\ - & - & - \end{bmatrix} = \begin{bmatrix} | & | & | \\ | & H_k^{(2)\prime}(\beta|\boldsymbol{\rho_m}|) & | \\ | & | & | \end{bmatrix}^T \quad (5-98)$$

$$\begin{bmatrix} - & - & - \\ - & J_k(\beta|\boldsymbol{\rho_{ob}}|) & - \\ - & - & - \end{bmatrix} = \begin{bmatrix} | & | & | \\ | & J_k(\beta|\boldsymbol{\rho_m}|) & | \\ | & | & | \end{bmatrix}^T \quad (5-99)$$

Next apply the boundary condition for the MFIE.

$$\begin{bmatrix} \cdots \\ H_{inc} \\ \cdots \end{bmatrix} = -\begin{bmatrix} \cdots \\ H_{ind} + J_C(\rho_m = \rho_n{}') \\ \cdots \end{bmatrix} \quad (5-47)$$

Using the matrices $\begin{bmatrix} \cdots & \cdots & \cdots \\ \cdots & H_k^{(2)\prime}(\beta|\boldsymbol{\rho_{ob}}|) & \cdots \\ \cdots & \cdots & \cdots \end{bmatrix}$ and $\begin{bmatrix} \cdots & \cdots & \cdots \\ \cdots & J_k(\beta|\boldsymbol{\rho_{ob}}|) & \cdots \\ \cdots & \cdots & \cdots \end{bmatrix}$, equation $(5-47)$ and $(5-77)$, and $(5-82)$, one may write equation $(5-100)$ to $(5-102)$

$$\begin{bmatrix} \cdots \\ H_{inc} \\ \cdots \end{bmatrix} = \begin{bmatrix} \cdots & \cdots & \cdots \\ \cdots & J_k(\beta|\boldsymbol{\rho_{ob}}|) & \cdots \\ \cdots & \cdots & \cdots \end{bmatrix} \begin{bmatrix} \cdots \\ \hat{\imath}_{SS,inc,Ie} \\ \cdots \end{bmatrix} \quad (5-100)$$

$$\begin{bmatrix} \cdots \\ H_{ind} + J_C(\rho_m = \rho_n{}') \\ \cdots \end{bmatrix} = \begin{bmatrix} \cdots & \cdots & \cdots \\ \cdots & H_k^{(2)\prime}(\beta|\boldsymbol{\rho_{ob}}|) & \cdots \\ \cdots & \cdots & \cdots \end{bmatrix} \begin{bmatrix} \cdots & \cdots & \cdots \\ \cdots & \cos(\gamma) & \cdots \\ \cdots & \cdots & \cdots \end{bmatrix}^T \begin{bmatrix} \cdots \\ \hat{\imath}_{SS,ind} \\ \cdots \end{bmatrix} \quad (5-101)$$

$$\begin{bmatrix} \cdots & \cdots & \cdots \\ \cdots & J_k(\beta|\boldsymbol{\rho_{ob}}|) & \cdots \\ \cdots & \cdots & \cdots \end{bmatrix} \begin{bmatrix} \cdots \\ \hat{\imath}_{SS,inc,Ie} \\ \cdots \end{bmatrix} = \begin{bmatrix} \cdots & \cdots & \cdots \\ \cdots & H_k^{(2)\prime}(\beta|\boldsymbol{\rho_{ob}}|) & \cdots \\ \cdots & \cdots & \cdots \end{bmatrix} \begin{bmatrix} \cdots & \cdots & \cdots \\ \cdots & \cos(\gamma) & \cdots \\ \cdots & \cdots & \cdots \end{bmatrix}^T \begin{bmatrix} \cdots \\ \hat{\imath}_{SS,ind} \\ \cdots \end{bmatrix}$$

$$(5-102)$$

Table 5-3: Summary of Line Sources.

Line Source Scattering EFIE	
Electric Line Source $(5-4)$	$E_z(\beta\|\boldsymbol{\rho}-\boldsymbol{\rho}'\|) = -\frac{\beta^2 I_e}{4\omega\varepsilon} H_0^{(2)}(\beta\|\boldsymbol{\rho}-\boldsymbol{\rho}'\|)e^{j\beta(\phi-\phi\prime)}$ Electric field TM^z
Line Source Scattering MFIE	
Magnetic Line Source $(5-6)$	$H_z(\beta\|\boldsymbol{\rho}-\boldsymbol{\rho}'\|) = -\frac{\beta^2 I_m}{4\omega\mu} H_0^{(2)}(\beta\|\boldsymbol{\rho}-\boldsymbol{\rho}'\|)e^{j\beta(\phi-\phi\prime)}$ Magnetic field TE^z

Table 5-4: Summary of Addition Theorem Equations.

Addition Theorem Equations	Condition
$H_m^{(2)}(\beta\lvert\boldsymbol{\rho}-\boldsymbol{\rho}'\rvert)e^{jm\phi''}=\sum_{n=-\infty}^{\infty}H_{m+n}^{(2)}(\beta\lvert\boldsymbol{\rho}\rvert)J_n(\beta\lvert\boldsymbol{\rho}'\rvert)e^{j[(m+n)\phi-n\phi']}$ Correlation of Spectral Signatures	$\rho > \rho'$
$H_m^{(2)}(\beta\lvert\boldsymbol{\rho}-\boldsymbol{\rho}'\rvert)e^{jm\phi''}=\sum_{n=-\infty}^{\infty}H_{m+n}^{(2)}(\beta\lvert\boldsymbol{\rho}'\rvert)J_n(\beta\lvert\boldsymbol{\rho}\rvert)e^{j[(m+n)\phi'-n\phi]}$ Correlation of Spectral Signatures	$\rho' > \rho$
$H_m^{(2)}(\beta\lvert\boldsymbol{\rho}+\boldsymbol{\rho}'\rvert)e^{jm\phi''}=\sum_{k=-\infty}^{\infty}H_{m-k}^{(2)}(\beta\lvert\boldsymbol{\rho}\rvert)J_k(\beta\lvert\boldsymbol{\rho}'\rvert)e^{j[(m-k)\phi-k\phi']}$ Convolution of Spectral Signatures	$\rho > \rho'$
$H_m^{(2)}(\beta\lvert\boldsymbol{\rho}+\boldsymbol{\rho}'\rvert)e^{jm\phi''}=\sum_{k=-\infty}^{\infty}H_{m-k}^{(2)}(\beta\lvert\boldsymbol{\rho}'\rvert)J_k(\beta\lvert\boldsymbol{\rho}\rvert)e^{j[(m-k)\phi'-k\phi]}$ Convolution of Spectral Signatures	$\rho' > \rho$
$H_0^{(2)}(\beta\lvert\boldsymbol{\rho}-\boldsymbol{\rho}'\rvert)\approx\sum_{k=-K}^{K}H_k^{(2)}(\beta\lvert\boldsymbol{\rho}\rvert)J_k(\beta\lvert\boldsymbol{\rho}'\rvert)e^{jk(\phi-\phi')}$ Projection of **J**-spectral signature onto the **H**-spectral signature	$\rho > \rho'$
$H_0^{(2)}(\beta\lvert\boldsymbol{\rho}-\boldsymbol{\rho}'\rvert)\approx\sum_{k=-K}^{K}H_k^{(2)}(\beta\lvert\boldsymbol{\rho}'\rvert)J_k(\beta\lvert\boldsymbol{\rho}\rvert)e^{jk(\phi'-\phi)}$ Projection of the **H**-spectral signature onto the **J**-spectral signature	$\rho' > \rho$

Table 5-5: Summary of Spectral Projection Model Equations.

EFIE
$\begin{bmatrix} \cdots \\ E_{inc} \\ \cdots \end{bmatrix} = \begin{bmatrix} \cdots & \cdots & \cdots \\ \cdots & J_k\ (\beta\|\boldsymbol{\rho}\|)e^{jk\phi} & \cdots \\ \cdots & \cdots & \cdots \end{bmatrix}^T \begin{bmatrix} \cdots \\ \hat{\imath}_{ss,inc,Ie} \\ \cdots \end{bmatrix}$ Incident Electric Field
$\begin{bmatrix} \cdots \\ E_{ind} \\ \cdots \end{bmatrix} = \begin{bmatrix} \cdots & \cdots & \cdots \\ \cdots & H_k\ (\beta\|\boldsymbol{\rho}\|)e^{jk\phi} & \cdots \\ \cdots & \cdots & \cdots \end{bmatrix}^T \begin{bmatrix} \cdots \\ \hat{\imath}_{iss,ind} \\ \cdots \end{bmatrix}$ Induced Electric Field
MFIE
$\begin{bmatrix} \cdots \\ H_{inc} \\ \cdots \end{bmatrix} = \begin{bmatrix} \cdots & \cdots & \cdots \\ \cdots & J_k\ (\beta\|\boldsymbol{\rho}\|)e^{jk\phi} & \cdots \\ \cdots & \cdots & \cdots \end{bmatrix}^T \begin{bmatrix} \cdots \\ \hat{\imath}_{ss,inc,Im} \\ \cdots \end{bmatrix}$ Incident Magnetic Field
$\begin{bmatrix} \cdots \\ H_{ind} \\ \cdots \end{bmatrix} = \left(\begin{bmatrix} \cdots & \cdots & \cdots \\ \cdots & \cos(\gamma) & \cdots \\ \cdots & \cdots & \cdots \end{bmatrix} \begin{bmatrix} \cdots & \cdots & \cdots \\ \cdots & H_k\ '(\beta\|\boldsymbol{\rho}\|)e^{jk\phi} & \cdots \\ \cdots & \cdots & \cdots \end{bmatrix} \right)^T \begin{bmatrix} \cdots \\ \hat{\imath}_{iss,ind} \\ \cdots \end{bmatrix}$ Induced Magnetic Field

Table 5-6: Spectral Signature Definitions.

EFIE	
$\hat{\imath}_{ss,inc,Ie}$	Spectral Signature of Incident Electric Line Source Current
$\hat{\imath}_{inc,Ie}$	Incident Electric Current
EFIE & MFIE	
$\hat{\imath}_{SS,ind}$	Spectral Signature of Induced Electric Current
$\hat{\imath}_{ind}$	Induced Electric Current
MFIE	
$\hat{\imath}_{ss,inc,Im}$	Spectral Signature of Incident Magnetic Line Source Current
$\hat{\imath}_{inc,Im}$	Incident Magnetic Current

Table 5-7: Spectral Signature Definitions.

EFIE
$\begin{bmatrix} \cdots \\ \hat{\imath}_{ss,inc,Ie} \\ \cdot\cdot \end{bmatrix} = -\frac{\beta^2 I_e}{4\omega\varepsilon}\begin{bmatrix} H_{-K}^{(2)}(\beta\lvert\boldsymbol{\rho}'\rvert)e^{jK\phi'} \\ \vdots \\ H_k^{(2)}(\beta\lvert\boldsymbol{\rho}'\rvert)e^{jk\phi'} \\ \vdots \\ H_K^{(2)}(\beta\lvert\boldsymbol{\rho}'\rvert)e^{-jK\phi'} \end{bmatrix}$ Spectral Signature of Incident Electric Line Source in Near-Field
$\begin{bmatrix} \vdots \\ i_{ss,inc,Ie}^{ff} \\ \vdots \end{bmatrix} = E_0\begin{bmatrix} e^{-jK\left(\phi'-\frac{\pi}{2}\right)} \\ \vdots \\ e^{jk\left(\phi'-\frac{\pi}{2}\right)} \\ \vdots \\ e^{jK\left(\phi'-\frac{\pi}{2}\right)} \end{bmatrix}$ Spectral Signature of Incident Electric Line Source in Far-Field
MFIE
$\begin{bmatrix} \cdots \\ \hat{\imath}_{ss,inc,Im} \\ \cdot\cdot \end{bmatrix} = -\frac{\beta^2 I_m}{4\omega\mu}\begin{bmatrix} H_{-K}^{(2)}(\beta\lvert\boldsymbol{\rho}'\rvert)e^{jK\phi'} \\ \vdots \\ H_k^{(2)}(\beta\lvert\boldsymbol{\rho}'\rvert)e^{jk\phi'} \\ \vdots \\ H_K^{(2)}(\beta\lvert\boldsymbol{\rho}'\rvert)e^{-jK\phi'} \end{bmatrix}$ Spectral Signature of Incident Magnetic Line Source in Near-Field
$\begin{bmatrix} \vdots \\ i_{ss,inc,Im}^{ff} \\ \vdots \end{bmatrix} = H_0\begin{bmatrix} e^{-jK\left(\phi'-\frac{\pi}{2}\right)} \\ \vdots \\ e^{jk\left(\phi'-\frac{\pi}{2}\right)} \\ \vdots \\ e^{jK\left(\phi'-\frac{\pi}{2}\right)} \end{bmatrix}$ Spectral Signature of Incident Magnetic Line Source in Far-Field

5.4 Far-field Scattering in Spectral Projection Model

In this section the large argument approximation of the Hankel function will be used to derive the far-field **H**-spectral signature matrix. To calculate the far-field electric field pattern, the **J**-spectral signature of the induced currents on the surface of a conducting cylinder are projected onto the far-field **H**-spectral signature subspace matrix. Taking the far-field **H**-spectral signature of the **J**-spectral signature of the induced currents will be shown to be the same as taking the Discrete Fourier Transform (DFT) of the **J**-spectral signature of the induced currents with a scaling factor.

5.4.1 Analytical Method for Calculating Far-field Patterns

A set of *N* isotropic antenna elements positioned at polar coordinates points $(\rho_n, \theta_n, \phi_n)$, $n \in \{1,2, \ldots N\}$ is illustrated in Figure 5-17.

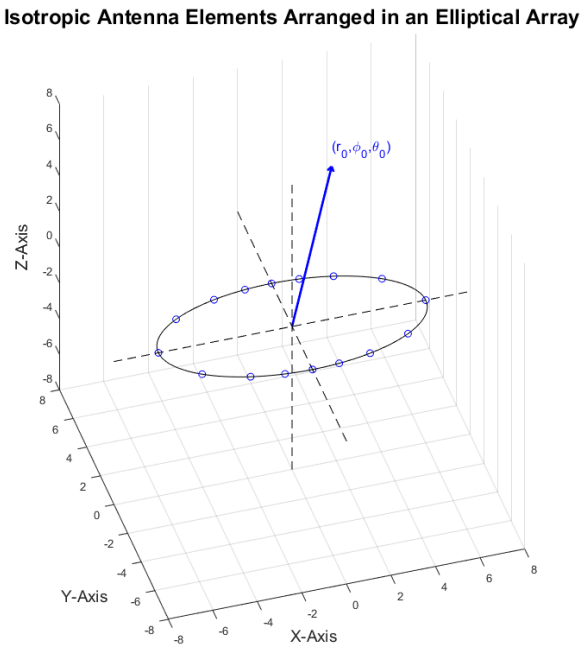

Figure 5-17: Isotropic point source radiating elements arranged in an elliptical array.

Consider a point source at $(\rho_n, \theta_n, \phi_n)$ and an incident plane wave arriving from angles (θ_0, ϕ_0), illustrated in Figure 5-18.

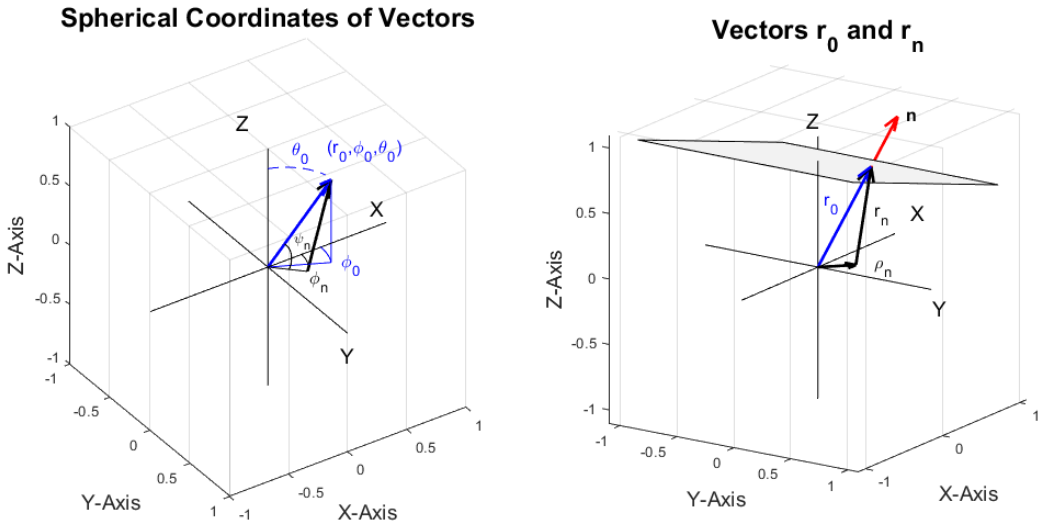

a) b)

Figure 5-18: Illustration of vectors. a) Vector $\boldsymbol{r_0}$ positioned at the origin and b) vector $\boldsymbol{r_n}$ positioned at $(\rho_n, \theta_n, \phi_n)$ in spherical coordinates.

If each element in the array is excited by a current of different amplitude and phase, $I_n e^{j\upsilon_n}$, then the electric far-field radiation pattern, E_{ff} , will be the sum of the radiation patterns due to all the elements.

$$E_{ff}(\theta,\phi) = \sum_{n=1}^{N} I_n e^{j\upsilon_n}\, e^{j\boldsymbol{\beta}\cdot\boldsymbol{r_n} cos(\varphi_n)} \qquad (5-103)$$

The angle φ_n is defined by the law of cosines,

$$r_n^2 = r_0^2 + \rho_n^2 - 2\rho_n r_0 cos(\varphi_n) \qquad (5-104)$$

To simplify calculation of r_n, one may use a square root approximation for $\rho_n \ll r_n$.

$$r_n \cong r_0 - \rho_n cos(\varphi_n) \qquad (5-105)$$

Now substituting for $cos(\varphi_n)$ from Figure 5-18, one obtains equation $(5-106)$.

$$r_n \cong r_0 - \rho_n \sin(\theta) cos(\phi_0 - \phi_n) \qquad (5-106)$$

Then the electric far-field can be written as $(5-107)$.

$$E_{ff}(\theta,\phi) = \sum_{n=1}^{N} I_n e^{j\upsilon_n}\, e^{j\beta r_0}\, e^{j\beta\rho_n \sin(\theta) cos(\phi_0-\phi_n)} \qquad (5-107)$$

A circular array of line sources is shown in Figure 5-19.

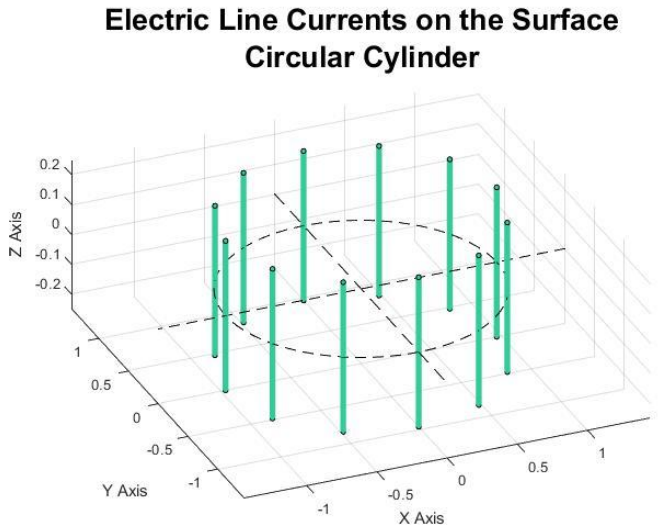

Figure 5-19: Line source antennas arranged in a circular array.

The total electric far-field for a circular array of line sources is given in equation $(5-108)$.

$$E_{ff}(\theta,\phi) = \sum_{n=1}^{N} I_n e^{j\upsilon_n} H_0^2(|\boldsymbol{\rho_0} - \boldsymbol{\rho_n}|)\, e^{-j\beta(\phi_0-\phi_n)} \qquad (5-108)$$

This differs from E_{ff} for point sources by the Green's function, and is a form of the discrete Fourier transform.

5.4.2 Far-field Spectral Signature and the Discrete Fourier Transform

To calculate the Hankel function for the far-field case $\rho \to \infty$, one uses the asymptotic approximation of the Hankel function for large arguments.

$$H_k^{(2)}(\beta|\boldsymbol{\rho}|) \approx= \sqrt{\frac{2}{\pi\rho}} e^{-j\left(\beta\rho-\frac{\pi}{4}\right)} e^{\frac{jk\pi}{2}} \qquad \rho \to \infty \quad (5-109)$$

Let $H_k^{(2)}(\beta|\boldsymbol{\rho}|)|_{\rho\to\infty}$ symbolize the asymptotic expansion of $H_k^{(2)}(\rho)$ for ρ being the distance from the line source in the far-field to the cylinder.

$$H_k^{(2)}(\beta|\boldsymbol{\rho}|)|_{\rho\to\infty} \sim f(\rho) e^{\frac{jk\pi}{2}} = f(\rho) e^{\frac{jk\pi}{2}} \qquad (5-110)$$

The symbol for the k^{th} order asymptotic expansion of the Hankel function of the second kind is given in equation $(5-111)$.

$$H_k^{(2)}(\beta|\boldsymbol{\rho}|)|_{\rho\to\infty} = e^{\frac{jk\pi}{2}} \qquad \rho\to\infty \quad (5-111)$$

with the amplitude term $f(\rho)$ omitted.

For an external electric line source receiver at infinity $\rho_0{}' \to \infty$ and angle of incidence ϕ_0, the large argument approximation for a Hankel function is given in equation $(5-112)$.

$$H_k^{(2)}(\beta|\boldsymbol{\rho}'|)|_{\rho'\to\infty} \Rightarrow e^{-jk\left(\phi_0{}'-\frac{\pi}{2}\right)} \qquad (5-112)$$

To write the far-field **H**-spectral signature matrix, $\begin{bmatrix}\cdots & \cdots & \cdots\\ \cdots & H_k^{(2)}(\beta|\boldsymbol{\rho}'|)|_{\rho'\to\infty} & \cdots\\ \cdots & \cdots & \cdots\end{bmatrix}$, for incident angles $\phi \in \{\phi_0, \phi_1, \ldots \phi_{N_S-1}\}$, one begins by substituting the large argument approximation into the matrix for $\begin{bmatrix}\vdots\\ H_k^{(2)}(\beta|\boldsymbol{\rho_n}'|)e^{-jk\phi_n'}\\ \vdots\end{bmatrix}$.

$$\begin{bmatrix}\cdots & \cdots & \cdots\\ \cdots & H_k^{(2)}(\beta|\boldsymbol{\rho}'|)|_{\rho'\to\infty} & \cdots\\ \cdots & \cdots & \cdots\end{bmatrix} = \begin{bmatrix} e^{-jK\left(\phi_0{}'-\frac{\pi}{2}\right)} & \cdots & \cdots & \cdots & e^{-jK\left(\phi_{N_S-1}{}'-\frac{\pi}{2}\right)}\\ \vdots & \vdots & \vdots & \vdots & \vdots\\ \vdots & \vdots & \vdots & \vdots & \vdots\\ \vdots & \vdots & \vdots & \vdots & \vdots\\ e^{jK\left(\phi_0{}'-\frac{\pi}{2}\right)} & \cdots & \cdots & \cdots & e^{jK\left(\phi_{N_S-1}{}'-\frac{\pi}{2}\right)}\end{bmatrix} \qquad (5-113)$$

This far-field **H**-spectral signature matrix may be used in two applications. One can project the **J**-spectral signature of the induced currents onto the far-field **H**-spectral signature to calculate the radiated electric far-field due to induced currents, E_{ind}^{ff}. Let $\begin{bmatrix}\vdots\\ E_{ind}^{ff}\\ \vdots\end{bmatrix}$ be defined for multiple infinitely long induced line sources at equally spaced angles on the surface $\Delta\phi = \phi_{n+1} - \phi_n$, and for *N* angles, and $n = \{0,1,2, \ldots N-1\}$,

$$\phi_n = \frac{2\pi}{N}k \qquad (5-114)$$

An illustration of *N = 16* points separated by equal angular spacing $\Delta\phi$ in the far-field is shown in Figure 5-20.

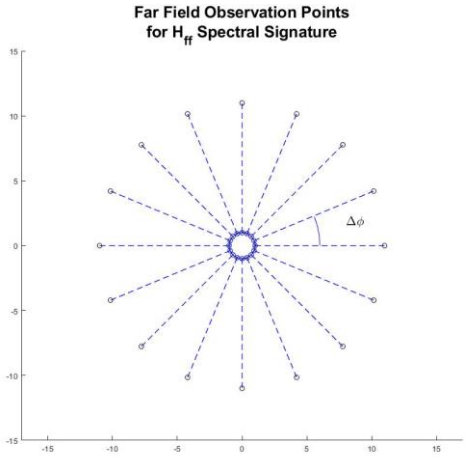

Figure 5-20: Observation points in the far-field uniformly spaced at equal angles for $N = 16$ receiving points.

One can calculate the **H**-spectral signature of an electric far-field for multiple sources using equation $(5-115)$.

$$\begin{bmatrix} \vdots \\ i_{ss,inc,Ie}^{ff} \\ \vdots \end{bmatrix} = \begin{bmatrix} e^{-jK\left(\phi_0{}'-\frac{\pi}{2}\right)} & \dots & \dots & \dots & e^{-jK\left(\phi_{N_S-1}{}'-\frac{\pi}{2}\right)} \\ \vdots & \vdots & \vdots & \vdots & \vdots \\ \vdots & \vdots & \vdots & \vdots & \vdots \\ \vdots & \vdots & \vdots & \vdots & \vdots \\ e^{jK\left(\phi_0{}'-\frac{\pi}{2}\right)} & \dots & \dots & \dots & e^{jK\left(\phi_{N_S-1}{}'-\frac{\pi}{2}\right)} \end{bmatrix} \begin{bmatrix} \vdots \\ \vdots \\ I_n \\ \vdots \\ \vdots \end{bmatrix} \qquad (5-115)$$

Each column in the matrix $\begin{bmatrix} \dots & \dots & \dots \\ \dots & H_k^{(2)}(\beta|\boldsymbol{\rho}'|)|_{\rho'\to\infty} & \dots \\ \dots & \dots & \dots \end{bmatrix}$ is the far-field **H**-spectral signature of a line source at infinity at a different angle $\phi_n{}'$. For a single source I_0 at angle $\phi_0{}'$, the current magnitude and phase vector $\begin{bmatrix} \vdots \\ \vdots \\ I_n \\ \vdots \\ \vdots \end{bmatrix}$ for incident line current $n = 0$ takes the form of equation $(5-116)$.

$$\begin{bmatrix} \vdots \\ \vdots \\ I_n \\ \vdots \\ \vdots \end{bmatrix} = \begin{bmatrix} I_0 \\ 0 \\ \vdots \\ \vdots \\ 0 \end{bmatrix} \qquad (5-116)$$

In this case, one may write the far-field **H**-spectral signature of $\begin{bmatrix} \vdots \\ i^{ff}_{ss,inc,Ie} \\ \vdots \end{bmatrix}$ as $(5-117)$, which is the spectral signature of an incident plane wave incident from angle ϕ_0. It is equal to a single column of the $\begin{bmatrix} \cdots & \cdots & \cdots \\ \cdots & H_k^{(2)}(\beta|\boldsymbol{\rho}'|)|_{\rho' \to \infty} & \cdots \\ \cdots & \cdots & \cdots \end{bmatrix}$ matrix weighted by the line source magnitude and phase coefficient I_0.

$$\begin{bmatrix} \vdots \\ i^{ff}_{ss,inc,Ie} \\ \vdots \end{bmatrix} = I_0 \begin{bmatrix} e^{-jK\left(\phi_0{}'-\frac{\pi}{2}\right)} \\ \vdots \\ e^{jk\left(\phi_0{}'-\frac{\pi}{2}\right)} \\ \vdots \\ e^{jK\left(\phi_0{}'-\frac{\pi}{2}\right)} \end{bmatrix} \qquad (5-117)$$

The discrete Fourier transform for the sequence $x[n]$ is given in equation $(5-118)$.

$$X[k] = \sum_{n=0}^{N} x[n] W_N^{-kn} \qquad (5-118)$$

and W_N are the roots of unity for $n \in \{0,1,\ldots,N-1\}$ defined as $W_N = e^{j\left(\frac{2\pi}{N}\right)}$.

For any spatial frequency $\phi_n{}' = 2\pi n/N$, notice that the angular spacing of the roots of unity for *N* points in Figure 5-21 are positioned the same as those shown in Figure 5-20, the far-field **H**-spectral signature.

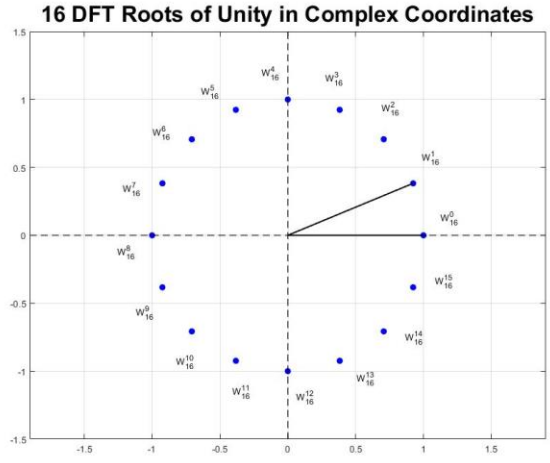

Figure 5-21: DFT roots of unity W_N^{-kn} for $N = 16$ points.

For the case in which the sinusoidal modes are *k = -K/2, -K/2+1, …K/2*, the shifted discrete Fourier transform operator, $\begin{bmatrix} \cdots & \cdots & \cdots \\ \cdots & \bar{F} & \cdots \\ \cdots & \cdots & \cdots \end{bmatrix}$, is shown in equation $(5-119)$.

$$\begin{bmatrix} \cdots & \cdots & \cdots \\ \cdots & \bar{F} & \cdots \\ \cdots & \cdots & \cdots \end{bmatrix} = \begin{bmatrix} e^{-jK\phi_{0}\prime} & \cdots & \cdots & \cdots & e^{-jK\phi_{\mathrm{N}-1}\prime} \\ \vdots & \vdots & \vdots & \vdots & \vdots \\ \vdots & \vdots & e^{-jk\phi_{\mathrm{n}}\prime} & \vdots & \vdots \\ \vdots & \vdots & \vdots & \vdots & \vdots \\ e^{jK\phi_{0}\prime} & \cdots & \cdots & \cdots & e^{jK\phi_{\mathrm{N}-1}\prime} \end{bmatrix} \quad (5-119)$$

This new shifted Fourier operator $\begin{bmatrix} \cdots & \cdots & \cdots \\ \cdots & \bar{F} & \cdots \\ \cdots & \cdots & \cdots \end{bmatrix}$ is the matrix product of the Fourier operator $\begin{bmatrix} \cdots & \cdots & \cdots \\ \cdots & F & \cdots \\ \cdots & \cdots & \cdots \end{bmatrix}$ and a matrix $\begin{bmatrix} \cdots & \cdots & \cdots \\ \cdots & S & \cdots \\ \cdots & \cdots & \cdots \end{bmatrix}$ that shifts the rows downward by $K/2$.

$$\begin{bmatrix} \cdots & \cdots & \cdots \\ \cdots & \bar{F} & \cdots \\ \cdots & \cdots & \cdots \end{bmatrix} = \begin{bmatrix} \cdots & \cdots & \cdots \\ \cdots & S & \cdots \\ \cdots & \cdots & \cdots \end{bmatrix} \begin{bmatrix} \cdots & \cdots & \cdots \\ \cdots & F & \cdots \\ \cdots & \cdots & \cdots \end{bmatrix} \quad (5-120)$$

The columns of $\begin{bmatrix} \cdots & \cdots & \cdots \\ \cdots & \bar{F} & \cdots \\ \cdots & \cdots & \cdots \end{bmatrix}$ take the same form as the $\begin{bmatrix} \cdots & \cdots & \cdots \\ \cdots & H_k^{(2)}(\beta|\boldsymbol{\rho}'|)|_{\rho\prime\to\infty} & \cdots \\ \cdots & \cdots & \cdots \end{bmatrix}$ matrix with a phase shift of the angle $\phi_n' = \phi_n' + \frac{\pi}{2}$. The far-field **H**-spectral signature matrix is equal to matrix product $\begin{bmatrix} \ddots & 0 & 0 \\ 0 & D_S & 0 \\ 0 & 0 & \ddots \end{bmatrix} \begin{bmatrix} \cdots & \cdots & \cdots \\ \cdots & \bar{F} & \cdots \\ \cdots & \cdots & \cdots \end{bmatrix}$ where the diagonal matrix $\begin{bmatrix} \ddots & 0 & 0 \\ 0 & D_S & 0 \\ 0 & 0 & \ddots \end{bmatrix}$ applies the $e^{jk\frac{\pi}{2}}$ phase shift to each column.

$$\begin{bmatrix} \ddots & 0 & 0 \\ 0 & D_S & 0 \\ 0 & 0 & \ddots \end{bmatrix} = \begin{bmatrix} \ddots & 0 & 0 \\ 0 & e^{jk\frac{\pi}{2}} & 0 \\ 0 & 0 & \ddots \end{bmatrix} \quad (5-121)$$

Thus, the matrix equality between the far-field **H**-spectral signature matrix and the DFT Fourier operator exists as given in equation $(5-122)$ and $(5-123)$.

$$\begin{bmatrix} \cdots & \cdots & \cdots \\ \cdots & H_k^{(2)}(\beta|\boldsymbol{\rho}|)|_{\rho\to\infty} & \cdots \\ \cdots & \cdots & \cdots \end{bmatrix} = \begin{bmatrix} \ddots & 0 & 0 \\ 0 & D_S & 0 \\ 0 & 0 & \ddots \end{bmatrix} \begin{bmatrix} \cdots & \cdots & \cdots \\ \cdots & S & \cdots \\ \cdots & \cdots & \cdots \end{bmatrix} \begin{bmatrix} \cdots & \cdots & \cdots \\ \cdots & F & \cdots \\ \cdots & \cdots & \cdots \end{bmatrix} \quad (5-122)$$

$$\begin{bmatrix} \cdots & \cdots & \cdots \\ \cdots & H_k^{(2)}(\beta|\boldsymbol{\rho}|)|_{\rho\to\infty} & \cdots \\ \cdots & \cdots & \cdots \end{bmatrix} = \begin{bmatrix} \ddots & 0 & 0 \\ 0 & D_S & 0 \\ 0 & 0 & \ddots \end{bmatrix} \begin{bmatrix} \cdots & \cdots & \cdots \\ \cdots & \bar{F} & \cdots \\ \cdots & \cdots & \cdots \end{bmatrix} \quad (5-123)$$

5.5 Waves Incident on a Circular Cylinder

Illustrated in Figure 5-22a are an incident and scattered TM^z wave. The incident wave angle is ϕ_i and the scattered wave angle is ϕ_s. Both are measured with respect to the positive X-axis. The unit vector $\boldsymbol{\beta_i}$ is the phase constant (or wave constant) normal to the plane of the incident TM^z wave. The unit vector $\boldsymbol{\beta_s}$ is the phase constant (or wave constant) normal to the plane of the scattered TM^z wave. The incident and scattered electric fields parallel to the axis of the circular cylinder are $\boldsymbol{E_z^i}$ and $\boldsymbol{E_z^s}$, respectively. Illustrated in Figure 5-22b are an incident and scattered TE^z wave. The incident wave angle is designated ϕ_i and the scattered wave angle is designated ϕ_s, as was the case for the TM^z wave. Similarly, the unit vectors $\boldsymbol{\beta_i}$ and $\boldsymbol{\beta_s}$ are the phase constant (or wave constant) normal to the planes of the incident and scattered TE^z waves. The incident and scattered magnetic fields parallel to the axis of the circular cylinder are $\boldsymbol{H_z^i}$ and $\boldsymbol{H_z^s}$, respectively.

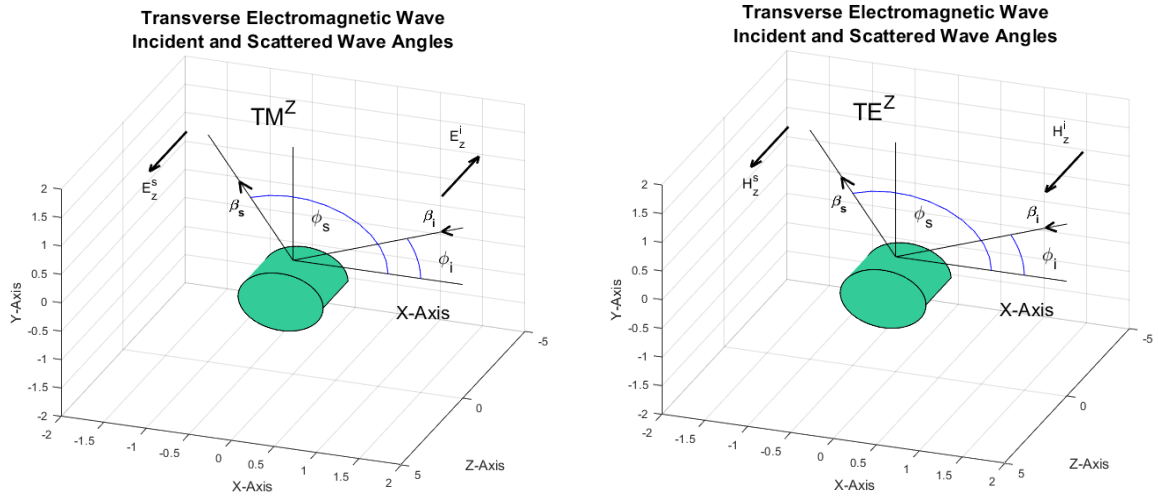

a) b)

Figure 5-22: Illustration of incident and scattered. a) TM^z waves upon circular cylinder. b) TE^z waves upon circular cylinder. Direction of incident waves is ϕ_i.

5.5.1 Spectral Projection Model using the EFIE for TM^z Waves incident upon a Circular Cylinder

For the discussion on circular cylinders, begin with the following matrix equation.

$$\begin{bmatrix} \cdots & \cdots & \cdots \\ \cdots & J_k(\beta|\boldsymbol{\rho_{ob}}|) & \cdots \\ \cdots & \cdots & \cdots \end{bmatrix}\begin{bmatrix} \cdots \\ \hat{\imath}_{SS,inc,Ie} \\ \cdots \end{bmatrix} = \begin{bmatrix} \cdots & \cdots & \cdots \\ \cdots & H_k^{(2)}(\beta|\boldsymbol{\rho_{ob}}|) & \cdots \\ \cdots & \cdots & \cdots \end{bmatrix}\begin{bmatrix} \cdots \\ \hat{\imath}_{SS,ind} \\ \cdots \end{bmatrix} \quad (5-96)$$

It is possible to solve this equation for a circular cylinder and reach a closed form solution for $\boldsymbol{\rho_{ob}} = \boldsymbol{a}$, or $\rho_{ob} = |\boldsymbol{a}|e^{j\phi_{ob}}$. Here $|\boldsymbol{a}|$ is the radius of the cylinder and ϕ_{ob} is the phase of each observation point.

Begin with the induced currents and examine again the **H**-spectral signature column space matrix for observation points $\rho_{ob} = \{\rho_0, \rho_1, \ldots \rho_{\mathrm{M}-1}\}$ as written as equation $(5-124)$.

$$\begin{bmatrix} | & | & | \\ | & H_k^{(2)}(\beta|\boldsymbol{\rho_m}|) & | \\ | & | & | \end{bmatrix} =$$

$$\begin{bmatrix} H_{-K}^{(2)}(\beta|\boldsymbol{\rho_0}|)e^{-jK\phi_0} & \cdots & \cdots & \cdots & H_{-K}^{(2)}(\beta|\boldsymbol{\rho_{M-1}}|)e^{-jK\phi_{\mathrm{M}-1}} \\ : & : & : & : & : \\ : & : & H_k^{(2)}(\beta|\boldsymbol{\rho_m}|)e^{jk\phi_m} & : & : \\ : & : & : & : & : \\ H_K^{(2)}(\beta|\boldsymbol{\rho_0}|)e^{jK\phi_0} & \cdots & \cdots & \cdots & H_K^{(2)}(\beta|\boldsymbol{\rho_{M-1}}|)e^{jK\phi_{\mathrm{M}-1}} \end{bmatrix}$$

$$(5-124)$$

Each column of $\begin{bmatrix} | & | & | \\ | & H_k^{(2)}(\beta|\boldsymbol{\rho_m}|) & | \\ | & | & | \end{bmatrix}$ is the **H**-spectral signature of an observation point.

For a circular cylinder $\rho_{\mathrm{m}} = a$ for $m = \{0, \ldots, M-1\}$, and equation $(5-124)$ may be diagonalized into equation $(5-125)$.

$$\begin{bmatrix} | & | & | \\ | & H_k^{(2)}(\beta|\boldsymbol{a}|) & | \\ | & | & | \end{bmatrix} =$$

$$\begin{bmatrix} H_{-K}^{(2)}(\beta|\boldsymbol{a}|) & \ddots & 0 & \ddots & 0 \\ 0 & \ddots & 0 & \ddots & 0 \\ 0 & \ddots & H_k^{(2)}(\beta|\boldsymbol{a}|) & \ddots & 0 \\ 0 & \ddots & 0 & \ddots & 0 \\ 0 & \ddots & 0 & \ddots & H_K^{(2)}(\beta|\boldsymbol{a}|) \end{bmatrix}\begin{bmatrix} e^{-jK\phi_0} & \cdots & \cdots & \cdots & e^{-jK\phi_{\mathrm{M}-1}} \\ : & : & : & : & : \\ : & : & : & : & : \\ : & : & : & : & : \\ e^{jK\phi_0} & \cdots & \cdots & \cdots & e^{jK\phi_{\mathrm{M}-1}} \end{bmatrix}$$

$$(5-125)$$

The exponential matrix on the right of equation $(5-125)$ is a column shifted version of the Fourier operator and will be designated as $\begin{bmatrix} \cdots & \cdots & \cdots \\ \cdots & \bar{\bar{F}} & \cdots \\ \cdots & \cdots & \cdots \end{bmatrix}$ for observation points.

$$\begin{bmatrix} \cdots & \cdots & \cdots \\ \cdots & \bar{F} & \cdots \\ \cdots & \cdots & \cdots \end{bmatrix} = \begin{bmatrix} e^{-jK\phi_0} & \cdots & \cdots & \cdots & e^{-jK\phi_{M-1}} \\ \vdots & \vdots & \vdots & \vdots & \vdots \\ \vdots & \vdots & \vdots & \vdots & \vdots \\ \vdots & \vdots & \vdots & \vdots & \vdots \\ e^{jK\phi_0} & \cdots & \cdots & \cdots & e^{jK\phi_{M-1}} \end{bmatrix} \qquad (5-126)$$

The diagonal matrix in equation $(5-125)$ may denoted as $\begin{bmatrix} \ddots & \ddots & \ddots \\ \ddots & D_H & \cdots \\ \ddots & \ddots & \ddots \end{bmatrix}$ and is given in equation $(5-127)$.

$$\begin{bmatrix} \ddots & 0 & 0 \\ 0 & D_H & 0 \\ 0 & 0 & \ddots \end{bmatrix} = \begin{bmatrix} H_{-K}^{(2)}(\beta|\boldsymbol{a}|) & \ddots & 0 & \ddots & 0 \\ 0 & \ddots & 0 & \ddots & 0 \\ 0 & \ddots & H_k^{(2)}(\beta|\boldsymbol{a}|) & \ddots & 0 \\ 0 & \ddots & 0 & \ddots & 0 \\ 0 & \ddots & 0 & \ddots & H_K^{(2)}(\beta|\boldsymbol{a}|) \end{bmatrix} \qquad (5-127)$$

From $(5-126)$ and $(5-127)$, matrix equation $(5-125)$ can take the form of a new equation $(5-128)$.

$$\begin{bmatrix} | & | & | \\ | & H_k^{(2)}(\beta|\boldsymbol{a}|) & | \\ | & | & | \end{bmatrix} = \begin{bmatrix} \ddots & 0 & 0 \\ 0 & D_H & 0 \\ 0 & 0 & \ddots \end{bmatrix} \begin{bmatrix} \cdots & \cdots & \cdots \\ \cdots & \bar{F} & \cdots \\ \cdots & \cdots & \cdots \end{bmatrix} \qquad (5-128)$$

Because the rows of $\begin{bmatrix} - & - & - \\ - & H_k^{(2)}(\beta|\boldsymbol{\rho_{ob}}|) & - \\ - & - & - \end{bmatrix}$ are the spectral signatures of the observation points, to write the induced field using this form one must take the conjugate transpose of both sides of $(5-129)$, This operation will be designated as $[\ ]^H$ to distinguish it from a transpose.

$$\begin{bmatrix} \cdots & \cdots & \cdots \\ \cdots & H_k^{(2)}(\beta|\boldsymbol{\rho_{ob}}|) & \cdots \\ \cdots & \cdots & \cdots \end{bmatrix} = \begin{bmatrix} \cdots & \cdots & \cdots \\ \cdots & H_k^{(2)}(\beta|\boldsymbol{a}|) & \cdots \\ \cdots & \cdots & \cdots \end{bmatrix}^H = \begin{bmatrix} \cdots & \cdots & \cdots \\ \cdots & \bar{F} & \cdots \\ \cdots & \cdots & \cdots \end{bmatrix}^H \begin{bmatrix} \ddots & \ddots & \ddots \\ \ddots & D_H & \cdots \\ \ddots & \ddots & \ddots \end{bmatrix} \qquad (5-129)$$

One may now rewrite the induced electric field vector $\begin{bmatrix} \cdots \\ \cdots \end{bmatrix}$ by substituting into equation $(5-95)$,

$$\begin{bmatrix} \cdots \\ \cdots \end{bmatrix} = \begin{bmatrix} - & - & - \\ - & H_k^{(2)}(\beta|\boldsymbol{\rho_{ob}}|) & - \\ - & - & - \end{bmatrix} \begin{bmatrix} \cdots \\ \cdots \end{bmatrix} \qquad (5-95)$$

and for a circular cylinder

$$\begin{bmatrix} \cdots \\ \cdots \end{bmatrix} = \begin{bmatrix} \cdots & \cdots & \cdots \\ \cdots & \bar{F} & \cdots \\ \cdots & \cdots & \cdots \end{bmatrix}^H \begin{bmatrix} \ddots & 0 & 0 \\ 0 & D_H & 0 \\ 0 & 0 & \ddots \end{bmatrix} \begin{bmatrix} \cdots \\ \cdots \end{bmatrix} \qquad (5-126)$$

The matrices on the left-hand side of equation $(5-96)$ represent the incident electric field. The rows of matrix $\begin{bmatrix} \cdots & \cdots & \cdots \\ \cdots & J_k(\beta|\boldsymbol{\rho_{ob}}|) & \cdots \\ \cdots & \cdots & \cdots \end{bmatrix}$ in equation $(5-96)$ represents the **J**-spectral signature subspace of the observation points,

$$\begin{bmatrix} \cdots \\ E_{inc} \\ \cdots \end{bmatrix} = \begin{bmatrix} - & - & - \\ - & J_k(\beta|\boldsymbol{\rho_{ob}}|) & - \\ - & - & - \end{bmatrix} \begin{bmatrix} | \\ \hat{\imath}_{SS,inc,Ie} \\ | \end{bmatrix} \qquad (5-94)$$

The column vector $\begin{bmatrix} \cdots \\ \hat{\imath}_{SS,inc,Ie} \\ \cdots \end{bmatrix}$ is the **H**-spectral signature of the incident external source. For circular cylinders, analogous to equation $(5-125)$, one may write equation $(5-127)$.

$$\begin{bmatrix} \cdots & \cdots & \cdots \\ \cdots & J_k(\beta|\boldsymbol{\rho_{ob}}|) & \cdots \\ \cdots & \cdots & \cdots \end{bmatrix} = \begin{bmatrix} \cdots & \cdots & \cdots \\ \cdots & J_k(\beta|\boldsymbol{a}|) & \cdots \\ \cdots & \cdots & \cdots \end{bmatrix}^H = \begin{bmatrix} \cdots & \cdots & \cdots \\ \cdots & \bar{F} & \cdots \\ \cdots & \cdots & \cdots \end{bmatrix}^H \begin{bmatrix} \ddots & 0 & 0 \\ 0 & D_J & 0 \\ 0 & 0 & \ddots \end{bmatrix} \qquad (5-127)$$

where

$$\begin{bmatrix} \cdots & \cdots & \cdots \\ \cdots & J_k(\beta|\boldsymbol{\rho_{ob}}|) & \cdots \\ \cdots & \cdots & \cdots \end{bmatrix} = \begin{bmatrix} \cdots & \cdots & \cdots \\ \cdots & \bar{F} & \cdots \\ \cdots & \cdots & \cdots \end{bmatrix}^H \begin{bmatrix} \ddots & 0 & 0 \\ 0 & D_J & 0 \\ 0 & 0 & \ddots \end{bmatrix} \qquad (5-128)$$

Matrix $\begin{bmatrix} \ddots & 0 & 0 \\ 0 & D_J & 0 \\ 0 & 0 & \ddots \end{bmatrix}$ is defined as a diagonal matrix $(5-129)$.

$$\begin{bmatrix} \ddots & 0 & 0 \\ 0 & D_J & 0 \\ 0 & 0 & \ddots \end{bmatrix} = \begin{bmatrix} J_{-K}(\beta|\boldsymbol{a}|) & \ddots & 0 & \ddots & 0 \\ 0 & \ddots & 0 & \ddots & 0 \\ 0 & \ddots & J_k(\beta|\boldsymbol{a}|) & \ddots & 0 \\ 0 & \ddots & 0 & \ddots & 0 \\ 0 & \ddots & 0 & \ddots & J_K(\beta|\boldsymbol{a}|) \end{bmatrix} \qquad (5-129)$$

Now one can solve equation $(5-96)$ for $\begin{bmatrix} \cdots \\ \hat{\imath}_{SS,ind} \\ \cdots \end{bmatrix}$.

$$\begin{bmatrix} \cdots \\ \hat{\imath}_{SS,ind} \\ \cdots \end{bmatrix} = \begin{bmatrix} \cdots & \cdots & \cdots \\ \cdots & H_k^{(2)}(\beta|\boldsymbol{\rho_{ob}}|) & \cdots \\ \cdots & \cdots & \cdots \end{bmatrix}^{-1} \begin{bmatrix} \cdots & \cdots & \cdots \\ \cdots & J_k^{(2)}(\beta|\boldsymbol{\rho_{ob}}|) & \cdots \\ \cdots & \cdots & \cdots \end{bmatrix} \begin{bmatrix} \cdots \\ \hat{\imath}_{SS,inc,Ie} \\ \cdots \end{bmatrix} \qquad (5-130)$$

Next substituting for $\begin{bmatrix} \cdots & \cdots & \cdots \\ \cdots & H_k^{(2)}(\beta|\boldsymbol{\rho_{ob}}|) & \cdots \\ \cdots & \cdots & \cdots \end{bmatrix}$ and $\begin{bmatrix} \cdots & \cdots & \cdots \\ \cdots & J_k^{(2)}(\beta|\boldsymbol{\rho_{ob}}|) & \cdots \\ \cdots & \cdots & \cdots \end{bmatrix}$, one obtains equation $(5-131)$.

$$\begin{bmatrix} \cdots \\ \hat{\imath}_{SS,ind} \\ \cdots \end{bmatrix} = \left(\begin{bmatrix} \cdots & \cdots & \cdots \\ \cdots & \bar{F} & \cdots \\ \cdots & \cdots & \cdots \end{bmatrix}^H \begin{bmatrix} \cdots & \cdots & \cdots \\ \cdots & D_H & \cdots \\ \cdots & \cdots & \cdots \end{bmatrix} \right)^{-1} \left(\begin{bmatrix} \cdots & \cdots & \cdots \\ \cdots & \bar{F} & \cdots \\ \cdots & \cdots & \cdots \end{bmatrix}^H \begin{bmatrix} \cdots & \cdots & \cdots \\ \cdots & D_J & \cdots \\ \cdots & \cdots & \cdots \end{bmatrix} \right) \begin{bmatrix} \cdots \\ \hat{\imath}_{SS,inc,Ie} \\ \cdots \end{bmatrix}$$

$$(5-131)$$

Since the shifted Fourier matrix $\begin{bmatrix} \cdots & \cdots & \cdots \\ \cdots & \bar{F} & \cdots \\ \cdots & \cdots & \cdots \end{bmatrix}$ is unitary,

$$\left(\begin{bmatrix} \cdots & \cdots & \cdots \\ \cdots & \bar{F} & \cdots \\ \cdots & \cdots & \cdots \end{bmatrix}^{H}\right) = \begin{pmatrix} \cdots & \cdots & \cdots \\ \cdots & \bar{F} & \cdots \\ \cdots & \cdots & \cdots \end{pmatrix}^{-1} \qquad (5-132)$$

then one can rewrite $(5-131)$ as $(5-133)$.

$$\begin{bmatrix} \cdots \\ \hat{\imath}_{SS,ind} \\ \cdot\cdot \end{bmatrix} = \begin{bmatrix} \ddots & 0 & 0 \\ 0 & D_H & 0 \\ 0 & 0 & \ddots \end{bmatrix}^{-1} \begin{bmatrix} \ddots & 0 & 0 \\ 0 & D_J & 0 \\ 0 & 0 & \ddots \end{bmatrix} \begin{bmatrix} \cdots \\ \hat{\imath}_{SS,inc,Ie} \\ \cdot\cdot \end{bmatrix} \qquad (5-133)$$

For plane wave incidence, the spectral signature of the source can be written using the far-field approximation to the Hankel function, with $\phi_i{}'$ equal to the angle of the incident wave.

$$\begin{bmatrix} \cdots \\ \hat{\imath}^{ff}_{\hat{\imath}_{SS,inc,Ie}} \\ \cdot\cdot \end{bmatrix} = [e^{-jK(\phi_i{}'-\pi/2)} \quad \cdots \quad e^{jk(\phi_i{}'-\pi/2)} \quad \cdots \quad e^{jK(\phi_i{}'-\pi/2)}]^T \qquad (5-134)$$

One can observe from the complex exponentials, the $\begin{bmatrix} \cdots \\ \hat{\imath}^{ff}_{\hat{\imath}_{SS,inc,Ie}} \\ \cdot\cdot \end{bmatrix}$ vector for plane waves is a Fourier series.

The expression for the k^{th} element of the spectral signature of the induced current $\hat{\imath}_{SS,ind,k}$ is written as $(5-135)$.

$$\hat{\imath}_{SS,ind,k} = \begin{bmatrix} \cdots & \dfrac{e^{-\frac{jk\pi}{2}} J_k(\beta|\boldsymbol{a}|)\, e^{-jk\phi_i{}'}}{H_k^{(2)}(\beta|\boldsymbol{a}|)} & \cdots \end{bmatrix}^T \qquad (5-135)$$

Note that $e^{-\frac{jk\pi}{2}} = j^{-k}$.

For the induced currents, the **J**-spectral signature of the induced source currents $\begin{bmatrix} \cdots \\ \hat{\imath}_{SS,ind} \\ \cdot\cdot \end{bmatrix}$ is related to the actual surface currents, $\begin{bmatrix} \cdots \\ \hat{\imath}_{ind} \\ \cdot\cdot \end{bmatrix}$, as equation $(5-136)$,

$$\begin{bmatrix} \cdots \\ \hat{\imath}_{SS,ind} \\ \cdot\cdot \end{bmatrix} = \begin{bmatrix} \cdots & \cdots & \cdots \\ \cdots & J_k(\beta|\boldsymbol{\rho_{ob}}|) & \cdots \\ \cdots & \cdots & \cdots \end{bmatrix} \begin{bmatrix} \cdots \\ \hat{\imath}_{ind} \\ \cdot\cdot \end{bmatrix} \qquad (5-136)$$

and using the linear transformation in equation $(5-127)$, one may write

$$\begin{bmatrix} \cdots \\ \hat{\imath}_{SS,ind} \\ \cdot\cdot \end{bmatrix} = \begin{bmatrix} \cdots & \cdots & \cdots \\ \cdots & J_k(\beta|\boldsymbol{a}|)) & \cdots \\ \cdots & \cdots & \cdots \end{bmatrix}^H \begin{bmatrix} \cdots \\ \hat{\imath}_{ind} \\ \cdot\cdot \end{bmatrix} \qquad (5-137)$$

$$\begin{bmatrix} \cdots \\ \hat{\imath}_{SS,ind} \\ \cdots \end{bmatrix} = \begin{bmatrix} \ddots & 0 & 0 \\ 0 & D_J & 0 \\ 0 & 0 & \ddots \end{bmatrix} \begin{bmatrix} \cdots & \cdots & \cdots \\ \cdots & \bar{F} & \cdots \\ \cdots & \cdots & \cdots \end{bmatrix} \begin{bmatrix} \cdots \\ \hat{\imath}_{ind} \\ \cdots \end{bmatrix} \quad (5-138)$$

The expression for the actual surface currents, $\begin{bmatrix} \cdots \\ \hat{\imath}_{ind} \\ \cdots \end{bmatrix}$, becomes

$$\begin{bmatrix} \cdots \\ \hat{\imath}_{ind} \\ \cdots \end{bmatrix} = \begin{bmatrix} \cdots & \cdots & \cdots \\ \cdots & \bar{F} & \cdots \\ \cdots & \cdots & \cdots \end{bmatrix}^H \begin{bmatrix} \ddots & 0 & 0 \\ 0 & D_J & 0 \\ 0 & 0 & \ddots \end{bmatrix}^{-1} \begin{bmatrix} \cdots \\ \hat{\imath}_{SS,ind} \\ \cdots \end{bmatrix} \quad (5-139)$$

The SPM expression for the surface current on a circular cylinder excited by an electric field plane wave may be written from equation $(5-139)$ as equation $(5-140)$.

$$\hat{\imath}(\rho,\phi) = \sum_{k=-K}^{K} \frac{j^{-k} e^{jk(\phi-\phi_i{}')}}{H_k^{(2)}(\beta|\boldsymbol{a}|)} \quad (5-140)$$

This normalized result agrees with the equation given by Balanis using modal analysis in reference book [36].

$$J_z(a,\phi_n) = \frac{2E_0}{\pi a \omega \mu} \sum_{k=-\infty}^{\infty} \frac{j^{-k} e^{jk(\phi_n-\phi_i{}')}}{H_k^{(2)}(\beta|\boldsymbol{a}|)} \quad (5-141)$$

For a near-field line current source at $(\rho_0{}', \phi_0{}')$, the spectral signature of this external source is given in equation $(5-142)$.

$$\begin{bmatrix} \cdots \\ \hat{\imath}_{SS,inc} \\ \cdots \end{bmatrix} = \left[H_{-K}^{(2)}(\beta|\boldsymbol{\rho_0}'|) e^{jK\phi_0'} \quad \cdots \quad H_k^{(2)}(\beta|\boldsymbol{\rho_0}'|) e^{-jk\phi_0'} \quad \cdots \quad H_K^{(2)}(\beta|\boldsymbol{\rho_0}'|) e^{-jK\phi_0'} \right]^T \quad (5-142)$$

The **H**-spectral signature of the surface current on the circular cylinder is given by equation $(5-143)$,

$$\begin{bmatrix} \cdots \\ \hat{\imath}_{SS,ind} \\ \cdots \end{bmatrix} = \begin{bmatrix} \cdots & \cdots & \cdots \\ \cdots & H_k^{(2)}(\beta|\boldsymbol{\rho_{ob}}|) & \cdots \\ \cdots & \cdots & \cdots \end{bmatrix}^{-1} \begin{bmatrix} \cdots \\ E_{ind} \\ \cdots \end{bmatrix} \quad (5-143)$$

and thus $\begin{bmatrix} \cdots \\ \hat{\imath}_{SS,ind} \\ \cdots \end{bmatrix}$ for a near field source excitation is given in equation $(5-144)$.

$$\begin{bmatrix} \cdots \\ \hat{\imath}_{SS,ind} \\ \cdots \end{bmatrix} = \begin{bmatrix} \cdots & \dfrac{H_k^{(2)}(\beta|\boldsymbol{\rho_{ob}}|) J_k(\beta|\boldsymbol{a}|)\, e^{-jk\phi_0'}}{H_k^{(2)}(\beta|\boldsymbol{a}|)} & \cdots \end{bmatrix}^T \quad (5-144)$$

Once again solving for the actual surface currents, $\begin{bmatrix} \cdots \\ \hat{\imath}_{ind} \\ \cdots \end{bmatrix}$,

$$\begin{bmatrix} \cdots \\ \hat{\imath}_{ind} \\ \cdot\cdot \end{bmatrix} = \begin{bmatrix} \cdots & \cdots & \cdots \\ \cdots & \bar{\bar{F}} & \cdots \\ \cdots & \cdots & \cdots \end{bmatrix}^{H} \begin{bmatrix} \ddots & 0 & 0 \\ 0 & D_J & 0 \\ 0 & 0 & \ddots \end{bmatrix}^{-1} \begin{bmatrix} \cdots \\ \hat{\imath}_{SS,ind} \\ \cdot\cdot \end{bmatrix} \qquad (5-145)$$

The normalized surface current on the circular cylinder excited by a near-field line current source is written as $(5-146)$.

$$\hat{\imath}(\rho,\phi) = \sum_{k=-K}^{K} \frac{H_k^{(2)}(\beta|\boldsymbol{\rho_0}'|)\, e^{jk(\phi-\phi_0')}}{H_k^{(2)}(\beta|\boldsymbol{a}|)} \qquad (5-146)$$

This solution agrees with the equation given by Balanis in reference book [36].

$$J_z(a,\phi_n) = -\frac{I_e}{2\pi a} \sum_{k=-\infty}^{\infty} \frac{H_k^{(2)}(\beta\rho')\, e^{jk(\phi_n-\phi')}}{H_k^{(2)}(\beta a)} \qquad (5-147)$$

5.5.2 Spectral Projection Model using the MFIE for TE^z Waves

To apply the boundary conditions for the Spectral Projection Model to the MFIE, one may begin with the same linear matrix equation as $(5-102)$.

$$\begin{bmatrix} \cdots & \cdots & \cdots \\ \cdots & J_k(\beta|\boldsymbol{\rho_{ob}}|) & \cdots \\ \cdots & \cdots & \cdots \end{bmatrix} \begin{bmatrix} \cdots \\ \hat{\imath}_{SS,inc,Ie} \\ \cdot\cdot \end{bmatrix} = \begin{bmatrix} \cdots & \cdots & \cdots \\ \cdots & H_k^{(2)\prime}(\beta|\boldsymbol{\rho_{ob}}|) & \cdots \\ \cdots & \cdots & \cdots \end{bmatrix} \begin{bmatrix} \ddots & 0 & 0 \\ 0 & \cos(\gamma) & 0 \\ 0 & 0 & \ddots \end{bmatrix}^{T} \begin{bmatrix} \cdots \\ \hat{\imath}_{SS,ind} \\ \cdot\cdot \end{bmatrix} \qquad (5-102)$$

For the case of the circular cylinder, $\gamma = \frac{\pi}{2}$, so the equation may be rewritten as

$$\begin{bmatrix} \cdots & \cdots & \cdots \\ \cdots & J_k(\beta|\boldsymbol{\rho_{ob}}|) & \cdots \\ \cdots & \cdots & \cdots \end{bmatrix} \begin{bmatrix} \cdots \\ \hat{\imath}_{SS,inc,Ie} \\ \cdot\cdot \end{bmatrix} = \begin{bmatrix} \cdots & \cdots & \cdots \\ \cdots & H_k^{(2)\prime}(\beta|\boldsymbol{\rho_{ob}}|) & \cdots \\ \cdots & \cdots & \cdots \end{bmatrix} \begin{bmatrix} \cdots \\ \hat{\imath}_{SS,ind} \\ \cdot\cdot \end{bmatrix} \qquad (5-148)$$

To calculate $\begin{bmatrix} \cdots \\ \hat{\imath}_{SS,ind} \\ \cdot\cdot \end{bmatrix}$, one again one substitutes $\boldsymbol{\rho_{ob}} = \boldsymbol{a}$, or $\rho_{ob} = |\boldsymbol{a}|e^{j\phi_{ob}}$, where $\boldsymbol{a}$ is the radius of the cylinder and ϕ_{ob} is the phase of each observation point.

The $N \times 1$ element vector, $\hat{\imath}_{SS,ind}$, is the **J**-spectral signature of the induced electric current sources on the surface of the conductor, as was the case for the EFIE.

Solving the MFIE the same way as the EFIE, one arrives at a similar expression for the diagonal matrix, except the diagonal terms are instead derivatives of the Hankel function.

$$\begin{bmatrix} \ddots & 0 & 0 \\ 0 & D_H{}' & 0 \\ 0 & 0 & \ddots \end{bmatrix} = \begin{bmatrix} H_{-K}^{(2)\prime}(\beta|\boldsymbol{a}|) & 0 & 0 & 0 & 0 \\ 0 & \ddots & 0 & 0 & 0 \\ 0 & 0 & H_k^{(2)\prime}(\beta|\boldsymbol{a}|) & 0 & 0 \\ 0 & 0 & 0 & \ddots & 0 \\ 0 & 0 & 0 & 0 & H_{K-1}^{(2)}{}'(\beta|\boldsymbol{a}|) \end{bmatrix} \qquad (5-149)$$

To solve for the normalized surface current on a circular cylinder at observation points (ρ, ϕ) excited by a magnetic field plane wave coming from incident angle $\phi' = \phi_0{}'$ using MFIE, one uses the same steps as for the EFIE. The surface current may be written as equation $(5-150)$.

$$\hat{\imath}(\rho,\phi) = \sum_{k=-K}^{K} \frac{j^{-k} e^{jk(\phi-\phi_0{}')}}{H_k^{(2)}{}'(\beta|\boldsymbol{a}|)} \qquad (5-150)$$

This agrees with the equation given by Balanis in reference book [36].

$$J_\phi(a,\phi_n) = j\frac{2H_0}{\pi\beta a} \sum_{k=-\infty}^{\infty} \frac{j^{-k} e^{jk(\phi_n-\phi_i{}')}}{H_k^{(2)}{}'(\beta a)} \qquad (5-151)$$

For a near-field magnetic line source, the actual normalized induced surface current on the circular cylinder at observation points (ρ, ϕ) is given in equation $(5-152)$.

$$\hat{\imath}(\rho,\phi) = \sum_{n=-K}^{K} \frac{H_k^{(2)}(\beta|\boldsymbol{\rho_0}'|)\, e^{jk(\phi-\phi_0{}')}}{H_k^{(2)}{}'(\beta|\boldsymbol{a}|)} \qquad (5-152)$$

This agrees with the equation given by Balanis in reference book [36].

$$J_\phi(a,\phi_n) = -\frac{jI_m}{2\eta\pi a} \sum_{k=-\infty}^{\infty} \frac{H_k^{(2)}(\beta\rho')\, e^{jk(\phi_n-\phi')}}{H_k^{(2)}{}'(\beta a)} \qquad (5-153)$$

5.5.3 Simulated Far-Field Patterns from SPM and Modal Analysis for Circular Cylinders

The Spectral Projection Model is applied here for calculating the electric far-field pattern for circular cylinders excited by plane wave with normal incidence at, i.e. $\phi_i = 90^o$. Results of the Spectral Projection Model agree well with analytical modal solutions excited by both TM^z and TE^z plane waves for circular cylinders of different radii. Shown in Figure 5-22a, 5-22b, and 5-22c are the far-field patterns of different radii circular cylinders. Angle of incidence is 90^o. Forward scattering is observed at $\phi_{scat} = 270^o$.

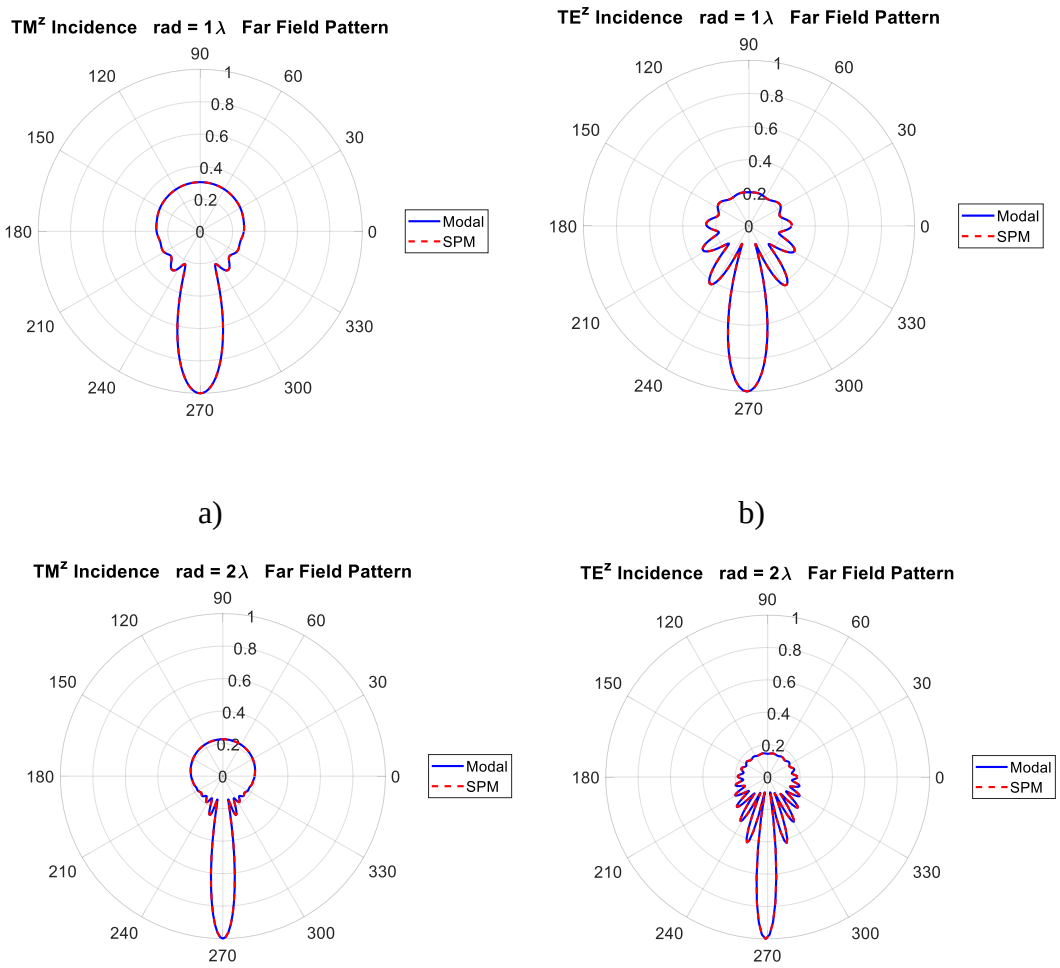

Figure 5-23: a) Polar plots of a) TM^z and b) TE^z far-field patterns for circular cylinders. Cylinders have radius 1λ. Polar plots of c) TM^z and d) TE^z far-field patterns for circular cylinders. Cylinders have radius 2λ.

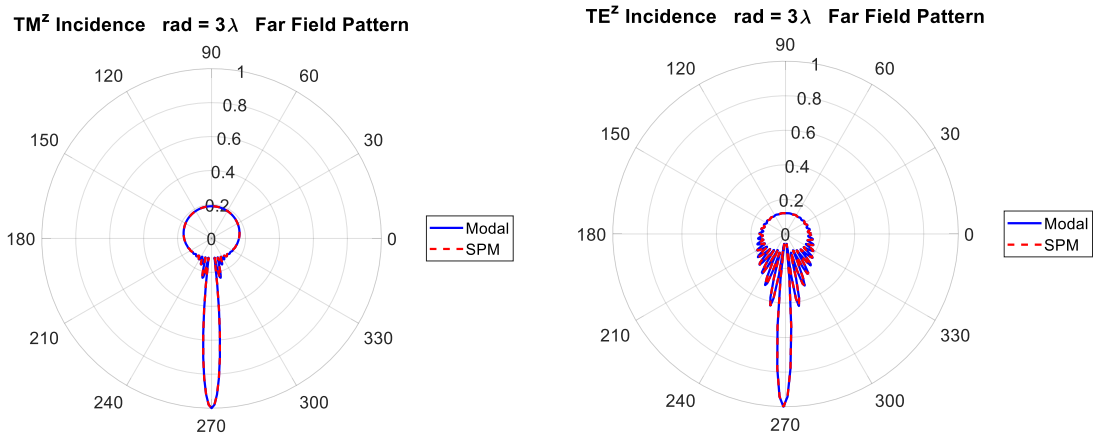

a) b)

Figure 5-24: Polar plots of a) TM^z and b) TE^z far-field patterns for circular cylinders. Cylinders have radius 3λ.

5.5.4 Validation of the Spectral Projection Model for Near-Field TM^z Wave

A near field electric current line current source I_e radiates an electric field with TM^z polarization upon a PEC infinitely long circular cylinder as in Figure 5-18a. The current density on the surface of a cylinder due to the incident TM^z polarized wave from angle $\phi_0{}'$ is given in equation $(5-154)$.

$$\boldsymbol{J}_s(a,\phi') = -\hat{\boldsymbol{z}}\frac{I_e}{2\pi a}\sum_{k=-\infty}^{\infty}\frac{H_k^{(2)}(\beta\rho_0{}')}{H_k^{(2)}(\beta a)}\,e^{jk(\phi\prime-\phi_0\prime)} \qquad (5-154)$$

The modal spectral signature of an infinitely long circular cylinder solved by analytical techniques, MOM and SPM for TM^z scattering are shown to have excellent agreement. See Figure 5-25.

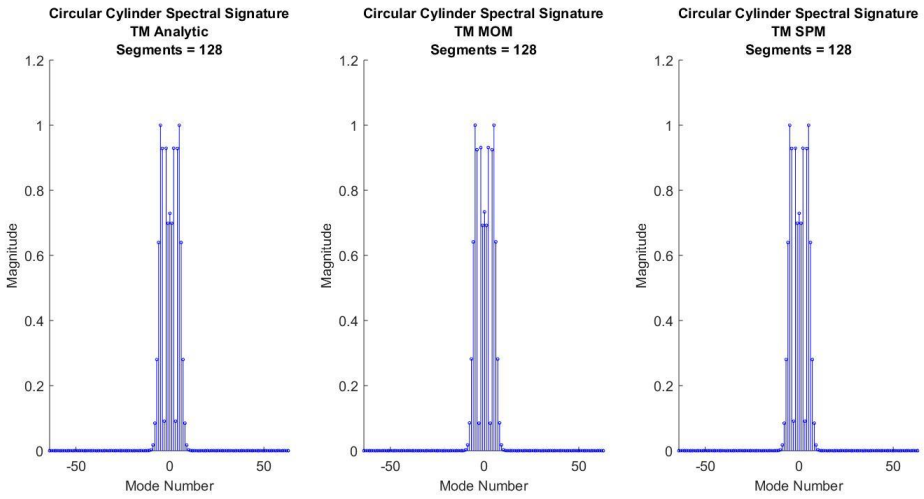

a) b) c)

Figure 5-25: Spectral signature of an infinitely long circular cylinder with radius = 1λ excited by a near-field TM^z wave from a line source calculated using a) analytical method b) Method of Moments and c) Spectral Projection Model.

In Figure 5-26 is shown the far-field pattern of the infinitely long circular cylinder of radius 1λ. calculated using the SPM and MOM. Angle of incidence is 90^o.

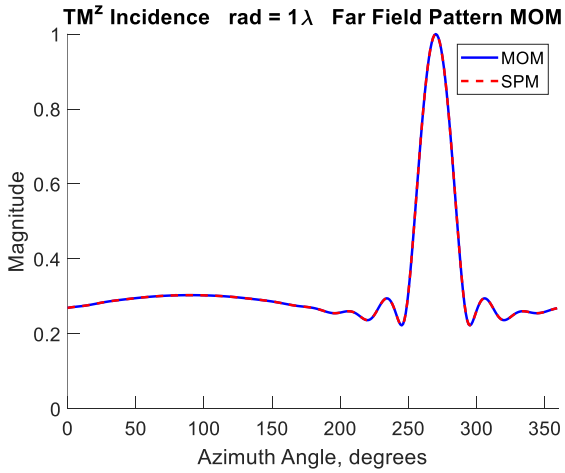

Figure 5-26: Calculated linear plot of far-field pattern for an infinitely long circular cylinder with radius = 1λ excited by a near-field TM^z wave from a line source calculated using the Method of Moments and Spectral Projection Model.

5.5.5 Validation of the Spectral Projection Model for Near-Field TE^z Wave

A near field magnetic current line current source I_m radiates a magnetic field with TE^z polarization upon a PEC infinitely long circular cylinder as in Figure 5-18b. The current density on the surface of a cylinder due to the incident TE^z polarized wave from incidence angle $\phi_0{}'$ is given in equation $(5-155)$. For these plots, angle of incidence is 90^o.

$$\boldsymbol{J_s}(a,\phi') = -\widehat{\boldsymbol{\phi}}\frac{jI_m}{2\eta\pi a}\sum_{k=-\infty}^{\infty}\frac{H_k^{(2)}(\beta\rho_0{}')}{H_k^{(2)}{}'(\beta a)}\,e^{jk(\phi'-\phi_0{}')} \qquad (5-154)$$

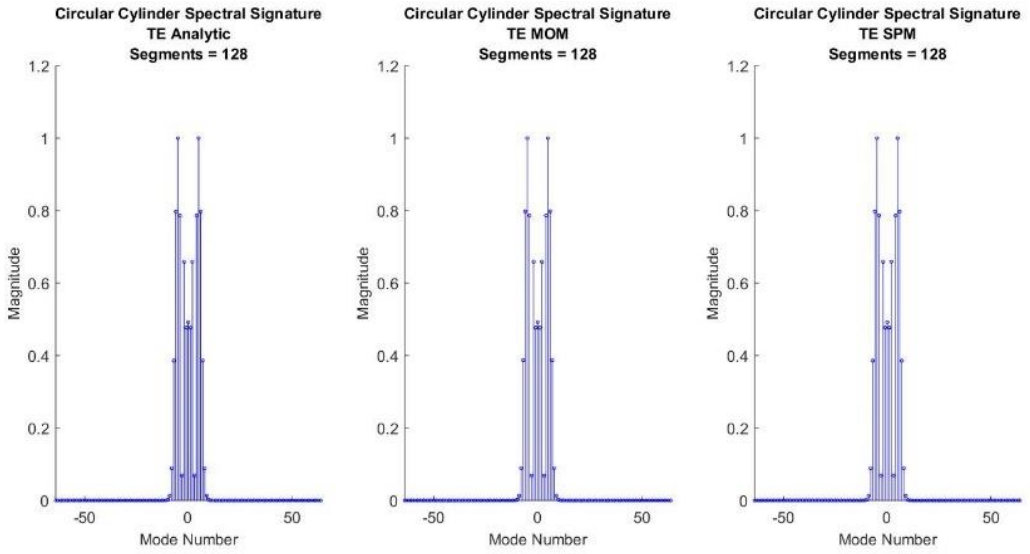

a) b) c)

Figure 5-27: Spectral signature of an infinitely long circular cylinder with radius = 1λ excited by a near-field TE^z wave from a line source calculated using a) analytical method b) Method of Moments and c) Spectral Projection Model.

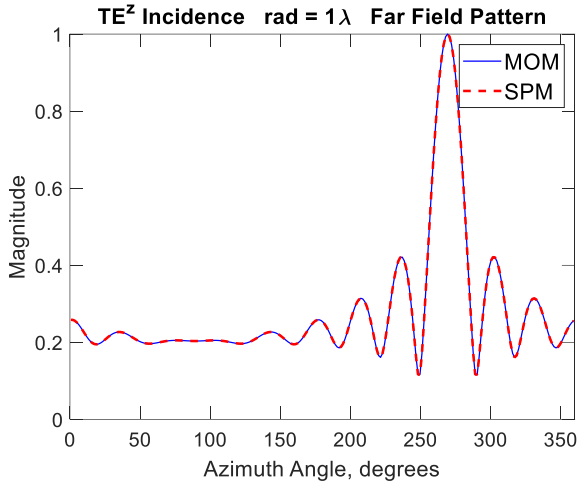

Figure 5-28: Calculated linear plot of far-field pattern for an infinitely long circular cylinder with radius = 1λ excited by a near-field TE^z wave from a line source calculated using the Method of Moments and Spectral Projection Model.

Comparison of the modal solution of an infinitely long circular cylinder with MOM and SPM for TE^z scattering is shown to have excellent agreement. See Figure 5-27. In Figure 5-28 is shown the far-field pattern of the infinitely long circular cylinder calculated using the SPM and MOM.

5.6 Limitation of SPM due to Bessel and Hankel Function Modes

The Spectral Projection Method as presented is limited by properties of the Bessel and Hankel functions much like the Method of Moments. The electric field for an infinitely long line source in the near and far-field are characterized using the zeroth order Hankel function of the second kind.

Plotted below in Figure 5-29 are the real and imaginary parts of the Hankel function $H_0^{(2)}(\beta|\boldsymbol{\rho}|)$.

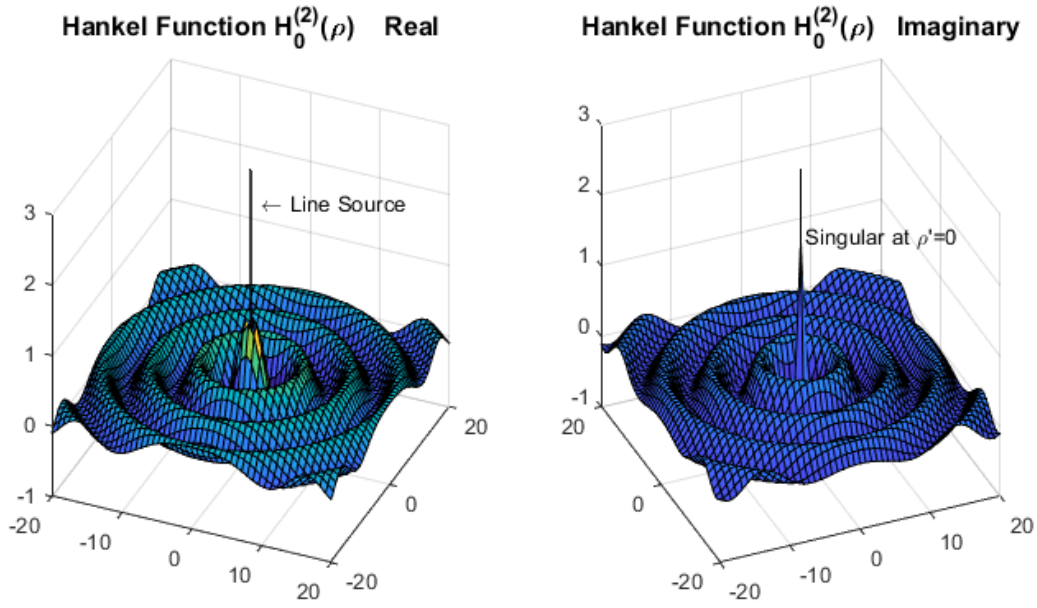

a) b)

Figure 5-29: The figure shows the real and imaginary components of the function $H_0^{(2)}(\beta|\boldsymbol{\rho}-\boldsymbol{\rho}'|)$ with $\rho' = 0$. a) Real part. b) Imaginary part.

The electric field from an electric line current source is illustrated in Figure 5-29. In this figure, the imaginary part of the electric field from the line source is singular at $\rho' = 0$. Hankel functions are cylindrically symmetric, and vary only with the ρ components.

The magnitude of a Bessel function increases as the absolute value of the mode number increases for near field arguments, i.e. small ρ values. In Figures 5-30a and 5-30b below, the decrease in magnitude is about 5-10 between Bessel function order -30 to 30. In the far-field, the magnitude of the Bessel functions decreases to zero, as seen in Figure 5-30c. This ensures convergence of the addition theorem, and thus the projection of the **J**-spectral signature onto the **H**-spectral signature.

The main obstacle limiting implementation of SPM for non-circular objects of small wavelength is the increase in magnitude of the Hankel function as the absolute value of the mode number increases. As seen in Figure 5-31a below, unlike the Bessel function, the magnitude of a Hankel function increases as the absolute value of the mode number increases for small wavelength ρ. In the far-field for increasing values of ρ, the magnitude of the Hankel function

decreases but the magnitude of the amplitude of each mode trends to the same absolute value, verifying the asymptotic approximation given in equation $(5-70)$. See Figures 5-31b, 5-31c and 5-32.

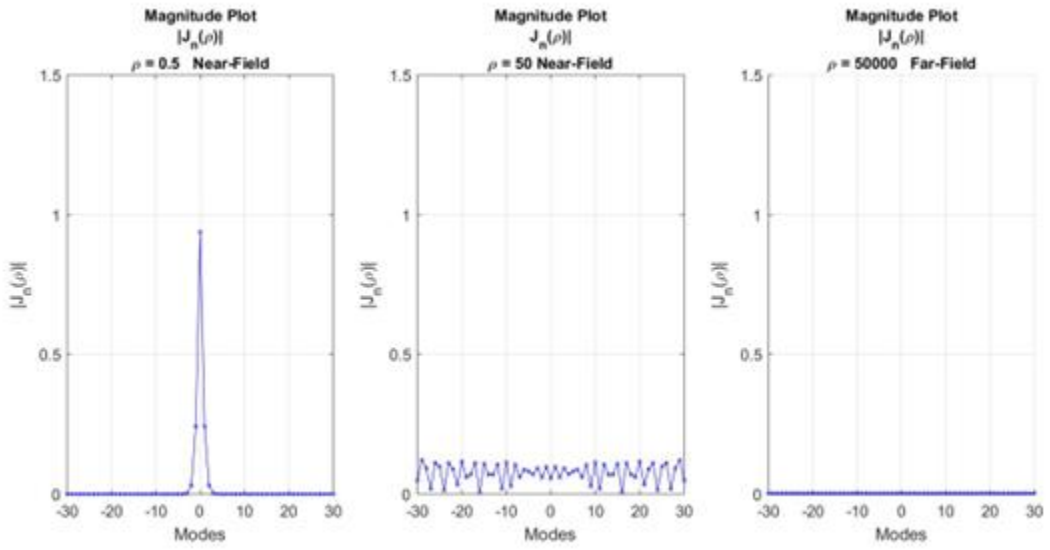

a) b) c)

Figure 5-30: Magnitude plots of Bessel functions versus modes for a) $\rho = .5\lambda$ b) $\rho = 50\lambda$ c) $\rho = 50000\lambda$.

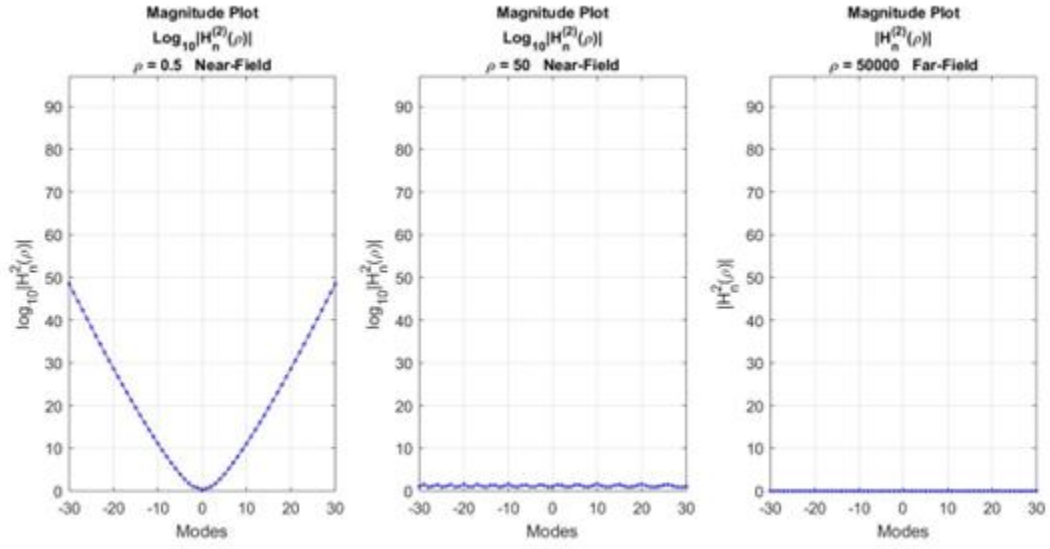

a) b) c)

Figure 5-31: Magnitude plots of Hankel functions versus modes for a) $\rho = .5\lambda$ b) $\rho = 50\lambda$ c) $\rho = 50000\lambda$.

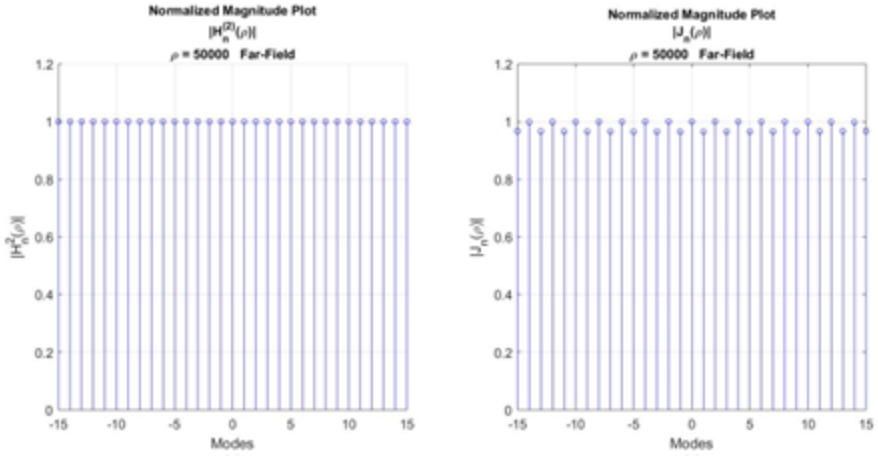

a) b)

Figure 5-32: Asymptotic expansion approximation to the far-field patterns for a) Hankel functions and b) Bessel functions.

5.6.1 Convergence of the Addition Theorem

For small radii, the higher order modes of the Hankel function increase in amplitude and decrease the numerical accuracy of the addition theorem. This is evident from conditions set by the addition theorem on requirements for the ρ and ρ' vectors. Recall the addition theorem in equation $(5-3)$. Equation $(5-156)$ writes the addition theorem as an infinite summation.

$$H_0^{(2)}(\beta|\boldsymbol{\rho}-\boldsymbol{\rho}'|) = \sum_{k=-\infty}^{\infty} J_k(\beta|\boldsymbol{\rho}'|)H_k^{(2)}(\beta|\boldsymbol{\rho}|)e^{jk(\phi-\phi')} \qquad \rho \geq \rho' \quad (5-156)$$

Figure 5-31 illustrates this requirement $\rho \geq \rho'$ when satisfied by a circular cylinder.

For a circle as in Figure 5-33, simply defining two circles with $\rho \geq \rho'$ satisfies the addition theorem. For the ellipse plotted in Figure 5-34, the ρ' vectors in red are not always smaller than the ρ vectors in blue. The addition theorem given in $(5-156)$ is not satisfied if the ρ' vectors are chosen on the surface of the elliptical cylinder. For this ellipse, ρ_1 is the major axis, and ρ_5 is the minor axis.

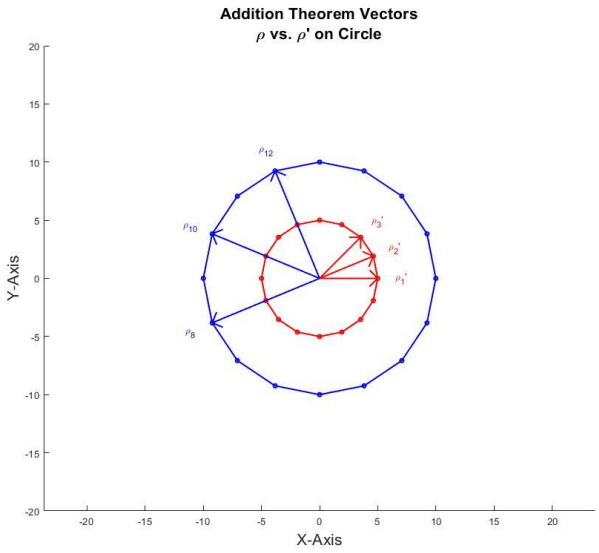

Figure 5-33: Vectors ρ and ρ' around a circular cylinder.

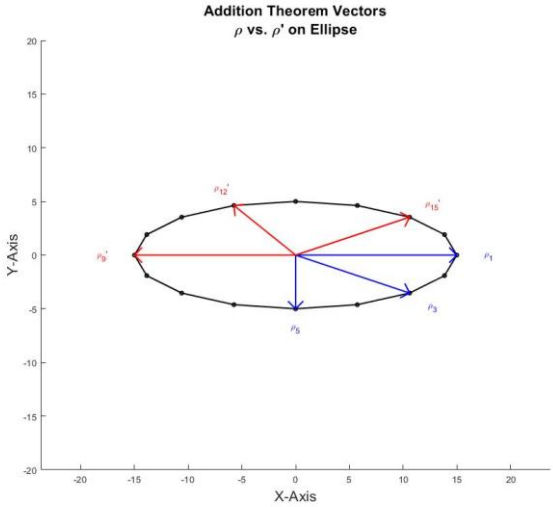

Figure 5-34: Vectors ρ and ρ' around an elliptical cylinder.

In Figure 5-35 the ρ' vectors in red are all smaller than the ρ vectors in blue. So, the addition theorem given in $(5-156)$ is always satisfied because the ρ' vectors fall inside the circular cylinder. In order to satisfy the addition theorem, the condition $\rho' \leq \rho_5$ for all ρ' must be met.

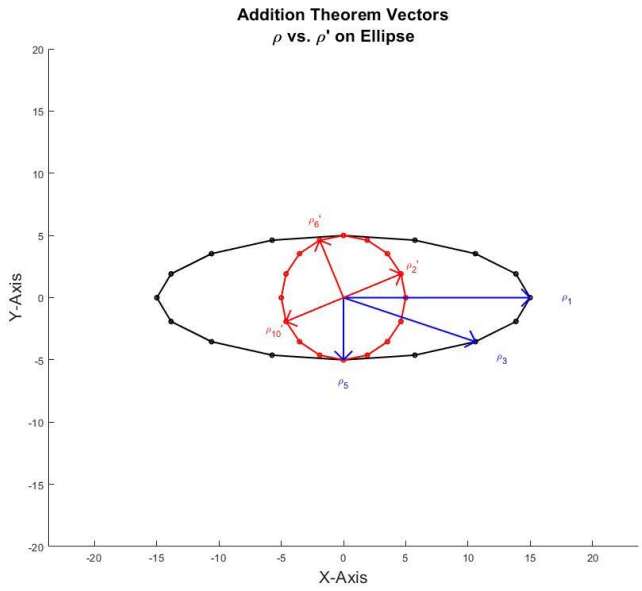

Figure 5-35: Vectors ρ and ρ' around an elliptical cylinder and inside circular cylinder.

5.6.2 Convolution Model for Spectral Signatures

In order to use the addition theorem for cases in which the cylinder shape is not circular, it is necessary to ensure that $\rho' < \rho$ using a different approach. The addition theorem given in equation $(5-2)$ may be written as a convolution. Equation $(5-157)$ gives the addition theorem in this form, with the symbol $\otimes$ signifying convolution.

$$H(m, \rho + \rho') = H(n, \rho) \otimes J(n, \rho') \qquad \rho \geq \rho' \quad (5-157)$$

Using this notation for convolution, methods of translating the origin for elliptically shaped surfaces will be discussed.

As stated earlier, the condition of the addition theorem states that in order for it to work for source point ρ and observation point ρ', the ρ vector with the larger radial distance from the origin will be the argument of the Hankel function and the smaller ρ must be for the Bessel function. This inequality $\rho \geq \rho'$ must be satisfied for the summation to converge.

For a closed conducting surface, the source (surface currents) and observation points (boundary conditions) are all located on the surface. Ideally, one would like the Hankel function to depend on the farther point, while the Bessel function will depend on the closer one. This is to ensure that the condition $\rho \geq \rho'$ stated in equation $(5-157)$ is complied with. But for a geometric shape other than a circle, depending on the angle, the distance of observation points

and source points from the origin changes. Since the radial distance depends on the origin, by translating the origin one can ensure that the condition $\rho \geq \rho'$ is always satisfied.

Figure 5-36a shows two source points, $\boldsymbol{so_1}$ and $\boldsymbol{so_2}$, and a single observation point ob_1. Begin by using O_1 as the origin. Since $\rho_{ob_1} > \rho_{so_1}$, in order to calculate the contribution of the source point so_1 at ob_1, ρ_{ob_1} must be the argument of the Hankel function and ρ_{so_1} must be the argument of the Bessel function. However, when calculating the contribution of ρ_{so_2} at ρ_{ob_1}since $\rho_{so_2} > \rho_{ob_1}$, the vector ρ_{ob_1} cannot be used as the argument of the Hankel function with origin O_1.

Now consider Figures 5-36b and 5-36c. If the origin is translated to O_2 via vector ρ_{trans}, $\rho'_{ob_1} > \rho'_{so_2}$, and ρ'_{ob_1} can be used as the argument for the Hankel function, while ρ'_{so_2} is used to calculate the Bessel function.

At the beginning of this chapter, two general forms of Graf's addition theorem were given in equations $(5-2)$ and $(5-3)$. Graf's addition theorem for Hankel functions of order *m* for the difference between two vectors is given in $(5-3)$,

$$H_m^{(2)}(\beta|\boldsymbol{\rho}-\boldsymbol{\rho}'|)e^{jm\phi''} = \sum_{n=-\infty}^{\infty} H_{m+n}^{(2)}(\beta|\boldsymbol{\rho}|)J_n(\beta|\boldsymbol{\rho}'|)e^{j[(m+n)\phi-n\phi']} \qquad \rho \geq \rho' \qquad (5-3)$$

and for the sum of two vectors the general form is $(5-2)$.

$$H_m^{(2)}(\beta|\boldsymbol{\rho}+\boldsymbol{\rho}'|)e^{jm\phi''} = \sum_{n=-\infty}^{\infty} H_{m-n}^{(2)}(\beta|\boldsymbol{\rho}|)J_n(\beta|\boldsymbol{\rho}'|)e^{j[(m-n)\phi-n\phi']} \qquad \rho \geq \rho' \qquad (5-2)$$

Vectors associated with the $|\boldsymbol{\rho}+\boldsymbol{\rho}'|$ form of the addition theorem are illustrated in Figure 5-36.

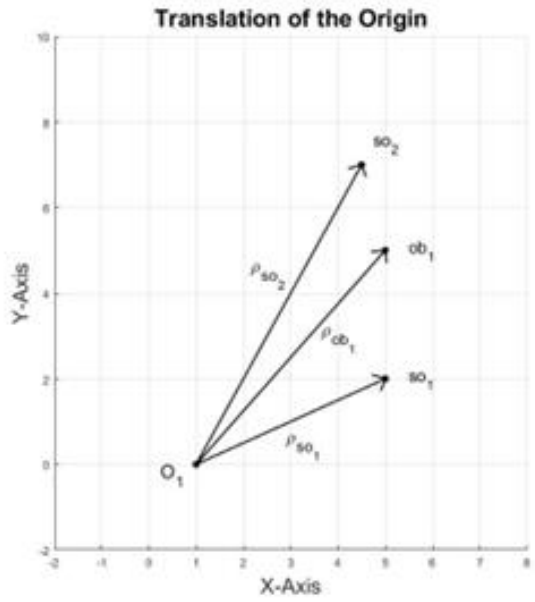

a)

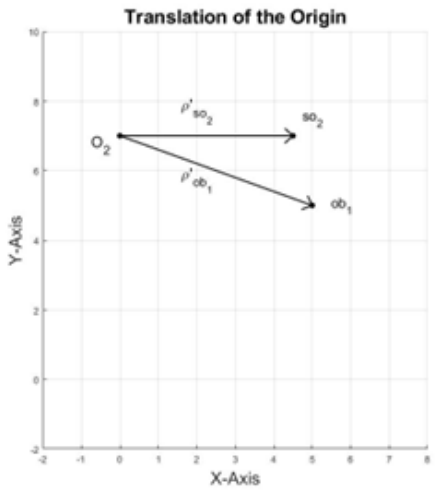

b)

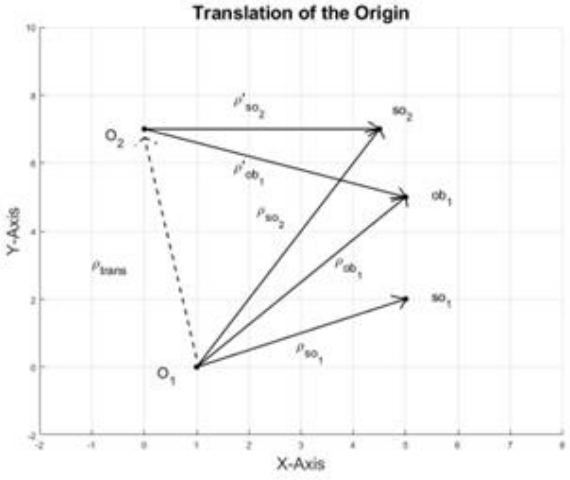

c)

Figure 5-36: a) Original origin, O_1, source and observation points. b) New origin, O_2, source and observation vectors. c) Translation of source and one observation point with new origin O_2.

Graf's addition theorem for the addition of two vectors $|\boldsymbol{\rho} + \boldsymbol{\rho}'|$ may be thought of as a discrete convolution between the **H**-spectral signature of an observation point at (ρ, ϕ) and the **J**-spectral signature of a source point at (ρ', ϕ'). Equation $(5-2)$ may be expressed in new notation as equation $(5-158)$.

$$H(m, \rho + \rho') = H(n, \rho) \otimes J(n, \rho') \qquad \rho \geq \rho' \quad (5-158)$$

To describe the convolution of two **J**-spectral signatures, the notation for the addition theorem is given in equation $(5-159)$.

$$J(m, \rho + \rho') = J(n, \rho) \otimes J(n, \rho') \qquad \rho \geq \rho' \quad (5-159)$$

The convolution operation permits one to define a relationship between two spectral signatures with respect to two separate origins.

The function $\boldsymbol{H}(m, \rho + \rho')$ represents the **H**-spectral signature with respect to the origin, O'**,** and $H(n, \rho)$ is **H**-spectral signature with respect to origin, O. $J(n, \rho')$ represents the **J**-spectral signature of the translation vector representing the translation of the origin from O' to O. See Figure 5-37 for an illustration.

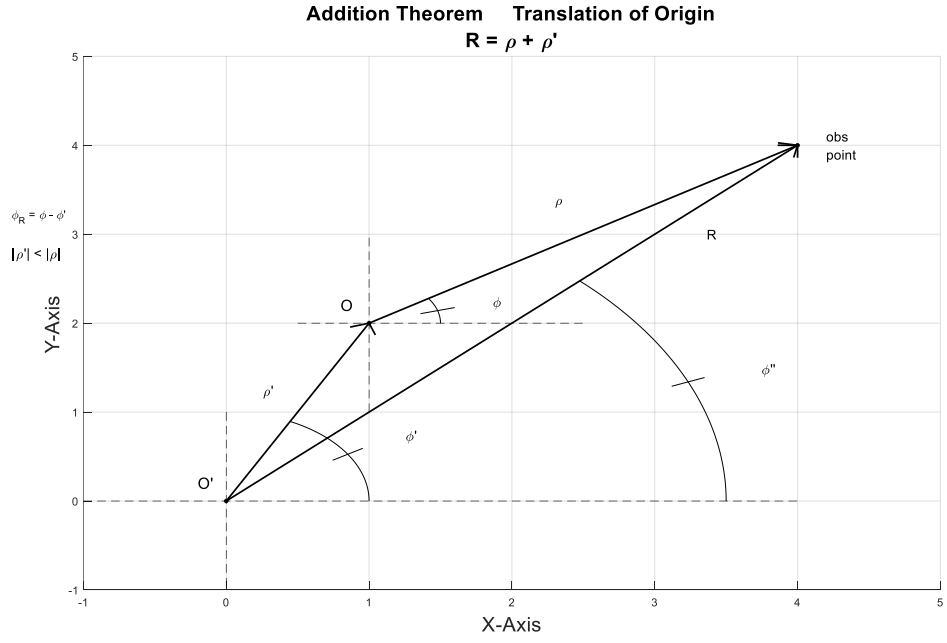

Figure 5-37: Illustration of Graf's addition theorem for $|\rho + \rho'|$ showing the translation of the origin.

The addition theorem may be written as the convolution of several Bessel functions as long as the condition $\rho \geq \rho'$ is met. For example if, $\rho' = {\rho_1}' + {\rho_2}'$, one may write

$$J(n, {\rho_1}' + {\rho_2}') = J(q, {\rho_1}') \otimes J(q, {\rho_2}') \qquad \rho \geq \rho' \quad (5-160)$$

And then one can write the Hankel function as the result of three convolutions.

$$H(m, \rho + \rho') = H(n, \rho) \otimes (J(q, {\rho_1}') \otimes J(q, {\rho_2}')) \qquad \rho \geq \rho' \quad (5-161)$$

A proof is given in Appendix A: SPM and Graf's Equation.

5.6.3 SPM and the Hadamard Product

To take advantage of the property of Graf's addition theorem to shift the origin, the Hadamard product of matrices in the DFT domain may be used to calculate the convolution of two vectors.

Assume a vector $\begin{bmatrix} | \\ \hat{h}_c \\ | \end{bmatrix}$ equals the convolution of two vectors, $\begin{bmatrix} | \\ \hat{h}_a \\ | \end{bmatrix}$ and $\begin{bmatrix} | \\ \hat{\jmath}_b \\ | \end{bmatrix}$.

$$\begin{bmatrix} | \\ \hat{h}_c \\ | \end{bmatrix} = \begin{bmatrix} | \\ \hat{h}_a \\ | \end{bmatrix} \otimes \begin{bmatrix} | \\ \hat{\jmath}_b \\ | \end{bmatrix} \qquad (5-162)$$

The convolution can be performed in the Fourier domain by taking the DFT of both sides of equation $(5-162)$, and writing it as the Hadamard product given in equation $(5-163)$.

$$\begin{bmatrix} \cdots & \cdots & \cdots \\ \cdots & F & \cdots \\ \cdots & \cdots & \cdots \end{bmatrix} \begin{bmatrix} | \\ \hat{h}_c \\ | \end{bmatrix} = \begin{bmatrix} \cdots & \cdots & \cdots \\ \cdots & F & \cdots \\ \cdots & \cdots & \cdots \end{bmatrix} \begin{bmatrix} | \\ \hat{h}_a \\ | \end{bmatrix} \odot \begin{bmatrix} \cdots & \cdots & \cdots \\ \cdots & F & \cdots \\ \cdots & \cdots & \cdots \end{bmatrix} \begin{bmatrix} | \\ \hat{\jmath}_b \\ | \end{bmatrix} \qquad (5-163)$$

To solve the matrix equation given below:

$$\begin{bmatrix} \cdots \\ e_i \\ \cdots \end{bmatrix} = \begin{bmatrix} \cdots & \cdots & \cdots \\ \cdots & H_c & \cdots \\ \cdots & \cdots & \cdots \end{bmatrix} \begin{bmatrix} \cdots \\ \hat{\imath}_{ss} \\ \cdots \end{bmatrix} \qquad (5-164)$$

where matrix $\begin{bmatrix} \cdots & \cdots & \cdots \\ \cdots & H_c & \cdots \\ \cdots & \cdots & \cdots \end{bmatrix}$ equals the column by column convolution of two matrices,

$$\begin{bmatrix} | & | & | \\ | & H_c & | \\ | & | & | \end{bmatrix} = \begin{bmatrix} | & | & | \\ | & H_a & | \\ | & | & | \end{bmatrix} \otimes_C \begin{bmatrix} | & | & | \\ | & J_b & | \\ | & | & | \end{bmatrix} \qquad (5-165)$$

one can write

$$\begin{bmatrix}\cdots\\ e_i\\ \cdots\end{bmatrix}=\left(\begin{bmatrix}| & | & |\\ | & H_a & |\\ | & | & |\end{bmatrix}\otimes_C\begin{bmatrix}| & | & |\\ | & J_b & |\\ | & | & |\end{bmatrix}\right)\begin{bmatrix}\cdots\\ \hat{\imath}_{ss}\\ ..\end{bmatrix} \qquad (5-166)$$

Now a diagonal matrix $\begin{bmatrix}\ddots & 0 & 0\\ 0 & D_{ii} & 0\\ 0 & 0 & \ddots\end{bmatrix}$ and its companion vector consisting of its diagonal elements $\begin{bmatrix}\cdots\\ d_i\\ \cdots\end{bmatrix}$, in which every element $D_{ii}=d_i$.

$$\begin{bmatrix}\cdots\\ d_i\\ \cdots\end{bmatrix}=diag\begin{bmatrix}\ddots & 0 & 0\\ 0 & D_{ii} & 0\\ 0 & 0 & \ddots\end{bmatrix} \qquad (5-167)$$

Then substituting $\begin{bmatrix}\cdots\\ \hat{\imath}_{ss}\\ ..\end{bmatrix}=\begin{bmatrix}\cdots\\ d_i\\ \cdots\end{bmatrix}$ into equation $(5-166)$ one obtains

$$\begin{bmatrix}\cdots\\ e\\ \cdots\end{bmatrix}=\left(\begin{bmatrix}| & | & |\\ | & H_a & |\\ | & | & |\end{bmatrix}\otimes\begin{bmatrix}| & | & |\\ | & J_b & |\\ | & | & |\end{bmatrix}\right)\begin{bmatrix}\cdots\\ d_i\\ \cdots\end{bmatrix} \qquad (5-168)$$

Next define the discrete Fourier transforms of the following matrices and vectors:

$$\begin{bmatrix}| & | & |\\ | & FH_a & |\\ | & | & |\end{bmatrix}=\begin{bmatrix}\cdots & \cdots & \cdots\\ \cdots & F & \cdots\\ \cdots & \cdots & \cdots\end{bmatrix}\begin{bmatrix}| & | & |\\ | & H_a & |\\ | & | & |\end{bmatrix} \qquad (5-169)$$

$$\begin{bmatrix}| & | & |\\ | & FJ_b & |\\ | & | & |\end{bmatrix}=\begin{bmatrix}\cdots & \cdots & \cdots\\ \cdots & F & \cdots\\ \cdots & \cdots & \cdots\end{bmatrix}\begin{bmatrix}| & | & |\\ | & J_b & |\\ | & | & |\end{bmatrix} \qquad (5-170)$$

$$\begin{bmatrix}| & | & |\\ | & FD_i & |\\ | & | & |\end{bmatrix}=\begin{bmatrix}\cdots & \cdots & \cdots\\ \cdots & F & \cdots\\ \cdots & \cdots & \cdots\end{bmatrix}\begin{bmatrix}\ddots & 0 & 0\\ 0 & D_{ii} & 0\\ 0 & 0 & \ddots\end{bmatrix} \qquad (5-171)$$

$$\begin{bmatrix}\cdots\\ Fd_i\\ \cdots\end{bmatrix}=\begin{bmatrix}\cdots & \cdots & \cdots\\ \cdots & F & \cdots\\ \cdots & \cdots & \cdots\end{bmatrix}\begin{bmatrix}\cdots\\ d_i\\ \cdots\end{bmatrix} \qquad (5-172)$$

$$\begin{bmatrix}| & | & |\\ | & Fe_i & |\\ | & | & |\end{bmatrix}=\begin{bmatrix}\cdots & \cdots & \cdots\\ \cdots & F & \cdots\\ \cdots & \cdots & \cdots\end{bmatrix}\begin{bmatrix}\cdots\\ e_i\\ \cdots\end{bmatrix} \qquad (5-173)$$

and then multiply both sides of $(5-166)$ by the Fourier operator,

$$\begin{bmatrix}\cdots & \cdots & \cdots\\ \cdots & F & \cdots\\ \cdots & \cdots & \cdots\end{bmatrix}\begin{bmatrix}\cdots\\ e_i\\ \cdots\end{bmatrix}=\begin{bmatrix}\cdots & \cdots & \cdots\\ \cdots & F & \cdots\\ \cdots & \cdots & \cdots\end{bmatrix}\left(\left(\begin{bmatrix}| & | & |\\ | & H_a & |\\ | & | & |\end{bmatrix}\otimes\begin{bmatrix}| & | & |\\ | & J_b & |\\ | & | & |\end{bmatrix}\right)\begin{bmatrix}\cdots\\ d_i\\ \cdots\end{bmatrix}\right) \qquad (5-174)$$

Equation $(5-174)$ may be written as a Hadamard product,

$$\begin{bmatrix} \cdots \\ Fe_i \\ \cdots \end{bmatrix} = \left(\begin{bmatrix} | & | & | \\ | & FH_a & | \\ | & | & | \end{bmatrix} \odot \begin{bmatrix} | & | & | \\ | & FJ_b & | \\ | & | & | \end{bmatrix} \right) \begin{bmatrix} \cdots \\ d_i \\ \cdots \end{bmatrix} \quad (5-175)$$

Using another property of Hadamard products one can rewrite equation $(5-175)$ as $(5-176)$..

$$\begin{bmatrix} \cdots \\ Fe_i \\ \cdots \end{bmatrix} = diag\left(\begin{bmatrix} | & | & | \\ | & FH_a & | \\ | & | & | \end{bmatrix} \begin{bmatrix} \ddots & 0 & 0 \\ 0 & D_{ii} & 0 \\ 0 & 0 & \ddots \end{bmatrix} \begin{bmatrix} | & | & | \\ | & FJ_b & | \\ | & | & | \end{bmatrix}^T \right) \quad (5-176)$$

Where $diag$ refers to the diagonal elements of the matrix in parentheses, and the diagonal elements of the matrix $\begin{bmatrix} \ddots & 0 & 0 \\ 0 & D_{ii} & 0 \\ 0 & 0 & \ddots \end{bmatrix}$ are the elements of column vector $\begin{bmatrix} | \\ d_i \\ | \end{bmatrix}$.

Recall that by applying singular value decomposition (SVD) to matrix $\begin{bmatrix} | & | & | \\ | & FH_a & | \\ | & | & | \end{bmatrix}$, it can be decomposed into three matrices shown below:

$$\begin{bmatrix} | & | & | \\ | & FH_a & | \\ | & | & | \end{bmatrix} = \begin{bmatrix} | & | & | \\ | & U_a & | \\ | & | & | \end{bmatrix} \begin{bmatrix} \ddots & 0 & 0 \\ 0 & D_{FH_a} & 0 \\ 0 & 0 & \ddots \end{bmatrix} \begin{bmatrix} | & | & | \\ | & V_a & | \\ | & | & | \end{bmatrix}^T \quad (5-177)$$

where

$\begin{bmatrix} | & | & | \\ | & U_a & | \\ | & | & | \end{bmatrix}$ and $\begin{bmatrix} | & | & | \\ | & V_a & | \\ | & | & | \end{bmatrix}$ are unitary matrices, while $\begin{bmatrix} \ddots & 0 & 0 \\ 0 & D_{FH_a} & 0 \\ 0 & 0 & \ddots \end{bmatrix}$ is a diagonal matrix whose diagonal entries are the singular values of the SVD.

One may use singular value decomposition on matrix $\begin{bmatrix} | & | & | \\ | & J_b & | \\ | & | & | \end{bmatrix}$ as well.

$$\begin{bmatrix} | & | & | \\ | & FJ_b & | \\ | & | & | \end{bmatrix} = \begin{bmatrix} | & | & | \\ | & U_b & | \\ | & | & | \end{bmatrix} \begin{bmatrix} \ddots & 0 & 0 \\ 0 & D_{FJ_b} & 0 \\ 0 & 0 & \ddots \end{bmatrix} \begin{bmatrix} | & | & | \\ | & V_b & | \\ | & | & | \end{bmatrix}^T \quad (5-178)$$

Substituting into equation $(5-176)$ one obtains equation $(5-179)$.

$$\begin{bmatrix} \cdots \\ Fe_i \\ \cdots \end{bmatrix} =$$

$$diag\left(\begin{bmatrix} | & | & | \\ | & U_a & | \\ | & | & | \end{bmatrix}\begin{bmatrix} \ddots & 0 & 0 \\ 0 & D_{H_a} & 0 \\ 0 & 0 & \ddots \end{bmatrix}\begin{bmatrix} | & | & | \\ | & V_a & | \\ | & | & | \end{bmatrix}^T\begin{bmatrix} \ddots & 0 & 0 \\ 0 & D_{ii} & 0 \\ 0 & 0 & \ddots \end{bmatrix}\begin{bmatrix} | & | & | \\ | & V_b & | \\ | & | & | \end{bmatrix}\begin{bmatrix} \ddots & 0 & 0 \\ 0 & D_{J_b} & 0 \\ 0 & 0 & \ddots \end{bmatrix}\begin{bmatrix} | & | & | \\ | & U_b & | \\ | & | & | \end{bmatrix}^T\right) \quad (5-179)$$

This expression may now be written in terms of diagonal element vectors corresponding to the diagonal matrices defined above.

$$\begin{bmatrix} \cdots \\ \hat{d}_{H_a} \\ \cdot\cdot \end{bmatrix} = \begin{bmatrix} \ddots & 0 & 0 & 0 & 0 \\ 0 & \ddots & 0 & 0 & 0 \\ 0 & 0 & D_{H_a} & 0 & 0 \\ 0 & 0 & 0 & \ddots & 0 \\ 0 & 0 & 0 & 0 & \ddots \end{bmatrix}\begin{bmatrix} 1 \\ \cdots \\ 1 \\ \cdot\cdot \\ 1 \end{bmatrix} \quad (5-180)$$

and

$$\begin{bmatrix} \cdots \\ \hat{d}_{J_b} \\ \cdot\cdot \end{bmatrix} = \begin{bmatrix} \ddots & 0 & 0 & 0 & 0 \\ 0 & \ddots & 0 & 0 & 0 \\ 0 & 0 & D_{J_b} & 0 & 0 \\ 0 & 0 & 0 & \ddots & 0 \\ 0 & 0 & 0 & 0 & \ddots \end{bmatrix}\begin{bmatrix} 1 \\ \cdots \\ 1 \\ \cdot\cdot \\ 1 \end{bmatrix} \quad (5-181)$$

Now equation $(5-179)$ may be written using the property given in equations $(5-175)$ and $(5-176)$ in a new form as the vector $\begin{bmatrix} \cdots \\ \hat{d}_{H_a} \\ \cdot\cdot \end{bmatrix}$ projected onto a Hadamard product.

$$\begin{bmatrix} \cdots \\ Fe_i \\ \cdots \end{bmatrix} = \left(\begin{bmatrix} | & | & | \\ | & U_a & | \\ | & | & | \end{bmatrix} \odot \begin{bmatrix} | & | & | \\ | & U_b & | \\ | & | & | \end{bmatrix}\begin{bmatrix} \ddots & 0 & 0 \\ 0 & D_{J_b} & 0 \\ 0 & 0 & \ddots \end{bmatrix}\begin{bmatrix} | & | & | \\ | & V_b & | \\ | & | & | \end{bmatrix}^T\begin{bmatrix} 0 & 0 & 0 \\ 0 & D_{ii} & 0 \\ 0 & 0 & 0 \end{bmatrix}\begin{bmatrix} | & | & | \\ | & V_a & | \\ | & | & | \end{bmatrix}\right)\begin{bmatrix} \cdots \\ \hat{d}_{H_a} \\ \cdot\cdot \end{bmatrix} \quad (5-182)$$

Then rearranging $(5-175)$ into $(5-183)$,

$$\begin{bmatrix} \cdots \\ Fe_i \\ \cdots \end{bmatrix} = \left(\begin{bmatrix} | & | & | \\ | & FJ_b & | \\ | & | & | \end{bmatrix} \odot \begin{bmatrix} | & | & | \\ | & FH_a & | \\ | & | & | \end{bmatrix}\right)\begin{bmatrix} \cdots \\ d_i \\ \cdots \end{bmatrix} \quad (5-183)$$

one can write $(5-183)$ as a different but equal matrix expression in which the vector $\begin{bmatrix} \cdots \\ \hat{d}_{J_b} \\ \cdot\cdot \end{bmatrix}$ is projected onto a different Hadamard product.

$$\begin{bmatrix} \cdots \\ Fe_i \\ \cdots \end{bmatrix} = \left(\begin{bmatrix} | & | & | \\ | & U_b & | \\ | & | & | \end{bmatrix} \odot \begin{bmatrix} | & | & | \\ | & U_a & | \\ | & | & | \end{bmatrix}\begin{bmatrix} \ddots & 0 & 0 \\ 0 & D_{H_a} & 0 \\ 0 & 0 & \ddots \end{bmatrix}\begin{bmatrix} | & | & | \\ | & V_a & | \\ | & | & | \end{bmatrix}^T\begin{bmatrix} 0 & 0 & 0 \\ 0 & D_{\hat{i}} & 0 \\ 0 & 0 & 0 \end{bmatrix}\begin{bmatrix} | & | & | \\ | & V_b & | \\ | & | & | \end{bmatrix}\right)\begin{bmatrix} \cdots \\ \hat{d}_{J_b} \\ \cdot\cdot \end{bmatrix} \quad (5-184)$$

Thus, if the vector $\begin{bmatrix} \cdots \\ e_i \\ \cdots \end{bmatrix}$ represents either the incident or induced electric or magnetic field, the projection of the **H**-spectral signature of the incident current $\begin{bmatrix} \cdots \\ \hat{d}_{H_a} \\ \cdot\cdot \end{bmatrix}$ onto the **J**-spectral signature of the observation points equals the projection of the **J**-spectral signature of the induced current $\begin{bmatrix} \cdots \\ \hat{d}_{J_b} \\ \cdot\cdot \end{bmatrix}$ onto the **H**-spectral signature of the observation points. This is the foundational principle of the Spectral Projection Model.

5.6.4 SPM with Translation for Ellipses of High Axial Ratio

The equation for the Spectral Projection Model that was given earlier is shown below:

$$\begin{bmatrix} \cdots & \cdots & \cdots \\ \cdots & J_k(\beta|\boldsymbol{\rho_{ob}}|) & \cdots \\ \cdots & \cdots & \cdots \end{bmatrix} \begin{bmatrix} \cdots \\ \hat{\imath}_{SS,inc} \\ \cdot\cdot \end{bmatrix} = \begin{bmatrix} \cdots & \cdots & \cdots \\ \cdots & H_k^{(2)}((\beta|\boldsymbol{\rho_{ob}}|) & \cdots \\ \cdots & \cdots & \cdots \end{bmatrix} \begin{bmatrix} \cdots \\ \hat{\imath}_{SS,ind} \\ \cdot\cdot \end{bmatrix} \qquad (5-185)$$

with the spectral signature vectors $\begin{bmatrix} \cdots \\ \hat{\imath}_{SS,inc} \\ \cdot\cdot \end{bmatrix}$ and $\begin{bmatrix} \cdots \\ \hat{\imath}_{SS,ind} \\ \cdot\cdot \end{bmatrix}$ being $M \times 1$ element vectors,

and the matrices in $(5-186)$ are equal.

$$\begin{bmatrix} - & - & - \\ - & H_k^{(2)}((\beta|\boldsymbol{\rho_{ob}}|) & - \\ - & - & - \end{bmatrix} = \begin{bmatrix} | & | & | \\ | & H_k\ (\beta|\boldsymbol{\rho}|)e^{jk\phi} & | \\ | & | & | \end{bmatrix}^T \qquad (5-186)$$

The observation matrix $\begin{bmatrix} - & - & - \\ - & H_k^{(2)}(\beta|\boldsymbol{\rho_{ob}}|) & - \\ - & - & - \end{bmatrix}$ consists of a set of row vectors which are the **H**-spectral signatures of the observation points. This may be written alternatively as

$$\begin{bmatrix} \cdots & \cdots & \cdots \\ \cdots & H_k^{(2)}(\beta|\boldsymbol{\rho_{ob}}|) & \cdots \\ \cdots & \cdots & \cdots \end{bmatrix} = \begin{bmatrix} H_{-K}^{(2)}(\beta|\boldsymbol{\rho_0}|)e^{-jK\phi_0} & \cdots & H_K^{(2)}(\beta|\boldsymbol{\rho_0}|)e^{jK\phi_0} \\ \cdots & \cdots & \cdots \\ H_{-K}^{(2)}(\beta|\boldsymbol{\rho_{M-1}}|)e^{-jK\phi_{M-1}} & \cdots & H_K^{(2)}(\beta|\boldsymbol{\rho_{M-1}}|)e^{jK\phi_{M-1}} \end{bmatrix} \qquad (5-187)$$

with each row being the **H**-spectral signature of an observation point $\rho_{a,n}$.

To generate an ellipse two constant radius vectors rotating in opposite directions may be summed together.

$\rho_{a,m}e^{j\phi_{a,m}} = ae^{jm\triangle\phi}$ $\quad m \in \{0,1,2,\ldots,M-1\}$ observation points along circle of radius a

$\rho_{b,m}e^{j\phi_{\mathrm{b,m}}} = be^{-jm\triangle\phi}$ $\quad m \in \{0,1,2,\ldots,M-1\}$ observation points along circle of radius b

$\rho_{e,m}e^{j\phi_{\mathrm{e,m}}} = \rho_{a,m} + \rho_{b,m}$ $\quad m \in \{0,1,2,\ldots,M-1\}$ observation points along ellipse e

For further details on how cylinders with non-circular cross sections can be generated using the sum of multiple vectors, see Appendix F and Figures 5-38, 5-39, and 5-40 below.

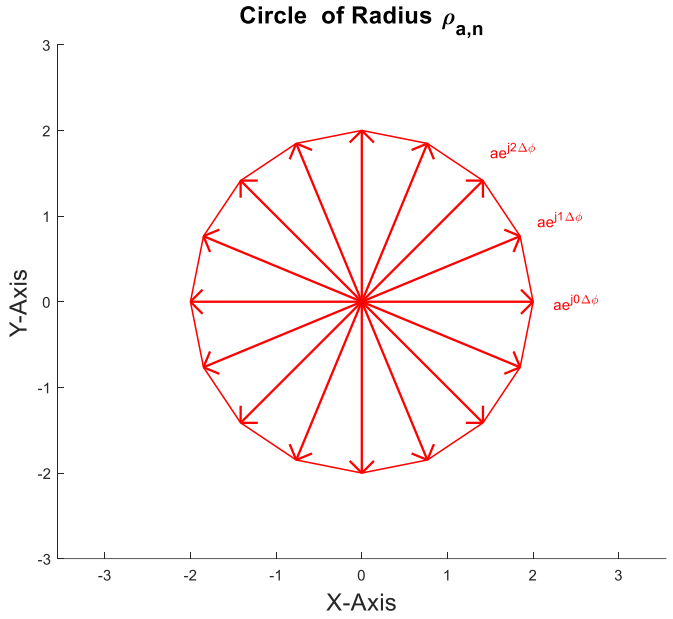

Figure 5-38: Counterclockwise rotating vector used to generate a circle with radius $\rho = a$.

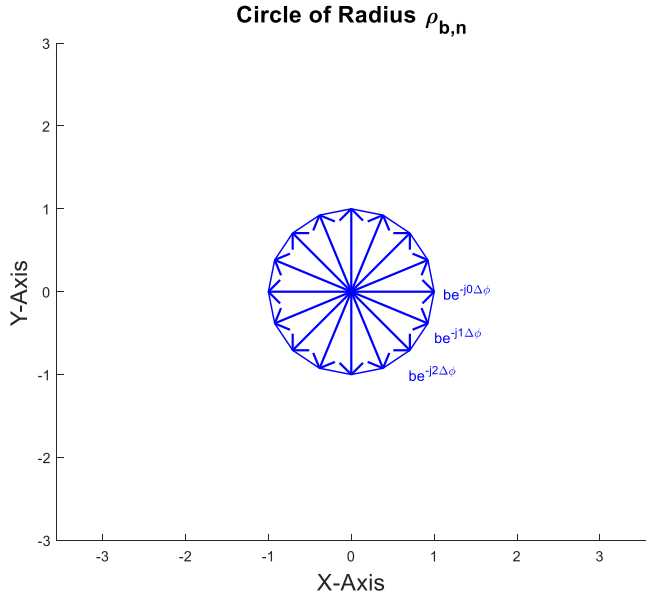

Figure 5-39: Clockwise rotating vector used to generate a circle with radius $\rho = b$.

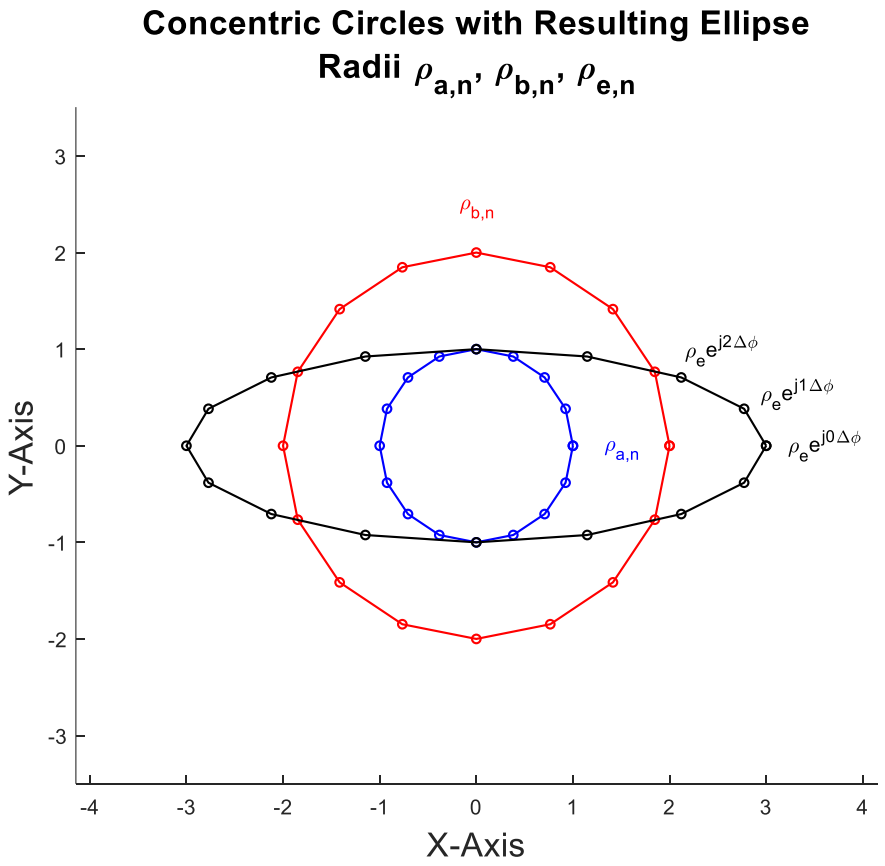

Figure 5-40: Sum of two vectors to generate an ellipse.

The resulting vector from both constant radius circles traces in Figure 5-36a and Figure 5-36b is an ellipse, so the observation points $\rho_{ob,m}$ on the ellipse are given below.

$\rho_{ob,m} = \rho_{e,m}$ $\quad m \in \{0,1,2,\ldots,M-1\}$ points along ellipse e

The Hankel spectral signature of the sum of the two rotating vectors at any discrete angle $m\Delta\phi$, and radius $\rho_{ob,n}$, may be calculated using the addition theorem shown in equation $(5-188)$ for $\rho_{b,m} \geq \rho_{a,m}$.

$$H_p^{(2)}\left(\beta\left|\boldsymbol{\rho_{ob,m}}\right|\right)e^{jm\phi_{e,m}} = \sum_{k=-\infty}^{\infty} H_{p-k}^{(2)}\left(\beta\left|\boldsymbol{\rho_{b,m}}\right|\right)J_k\left(\beta\left|\boldsymbol{\rho_{a,m}}\right|\right)e^{j[(p-k)\phi_{b,m}-k\phi_{a,m}]} \qquad (5-188)$$

The addition theorem in equation $(5-188)$ for observation point $(\rho_{ob,m}, \phi_{ob,m})$ may be written as a convolution between the **H**-spectral signature of $(\rho_{b,m}, \phi_{b,m})$ and **J**-spectral signature of $(\rho_{a,m}, \phi_{a,m})$.

$$H(p, \rho_{ob,m}) = H(k, \rho_{b,m}) \otimes J(k, \rho_{a,m}) \qquad (5-189)$$

In the equation $(5-189)$, the **H**-spectral signature vector defined in truncated form for point $(\rho_{b,m}, \phi_{b,m})$ is defined as

$$H(k, \rho_{b,m}) = \left[H_{-K}^{(2)}(\beta|\boldsymbol{\rho_b}|)e^{-jK\phi_{b,m}} \quad \ldots \quad H_k^{(2)}(\beta|\boldsymbol{\rho_b}|)e^{jk\phi_{b,m}} \quad \ldots \quad H_K^{(2)}(\beta|\boldsymbol{\rho_b}|)e^{jK\phi_{b,m}}\right] \qquad (5-190)$$

and the **J**-spectral signature vector defined in truncated form for point $(\rho_{a,m}, \phi_{a,m})$ as

$$J(k, \rho_{a,m}) = [J_{-K}(\beta|\boldsymbol{\rho_a}|)e^{-jK\phi_{a,m}} \quad \cdots \quad J_k(\beta|\boldsymbol{\rho_a}|)e^{jk\phi_{a,m}} \quad \cdots \quad J_K(\beta|\boldsymbol{\rho_a}|)e^{jK\phi_{a,m}}] \qquad (5-191)$$

For a cross-sectional contour generated by two rotating vectors, each row of the **H**-spectral signature observation point matrix, $\begin{bmatrix} \cdots & \cdots & \cdots \\ \cdots & H_k^{(2)}(\beta|\boldsymbol{\rho_{ob}}|) & \cdots \\ \cdots & \cdots & \cdots \end{bmatrix}$, equals the convolution of the Hankel spectral signature of point $(\rho_{b,m}, \phi_{b,m})$ and Bessel spectral signature of point $(\rho_{a,m}, \phi_{a,m})$. This matrix consisting of all observation points may be decomposed into two matrices using the convolution product in equation $(5-189)$, and written as equation $(5-192)$.

$$\begin{bmatrix} - & - & - \\ - & H_k^{(2)}(\beta|\boldsymbol{\rho_{ob}}|) & - \\ - & - & - \end{bmatrix} = \begin{bmatrix} - & - & - \\ - & H_k^{(2)}(\beta|\boldsymbol{\rho_b}|) & - \\ - & - & - \end{bmatrix} \otimes \begin{bmatrix} - & - & - \\ - & J_k(\beta|\boldsymbol{\rho_a}|) & - \\ - & - & - \end{bmatrix} \qquad (5-192)$$

The matrices in $(5-192)$ are written with -- notation to emphasize that each row is the spectral signature of an individual observation point.

In order to efficiently perform this convolution, one may use the relationship in equation $(5-162)$. For a column vector $\begin{bmatrix} | \\ \hat{h}_{ob} \\ | \end{bmatrix}$ that equals the convolution of column vectors $\begin{bmatrix} | \\ \hat{h}_{a,1} \\ | \end{bmatrix}$ and $\begin{bmatrix} | \\ \hat{J}_{b,1} \\ | \end{bmatrix}$, i.e.

$$\begin{bmatrix} | \\ \hat{h}_{ob} \\ | \end{bmatrix} = \begin{bmatrix} | \\ \hat{h}_{a,1} \\ | \end{bmatrix} \otimes \begin{bmatrix} | \\ \hat{j}_{b,1} \\ | \end{bmatrix} \quad (5-193)$$

the discrete Fourier transform of the column vector $\begin{bmatrix} | \\ \hat{h}_{ob} \\ | \end{bmatrix}$ equals the Hadamard product of the discrete Fourier transform of the column vectors $\begin{bmatrix} | \\ \hat{h}_{a,1} \\ | \end{bmatrix}$ and $\begin{bmatrix} | \\ \hat{j}_{b,1} \\ | \end{bmatrix}$.

$$\begin{bmatrix} \cdots & \cdots & \cdots \\ \cdots & F & \cdots \\ \cdots & \cdots & \cdots \end{bmatrix} \begin{bmatrix} | \\ \hat{h}_{ob} \\ | \end{bmatrix} = \begin{bmatrix} \cdots & \cdots & \cdots \\ \cdots & F & \cdots \\ \cdots & \cdots & \cdots \end{bmatrix} \begin{bmatrix} | \\ \hat{h}_{a,1} \\ | \end{bmatrix} \odot \begin{bmatrix} \cdots & \cdots & \cdots \\ \cdots & F & \cdots \\ \cdots & \cdots & \cdots \end{bmatrix} \begin{bmatrix} | \\ \hat{j}_{b,1} \\ | \end{bmatrix} \quad (5-194)$$

with $\odot$ denoting the Hadamard product operator.

In order to use this property to calculate the **H**-spectral signature and **J**-spectral signature given equation $(5-194)$ consider the following matrix $\begin{bmatrix} - & - & - \\ - & M & - \\ - & - & - \end{bmatrix}$. First one takes the transpose of the matrix, and it can be subdivided into columns as shown in equation $(5-195)$,

$$\begin{bmatrix} - & - & - \\ - & M & - \\ - & - & - \end{bmatrix}^T = \left\{ \begin{bmatrix} | \\ M_{k,1} \\ | \end{bmatrix} \; \begin{bmatrix} | \\ M_{k,m} \\ | \end{bmatrix} \; \begin{bmatrix} | \\ M_{k,M} \\ | \end{bmatrix} \right\} \quad (5-195)$$

each column being the spectral signature of a point,

$$\begin{bmatrix} | \\ M_{k,m} \\ | \end{bmatrix} = \begin{bmatrix} M_{-K,m} \\ | \\ M_{k,m} \\ | \\ M_{K,m} \end{bmatrix} \quad (5-196)$$

The Fourier transform of matrix $\begin{bmatrix} - & - & - \\ - & M & - \\ - & - & - \end{bmatrix}^T$ is the Fourier transform of each column given that $\begin{bmatrix} | \\ M_{k,m} \\ | \end{bmatrix}$ is column *m* of the matrix corresponding to observation point *m-1*.

$$\begin{bmatrix} \cdots & \cdots & \cdots \\ \cdots & \bar{F} & \cdots \\ \cdots & \cdots & \cdots \end{bmatrix} \begin{bmatrix} - & - & - & - & - & - \\ - & - & M & & - & - \\ - & - & - & - & - & - \end{bmatrix}^T =$$

$$\left\{ \begin{bmatrix} \cdots & \cdots & \cdots \\ \cdots & \bar{F} & \cdots \\ \cdots & \cdots & \cdots \end{bmatrix} \begin{bmatrix} | \\ M_{k,1} \\ | \end{bmatrix} \cdots \begin{bmatrix} \cdots & \cdots & \cdots \\ \cdots & F & \cdots \\ \cdots & \cdots & \cdots \end{bmatrix} \begin{bmatrix} | \\ M_{k,m} \\ | \end{bmatrix} \cdots \begin{bmatrix} \cdots & \cdots & \cdots \\ \cdots & F & \cdots \\ \cdots & \cdots & \cdots \end{bmatrix} \begin{bmatrix} | \\ M_{k,M} \\ | \end{bmatrix} \right\} \quad (5-197)$$

Now one can apply this property to the transpose of the Hankel observation matrix

$\begin{bmatrix} \cdots & \cdots & \cdots \\ \cdots & H_k^{(2)}((\beta|\boldsymbol{\rho_{ob}}|) & \cdots \\ \cdots & \cdots & \cdots \end{bmatrix}^T$ using the shifted Fourier operator.

$$\begin{bmatrix} \cdots & \cdots & \cdots \\ \cdots & \bar{F} & \cdots \\ \cdots & \cdots & \cdots \end{bmatrix} \begin{bmatrix} \cdots & \cdots & \cdots \\ \cdots & H_k^{(2)}(\beta|\boldsymbol{\rho_{ob}}|) & \cdots \\ \cdots & \cdots & \cdots \end{bmatrix}^T =$$

$$\begin{bmatrix} \cdots & \cdots & \cdots \\ \cdots & \bar{F} & \cdots \\ \cdots & \cdots & \cdots \end{bmatrix} \begin{bmatrix} \cdots & \cdots & \cdots \\ \cdots & H_k^{(2)}(\beta|\boldsymbol{\rho_b}|) & \cdots \\ \cdots & \cdots & \cdots \end{bmatrix}^T \odot \begin{bmatrix} \cdots & \cdots & \cdots \\ \cdots & \bar{F} & \cdots \\ \cdots & \cdots & \cdots \end{bmatrix} \begin{bmatrix} \cdots & \cdots & \cdots \\ \cdots & J_k(\beta|\boldsymbol{\rho_a}|) & \cdots \\ \cdots & \cdots & \cdots \end{bmatrix}^T \quad (5-198)$$

The matrices on the right of $(5-198)$ are defined below. Each column of

$\begin{bmatrix} - & - & - & - & - & - \\ - & - & H_k^{(2)}(\beta|\boldsymbol{\rho_b}|) & & - & - \\ - & - & - & - & - & - \end{bmatrix}^T$ is the spectral signature of a point $(\rho_{b,m}, \phi_{b,m})$ on the circle with radius *b*.

$$\begin{bmatrix} - & - & - & - & - & - \\ - & - & H_k^{(2)}((\beta|\boldsymbol{\rho_b}|) & & - & - \\ - & - & - & - & - & - \end{bmatrix}^T =$$

$$\left\{ \begin{bmatrix} H_{-K}^{(2)}(\beta|\boldsymbol{\rho_{b,0}}|)e^{-jK\phi_{b,0}} \\ | \\ | \\ | \\ H_K^{(2)}(\beta|\boldsymbol{\rho_{b,0}}|)e^{jK\phi_{b,0}} \end{bmatrix} \middle| \begin{bmatrix} H_{-K}^{(2)}(\beta|\boldsymbol{\rho_{b,m}}|)e^{-jK\phi_{b,m}} \\ | \\ | \\ | \\ H_K^{(2)}(\beta|\boldsymbol{\rho_{b,m}}|)e^{jK\phi_{b,m}} \end{bmatrix} \middle| \begin{bmatrix} H_{-K}^{(2)}(\beta|\boldsymbol{\rho_{b,M-1}}|)e^{-jK\phi_{b,M-1}} \\ | \\ | \\ | \\ H_K^{(2)}(\beta|\boldsymbol{\rho_{b,M-1}}|)e^{jK\phi_{b,M-1}} \end{bmatrix} \right\} \quad (5-199)$$

Each column of $\begin{bmatrix} - & - & - & - & - & - \\ - & - & J_K(\beta|\boldsymbol{\rho_{ob}}|) & & - & - \\ - & - & - & - & - & - \end{bmatrix}^T$ is the spectral signature of a point $(\rho_{a,m}, \phi_{a,m})$ on the circle with radius *a*.

$$\begin{bmatrix} - & - & - & - & - & - \\ - & - & J_K(\beta|\boldsymbol{\rho_{ob}}|) & - & - & - \\ - & - & - & - & - & - \end{bmatrix}^T =$$

$$\left\{\begin{bmatrix} J_{-K}(\beta|\boldsymbol{\rho_{a,0}}|)e^{-jK\phi_{b,0}} \\ | \\ | \\ | \\ J_K(\beta|\boldsymbol{\rho_{a,0}}|)e^{jK\phi_{b,0}} \end{bmatrix} \middle| \begin{bmatrix} J_{-K}(\beta|\boldsymbol{\rho_{a,m}}|)e^{-jK\phi_{b,m}} \\ | \\ | \\ | \\ J_K(\beta|\boldsymbol{\rho_{a,m}}|)e^{jK\phi_{b,m}} \end{bmatrix} \middle| \begin{bmatrix} J_{-K}(\beta|\boldsymbol{\rho_{a,M-1}}|)e^{-jK\phi_{b,M-1}} \\ | \\ | \\ | \\ J_K(\beta|\boldsymbol{\rho_{a,M-1}}|)e^{jK\phi_{b,M-1}} \end{bmatrix}\right\}$$

$$(5-200)$$

Next one needs to use this convolution principle to examine cylinders generated by circles of different radii. Thus, for the induced electric field, $\begin{bmatrix} \cdots \\ \cdot\cdot \end{bmatrix}$,

$$\begin{bmatrix} - & - & - & - & - & - \\ - & - & H_k^{(2)}((\beta|\boldsymbol{\rho_b}|) & - & - & - \\ - & - & - & - & - & - \end{bmatrix}\begin{bmatrix} \cdots \\ \cdot\cdot \end{bmatrix} = \begin{bmatrix} \cdots \\ \cdot\cdot \end{bmatrix} \qquad (5-201)$$

The term $\begin{bmatrix} - & - & - & - & - & - \\ - & - & H_k^{(2)}(\beta|\boldsymbol{\rho_b}|) & - & - & - \\ - & - & - & - & - & - \end{bmatrix}$ may be reformed by the matrix equation in $(5-202)$.

$$\begin{bmatrix} - & - & - & - & - & - \\ - & - & H_k^{(2)}(\beta|\boldsymbol{\rho_b}|) & - & - & - \\ - & - & - & - & - & - \end{bmatrix} = \left(\begin{bmatrix} \cdots & \cdots & \cdots \\ \cdots & \bar{F} & \cdots \\ \cdots & \cdots & \cdots \end{bmatrix}\begin{bmatrix} - & - & - & - & - & - \\ - & - & H_k^{(2)}(\beta|\boldsymbol{\rho_b}|) & - & - & - \\ - & - & - & - & - & - \end{bmatrix}^T\right)^T \begin{bmatrix} \cdots & \cdots & \cdots \\ \cdots & \bar{F} & \cdots \\ \cdots & \cdots & \cdots \end{bmatrix}$$

$$(5-202)$$

Substituting equation $(5-202)$ into equation $(5-201)$, one obtains

$$\left(\begin{bmatrix} \cdots & \cdots & \cdots \\ \cdots & \bar{F} & \cdots \\ \cdots & \cdots & \cdots \end{bmatrix}\begin{bmatrix} - & - & - & - & - & - \\ - & - & H_k^{(2)}(\beta|\boldsymbol{\rho_b}|) & - & - & - \\ - & - & - & - & - & - \end{bmatrix}^T\right)^T \begin{bmatrix} \cdots & \cdots & \cdots \\ \cdots & \bar{F} & \cdots \\ \cdots & \cdots & \cdots \end{bmatrix}\begin{bmatrix} \cdots \\ \cdot\cdot \end{bmatrix} = \begin{bmatrix} \cdots \\ \cdot\cdot \end{bmatrix} \qquad (5-203)$$

Now expanding using the Hadamard product, one can write the induced fields.

$$\begin{bmatrix} \cdots \\ \cdot\cdot \end{bmatrix} = \left(\begin{bmatrix} \cdots & \cdots & \cdots \\ \cdots & \bar{F} & \cdots \\ \cdots & \cdots & \cdots \end{bmatrix}\begin{bmatrix} \cdots & \cdots & \cdots \\ \cdots & H_k^{(2)}(\beta|\boldsymbol{\rho_b}|) & \cdots \\ \cdots & \cdots & \cdots \end{bmatrix}^T \odot \begin{bmatrix} \cdots & \cdots & \cdots \\ \cdots & \bar{F} & \cdots \\ \cdots & \cdots & \cdots \end{bmatrix}\begin{bmatrix} \cdots & \cdots & \cdots \\ \cdots & J_k(\beta|\boldsymbol{\rho_a}|) & \cdots \\ \cdots & \cdots & \cdots \end{bmatrix}^T\right)^T \cdot$$

$$\begin{bmatrix} \cdots & \cdots & \cdots \\ \cdots & \bar{F} & \cdots \\ \cdots & \cdots & \cdots \end{bmatrix}\begin{bmatrix} \cdots \\ \cdot\cdot \end{bmatrix} \qquad (5-204)$$

One can use the boundary condition to equate $\begin{bmatrix} \cdots \\ \cdot\cdot \end{bmatrix}$ and $\begin{bmatrix} \cdots \\ \cdot\cdot \end{bmatrix}$,

$$\begin{bmatrix} \cdots \\ \cdots \end{bmatrix} = -\begin{bmatrix} \cdots \\ \cdots \end{bmatrix} \qquad (5-43)$$

i.e. the scattered field to the incident field. Incident fields may also be defined in a similar manner, i.e., as the **J**-spectral signature of two rotating vectors. One may begin with equation $(5-205)$,

$$\begin{bmatrix} \cdots \\ E_{inc} \\ \cdots \end{bmatrix} = \begin{bmatrix} \cdots & \cdots & \cdots \\ \cdots & J_k(\beta|\boldsymbol{\rho_{ob}}|) & \cdots \\ \cdots & \cdots & \cdots \end{bmatrix} \begin{bmatrix} \cdots \\ \hat{\imath}_{SS,inc} \\ \cdots \end{bmatrix} \tag{5-205}$$

then using similar reasoning as in equation $(5-205)$, one obtains equation $(5-206)$.

$$\begin{bmatrix} \cdots \\ E_{inc} \\ \cdots \end{bmatrix} = \left(\begin{bmatrix} \cdots & \cdots & \cdots \\ \cdots & \bar{\bar{F}} & \cdots \\ \cdots & \cdots & \cdots \end{bmatrix} \begin{bmatrix} \cdots & \cdots & \cdots \\ \cdots & J_k(\beta|\boldsymbol{\rho_b}|) & \cdots \\ \cdots & \cdots & \cdots \end{bmatrix}^T \odot \begin{bmatrix} \cdots & \cdots & \cdots \\ \cdots & \bar{\bar{F}} & \cdots \\ \cdots & \cdots & \cdots \end{bmatrix} \begin{bmatrix} \cdots & \cdots & \cdots \\ \cdots & J_k(\beta|\boldsymbol{\rho_a}|) & \cdots \\ \cdots & \cdots & \cdots \end{bmatrix}^T \right)^T \cdot$$

$$\begin{bmatrix} \cdots & \cdots & \cdots \\ \cdots & \bar{\bar{F}} & \cdots \\ \cdots & \cdots & \cdots \end{bmatrix} \begin{bmatrix} \cdots \\ \hat{\imath}_{SS,inc} \\ \cdots \end{bmatrix} \tag{5-206}$$

and the term $\begin{bmatrix} \cdots & \cdots & \cdots \\ \cdots & \bar{\bar{F}} & \cdots \\ \cdots & \cdots & \cdots \end{bmatrix} \begin{bmatrix} \cdots \\ \hat{\imath}_{SS,inc} \\ \cdots \end{bmatrix}$ is the discrete Fourier transform of the spectral signature of the incident current.

5.6.5 Generating an Ellipse by Summing Circles of Different Radii

The previous section discusses a method for translating the origin to satisfy the requirements of the addition theorem and allow the possibility of solving problems with large axial ratios. In this section, a brief explanation of a technique for generating an ellipse of any major and minor axis dimensions from circular shapes is explained. To begin it is important to review the basic terms relating to an ellipse. See Figure 5-41.

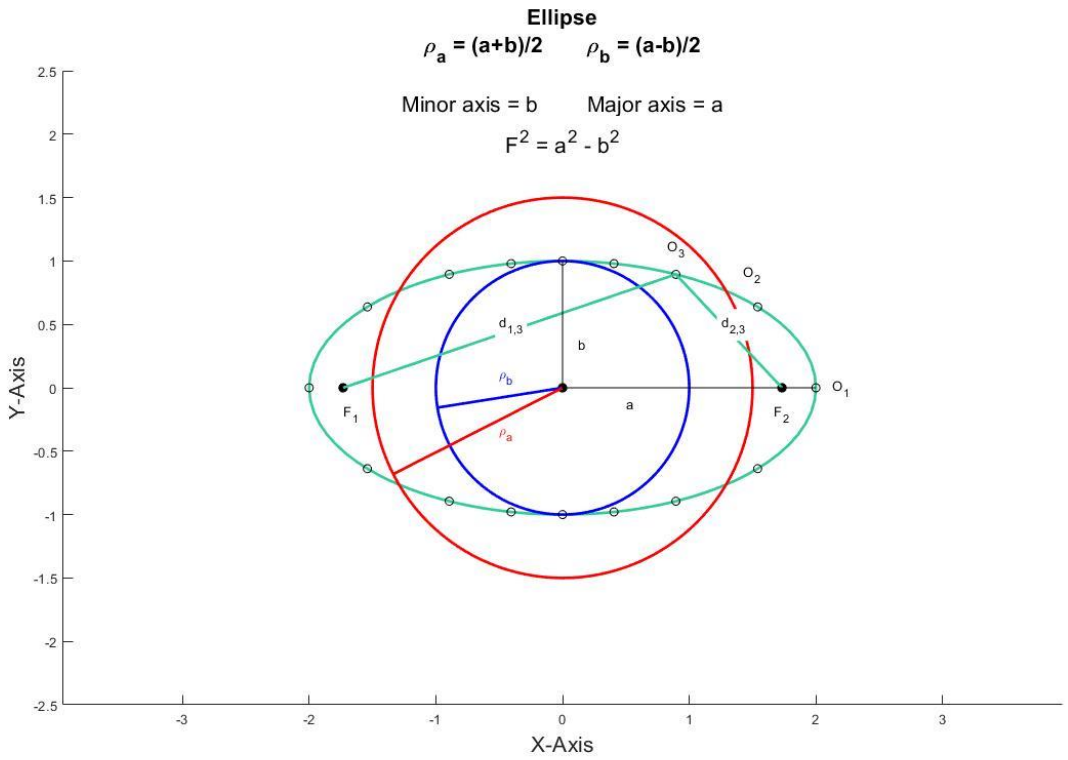

Figure 5-41: Ellipse in black, and focal points are F_1 and F_2. Two concentric circles of radii ρ_a and ρ_b are drawn overlapping.

The set of n points forming the locus of an ellipse are those points in a plane whose distance sum $d_{1,n} + d_{1,n}$ from two foci always equals a constant. An ellipse can be generated by summing vectors along two circles of different radii, one rotating clockwise and the other rotating counterclockwise. See equation $(5-207)$.

$$\rho_{a,n} + \rho_{b,n} = \rho_{e,n} \qquad (5-207)$$

$\rho_{a,n}$	$n \in \{0,1,2,\dots,N-1\}$	points along circle of radius a
$\rho_{b,n}$	$n \in \{0,1,2,\dots,N-1\}$	points along circle of radius b
$\rho_{e,n}$	$n \in \{0,1,2,\dots,N-1\}$	points along ellipse e

In Figure 5-42, points along two circles of radii ρ_a and ρ_b, with $\rho_a > \rho_b$, are illustrated. These points are summed to generate an ellipse with major axis length $\rho_a + \rho_b$ and minor axis length $\rho_a - \rho_b$, illustrated in Figure 5-43.

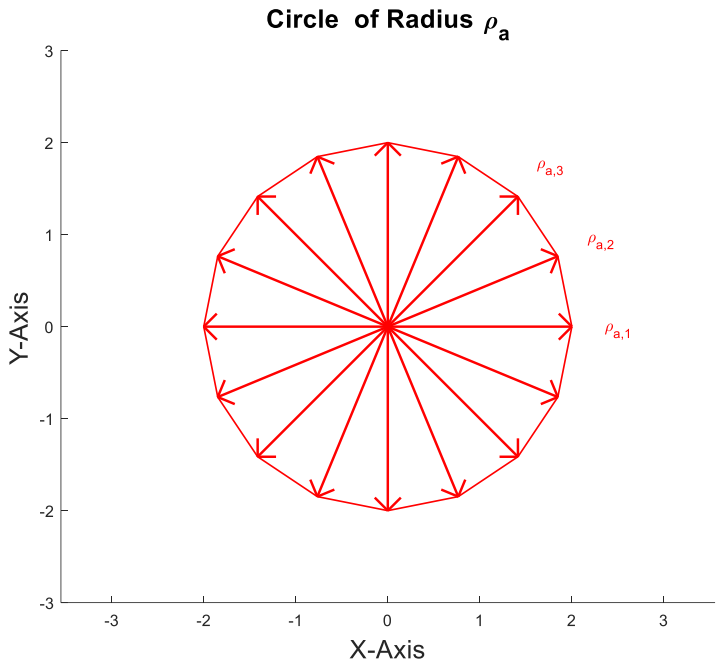

a)

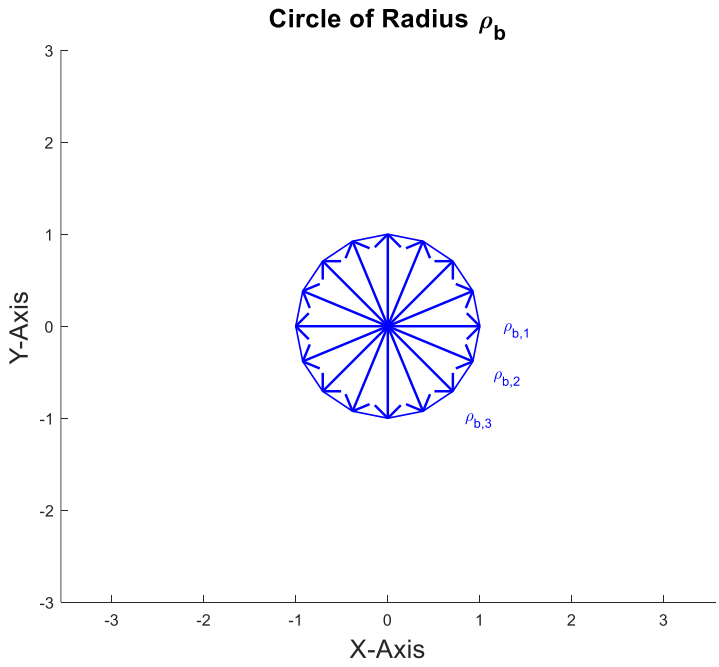

b)

Figure 5-42: Two circles of different radii a) 1λ and b) 2λ.

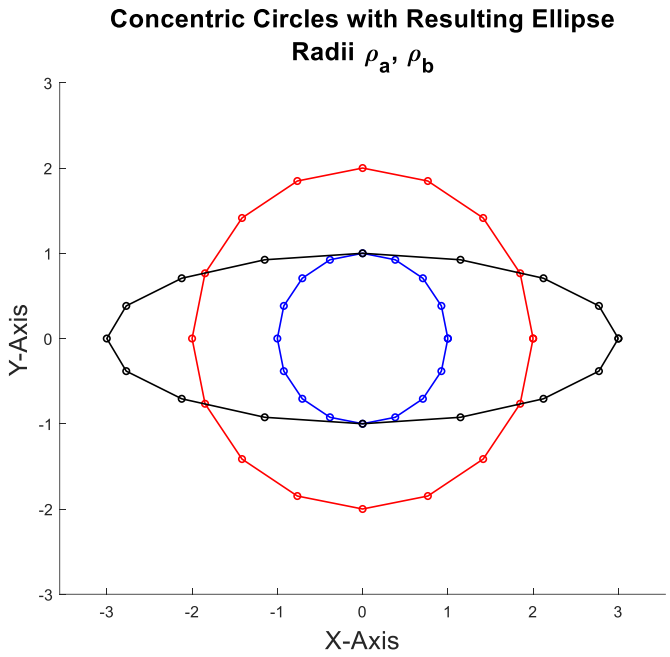

Figure 5-43: Superposition of points along two circles of radius 1λ and 2λ to generate an ellipse.

In Figure 5-43 sampled points along circles of radii ρ_a and ρ_b are summed together to form the ellipse shown in black. Vectors 1, 5, 8, and 11 for the circle of radius $\rho_{a,n}$ are shown in Figure 5-44a, and for $\rho_{b,n}$ is illustrated in Figure 5-44b. Summation of all points, $\rho_{a,n} + \rho_{b,n}$, for $n \in \{1,2,\dots,N\}$ trace out the lotus of the ellipse shown in Figure 5-44c.

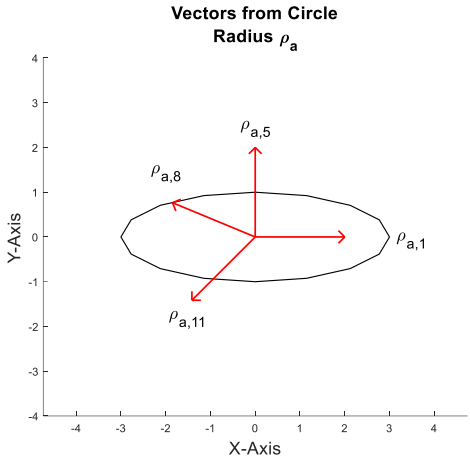

a)

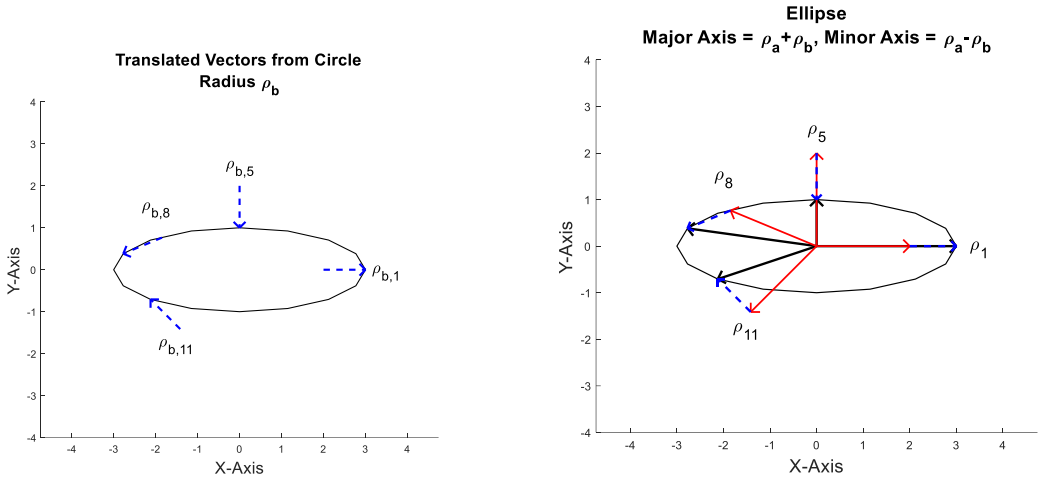

b) c)

Figure 5-44: a) Vectors from circle of radius $\rho_{a,n}$ for $n \in \{1,5,8,11\}$. b) Vectors from circle of radius $\rho_{b,n}$, $n \in \{1,5,8,11\}$. c) Resulting vectors generate the locus on an ellipse.

Unfortunately, although summing rotating vectors is helpful in generating different figures, it is only sufficient to solving SPM scattering problems for geometries with small axial ratios. For larger axial ratios, it is necessary to translate the axis of the source points to ensure that the addition theorem condition $\rho > \rho'$ is met. The next section will discuss a technique for translating the axis to new coordinates.

5.6.6 Application of Translating of the Origin to SPM

By decomposing an ellipse into a sum of three vectors, the addition theorem may be treated as the convolution of three vectors. The observation points ρ_n may be defined as in equation $(5-208)$ for $n \in \{1,2,\dots,N\}$.

$$\rho_{ob} = \rho_{a,n} + \rho_{b,n} \qquad (5-208)$$

The addition theorem can then be written as the convolution of three vectors $(5-209)$.

$$H(m,\rho+\rho') = H\left(n,\rho_{c,n}\right) \otimes \left[J(n,\rho_{t_1,n}') \otimes \ J(n,\rho_{t_2,n}')\right] \qquad (5-209)$$

For example, consider an ellipse with major axis a and minor axis b, and traced out by vector function $\boldsymbol{f}$. The vector $\boldsymbol{f}$ is the sum of three vectors, $\boldsymbol{f} = \boldsymbol{c} + \boldsymbol{t_1} + \boldsymbol{t_2}$. The vector $\boldsymbol{c}$ is a constant amplitude vector rotating in the counterclockwise direction. The vectors $\boldsymbol{t_1}$ and $\boldsymbol{t_1}$ are constant amplitude vectors rotating in the clockwise and counterclockwise directions, respectively. See Figure 5-45.

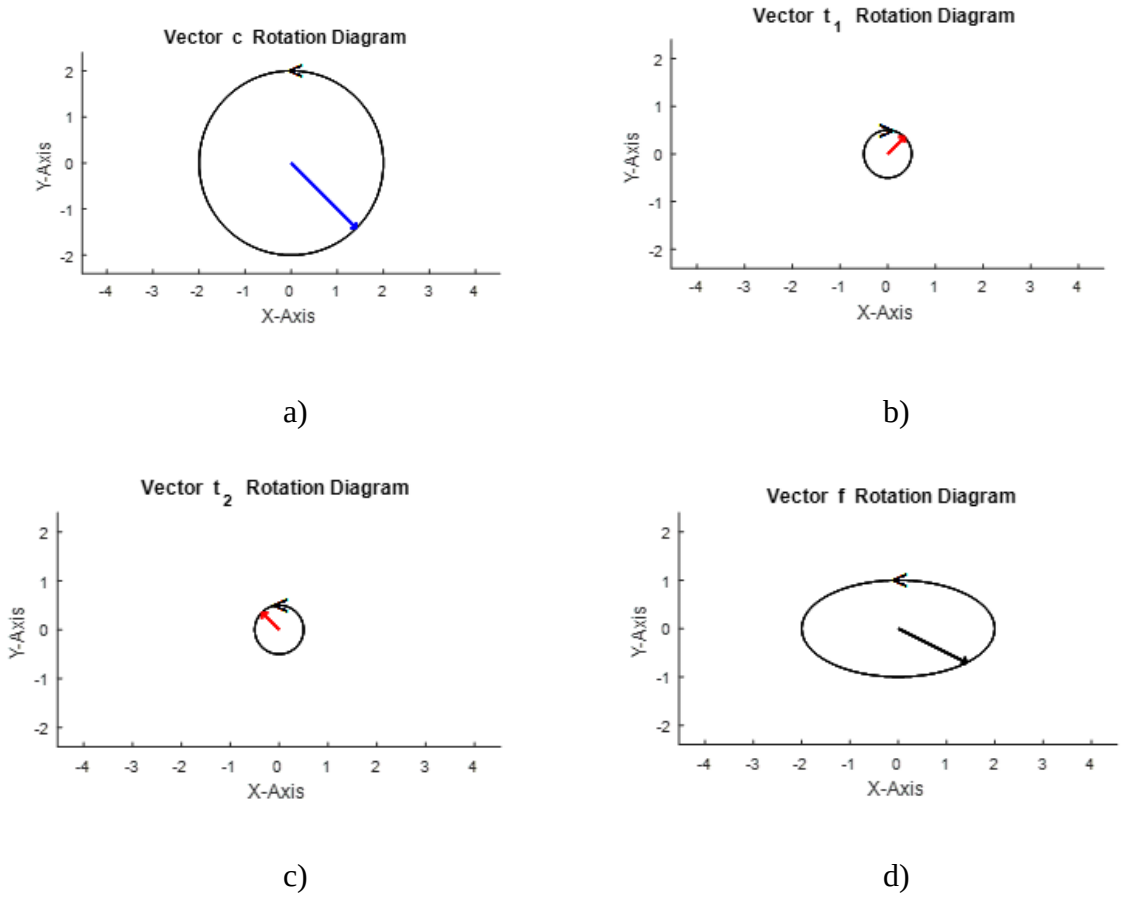

Figure 5-45: Generating circles for an ellipse from a) vector **c** (ccw) b) vector $\mathbf{t_1}$ (cw) c) vector $\mathbf{t_2}$ (ccw) and d) vector **f** (ccw).

The vectors meet the condition of the addition theorem, $|\boldsymbol{c}| = |\boldsymbol{t_1} + \boldsymbol{t_2}|$. The ellipse and example vectors are illustrated in Figure 5-46.

$$\boldsymbol{c} = ae^{j\phi} \qquad |\boldsymbol{c}| = a \qquad (5-210)$$

$$\boldsymbol{t_1} = \frac{(a-b)}{2}e^{-j\phi} \qquad (5-211)$$

$$\boldsymbol{t_2} = \frac{(b-a)}{2}e^{j\phi} \qquad (5-212)$$

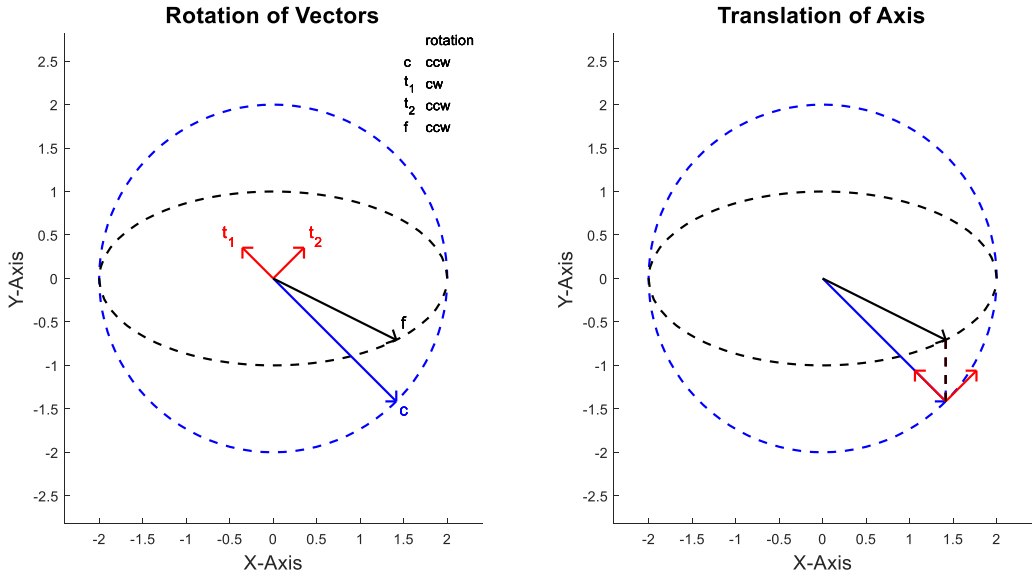

a) b)

Figure 5-46: a) Rotation and b) translation of the source origin. Vector *f* traces out the ellipse, vector *c* traces out the circle with radius equal to the length of the major axis, and vectors $\boldsymbol{t_1}$ and $\boldsymbol{t_2}$ represent the translation vectors. The vertical dotted line is the actual translation from the source on the ellipse (Bessel functions) to the outer circle (Hankel function).

From Figure 5-46, the following vector addition translates the origin in the Y-direction.

$$\boldsymbol{t_1} + \boldsymbol{t_2} = (b-a)sin\phi\hat{\boldsymbol{y}} \qquad (5-213)$$

After doing some elementary trigonometry, the equation of an ellipse is verified for function f.

$$f_x = acos\phi \qquad (5-214)$$

$$f_y = bsin\phi \qquad (5-215)$$

Using this formulation, the addition theorem requirement will always be satisfied as long as $\boldsymbol{c}$ is calculated with the Hankel function, and vectors $\boldsymbol{t_1}$ and $\boldsymbol{t_2}$ are assigned to the Bessel functions.

5.7 Validation of the Spectral Projection Model

In this section the relationship between axial ratio of infinitely long conducting cylinders and the accuracy of the Spectral Projection Model will be discussed [30]. Results will be compared to analyses using the Method of Moments.

5.7.1 Validation of the Spectral Projection Model for plane wave TM^z scattering without Translation

For an infinitely long elliptical cylinder subjected to an incident TM^z wave, the current distribution is not calculated using the Spectral Projection Model because the far-field pattern can be calculated directly from the **J**-spectral signature. The surface current calculated using MOM for a PEC elliptical cylinder with axial ratio 2:1 is shown in Figure 5-47b. Shown in Figure 5-48a and 5-48b is the spectral signature of the surface current distribution due to the TM^z wave scattering for an elliptical cylinder with axial ratio 2:1 using MOM and SPM. This is band-limited to the center 25% of the 128 modes, which is approximately $ka \cong 12$. The value of a is the major axis of the ellipse, and b is the minor axis. The far-field electric field pattern calculated using the MOM and SPM agree well too as seen in Figures 5-48c and 5-48d. Incidence angle is 90°.

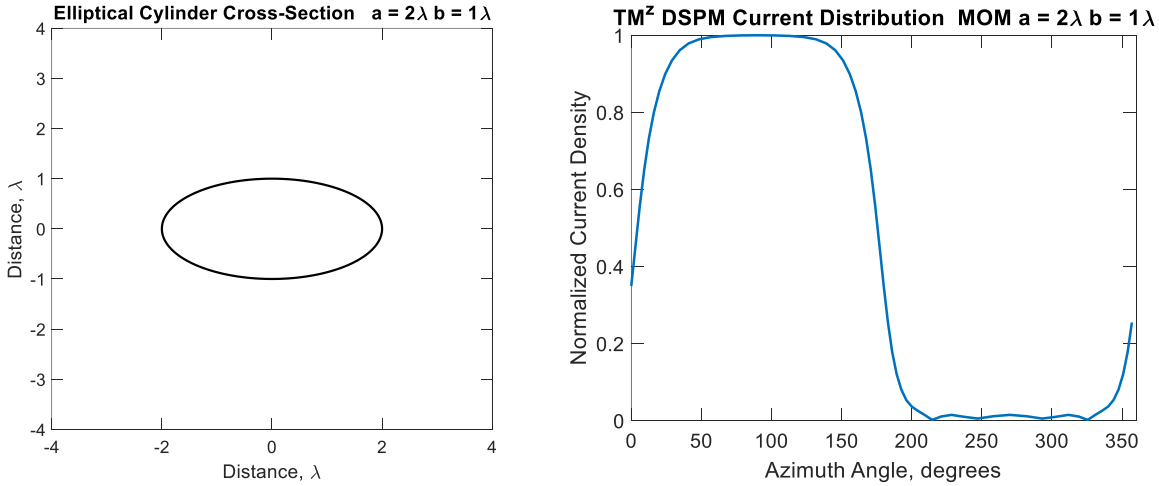

a) b)

Figure 5-47: a) Infinitely long elliptical cylinder $a = 2\lambda$ and $b = 1\lambda$. b) Current distribution calculated using the Method of Moments for TM^z polarization

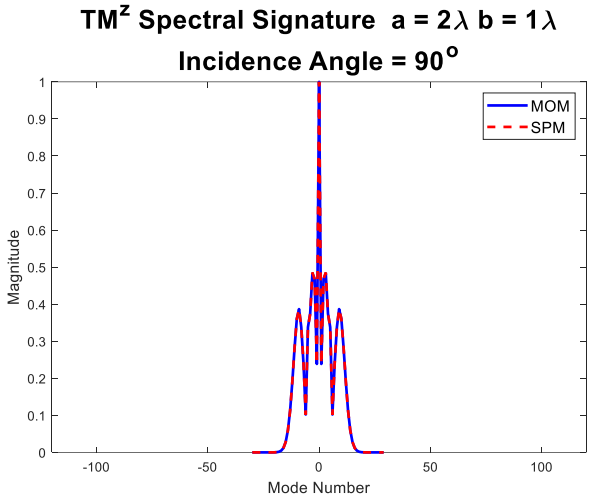

a)

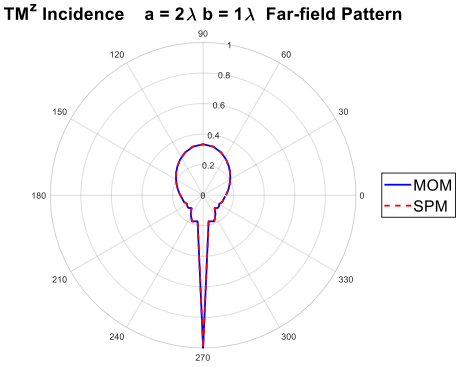

b)

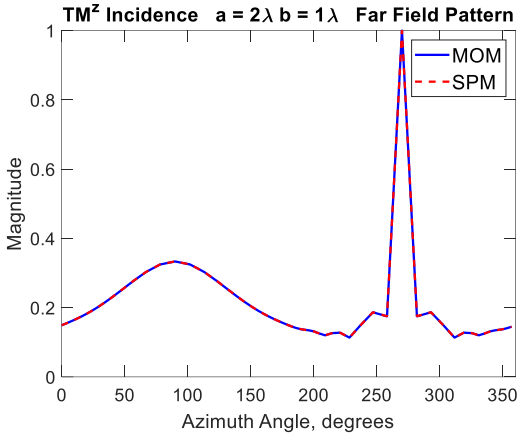

c)

Figure 5-48: a) Spectral signature of surface current from Method of Moments and SPM for TM^z polarization on elliptical cylinder $a = 2\lambda$ and $b = 1\lambda$. b) Electric far-field pattern in polar coordinates. c) Electric far-field pattern linear plot.

The direct application of SPM works well for small axial ratios, i.e. 4:1 or less. Results for a TM^z wave incident on an ellipse with a higher axial ratio 4:1 is shown in Figure 5-49. For higher axial ratios, the SPM without translation does not work as well. For these larger axial ratios, the direct application of SPM suffers from a 'low pass' effect in which the higher order modes are cut-off. This cut-off is determined by the size of the minor axis, where the

requirement $\rho_{ob} \geq \rho_{so}$ fails. Some translation using the convolution property of the addition theorem is necessary to overcome this limitation. Angle of incidence is 90°

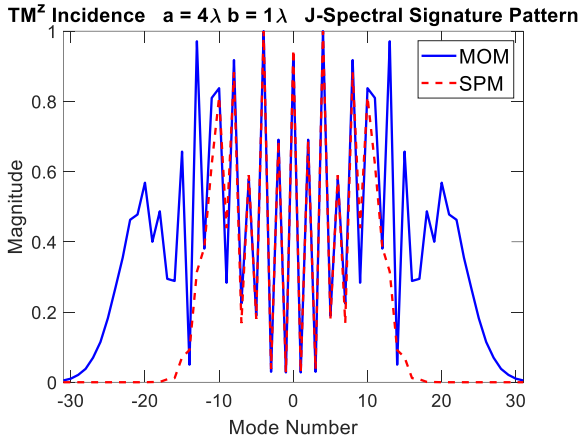

a)

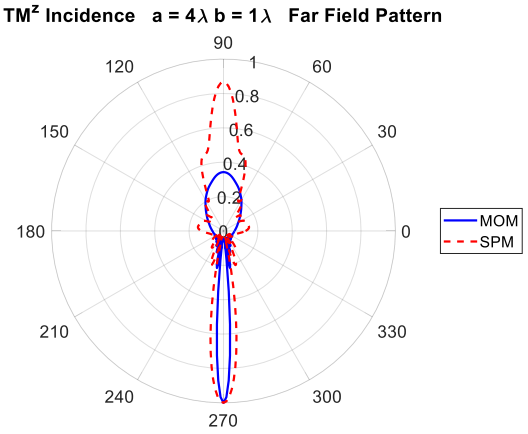

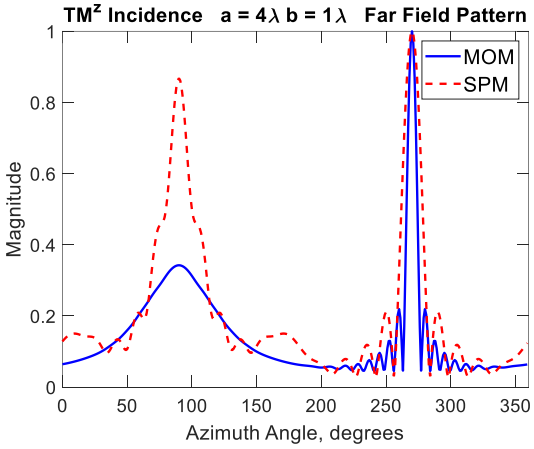

b) c)

Figure 5-49: a) Spectral signature of surface current from Method of Moments and SPM for TM^z polarization on elliptical cylinder $a = 4\lambda$ and $b = 1\lambda$. b) Electric far-field pattern in polar coordinates. c) Electric far-field pattern linear plot.

5.7.2 Validation of the Spectral Projection Model for plane wave TE^z scattering without Translation

For an infinitely long elliptical cylinder subjected to an incident TE^z wave, calculation of the current distribution is slightly different than TM^z using the Spectral Projection Model. In equation $(5-216)$, one can substitute the product of the matrix and derivative of the Green's function for the $\begin{bmatrix} \cdots & \cdots & \cdots \\ \cdots & H_k^{(2)}(\beta|\boldsymbol{\rho_m}|) & \cdots \\ \cdots & \cdots & \cdots \end{bmatrix}$ term, and then solve for the spectral signature of the surface current as before.

$$\begin{bmatrix} \cdots \\ H_{ind} \\ \cdots \end{bmatrix} = \left(\begin{bmatrix} \cdots & \cdots & \cdots \\ \cdots & \cos(\gamma) & \cdots \\ \cdots & \cdots & \cdots \end{bmatrix} \begin{bmatrix} \cdots & \cdots & \cdots \\ \cdots & H_k{}'(\beta|\boldsymbol{\rho_m}|)e^{jk\phi} & \cdots \\ \cdots & \cdots & \cdots \end{bmatrix} \right)^T \begin{bmatrix} \cdots \\ \hat{\imath}_{SS,ind} \\ \cdots \end{bmatrix} \qquad (5-216)$$

Using the method of least squares, one may solve for the **J**-spectral signature of the current. The right side of the equation becomes the **J**-spectral signature of the surface current for a TE^z wave incident on a PEC cylinder. Now define the matrix product above as $(5-217)$.

$$\begin{bmatrix} \cdots & \cdots & \cdots \\ \cdots & H_k{}'\cos(\gamma) & \cdots \\ \cdots & \cdots & \cdots \end{bmatrix} = \left(\begin{bmatrix} \cdots & \cdots & \cdots \\ \cdots & \cos(\gamma) & \cdots \\ \cdots & \cdots & \cdots \end{bmatrix} \begin{bmatrix} \cdots & \cdots & \cdots \\ \cdots & H_k{}'(\beta|\boldsymbol{\rho_m}|)e^{jk\phi} & \cdots \\ \cdots & \cdots & \cdots \end{bmatrix} \right)^T \qquad (5-217)$$

Next one can solve for the **J**-spectral signature of the induced currents.

$$\begin{bmatrix} \cdots \\ \hat{\imath}_{SS,ind} \\ \cdots \end{bmatrix} =$$

$$\frac{4}{\omega\mu} \left(\begin{bmatrix} \cdots & \cdots & \cdots \\ \cdots & H_k{}'\cos(\gamma) & \cdots \\ \cdots & \cdots & \cdots \end{bmatrix} \begin{bmatrix} \cdots & \cdots & \cdots \\ \cdots & H_k{}'\cos(\gamma) & \cdots \\ \cdots & \cdots & \cdots \end{bmatrix}^T \right)^{-1} \begin{bmatrix} \cdots & \cdots & \cdots \\ \cdots & H_k{}'\cos(\gamma) & \cdots \\ \cdots & \cdots & \cdots \end{bmatrix} \begin{bmatrix} \cdots \\ E_{inc} \\ \cdots \end{bmatrix} \quad (5-218)$$

As mentioned earlier, to calculate the **J**-spectral signature of the surface current for TE^z wave scattering, one substitutes the derivative term $H_0^{(2)\prime}(\beta|\boldsymbol{\rho_m}-\boldsymbol{\rho}'|)$ for $H_0^{(2)}(\beta|\boldsymbol{\rho_m}-\boldsymbol{\rho}'|)$. This is because one is calculating the incident magnetic field from the electric field in Faraday's law which involves a curl operation. Calculation of the current distribution due to the TE^z wave scattering for an elliptical cylinder with axial ratio 1.25:1 using MOM is shown below in Figure 5-50b. A comparison of the spectral signatures using the MOM and SPM is shown in Figures 5-50c and 5-50d. A comparison of the MOM and SPM far-field patterns is shown in Figures 5-51a and 5-51b in both polar and linear coordinates.

The plot of the TE^z wave far-field pattern for a 2:1 axial ratio showed poor agreement between the MOM and SPM results. Adjustments to the SPM method with translation vectors is again required to rectify this problem, same as the TM^z case. Angle of incidence is 90^o.

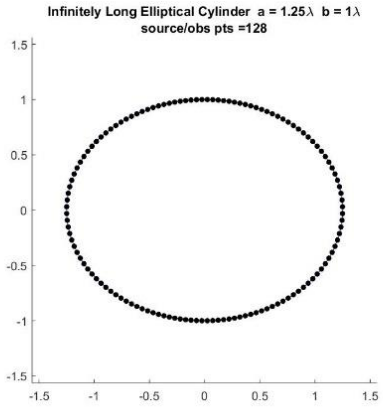

a)

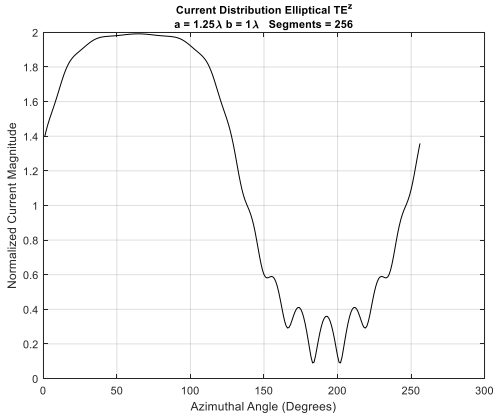

b)

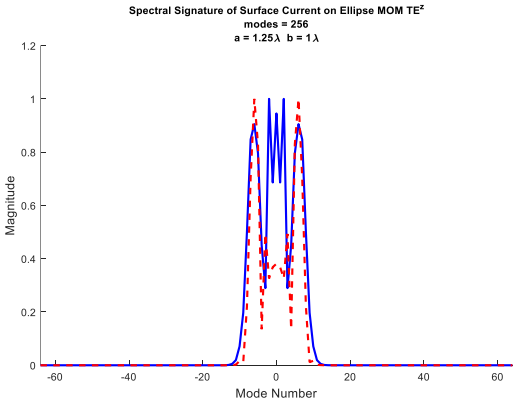

c)

Figure 5-50: a) Infinitely long elliptical cylinder $a = 1.25\lambda$ and $b = 1\lambda$. b) Current distribution calculated using the Method of Moments for TE^z polarization. c) Spectral signature of surface current from Method of Moments and SPM for TE^z polarization.

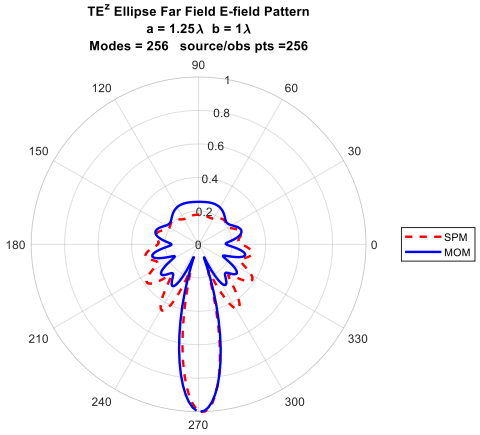

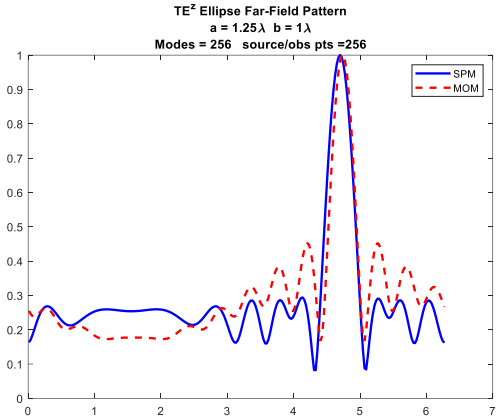

a) b)

Figure 5-51: a) SPM electric far-field pattern in polar coordinates for elliptical cylinder $a = 1.25\lambda$ and $b = 1\lambda$. b) SPM electric far-field pattern linear plot.

5.7.3 Validation of the Spectral Projection Model for Plane Wave TM^z Scattering with Translation

For an infinitely long elliptical cylinder subjected to an incident TM^z wave using translation of the source axis, larger axial ratio problems may be solved [53]. Figure 5-52 and Figure 5-53 show the results of an ellipse with axial ratio $\frac{a}{b} = 10$ as good agreement with the MOM. Angle of incidence is 90^o.

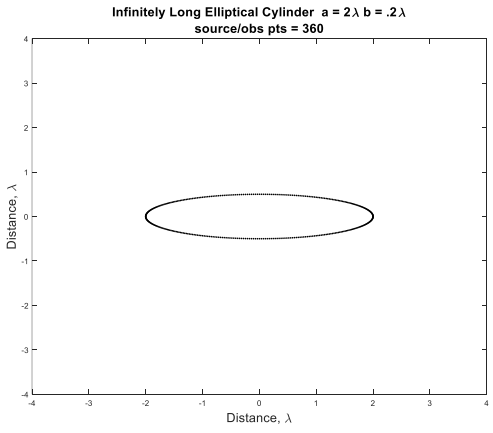

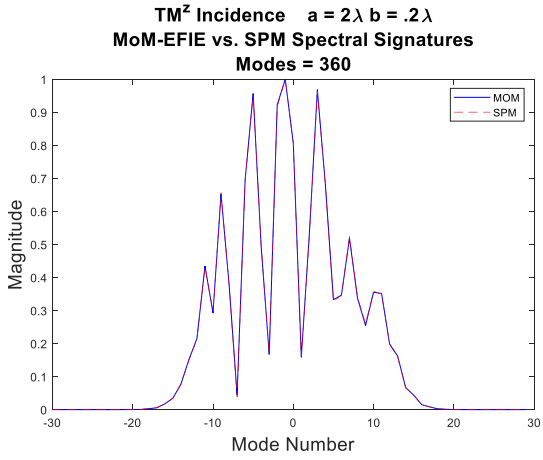

a) b)

Figure 5-52: a) Elliptical cylinder $a = 2\lambda$ and $b = .2\lambda$. b) Spectral signature of the surface current using Spectral Projection Model vs. MOM for TM^z polarization.

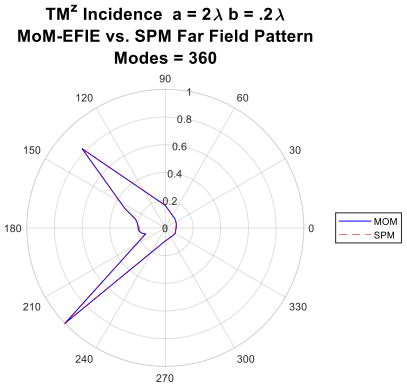

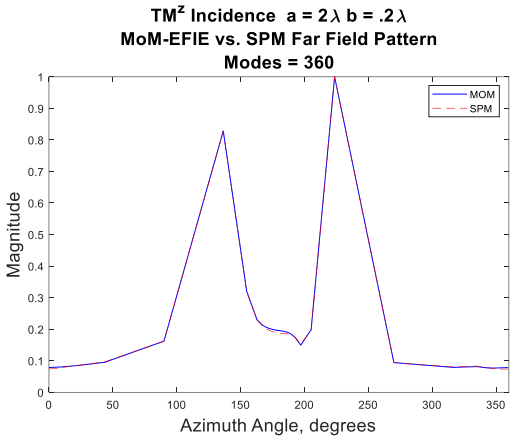

a) b)

Figure 5-53: a) Electric far-field pattern for SPM vs. MOM,in polar coordinates for elliptical cylinder $a = 2\lambda$ and $b = .2\lambda$ for TM^z polarization. b) Electric far-field pattern for SPM vs. MOM linear plot.

5.7.4 Validation of the Spectral Projection Model for plane wave TE^z scattering with Translation

For an infinitely long elliptical cylinder subjected to an incident TE^z wave using translation of the source axis, the axial ratio $\frac{a}{b} = 10$ has good agreement with the MOM [53]. In Figure 5-54 and Figure 5-55 are plots of the cylinder, modal spectral signature, far-field pattern, and a polar plot of the far-field pattern.

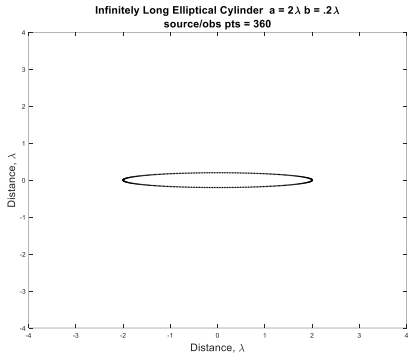

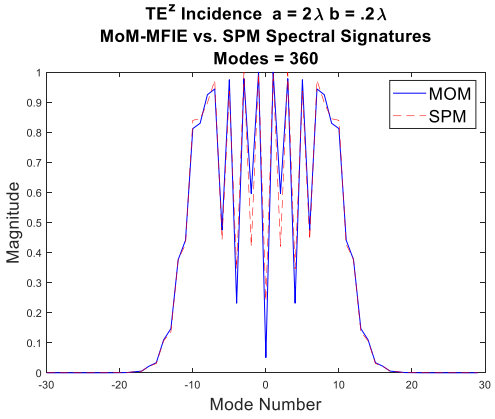

a) b)

Figure 5-54: a) Elliptical cylinder $a = 2\lambda$ and $b = .2\lambda$. b) Spectral signature of the surface current using Spectral Projection Model vs. MOM for TE^z polarization.

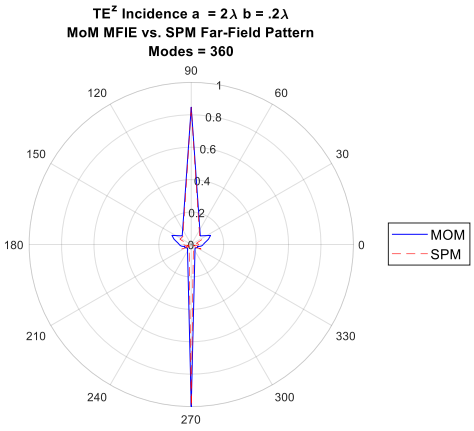

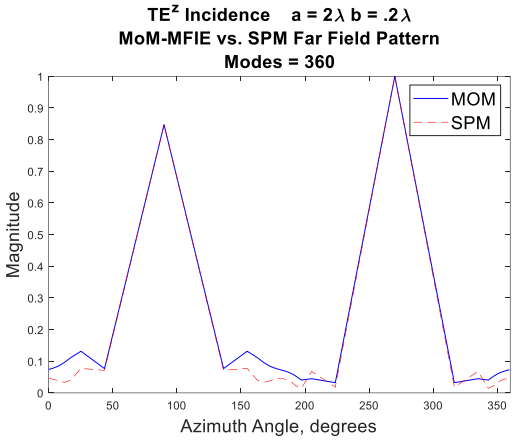

a) b)

Figure 5-55: a) Electric far-field pattern for Spectral Projection Method vs. MOM,in polar coordinates for elliptical cylinder $a = 2\lambda$ and $b = .2\lambda$ for TE^z polarization. b) Electric far-field pattern for Spectral Projection Method vs. MOM linear plot.

Chapter 6: Direct Spectral Projection Model

6.1 Introduction to the Direct Spectral Projection Model

An improvement to the SPM model is presented in this section. This improvement is known as the Direct Spectral Projection Method (DSPM). The DSPM derives a set of eigenfunctions which are a set of solutions to scattering from cylinders of arbitrary cross-sections. The eigenfunctions are designed to satisfy the boundary conditions for the scattering problem. Having found the eigenfunctions for the problem at hand, any external stimulus may be described as a weighted sum of these eigenfunctions. The weights of these eigenfunctions are obtained by assuming the spectral signatures of the external source are approximately equal to the collective spectral signatures of the eigenfunctions. Boundary conditions are satisfied by both sides of the equation by being projected onto the **J**-spectral signatures of the observation points. This eliminates the need to solve the boundary conditions directly. Since the eigenfunctions are found so that they satisfy the boundary conditions, writing the external stimulus in terms of these eigenfunctions implicitly satisfies the boundary conditions for the problem at hand [54].

With the direct SPM method, once this matrix is set up, one can calculate the vector current distribution for many different cross-sectional geometries and external excitations, whether the external stimuli be a single line source, multiple line sources or a plane wave.

6.2 Line Sources Near a Circular Cylinder

As shown in Chapter 5, an electric current on the surface of a PEC circular cylinder of radius $\rho = a$ is induced by an incident electric field from an external line source. If the external line source is located at polar coordinates $(\rho_0{}', \phi_0{}')$, this induced current is described by equation $(6-1)$.

$$i_{ind}(\rho', \phi') = \sum_{k=-\infty}^{\infty} \frac{H_k^{(2)}(\beta|\boldsymbol{\rho_0}'|)\, e^{jk(\phi\prime-\phi_0\prime)}}{H_k^{(2)}(\beta|\boldsymbol{\rho}'|)} \qquad (6-1)$$

Assume points (ρ', ϕ') on the surface of the cylinder are at discrete locations $(\rho_n{}', \phi_n{}')$ for $n \in \{0,1, N-1\}$. In the case of a circular cylinder $\rho_n' = a$ for all n.

As illustrated in Figure 6-1, if the external line source at angle $\phi_0{}'$ is moved close to the surface of the circular cylinder with $\rho_0{}' = a + \varepsilon$, an induced line current source flows opposite at the same location as the electric line source $\rho_0{}' = a - \varepsilon$, as $\varepsilon \to 0$.

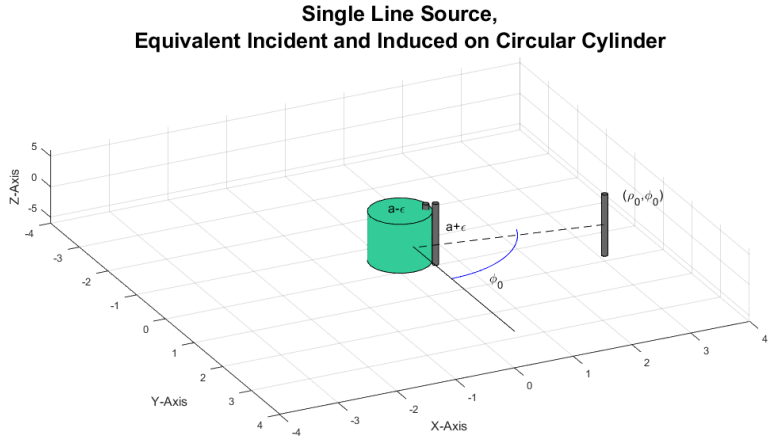

a)

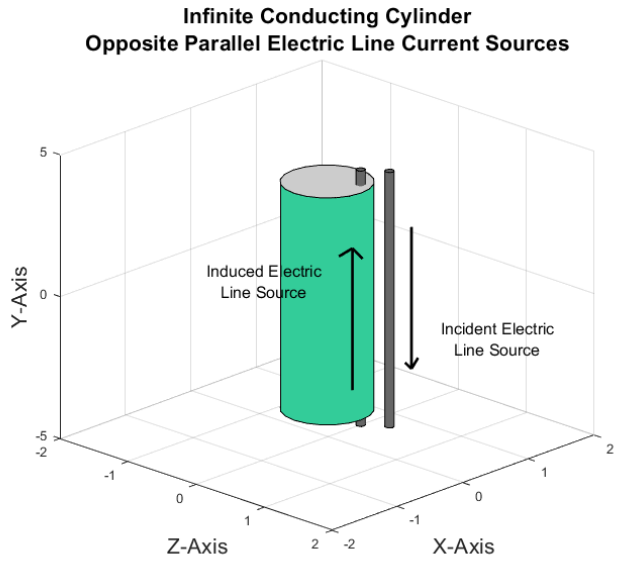

b)

Figure 6-1: a) Infinitely long external line source at (ρ_0, ϕ_0) moved near the surface of an infinitely long circular cylinder to a distance $a + \varepsilon$, and the induced line current at $a - \varepsilon$, as $\varepsilon \to 0$. b) Infinitely long electric line source moved near the surface of an infinitely long circular cylinder, and its induced electric line current which is equal and opposite.

The new distance of the line source near the surface of the circular cylinder is given in equation $(6-2)$,

$$\rho_{0,inc}{}' = a + \varepsilon \qquad \varepsilon \to 0 \qquad (6-2)$$

By substituting $(6-2)$ into equation $(6-1)$,

$$H_k^{(2)}(\beta|\boldsymbol{\rho_0}'|) = H_k^{(2)}(\beta|\boldsymbol{a}|) \qquad (6-3)$$

Now substituting $(6-3)$ into $(6-1)$, the induced current on the surface at any point (ρ_n', ϕ_n') can be described as a delta function.

$$\delta(\rho' - a, \phi_n{}' - \phi_0) = \sum_{k=-\infty}^{\infty} e^{jk(\phi_n{}' - \phi_0)} \qquad (6-4)$$

and $\delta(\rho' - a, \phi_n' - \phi_0) = 1$ when $\rho' = a$ and $\phi_n' = \phi_0$.

As further evidence that the surface current distribution trends toward a delta function, a plot of the surface current for line currents at different distances ρ from a circular cylinder is shown in the Figure 6-2 below. From the plot of equation $(6-1)$, as an electric line source approaches the surface of a circular cylinder of radius $a = 5\lambda$, the induced current magnitude approaches that of a single spike (delta function). So, it radiates only from the surface at one point. The incident electric current at the surface distance $a + \varepsilon$ from the line source will hereafter be referred to as the "virtual current." Its induced surface current J_n^{ind} at location $(\rho_n{}', \phi_n{}')$ on the other side of the surface approaches a magnitude that is equal and opposite in phase to the virtual current, and zero everywhere else.

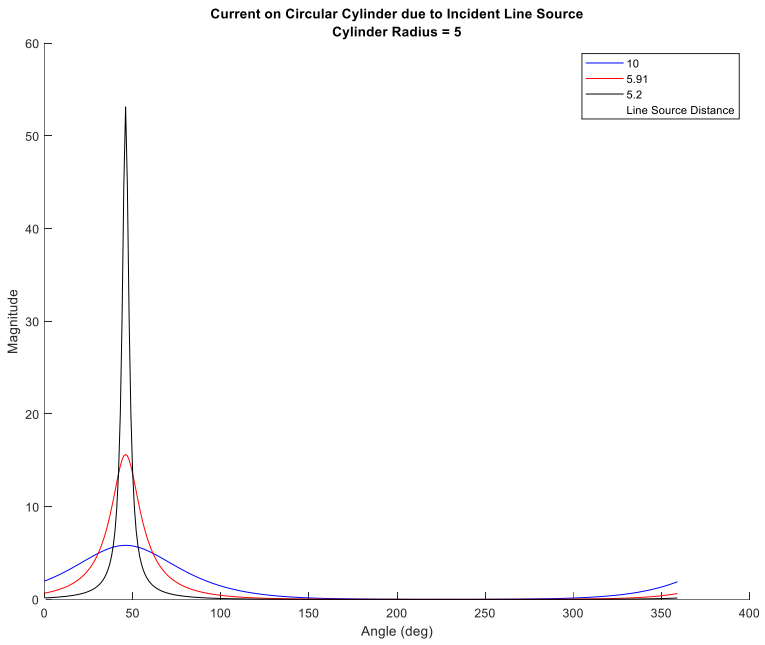

Figure 6-2: Current distribution of a line source near an infinitely long circular cylinder of radius 5λ at distances $\rho = 10\lambda, \rho = 5.91\lambda, \rho = 5.2\lambda$.

For an external line source at coordinates $(\rho_n, '\phi_n')$, the weight of each eigenfunction $\delta(\rho' - \rho_n', \phi' - \phi_n')$ corresponding to a virtual current can be represented in vector form as an $N \times 1$ column vector of all zeros and a single value of α_n placed in the n^{th} row.

$$\begin{bmatrix} | \\ \hat{\imath}_{vir,n} \\ | \end{bmatrix} = \begin{bmatrix} 0 \\ | \\ \alpha_n \\ | \\ 0 \end{bmatrix} \tag{6-5}$$

The virtual current may be written as the sum of these $N \times 1$ column vectors,

$$\begin{bmatrix} | \\ \hat{\imath}_{vir,sum} \\ | \end{bmatrix} = \begin{bmatrix} | \\ | \\ \hat{\imath}_{vir,0} \\ | \\ | \end{bmatrix} + \cdots + \begin{bmatrix} | \\ | \\ \hat{\imath}_{vir,n} \\ | \\ | \end{bmatrix} + \cdots . \begin{bmatrix} | \\ | \\ \hat{\imath}_{vir,N-1} \\ | \\ | \end{bmatrix} \tag{6-6}$$

The sum of these virtual current vectors, $\begin{bmatrix} | \\ \hat{\imath}_{vir,sum} \\ | \end{bmatrix}$, can be written as equation $(6-7)$.

$$\begin{bmatrix} | \\ \hat{\imath}_{vir,sum} \\ | \end{bmatrix} = \begin{bmatrix} \alpha_0 \\ | \\ \alpha_n \\ | \\ \alpha_{N-1} \end{bmatrix} \tag{6-7}$$

Similarly, the induced current vector $\begin{bmatrix} | \\ \hat{\imath}_{ind,sum} \\ | \end{bmatrix}$ corresponding to the induced surface currents can be written as equation $(6-8)$.

$$\begin{bmatrix} | \\ \hat{\imath}_{ind,sum} \\ | \end{bmatrix} = \begin{bmatrix} \beta_0 \\ | \\ \beta_n \\ | \\ \beta_{N-1} \end{bmatrix} \tag{6-8}$$

One may write the DSPM equation as an eigenvector relation in terms of $\begin{bmatrix} | \\ \hat{\imath}_{vir,sum} \\ | \end{bmatrix}$ and $\begin{bmatrix} | \\ \hat{\imath}_{ind,sum} \\ | \end{bmatrix}$, in which every $\alpha_n = -\beta_n$.

6.3 Derivation of DSPM from Modal Analysis for a Circular Cylinder

For TM^z waves incident upon a PEC circular cylinder, the modal matrix solution given in equation $(6-1)$ can be written in terms of an induced current vector $\begin{bmatrix} \cdots \\ \hat{\imath}_{ind,sum} \\ \cdot\cdot \end{bmatrix}$ for *N-1* equations as shown in equation $(6-9)$.

$$\begin{bmatrix} \ddots & 0 & 0 \\ 0 & H_k^{(2)}(\beta|\boldsymbol{a}|) & 0 \\ 0 & 0 & \ddots \end{bmatrix} \begin{bmatrix} \cdots & \cdots & \cdots \\ \cdots & \bar{F} & \cdots \\ \cdots & \cdots & \cdots \end{bmatrix} \begin{bmatrix} | \\ \hat{\imath}_{ind,sum} \\ | \end{bmatrix} = \begin{bmatrix} | \\ \hat{\imath}_{ss,inc,I_n} \\ | \end{bmatrix} \tag{6-9}$$

If the excitation is a single external current line source I_n at coordinates (ρ_n', ϕ_n'), using equation $(5-68)$ one may write

$$\begin{bmatrix} | \\ \hat{\imath}_{ss,inc,I_n} \\ | \end{bmatrix} = \begin{bmatrix} H_{-K}^{(2)}(\beta|\boldsymbol{\rho_0}'|)e^{jK\phi_0'} & \cdots & \cdots & \cdots & H_{-K}^{(2)}\left(\beta\left|\boldsymbol{\rho_{N_S-1}}'\right|\right)e^{jK\phi_{N_S-1}'} \\ \vdots & \vdots & \vdots & \vdots & \vdots \\ \vdots & \vdots & \vdots & \vdots & \vdots \\ \vdots & \vdots & \vdots & \vdots & \vdots \\ H_{K}^{(2)}(\beta|\boldsymbol{\rho_0}'|)e^{-jK\phi_0'} & \cdots & \cdots & \cdots & H_{K}^{(2)}\left(\beta\left|\boldsymbol{\rho_{N_S-1}}'\right|\right)e^{-jK\phi_{N_S-1}'} \end{bmatrix} \begin{bmatrix} 0 \\ \vdots \\ I_n \\ \vdots \\ 0 \end{bmatrix} \tag{6-10}$$

As the external line source approaches the surface of the conductor, $\boldsymbol{\rho_0}' = \boldsymbol{a}$, and the matrix product $(6-10)$ reduces to equation $(6-11)$.

$$\begin{bmatrix} | \\ \hat{\imath}_{ind,sum} \\ | \end{bmatrix} = I_n \begin{bmatrix} \cdots & \cdots & \cdots \\ \cdots & \bar{F} & \cdots \\ \cdots & \cdots & \cdots \end{bmatrix}^H \begin{bmatrix} | \\ e^{jk\phi_n'} \\ | \end{bmatrix} \tag{6-11}$$

where

$$\begin{bmatrix} | \\ e^{jk\phi_n} \\ | \end{bmatrix} = \begin{bmatrix} e^{-jK\phi_n'} \\ \vdots \\ e^{jk\phi_n'} \\ \vdots \\ e^{jK\phi_n'} \end{bmatrix} \tag{6-12}$$

If matrices $\begin{bmatrix} | \\ e^{jK\phi_n'} \\ | \end{bmatrix}$ and $\begin{bmatrix} \cdots & \cdots & \cdots \\ \cdots & \bar{F} & \cdots \\ \cdots & \cdots & \cdots \end{bmatrix}$ are infinite dimensional in column length $K \to \infty$, the induced current vector becomes a set of infinite sums of exponentials corresponding to Fourier series expansions.

$$\begin{bmatrix} | \\ \hat{\imath}_{ind,sum} \\ | \end{bmatrix} = I_n \begin{bmatrix} \sum_{k=-\infty}^{\infty} e^{jk(\phi_0'-\phi_n')} \\ \vdots \\ \sum_{k=-\infty}^{\infty} e^{jk(\phi_n'-\phi_n')} \\ \vdots \\ \sum_{k=-\infty}^{\infty} e^{jk\left(\phi_{N_{S-1}}'-\phi_n'\right)} \end{bmatrix} \tag{6-13}$$

Equation $(6-13)$ reduces to equation $(6-14)$ according to the Fourier series expansion for a delta function given in equation $(6-4)$.

$$\begin{bmatrix} | \\ \hat{\imath}_{ind,sum} \\ | \end{bmatrix} = I_n \begin{bmatrix} 0 \\ 0 \\ 1 \\ \vdots \\ 0 \end{bmatrix} \quad (6-14)$$

In equation $(6-14)$, the delta function has the following property, $\delta(\phi_n' - \phi_n{}') = 1$ for $\delta(0)$, and zero otherwise. Thus, we can write equation $(6-14)$ as $(6-15)$.

$$\begin{bmatrix} 0 \\ \vdots \\ i_{ind,n} \\ \vdots \\ 0 \end{bmatrix} = I_n \begin{bmatrix} 0 \\ \vdots \\ 1 \\ \vdots \\ 0 \end{bmatrix} \quad (6-15)$$

Equation $(6-15)$ reveals that every induced current can be generated by an equal and opposite incident current at the surface at the same location. This incident current may be considered a virtual current. Taking equation $(6-11)$, one may rewrite it using $(6-16)$, in terms of virtual currents,

$$\begin{bmatrix} \cdots & \cdots & \cdots \\ \cdots & \bar{F} & \cdots \\ \cdots & \cdots & \cdots \end{bmatrix} \begin{bmatrix} | \\ \hat{\imath}_{vir,sum} \\ | \end{bmatrix} = -I_n \begin{bmatrix} | \\ e^{jk\phi_n{}'} \\ | \end{bmatrix} \quad (6-16)$$

When $i_{vir,n}$ is the magnitude of the virtual current at coordinates (ρ_n, ϕ_n), from equation $(6-15)$ one may rewrite equation $(6-16)$.

$$\begin{bmatrix} \cdots & \cdots & \cdots \\ \cdots & \bar{F} & \cdots \\ \cdots & \cdots & \cdots \end{bmatrix} \begin{bmatrix} 0 \\ \hat{\imath}_{vir,n} \\ 0 \end{bmatrix} = i_{vir,n} \begin{bmatrix} | \\ e^{jk\phi_n{}'} \\ | \end{bmatrix} \quad (6-17)$$

From equation $(6-17)$, the virtual currents can be represented as eigenfunctions which satisfy the electric field boundary conditions at every pair of points opposite on the surface, i.e. virtual currents at $(\rho_n{}', \phi_n{}')$ by induced currents at $(\rho_m{}', \phi_m{}')$. For a circular cylinder, the eigenfunctions are the columns of the $\begin{bmatrix} \cdots & \cdots & \cdots \\ \cdots & \bar{F} & \cdots \\ \cdots & \cdots & \cdots \end{bmatrix}$ matrix. These electric line currents generate equal and opposite electric fields that satisfy the boundary conditions which require that the electric field on the surface equal zero according to equation $(6-18)$.

$$E^{scat}(\rho, \phi) = -E^{inc}(\rho', \phi') \quad (6-18)$$

If one rearranges equation $(6-9)$, one obtains equation $(6-19)$, for excitation of a circular cylinder by a TM^z incident wave from a near-field line source.

$$\begin{bmatrix} \ddots & 0 & 0 \\ 0 & H_k^{(2)}(\beta|\boldsymbol{a}|) & 0 \\ 0 & 0 & \ddots \end{bmatrix} \begin{bmatrix} \cdots & \cdots & \cdots \\ \cdots & \bar{\bar{F}} & \cdots \\ \cdots & \cdots & \cdots \end{bmatrix} \begin{bmatrix} | \\ \hat{\imath}_{ind,sum} \\ | \end{bmatrix} = \begin{bmatrix} | \\ \hat{\imath}_{ss,inc,I_n} \\ | \end{bmatrix} \quad (6-19)$$

As shown in Chapter 5 equation $(5-124)$, the matrix product in equation $(6-19)$ originated from the **H**-spectral signature matrix when $\boldsymbol{\rho_m = a}$**.**

$$\begin{bmatrix} \vdots & & \vdots \\ \vdots & H_k^{(2)}(\beta|\boldsymbol{\rho_m}'|)e^{jk\phi_{m'}} & \vdots \\ \vdots & & \vdots \end{bmatrix} = \begin{bmatrix} \ddots & 0 & 0 \\ 0 & H_k^{(2)}(\beta|\boldsymbol{a}|) & 0 \\ 0 & 0 & \ddots \end{bmatrix} \begin{bmatrix} \cdots & \cdots & \cdots \\ \cdots & \bar{\bar{F}} & \cdots \\ \cdots & \cdots & \cdots \end{bmatrix} \quad (6-20)$$

Substituting into equation $(6-19)$, one obtains for a circular cylinder equation $(6-21)$.

$$\begin{bmatrix} \vdots & & \vdots \\ \vdots & H_k^{(2)}(\beta|\boldsymbol{\rho_m}'|)e^{jk\phi_{m'}} & \vdots \\ \vdots & & \vdots \end{bmatrix} \begin{bmatrix} | \\ \hat{\imath}_{ind,sum} \\ | \end{bmatrix} = \begin{bmatrix} | \\ \hat{\imath}_{ss,inc,I_n} \\ | \end{bmatrix} \quad (6-21)$$

If one replaces $\begin{bmatrix} | \\ \hat{\imath}_{ind,sum} \\ | \end{bmatrix}$ by $\begin{bmatrix} | \\ \hat{\imath}_{vir,sum} \\ | \end{bmatrix}$ on the surface of the cylinder, one can write the new equation for virtual sources at (ρ_m', ϕ_m') as $(6-22)$.

$$\begin{bmatrix} \vdots & & \vdots \\ \vdots & H_k^{(2)}(\beta|\boldsymbol{\rho_m}'|)e^{jk\phi_{m'}} & \vdots \\ \vdots & & \vdots \end{bmatrix} \begin{bmatrix} | \\ \hat{\imath}_{vir,sum} \\ | \end{bmatrix} = \begin{bmatrix} | \\ \hat{\imath}_{ss,inc,I_n} \\ | \end{bmatrix} \quad (6-22)$$

One may expand the possibilities of this equation for TM^z incidence on a circular cylinder, by writing it for an excitation by an electric line source Ie in the far-field at angle ϕ_n'. The spectral signature of an incident electric field from an electric line source in the far-field was given earlier in equation $(5-72)$.

$$\begin{bmatrix} \vdots \\ i_{ss,inc,Ie}^{ff} \\ \vdots \end{bmatrix} = E_0 \begin{bmatrix} e^{-jK\left(\phi_{n'}-\frac{\pi}{2}\right)} \\ \vdots \\ e^{jk\left(\phi_{n'}-\frac{\pi}{2}\right)} \\ \vdots \\ e^{jK\left(\phi_{n'}-\frac{\pi}{2}\right)} \end{bmatrix} \quad (6-23)$$

As long as the vector $\begin{bmatrix} \vdots \\ i_{ss,inc,Ie}^{ff} \\ \vdots \end{bmatrix}$ is in the column space of the **H**-spectral signature matrix, one may replace the spectral signature $\begin{bmatrix} | \\ \hat{\imath}_{ss,inc,I_n} \\ | \end{bmatrix}$ by $\begin{bmatrix} \vdots \\ i_{ss,inc,Ie}^{ff} \\ \vdots \end{bmatrix}$ and arrive at equation $(6-24)$.

$$\begin{bmatrix} \vdots & & \vdots \\ \cdots & H_k^{(2)}(\beta|\boldsymbol{\rho_m}'|)e^{jk\phi_{m'}} & \cdots \\ \vdots & & \vdots \end{bmatrix}\begin{bmatrix} | \\ \hat{\imath}_{ind,sum} \\ | \end{bmatrix} = \begin{bmatrix} \vdots \\ i_{ss,inc,Ie}^{ff} \\ \vdots \end{bmatrix} \quad (6-24)$$

By replacing $\begin{bmatrix} | \\ \hat{\imath}_{ind,sum} \\ | \end{bmatrix}$ by $\begin{bmatrix} | \\ \hat{\imath}_{vir,sum} \\ | \end{bmatrix}$, one arrives at the DSPM equation for a circular cylinder in equation $(6-25)$.

$$\begin{bmatrix} \vdots & & \vdots \\ \cdots & H_k^{(2)}(\beta|\boldsymbol{\rho_m}'|)e^{jk\phi_{m'}} & \cdots \\ \vdots & & \vdots \end{bmatrix}\begin{bmatrix} | \\ \hat{\imath}_{vir,sum} \\ | \end{bmatrix} = -\begin{bmatrix} \vdots \\ i_{ss,inc,Ie}^{ff} \\ \vdots \end{bmatrix} \quad (6-25)$$

Another way of stating equation $(6-25)$ is in the written statement below.

H-Spectral Signature of Virtual Sources or Eigenfunctions	=	**H**-Spectral Signature of the Incident Sources

6.4 Application of DSPM to TM^z and TE^z Waves incident upon a Circular Cylinder

For electric line source located in the near-field at (ρ_0', ϕ_0'), the **H**-spectral signature of the incident field due to the line current is given in equation $(6-26)$, from equation $(5-69)$.

$$\begin{bmatrix} | \\ \hat{\imath}_{ss,inc,I0} \\ | \end{bmatrix} = I_0\left[H_{-K}^{(2)}(\beta|\boldsymbol{\rho_0}'|)e^{jK\phi_{0'}} \ldots H_k^{(2)}(\beta|\boldsymbol{\rho_0}'|)e^{jk\phi_{0'}} \ldots H_K^{(2)}(\beta|\boldsymbol{\rho_0}'|)e^{-jK\phi_{0'}}\right]^T \quad (6-26)$$

where ρ_0' and ϕ_0' are the radial distance and azimuthal angle of the line source, and $I_0 = -\frac{\beta^2 I_e}{4\omega\varepsilon}$.

For an electric plane wave E_0 incident from a line source at the angle, ϕ_0', the spectral signature of the incident field was written earlier using the large argument approximation in equation $(5-71)$.

$$\begin{bmatrix} \vdots \\ i_{ss,inc,Ie}^{ff} \\ \vdots \end{bmatrix} = E_0[e^{-jK(\phi_{0'}-\pi/2)} \quad \ldots \quad e^{jk(\phi_{0'}-\pi/2)} \quad \ldots \quad e^{jK(\phi_{0'}-\pi/2)}]^T \quad (5-69)$$

For a circular cylinder with constant radius, $\rho = a$, the DSPM equation was given in equation $(6-21)$. For an incident line current I_0,

$$\begin{bmatrix} \vdots & & \vdots \\ \cdots & H_k^{(2)}(\beta|\boldsymbol{\rho_m}|)e^{jk\phi_m} & \cdots \\ \vdots & & \vdots \end{bmatrix}\begin{bmatrix} | \\ \hat{\imath}_{ind,sum} \\ | \end{bmatrix} = \begin{bmatrix} | \\ \hat{\imath}_{ss,inc,I_0} \\ | \end{bmatrix} \quad (6-27)$$

Solving equation $(6-27)$ for the induced current vector $\begin{bmatrix} \cdots \\ \hat{\imath}_{ind,sum} \\ \cdots \end{bmatrix}$, equation $(6-28)$ results.

$$\begin{bmatrix} | \\ \hat{\imath}_{ind,sum} \\ | \end{bmatrix} = \begin{bmatrix} \cdots & \cdots & \cdots \\ \cdots & \bar{F} & \cdots \\ \cdots & \cdots & \cdots \end{bmatrix}^H \begin{bmatrix} \ddots & 0 & 0 \\ 0 & 1/H_k^{(2)}(\beta|\boldsymbol{a}|) & 0 \\ 0 & 0 & \ddots \end{bmatrix} \begin{bmatrix} | \\ \hat{\imath}_{ss,inc,I0} \\ | \end{bmatrix} \qquad (6-28)$$

The induced current vector depends on the type of external source excitation. The **H**-spectral signature matrix $\begin{bmatrix} \vdots & \vdots & \vdots \\ \vdots & H_k^{(2)}(\beta|\boldsymbol{\rho_m}|)e^{jk\phi_m} & \vdots \\ \vdots & \vdots & \vdots \end{bmatrix}$ is the product of the inverse shifted DFT Fourier operator $\begin{bmatrix} \cdots & \cdots & \cdots \\ \cdots & \bar{F} & \cdots \\ \cdots & \cdots & \cdots \end{bmatrix}^H$ and the diagonal matrix $\begin{bmatrix} \ddots & 0 & 0 \\ 0 & 1/H_k^{(2)}(\beta|\boldsymbol{a}|) & 0 \\ 0 & 0 & \ddots \end{bmatrix}$. The columns of the diagonal matrix are $[\,0 \quad \ldots \quad \frac{1}{H_k}^{(2)}(\beta|\boldsymbol{a}|) \quad \ldots \quad 0]^T$, and make up the spectral response of the circular cylinder. In order to calculate the induced current distribution in the spatial domain, one must take the inverse Fourier transform of the **H**-spectral signature of the incident currents modified by the spectral response of the circular cylinder.

For electric lines source I_0 located in the near-field at (ρ_0, ϕ_0), the spectral signature of the incident current was given in equation $(5-142)$. For this near field line source from the $\phi_0{}'$ direction, the induced electric surface current in matrix equation $(6-28)$ may be written in summation form for any point (ρ', ϕ') as equation $(6-29)$.

$$i_{ind}(a,\phi') = \sum_{k=-K}^{K} \frac{H_k^{(2)}(\beta|\boldsymbol{\rho_0}'|)\, e^{jk(\phi'-\phi_0')}}{H_k^{(2)}(\beta|\boldsymbol{a}|)} \qquad (6-29)$$

This result is also in agreement with reference text [36].

$$J_z(a,\phi_n) = -\frac{I_e}{2\pi a} \sum_{k=-\infty}^{\infty} \frac{H_k^{(2)}(\beta|\boldsymbol{\rho_n}|)\, e^{jk(\phi_n-\phi_0')}}{H_k^{(2)}(\beta|\boldsymbol{a}|)} \qquad (5-147)$$

For the case of TM^z plane waves incident from the $\phi_0{}'$ direction, the induced electric surface current in matrix equation $(6-28)$ may be written in summation form for any point (ρ, ϕ) as equation $(6-30)$.

$$i_{ind}(a,\phi') = \sum_{k=-K}^{K} \frac{j^{-k} e^{jk(\phi'-\phi_0)}}{H_k^{(2)}(\beta|\boldsymbol{a}|)} \qquad (6-30)$$

This result agrees with reference text [36].

$$J_z(a,\phi_n{}') = \frac{2E_0}{\pi a\omega\mu}\sum_{k=-\infty}^{\infty}\frac{j^{-k}e^{jk(\phi_n{}'-\phi_i)}}{H_k^{(2)}(\beta|\boldsymbol{a}|)} \qquad (5-141)$$

where $\phi_i = \phi_0$.

See Figure 6-3 for plots of the induced current, spectral signature, and far-field pattern for incident wave with TM^z polarization upon a circular cylinder.

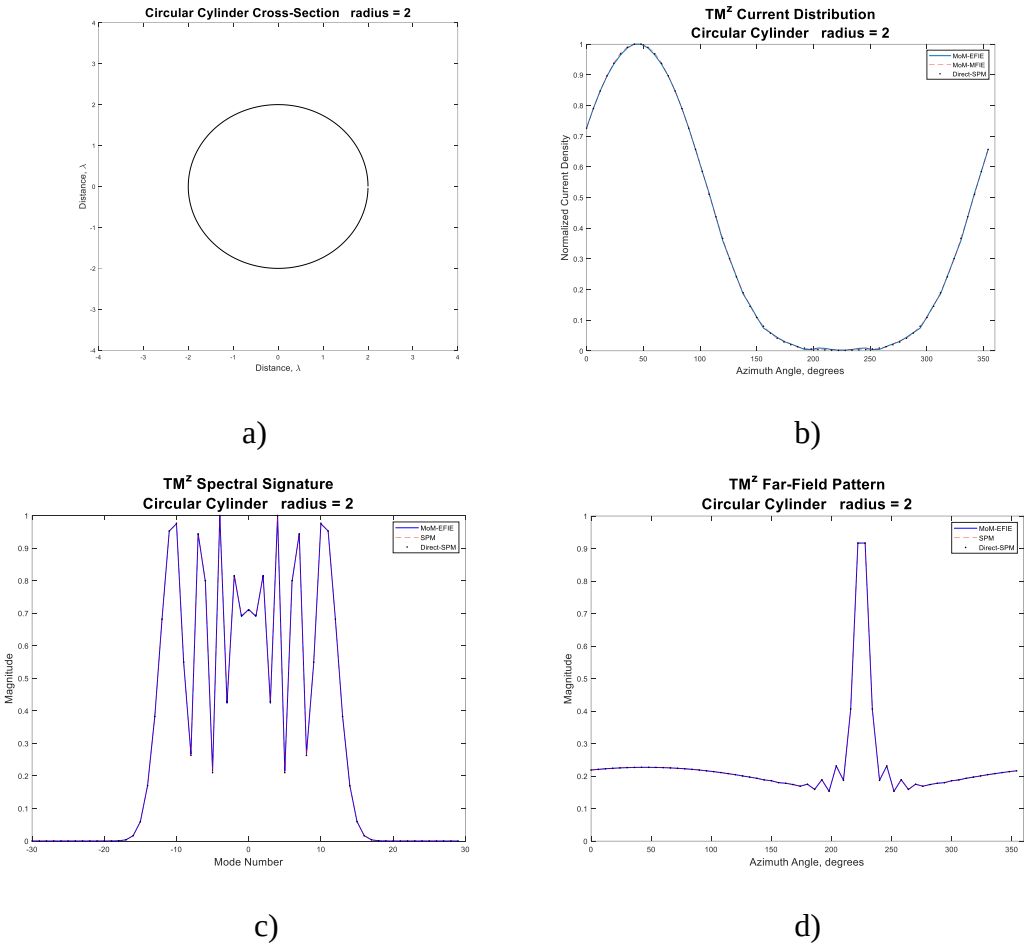

Figure 6-3: a) Infinitely long circular cylinder of $\rho = 2\lambda$. b) Plot of surface current around an infinitely long circular cylinder using DSPM, SPM and MOM for TM^Z Wave. c) Spectral signature plot of modes using DSPM, SPM, and MOM. d) Far-field pattern using DSPM, SPM and MOM.

For TE^z plane waves incident upon a PEC circular cylinder, derivation of the induced current on the surface follows a similar derivation. The solution of the MFIE the yields another

diagonal matrix form of matrix $\begin{bmatrix} : & : & : \\ : & H_k^{(2)\prime}(\beta|\boldsymbol{\rho_m}|)e^{jk\phi_m} & : \\ : & : & : \end{bmatrix}$, and the spectral response of the circular cylinder consists of derivatives of the Hankel function $(6-31)$.

$$\begin{bmatrix} : & : & : \\ : & H_k^{(2)\prime}(\beta|\boldsymbol{\rho_m}|)e^{jk\phi_m} & : \\ : & : & : \end{bmatrix} = \begin{bmatrix} \dots & 0 & 0 \\ 0 & H_k^{(2)\prime}(\beta|\boldsymbol{a}|) & 0 \\ 0 & 0 & \dots \end{bmatrix} \begin{bmatrix} \dots & \dots & \dots \\ \dots & \bar{F} & \dots \\ \dots & \dots & \dots \end{bmatrix} \quad (6-31)$$

The general DSPM equation for TE^z plane waves is given below in equation $(6-32)$.

$$\begin{bmatrix} | \\ \hat{\imath}_{ind,sum} \\ | \end{bmatrix} = \begin{bmatrix} \dots & \dots & \dots \\ \dots & \bar{F} & \dots \\ \dots & \dots & \dots \end{bmatrix}^H \begin{bmatrix} \dots & 0 & 0 \\ 0 & 1/H_k^{(2)\prime}(\beta|\boldsymbol{a}|) & 0 \\ 0 & 0 & \dots \end{bmatrix} \begin{bmatrix} | \\ \hat{\imath}_{ss,inc,Im0} \\ | \end{bmatrix} \quad (6-32)$$

For a near-field magnetic line source at (ρ_0', ϕ_0'), the spectral signature of the incident magnetic line source is written in $(5-88)$. Substituting for $I_{m0} = -\frac{\beta^2 I_m}{4\omega\varepsilon}$,

$$\begin{bmatrix} | \\ \hat{\imath}_{ss,inc,Im0} \\ | \end{bmatrix} = Im0\left[H_{-K}^{(2)}(\beta|\boldsymbol{\rho_0}'|)e^{jK\phi_0'} \dots H_k^{(2)}(\beta|\boldsymbol{\rho_0}'|)e^{jk\phi_0'} \dots H_K^{(2)}(\beta|\boldsymbol{\rho_0}'|)e^{-jK\phi_0'}\right]^T \quad (5-88)$$

The induced electric surface current on the circular cylinder at observation points (ρ, ϕ) for excitation by a magnetic line source I_{m0} is given in equation $(6-33)$.

$$i_{ind}(a, \phi') = \sum_{k=-K}^{K} \frac{H_k^{(2)}(\beta|\boldsymbol{\rho_0}'|)\, e^{jk(\phi'-\phi_0')}}{H_k^{(2)\prime}(\beta|\boldsymbol{a}|)} \quad (6-33)$$

This agrees with the equation given by Balanis in reference book [36].

$$J_\phi(a, \phi_n') = -\frac{jI_m}{2\eta\pi a} \sum_{k=-\infty}^{\infty} \frac{H_k^{(2)}(\beta|\boldsymbol{\rho}'|)\, e^{jk(\phi_n'-\phi_0')}}{H_k^{(2)\prime}(\beta|\boldsymbol{a}|)} \quad (5-153)$$

For TE^z plane waves incident from the ϕ_0' direction, the **H**-spectral signature of the magnetic field was given in equation $(5-91)$, where *ff* refers to far-field.

$$\begin{bmatrix} | \\ \hat{\imath}_{s,inc,Im}^{ff} \\ | \end{bmatrix} = H_0\left[e^{-jK\left(\phi_0'-\frac{\pi}{2}\right)} \quad \dots \quad e^{jk\left(\phi_0'-\frac{\pi}{2}\right)} \quad \dots \quad e^{jK\left(\phi_0'-\frac{\pi}{2}\right)}\right]^T \quad (5-91)$$

For a circular cylinder excited by a TE^z plane wave, the induced electric surface current in matrix equation $(6-32)$ may be written in summation form for any point (ρ', ϕ') as $(6-34)$.

$$i_{ind}(a,\phi') = \sum_{k=-K}^{K} \frac{j^{-k} e^{jk(\phi\prime-\phi_0\prime)}}{H_k^{(2)\prime}(\beta|\boldsymbol{a}|)} \qquad (6-34)$$

This agrees with the equation given by Balanis in reference book [36] and equation $(5-151)$.

$$J_\phi(a,\phi_n') = j\frac{2H_0}{\pi\beta a} \sum_{k=-\infty}^{\infty} \frac{j^{-k} e^{jk(\phi_n\prime-\phi_i\prime)}}{H_k^{(2)\prime}(\beta|\boldsymbol{a}|)} \qquad (5-151)$$

A comparison of DSPM and MOM plots for incident TE^z waves is shown in Figure 6-4. All three plots show good agreement for cylinder radius $a = 2\lambda$.

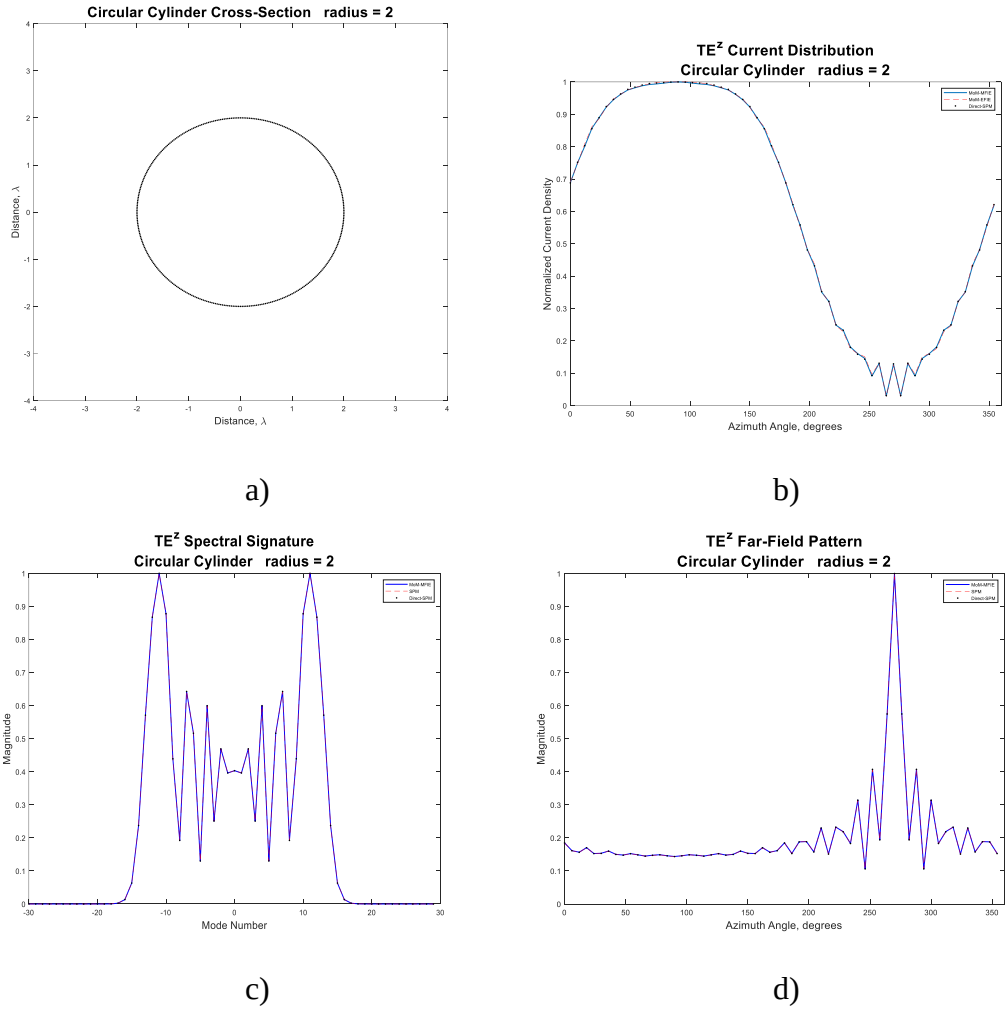

Figure 6-4: a) Infinitely long circular cylinder of $\rho = 2\lambda$. b) Plot of surface current around an infinitely long circular cylinder using DSPM, SPM and MOM for TE^Z Wave. c) Spectral signature plot of modes using DSPM, SPM, and MOM. d) Far-field pattern using DSPM, SPM and MOM.

The application of DSPM works well for small axial ratios radius $\frac{a}{b} < 4$. For larger axial ratios, the direct application of SPM fails because of the 'low pass' effect where the higher order modes are cut-off. This cut-off is dependent upon the size of the minor axis, where the requirement $\rho' < \rho$ for the source fails. To eliminate the 'low pass' effect, translation of the origin is necessary. Similar to the Spectral Projection Model, it will be shown that translation of the origin yields better results for ellipses with larger axial ratios and larger major axes.

6.5 Derivation of Direct SPM from SPM assuming Line Sources

From equation, DSPM can be generalized from a circular cylinder to any geometry. Each eigenfunction can be represented as an eigenvector in a matrix equation. So, each eigenvector is a solution to the TM^z scattering problem, and any incident waveform may be decomposed into a set of weighted eigenfunctions distributed across the entirety of the object's surface.

The electric field boundary condition for a PEC object was given previously as

$$E^{inc}(\rho,\phi) = -E^{scat}(\rho',\phi') \qquad (6-35)$$

The EFIE for 2D infinitely long cylinders aligned with the Z-axis excited by a TM^z wave was given in equation $(2-15)$.

$$E_z^{inc}(\rho) = \frac{\omega\mu}{4}\oint_C J_z(\beta|\boldsymbol{\rho}'|)H_0^{(2)}(\beta|\boldsymbol{\rho}-\boldsymbol{\rho}'|)dc' \qquad (2-15)$$

The left-hand side is generated by the external stimulus (incident fields) and right side of the equation is the scattered field from the unknown induced current $J(\rho',\phi')$ which is embedded in the integral on the right.

The EFIE can be discretized and applied to a set of known observation points (ρ_m,ϕ_m) on the boundary, and be written in matrix form $(6-36)$.

$$\begin{bmatrix} | \\ E_i(\rho_m) \\ | \end{bmatrix} = \frac{\omega\mu}{4}\begin{bmatrix} \cdots & \cdots & \cdots \\ \cdots & H_0^{(2)}(\beta|\boldsymbol{\rho_m}-\boldsymbol{\rho_n'}|) & \cdots \\ \cdots & \cdots & \cdots \end{bmatrix}\begin{bmatrix} | \\ J\,(\rho_n',\phi_n') \\ | \end{bmatrix} \qquad (6-36)$$

where (ρ_m, ϕ_m) are a set of observation points on the boundary and $(\rho_n, '\phi_n')$ are the locations of the induced current sources. One can solve this matrix equation for the vector corresponding to the unknown induced currents $\begin{bmatrix} | \\ J\ (\rho_n', \phi_n') \\ | \end{bmatrix}$.

To solve this equation, one begins with an external stimulus that is a line source aligned with the conductor axis (in the Z-direction) as illustrated in Figure 6-5.

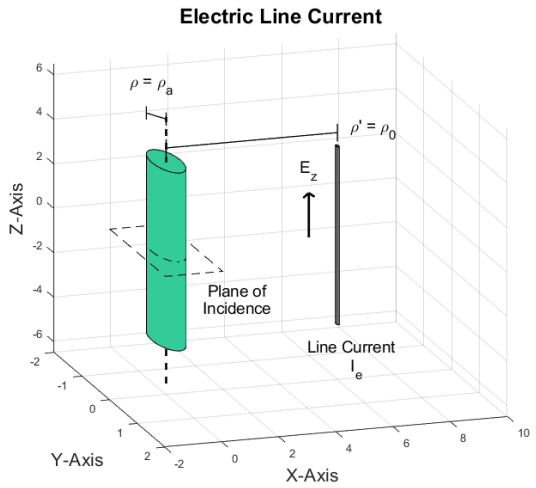

Figure 6-5: Infinitely long electric line source at coordinates $(\rho_{0,}\phi_0)$ near an infinitely long circular cylinder.

From Chapter 5 the incident electric field from a line source at originating at location (ρ_0', ϕ_0') and measured at (ρ_m, ϕ_m) may be described using a zeroth order Hankel function of the second kind,

$$\begin{bmatrix} | \\ E_{inc}(\rho_m) \\ | \end{bmatrix} = \frac{\beta^2 I_e}{4\omega\varepsilon} \begin{bmatrix} | \\ H_0^{(2)}\ (\beta|\boldsymbol{\rho_0}' - \boldsymbol{\rho_m}|) \\ | \end{bmatrix} \qquad (5-69)$$

where the magnitude of the current can be rewritten as I_0.

$$I_0 = -\frac{\beta^2 I_e}{4\omega\varepsilon} \qquad (6-37)$$

Using the addition theorem, the incident electric field from an external line source can be decomposed into two matrices which represent the **H**-spectral signature of the incident line source $\begin{bmatrix} | \\ H_k^{(2)}(\beta|\boldsymbol{\rho_0}'|) \\ | \end{bmatrix}$ projected onto the **J**-spectral signature of the observation points (ρ_m, ϕ_m).

$$\begin{bmatrix} | \\ E_{inc}(\rho_m) \\ | \end{bmatrix} = I_0 \begin{bmatrix} \cdots & \cdots & \cdots \\ \cdots & J_k(\beta|\boldsymbol{\rho_m}|) & \cdots \\ \cdots & \cdots & \cdots \end{bmatrix}^T \begin{bmatrix} | \\ H_k^{(2)}(\beta|\boldsymbol{\rho_0}'|) \\ | \end{bmatrix} \qquad (6-38)$$

The **H**-spectral signature of a single external line source $\begin{bmatrix} | \\ \hat{\imath}_{ss,inc,I_0} \\ | \end{bmatrix}$ at location (ρ_0', ϕ_0') is given in equation $(6-39)$. This is found by taking equation $(5-69)$ and then setting $I_0 = \frac{\beta^2 I_e}{4\omega\varepsilon}$.

$$\begin{bmatrix} | \\ \hat{\imath}_{ss,inc,I_0} \\ | \end{bmatrix} = I_0 \begin{bmatrix} H_{-K}^{(2)}(\beta|\boldsymbol{\rho_0}'|e^{jk\phi_0'} \\ | \\ H_k^{(2)}(\beta|\boldsymbol{\rho_0}'|e^{jk\phi_0'} \\ | \\ H_K^{(2)}(\beta|\boldsymbol{\rho_0}'|e^{jk\phi_0'} \end{bmatrix} \qquad (6-39)$$

Multiple line sources radiating from a set of infinitely long cylinders each contribute individually to the **H**-spectral signature of the electric field on the surface of the conducting cylinder. Illustrated in the Figure 6-6 is a circular cylinder excited by multiple line sources near its surface at angles ϕ_0, ϕ_1, and ϕ_2.

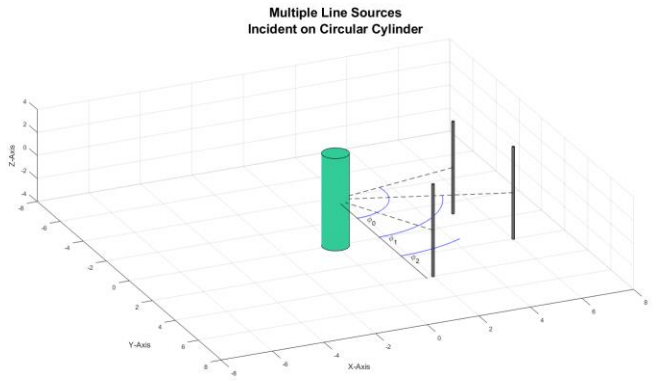

Figure 6-6: Three external line sources outside a circular cylinder.

If these electric line sources are moved close to the surface of the conductor, each becomes a virtual current on the surface. Every virtual current generates its own equal and opposite induced current. The Figure 6-7 shows three virtual current sources on the surface of a circular cylinder.

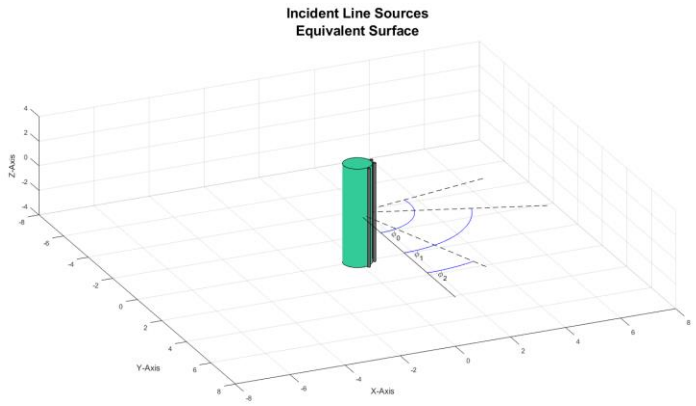

Figure 6-7: Three external line sources moved to a distance ε outside a circular cylinder.

The **H**-spectral signature of a single virtual current source at surface location $(\rho_n{}', \phi_n{}')$ can be represented as a column vector, $\begin{bmatrix} | \\ h_n \\ | \end{bmatrix}$.

$$\begin{bmatrix} | \\ h_n \\ | \end{bmatrix} = \begin{bmatrix} H_{-K}^{(2)}(\beta|\boldsymbol{\rho_n}'|)e^{jk\phi_n'} \\ | \\ H_{k}^{(2)}(\beta|\boldsymbol{\rho_n}'|)e^{jk\phi_n'} \\ | \\ H_{K}^{(2)}(\beta|\boldsymbol{\rho_n}'|)e^{jk\phi_n'} \end{bmatrix} \qquad (6-40)$$

When multiple line current sources are moved to the surface of the cylinder, the weighted sum of the **H**-spectral signatures of the virtual current sources from *N* line sources is given in equation $(6-41)$.

$$\begin{bmatrix} | \\ \hat{\imath}_{ss,vir,sum} \\ | \end{bmatrix} = \begin{bmatrix} | \\ | \\ h_0 \\ | \\ | \end{bmatrix}\alpha_0 + \begin{bmatrix} | \\ | \\ h_1 \\ | \\ | \end{bmatrix}\alpha_1 \quad + \quad \ldots + \quad \begin{bmatrix} | \\ | \\ h_{N-1} \\ | \\ | \end{bmatrix}\alpha_{N-1} \qquad (6-41)$$

The weighting factors of the virtual current sources are $\alpha_n \in \{\alpha_0, \alpha_1, \ldots, \alpha_{N-1}\}$.

$$\begin{bmatrix} | \\ \hat{\imath}_{vir,sum} \\ | \end{bmatrix} = \begin{bmatrix} \alpha_0 \\ | \\ \alpha_n \\ | \\ \alpha_{N-1} \end{bmatrix} \tag{6-42}$$

These coefficients α_n are the magnitude and phase of the virtual current sources.

This is analogous to SPM in Chapter 5 using equation $(5-69)$ to aggregate the spectral signatures of multiple line sources $\begin{bmatrix} | \\ \hat{\imath}_{ss,inc,Ie} \\ | \end{bmatrix}$ into a single matrix. The sum of the **H**-spectral signatures of multiple virtual line current sources at coordinates $\phi' = \phi_n{}'$ for $n \in \{0,1,N-1\}$ equals the **H**-spectral signature of the total virtual electric current. See equation $(6-43)$.

$$\begin{bmatrix} | \\ \hat{\imath}_{ss,vir,sum} \\ | \end{bmatrix} = \begin{bmatrix} H_{-K}^{(2)}(\beta|\boldsymbol{\rho_0}'|)e^{jk\phi_0'} \\ | \\ H_k^{(2)}(\beta|\boldsymbol{\rho_0}'|)e^{jk\phi_0'} \\ | \\ H_K^{(2)}(\beta|\boldsymbol{\rho_0}'|)e^{jk\phi_0'} \end{bmatrix} I_0 + \begin{bmatrix} H_{-K}^{(2)}(\beta|\boldsymbol{\rho_1}'|)e^{jk\phi_1'} \\ | \\ H_k^{(2)}(\beta|\boldsymbol{\rho_1}'|)e^{jk\phi_1'} \\ | \\ H_K^{(2)}(\beta|\rho_1'|)e^{jk\phi_1'} \end{bmatrix} I_1 + \cdots$$

$$+ \begin{bmatrix} H_{-K}^{(2)}(\beta|\boldsymbol{\rho_{N-1}}'|)e^{jk\phi_{N-1}'} \\ | \\ H_k^{(2)}(\beta|\boldsymbol{\rho_{N-1}}'|)e^{jk\phi_{N-1}'} \\ | \\ H_K^{(2)}(\beta|\boldsymbol{\rho_{N-1}}'|)e^{jk\phi_{N-1}'} \end{bmatrix} I_{N-1} \tag{6-43}$$

If the external stimulus is an electric field plane wave E_0 from a distant electric line source I_0, then the **H**-spectral signature of the incident electric field is given in equation $(6-44)$.

$$\begin{bmatrix} | \\ i_{ss,vir,I_0}^{ff} \\ | \end{bmatrix} = E_0 \begin{bmatrix} e^{-jK\left(\phi_0'-\frac{\pi}{2}\right)} \\ | \\ e^{jk\left(\phi_0'-\frac{\pi}{2}\right)} \\ | \\ e^{jK\left(\phi_0'-\frac{\pi}{2}\right)} \end{bmatrix} \tag{6-44}$$

For DSPM, this equation is similar to equation $(5-72)$ except that the equivalent far-field spectral signature originates from the virtual sources on the conductor and not a line source at

infinity. This is because DSPM differs from SPM in that the virtual currents are at the surface of the conductor.

The weighted sum of the **H**-spectral signatures of the virtual current sources set up a surface current equivalent to that of the **H**-spectral signature of an incident electric field. The electric field produces induced current sources that are equal and opposite to the virtual current sources. See Figure 6-8.

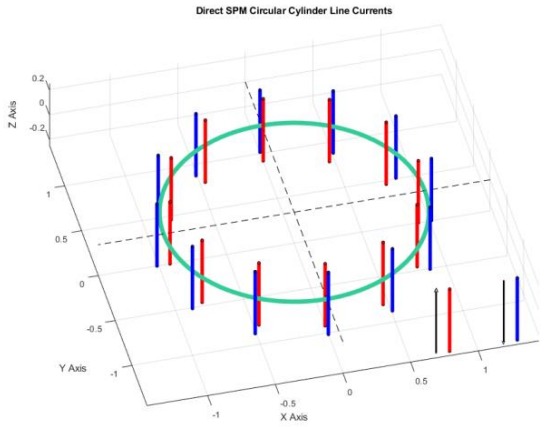

Figure 6-8: Illustration of virtual current sources on an infinitely long circular cylinder in blue, and induced surface line currents in red. Surface and induced currents are in opposite directions. The cylinder is in green.

In DSPM the far-field **H**-spectral signature of an incident line source(s) can be set equal to the **H**-spectral signature of a set of virtual currents on the surface of the conductor. An illustration of a line source in the far-field generating an external plane wave incident upon an infinitely long PEC cylinder is shown in Figure 6-9. The DSPM equation is also shown in the figure.

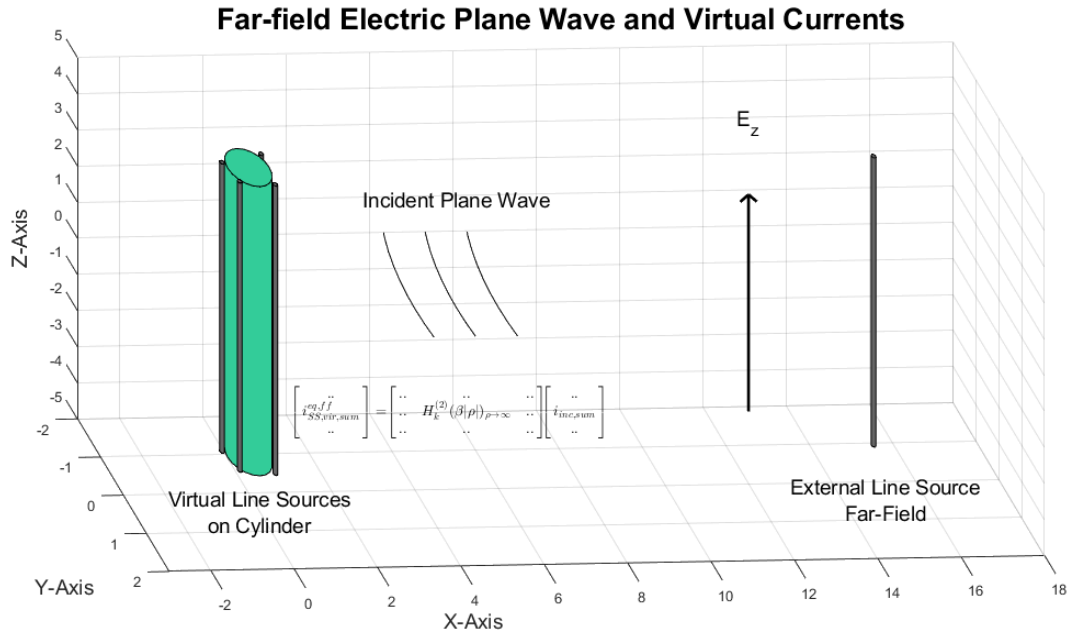

Figure 6-9: External current source, virtual current sources, and **H**-spectral signature of the incident plane wave set equal to the weighted sum of the **H**-spectral signatures of the virtual currents.

The magnitude and phase of each induced current source equals the weighting factor $\beta_n \in \{\beta_0, \beta_1, \dots, \beta_{N-1}\}$. The vector representation of the magnitude and phase of the sum of the induced currents $\begin{bmatrix} | \\ \hat{\imath}_{ind,sum} \\ | \end{bmatrix}$ may be written as equation $(6-45)$.

$$\begin{bmatrix} | \\ \hat{\imath}_{ind,sum} \\ | \end{bmatrix} = \begin{bmatrix} \beta_0 \\ | \\ \beta_n \\ | \\ \beta_{N-1} \end{bmatrix} \qquad (6-45)$$

where $\alpha_n = -\beta_n$.

The left side of the discretized EFIE represents the incident field. For a single line current source I_0 at (ρ_0', ϕ_0'), $\begin{bmatrix} \dots \\ E_{inc}(\rho_m) \\ \dots \end{bmatrix}$ at observation point (ρ_m, ϕ_m) equals the **H**-spectral signature of the external source projected onto the **J**-spectral signature of the observation points.

$$\begin{bmatrix} | \\ E_{inc}(\rho_m) \\ | \end{bmatrix} = I_0 \begin{bmatrix} \cdots & \cdots & \cdots \\ \cdots & J_k\,(\beta|\boldsymbol{\rho_m}|) & \cdots \\ \cdots & \cdots & \cdots \end{bmatrix}^T \begin{bmatrix} | \\ H_k^{(2)}\,(\beta|\boldsymbol{\rho_0}'|e^{jk\phi_{0'}} \\ | \end{bmatrix} \qquad (6-46)$$

For a line current near the surface of the conductor, one can write the left side of the EFIE equation for the **H**-spectral signature of a single virtual line current source $\begin{bmatrix} | \\ h_n \\ | \end{bmatrix}$,

$$\begin{bmatrix} | \\ E_{inc}(\rho_m) \\ | \end{bmatrix} = \begin{bmatrix} \cdots & \cdots & \cdots \\ \cdots & J_k\,(\beta|\boldsymbol{\rho_m}|) & \cdots \\ \cdots & \cdots & \cdots \end{bmatrix}^T \begin{bmatrix} | \\ h_n \\ | \end{bmatrix} \qquad (6-47)$$

where $\begin{bmatrix} | \\ h_n \\ | \end{bmatrix}$ is the **H**-spectral signature of a single virtual current source defined in equation $(6-40)$. This equation is equivalent to the incident electric field $\begin{bmatrix} | \\ E_{inc} \\ | \end{bmatrix}$written as the **H**-spectral signature of the incident current source projected onto the **J**-spectral signature of the observation point (ρ_m, ϕ_m).

$$\begin{bmatrix} | \\ E_{inc} \\ | \end{bmatrix} = \begin{bmatrix} \cdots & \cdots & \cdots \\ \cdots & J_k\,(\beta|\boldsymbol{\rho_m}|) & \cdots \\ \cdots & \cdots & \cdots \end{bmatrix}^T \begin{bmatrix} | \\ i_{ss,inc} \\ | \end{bmatrix} \qquad SPM \qquad (6-48)$$

DSPM decomposes the HSS of the incident sources into the weighted sum of the HSS of the virtual currents. By finding the virtual currents we can easily calculate the induced currents which are equal and opposite. Once the induced currents are calculated, one may calculate the far-field pattern. The far-field patten is the Fourier transform of the **J**-spectral signature of the induced currents. These weights are equal to the virtual current source vector and negative the induced current vector.

The steps for calculating the induced current and therefore the far-field pattern using DSPM can be summarized in the block diagram below in Figure 6-10.

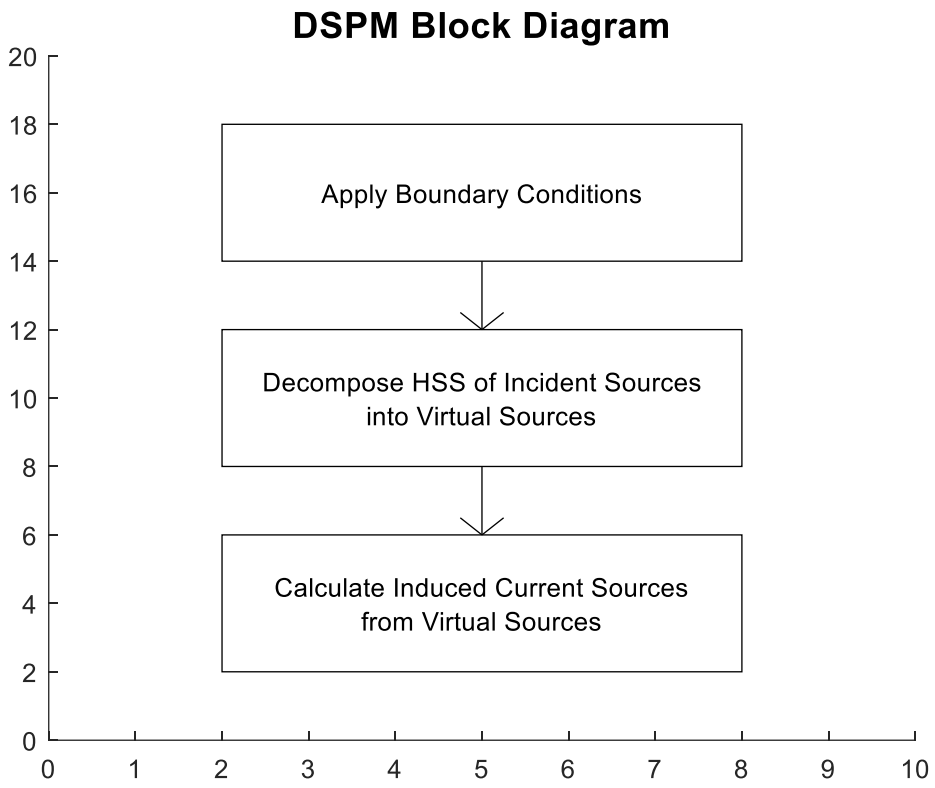

Figure 6-10: Block diagram of steps for calculating currents through DSPM process.

One may write the eigenvector matrix equation for the electric field boundary conditions as equation $(6-49)$ to ensure that the B.C.s are satisfied. Because the virtual currents represent eigenvectors of eigenfunction solutions to the boundary value scattering problem, we can also write $\begin{bmatrix} | \\ E_{inc} \\ | \end{bmatrix}$ as a weighted sum of a set of eigenfunctions. This is the DSPM equation shown in addition theorem form.

$$\begin{bmatrix} \cdots & \cdots & \cdots \\ \cdots & J_k\left(\beta|\boldsymbol{\rho_m}|\right) & \cdots \\ \cdots & \cdots & \cdots \end{bmatrix}^T \begin{bmatrix} | \\ i_{ss,inc,sum} \\ | \end{bmatrix} = \begin{bmatrix} \cdots & \cdots & \cdots \\ \cdots & J_k\left(\beta|\boldsymbol{\rho_m}|\right) & \cdots \\ \cdots & \cdots & \cdots \end{bmatrix}^T \begin{bmatrix} | \\ i_{ss,vir,sum} \\ | \end{bmatrix} \qquad (6-49)$$

From equation $(6-49)$, for a single line source, the **H**-spectral signature of the incident line current can be set equal to the weighted sum of the **H**-spectral signatures of the virtual currents. The weighting factors are the coefficients of the incident line current and virtual currents.

$$\begin{bmatrix} \cdots & \cdots & \cdots \\ \cdots & H_k^{(2)}(\beta|\boldsymbol{\rho_{n,vir}}|) & \cdots \\ \cdots & \cdots & \cdots \end{bmatrix} \begin{bmatrix} | \\ \hat{\imath}_{vir,sum} \\ | \end{bmatrix} = \begin{bmatrix} \cdots & \cdots & \cdots \\ \cdots & H_k^{(2)}(\beta|\boldsymbol{\rho_{n,inc}}|) & \cdots \\ \cdots & \cdots & \cdots \end{bmatrix} \begin{bmatrix} | \\ \hat{\imath}_{inc,sum} \\ | \end{bmatrix} \qquad (6-50)$$

Incident current sources can be either one or multiple external sources as explained in Figure 6-11.

Single external line source (near field)
Multiple external line sources (near field) $\rightarrow$ $\begin{bmatrix} | \\ \hat{\imath}_{inc,Ie} \\ | \end{bmatrix}$
Single external line source (far − field) or plane wave

Figure 6-11: External incident line sources using DSPM.

The general DSPM equation for any incident sources is given in equation $(6-51)$, Figure 6-12, and reference [54].

$$\begin{bmatrix} \cdots & \cdots & \cdots \\ \cdots & H_k^{(2)}(\beta|\boldsymbol{\rho_{n,vir}}|) & \cdots \\ \cdots & \cdots & \cdots \end{bmatrix} \begin{bmatrix} | \\ \hat{\imath}_{vir,sum} \\ | \end{bmatrix} = \begin{bmatrix} | \\ \hat{\imath}_{ss,inc,sum} \\ | \end{bmatrix} \qquad (6-51)$$

Weighted sum of the **H**-Spectral Signatures of the Virtual Sources

H-Spectral Signature of Incident Current Sources

Figure 6-12: General DSPM equation for incident sources.

Any external source can be represented by the weighted sum of virtual sources. So, an equivalent electric field waveform in matrix equation $(6-51)$ can be generated by a set of virtual sources with appropriate magnitudes, phases, and locations on the surface of the conductor. For example, the excitation generated by the virtual sources can be the equivalent of an incident electric field plane wave E_0 from the far-field impingent on the surface of the

cylinder at observation points (ρ_m, ϕ_m). The virtual and induced current sources will occupy the same surface coordinates pairs on the surface of the conductor. The excitation waveform may also be any arbitrary incident electric field pattern generated by *N* external line sources. The virtual line sources on the surface of the cylinder can also generate the same arbitrary electric field pattern. For example, the weighted sum of the **H**-spectral signature of the virtual currents equals the equivalent spectral signature of an electric plane wave produced by incident sources as shown in equation $(6-52)$ in Figure 6-13.

$$\begin{bmatrix} \cdots & \cdots & \cdots \\ \cdots & H_k^{(2)}(\beta|\boldsymbol{\rho_{n,vir}}|) & \cdots \\ \cdots & \cdots & \cdots \end{bmatrix} \begin{bmatrix} | \\ \hat{\imath}_{vir,sum} \\ | \end{bmatrix} = \begin{bmatrix} | \\ i_{ss,inc,sum}^{ff} \\ | \end{bmatrix} \qquad (6-52)$$

Weighted sum of the **H**-Spectral Signatures of the Virtual Sources

H-Spectral Signature of Incident Far-Field Current Source

Figure 6-13: General DSPM equation for far-field sources.

The actual eigenfunctions of equation $(6-52)$ depend upon the geometry of the object being analyzed.

A real incident plane can only be represented by a vector of infinite dimensional space. But to solve any scattering problem computationally, the object and the plane wave both must be discretized and limited to a finite number of modes. Depending on the largest radius of the object, the value of the Hankel function increases exponentially after a certain number of modes K. To solve a circular cylinder for its induced currents, both sides of the DSPM equation are multiplied by the inverse of the diagonal matrix $H_k^{(2)}(\beta|\boldsymbol{\rho}|)$. Because the inverse diagonal matrix is made up of $1/H_k^{(2)}(\beta|\boldsymbol{\rho}|)$ elements, the magnitude of the $1/H_k^{(2)}(\beta|\boldsymbol{\rho}|)|_{k\to\infty} = 0$ for higher order modes k.

Even though a plane wave occupies infinite space, when it is multiplied by$1/H_k^{(2)}(\beta|\boldsymbol{\rho}|)$, its higher order modes are filtered out. So, one can truncate the vector representation of the plane wave to a finite $\pm K$ due to this lowpass filtering process and not affect the solution. The

inverse of the **H**-spectral signature subspace matrix exhibits a lower cut-off effect for a value of K.

In DSPM the cut-off K of the lower order modes is determined by the largest dimension of the object. Inv of $H_k^{(2)}(\beta|\boldsymbol{\rho}|)$causes the magnitude of the **H**-spectral signature to cut off at mode number K when $H_k^{(2)}(\beta|\boldsymbol{\rho}|)$starts to grow large. This is where the lowpass filter effect begins to occur.

For the initial analyses of the ellipse using DSPM, the lowpass filter effect became pronounced because the smallest dimension of the ellipse determined the cutoff mode rendering many of the higher order modes insignificant. By translating the origin, the largest dimension was set with the Hankel function. This was necessary because Bessel functions do exhibit this lowpass filter effect.

$H_k^{(2)}(\beta|\boldsymbol{\rho}|)$is set to the largest dimension sot it determines the cut-off of the modes and $1/H_k^{(2)}(\beta|\boldsymbol{\rho}|)|_{k\to\infty} = 0$. So, we get the lowpass filter effect on the largest dimension using the two-vector model.

We can take any waveform that is infinite space and this property of the Hankel function provides a built-in filtering of the higher order modes. The spectral signatures are all band limited and do not need to occupy infinite dimensional space. The incident waveforms can be any configuration of waves, or far-field or near field waves, and for modes higher than the cutoff, the **H**-spectral signature matrix will filter out all the energy over the cut-off mode.

All the higher modal energy in the incident field does not affect the solution of the problem. Modes that are high frequency terms get filtered out. So, if the incident sources are a set of plane waves over a range of angles $\phi' = \{\phi_0', \phi_1', \ldots, \phi_P'\}$, it does not exhibit an infinite spectrum, but is band limited and the higher order energy goes to zero. The scattering process using DSPM is independent of the higher order modes.

Solving for the boundary conditions are the initial step to the DSPM solution. Scattered fields induced by the induced currents and incident fields due to incident currents. DSPM replaces the incident sources by virtual sources. In SPM the incident electric field is found when one projects the **H**-spectral signature of the source points onto the **J**-spectral signature of the observation points at the surface. DSPM uses equation 6-52 to find the equivalent electric field due to virtual sources. Then one can project the **H**-spectral signature of the virtual current

sources onto the **J**-spectral signature of the observation points and set it equal to **H**-spectral signature of the incident sources projected onto the **J**-spectral signature of the observation points. Once the equation is solved for the virtual currents, the amplitude of the virtual currents equals the amplitude of the induced currents.

6.6 Spectral Features of 2D Circular Cylinders excited by TM^z Waves using DSPM

The spectral signature of circular cylinders varies according to the radius of the cylinder cross section. For circular cylinders, the number of modes in the spectral signature increases with the radius of the cylinder. The cylinder exhibits a low-pass filter pattern, and the modal magnitudes decrease for higher order spectral modes. This is due to the addition theorem product $H_k^{(2)}(\beta|\boldsymbol{\rho}|)J_k(\beta|\boldsymbol{\rho}'|) \to 0$ as modes $k \to \infty$. See Figures 6-14 and 6-15.

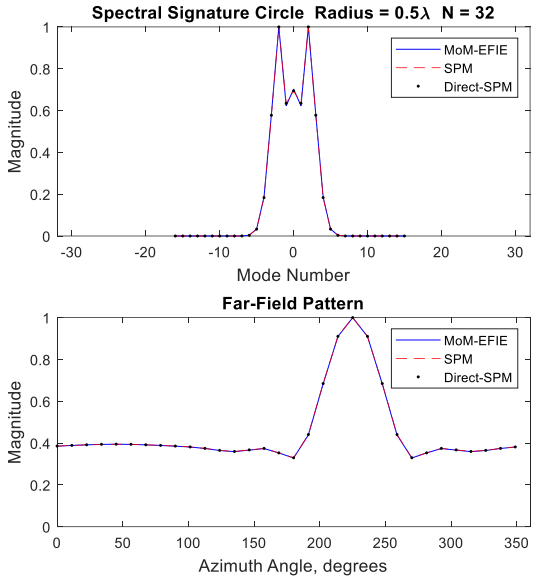

Figure 6-14: Comparison of spectral signature and far-field pattern of infinitely long circular cylinder of $\rho = .5\lambda$ using MOM, SPM and DSPM for TM^z wave.

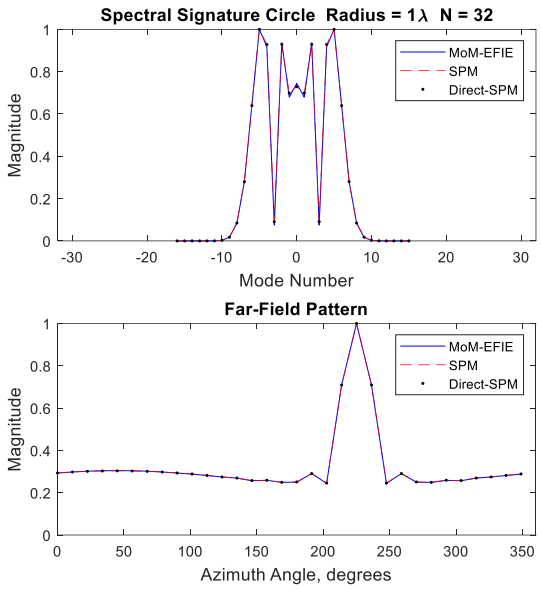

a)

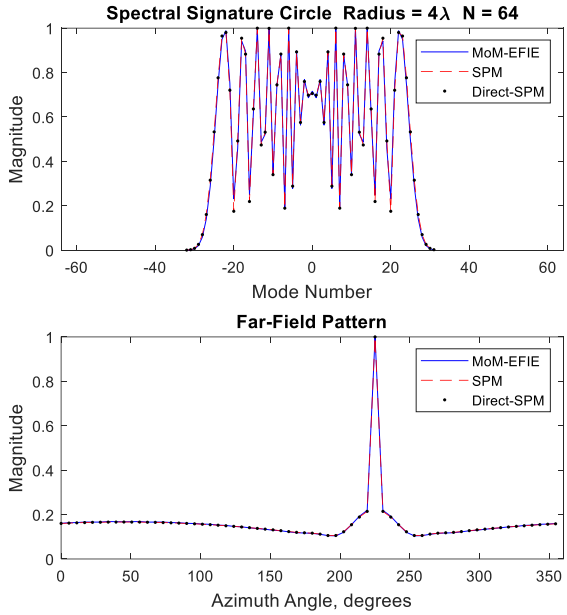

b)

Figure 6-15: a) Comparison of spectral signature and far-field pattern of infinitely long circular cylinder of $\rho = 1\lambda$ using MOM, SPM and DSPM for TM^z wave. b) Comparison of spectral signature and far-field pattern of infinitely long circular cylinder of $\rho = 4\lambda$ using MOM, SPM and DSPM for TM^z wave.

Figure 6-14 and Figure 6-15 make clear that besides broadening the spectral signature, increasing the radius of the cylinder also narrows the angular bandwidth of the far-field pattern. Comparing the far-field pattern between radii $\rho = .5\lambda$ and $\rho = 4\lambda$, the angular bandwidth decreased from about 50 degrees to 10 degrees. In order to achieve proper resolution of the peak, the number of modes had to be increased from 32 to 64 in the calculations. The sharpening of the peaks and greater directivity was made possible by the increase in the number of harmonics in the spectral signature.

This lowpass filtering effect resembles the lowpass filtering caused by introduction of basis functions when using the Method of Moments. For MOM pulse functions, the spatial frequency domain representation was a sinc function. The MOM Fourier domain bandwidth of these basis functions was broader for narrower spatial lengths, similar to the above results for DSPM.

When less basis functions were used to cover the spatial domain of the scattering problem, wider basis functions were needed. The bandwidth of the wider pulses was smaller than the narrow pulses. This decrease in spatial frequency bandwidth came at the cost of less resolution for the current distribution pattern. The resolution of the far-field pattern resolution was also adversely affected by these changes.

6.7 Translation of the Origin for DSPM Solutions

The collective spectral signature of the actual sources equals the collective spectral signature of the sources on the surface. One may use the convolution principle to examine general 2D objects generated by circular cylinders of different radii to examine this property of DSPM. Just as in SPM, translation of the origin enables the Direct Spectral Projection Model to be used to analyze large axial ratio objects with good convergence of the addition theorem. TM^z waves incident on an arbitrarily shaped cylinder will only be explained, but the results are similar for TE^z waves as well. For an induced electric current, $\begin{bmatrix} \cdots \\ \hat{\imath}_{ind} \\ \cdot\cdot \end{bmatrix}$, the columns of the eigenvector matrix correspond to the **H**-spectral signature of the virtual currents at ϕ_{N_S}different points $(6-53)$.

$$\begin{bmatrix} | & | & | \\ | & H_k^{(2)}(\beta|\boldsymbol{\rho_n}'|) & | \\ | & | & | \end{bmatrix} = \begin{bmatrix} H_{-K}^{(2)}(\beta|\boldsymbol{\rho_0}'|)e^{jK\phi_{0'}} & \cdots & \cdots & \cdots & H_{-K}^{(2)}\left(\beta\left|\boldsymbol{\rho_{N_S-1}}'\right|\right)e^{jK\phi_{N_S-1'}} \\ \vdots & \vdots & \vdots & \vdots & \vdots \\ \vdots & \vdots & \vdots & \vdots & \vdots \\ \vdots & \vdots & \vdots & \vdots & \vdots \\ H_K^{(2)}(\beta|\boldsymbol{\rho_0}'|)e^{-jK\phi_{0'}} & \cdots & \cdots & \cdots & H_K^{(2)}\left(\beta\left|\boldsymbol{\rho_{N_S-1}}'\right|\right)e^{-jK\phi_{N_S-1'}} \end{bmatrix} \quad (6-53)$$

The **H**-spectral signature subspace $\begin{bmatrix} | & | & | \\ | & H_k^{(2)}(\beta|\boldsymbol{\rho_n}'|) & | \\ | & | & | \end{bmatrix}$ may be rewritten as the matrix equation in $(6-54)$.

$$\begin{bmatrix} | & | & | \\ | & H_k^{(2)}(\beta|\boldsymbol{\rho_n}'|) & | \\ | & | & | \end{bmatrix} = \left(\begin{bmatrix} \cdots & \cdots & \cdots \\ \cdots & \bar{F} & \cdots \\ \cdots & \cdots & \cdots \end{bmatrix} \begin{bmatrix} | & | & | \\ | & H_k^{(2)}(\beta|\boldsymbol{\rho_n}'|) & | \\ | & | & | \end{bmatrix}^H \right)^H \begin{bmatrix} \cdots & \cdots & \cdots \\ \cdots & \bar{F} & \cdots \\ \cdots & \cdots & \cdots \end{bmatrix} \quad (6-54)$$

Substituting equation $(6-54)$ into equation $(6-51)$, one gets $(6-55)$.

$$\left(\begin{bmatrix} \cdots & \cdots & \cdots \\ \cdots & \bar{F} & \cdots \\ \cdots & \cdots & \cdots \end{bmatrix} \begin{bmatrix} | & | & | \\ | & H_k^{(2)}((\beta|\boldsymbol{\rho_n}'|) & | \\ | & | & | \end{bmatrix}^H \right)^H \begin{bmatrix} \cdots & \cdots & \cdots \\ \cdots & \bar{F} & \cdots \\ \cdots & \cdots & \cdots \end{bmatrix} \begin{bmatrix} \cdots \\ \hat{\imath}_{vir,sum} \\ \cdot\cdot \end{bmatrix} = \begin{bmatrix} \cdots \\ \hat{\imath}_{ss,inc,sum} \\ \cdot\cdot \end{bmatrix} \quad (6-55)$$

When the geometry of the object can be generated by convolving two constant magnitude vectors $\boldsymbol{\rho_a}$ and $\boldsymbol{\rho_b}$ rotating in opposite directions, as explained in Chapter 5 and Appendix M, equation $(6-56)$ may be expanded using the following property of a Hadamard product $\odot$.

$$\left(\begin{bmatrix} \cdots & \cdots & \cdots \\ \cdots & \bar{F} & \cdots \\ \cdots & \cdots & \cdots \end{bmatrix} \begin{bmatrix} | & | & | \\ | & H_k^{(2)}((\beta|\boldsymbol{\rho_b}|) & | \\ | & | & | \end{bmatrix}^H \odot \begin{bmatrix} \cdots & \cdots & \cdots \\ \cdots & \bar{F} & \cdots \\ \cdots & \cdots & \cdots \end{bmatrix} \begin{bmatrix} \cdots & \cdots & \cdots \\ \cdots & J_k(\beta|\boldsymbol{\rho_a}|) & \cdots \\ \cdots & \cdots & \cdots \end{bmatrix}^H \right)^H .$$

$$\begin{bmatrix} \cdots & \cdots & \cdots \\ \cdots & \bar{F} & \cdots \\ \cdots & \cdots & \cdots \end{bmatrix} \begin{bmatrix} \cdots \\ \hat{\imath}_{vir,sum} \\ \cdot\cdot \end{bmatrix} = \begin{bmatrix} \cdots \\ \hat{\imath}_{ss,inc,sum} \\ \cdot\cdot \end{bmatrix} \quad (6-56)$$

This technique enables one to analyze elliptically shaped two-dimensional cylinders with large axial ratios with good accuracy using DSPM. The following results validate this technique.

Figure 6-16 and Figure 6-17 show current flows for TM^z waves in the same direction as the electric field.

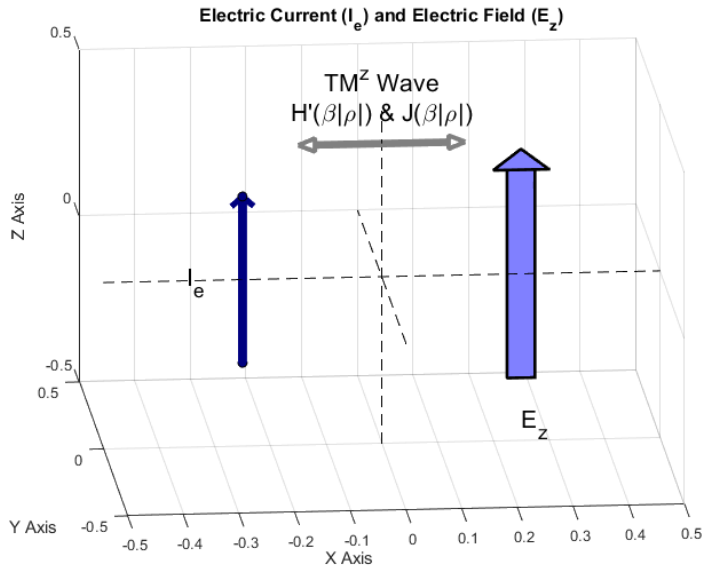

Figure 6-16: Illustration of the Z-direction of current versus electric field for a TM^z incident wave vertical view.

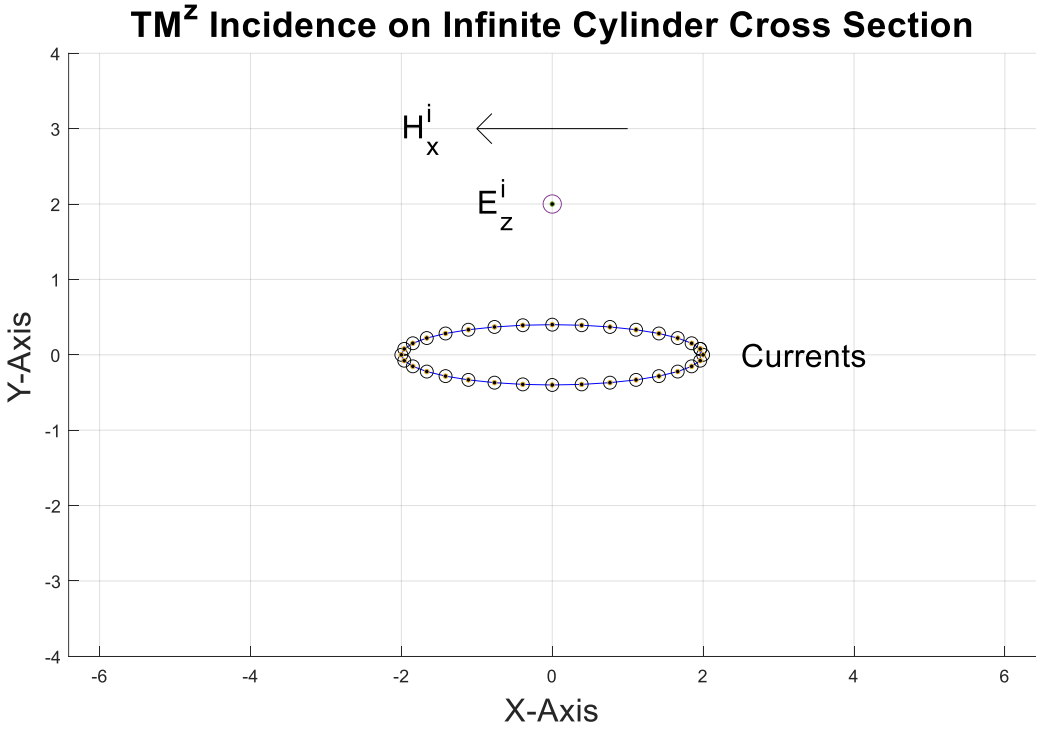

Figure 6-17: Illustration of the Z-direction of current versus electric field for a TM^z incident wave cross sectional view.

Results for TM^z incident waves for cylinders of axial ratios of $\frac{a}{b} = 5$ and $\frac{a}{b} = 10$ are calculated and plotted in Figure 6-18 and Figure 6-19. The calculations were performed using the Method of Moments, Spectral Projection Model and Direct Spectral Projection Model, and are in good agreement.

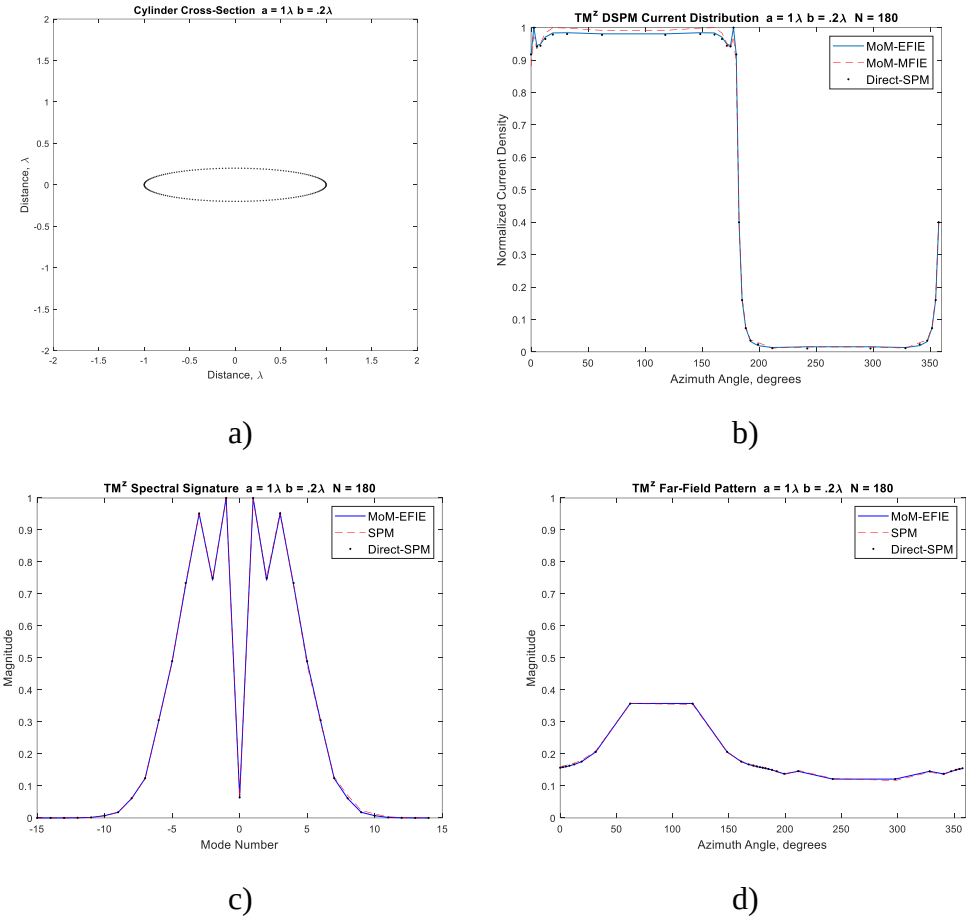

Figure 6-18: a) Infinitely long elliptical cylinder of axial ratios $\frac{a}{b} = 5$. b) Plot of surface current around an infinitely long circular cylinder using DSPM, SPM and MOM for TM^Z wave.
c) Spectral plot of modes using DSPM, SPM, and MOM d) Far-field pattern using DSPM, SPM and MOM.

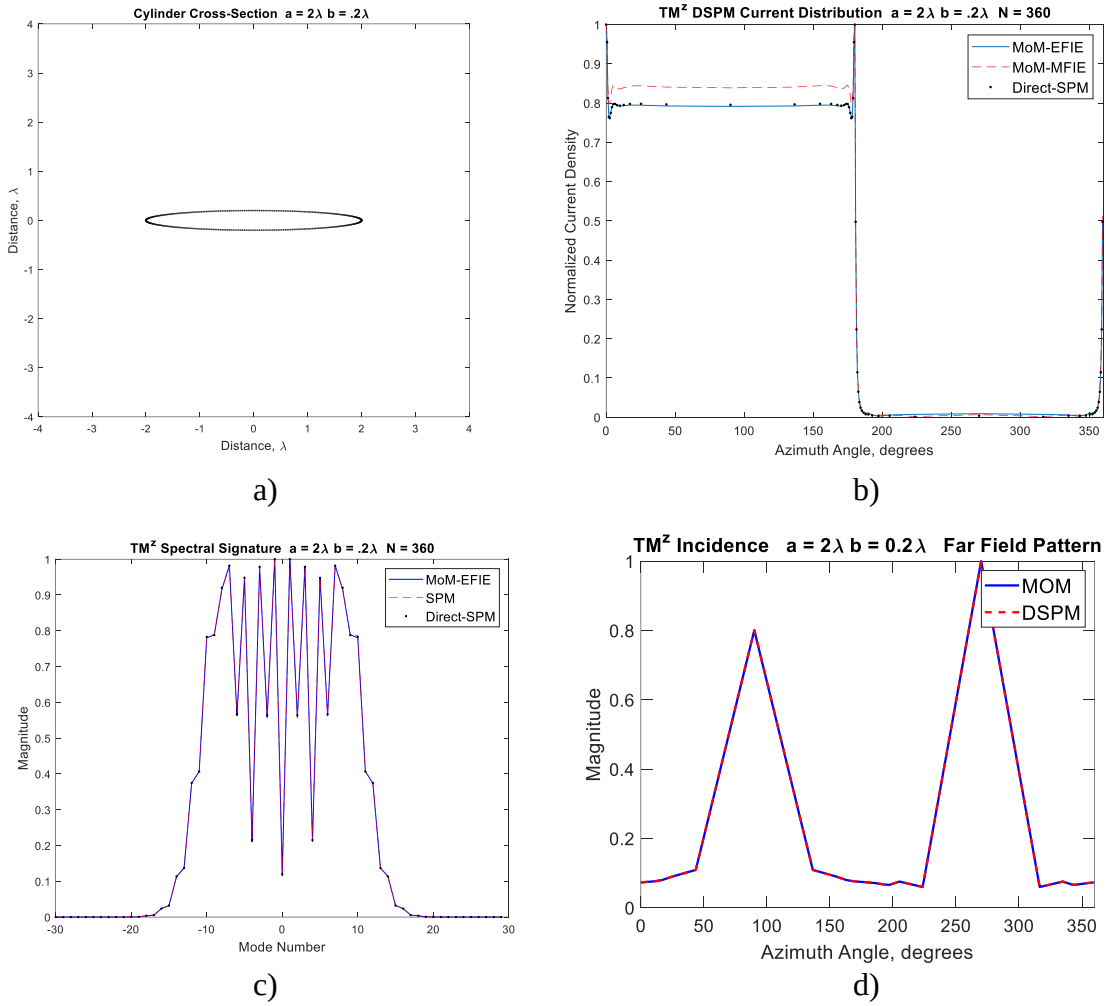

Figure 6-19: a) Infinitely long elliptical cylinder of axial ratios $\frac{a}{b} = 10$. b) Plot of surface current around an infinitely long circular cylinder using DSPM, SPM and MOM for TM^Z wave. c) Spectral plot of modes using DSPM, SPM, and MOM. d) Far-field pattern using DSPM, SPM and MOM.

The main lobe and side lobes of the far-field pattern of an antenna scatterer are determined by the size of the scatterer with respect to the excitation wavelength, the geometry of the scatterer, and the shape of the excitation waveform. For the same TM^z plane wave excitation on different elliptical cylinders using DSPM, larger structures produce wider spectral signature bandwidths as evidenced by the difference in plots from Figure 6-18c, 6-19c, and 6-20. When the size of the major axis is increased, the spectral signature broadens and thus the number of modes also increases.

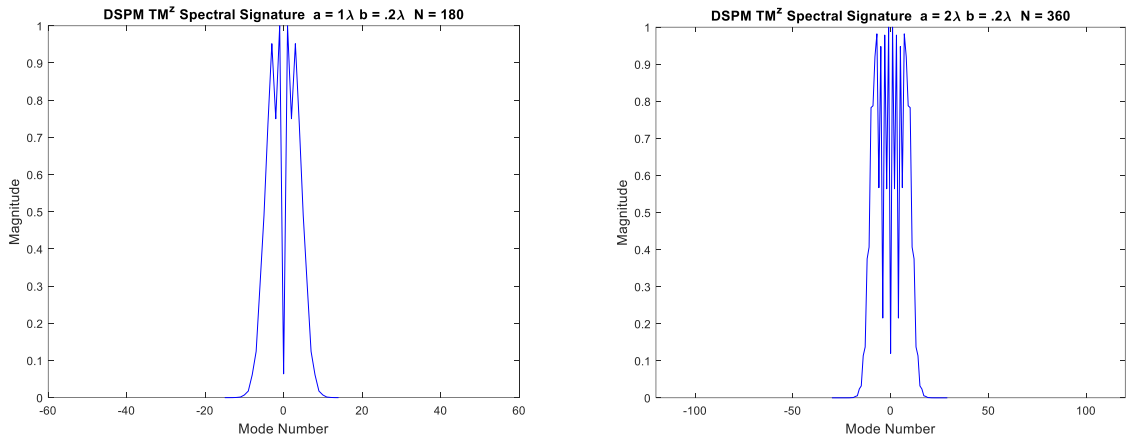

a) b)

Figure 6-20: Comparison of spectral plots of infinitely long elliptical cylinder of axial ratios a) $\frac{a}{b} = 5$ and b) $\frac{a}{b} = 10$ using DSPM for TM^Z wave excitation.

For axial ratios $\frac{a}{b} = 5$ and $\frac{a}{b} = 10$, the radiation lobe(s) are aligned with the minor axis of the ellipse where the average current distribution is greatest. These lobes are at 90^o and 270^o for a plane wave angle of incidence of 90^o. See the far-field plots in Figures 6- 18 and 6-19. Higher order modes in the spectral signature were the major contributors to the current spikes shown in the current distribution. Current spikes along the major axis are "end effects" due to the curvature of the scattering object, where a greater number of near-field interactions occur. The end effect in the current distribution of the ellipse with axial ratio $\frac{a}{b} = 10$ in Figure 6-21b is much greater than that in the ellipse with the lower axial ratio $\frac{a}{b} = 5$ in Figure 6-21a. Current spikes do not appear in the current distribution pattern of a circular cylinder because of its uniform geometry and curvature (Figure 6-4b).

The higher axial ratio and larger major axis, i.e. $\frac{a}{b} = 10$ compared to $\frac{a}{b} = 5$, causes the far-field pattern of an ellipse to exhibit narrower major lobes in Figure 6-16 versus Figure 6-15. The change in magnitude and phase appears at the ends where the major axis intersects the ellipse, due to the greater spiking effect.

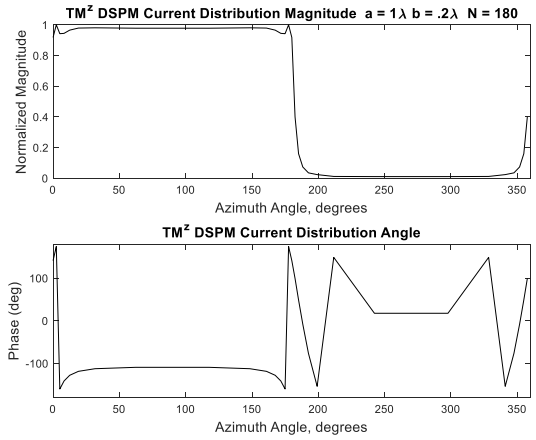

a)

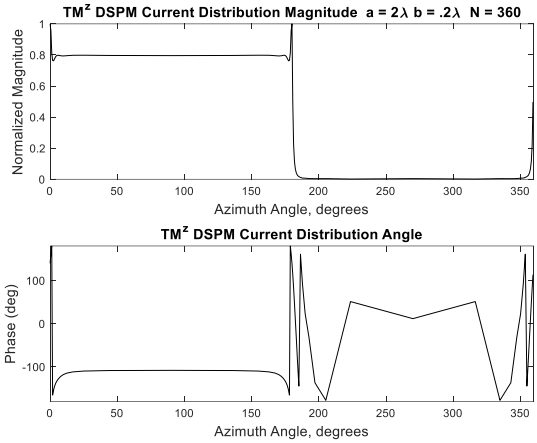

b)

Figure 6-21: a) Linear plot of surface current on an infinitely long elliptical cylinder using DSPM $\frac{a}{b} = 5$. b) Linear plot of surface current on an infinitely long elliptical cylinder using DSPM $\frac{a}{b} = 10$.

Results for TE^z incident waves incident on cylinders of axial ratios of $\frac{a}{b} = 5$ and $\frac{a}{b} = 10$ are calculated and plotted in Figure 6-24 and Figure 6-25. These results for incident magnetic field waves are similar to the waveform patterns of TM^z waves. Note the current flow for the TE^z excitation is azimuthal around the contour of the cylinder, as shown in Figure 6-22 and Figure 6-23.

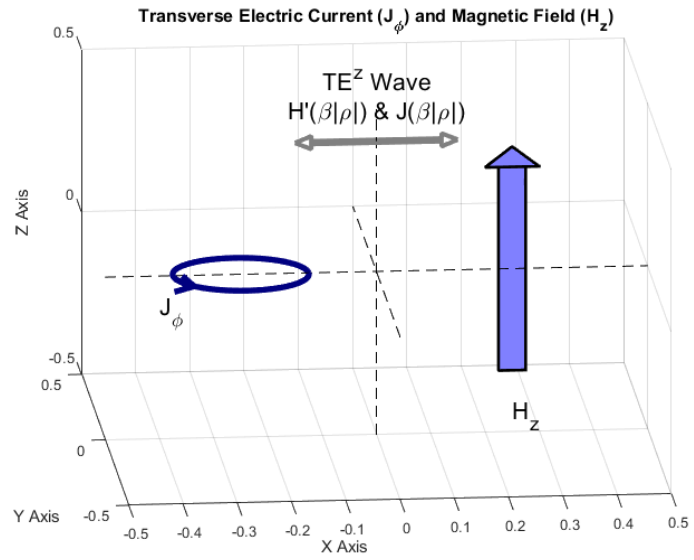

Figure 6-22: Illustration of the azimuthal direction of current around the contour of the cylinder versus magnetic field for a TE^z incident wave vertical view.

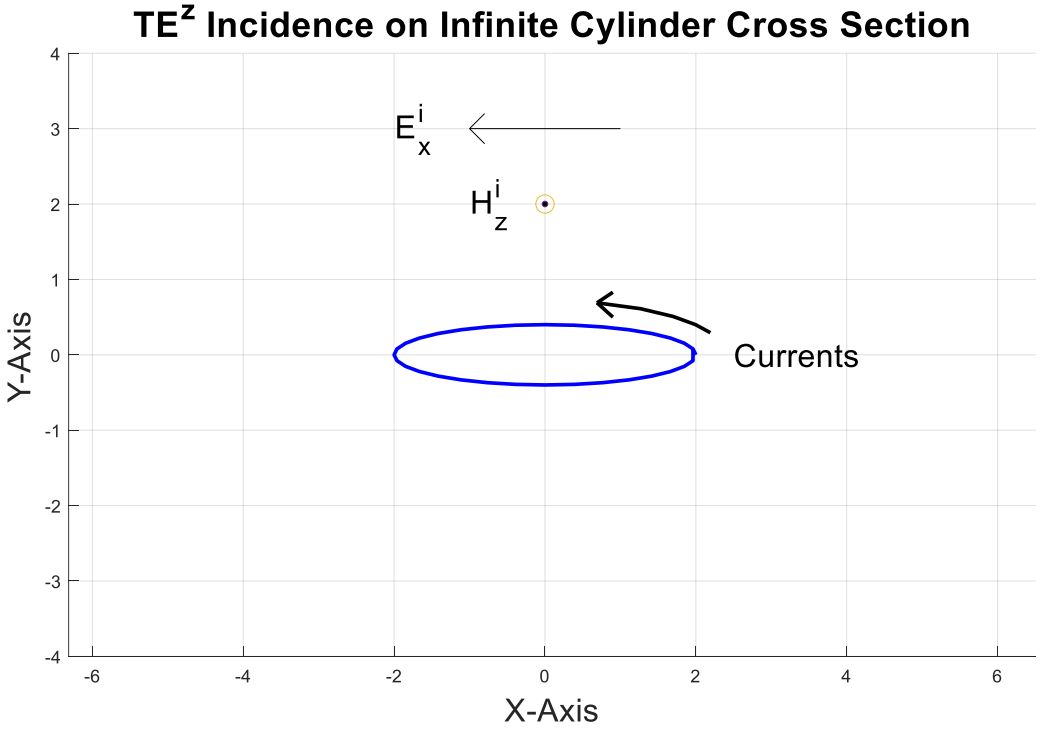

Figure 6-23: Illustration of the azimuthal direction of current around the contour of the cylinder versus magnetic field for a TE^z incident wave cross sectional view.

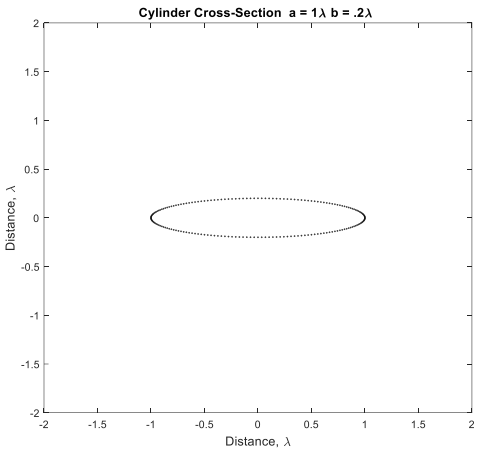

a)

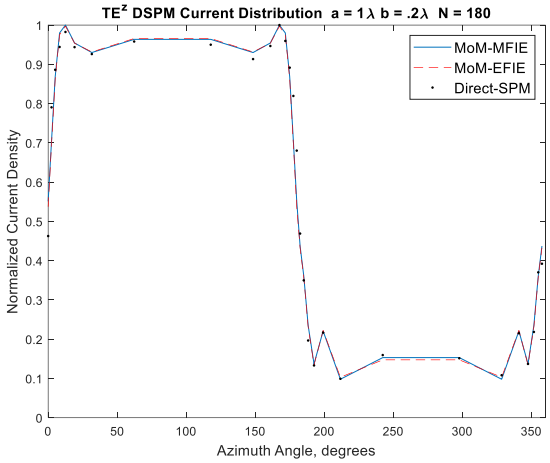

b)

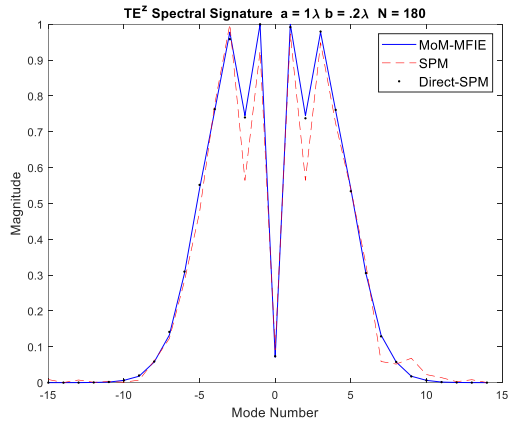

c)

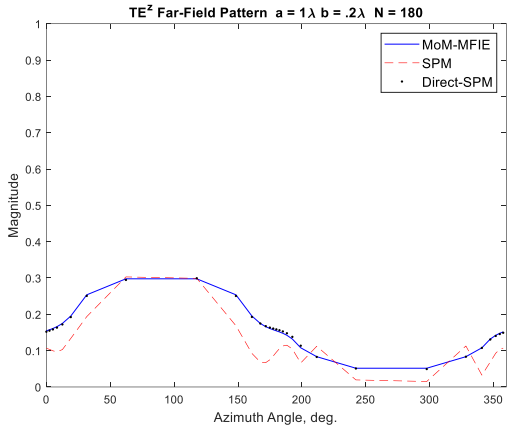

d)

Figure 6-24: a) Infinitely long elliptical cylinder of axial ratio $\frac{a}{b} = 5$. b) Plot of surface current around an infinitely long elliptical cylinder using DSPM, SPM and MOM for TE^Z wave. c) Spectral plot of modes using DSPM, SPM, and MOM d) Far-field pattern using DSPM, SPM and MOM.

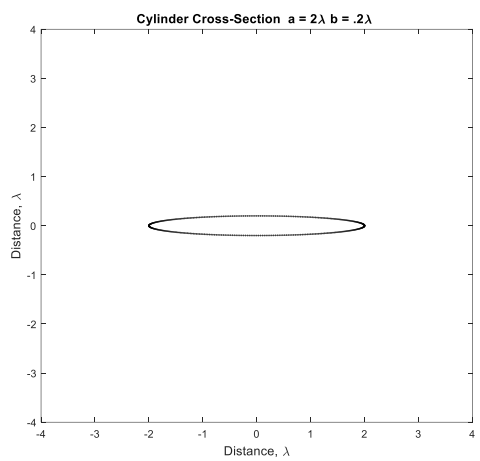

a)

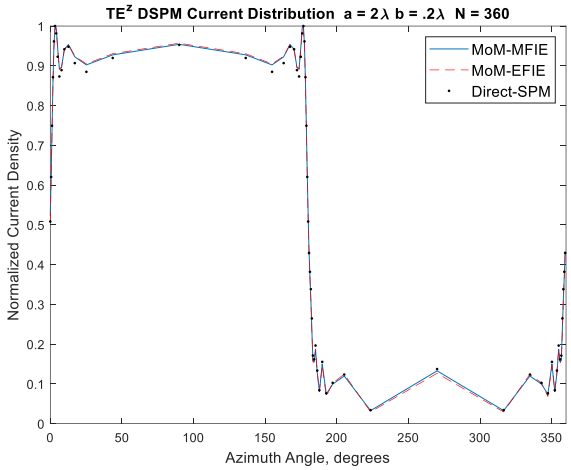

b)

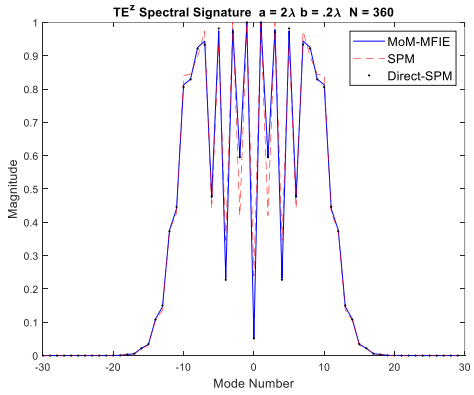

c)

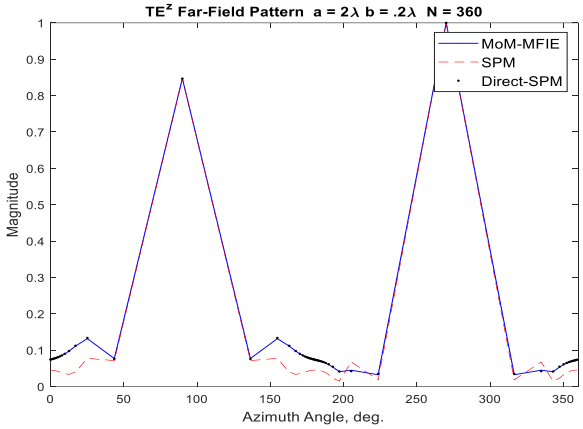

d)

Figure 6-25: a) Infinitely long elliptical cylinder of axial ratio $\frac{a}{b} = 10$. b) Plot of surface current around an infinitely long elliptical cylinder using DSPM, SPM and MOM for TE^Z wave. c) Spectral plot of modes using DSPM, SPM, and MOM d) Far-field pattern using DSPM, SPM and MOM.

The spectral signature bandwidth for TE^z excitation resembles that of the ellipses for TM^z excitation. The side of the ellipse subject to the transverse electric field radiation experiences the greatest current flow, and but for this TE^z case it emits a front and back electric field radiation lobe. Calculation of the current distribution and phase in Figures 6-21 and 6-26 show the difference in current patterns for TM^z and TE^z excitation. The spikes in the current for TE^z incidence mimic those of the elliptical cylinders excited by TM^z waves. However, the magnitude

and phase of the current are significantly different. Recall that the current flow for TE^z waves is azimuthal around the contour, not along the axis of the cylinder. Also, the phase of the current for the TE^z incidence on the radiated side is positive, but for the TM^z incidence it is mostly negative.

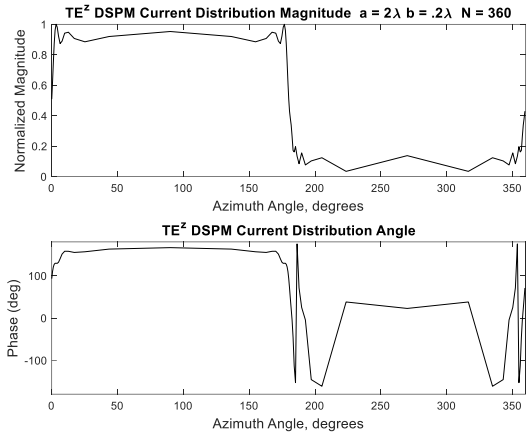

Figure 6-26: Linear plot of surface current and phase on an infinitely long elliptical cylinder using DSPM for TE^z incidence and axial ratio $\frac{a}{b} = 10$.

6.8 Excitation of Elliptical Cylinders using DSPM Model by Plane Wave Excitation

In this section excitation of elliptical cylinders of different major and minor axes and axial ratios are calculated excited by TM^z plane waves to examine the modal spectrum of these geometries using DSPM.

Eight plots are calculated in Figure 6-27 and Figure 6-28. Increasing the size of the major axis from $a = 1\lambda$ to $a = 2\lambda$ and $a = 4\lambda$ while keeping the minor axis at $b = .2\lambda$ increases the bandwidth of the spectral signature. Comparing the plots of ellipses with $a = 2\lambda$ and $b = .2\lambda$ with $a = 2\lambda$ and $b = .4\lambda$, increasing the size of the minor axis does not increase the bandwidth of the spectral signature.

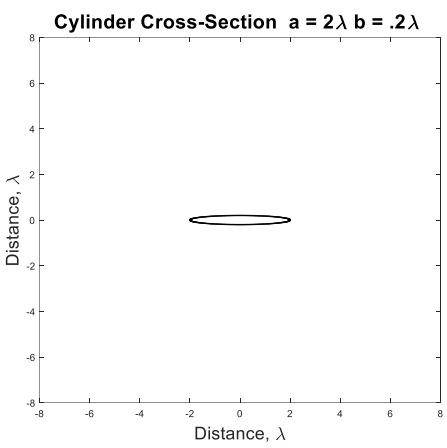

a)

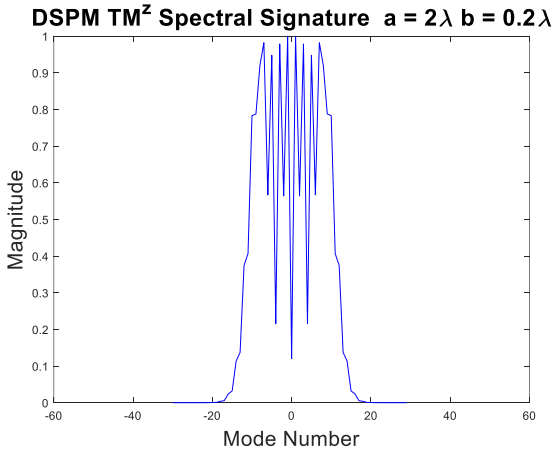

b)

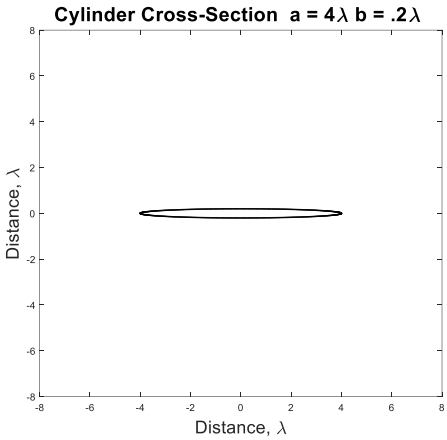

c)

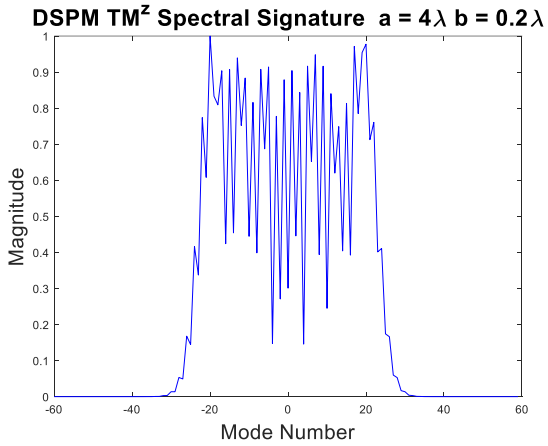

d)

Figure 6-27: Plots of modal spectrum for elliptical cylinders $\frac{a}{b} = 10$ and $\frac{a}{b} = 20$ under TM^z plane wave excitation. a, c) Illustrations of ellipses and b, d) corresponding **J**-spectral signatures.

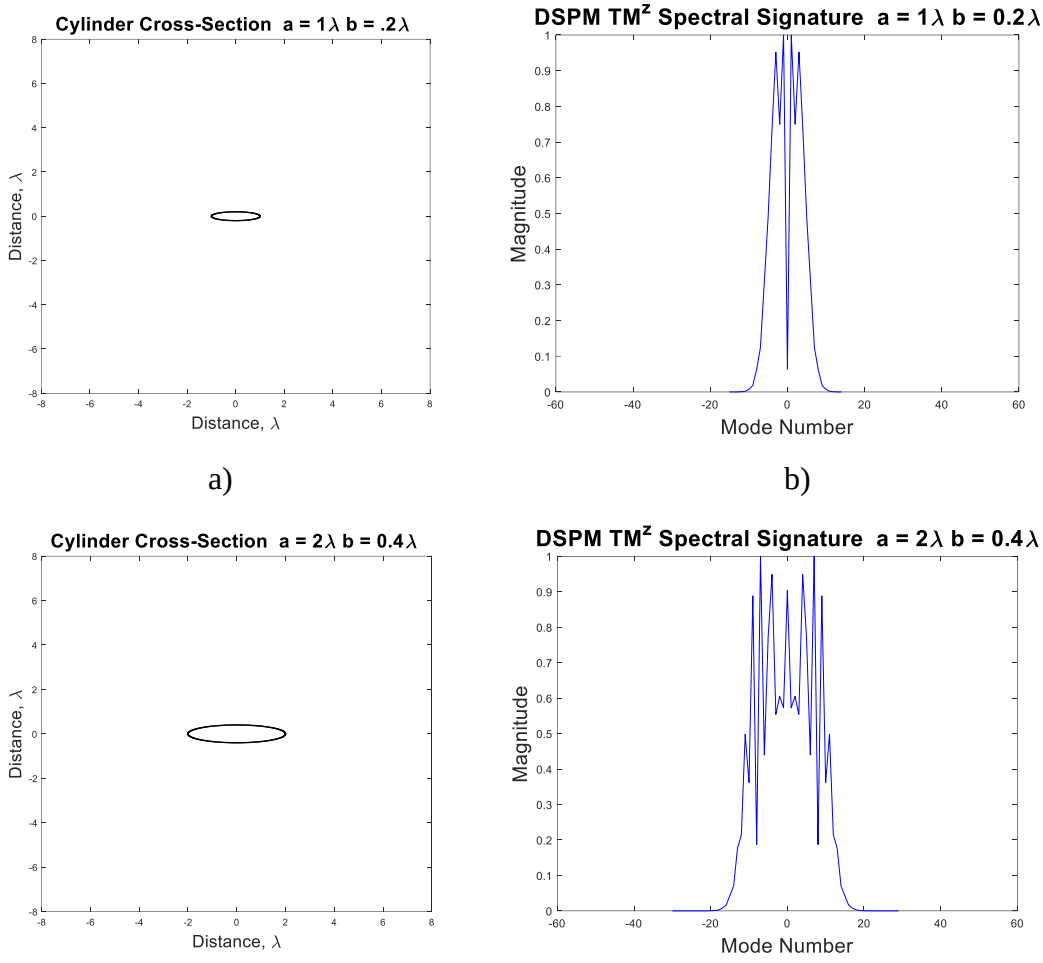

Figure 6-28: Plots of modal spectrum for elliptical cylinders $\frac{a}{b} = 5$ under TM^z plane wave excitation. a, c) Illustrations of ellipses and b, d) corresponding **J**-spectral signatures.

6.9 Excitation of Elliptical Cylinders using DSPM Model for Different Incidence Angles

Excitation of an elliptical cylinder with axial ratio of $\frac{a}{b} = 5$ by a TM^z wave at an angle of $\phi_0 = 45^o$ significantly changes its current distribution from normal incidence, eliminating the spike in the far-end of the cylinder, and increasing the spike at the end closest to the impingent wavefront. This redistribution of current causes the two major sidelobes to radiate almost equally in a direction 45^o to the major axis away from the wavefront. This effect is shown in Figure 6-29. The opposite effect results if the ellipse is radiated by a TM^z wave at $\phi_0 = 135^o$, as shown

in Figure 6-30. Incidence from an angle of $\phi_0 = 0^o$ in Figure 6-31 yields a more directional pattern away from the incident wave.

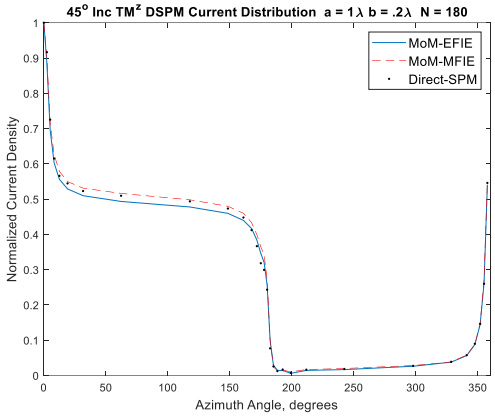

a)

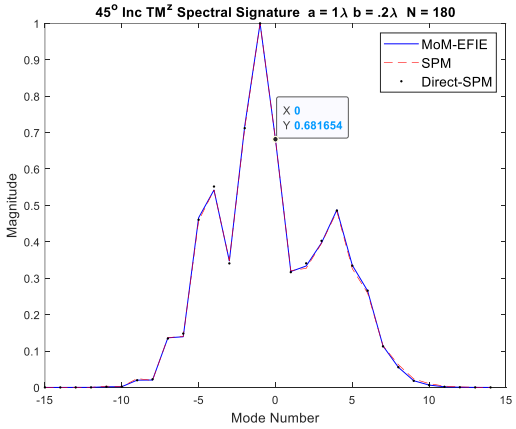

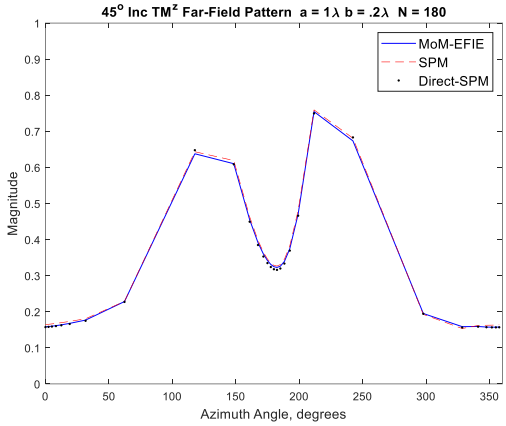

b) c)

Figure 6-29: Infinitely long elliptical cylinder TM^z wave angle of incidence 45^o. a) Current distribution. b) **J**-spectral signature modal distribution. c) Far-field pattern linear plot.

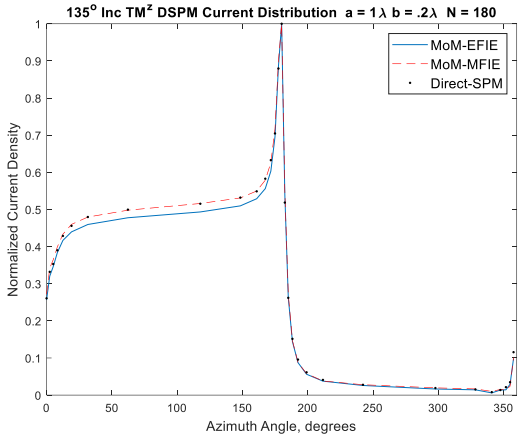

a)

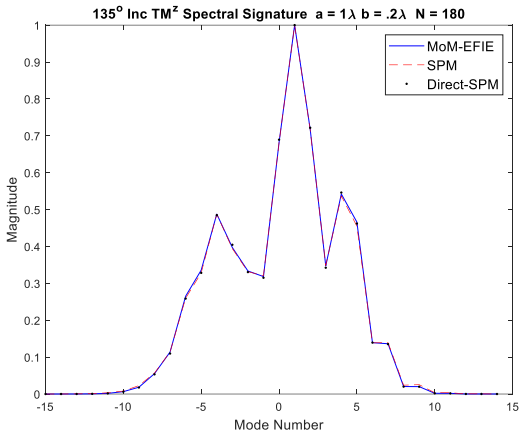

b)

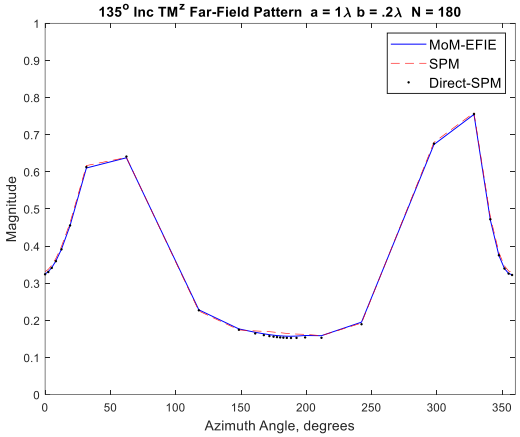

c)

Figure 6-30: Infinitely long elliptical cylinder TM^z wave angle of incidence 135°. a) Current distribution. b) **J**-spectral signature modal distribution. c) Far-field pattern linear plot.

Besides circular and elliptical cylinders, applying the two-vector model to DSPM also allows one to calculate the scattering pattern of arbitrarily shaped PEC cylinders subjected to any incident electric or magnetic field. Some of these results are discussed next.

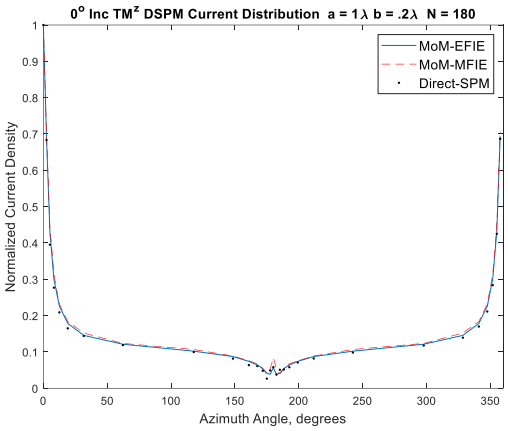

a)

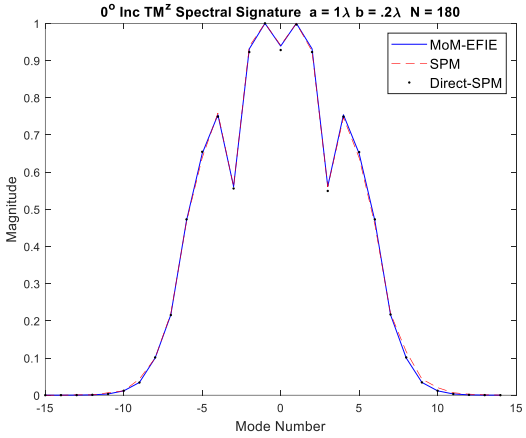

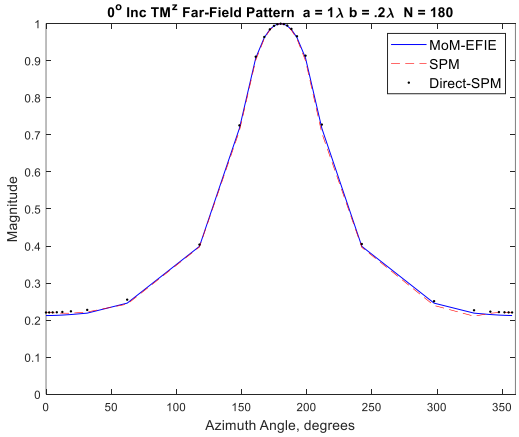

b) c)

Figure 6-31: Infinitely long elliptical cylinder TM^z wave angle of incidence 0^o. a) Current distribution. b) **J**-spectral signature modal distribution. c) Far-field pattern linear plot.

6.10 Validation of the DSPM Model for Arbitrary Shaped Cylinders

An infinitely long 2D cylinder with random corrugations, its current distribution, and its spectral and far-field patterns are illustrated in Figure 6-32 and Figure 6-33. As shown in the results for TM^z wave excitation, the current distribution, **J**-spectral signature, and far-field pattern are in good agreement. For a greater number of corrugations, the spectral signature necessarily grows broader in order to model the abrupt changes in the current distribution with angle.

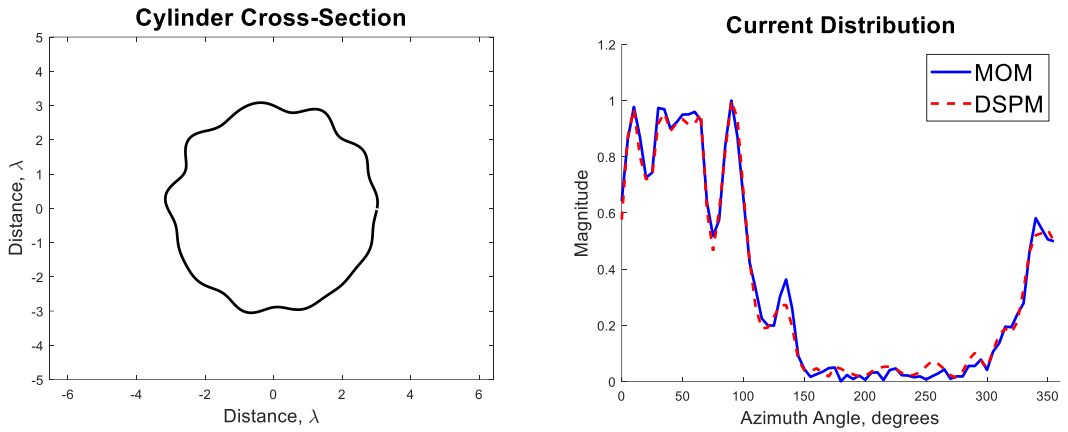

a) b)

Figure 6-32: a) Infinitely long cylinder of arbitrary shape type A. b) Plot of surface current around an infinitely long arbitrarily shaped cylinder using DSPM and MOM for TM^Z wave excitation.

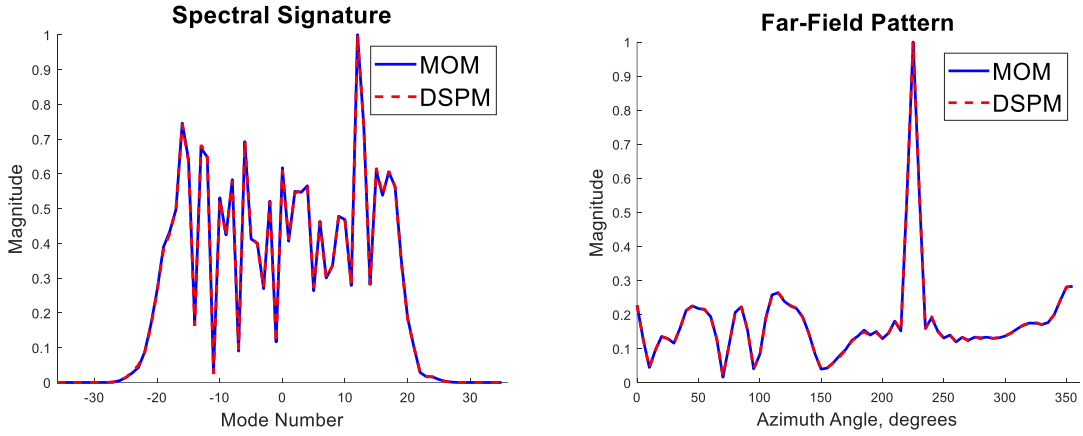

a) b)

Figure 6-33: a) For an infinitely long cylinder of arbitrary shape of A under TM^z excitation, **J**-spectral plot of modes using DSPM and MOM. b) Far-field pattern using DSPM and MOM.

Numerous other shapes have been analyzed with DSPM and have shown good agreement with the Method of Moments. The other shapes and their results are shown in Figures 6-34 to Figure 6-41.

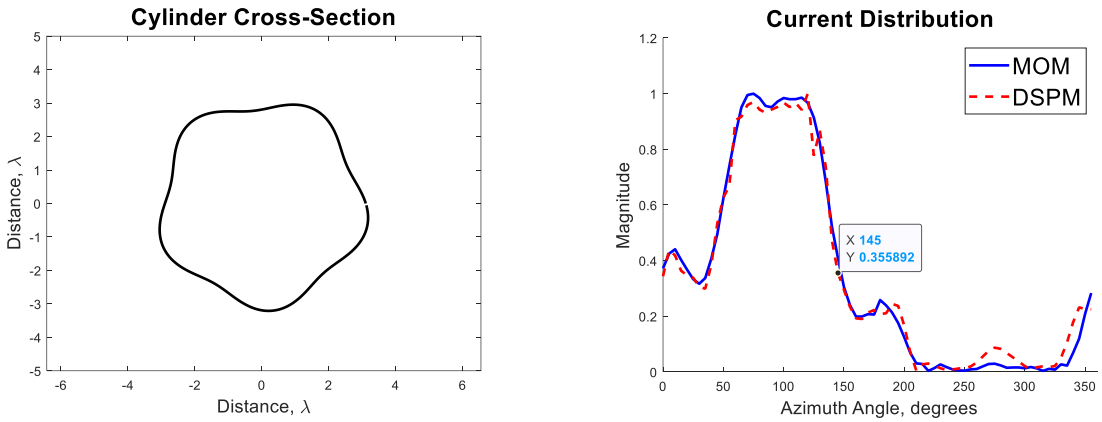

a) b)

Figure 6-34: a) Infinitely long cylinder of arbitrary shape type B. b) Plot of surface current around infinitely long arbitrarily shaped cylinder B using DSPM and MOM for TM^Z wave excitation.

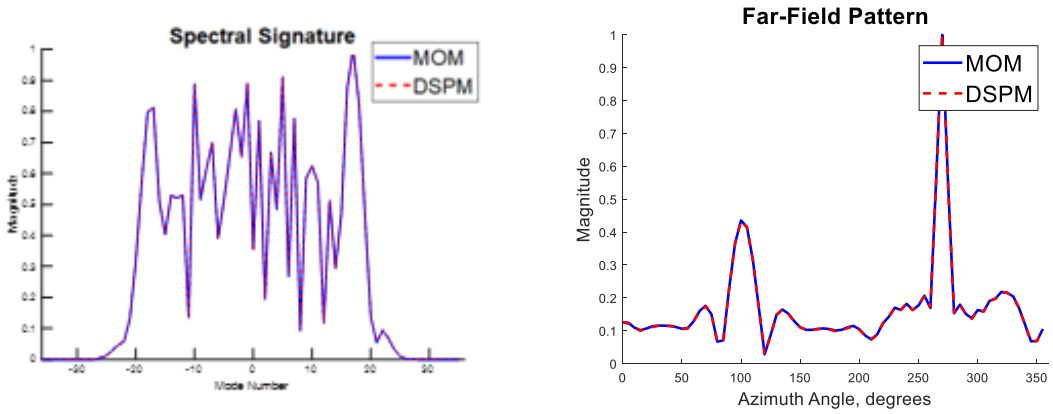

a) b)

Figure 6-35: a) For an infinitely long cylinder of arbitrary shape type B under TM^z excitation, **J**-spectral plot of modes using DSPM and MOM. b) Far-field pattern using DSPM and MOM.

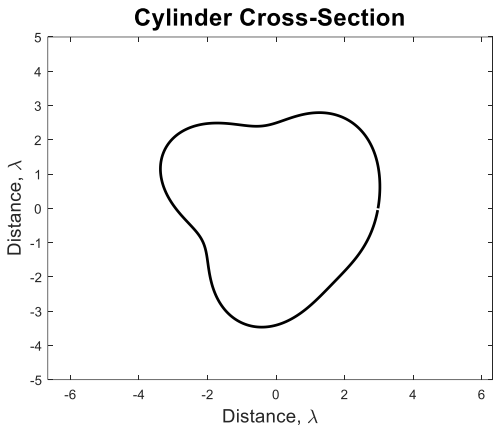

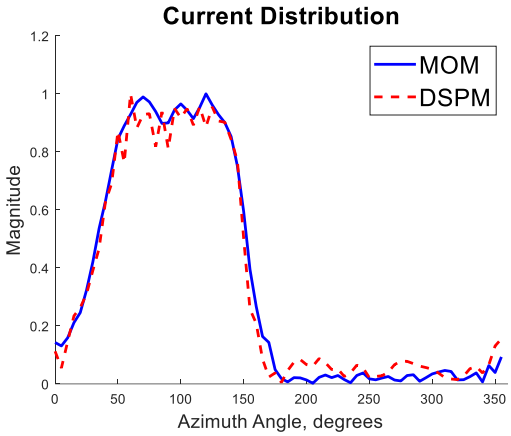

a) b)

Figure 6-36: a) Infinitely long cylinder of arbitrary shape type C. b) Plot of surface current around infinitely long arbitrarily shaped cylinder C using DSPM and MOM for TM^Z wave excitation.

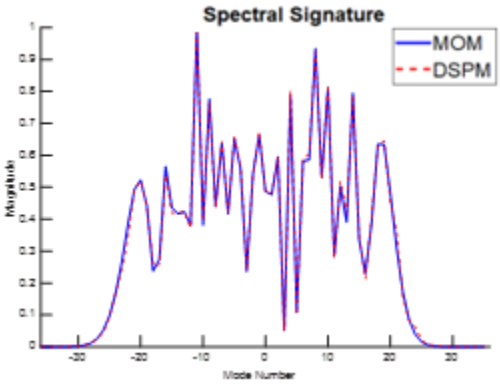

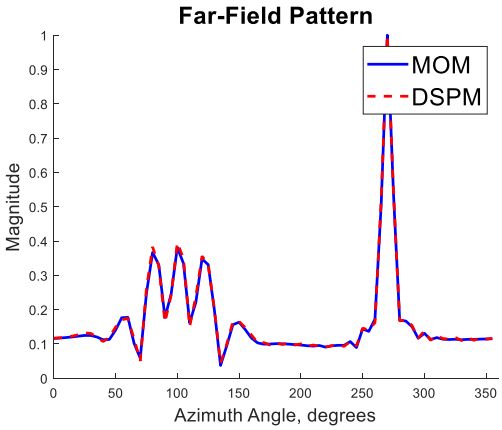

a) b)

Figure 6-37: a) For an infinitely long cylinder of arbitrary shape type C under TM^z excitation, **J**-spectral plot of modes using DSPM, and MOM. b) Far-field pattern using DSPM and MOM.

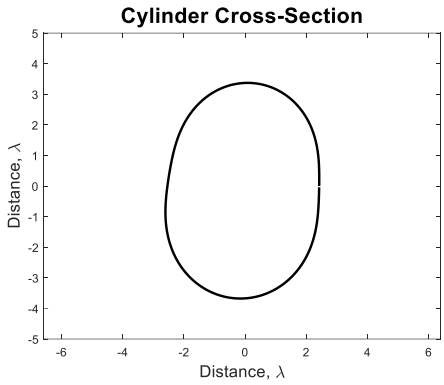

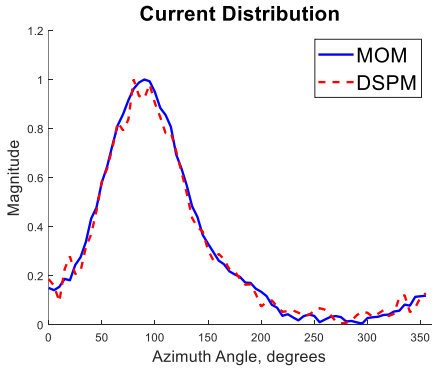

a) b)

Figure 6-38: a) Infinitely long cylinder of arbitrary shape type D. b) Plot of surface current around infinitely long arbitrarily shaped cylinder D using DSPM and MOM for TM^{Z} wave excitation.

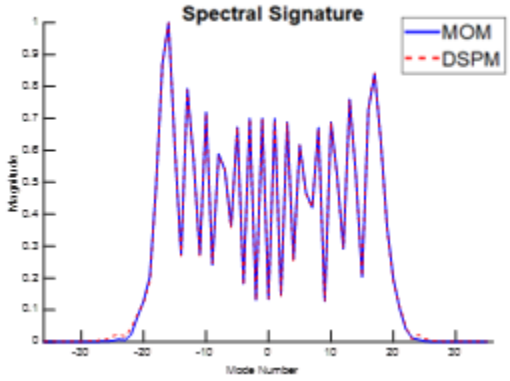

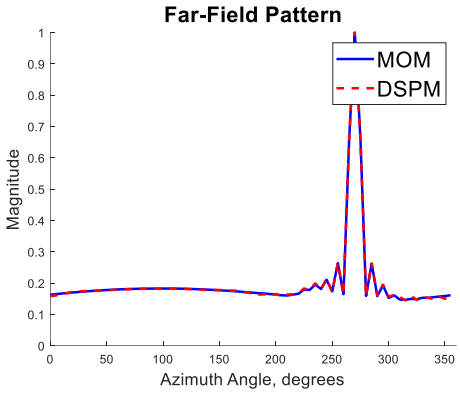

a) b)

Figure 6-39: a) For an infinitely long cylinder of arbitrary shape type D under TM^{z} excitation, **J**-spectral plot of modes using DSPM, and MOM. b) Far-field pattern using DSPM and MOM.

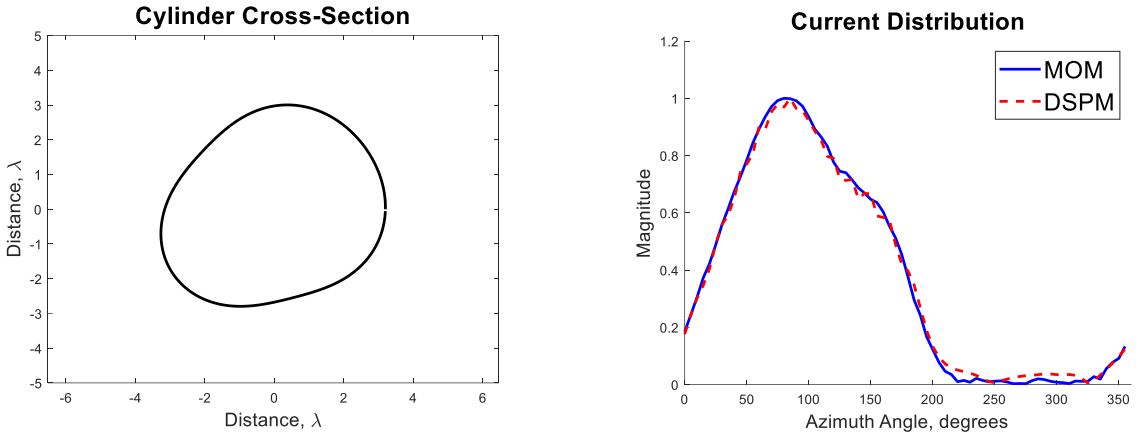

a) b)

Figure 6-40: a) Infinitely long cylinder of arbitrary shape type E. b) Plot of surface current around infinitely long arbitrarily shaped cylinder E using DSPM and MOM for TM^{Z} wave excitation.

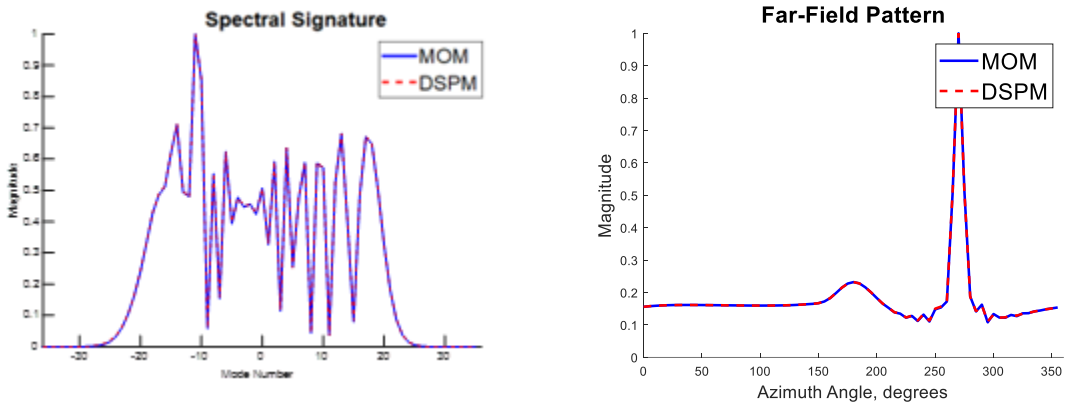

a) b)

Figure 6-41: a) For an infinitely long cylinder of arbitrary shape type E under TM^{z} excitation, **J**-spectral plot of modes using DSPM, and MOM. b) Far-field pattern using DSPM and MOM.

Application of DSPM for arbitrarily shaped cylinders is limited by the depth of the corrugations in their cross section. For deep corrugations in the cross section, the current density deviates from the MOM solution significantly without translation. Therefore, in these analyses

the corrugations were kept small compared to the radius of the cylinder. This was necessary in order to achieve convergence of the addition theorem and stable inversion of the matrix.

6.11 Validation of the DSPM Model for Large Circular and Elliptical Cylinders

In this section large wavelength infinitely long circular structures and elliptical structures with an axial ratio of 5:1 have been analyzed. Infinitely long 2D circular cylinder with radius = 40λ is illustrated in Figure 6-42 to Figure 6-45. As shown in the results for TM^z wave excitation, the current distribution and far-field pattern for DSPM and modal analysis agree for this circular cylinder of radius $a = 40\lambda$.

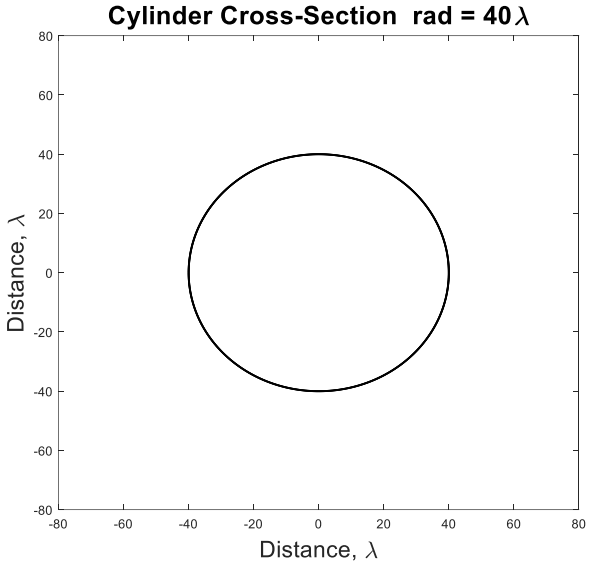

Figure 6-42: Infinitely long circular cylinder of radius = 40λ.

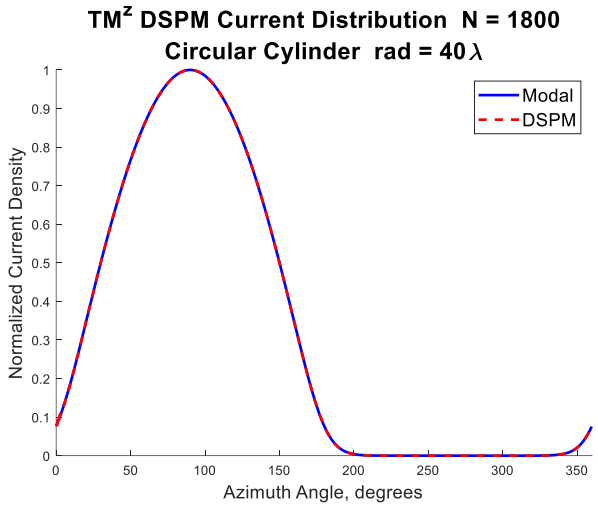

b)

Figure 6-43: Plot of surface current around an infinitely long circular cylinder with radius = 40λ using modal analysis and DSPM under TM^Z wave excitation.

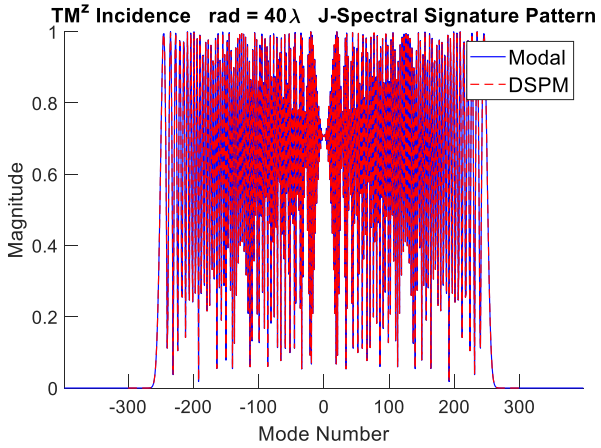

Figure 6-44: **J**-spectral signature plot of an infinitely long circular cylinder with radius = 40λ using modal analysis and DSPM under TM^Z wave excitation.

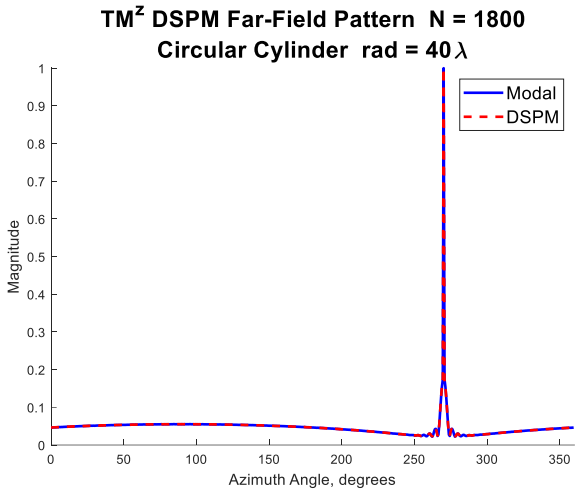

Figure 6-45: Far-field pattern of an infinitely long circular cylinder with radius = 40λ using modal analysis and DSPM under TM^Z wave excitation.

For TM^z wave excitation, the current distribution and far-field pattern for DSPM and modal analysis are in good agreement for circular cylinder of radius $a = 100\lambda$ in Figure 6-46 to Figure 6-49.

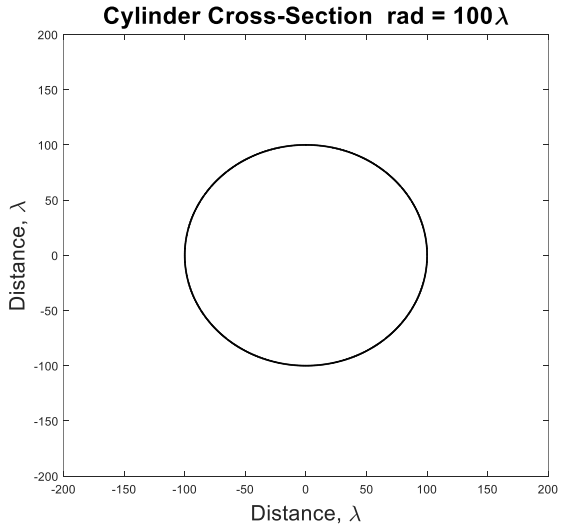

Figure 6-46: a) Infinitely long circular cylinder radius = 100λ.

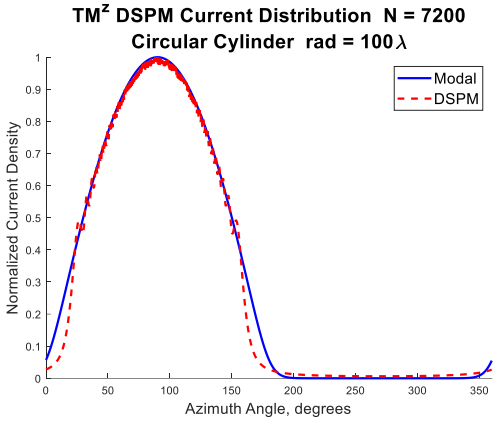

Figure 6-47: Plot of surface current around an infinitely long circular cylinder with radius = 100λ using modal analysis and DSPM under TM^Z wave excitation.

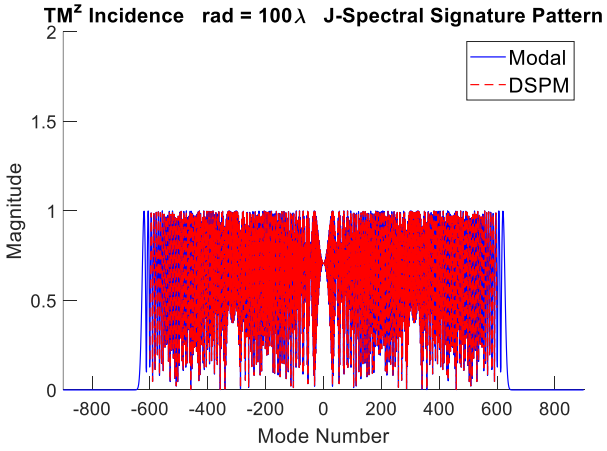

Figure 6-48: **J**-spectral signature plot of an infinitely long circular cylinder with radius = 100λ using modal analysis and DSPM for TM^Z wave excitation.

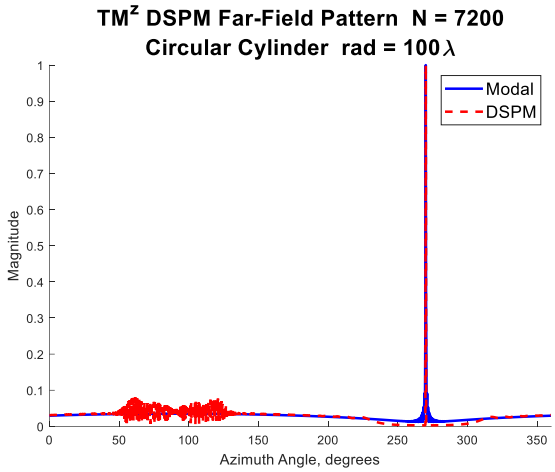

Figure 6-49: Far-field pattern an infinitely long circular cylinder with radius = 100λ using modal analysis and DSPM for TM^Z wave excitation.

For TM^z wave excitation, the current distribution, **J**-spectral signature, and far-field pattern agree for an elliptical cylinder with major axis $a = 20\lambda$ and minor axis $b = 4\lambda$, and axial ratio $\frac{a}{b} = 5$. Plots are shown in Figure 6-50 to Figure 6-53.

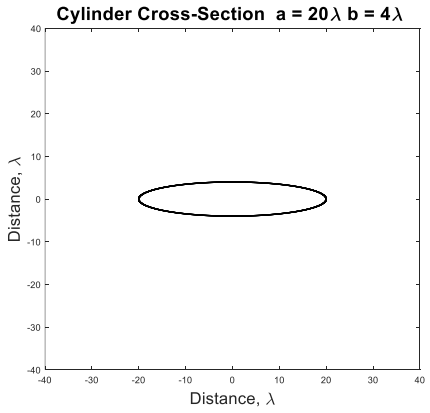

Figure 6-50: Infinitely long elliptical cylinder with axial ratio $\frac{a}{b} = 5$ and $a = 20\lambda$.

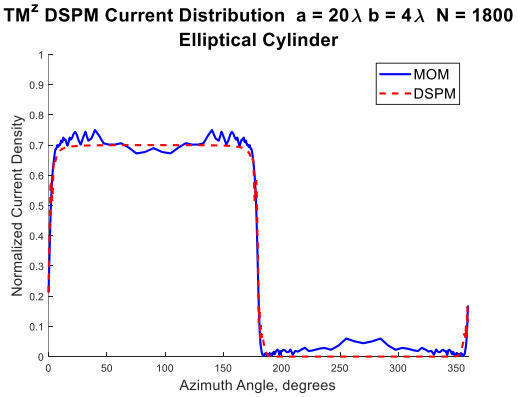

Figure 6-51: Plot of surface current around an infinitely long elliptical cylinder with ratio $\frac{a}{b} = 5$ and $a = 20\lambda$ using MOM and DSPM under TM^Z wave excitation.

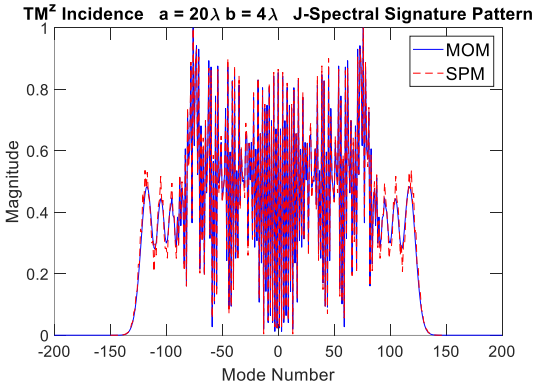

Figure 6-52: Plot of **J**-spectral signature of an infinitely long elliptical cylinder with ratio $\frac{a}{b} = 5$ and $a = 20\lambda$ using MOM and DSPM under TM^Z wave excitation.

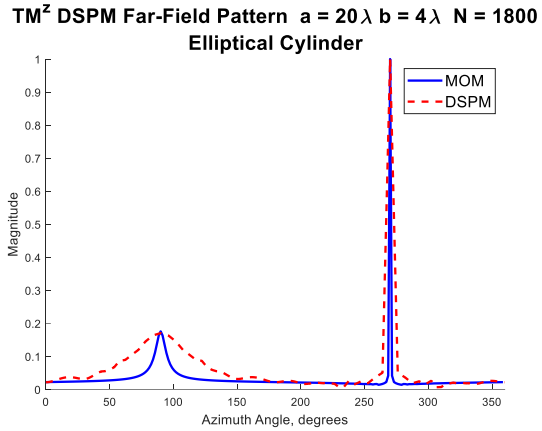

Figure 6-53: Plot of far field pattern for an infinitely long elliptical cylinder with ratio $\frac{a}{b} = 5$ and $a = 20\lambda$ using MOM and DSPM under TM^Z wave excitation.

For TM^z wave excitation, the current distribution, **J**-spectral signature, and far-field pattern for an elliptical cylinder with major axis $a = 40\lambda$ and minor axis $b = 8\lambda$, and axial ratio $\frac{a}{b} = 5$, are shown in Figure 6-54 to Figure 6-57.

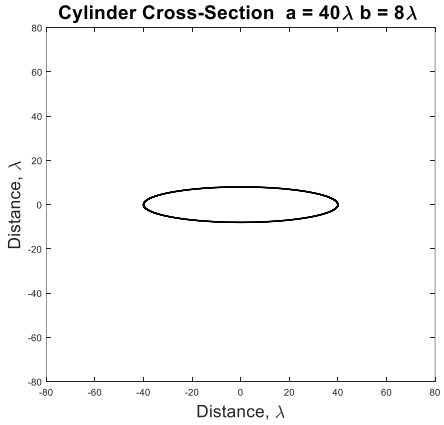

Figure 6-54: Infinitely long elliptical cylinder with axial ratio $\frac{a}{b} = 5$ and $a = 40\lambda$.

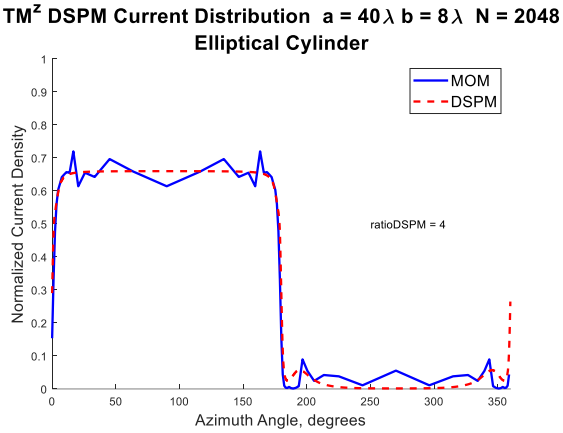

Figure 6-55: Plot of surface current around an infinitely long elliptical cylinder with ratio $\frac{a}{b} = 5$ and $a = 40\lambda$ using MOM and DSPM under TM^Z wave excitation.

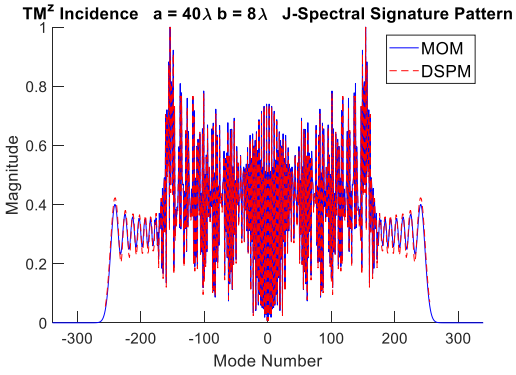

Figure 6-56: Plot of **J**-spectral signature of an infinitely long under cylinder with ratio $\frac{a}{b} = 5$ and $a = 40\lambda$ using MOM and DSPM under TM^Z wave excitation.

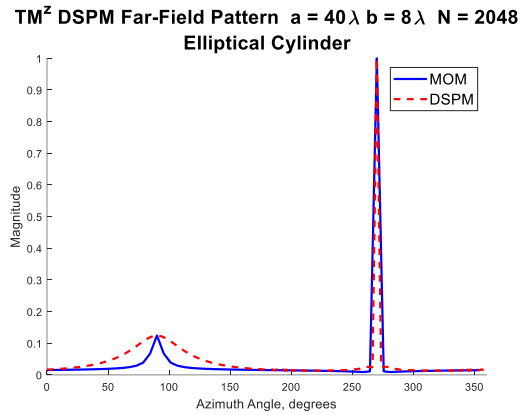

Figure 6-57: Plot of far-field pattern for an infinitely long elliptical cylinder with ratio $\frac{a}{b} = 5$ and $a = 40\lambda$ using MOM and DSPM under TM^Z wave excitation.

In Figure 6-58 to Figure 6-61, the current distribution, **J**-spectral signature, and far-field pattern agree for elliptical cylinder under TM^z wave excitation with major axis $a = 90\lambda$ and minor axis $b = 18\lambda$, i.e. axial ratio $\frac{a}{b} = 5$, are given.

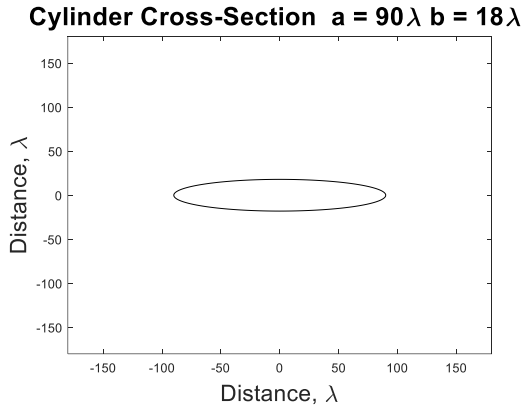

Figure 6-58: Infinitely long elliptical cylinder with axial ratio $\frac{a}{b} = 5$ and $a = 90\lambda$.

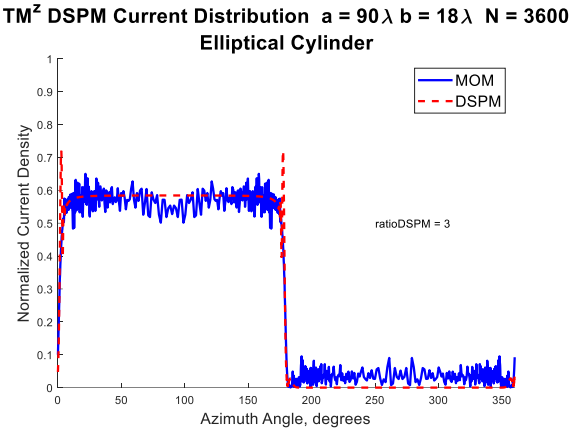

Figure 6-59: Plot of surface current around an infinitely long elliptical cylinder with ratio $\frac{a}{b} = 5$ and $a = 90\lambda$ using MOM and DSPM under TM^Z wave excitation.

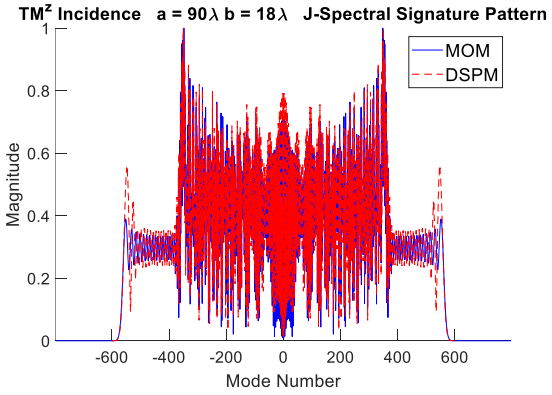

Figure 6-60: Plot of **J**-spectral signature of an infinitely long elliptical cylinder with ratio $\frac{a}{b} = 5$ and $a = 90\lambda$ using MOM and DSPM under TM^Z wave excitation.

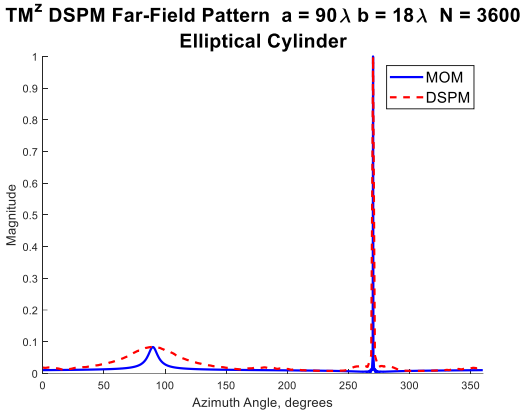

Figure 6-61: Plot of far-field pattern for an infinitely long elliptical cylinder with ratio $\frac{a}{b} = 5$ and $a = 90\lambda$ using MOM and DSPM under TM^Z wave excitation.

Application of DSPM for large cylinders is limited by the matrix size and the length of the cross section in wavelengths. The current density deviates from the MOM solution at the ends exhibiting a small spike, but the far field patterns are in better agreement except for the minor backscattering sidelobe. To achieve convergence of the addition theorem and stable inversion of the matrix, large modal limits and translation of the origin were necessary.

6.12 Validation of the DSPM Model for Rectangular Cylinders

Infinitely long square cylindrical structures with side lengths of 2λ and 4λ have been analyzed. These infinitely long 2D cylinders exhibited current distributions and far-field patterns similar to the Method of Moments as seen in Figure 6-62 through Figure 6-69. The DSPM failed to properly calculate the current spikes at the ends of the major axes. The right side DSPM plot of current distribution in Figure 6-63b has current end spikes closer to those calculated using MOM analysis, but at the expense of greater sidelobes. The results shown are for TM^z wave excitation using DSPM and MOM only.

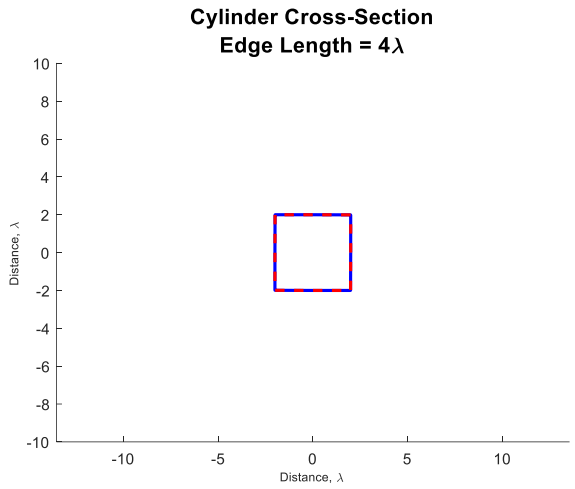

Figure 6-62: Infinitely long square cylinder with edge length $= 4\lambda$.

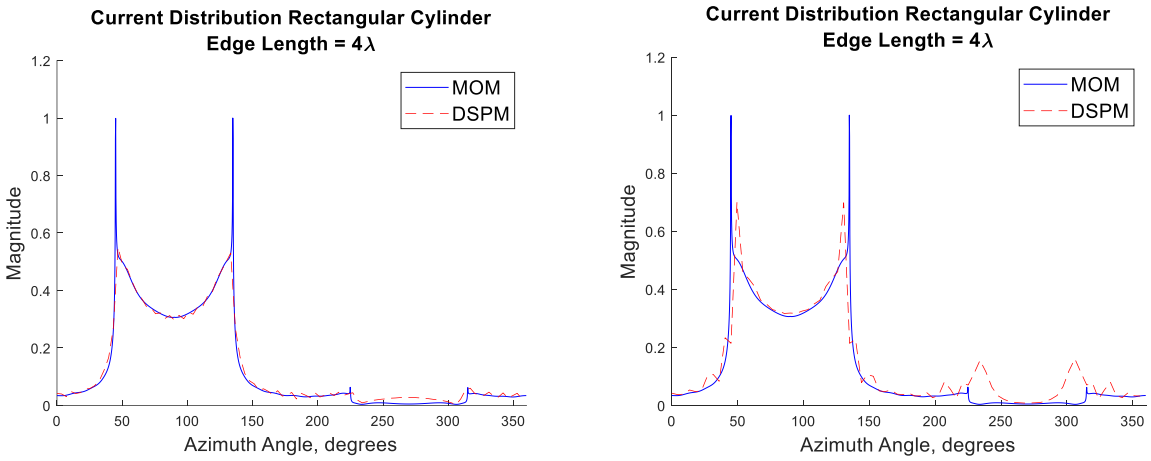

a) b)

Figure 6-63: Two plots of surface current around an infinitely long square cylinder with edge length $= 4\lambda$ using MOM and DSPM for TM^z wave excitation using different translations. a) Smaller translation. b) Larger translation.

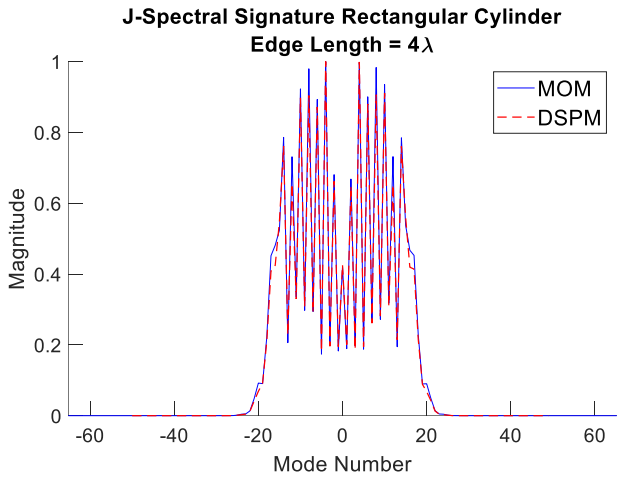

Figure 6-64: Plot of **J**-spectral signature of infinitely long square cylinder (63a) with edge length $= 4\lambda$ using MOM and DSPM under TM^Z wave excitation.

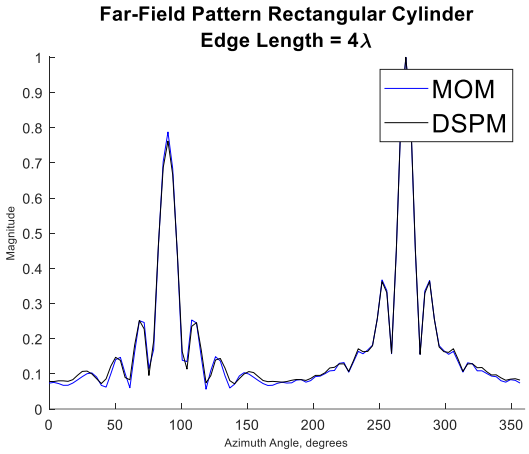

Figure 6-65: Plot of far field pattern for infinitely long square cylinder (63a) with edge length $= 4\lambda$ using MOM and DSPM under TM^Z wave excitation.

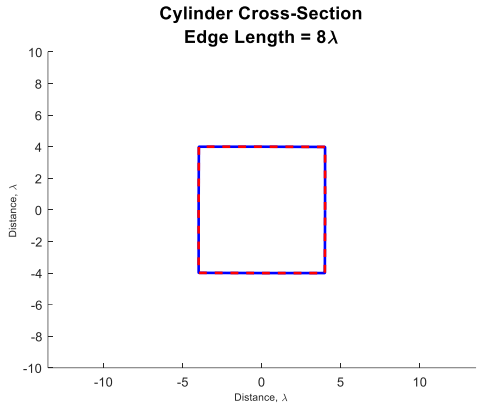

Figure 6-66: Infinitely long square cylinder with edge length $= 8\lambda$.

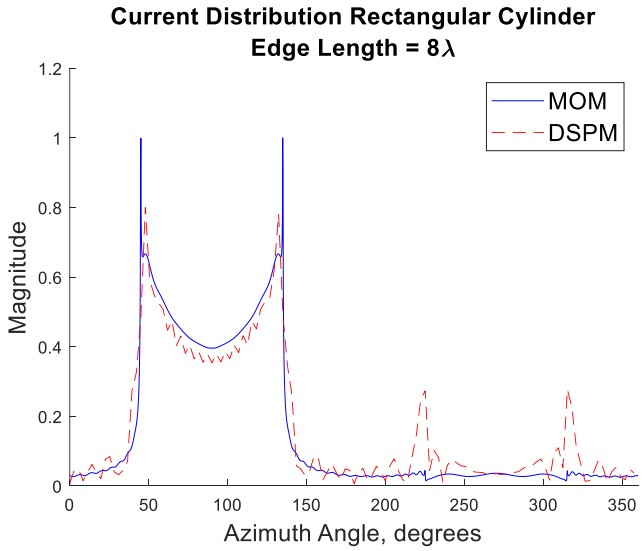

Figure 6-67: Plot of surface current around an infinitely long square cylinder with edge length $= 8\lambda$ using MOM and DSPM under TM^z wave excitation.

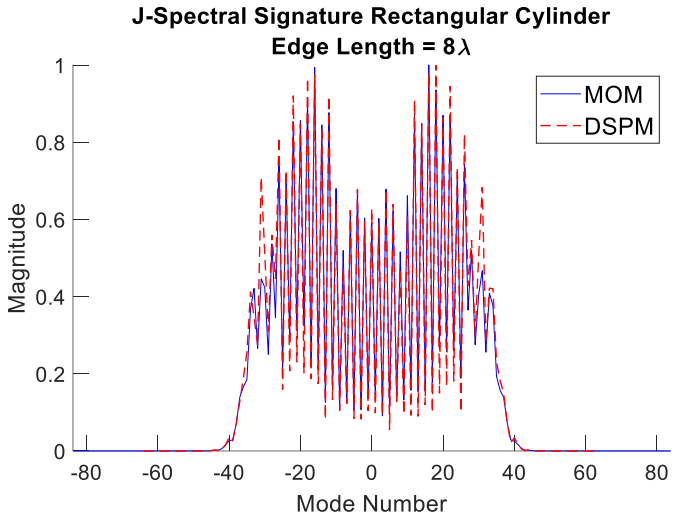

Figure 6-68: Plot of **J**-spectral signature of infinitely long square cylinder with edge length $= 8\lambda$ using MOM and DSPM under TM^z wave excitation.

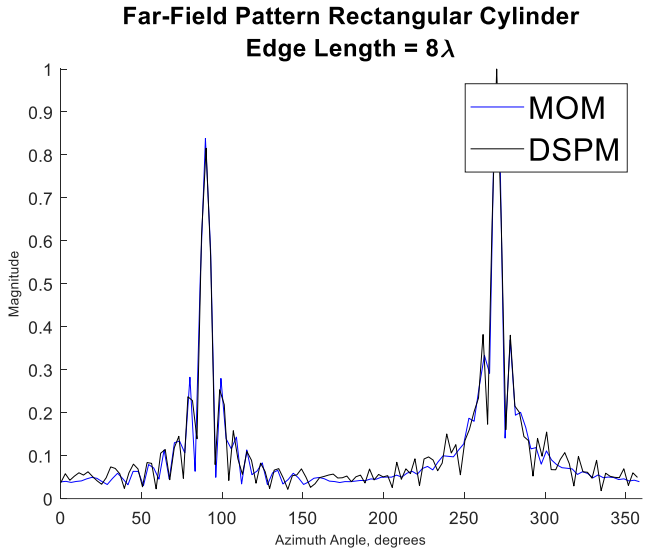

Figure 6-69: Plot of far field pattern for infinitely long square cylinder with edge length $= 8\lambda$ using MOM and DSPM under TM^z wave excitation.

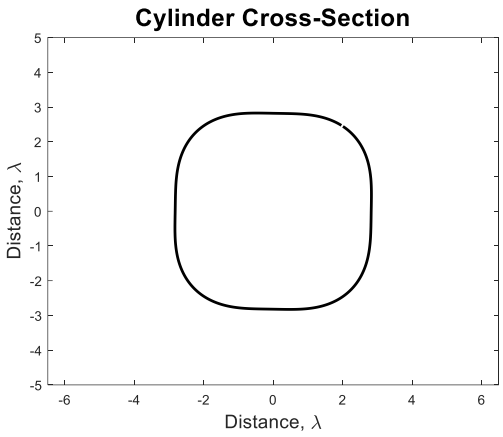

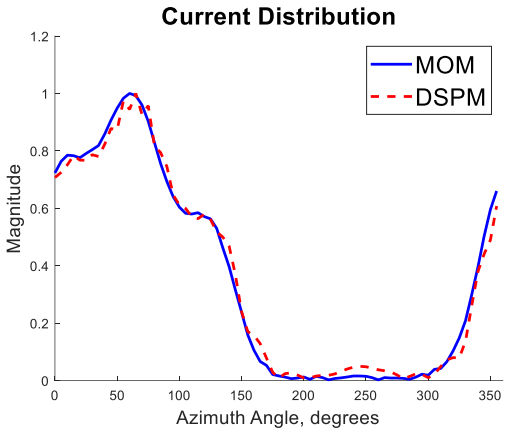

a) b)

Figure 6-70: a) Infinitely long semi-rectangular cylinder with rounded corners and edge length 4λ. b) Plot of surface current around an infinitely long semi-rectangular cylinder with rounded corners using DSPM and MOM under TM^z wave excitation.

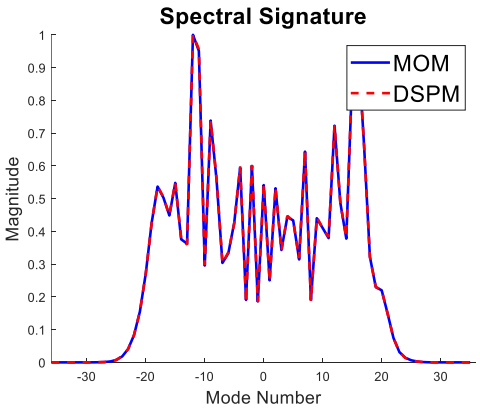

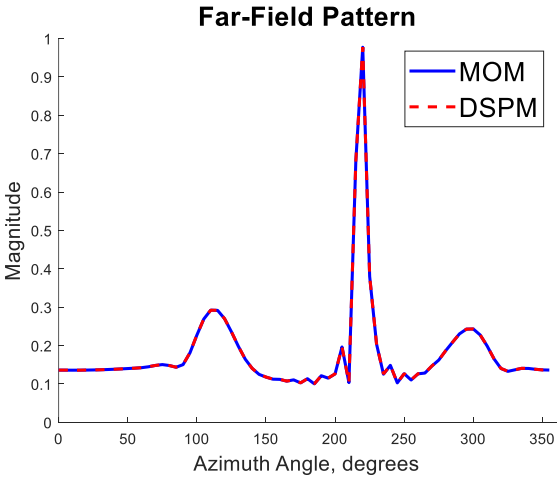

a) b)

Figure 6-71: a) For an infinitely long semi-rectangular cylinder with rounded corners, **J**-spectral plot of modes using DSPM, and MOM. b) Far-field pattern using DSPM and MOM.

6.13 Validation of the DSPM Model for Cardioid Shaped Cylinders

Infinitely long cardioid cylindrical structures with edge length of $.5\lambda$ and has been analyzed. This infinitely long 2D cylinder exhibited current distributions and far-field patterns similar to the Method of Moments as seen in Figure 6-72 to Figure 6-75.

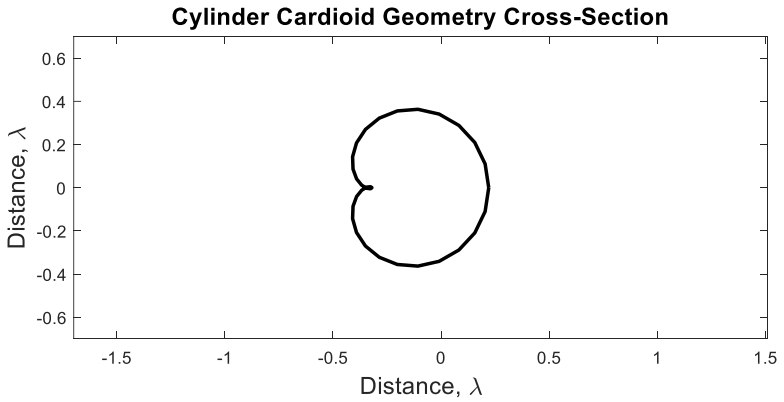

Figure 6-72: Infinitely long cardioid geometry cylinder.

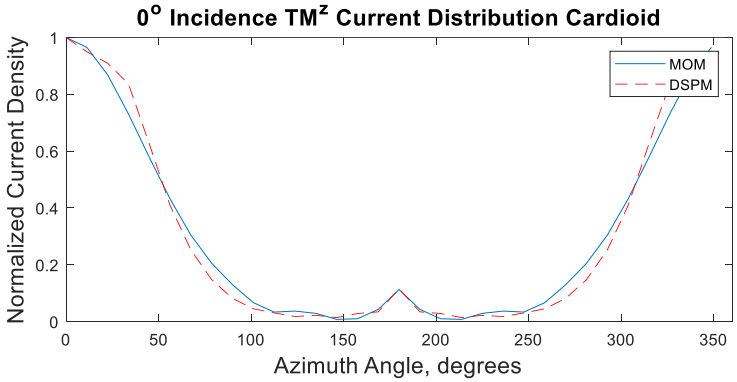

Figure 6-73: Plot of surface current around an infinitely long cardioid cylinder using MOM and DSPM for TM^Z wave excitation.

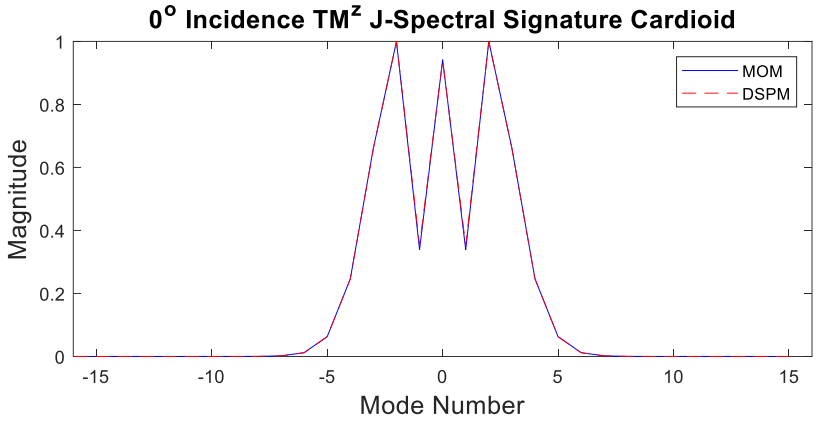

Figure 6-74: Plot of **J**-spectral signature of an infinitely long cardioid cylinder using MOM and DSPM for TM^Z wave excitation.

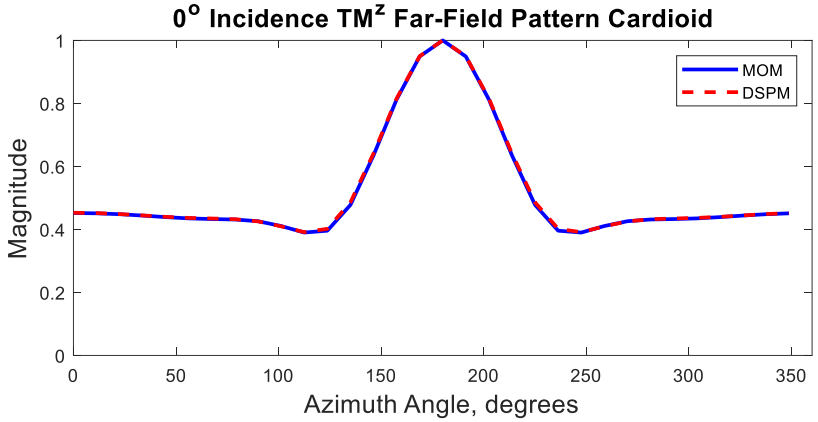

Figure 6-75: Plot of far field pattern for an infinitely long cardioid cylinder using MOM and DSPM for TM^Z wave excitation.

Application of DSPM for cardioid cylinders is limited by the indentation and the length of the cross section in wavelengths. To achieve convergence of the addition theorem and stable inversion of the matrix, translation of the origin was necessary again.

6.14 Comparison Matrix Inversion Speed for DSPM Model vs. Method of Moments

Data comparing the speed of populating and inverting matrices using the Method of Moments and DSPM are shown in Table 6-1. Ellipses of axial ratio $\frac{a}{b} = 4$ were analyzed. The results are given for TM^z wave excitation, and an equal number of source/observation points.

The sampling ratio (SR) helped stabilize the matrices used in DSPM. The results of DSPM compared faster against MOM for both population of the matrices and inversion.

Table 6-1: Timing Analysis of DSPM vs. MOM for Populating and Inverting Matrices

Major Axis Length	MOM POP Timing	DSPM POP Timing	MOM INV Timing	DSPM INV Timing	Inversion Time Ratio
20	3.1643	1.3286	0.4744	0.0189	25.0558
32	8.7049	3.9152	1.6910	0.0562	30.0653
40	13.6255	6.4856	3.1556	0.1047	30.1479
48	21.8877	11.4291	6.1098	0.2008	30.4235
60	39.249	16.3238	9.660	.2755	35.064
72	53.3787	27.5159	21.9838	0.6192	35.5037
88	84.1849	43.3463	32.5841	0.8223	39.6268
100	110.0659	61.3263	50.0294	1.2643	39.5717

The same data comparing the speed of populating and inverting matrices using the Method of Moments and DSPM is shown graphically in Figures 6-76 to Figure 6-78. The DSPM was considerably faster for populating matrices and inverting them as seen in the graphs.

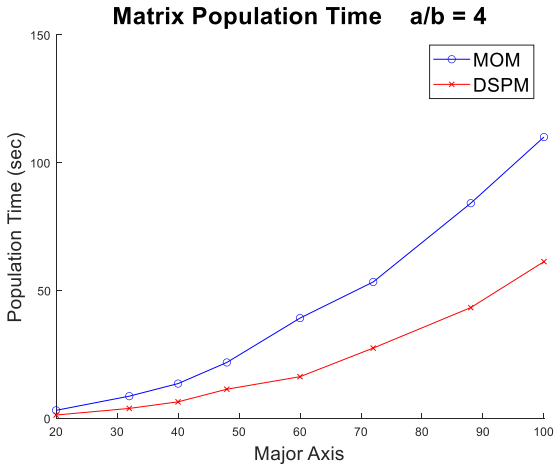

Figure 6-76: Comparison plot of speed to populate the same size matrices using MOM vs. DSPM for various elliptical cylinder major axes with axial ratio. $\frac{a}{b} = 4$.

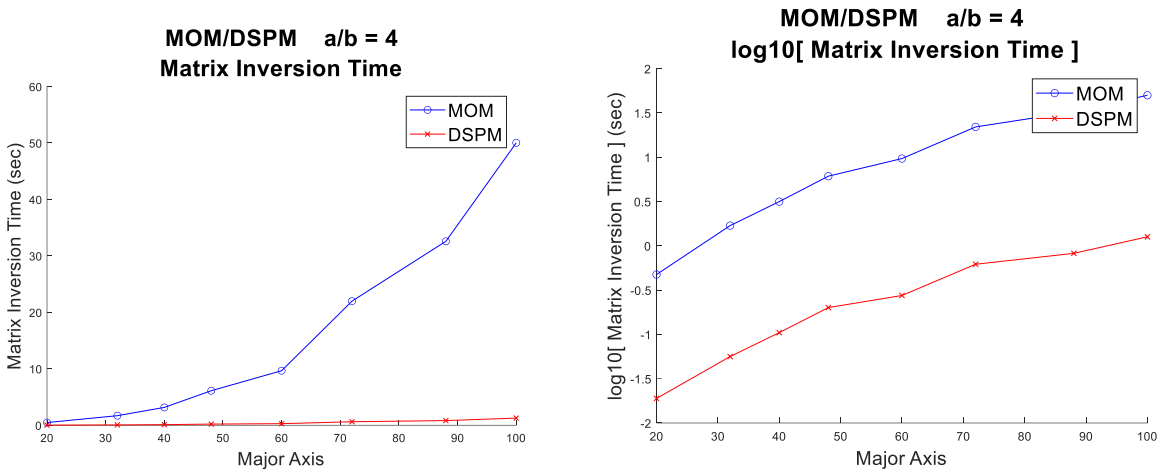

a) b)

Figure 6-77: Comparison plot of speed to invert the same size matrices using MOM vs. DSPM for elliptical cylinder major axes with axial ratio $\frac{a}{b} = 4$. a) Linear scale. b) Logarithmic scale.

The DSPM showed considerable speed improvement (22+) for inverting matrices as seen in the graphs shown in Figure 6-77 and Figure 6-78. The speed improvement increased with increasing size of the cylinder and matrix size as seen from the IR trend given in Figure 6-78.

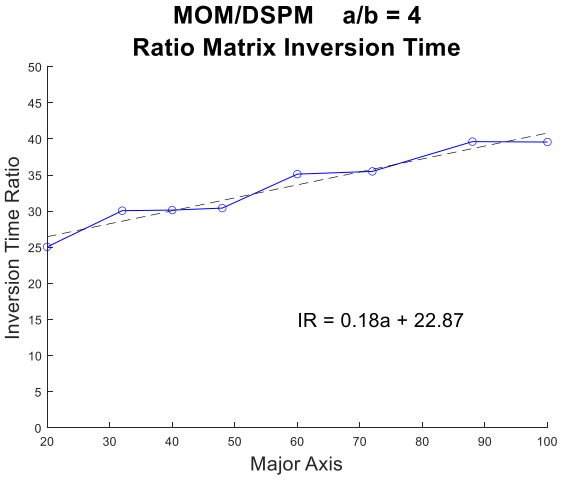

Figure 6-78: Plot of ratio of speed to invert the same size matrices using MOM vs. DSPM for various elliptical cylinder major axes with axial ratio $\frac{a}{b} = 4$.

6.15 Summary of Results for DSPM

The Direct Spectral Projection Model has been shown to be accurate in modelling infinitely long circular cylinders in two-dimensions. The convolution property of the addition theorem improves DSPM results significantly over those calculated using simple DSPM. Results of the DSPM closely mimic those of MOM for elliptical cylinders of high axial ratio and arbitrary shapes for TM^z incidence. For TE^z incidence, the model also performed well with elliptical cylinders of high axial ratio. The modal bandwidth of elliptical cylinders increases with the length of the major axis, and thus becomes a limiting factor for ellipses whose major axis is long in wavelength. For short wavelength structures, DSPM performs well in accurately modelling the current distribution and far-field patterns. DSPM has also been shown to populate and invert matrices faster than MOM. DSPM is a promising alternative to other techniques for scattering analysis of objects with different materials.

Table 6-2: Summary of Spectral Signatures of Virtual and Induced Current Sources.

$\begin{bmatrix} \vert \\ h_n \\ \vert \end{bmatrix} = \begin{bmatrix} H_{-K}^{(2)}(\beta\lvert\boldsymbol{\rho_n}\rvert)e^{jk\phi_n} \\ \vert \\ H_k^{(2)}(\beta\lvert\boldsymbol{\rho_n}\rvert)e^{jk\phi_n} \\ \vert \\ H_K^{(2)}(\beta\lvert\boldsymbol{\rho_n}\rvert)e^{jk\phi_n} \end{bmatrix}$ The **H**-spectral signature of a single virtual current source at surface location (ρ_n, ϕ_n)
$\begin{bmatrix} \vert \\ \hat{\imath}_{vir,sum} \\ \vert \end{bmatrix} = \begin{bmatrix} \alpha_0 \\ \vert \\ \alpha_n \\ \vert \\ \alpha_{N-1} \end{bmatrix}$ The weighting factors of the virtual current sources
$\begin{bmatrix} \vert \\ \hat{\imath}_{ss,vir,sum} \\ \vert \end{bmatrix} = \left(\begin{bmatrix} \vert & \vert & \vert \\ \vert & h_n & \vert \\ \vert & \vert & \vert \end{bmatrix} \begin{bmatrix} \ddots & 0 & 0 \\ 0 & \alpha_n & \\ 0 & 0 & \ddots \end{bmatrix} \right) \begin{bmatrix} \vdots \\ 1 \\ \vdots \end{bmatrix}$ Sum of the **H**-spectral signatures of the virtual current sources
$\begin{bmatrix} \vert \\ e_n \\ \vert \end{bmatrix} = \begin{bmatrix} J_{-K}(\beta\lvert\boldsymbol{\rho_n}'\rvert)e^{-jK\phi_n'} \\ \vert \\ J_k(\beta\lvert\boldsymbol{\rho_n}'\rvert)e^{jk\phi_n'} \\ \vert \\ J_K(\beta\lvert\boldsymbol{\rho_1}'\rvert)e^{jK\phi_n'} \end{bmatrix}$ The **J**-spectral signature of a single induced current source point at location (ρ_n', ϕ_n')
$\begin{bmatrix} \vert \\ \hat{\imath}_{ind,sum} \\ \vert \end{bmatrix} = \begin{bmatrix} \beta_0 \\ \vert \\ \beta_n \\ \vert \\ \beta_{N-1} \end{bmatrix} = \begin{bmatrix} \vert \\ J(\rho_n', \phi_n') \\ \vert \end{bmatrix}$ The vector representation of the magnitude and phase of the sum of the induced currents
$\begin{bmatrix} \vert \\ \hat{\imath}_{ss,ind,sum} \\ \vert \end{bmatrix} = \left(\begin{bmatrix} \vert & \vert & \vert \\ \vert & e_n & \vert \\ \vert & \vert & \vert \end{bmatrix} \begin{bmatrix} \ddots & 0 & 0 \\ 0 & \beta_n & \\ 0 & 0 & \ddots \end{bmatrix} \right) \begin{bmatrix} \vdots \\ 1 \\ \vdots \end{bmatrix}$ The sum of the **J**-spectral signature of the induced current sources

Table 6-3: Summary of DSPM Equations.

$\begin{bmatrix} \cdots & \cdots & \cdots \\ \cdots & H_k^{(2)}(\beta\lvert\boldsymbol{\rho_n}\rvert) & \cdots \\ \cdots & \cdots & \cdots \end{bmatrix} \begin{bmatrix} \\ \hat{\imath}_{vir,sum} \\ \\ \end{bmatrix} = \begin{bmatrix} \\ i_{ss,inc,sum}^{ff} \\ \\ \end{bmatrix}$ Equation for the DSPM for scattering problems with far-field excitation
$\begin{bmatrix} \vdots & \vdots & \vdots \\ \vdots & H_k^{(2)}(\beta\lvert\boldsymbol{\rho_m}\rvert)e^{jk\phi_m} & \vdots \\ \vdots & \vdots & \vdots \end{bmatrix} \begin{bmatrix} \\ \hat{\imath}_{ind} \\ \\ \end{bmatrix} = \begin{bmatrix} \\ \hat{\imath}_{ss,inc,Ie} \\ \\ \end{bmatrix}$ DSPM eigenvector equation for near field electric line source excitation
$\left(\begin{bmatrix} \cdots & \cdots & \cdots \\ \cdots & \bar{F} & \cdots \\ \cdots & \cdots & \cdots \end{bmatrix} \begin{bmatrix} \\ H_k^{(2)}((\beta\lvert\boldsymbol{\rho_b}\rvert) \\ \\ \end{bmatrix}^H \odot \begin{bmatrix} \cdots & \cdots & \cdots \\ \cdots & \bar{F} & \cdots \\ \cdots & \cdots & \cdots \end{bmatrix} \begin{bmatrix} \cdots & \cdots & \cdots \\ \cdots & J_k(\beta\lvert\boldsymbol{\rho_a}\rvert) & \cdots \\ \cdots & \cdots & \cdots \end{bmatrix}^H \right)^H \cdot$ $\begin{bmatrix} \cdots & \cdots & \cdots \\ \cdots & \bar{F} & \cdots \\ \cdots & \cdots & \cdots \end{bmatrix} \begin{bmatrix} \cdots \\ \hat{\imath}_{ind} \\ \cdots \end{bmatrix} = \begin{bmatrix} \cdots \\ \hat{\imath}_{ss,inc,Ie} \\ \cdots \end{bmatrix}$ DSPM matrix equation for near field electric line source excitation and two vector convolution model.

Chapter 7: Conclusions and Future Work

7.1 Spectral Projection Model and Direct Spectral Projection Model Summary

This dissertation introduces a new technique for solving two-dimensional electromagnetic field scattering problems called the Spectral Projection Model. Some techniques like the Finite Element Method and the Finite Difference Time Domain are developed directly from the differential form of Maxwell's equations. The Spectral Projection Model is a boundary element method, much like the Method of Moments and Fast Multipole Method, and a spectral method like the Spatial Frequency Technique, explained in Chapters 2, 3, and 4. Beginning with the differential form of Maxwell's equations, the boundary element method enforces the tangential electric and magnetic field boundary conditions to the surface of an object to find the integral form solution of the electric and magnetic fields. The resulting solutions are called the Electric Field Integral Equation (EFIE) and the Magnetic Field Integral Equation (MFIE). Depending upon whether the excitation is a transverse electric or transverse magnetic plane wave, an electric or magnetic line source, or multiple sources will determine the form that the EFIE or MFIE takes. The scattering object is then discretized and a set of linear equations in matrix form are solved.

The Method of Moments, Fast Multipole Method, and Spatial Frequency technique solve a matrix equation for the currents on the surface of the conducting body, and then the far-field radiation pattern may be calculated from the current distribution. The Spectral Projection Model uses elements of all three techniques to solve for the Bessel spectral signature of the electric current, from which the far-field pattern may be found by application of discrete Fourier transform. The Direct Spectral Projection Model solves for the current on the surface of the conductor directly using an eigenfunction approach.

The Spectral Projection Model and Direct Spectral Projection Model is a new spectral domain method that has certain features with advantages over the techniques just mentioned. These features, validation results and future research directions are listed below:

- Electric and Magnetic Fields are written as Projections of Spectral Signatures
- The Boundary Conditions are written as Projections and not Integral Equations
- Irregular Grid Spacing and Source and Observation Points are not Collocated
- Far-field Pattern Calculated Directly from Spectral Signature (SPM Only)
- Boundary Conditions are Implicitly Enforced (DSPM Only)
- Validation of SPM and DSPM using MOM
- Application and Future Directions of SPM and DSPM for Dielectric and 3D Objects

7.2 Electric and Magnetic Field Representation using SPM and DSPM

The Spectral Projection Model (SPM) has its origin in the Hankel form of the addition theorem, and its antecedent known as Graf's addition theorem [56]. The addition theorem is a method for calculating a Bessel or Hankel function as an infinite sum of Bessel and Hankel functions. For the Spectral Projection Model, the addition theorem is used to decompose the Green's function in the scattered electric and magnetic fields as a projection of the **J**-spectral signature of source points onto the **H**-spectral signature of observation points along the surface of the object. The wave transformation equation described by Harrington [17] and the asymptotic form of the Hankel function are used to define plane wave behavior as the weighted sum of **H**-spectral signatures.

7.3 Boundary Condition Enforcement using SPM and DSPM

Boundary conditions for the Electric Field Integral Equation and the Magnetic Field Integral Equation are written as a result of applying boundary conditions at the surface of the PEC. For the EFIE, the incident and scattered electric fields are summed together. The equation contains an integral with a Green's function and basis functions. Selection of the basis functions depends on the Green's function, and integration of the Green's function at the singularity must be performed. Similarly, the MFIE sets the difference in the tangential magnetic fields equal to the surface current, and contains an integral with a Green's function and basis functions.

Both SPM and DSPM write the boundary conditions for the EFIE and MFIE as the projection of one spectral signature onto another spectral signature by decomposing the Green's function into Hankel and Bessel functions using the addition theorem. Unlike MOM, FMM and SFT, no basis functions are required, and there is no need to integrate the product of those functions with the Green's function. So, this method offers a simple solution to enforcing the boundary conditions without the messy mathematics of integrating complex functions at the singularity of a Green's function.

7.4 Irregular Grid Spacing using SPM and DSPM

One disadvantage of the Spatial Frequency Technique is that in order to effectively use the FFT in problem formulations, it is necessary to define the objects under illumination with regularly spaced grids. Most Method of Moments problems generally use regular grid spacing, but the Method of Moments can accommodate irregular grids with hybrid approaches. The SPM and DSPM do not suffer from this constraint when solving scattering problems with low axial ratios. For higher axial ratios in which the addition theorem is used as a convolution product, angular spacing of rotating vectors must be defined before an FFT algorithm is used.

7.5 Far-field Calculations using SPM

The solution of scattering problems using the Spectral Projection Model yields the **J**-spectral signature of the induced current on the surface of a PEC conductor. Rather than solve for the induced current, the far-field pattern for the object can be calculated directly from the **J**-spectral signature by using a form of the Discrete Fourier Transform. When solving for the current distribution is necessary, the DSPM offers a simple way of calculating the induced currents.

7.6 Boundary Conditions are Implicitly Enforced using DSPM

DSPM analysis is a way to calculate the scattered fields by describing them in terms of eigenfunctions. Virtual currents on the surface of a conductor act as eigenfunctions with equal and opposite induced currents on the surface of the object sharing the same points. Virtual currents are used to describe incident and induced currents by defining them as the weighting factors of **H**-spectral signatures. The weighted sum of the **H**-spectral signatures of the incident and virtual currents are set equal to each other in a matrix equation, and solving for the virtual currents enables one to calculate the induced currents. The boundary conditions are implicitly enforced by the eigenfunctions, because any induced current produces a scattered field equal and opposite that of a virtual current. Projecting the **H**-spectral signature on each side of the equation onto the same $\mathbf{J}^{\mathbf{T}}$-spectral signatures defined at a set of observation points on the surface ensures that the incident field and the scattered field cancel.

7.7 Validation of SPM and DSPM using MOM

Both SPM and DSPM have been tested and verified for scattering from 2D, conducting objects for TM and TE waves using both EFIE and MFIE. The SPM was developed originally and led to the development of the faster analytical tool called the DSPM. Both techniques can solve a variety of 2D electromagnetic scattering problems, and DSPM has been shown to solve TM^z scattering from arbitrary shaped objects with the same accuracy as the MOM.

7.8 Application and Future Directions of SPM and DSPM for Dielectric and 3D Objects

SPM and DSPM are spectral techniques that have been used to solve a variety of scattering problems on 2D conducting bodies without the necessity of integrating the singularity of a Green's function or specifying a regular spatial grid. By taking advantage of the convolution property of the addition theorem, a larger class of problems has been solved with excellent accuracy. Further study of the convolution theorem and its implementation on objects with corrugated surfaces can expand the usefulness of these methods. These techniques show promise in solving problems involving scattering from 2D dielectric objects by applying both the electric

field and magnetic field boundary conditions. In order to solve 3D conducting body scattering problems, spherical Hankel functions can be employed with application of both the electric field and magnetic field boundary conditions. SPM and DSPM techniques can be validated for 3D problems by comparison with results using MOM RWG elements.

References

[1] "A Brief History of Calculus," www.wyzant.com. https://www.wyzant.com/resources/lessons/math/calculus/introduction/history_of_calculus/ (accessed February 2, 2023).

[2] J. Christensen, "A Brief History of Linear Algebra," http:www.math.utah.edu/. http://www.math.utah.edu/~gustafso/s2012/2270/web-projects/christensen-HistoryLinearAlgebra.pdf (accessed February 2, 2023).

[3] "d'Alembert Solution of the Wave Equation," www.math.uiuc.edu. http://www.math.uiuc.edu/~jlebl/286-dalemb.pdf (accessed February 25, 2023).

[4] M. Hancock. "The 1-D Wave Equation," https://ocw.mit.edu. http://ocw.mit.edu/courses/mathematics/18-303-linear-partial-differential-equations-fall-2006/lecture-notes/waveeqni.pdf (accessed November 5, 2020).

[5] "Bessel functions," onlinelibrary.wiley.com. http://onlinelibrary.wiley.com/doi/10.1002/9781118093184.app4/pdf (accessed November 5, 2020).

[6] P. P. Silvester, R. L. Ferrari, Finite Elements for Electrical Engineers, Cambridge University Press, Cambridge, England, 1986.

[7] A. Taflove, S. C. Hagness, Computational Electrodynamics: The Finite-Difference Time-Domain Method, 3rd Edition, Artech House, Norwood, MA, 1995.

[8] R. F. Harrington, "Matrix Methods for Field Problems," Proc. IEEE, Vol. 55, No. 2, Feb 1967, pp. 136-149.

[9] R. Coifman, V. Rokhlin, and S. Wandzura, "The fast multipole method for the wave equation: A pedestrian prescription," IEEE Trans. Antennas Propagation, Vol. 35, No. 3, 1993, pp. 7-12.

[10] N. N. Bojarski , "k-space Formulation of the electromagnetic scattering problem, Air Force Avionics Lab," Technical Report AFAL - TR - 71 - 75, 1971.

[11] T. K. Sarkar, E. Arvas, and S. M. Rao, "Application of FFT and the conjugate gradient method for the solution of electromagnetic radiation from electrically large and small

conducting bodies," IEEE Trans. Antennas Propagation, Vol. 34, No. 5, 1986, pp. 635 – 640.

[12] D. L. Logan, A First Course in the Finite Element Method, 3rd Edition, Brooks/Cole Thomson Learning, Pacific Grove, CA, 2002.

[13] S. S. Rao, Applied Numerical Methods for Engineers and Scientists, Prentice Hall, Hoboken, NJ, 2002.

[14] "The Finite Difference Time Domain Method," www.slideserve.com. https://www.slideserve.com/kaliska-parker/finite-difference-time-domain-method-fdtd (accessed November 5, 2020).

[15] M. Spiegel, Schaum's Outline of Calculus of Finite Differences and Difference Equations, McGraw Hill, New York, NY, 1971.

[16] "Chapter 14 Stability of Finite Difference Methods," http://web.mit.edu. http://web.mit.edu/16.90/BackUp/www/pdfs/Chapter14.pdf (accessed February 2, 2023).

[17] R. F. Harrington, Field Computation by Moment Methods, Krieger, Malabar, FL, 1968.

[18] R. Mittra, Editor, Computer Techniques for Electromagnetics, Elmsford, Pergamon Press, New York, NY, 1973.

[19] A. F. Peterson, S. L. Ray, and R. Mittra, Computational Methods for Electromagnetics, IEEE Press, New York, NY, 1997.

[20] W. C. Gibson, The Method of Moments in Electromagnetics, Chapman & Hall/ CRC, Boca Raton, FL, 2008.

[21] R. Bancroft, Understanding Electromagnetic Scattering Using the Moment Method, Artech House, Norwood, MA, 1996.

[22] S. N. Makarov, Antenna and EM Modeling with MATLAB, John Wiley & Sons, New York, NY, 2002

[23] "Classical Iterative Methods for the Solution of Linear Systems," www.math.iit.edu. http://www.math.iit.edu/~fass/477577_Chapter_13.pdf (accessed February 2 2023).

[24] "Splitting Methods," www.asc.tuwien.ac.at. http://www.asc.tuwien.ac.at/~winfried/teaching/106.079/SS2011/downloads/script-p-035-045.pdf (accessed February 5, 2023).

[25] R. Bracewell, The Fourier Transform and its Applications, McGraw Hill, New York, NY, 1999.

[26] C. Y. Shen, K. J. Glover, M. I. Sancer, and A. D. Varvatsis, “The discrete Fourier transform method of solving differential – integral equations in scattering theory,” IEEE Trans. Antennas Propagation, Vol. 37, No. 8, 1989, 1032 – 1041.

[27] J. Jin, Theory, Computation of Electromagnetic Fields, John Wiley & Sons, Hoboken, NJ, 2010.

[28] E. K. Miller, L. Medgyesi-Mitschang, and E. H. Newman, Eds., Computational Electromagnetics: Frequency-Domain Method of Moments, IEEE Press, New York, NY, 1992.

[29] Y. Liu, The Fast Multipole Boundary Element Method Theory and Applications in Engineering, Cambridge University Press, Cambridge, England, 2009.

[30] D. Kasilingam, A. Fascia, and V. Sivalingam, “Spectral Projection Model for Analyzing Electromagnetic Scattering from Two Dimensional Conducting Objects,” ICEAA, 2019.

[31] J. A. Stratton, Electromagnetic Theory, McGraw Hill, New York, NY, 1941.

[32] “Digital Library of Mathematical Functions (DLMF),” https://dlmf.nist.gov. https://dlmf.nist.gov/10.23 (accessed February 2, 2023).

[33] D. R. Wilton, “A New Numerical Approach to the Calculation of Electromagnetic Scattering Properties of Two-Dimensional Bodies of Arbitrary Cross Section,” University of Illinois at Urbana-Champaign, Ph.D. Dissertation, 1970.

[34] D. R. Wilton, R. Mittra, “A New Numerical Approach to the Calculation of Electromagnetic Scattering Properties of Two-Dimensional Bodies of Arbitrary Cross Section,” IEEE Trans. Antennas Propagation, Vol. 20, 1972, pp. 310-317.

[35] R. F. Harrington, Time Harmonic Electromagnetic Fields, McGraw Hill, New York, NY, 1962.

[36] C. A. Balanis, Advanced Engineering Electromagnetics, 1rst Edition, John Wiley & Sons Inc., Hoboken, NJ, 1989.

[37] A. Lindquist, “On Fredholm Integral Equations, Toeplitz Equations and Kalman-Bucy Filtering,” Applied Mathematics and Optimization, Vol. 1, No. 4, 355-373.

[38] F. G. Tricomi, Integral Equations, Dover Publications, New York, NY 1957.

[39] C. A. Balanis, Antenna Theory, Harper Collins Publishers, New York, NY, 1982.

[40] P. J. Davis, Circulant Matrices, John Wiley & Sons, New York, NY, 1979.

[41] S. M. Rao, D.R. Wilton, and A.W. Glisson, "Electromagnetic Scattering by Surfaces of Arbitrary Shape," IEEE Trans. Antennas Propagation, Vol. 30, No. 3, 1982, pp. 409-419.

[42] R. M. Gray, "Toeplitz and Circulant Matrices: A Review," https://ee.stanford.edu. https://ee.stanford.edu/~gray/toeplitz.pdf (accessed June 5, 2021).

[43] P. G. Martinsson, "A Fast Algorithm for the Inversion of General Toeplitz Matrices," https://dl.acm.org. https://dl.acm.org/doi/abs/10.1016/j.camwa.2005.03.011 (accessed February 2, 2023).

[44] M. Chen, "On the Solution of Linear Circulant Systems," SIAM, Vol. 24, Iss. 3, 1987.

[45] L. F. Chaparro, Signals and Systems using MATLAB, Elsevier, London, U.K., 2001.

[46] M. Spiegel, Schaum's Outline of Fourier Analysis with Applications to Boundary Value Problems, McGraw Hill, New York, NY, 1974.

[47] D. Kasilingam, A. Fascia, "Two-Dimensional Spatial Frequency Technique for Calculating Electromagnetic Scattering from Large Objects," Progress in Electromagnetics Symposium (PIERS), July 2015.

[48] J. R. Phillips, J. K. White, "A precorrected–FFT method for electrostatic analysis of complicated 3D structures," IEEE Trans. Computer Aided Design, Vol. 16, 1059–1072, 1997.

[49] D. Kasilingam, A. Fascia, M. Ahmad, and J. Summerfield, "Fast Spatial Frequency Based Analysis Technique for Electromagnetic Scattering," IEEE International Symposium on Antennas and Propagation and North American Radio Science Meeting, 2015.

[50] D. Kasilingam, A. Fascia, and M. Ahmad, "Fast Algorithm for Implementing Spatial Frequency Analysis of Electromagnetic Scattering," IEEE APS/URSI, Fajardo, Puerto Rico, 2016.

[51] T. K. Sarkar, "The application of the conjugate gradient method for the solution of operator equations arising in electromagnetic scattering from wire antennas," Radio Science, Vol. 19, Issue 5, 1984, 1156-1172.

[52] J. Demmel, Applied Numerical Linear Algebra, SIAM, Philadelphia, PA, 1997.

[53] D. Kasilingam, A. Fascia and V. Sivalingam, “The Extension of the Spectral Projection Model for Electromagnetic Scattering,” IEEE APS/URSI, Denver, CO, 2022.

[54] D. Kasilingam, A. Fascia and V. Sivalingam, “The Direct Spectral Projection Model for Electromagnetic Scattering,” IEEE APS/URSI, Portland, OR, 2023.

[55] S. Rao, Applied Numerical Methods for Engineers and Scientists, Prentice Hall, 2000.

[56] M. Abramowitz, and I. Stegun, Handbook of Mathematical Functions, Dover Publications, New York, NY, 1982.

[57] I. Gradshteyhn, I. Ryzhik, Table of Integrals, Series and Products, Academic Press, New York, NY, 1980.

[58] A. Gray, G. B. Matthews, Treatise on Bessel Functions and Their Applications to Physics, Merchant Books, Mile End, Canada, 2007.

[59] G. N. Watson, Theory of Bessel Functions, Merchant Books, Mile End, Canada, 2008.

[60] F. Bowman, Introduction to Bessel Functions, Dover Publications, New York, NY, 1958.

[61] L. Tsang, J. Kong, and K. Ding, Scattering of Electromagnetic Waves: Theories and Applications, John Wiley & Sons, Hoboken, NJ, 2000.

[62] C. Bourlier, N. Pinel, and G. Kubicke, Method of Moments for 2D Scattering Problems, John Wiley & Sons, Hoboken, NJ, 2013.

[63] E. Yamashita, Editor, Analysis Methods for Electromagnetic Wave Problems, Vol. 2, Artech House, Norwood, MA, 1996.

[64] A. E. Taylor, Advanced Calculus, Ginn and Company, Boston, MA, 1955.

[65] Wolfram Mathworld, https://mathworld.wolfram.com. https://mathworld.wolfram.com/LeibnizIntegralRule.html (accessed February 5, 2023).

[66] C. Bray, Multivariable Calculus, Clark Bray, Durham, NC, 2009.

[67] The Wolfram Functions Site, https://functions.wolfram.com. https://functions.wolfram.com/Bessel-TypeFunctions/BesselY/introductions/Bessels/05/ (accessed Feb 25, 2023).

[68] The Great Soviet Encyclopedia, 3rd Edition, “Carl Gottfried Neumann,” http://encyclopedia2.thefreedictionary.com. http://encyclopedia2.thefreedictionary.com/Carl+Gottfried+Neumann (accessed February 2, 2023.

[69] "Carl Gottried Neumann," www.encyclopedia.com. http://www.encyclopedia.com/doc/1G2-2830903142.html (accessed February 5, 2023).

[70] AMS, "Partial Differential Equations of Mathematical Physics," http://www.ams.org. http://www.ams.org/journals/bull/1901-08-02/S0002-9904-1901-00858-0 (accessed June 8, 2020).

[71] Bibliotheca Teubneriana, "Theory of Bessel functions: An Analogue of the Theory of Spherical Harmonics," https://en.wikipedia.org. https://en.wikipedia.org/wiki/Bibliotheca_Teubneriana (accessed February 2, 2023).

[72] A. Borji, "Bessel, Hankel and Neumann Functions," http://sharif.edu. http://sharif.edu/~aborji/25735/files/bessel%20functions.pdf (accessed February 25, 2023).

[73] M. R. Spiegel, J. Liu, Schaum's Outline Series, Mathematical Handbook of Formulas and Tables, 2nd Edition, McGraw Hill, New York, NY, 1999.

[74] T. K. Sarkar, "The application of the conjugate gradient method for the solution of operator equations arising in electromagnetic scattering from wire antennas," Radio Science, Vol. 19, Issue 5, Sept. 1984, 1156-1172.

[75] R. Hon-Fu Chan and X. Q. Jin, "An Introduction to Iterative Toeplitz Solvers," https://epubs.siam.org. https://epubs.siam.org/doi/pdf/10.1137/1.9780898718850.fm (accessed February 2, 2023).

[76] V. B. K. Vatti, Numerical Analysis Iterative Methods, I. K. International Publishing House Pvt. Ltd., 2016.

[77] J. Malek, Z. Strakos, Preconditioning and the Conjugate Gradient Method in the Context of Solving PDEs, SIAM, 2015.

[78] H. A. van der Vorst, Iterative Krylov Methods for Large Linear Systems, Cambridge University Press, Cambridge, England, 2003.

[79] M. R. Hestenes, E. Stiefel, "Methods of Conjugate Gradients for Solving Linear Systems," Journal of Research of the National Bureau of Standards, Vol. 49, No. 6, 1952.

[80] H. Belhadj, T. Aguili, "Finite Step Conjugate Gradient Methods for the Solution of an Impedance Operator Equation Arising in Electromagnetics," Journal of Electromagnetic Analysis and Applications, Vol. 3, 2011, 416-422.

[81] R. H. Chan. X. Jin, An Introduction to Iterative Toeplitz Solvers, SIAM, 2007.

[82] G. Birkoff, E. Kreysig. "The Establishment of Functional Analysis," www.sciencedirect.com. http://www.sciencedirect.com/science/article/pii/0315086084900363 (accessed February 2, 2023).

[83] F. Hildebrand, Methods of Applied Mathematics, 2nd Edition, Dover Publications, New York, NY, 1965.

[84] G. E. Shilov, Elementary Functional Analysis, Dover Publications, New York, NY, 1974.

[85] S. Lipschutz, Schaum's Outline of Linear Algebra, McGraw Hill, New York, NY, 1968.

[86] F. M. Stewart, Introduction to Linear Algebra, D. Van Nostrand Company, New York, NY, 1963.

[87] H. G. Moore, A. Yaqub, A First Course in Linear Algebra with Applications, 3rd Edition, Academic Press, New York, NY, 1998.

[88] D. Zelinsky, A First Course in Linear Algebra with Applications, Academic Press, New York, NY, 1968.

[89] W. Cheney, D. Kincaid, Numerical Mathematics and Computing, 4th Edition, Brooks/Cole Publishing, Three Lakes, WI, 1999.

[90] D. J. Griffiths, Introduction to Electrodynamics, 4th Edition, Pearson Education Limited, Essex, England, 2014.

[91] J. D. Jackson, Classical Electrodynamics, 2nd Edition, John Wiley & Sons, Hoboken, NJ, 1975.

[92] A. D. Poularikas, The Transforms and Applications Handbook, 2nd Edition, CRC Press, Boca Raton, FL, 1961.

[93] J. O. Smith III, Mathematics of the Discrete Fourier Transform with Audio Applications, W3K Publishing, Middletown, DE, 2007.

[94] J. Smith III, Mathematics of the Discrete Fourier Transform, W3K Publishing, Middletown, DE, 2014.

[95] T. S. El Ali, Discrete Systems and Digital Signal Processing with Matlab, CRC Press, Boca Raton, FL, 2004.

[96] A. Oppenheim, R. Schafer, with J. Buck, Discrete Time Signal Processing, Pearson Education, New York, NY, 1999.

[97] F. Oberhettinger, Fourier Transforms of Distributions and Their Inverses, Academic Press, New York, NY, 1973.

[98] R. Schwartz, "Multiplication and the Fast Fourier Transform," www.math.brown.edu. https://www.math.brown.edu/reschwar/MathNotes/FFT.pdf (accessed February 2, 2023).

[99] J. W. Cooley, J. W. Tukey, "An algorithm for the machine calculation of complex Fourier series," Mathematics of Computation, vol.19, no.2, pp.297-301, April 1965.

[100] E. Million, "Hadamard Product," http://buzzard.ups.edu. http://buzzard.ups.edu/courses/2007spring/projects/million-paper.pdf (accessed February 2, 2023).

Appendix A: SPM and Graf's Equation

A.1 Graf's Addition Theorem – Correlation Product

The addition theorem used in Fast Multipole Method and Spectral Projection Model is given in equation $(3-13)$ below from references [56-58]. This equation is specific to $H_0^{(2)}(\beta|\boldsymbol{\rho}-\boldsymbol{\rho}'|)$, the zeroth order Hankel function of the second kind. Note the sign of the angles are the same as the sign of the vectors $\boldsymbol{\rho}$ and $\boldsymbol{\rho}'$.

$$H_0^{(2)}(\beta|\boldsymbol{\rho}-\boldsymbol{\rho}'|)=\sum_{k=-\infty}^{\infty} J_k(\beta|\boldsymbol{\rho}|)H_k^{(2)}(\beta|\boldsymbol{\rho}'|)e^{jk(\phi-\phi')} \qquad \rho<\rho' \qquad (3-13)$$

This addition theorem is one of Neumann's formulas, but the addition theorem was generalized by Johann Heinrich Graf. The addition theorem equation of Graf given by Watson [59] is shown in equation (A-1). Figure A-1 is an illustration of the corresponding coordinates and angles.

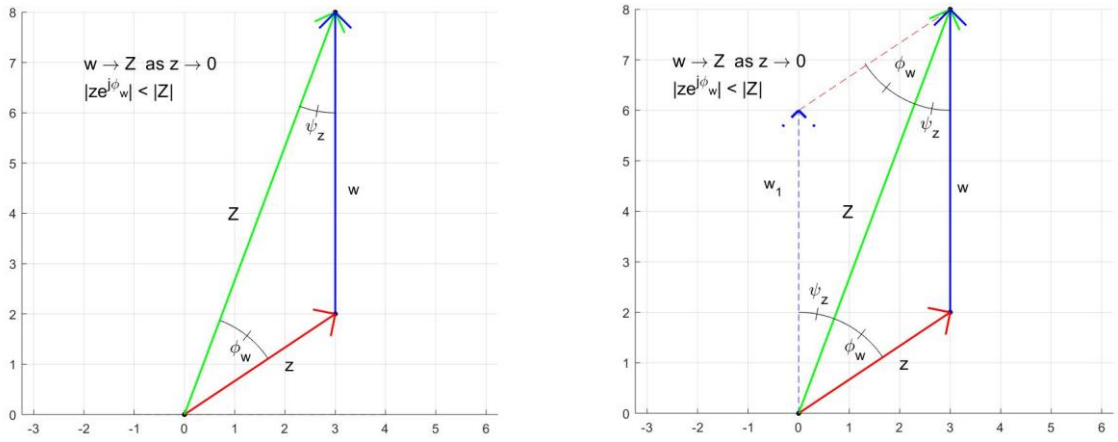

a) b)

Figure A-1: a) Illustration of vectors and corresponding angles for Graf's addition theorem. b) Graf's addition theorem with parallelogram for vector association.

$$H_m^{(2)}(w)e^{jm\psi_z}=\sum_{n=-\infty}^{\infty} H_{m+n}^{(2)}(Z)J_n(z)e^{jn\phi_w} \qquad (A-1)$$

Equation $(A-1)$ may be viewed as a discrete a correlation operation because of the (m+n) order term on the Hankel function $H_{m+n}^{(2)}$. To change the equation into a convolution product, the order term needs to be (m-n).

A.2 Reflection Properties of Bessel and Hankel Functions

The reflection properties of the Bessel and the Hankel function in equations $(A-2)$ to $(A-6)$ may be used to change equation $(A-1)$ into equation $(A-7)$ [60].

$$(-1)^n = e^{-jn\pi} \qquad (A-2)$$

$$J_{-n}(w) = J_n(-w) \qquad (A-3)$$

$$J_{-n}(w) = e^{-jn\pi} J_n(w) \qquad (A-4)$$

$$H_n^{(2)}(w) = H_n^{(2)}(-w) \qquad (A-5)$$

$$H_{-n}^{(2)}(w) = e^{-jn\pi} H_n^{(2)}(w) \qquad (A-6)$$

A.3 Graf's Addition Theorem – Convolution Product

As mentioned above, equation $(A-1)$ is a correlation operation because of the (m+n) order term on the Hankel function $H_{m+n}^{(2)}$. By using the reflection properties listed above, equation $(A-1)$ can be transformed into equation $(A-7)$, which is the convolution product form $H_{m-n}^{(2)}$ of Graf's generalized addition formula.

$$H_m^{(2)}(w)e^{jm\varphi_z} = \sum_{n=-\infty}^{\infty} H_{m-n}^{(2)}(Z)J_n(z)e^{jn(\phi_w-\pi)} \qquad (A-7)$$

The correlation and convolution products of the Bessel function are given in equations $(A-8)$ and $(A-9)$. These equations are forms of the Neumann addition theorem, which is less general than the Graf form of the addition theorem.

$$J_m(w)e^{jm\varphi_z} = \sum_{n=-\infty}^{\infty} J_{m+n}(Z)J_n(z)e^{jn(\phi_w)} \qquad (A-8)$$

$$J_m(w)e^{jm\varphi_z} = \sum_{n=-\infty}^{\infty} J_{m-n}(Z)J_n(z)e^{jn(\phi_w-\pi)} \qquad (A-9)$$

A.4 Graf's Addition Theorem - Coordinate Change

In order to implement the Spectral Projection Model, a more convenient coordinate system needed to be considered that defined angles from the positive horizontal X-axis rotating counterclockwise. This section illustrates how the Graf addition theorem can be rewritten using a different set of coordinates. Taking the difference between two vectors, $\mathbf{R} = \boldsymbol{\rho} - \boldsymbol{\rho}'$, to enact a change in coordinates and angles, one can substitute from equations $(A-4)$ and $(A-6)$ into equation $(A-1)$. Figure A-2 is an illustration of the vector subtraction.

$$\varphi_z = \phi'' - \phi \qquad (A-10)$$

$$\phi_w = \phi - \phi' \qquad (A-11)$$

The corresponding expression for R are in equations $(A-12)$ and $(A-13)$, besides in Figure A-2.

$$R = \sqrt{\rho^2 + \rho'^2 + 2\rho\rho' cos(\alpha)} \qquad (A-12)$$

$$R = \sqrt{\rho^2 + \rho'^2 - 2\rho\rho' cos(\gamma)} \qquad (A-13)$$

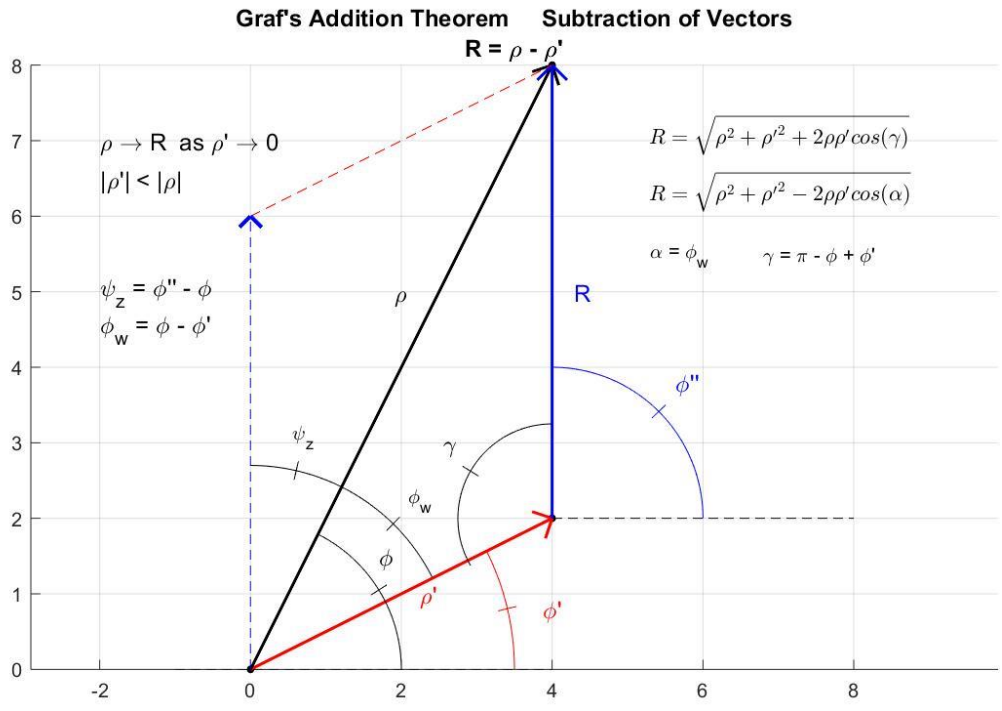

Figure A-2: Illustration of vectors and corresponding angles for Graf's addition theorem for the difference between two vectors with a change in coordinates.

The new equation for Graf's addition theorem for the subtraction of vectors is in equation $(A-14)$.

$$H_m^{(2)}(\beta|\boldsymbol{\rho}-\boldsymbol{\rho}'|)e^{jm\phi''} = \sum_{n=-\infty}^{\infty} H_{m+n}^{(2)}(\beta|\boldsymbol{\rho}|)J_n(\beta|\boldsymbol{\rho}'|)e^{j[(m+n)\phi-n\phi']} \qquad (A-14)$$

The new equation for Graf's addition theorem for the addition of vectors is in equation $(A-15)$.

$$H_m^{(2)}(\beta|\boldsymbol{\rho}+\boldsymbol{\rho}'|)e^{jm\phi''} = \sum_{n=-\infty}^{\infty} H_{m-n}^{(2)}(\beta|\boldsymbol{\rho}|)J_n(\beta|\boldsymbol{\rho}'|)e^{j[(m-n)\phi-n\phi']} \qquad (A-15)$$

Illustrations of Graf's addition theorem for the addition of two vectors is shown in Figure A-3 and Figure A-4.

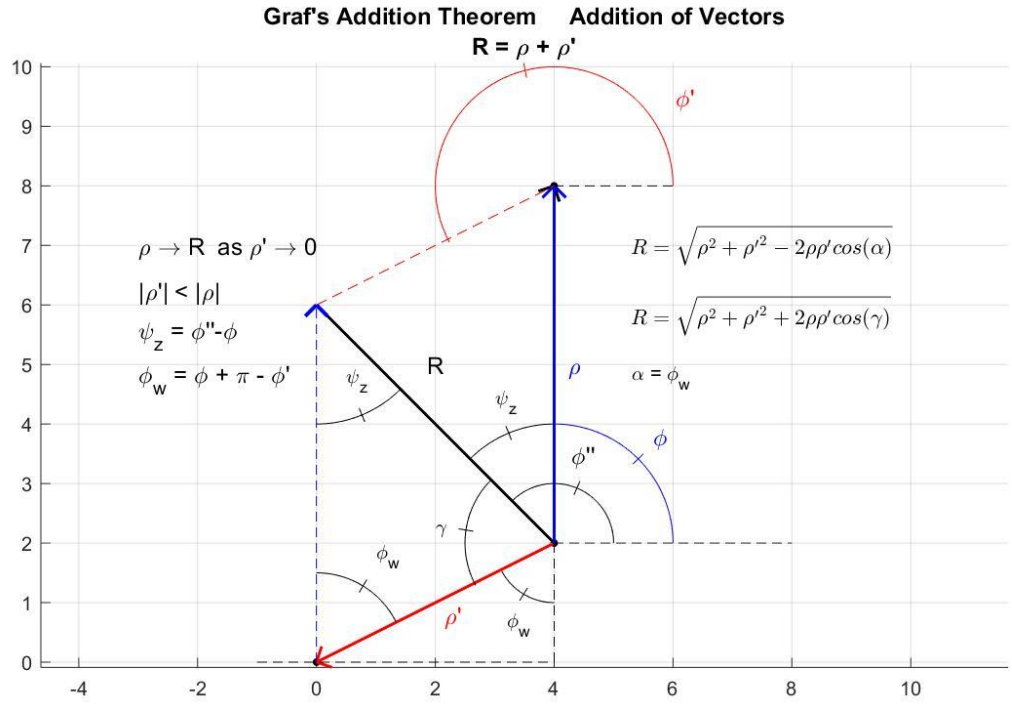

Figure A-3: Illustration of Graf's addition theorem for a vector sum with a change in coordinates ψ_z, ϕ_w, γ to coordinates ϕ, ϕ', ϕ'' view one.

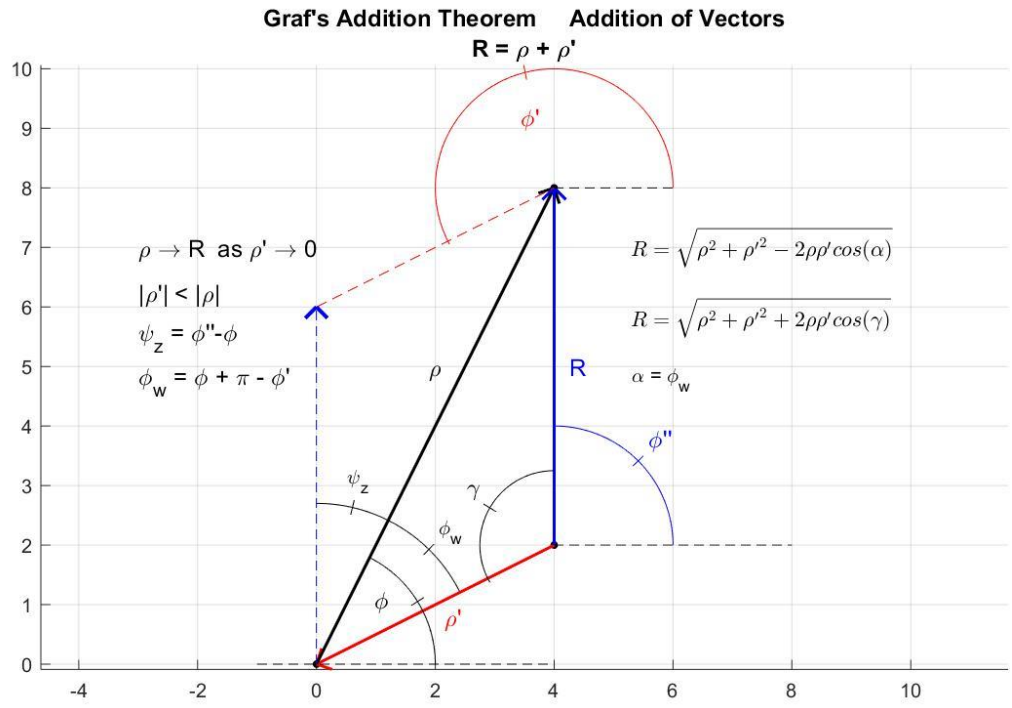

Figure A-4: Illustration of Graf's addition theorem for a vector sum with a change in coordinates ψ_z, ϕ_w, γ to coordinates ϕ, ϕ', ϕ'' view two.

Equations $(A-8)$ and $(A-9)$ may be rewritten in terms of the new angle too. They are shown in equations $(A-16)$ and $(A-17)$.

$$J_m(\beta|\boldsymbol{\rho}-\boldsymbol{\rho}'|)e^{jm\phi''} = \sum_{n=-\infty}^{\infty} J_{m+n}(\beta|\boldsymbol{\rho}|)J_n(\beta|\boldsymbol{\rho}'|)e^{j[(m+n)\phi-n\phi']} \qquad (A-16)$$

$$J_m(\beta|\boldsymbol{\rho}+\boldsymbol{\rho}'|)e^{jm\phi''} = \sum_{n=-\infty}^{\infty} J_{m-n}(\beta|\boldsymbol{\rho}|)J_n(\beta|\boldsymbol{\rho}'|)e^{j[(m-n)\phi-n\phi']} \qquad (A-17)$$

A.5 Neumann's Addition Theorem – Convolution of Two Vectors

The connection between the spectral signature of a set of points and the Neumann addition theorem is evident when one considers the product and sum of vectors.

$$|\boldsymbol{\rho}-\boldsymbol{\rho}'|^2 = (\boldsymbol{\rho}-\boldsymbol{\rho}')\cdot(\boldsymbol{\rho}-\boldsymbol{\rho}') \qquad (A-18)$$

$$|\boldsymbol{\rho}-\boldsymbol{\rho}'|^2 = \boldsymbol{\rho}\cdot\boldsymbol{\rho}+\boldsymbol{\rho}'\cdot\boldsymbol{\rho}'-2\boldsymbol{\rho}\cdot\boldsymbol{\rho}' \qquad (A-19)$$

$$cos(\phi) = \frac{\boldsymbol{\rho} \cdot \boldsymbol{\rho}'}{|\boldsymbol{\rho}||\boldsymbol{\rho}'|} \qquad (A-20)$$

$$|\boldsymbol{\rho} - \boldsymbol{\rho}'|^2 = |\boldsymbol{\rho}|^2 + |\boldsymbol{\rho}'|^2 - 2|\boldsymbol{\rho}||\boldsymbol{\rho}'|cos(\phi) \qquad (A-21)$$

Similarly, one can prove for the addition of two vectors,

$$|\boldsymbol{\rho} + \boldsymbol{\rho}'|^2 = |\boldsymbol{\rho}|^2 + |\boldsymbol{\rho}'|^2 + 2|\boldsymbol{\rho}||\boldsymbol{\rho}'|cos(\phi) \qquad (A-22)$$

If vector $\boldsymbol{\rho}' = \boldsymbol{\rho_a}' + \boldsymbol{\rho_b}'$, the vector sum can be represented as equation $(A-23)$.

$$|\boldsymbol{\rho} + (\boldsymbol{\rho_a}' + \boldsymbol{\rho_b}')|^2 = (\boldsymbol{\rho} + \boldsymbol{\rho_a}' + \boldsymbol{\rho_b}') \cdot (\boldsymbol{\rho} + \boldsymbol{\rho_a}' + \boldsymbol{\rho_b}') \qquad (A-23)$$

One can write these vector sums using the addition theorem for Bessel functions.

$$J_n\,(\beta|\boldsymbol{\rho} + \boldsymbol{\rho}'|)e^{jm\phi''} =$$

$$\sum_{m=-\infty}^{\infty} J_{n-m}(\beta|\boldsymbol{\rho}|)J_m(\beta|\boldsymbol{\rho}'|)e^{j[(m-n)\phi - n\phi']} \qquad (A-24)$$

$$J_m(\beta|\boldsymbol{\rho_a}' + \boldsymbol{\rho_b}'|)e^{jm\phi} =$$

$$\sum_{l=-\infty}^{\infty} J_{m-l}(\beta|\boldsymbol{\rho_a}'|)J_l(\beta|\boldsymbol{\rho_b}'|)e^{j[(m-l)\phi_{a'} - l\phi_{b'}]} \qquad (A-25)$$

$$J_n\,(\beta|\boldsymbol{\rho} + \boldsymbol{\rho_a}' + \boldsymbol{\rho_b}'|)e^{jm\phi''} =$$

$$\sum_{m=-\infty}^{\infty} J_{n-m}(\beta|\boldsymbol{\rho}|) \sum_{l=-\infty}^{\infty} J_{m-l}(\beta|\boldsymbol{\rho_a}'|)J_l(\beta|\boldsymbol{\rho_b}'|)e^{j[(m-l)\phi_{a'} - l\phi_{b'}]} \qquad (A-26)$$

The expression in $(A-24)$ may be written in shorter form as equation $(A-27)$.

$$J(n, \boldsymbol{\rho} + \boldsymbol{\rho}') = J(n, \boldsymbol{\rho}) \otimes J(n, \boldsymbol{\rho}') \qquad (A-27)$$

with the symbol $\otimes$ meaning convolution, and the arguments being the order of the Bessel function and then the vectors.

The expression in $(A-26)$ may be written in shorter form as equation $(A-28)$.

$$J(n, \boldsymbol{\rho} + \boldsymbol{\rho_a}' + \boldsymbol{\rho_b}') = J(n, \boldsymbol{\rho}) \otimes \left(J(n, \boldsymbol{\rho_a}') \otimes J(n, \boldsymbol{\rho_b}')\right) \qquad (A-28)$$

Similarly, one can write the addition theorem for Hankel functions, and correlation $\circledast$ between spectral signatures. For equation $(A-29)$,

$$H(m, \boldsymbol{\rho} - \boldsymbol{\rho}') = H(n, \boldsymbol{\rho}) \circledast J(n, \boldsymbol{\rho}') \qquad \rho \geq \rho' \qquad (A-29)$$

the equation can be seen as the discrete correlation between the **H**-spectral signature of the observation point and the **J**-spectral signature of the source point.

The convolution operation allows one to define a relationship between two spectral signatures defined with respect to two separate origins.

$$H(m, \boldsymbol{\rho} + \boldsymbol{\rho}') = H(n, \boldsymbol{\rho}) \otimes J(n, \boldsymbol{\rho}') \qquad (A - 30)$$

The term $H(m, \boldsymbol{\rho} + \boldsymbol{\rho}')$ represents the **H**-spectral signature with respect to the origin, **o',** and $H(n, \boldsymbol{\rho})$ is **H**-spectral signature with respect to origin, **o**. $J(n, \boldsymbol{\rho}')$ represents the **J**-spectral signature of the translation vector which translates of the origin.

The important conclusion of this appendix is the property that the convolution of the spectral signature of one vector with the spectral signature of another vector will yield the spectral signature of the vector sum. The first vector may be either the Hankel spectral signature or the Bessel spectral signature and the second vector is always a Bessel spectral signature. This amounts to decomposing the vector into a convolution operation, and follows from the addition theorem. The resultant spectral signature of the sum vector will be the same as the spectral signature of the original vector. This property may be shown to extend to the sum of any number of vectors.

Appendix B: TM and TE Waves on Infinitely Long Cylinders

B.1 Magnetic Field Integral Equation and Electric Field Integral Equations

This section contains the derivation of the MFIE for TE^z polarized waves and the EFIE for TM^z polarized waves. The following derivations may be found in many electromagnetics texts [27]. Two of the more popular ones are by Harrington [35] and Balanis [36].

B.2 Perfect Electric Conductor Boundary Conditions

The boundary conditions for a perfect electric conductor are stated as follows. The tangential component of electric field is continuous across the air/conductor interface as is the normal component of magnetic flux density. The current normal to the surface boundary equals zero.

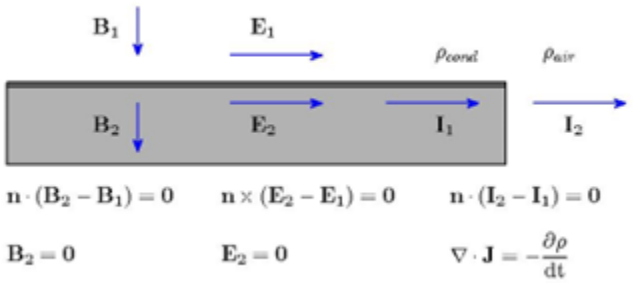

Figure B-1: PEC Boundary Conditions: Magnetic field normal to the boundary, electric field tangential to the boundary, and current on the surface of the interface.

B.3 Helmholtz Wave Equation

Calculation of the Helmholtz wave equation for the magnetic vector potential $\boldsymbol{A}$ in cylindrical coordinates begins with equation $(B-1)$, the curl of the magnetic vector potential is equal to the magnetic flux density $\boldsymbol{B}$.

$$\boldsymbol{\nabla} \times \boldsymbol{A} = \boldsymbol{B} \qquad (B-1)$$

Now taking the curl of both sides of the equation,

$$\boldsymbol{\nabla} \times \boldsymbol{\nabla} \times \boldsymbol{A} = \boldsymbol{\nabla} \times \boldsymbol{B} \qquad (B-2)$$

and expressing the magnetic flux density in terms of the magnetic field intensity $\boldsymbol{H}$,

$$\boldsymbol{\nabla} \times \boldsymbol{\nabla} \times \boldsymbol{A} = \boldsymbol{\nabla} \times \mu \boldsymbol{H} \qquad (B-3)$$

The vector $\boldsymbol{A}$ may be expanded using the identity shown in equation $(B-4)$.

$$\boldsymbol{\nabla} \times \boldsymbol{\nabla} \times \boldsymbol{A} = \boldsymbol{\nabla}(\boldsymbol{\nabla} \cdot \boldsymbol{A}) - \boldsymbol{\nabla^2 A} \qquad (B-4)$$

Substituting equation $(B-3)$ into equation $(B-4)$, one gets $(B-5)$.

$$\boldsymbol{\nabla}(\boldsymbol{\nabla} \cdot \boldsymbol{A}) - \boldsymbol{\nabla^2 A} = \boldsymbol{\nabla} \times \mu \boldsymbol{H} \qquad (B-5)$$

Recall Ampere's law in equation $(B-6)$.

$$\boldsymbol{\nabla} \times \boldsymbol{H} = \mathbf{J} + j\omega\varepsilon \boldsymbol{E} \qquad (B-6)$$

Assuming the medium is homogeneous, i.e. μ is a constant, the right-hand side of equation $(B-5)$ is replaced with the right-hand side of Ampere's law.

$$\boldsymbol{\nabla}(\boldsymbol{\nabla} \cdot \boldsymbol{A}) - \boldsymbol{\nabla^2 A} = \mu \mathbf{J} + j\omega\mu\varepsilon \boldsymbol{E} \qquad (B-7)$$

Faraday's law for time harmonic fields is written in equation $(B-8)$.

$$\boldsymbol{\nabla} \times \boldsymbol{E} = -j\omega \boldsymbol{B} \qquad (B-8)$$

Substituting equation $(B-1)$ into $(B-8)$ and rearranging one obtains equation $(B-9)$.

$$\boldsymbol{\nabla} \times (\boldsymbol{E} + j\omega \mathbf{A}) = 0 \qquad (B-9)$$

Using the vector identity in equation $(B-10)$, with ϕ_e defined as the scalar electric potential, one may write

$$\boldsymbol{\nabla} \times (-\boldsymbol{\nabla}\phi_e) = 0 \qquad (B-10)$$

Substitution into equation $(B-9)$ yields equation $(B-11)$.

$$\boldsymbol{\nabla} \times (\boldsymbol{E} + j\omega \mathbf{A}) = \boldsymbol{\nabla} \times (-\boldsymbol{\nabla}\phi_e) \qquad (B-11)$$

Then an equation for electric field may be written as equation $(B-12)$.

$$\boldsymbol{E} = -\boldsymbol{\nabla}\phi_e - j\omega \mathbf{A} \qquad (B-12)$$

Equation $(B-12)$ is substituted into equation $(B-7)$,

$$\boldsymbol{\nabla}(\boldsymbol{\nabla} \cdot \boldsymbol{A}) - \boldsymbol{\nabla^2 A} = \mu \mathbf{J} + j\omega\mu\varepsilon(-\boldsymbol{\nabla}\phi_e - j\omega \mathbf{A}) \qquad (B-13)$$

The terms of equation $(B-13)$ when reordered becomes equation $(B-14)$.

$$\boldsymbol{\nabla^2 A} + \omega^2\mu\varepsilon \boldsymbol{A} = -\mu \mathbf{J} + \boldsymbol{\nabla}(\boldsymbol{\nabla} \cdot \boldsymbol{A} + j\omega\mu\varepsilon\phi_e) \qquad (B-14)$$

Defined in equation $(B-15)$ is the Lorentz gauge,

$$\boldsymbol{\nabla} \cdot \boldsymbol{A} + j\omega\mu\varepsilon\phi_e = 0 \qquad (B-15)$$

Now substituting $(B-15)$ into equation $(B-14)$ yields the free space wave equation for the magnetic vector potential $(B-16)$ where $\beta^2 = \omega_0^2\mu\varepsilon$.

$$\boldsymbol{\nabla}^2\boldsymbol{A} + \beta^2\boldsymbol{A} = -\mu\mathbf{J} \qquad (B-16)$$

The term β is the free space wavenumber.

B.4 Free Space Helmholtz Wave Equation Source Free

For a source free region, $\mathbf{J} = \mathbf{0}$, the homogeneous wave equation is given in equation $(B-17)$.

$$\nabla^2\boldsymbol{A} + \beta^2\boldsymbol{A} = 0 \qquad (B-17)$$

The Laplacian operator in spherical coordinates is shown in equation $(B-18)$.

$$\nabla^2 = \frac{1}{R^2}\frac{\partial}{\partial R}\left(R^2\frac{\partial}{\partial R}\right) + \frac{1}{R^2 sin\theta}\frac{\partial}{\partial\theta}\left(sin\theta\frac{\partial}{\partial\theta}\right) + \frac{1}{R^2 sin^2\theta}\frac{\partial^2}{\partial\phi^2} \qquad (B-18)$$

For a plane wave using cylindrical coordinates with the magnetic vector potential aligned with the Z-axis, A_z = constant, then $\frac{\partial A_z}{\partial\theta} = 0$ and $\frac{\partial A_z}{\partial\phi} = 0$. The solution of the homogenous wave equation (source free, free space) for the magnetic vector potential $\boldsymbol{A} = \hat{\boldsymbol{a}}_{\boldsymbol{z}}A_z$, in which $\boldsymbol{A}$ is a plane wave, is given in equations$(B-19)$ through $(B-22)$.

$$\frac{1}{R^2}\frac{\partial}{\partial R}\left(R^2\frac{\partial A_z}{\partial R}\right) + \beta^2 A_z = 0 \qquad (B-19)$$

$$\frac{1}{R^2}\left(2R\frac{\partial A_z}{\partial R} + R^2\frac{\partial^2 A_z}{\partial R^2}\right) + \beta^2 A_z = 0 \qquad (B-20)$$

$$\frac{\partial^2 A_z}{\partial R^2} + \frac{2}{R}\frac{\partial A_z}{\partial R} + \beta^2 A_z = 0 \qquad (B-21)$$

$$\frac{\partial^2}{\partial R^2}(RA_z) + \beta^2 RA_z = 0 \qquad (B-22)$$

The solution to the equation $(B-22)$ in free space is given in equation $(B-23)$ in which A_z^i is the incident magnetic vector potential constant and A_z^s is the scattered magnetic vector potential constant for the homogeneous wave equation.

$$A_z = A_z^i\frac{e^{-j\beta R}}{R} + A_z^s\frac{e^{jk\beta R}}{R} \qquad (B-23)$$

The function A_z is a Green's function, specifically the zeroth order spherical Hankel function of the second kind, and is written in equation $(B-24)$,

$$h_0^{(2)}(R) = \frac{e^{j\beta R}}{R} \qquad (B-24)$$

with

$$R = \sqrt{|\rho - \rho'|^2 + (z - z')^2} \qquad (B-25)$$

Equation $(B-16)$ is called the Helmholtz vector wave equation for the magnetic vector potential with source current **J**. On the surface of a conducting body, $\boldsymbol{J_s} = \boldsymbol{J}$. The solution to the wave equation is an integral expression given in equation $(B-26)$.

$$\boldsymbol{A}(\rho) = \frac{\mu}{4\pi}\iint_S \boldsymbol{J_s}(\rho')h_0^{(2)}(\beta R)dS' \qquad (B-26)$$

The excitation current for the magnetic vector potential $\boldsymbol{A}$ is $J_z(\rho')$, and the Green's function is $h_0^{(2)}(R)$.

The magnetic vector potential may then be written as

$$A_z(\rho) = \frac{\mu}{4\pi}\iint_S J_z(\rho')h_0^{(2)}(\beta R)dS' \qquad (B-27)$$

B.5 General Helmholtz Wave Equation with Sources

Starting with equation $(B-15)$, one substitutes from equation $(B-12)$ the expression for Φ_e to calculate the electric field equation for a source free homogeneous region, i.e. μ, ε are constant.

$$\boldsymbol{E} = -j\omega\boldsymbol{A} - \frac{j}{\omega\mu\varepsilon}\boldsymbol{\nabla}(\boldsymbol{\nabla}\cdot\boldsymbol{A}) \qquad (B-28)$$

The scalar electric potential Φ_e wave equation is given as

$$\nabla^2\Phi_e + \beta^2\Phi_e = \rho_e \qquad (B-29)$$

For TM^z incident waves, $\boldsymbol{A}$ has no normal component, and $\rho_e = 0$. Therefore, from equation $(B-29)$, $\Phi_e = 0$. The divergence of the magnetic vector potential is given in equation $(B-30)$.

$$\boldsymbol{\nabla}\cdot\boldsymbol{A} = \Phi_e \qquad (B-30)$$

and so $\Phi_e = 0$, and one can then write $(B-31)$.

$$\boldsymbol{\nabla}\cdot\boldsymbol{A} = \boldsymbol{0} \qquad (B-31)$$

Now it follows that

$$\boldsymbol{\nabla}(\boldsymbol{\nabla}\cdot\boldsymbol{A}) = \boldsymbol{0} \qquad (B-32)$$

and equation $(B-28)$ can be simplified. The resulting equation becomes

$$\mathbf{E} = -j\omega \boldsymbol{A} \qquad (B-33)$$

For TM^z wave, because the current density on the surface of the cylinder is in the Z-direction only, $\boldsymbol{J_s} = J_z\hat{\boldsymbol{z}}$, and the current is a function of ρ and ϕ only, $J_z = f(\rho, \phi)$. From the continuity equation,

$$\boldsymbol{\nabla} \cdot \boldsymbol{J_s} = \frac{\boldsymbol{\partial \rho_e}}{\boldsymbol{\partial t}} \text{ with } \rho_e = 0. \qquad (B-34)$$

B.6 EFIE and TM^z Waves on PEC Infinitely Long Cylinders

If the incident field has only a Z-direction, i.e. $\boldsymbol{E^i} = \hat{\boldsymbol{z}}E^i$, then $\boldsymbol{E^s} = \hat{\boldsymbol{z}}E^s$, which satisfies the boundary condition that the tangential electric field must equal zero. Therefore, for TM^z incidence, the $\boldsymbol{A}$ must have only a $\hat{\boldsymbol{z}}$ component. Equating the $\hat{\boldsymbol{z}}$ vectors in both sides of equation $(B-34)$ one obtains equation $(B-35)$ for a time harmonic wave.

$$\mathrm{E}_z\hat{\boldsymbol{z}} = -j\omega A_z\hat{\boldsymbol{z}} \qquad (B-35)$$

Using equation $(B-27)$ and substituting the term R from $(B-25)$ into equation $(B-27)$, one may integrate with respect to z to obtain equation $(B-36)$

$$A_z(\rho) = \frac{\mu}{4\pi}\int_L J_z(\rho')\int_{-\infty}^{\infty}\left[\frac{e^{-j\beta\sqrt{|\rho-\rho'|^2+(z-z\prime)^2}}}{\sqrt{|\rho-\rho'|^2+(z-z')^2}}dz'\right]d\rho' \qquad (B-36)$$

to find a simplified expression for the magnetic vector potential for TM^z incidence.

$$A_z(\rho) = -j\frac{\mu}{4}\iint_S J_z(\rho')'\,H_0{}^{(2)}(\beta|\rho-\rho'|)d\rho' \qquad (B-37)$$

Substituting back into equation $(B-35)$, one obtains a new equation. For an infinitely long cylinder, the appropriate Green's function is the zeroth order Hankel function of the second kind $H_0{}^{(2)}$ and the expression for the scattered electric field becomes $(B-38)$.

$$E^s = -\frac{\omega\mu}{4}\iint_S J_z(\rho')'\,H_0{}^{(2)}(\beta|\rho-\rho'|)d\rho' \qquad (B-38)$$

B.7 MFIE and TE^z Waves on PEC Infinitely Long Cylinders

A TE^z polarized wave with the magnetic field aligned with the Z-axis of the cylinder is written in equation $(B-39)$,

$$\boldsymbol{H^i} = \hat{\boldsymbol{z}}H_z^i(\rho,\phi) \qquad (B-39)$$

Enforcing boundary conditions on the surface of the infinitely long PEC cylinder, one applies the magnetic field boundary conditions to equation $(B-40)$, and arrives at equation $(B-41)$ along contour C.

$$\boldsymbol{J_s}(\rho) = \hat{\boldsymbol{n}} \times (\boldsymbol{H^i} + \boldsymbol{H^s})|_C \qquad (B-40)$$

$$\boldsymbol{J_s}(\rho) = \hat{\boldsymbol{n}} \times \boldsymbol{H^i} + (\hat{\boldsymbol{n}} \times \boldsymbol{H^s})|_C \qquad (B-41)$$

For TE^z polarization, $\boldsymbol{H^i} = \hat{\boldsymbol{z}} H_z^i$, and one can write

$$\boldsymbol{J_s}(\rho) = \hat{\boldsymbol{n}} \times \hat{\boldsymbol{z}} H_z^i + (\hat{\boldsymbol{n}} \times \boldsymbol{H^s})|_C \qquad (B-42)$$

Replacing the cross product with the tangential unit vector $\hat{\boldsymbol{t}}$,

$$\boldsymbol{J_s}(\rho) = -\hat{\boldsymbol{t}} H_z^i|_C + (\hat{\boldsymbol{n}} \times \boldsymbol{H^s})|_C \qquad (B-43)$$

Now taking the dot product of both sides of the equation by $\hat{\boldsymbol{t}}$,

$$\hat{\boldsymbol{t}} \cdot \boldsymbol{J_s}(\rho) = \hat{\boldsymbol{t}} \cdot \left(-\hat{\boldsymbol{t}} H_z^i|_C + (\hat{\boldsymbol{n}} \times \boldsymbol{H^s})|_C\right) \qquad (B-44)$$

and one can write the surface current as $J_{S,t}(\rho, \phi)$.

$$J_{S,t}(\rho, \phi) = -H_z^i|_C + (\hat{\boldsymbol{t}} \cdot \hat{\boldsymbol{n}} \times \boldsymbol{H^s})|_C \qquad (B-45)$$

The surface current $\boldsymbol{J_s}$ along the cross-sectional contour C of an infinitely long cylinder equal to the tangential current $J_{S,t}$ and is given in equation $(B-46)$, with $\hat{\boldsymbol{t}}$ representing the tangential unit vector at coordinates (ρ, ϕ). The current is tangential to the surface along the contour C.

$$\boldsymbol{J_s}(\rho, \phi) = \hat{\boldsymbol{t}} J_{S,t}(\rho, \phi)|_C \qquad (B-46)$$

B.7.1 Expressing the Scattered Magnetic Field as an Integral

This section aims to rewrite the expression for the scattered magnetic field, $\boldsymbol{H^s}$. One can then derive a simpler expression for the surface current along the cross-sectional contour C. Several texts present different methods to approach deriving the MFIE and its associated terms [61-65]. One begins with

$$\boldsymbol{H^s} = \frac{1}{\mu} \boldsymbol{\nabla} \times \boldsymbol{A} \qquad (B-47)$$

For an infinitely long cylinder in the Z-direction, one substitutes for the magnetic vector potential from equation $(B-26)$. Integration must be performed to infinity in the Z-direction as shown in equation $(B-48)$.

$$\boldsymbol{H^s} = \frac{1}{\mu}\boldsymbol{\nabla} \times \frac{\mu}{4\pi}\int_C \int_{-\infty}^{\infty} \boldsymbol{J_s}(\rho')\frac{e^{-j\beta R}}{R} dz' dc' \qquad (B-48)$$

Once one integrates equation $(B-48)$ in the Z-direction, one obtains equation $(B-49)$, according to the same reason as in equation $(B-37)$ for TM^z incidence.

$$\boldsymbol{H^s} = \frac{-j}{4}\boldsymbol{\nabla} \times \int_C \boldsymbol{J_s}(\rho')H_0^{(2)}(\beta R) dC \qquad (B-49)$$

The variable R is newly defined as

$$R = \sqrt{|\rho - \rho'|^2} \qquad (B-50)$$

because the z term has been integrated out.

B.7.2 Leibniz Integral Rule

In order to simplify equation $(B-49)$ further, it is necessary to use Leibniz integral rule [65] for differentiation to bring the curl operator inside the integral. For the variable ρ in equations $(B-49)$ and $(B-50)$, one can write Leibniz integral rule as equation $(B-51)$.

$$\frac{d}{d\rho}\left(\int_{C_1(\rho)}^{C_2(\rho)} f(\rho,\rho')d\rho'\right) =$$

$$f\big(\rho, C_2(\rho)\big)\frac{d}{d\rho}C_2(\rho) - f\big(\rho, C_1(\rho)\big)\frac{d}{d\rho}C_1(\rho) + \int_{C_1(\rho)}^{C_2(\rho)} \frac{d}{d\rho} f(\rho,\rho')d\rho' \qquad (B-51)$$

If $C_1(\rho) = C_1$ is a constant, and $C_2(\rho) = C_2$ is a constant, Leibniz rule reduces to the equation $(B-52)$.

$$\frac{d}{d\rho}\left(\int_{C_1}^{C_2} f(\rho,\rho')d\rho'\right) = \int_{C_1}^{C_2} \frac{d}{d\rho} f(\rho,\rho')d\rho' \qquad (B-52)$$

Equation $(B-51)$ may be written for ρ' as well.

The curl operator may be moved inside the integral using Leibniz rule because the limits of integration C_1 and C_2 are taken at constant points along the contour, i.e. one can say $\frac{\partial C}{\partial \phi} = \frac{\partial C}{\partial z} = \frac{\partial C}{\partial \rho} = 0$.

B.7.3 Simplifying the Scattered Magnetic Field using Leibniz Integral Rule

The equation $(B-49)$ may be written as follows.

$$\boldsymbol{H^s} = \frac{-j}{4}\int_C \boldsymbol{\nabla} \times \boldsymbol{J_s}(\rho')H_0^{(2)}(\beta R)dC \qquad (B-53)$$

For the term $\boldsymbol{J_s}(\rho')H_0^{(2)}(\beta R)$ one can apply the vector identity given in equation $(B-54)$.

$$\boldsymbol{\nabla} \times (\psi \boldsymbol{W}) = \boldsymbol{\nabla}\psi \times \boldsymbol{W} + \psi \boldsymbol{\nabla} \times \boldsymbol{W} \qquad (B-54)$$

Substituting in the identity above, the integrand in $(B-54)$ may be written as $(B-55)$, where the derivative is taken with respect to ρ.

$$\boldsymbol{\nabla} \times \left(H_0^{(2)}(\beta R)\boldsymbol{J_s}(\rho')\right) = H_0^{(2)}(\beta R)\boldsymbol{\nabla} \times \boldsymbol{J_s}(\rho') - \boldsymbol{J_s}(\rho') \times \boldsymbol{\nabla}H_0^{(2)}(\beta R) \qquad (B-55)$$

The curl of the surface current term with respect to ρ in equation $(B-56)$ equals zero.

$$\boldsymbol{\nabla} \times \boldsymbol{J_s}(\rho') = 0 \qquad (B-56)$$

which yields equation $(B-57)$

$$\boldsymbol{H^s} = \frac{j}{4}\int_C \boldsymbol{J_s}(\rho') \times \boldsymbol{\nabla}H_0^{(2)}(\beta R)dC \qquad (B-57)$$

Now taking the $\widehat{\boldsymbol{n}'}$ cross product and substituting $(B-46)$ into equation $(B-53)$, one arrives at equation $(B-58)$.

$$\widehat{\boldsymbol{n}'} \times \boldsymbol{H^s} = \widehat{\boldsymbol{n}'} \times \frac{j}{4}\int_C \widehat{\boldsymbol{t}'}J_{S,t}(\rho') \times \boldsymbol{\nabla}H_0^{(2)}(\beta R)dC \qquad (B-58)$$

B.7.4 Scattered Magnetic Field Expression

To simplify the expression of the cross product of the normal vector with the scattered magnetic field, $\widehat{\boldsymbol{n}'} \times \boldsymbol{H^s}$, one begins by taking the dot product of both sides of equation $(B-58)$ with the unit vector $\widehat{\boldsymbol{t}'}$ tangential to the contour C. Also, one substitutes $J_{S,t} = J_C$ for current around the contour.

$$\widehat{\boldsymbol{t}'} \cdot \widehat{\boldsymbol{n}'} \times \boldsymbol{H^s} = \widehat{\boldsymbol{t}'} \cdot \widehat{\boldsymbol{n}'} \times \frac{j}{4}\int_C \widehat{\boldsymbol{t}'}J_C(\rho') \times \boldsymbol{\nabla}H_0^{(2)}(\beta R)dC \qquad (B-59)$$

Rearranging terms, equation $(B-59)$ results.

$$\widehat{\boldsymbol{t}'} \cdot \widehat{\boldsymbol{n}'} \times \boldsymbol{H^s} = \widehat{\boldsymbol{t}'} \cdot \widehat{\boldsymbol{n}'} \times \frac{j}{4}\int_C J_C(\rho')\left(\widehat{\boldsymbol{t}'} \times \boldsymbol{\nabla}H_0^{(2)}(\beta R)\right)dC \qquad (B-60)$$

The tangential vector to the contour $\widehat{\boldsymbol{t}'}$ for TE^z waves is equal to the cross-product expression in equation $(B-61)$.

$$\widehat{\boldsymbol{t}}' = -\widehat{\boldsymbol{n}}' \times \hat{\boldsymbol{z}} \qquad (B-61)$$

Now working with the vector dot product in parenthesis in the integrand of equation $(B-61)$, one obtains equation $(B-62)$.

$$\widehat{\boldsymbol{t}}' \times \boldsymbol{\nabla} H_0^{(2)}(\beta R) = \; -\widehat{\boldsymbol{n}}' \times \hat{\boldsymbol{z}} \times \boldsymbol{\nabla} H_0^{(2)}(\beta R) \qquad (B-62)$$

Now one uses the vector identity in equation $(B-63)$

$$\boldsymbol{A} \times (\boldsymbol{B} \times \boldsymbol{C}) = \boldsymbol{B}(\boldsymbol{A} \cdot \boldsymbol{C}) - \boldsymbol{C}(\boldsymbol{A} \cdot \boldsymbol{B}) \qquad (B-63)$$

with equation $(B-61)$ and write

$$-\widehat{\boldsymbol{n}}' \times \hat{\boldsymbol{z}} \times \boldsymbol{\nabla} H_0^{(2)}(\beta R) = -\hat{\boldsymbol{z}} \left(\widehat{\boldsymbol{n}}' \cdot \boldsymbol{\nabla} H_0^{(2)}(\beta R) \right) + \widehat{\boldsymbol{n}}' \left(\hat{\boldsymbol{z}} \cdot \boldsymbol{\nabla} H_0^{(2)}(\beta R) \right) \qquad (B-64)$$

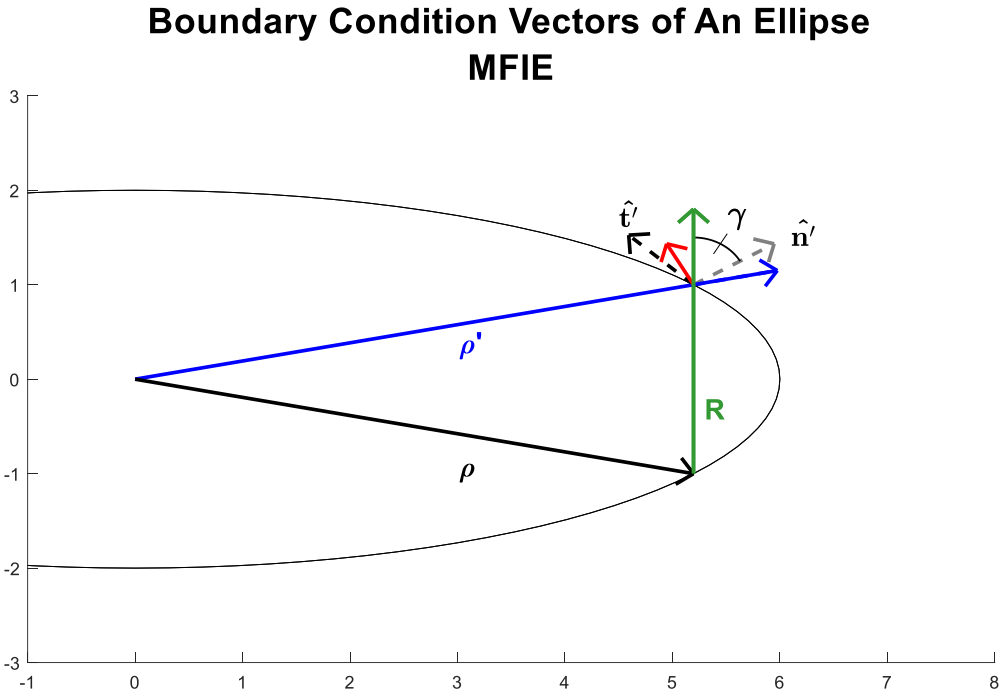

Figure B-2: Illustration of vectors associated with TE^z waves incident on an infinitely long conducting cylinder.

The unit normal vector at (ρ, ϕ) is $\widehat{\boldsymbol{n}}'$. The gradient of $H_0^{(2)}(\beta R)$ is cylindrically symmetric and cannot lie in the Z-direction. Thus, one writes

$$\hat{\boldsymbol{z}} \cdot \boldsymbol{\nabla} H_0^{(2)}(\beta R) = \boldsymbol{0} \qquad (B-65)$$

and arrives at equation $(B-66)$,

$$\widehat{\boldsymbol{t}}' \times \boldsymbol{\nabla} H_0^{(2)}(\beta R) = -\hat{\boldsymbol{z}}\left(\widehat{\boldsymbol{n}}' \cdot \boldsymbol{\nabla} H_0^{(2)}(\beta R)\right) \qquad (B-66)$$

Next taking the dot product of $(B-64)$ with the tangential unit vector,

$$\widehat{\boldsymbol{t}}' \cdot \widehat{\boldsymbol{n}}' \times \left(\widehat{\boldsymbol{t}}' \times \boldsymbol{\nabla} H_0^{(2)}(\beta R)\right) = -\widehat{\boldsymbol{t}}' \cdot \widehat{\boldsymbol{n}}' \times \hat{\boldsymbol{z}}\left(\widehat{\boldsymbol{n}}' \cdot \boldsymbol{\nabla} H_0^{(2)}(\beta R)\right) \qquad (B-67)$$

and

$$\widehat{\boldsymbol{t}}' \cdot \widehat{\boldsymbol{n}}' \times \left(\widehat{\boldsymbol{t}}' \times \boldsymbol{\nabla} H_0^{(2)}(\beta R)\right) = \widehat{\boldsymbol{n}}' \cdot \boldsymbol{\nabla} H_0^{(2)}(\beta R) \qquad (B-68)$$

because $\widehat{\boldsymbol{n}}' \times \hat{\boldsymbol{z}} = -\widehat{\boldsymbol{t}}'$ and $\widehat{\boldsymbol{t}}' \cdot \widehat{\boldsymbol{t}}' = 1$.

Now one can substitute $(B-68)$ into equation $(B-58)$, and equation $(B-69)$ results.

$$J_{S,t}(\rho,\phi) = -H_z^i|_C + \lim_{\rho \to C} \frac{j}{4} \int_C J_C(\rho')\left(\widehat{\boldsymbol{n}}' \cdot \boldsymbol{\nabla} H_0^{(2)}(\beta R)\right) dC \qquad (B-69)$$

The slope of the surface defined by the function f in the direction of the normal unit vector is called the directional derivative of f. The dot product of the normal vector $\widehat{\boldsymbol{n}}$ and the gradient of the function, $\boldsymbol{\nabla} f$, equals the derivative of the function f with respect to the normal [21,27,66].

$$\frac{\partial f}{\partial n'} = \widehat{\boldsymbol{n}}' \cdot \boldsymbol{\nabla} f \qquad (B-70)$$

Using this property of the normal vector, one can rewrite the expression in parenthesis from equation $(B-70)$ as

$$\widehat{\boldsymbol{n}}' \cdot \boldsymbol{\nabla} H_0^{(2)}(\beta R) = \frac{\partial H_0^{(2)}(\beta R)}{\partial \hat{n}} \qquad (B-71)$$

This gives an expression for the surface current density due to TE^z wave incidence on an infinitely conducting cylinder.

$$J_{S,t}(\rho,\phi) = -H_z^i|_C + \frac{j}{4} \int_C J_{S,t}(\rho') \frac{\partial H_0^{(2)}(\beta R)}{\partial \widehat{n'}} dC \qquad (B-72)$$

By taking the derivative of $H_0^{(2)}(\beta R)$ with respect to the vector ρ', the dot product $\widehat{\boldsymbol{n}} \cdot \boldsymbol{\nabla} H_0^{(2)}$ can be written as equation $(B-73)$, where $\widehat{\boldsymbol{R}}$ is the unit vector of $\boldsymbol{R}$ from coordinates (ρ', ϕ') to (ρ, ϕ).

$$\widehat{\boldsymbol{n}}' \cdot \boldsymbol{\nabla} H_0^{(2)}(\beta R) = \left(\widehat{\boldsymbol{n}}' \cdot \widehat{\boldsymbol{R}}\right) \beta H_1^{(2)}(\beta R) \qquad (B-73)$$

and equation $(B-72)$ may be written as $(B-74)$,

$$J_C(\rho,\phi) = -H_z^i|_C + \frac{j}{4}\int_C J_C(\rho')\left(\widehat{\boldsymbol{n}}' \cdot \widehat{\boldsymbol{R}}\right)\beta H_1^{(2)}(\beta R)\, dC \qquad (B-74)$$

The dot product in equation $(B-74)$ may also be written as a cosine function. See Figure B-1 for an illustration of the vectors and angle γ.

$$\widehat{\boldsymbol{n}}' \cdot \boldsymbol{\nabla} H_0^{(2)}(\beta R) = cos(\gamma)\beta H_1^{(2)}(\beta R) \qquad (B-75)$$

This gives another expression for the current density due to TE^z wave incidence on an infinitely conducting cylinder.

$$J_C(\rho,\phi) = -H_z^i|_C + \frac{j\beta}{4}\int_C J_C(\rho')cos(\gamma)H_1^{(2)}(\beta R)\, dC \qquad (B-76)$$

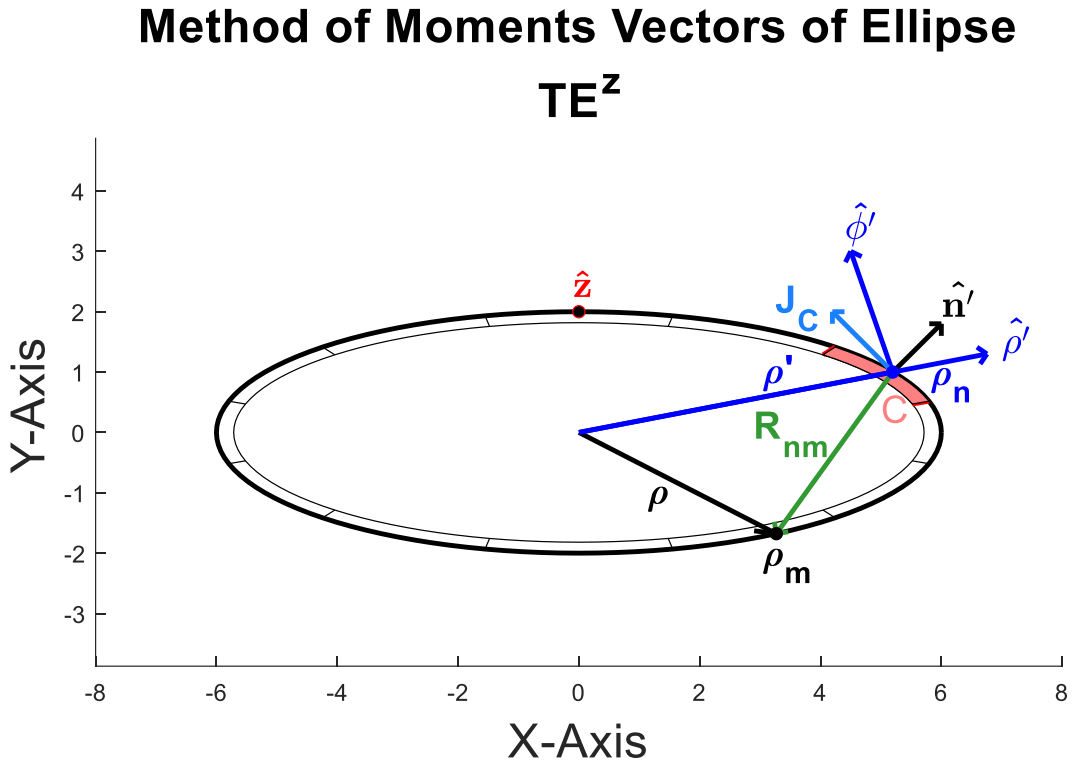

Figure B-3: Illustration of vectors $\widehat{\boldsymbol{\rho}}'$, $\widehat{\boldsymbol{\phi}}'$, and $\widehat{\boldsymbol{n}}'$ associated with TE^z waves incident on an infinitely long elliptical conducting cylinder at contour segment C. The contour current $J_C(\rho')$ is tangential to the surface.

Appendix C: SPM and Modal Analysis of Circular Cylinder

C.1 SPM for Incident Electric Line Sources and Magnetic Line Sources

In this section a comparison of the Spectral Projection Model to modal analysis for TM^z and TE^z incident waves impingent upon the surface of a PEC infinitely long circular cylinder is presented. These fields were calculated using modal analysis in Balanis [36]. Two external sources are covered, a near-field excitation from an electric line current, and a far-field excitation from a TM^z plane wave. The same fields are then calculated using the Spectral Projection Model and the results are compared.

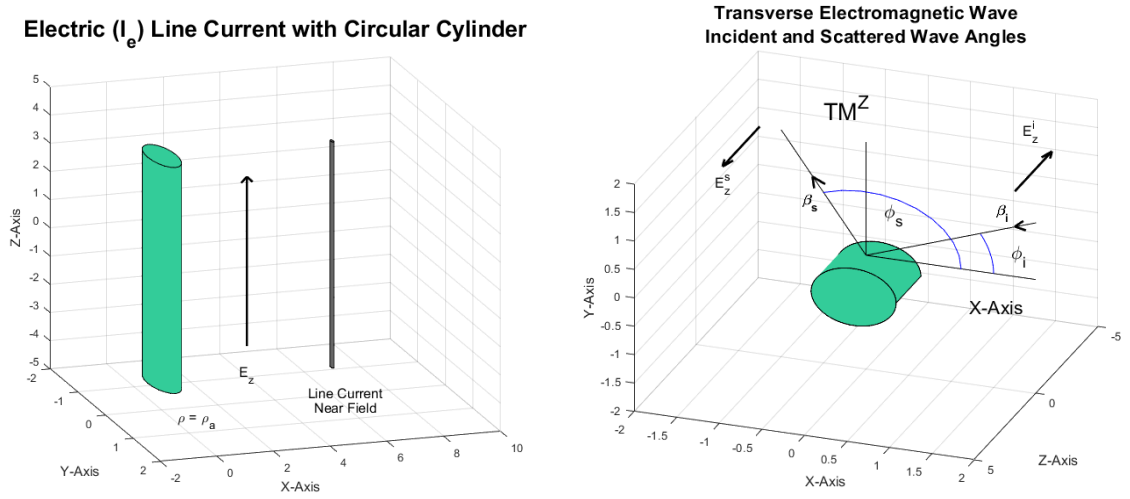

a) b)

Figure C-1: a) Near-field and b) far-field TM^z plane wave incident on a conducting cylinder.

C.2 Modal Analysis and SPM for Electric Line Sources

In Figure C-1 an electric line source is illustrated. The electric line source is located at polar coordinates $(\rho', \phi') = (\rho_0, \phi_0)$. The radiated electric near-field E_z of an electric line current is parallel to the axis of the cylinder and line source (Z-axis). The electromagnetic fields are TM^z polarized in the far-field. See equation $(C-1)$.

$$E_z(\beta|\boldsymbol{\rho}-\boldsymbol{\rho}'|) = -\frac{\beta^2 I_e}{4\omega\varepsilon} H_0^{(2)}(\beta|\boldsymbol{\rho}-\boldsymbol{\rho}'|) \qquad (C-1)$$

The electric current line source is constant magnitude, I_e, and time harmonic. The magnetic field has both radial and azimuthal components which are transverse to the axis of the cylinder.

To satisfy boundary conditions, the total modal solution for the TM^z tangential component of the electric field E_z^t near the surface of a circular cylinder is the sum of the incident and scattered fields. Equation $(C-2)$ expresses the boundary condition for the incident and scattered electric fields in the Z-direction for a circular cylinder of radius, $\rho = a$.

$$E_z^t(\rho) = E_z^i(\rho) + E_z^s(\rho) = 0 \qquad (C-2)$$

The modal solution [47] for the tangential electric field for the condition $a \le \rho \le \rho'$ is shown below in equation $(C-3)$.

$$E_z^t = -\frac{\beta^2 I_e}{4\omega\varepsilon}\sum_{k=-\infty}^{\infty} H_k^{(2)}(\beta|\boldsymbol{\rho}'|)\left[J_k(\beta|\boldsymbol{\rho}|) - \frac{J_k(\beta a)}{H_k^{(2)}(\beta a)}H_k^{(2)}(\beta|\boldsymbol{\rho}|)\right]e^{jk(\phi-\phi')} \qquad (C-3)$$

Equation $(C-3)$ may also be derived using the Spectral Projection Model. Firstly, begin with the incident electric field E_z^i written as the projection of the **H**-spectral signature of the source points (ρ', ϕ') onto the **J**-spectral signature of the observation points (ρ, ϕ) multiplied by the magnitude of the electric line current, I_e and a scaling factor $\frac{\beta^2}{4\omega\varepsilon}$.

$$E_z^i = -\frac{\beta^2 I_e}{4\omega\varepsilon} e_{om}^T e_{sn} \qquad a \le \rho \le \rho' \qquad (C-4)$$

The Hankel spectral signature of a source point at (ρ', ϕ') is designated as e_{sn},

$$e_{sn} = \left[H_K^{(2)}(\beta|\boldsymbol{\rho}'|)e^{-jK\phi'} \quad .. \quad H_k^{(2)}(\beta|\boldsymbol{\rho}'|)e^{jk\phi'} \quad ... \quad H_{-K}^{(2)}(\beta|\boldsymbol{\rho}'|)e^{jK\phi'}\right]^T \qquad (C-5)$$

and the Bessel spectral signature of an observation point, (ρ, ϕ), is e_{om}.

$$e_{om} = \left[J_{-K}(\beta|\boldsymbol{\rho}|)e^{-jK\phi} \quad .. \quad J_k(\beta|\boldsymbol{\rho}|)e^{jk\phi} \quad ... \quad J_K(\beta|\boldsymbol{\rho}|)e^{jK\phi}\right]^T \qquad (C-6)$$

After projecting e_{sn} onto e_{om} and multiplying by a scaling factor, $-\frac{\beta^2}{4\omega\varepsilon}$, the resulting incident electric field E_z^i is equivalent to the modal solution truncated to $2K+1$ modes. Both are written in equations $(C-7)$ and $(C-8)$.

$$E_z^i = -\frac{\beta^2 I_e}{4\omega\varepsilon}\sum_{k=-\infty}^{\infty} H_k^{(2)}(\beta|\boldsymbol{\rho}'|)J_k(\beta|\boldsymbol{\rho}|)e^{jk(\phi-\phi')} \qquad a \le \rho \le \rho' \qquad (C-7)$$

Modal Solution Electric Line Source – Incident Field

$$E_z^i = -\frac{\beta^2 I_e}{4\omega\varepsilon}\sum_{k=-K}^{K} H_k^{(2)}(\beta|\boldsymbol{\rho}'|)J_k(\beta|\boldsymbol{\rho}|)e^{jk(\phi-\phi')} \qquad a \le \rho \le \rho' \qquad (C-8)$$

Spectral Projection Model Electric Line Source - Incident Field

The scattered electric field for these two points may now be written in projection form as equation $(C-9)$. To determine the scattered electric field from a circular cylinder, the **J**-spectral signature of every induced electric line currents at (ρ', ϕ') is projected onto the **H**-spectral signature of the observation points located at (ρ, ϕ).

$$E_z^s = -\frac{\beta^2 I_e}{4\omega\varepsilon} e_{om}^T e_{sn} \qquad a \le \rho \le \rho' \qquad (C-9)$$

The spectral signature of an induced electric line current at (ρ', ϕ') is given in equation $(C-10)$, with factors c_k used to satisfy the boundary conditions. The vector in equation $(C-10)$ equivalently represents the **J**-spectral signature of the induced currents.

$$e_{sn} = \left[c_K e^{-jK\phi'} \quad .. \quad c_k e^{jk\phi'} \quad ... \quad c_{-K} e^{j(K-1)\phi'}\right]^T \qquad (C-10)$$

The **H**-spectral signature of an observation point, (ρ, ϕ) is e_{om}.

$$e_{om} = \left[H_{-K}^{(2)}(\beta|\boldsymbol{\rho}|)e^{-jK\phi} \quad .. \quad H_k^{(2)}(\beta|\boldsymbol{\rho}|)e^{jk\phi} \quad ... \quad H_K^{(2)}(\beta|\boldsymbol{\rho}|)e^{jK\phi}\right]^T \qquad (C-11)$$

To determine the terms c_k, the boundary conditions must be applied, and these c_k terms ensure that the boundary conditions at the surface of the conductor are satisfied. The term is $c_k = \frac{J_k(\beta a)H_k^{(2)}(\beta\rho')}{H_k^{(2)}(\beta a)}$. This equals the modal reflection coefficient of the electric field at the surface of the conductor multiplied by the Hankel function. The scattered electric field from the modal solution is given in equation $(C-12)$.

$$E_z^s = \frac{\beta^2 I_e}{4\omega\varepsilon}\sum_{k=-\infty}^{\infty} H_k^{(2)}(\beta|\boldsymbol{\rho}|)\frac{J_k(\beta a)}{H_k^{(2)}(\beta a)}H_k^{(2)}(\beta|\boldsymbol{\rho}'|)e^{jk(\phi-\phi')} \qquad a \le \rho \le \rho' \qquad (C-12)$$

The equivalent **J**-spectral signature of an induced current source point e_{sn} is written in equation $(C-13)$.

$$e_{sn} = \left[\frac{J_{-K}(\beta a)}{H_{-K}^{(2)}(\beta a)}H_{-K}^{(2)}(\beta|\boldsymbol{\rho}'|)e^{jK\phi'} \quad ... \quad \frac{J_{-k}(\beta a)}{H_{-k}^{(2)}(\beta a)}H_{-k}^{(2)}(\beta|\boldsymbol{\rho}'|)e^{jk\phi'} \quad ...\right.$$

$$\left.\frac{J_K(\beta a)}{H_K^{(2)}(\beta a)}H_K^{(2)}(\beta|\boldsymbol{\rho}'|)e^{-jK\phi'}\right]^T \qquad (C-13)$$

The projection of e_{sn} onto e_{om} is now equal to the scattered electric field E_z^s in equation $(C-15)$ truncated to $2K+1$ modes.

$$E_z^s = \frac{\beta^2 I_e}{4\omega\varepsilon}\sum_{k=-\infty}^{\infty} H_k^{(2)}(\beta|\boldsymbol{\rho}|)\frac{J_k(\beta a)}{H_k^{(2)}(\beta a)}H_k^{(2)}(\beta|\boldsymbol{\rho}'|)e^{jk(\phi-\phi')} \qquad a \le \rho \le \rho' \qquad (C-14)$$

Modal Solution Electric Line Source - Scattered Field

$$E_z^s = \frac{\beta^2 I_e}{4\omega\varepsilon}\sum_{k=-K}^{K} H_k^{(2)}(\beta|\boldsymbol{\rho}|)\frac{J_k(\beta a)}{H_k^{(2)}(\beta a)}H_k^{(2)}(\beta|\boldsymbol{\rho}'|)e^{jk(\phi-\phi')} \qquad a \le \rho \le \rho' \qquad (C-15)$$

Spectral Projection Model Electric Line Source - Scattered Field

For an infinitely long circular cylinder excited by a TM^z plane wave using modal analysis the far-field solution $\rho' > \rho$ to the tangential electric field is given in equation $(C-16)$.

$$E_z^t = E_0\sum_{k=-\infty}^{\infty} j^{-k}\left[J_k(\beta|\boldsymbol{\rho}|) - \frac{J_k(\beta a)}{H_k^{(2)}(\beta a)}H_k^{(2)}(\beta|\boldsymbol{\rho}|)\right]e^{jk(\phi-\phi_i)} \qquad (C-16)$$

The incident plane wave from the modal solution in equation $(C-16)$ is shown in equation $(C-17)$. This can be recognized as the wave equation.

$$E_z^i = E_0\sum_{k=-\infty}^{\infty} j^{-k}J_k(\beta|\boldsymbol{\rho}|)e^{jk(\phi-\phi_i)} \qquad (C-17)$$

For an incident plane wave coming from $(\rho' \to \infty, \phi' = \phi_i)$ one simply replaces the Hankel function $H_k^{(2)}(\beta|\boldsymbol{\rho}'|)$ with its asymptotic approximation $e^{-\frac{jk\pi}{2}}$. The Hankel spectral signature of the plane wave source is e_{sn}, and written as $(C-18)$, but instead using the asymptotic expansion.

$$e_{sn} = \left[e^{-jK\left(\phi'+\frac{\pi}{2}\right)} \quad \ldots \quad e^{jk\left(\phi'+\frac{\pi}{2}\right)} \quad \ldots \quad e^{jK\left(\phi'+\frac{\pi}{2}\right)}\right]^T \qquad (C-18)$$

The Bessel spectral signature of an observation point, (ρ, ϕ), is still e_{om}.

$$e_{om} = \left[J_{-K}(\beta|\boldsymbol{\rho}|)e^{-jK\phi} \quad \ldots \quad J_k\,(\beta|\boldsymbol{\rho}|) \quad \ldots \quad J_{K-1}(\beta|\boldsymbol{\rho}|)e^{jK\phi}\right]^T \qquad (C-19)$$

Now projecting e_{sn} onto e_{om} and multiplying by E_0, the incident electric field E_z^i is given in equation $(C-20)$.

$$E_z^i = E_0 e_{om}^T e_{sn} \qquad (C-20)$$

$$E_z^i = E_0 \sum_{k=-\infty}^{\infty} j^{-k} J_k(\beta|\boldsymbol{\rho}|) e^{jk(\phi-\phi_i)} \qquad (C-21)$$

Modal Solution TM^z Plane Wave – Incident Field

$$E_z^i = E_0 \sum_{k=-K}^{K} j^{-k} J_k(\beta|\boldsymbol{\rho}|) e^{jk(\phi-\phi_i)} \qquad (C-22)$$

Spectral Projection Model TM^z Plane Wave - Incident Field

The scattered electric field may be written as the projection of e_{sn} onto e_{om}, shown in equation $(C-23)$.

$$E_z^s = E_0 e_{om}^T e_{sn} \qquad (C-23)$$

The equivalent **J**-spectral signature of the induced current is given in equation $(C-24)$,

$$e_{sn} = \left[j^{-K} \frac{J_{-K}(\beta|\boldsymbol{a}|)}{H_{-K}^{(2)}(\beta|\boldsymbol{a}|)} e^{jK\phi'} \quad \ldots \quad j^{-k} \frac{J_{-k}(\beta|\boldsymbol{a}|)}{H_{-k}^{(2)}(\beta|\boldsymbol{a}|)} e^{jk\phi'} \quad \ldots \quad j^{K} \frac{J_K(\beta|\boldsymbol{a}|)}{H_K^{(2)}(\beta|\boldsymbol{a}|)} e^{-jK\phi'} \right]^T \qquad (C-24)$$

and the Hankel spectral signature of the observation points given in equation $(C-25)$,

$$e_{om} = \left[H_{-K}^{(2)}(\beta|\boldsymbol{\rho}|) e^{-jK\phi} \quad .. \quad H_{-k}^{(2)}(\beta|\boldsymbol{\rho}|) e^{-jk\phi} \quad \ldots \quad H_K^{(2)}(\beta|\boldsymbol{\rho}|) e^{jK\phi} \right]^T \qquad (C-25)$$

The modal solution to the scattered electric field E_z^s from equation $(C-14)$ for the near field is instead written as equation $(C-26)$ with the Hankel function term $H_k^{(2)}(\beta|\boldsymbol{\rho}'|)e^{jk\phi'}$ replaced with j^{-n}. The SPM scattered field in equation $(C-23)$ truncated to $2K+1$ modes is E_z^s from SPM and shown in equation $(C-27)$.

$$E_z^s = -E_0 \sum_{k=-\infty}^{\infty} j^{-k} \frac{J_k(\beta|\boldsymbol{a}|)}{H_k^{(2)}(\beta|\boldsymbol{a}|)} H_k^{(2)}(\beta|\boldsymbol{\rho}|) e^{jk(\phi-\phi')} \qquad (C-26)$$

Modal Solution TM^z Plane Wave - Scattered Field

$$E_z^s = -E_0 \sum_{k=-K}^{K} j^{-k} \frac{J_k(\beta|\boldsymbol{a}|)}{H_k^{(2)}(\beta|\boldsymbol{a}|)} H_k^{(2)}(\beta|\boldsymbol{\rho}|) e^{jk(\phi-\phi')} \qquad (C-27)$$

Spectral Projection Model TM^z Plane Wave - Scattered Field

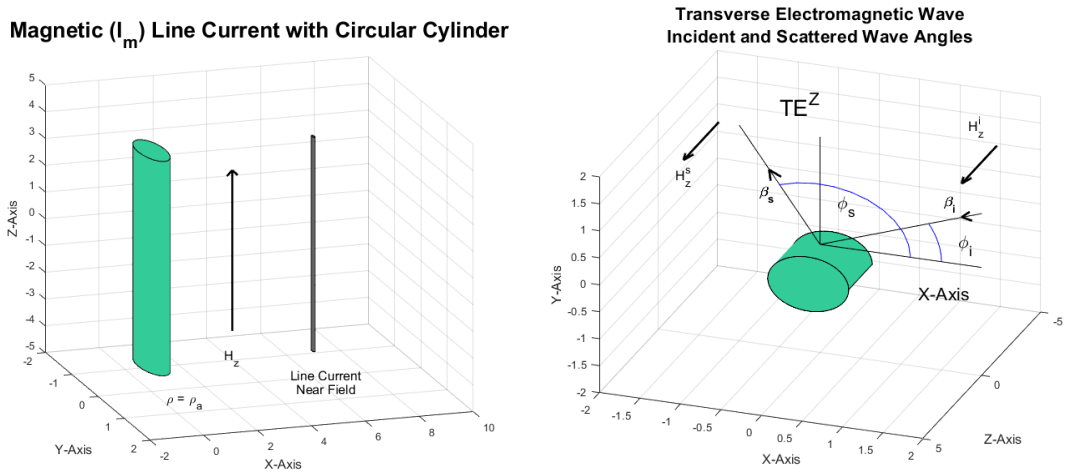

a) b)

Figure C-2: a) Near-field and b) far-field TE^z plane wave incident on a conducting cylinder.

C.3 Modal Analysis and SPM for Magnetic Line Sources

In this section the tangential magnetic field on the surface of an infinitely long circular cylinder is presented. These fields are calculated using modal analysis and can be found in Balanis [36]. A near-field excitation from a magnetic line current and a far-field excitation from a TE^z plane wave will be the two external sources. The Spectral Projection Model is used to calculate these fields.

In Figure C-2 a magnetic line source is shown. The magnetic line source is located at polar coordinates $(\rho', \phi') = (\rho_0, \phi_0)$. The radiated magnetic near-field H_z from a magnetic line current is parallel to the axis of the line source and the cylinder. From equation $(C-28)$ given earlier, the magnetic field is described by a Hankel function $H_0^{(2)}(\beta|\boldsymbol{\rho}-\boldsymbol{\rho}'|)$.

$$H_z(\beta|\boldsymbol{\rho}-\boldsymbol{\rho}'|) = -\frac{\beta^2 I_m}{4\omega\mu} H_0^{(2)}(\beta|\boldsymbol{\rho}-\boldsymbol{\rho}'|) \qquad (C-28)$$

The magnetic current line source is constant magnitude, I_m, and time harmonic. The radiated electric field has both radial and azimuthal components which are transverse to the axis of the cylinder.

To satisfy magnetic field boundary conditions for TE^z waves, the tangential component of the magnetic field H_z^t at the surface of a circular cylinder is related to the surface current by equation $(C-29)$.

$$\boldsymbol{J_S} = \hat{\boldsymbol{n}} \times (\boldsymbol{H^i} + \boldsymbol{H^s}) \qquad (C-29)$$

Equation $(C-29)$ expresses the boundary condition for the incident and scattered magnetic fields in the Z-direction for a circular cylinder of radius, $\rho = a$. The term $J_C(\rho_m)$ is the self-term which is normally absorbed into the scattered field expression.

$$H_z^i = -[H_z^s + J_C(\rho_m = a)] \qquad (C-30)$$

The modal solution for the H_z^{tan} tangential components of the magnetic field are shown below in equations $(C-31)$.

$$H_z^t = -\frac{\beta^2 I_m}{4\omega\mu} \sum_{k=-\infty}^{\infty} H_k^{(2)}(\beta|\boldsymbol{\rho}'|) \left[J_k(\beta|\boldsymbol{\rho}|) - \frac{J_k{}'(\beta a)}{H_k^{(2)}{}'(\beta a)} H_k^{(2)}(\beta|\boldsymbol{\rho}|) \right] e^{jk(\phi-\phi')} \qquad a \le \rho \le \rho' \qquad (C-31)$$

To determine the H_z^{tan} tangential solution using SPM, the incident magnetic field H_z^i is found first. It is the projection of the **H**-spectral signature of the source points onto the **J**-spectral signature of the observation points multiplied by the magnitude of the magnetic line current I_m and a scaling factor $-\frac{\beta^2}{4\omega\mu}$.

The Hankel spectral signature of a source point at (ρ', ϕ') is e_{sn}, shown in equation $(C-32)$.

$$e_{sn} = \left[H_{-K}^{(2)}(\beta|\boldsymbol{\rho}'|) e^{jK\phi'} \quad .. \quad H_{-k}^{(2)}(\beta|\boldsymbol{\rho}'|) e^{jk\phi'} \quad ... \quad H_K^{(2)}(\beta|\boldsymbol{\rho}'|) e^{-jK\phi'} \right]^T \qquad (C-32)$$

The Bessel spectral signature of an observation point, (ρ, ϕ) is e_{om}.

$$e_{om} = \left[J_{-K}(\beta|\boldsymbol{\rho}|) e^{-jK\phi} \quad .. \quad J_k\,(\beta|\boldsymbol{\rho}|) \quad ... \quad J_K(\beta|\boldsymbol{\rho}|) e^{jK\phi} \right]^T \qquad (C-33)$$

By projecting e_{sn} onto e_{om} and multiplying by a scaling factor, $-\frac{\beta^2 I_m}{4\omega\mu}$, the incident magnetic field is now be written as equation $(C-34)$.

$$H_z^i = -\frac{\beta^2 I_m}{4\omega\mu} e_{om}^T e_{sn} \qquad a \le \rho \le \rho' \qquad (C-34)$$

The incident tangential component of the magnetic field H_z^i from the modal solution is written in $(C-35)$.

$$H_z^i = -\frac{\beta^2 I_m}{4\omega\mu}\sum_{k=-\infty}^{\infty} J_k(\beta|\boldsymbol{\rho}|)H_k^{(2)}(\beta|\boldsymbol{\rho}'|)e^{jk(\phi-\phi')} \qquad a \le \rho \le \rho' \qquad (C-35)$$

The incident tangential component of the magnetic field H_z^i from the SPM truncated to $2K+1$ modes is written in $(C-37)$.

$$H_z^i = -\frac{\beta^2 I_m}{4\omega\mu}\sum_{k=-\infty}^{\infty} J_k(\beta|\boldsymbol{\rho}|)H_k^{(2)}(\beta|\boldsymbol{\rho}'|)e^{jk(\phi-\phi')} \qquad a \le \rho \le \rho' \qquad (C-36)$$

Modal Solution Magnetic Line Source – Incident Field

$$H_z^i = -\frac{\beta^2 I_m}{4\omega\mu}\sum_{k=-K}^{K} J_k(\beta|\boldsymbol{\rho}|)H_k^{(2)}(\beta|\boldsymbol{\rho}'|)e^{jk(\phi-\phi')} \qquad a \le \rho \le \rho' \qquad (C-37)$$

Spectral Projection Model Solution Magnetic Line Source – Incident Field

The scattered magnetic field H_z^s is due to induced electric currents on the surface of the conductor. From the modal solution, H_z^s is written in equation $(C-38)$.

$$H_z^s = \frac{\beta^2 I_m}{4\omega\mu}\sum_{k=-\infty}^{\infty} \frac{J_k{}'(\beta a)}{H_k^{(2)\prime}(\beta a)} H_k^{(2)}(\beta|\boldsymbol{\rho}|)H_k^{(2)}(\beta|\boldsymbol{\rho}'|)e^{jk(\phi-\phi')} \qquad a \le \rho \le \rho' \qquad (C-38)$$

For $a \le \rho \le \rho'$, H_z^s is equal to the **J**-spectral signature of the source currents projected onto the **H**-spectral signature of the observation points. For the scattered tangential magnetic field, the vector e_{sn} is projected onto e_{om} and multiplied the magnetic current I_m and a scaling factor $\frac{\beta^2}{4\omega\mu}$. The scattered magnetic field is written in equation $(C-39)$.

$$H_z^s = \frac{\beta^2 I_m}{4\omega\mu} e_{om}^T e_{sn} \qquad a \le \rho \le \rho' \qquad (C-39)$$

The Hankel spectral signature of the observation points given in equation $(C-40)$,

$$e_{om} = \left[H_{-K}^{(2)}(\beta|\boldsymbol{\rho}|)e^{jK\phi} \quad .. \quad H_{-k}^{(2)}(\beta|\boldsymbol{\rho}|)e^{jk\phi} \quad ... \quad H_{K-1}^{(2)}(\beta|\boldsymbol{\rho}|)e^{-jK\phi}\right]^T \qquad (C-40)$$

The Bessel spectral signature of an induced electric current source point at the circular cylinder surface is e_{sn} shown in equation $(C-41)$.

$$e_{sn} = \left[\frac{J_{-K}{}'(\beta a)}{H_{-K}^{(2)\prime}(\beta a)} H_{-K}^{(2)}(\beta|\boldsymbol{\rho}'|)e^{jK\phi'} \quad ... \quad \frac{J_{-k}{}'(\beta a)}{H_{-k}^{(2)\prime}(\beta a)} H_{-k}^{(2)}(\beta|\boldsymbol{\rho}'|)e^{jk\phi'} \quad ...\right.$$

$$\left.\frac{J_K(\beta a)'}{H_K^{(2)}(\beta a)'} H_K^{(2)}(\beta|\boldsymbol{\rho}'|)e^{-jK\phi'}\right]^T \qquad (C-41)$$

The term $\frac{J_n{}'(\beta a)}{H_n^{(2)}{}'(\beta a)}$ is the modal reflection coefficient. The projection product $e_{om}^T e_{sn}$ is given in equation $(C-42)$.

$$H_z^s = \frac{\beta^2 I_m}{4\omega\mu}\sum_{k=-\infty}^{\infty}\frac{J_k{}'(\beta a)}{H_k^{(2)}{}'(\beta a)}H_k^{(2)}(\beta|\boldsymbol{\rho}|)H_k^{(2)}(\beta|\boldsymbol{\rho}'|)e^{jk(\phi-\phi')} \qquad a \le \rho \le \rho' \qquad (C-38)$$

Modal Solution Magnetic Line Source – Scattered Field

$$H_z^s = \frac{\beta^2 I_m}{4\omega\mu}\sum_{k=-K}^{K}\frac{J_k{}'(\beta a)}{H_k^{(2)}{}'(\beta a)}H_k^{(2)}(\beta|\boldsymbol{\rho}|)H_k^{(2)}(\beta|\boldsymbol{\rho}'|)e^{jk(\phi-\phi')} \qquad a \le \rho \le \rho' \qquad (C-42)$$

Spectral Projection Model Solution Magnetic Line Source – Scattered Field

For a magnetic line current source in the far-field radiates a magnetic field with TE^z polarization upon a PEC infinitely long circular cylinder the radiated magnetic field is parallel to the axis of the cylinder and line source. The electric field has both radial and azimuthal components which are transverse to the axis of the cylinder.

The modal solution for the H_z^t tangential components of the magnetic field due to far-field excitation is shown below.

$$H_z^t = H_0\sum_{k=-\infty}^{\infty} j^{-k}\left[J_k(\beta\rho) - \frac{J_k{}'(\beta a)}{H_k^{(2)}{}'(\beta a)}H_k^{(2)}(\beta\rho)\right]e^{jk\phi} \qquad (C-43)$$

The incident magnetic field is given in equations $(C-46)$ and $(C-48)$ as the projection of the Hankel spectral signature of the magnetic far-field $(C-44)$ onto **J**-spectral signature of an observation point on the cylinder surface $(C-45)$ truncated to $2K+1$ modes. This agrees with the modal solution $(C-47)$.

The Hankel spectral signature of the incident plane wave source is e_{sn}, and written as $(C-45)$.

$$e_{sn} = \left[e^{-jK\left(\phi'+\frac{\pi}{2}\right)} \quad \dots \quad e^{jk\left(\phi'+\frac{\pi}{2}\right)} \quad \dots \quad e^{jK\left(\phi'+\frac{\pi}{2}\right)}\right]^T \qquad (C-44)$$

The Bessel spectral signature of an observation point, (ρ,ϕ), is still e_{om}.

$$e_{om} = \left[J_{-K}(\beta|\boldsymbol{\rho}|)e^{-jK\phi} \quad \dots \quad J_k\,(\beta|\boldsymbol{\rho}|) \quad \dots \quad J_{K-1}(\beta|\boldsymbol{\rho}|)e^{jK\phi}\right]^T \qquad (C-45)$$

$$H_t^i = H_0 e_{om}^T e_{sn} \qquad (C-46)$$

$$H_i^t = H_0 \sum_{k=-\infty}^{\infty} j^{-k} J_k(\beta|\boldsymbol{\rho}|) e^{jk\phi} \qquad (C-47)$$

Modal Solution TE^z Plane Wave - Incident Field

$$H_i^t = H_0 \sum_{k=-K}^{K} j^{-k} J_k(\beta|\boldsymbol{\rho}|) e^{jk\phi} \qquad (C-48)$$

Spectral Projection Model Solution TE^z Plane Wave - Incident Field

The scattered magnetic field H_z^S is due to induced currents on the surface of the conductor. It is equal to the spectral signature of the source points projected onto the **H**-spectral signature of the observation points multiplied by the magnitude of the magnetic field H_0. Using SPM, the spectral signature of the induced currents comes from equation $(C-49)$.

$$e_{sn} = \left[j^{-K} \frac{J_K{}'(\beta|\boldsymbol{a}|)}{H_K^{(2)\prime}(\beta|\boldsymbol{a}|)} e^{jK\phi'} \quad \ldots \quad j^{-k} \frac{J_k{}'(\beta|\boldsymbol{a}|)}{H_k^{(2)\prime}(\beta|\boldsymbol{a}|)} e^{jk\phi'} \quad \ldots \quad j^{K} \frac{J_{-K}{}'(\beta|\boldsymbol{a}|)}{H_{-K}^{(2)\prime}(\beta|\boldsymbol{a}|)} e^{-jK\phi'} \right]^T \qquad (C-49)$$

The vector e_{sn} is projected onto the Hankel spectral signature of the observation points.

$$e_{om} = \left[H_{-K}^{(2)}(\beta|\boldsymbol{\rho}|) e^{-jK\phi} \quad .. \quad H_{-k}^{(2)}(\beta|\boldsymbol{\rho}|) e^{-jk\phi} \quad \ldots \quad H_K^{(2)}(\beta|\boldsymbol{\rho}|) e^{jK\phi} \right]^T \qquad (C-50)$$

Thus, the scattered magnetic field may be written as the projection of e_{sn} onto e_{om}, shown in equation $(C-51)$.

$$H_z^S = H_0 e_{om}^T e_{sn} \qquad (C-51)$$

Equation $(C-51)$, shown in summation form in equation $(C-53)$ and truncated to $2K+1$ modes, agrees with the modal model scattered field given in Balanis [36] equation $(C-52)$.

$$H_z^S = -H_0 \sum_{k=-\infty}^{\infty} j^{-k} \frac{J_k{}'(\beta a)}{H_k^{(2)\prime}(\beta a)} H_k^{(2)}(\beta\rho) e^{jk\phi} \qquad (C-52)$$

Modal Solution TE^z Plane Wave - Scattered Field

$$H_z^s = -H_0 \sum_{k=-\infty}^{\infty} j^{-k} \frac{J_k{}'(\beta a)}{H_k^{(2)}{}'(\beta a)} H_k^{(2)}(\beta\rho) e^{jk\phi} \qquad (C-53)$$

Spectral Projection Model Solution TE^z Plane Wave – Scattered Field

Appendix D: Bessel Functions

D.1 Bessel's Equation

The following derivations may be found in many electromagnetics texts. Many years before Bessel's investigation into cylindrical functions, Joseph Fourier used a form of Bessel's differential equation in his famous work Analytic Theory of Heat [1-5]. This equation is now known as Bessel's equation of order n,

$$x^2 \frac{\partial^2 y}{\partial^2 x} + x \frac{\partial y}{\partial x} + (x^2 - n^2)y = 0 \qquad (D-1)$$

Friedrich Bessel, for whom the functions are named, derived the Bessel differential equation by investigating a problem dealing with elliptical motion and did an extensive study of Bessel functions and their solutions [58]. Bessel's equation and its associated Bessel functions $J_n(x)$ are used to describe the electric potential in objects that have cylindrical symmetry. Bessel functions are also used in solving time harmonic electromagnetic field problems too. The Spectral Projection Model in this dissertation deals exclusively with solving time harmonic electric field scattering problems in 2D for objects with cylindrical symmetry. A plot of several Bessel functions of the first kind is shown in Figure D-1.

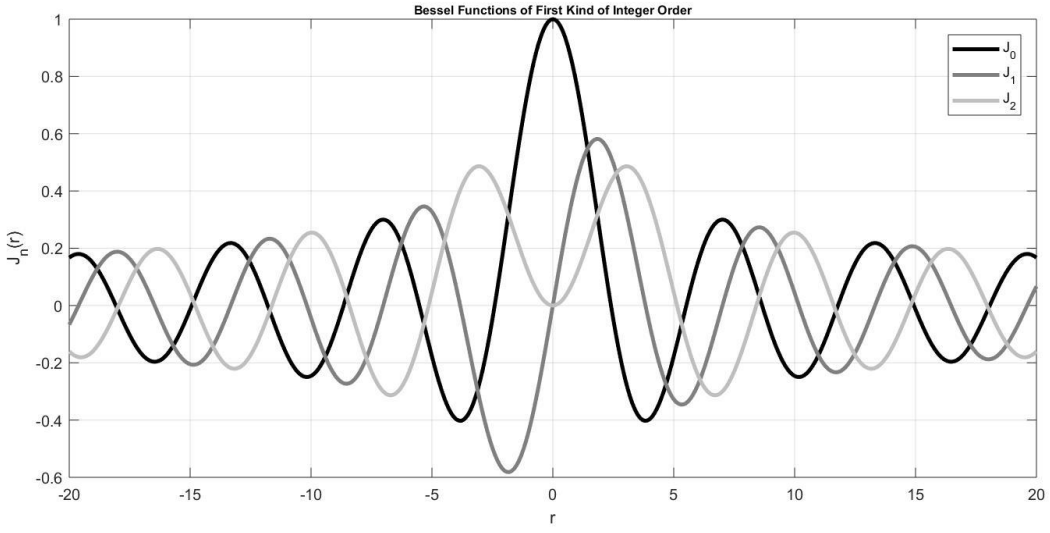

Figure D-1: Plot of Bessel function of the first kind for several orders.

In 1824 Friedrich Bessel wrote extensively on functions describing planetary motion [5,59]. He derived many properties of the function described below:

$$J_n(x) = \frac{1}{2\pi}\int_0^{2\pi} cos(n\theta - xsin\theta)d\theta \qquad (D-2)$$

He also introduced the equation below, known as Bessel's differential equation.

$$x^2\frac{\partial^2 J_n(x)}{\partial x^2} + x\frac{dJ_n(x)}{dx} + (x^2 - n^2)J_n(x) = 0 \qquad (D-3)$$

Bessel's differential equation can be written in many forms. One differential form commonly used is shown below:

$$\frac{d^2y}{dx^2} + \frac{1}{x}\frac{dy}{dx} - \left(1 + \frac{v^2}{x^2}\right)y = 0 \qquad (D-4)$$

Bessel functions of the second kind, also known as Neumann or Weber functions, were named because of the mathematical contributions of German mathematicians Carl Gottfried Neumann (1832-1925) and Heinrich Martin Weber (1842-1913) [67-70]. The series expansion of Neumann's Bessel function of the second kind, $N_v(x)$, is defined below:

$$N_v(x) = J_v(x)log(x) - \frac{1}{2}\sum_{k=0}^{v-1}\frac{(v-k-1)!}{k!}\left(\frac{x}{2}\right)^{2k-v} +$$

$$\frac{1}{2}\sum_{k=0}^{\infty}\frac{(-1)^{k-1}\left[\left(1+\frac{1}{2}+\cdots+\frac{1}{k}\right)+\left(1+\frac{1}{2}+\cdots+\frac{1}{k+v}\right)\right]}{k!\,(k+v)!}\left(\frac{x}{2}\right)^{2k+v} \qquad (D-5)$$

Neumann functions have a logarithmic term and singularity at the origin (x = 0). Neumann's work, *Theory of Bessel functions: An Analogue of the Theory of Spherical Harmonics* (1867), investigated these functions [71]. Many other references exist as well [72].

The Weber Bessel function of the second kind [60], $Y_v(x)$, as shown in equation $(D-6)$ below,

$$Y_v(x) = \frac{2}{\pi}J_v(x)\left(ln\frac{x}{2}+\gamma\right) - \frac{1}{\pi}\sum_{k=0}^{v-1}\frac{(v-k-1)!}{k!}\left(\frac{x}{2}\right)^{2k-v} +$$

$$\frac{1}{\pi}\sum_{k=0}^{\infty}\frac{(-1)^{k-1}\left[\left(1+\frac{1}{2}+\cdots+\frac{1}{k}\right)+\left(1+\frac{1}{2}+\cdots+\frac{1}{k+v}\right)\right]}{k!\,(k+v)!}\left(\frac{x}{2}\right)^{2k+v} \qquad (D-6)$$

Weber's Bessel function of the second kind also has a logarithmic term. Weber's function is that form which is most frequently tabulated and used. The gamma term γ denotes Euler's constant ($\gamma = 1.781$). A plot of several Bessel functions of the second kind is shown in Figure D-2.

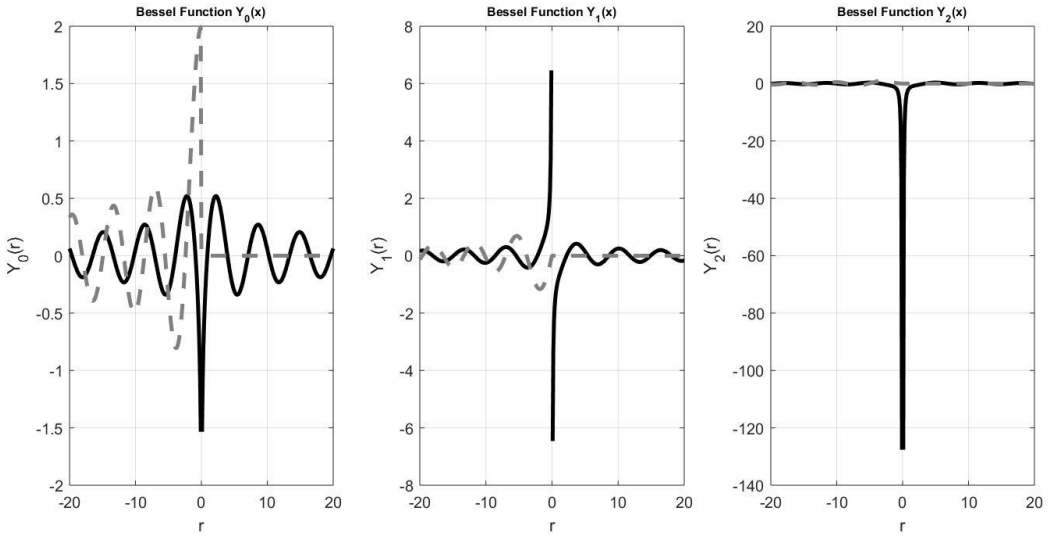

a) b) c)

Figure D-2: Plot of Weber's Bessel function of the second kind for several orders: a) $Y_0(x)$, b) $Y_1(x)$, and c) $Y_2(x)$.

The general solution to the Bessel's equation is written as

$$y = AJ_0(x) + BY_0(x) \qquad (D-7)$$

where *A* and *B* are arbitrary constants.

D.2 Hankel Functions

Bessel functions of the second kind combined with Bessel functions of the first kind form Hankel functions. Because Hankel functions are a linear combination of $J_n(x)$ and $Y_n(x)$, Hankel functions are also solutions to Bessel's equation [36,46,57,73]. See equations $(D-8)$ and $(D-9)$.

$$H_n^{(1)} = J_n(x) + jY_n(x) \qquad (D-8)$$

$$H_n^{(2)} = J_n(x) - jY_n(x) \qquad (D-9)$$

Other important properties of Bessel functions are given in the table below. These are helpful in finding new properties of these function.

Hankel functions are used extensively in electromagnetic theory. They frequently act as Green's functions and have many useful properties. Because they are cylindrically symmetrical, they are often used to characterize waves. The singularity in Weber's function often requires special attention when integrating self-terms especially with the Electric Field Integral Equation and the Magnetic Field Integral Equation. The Spectral Projection Model uses Hankel functions of the second kind in modelling electromagnetic behavior. The singularity in the function is avoided by using the addition theorem sum to calculate the Hankel functions.

D.3 Bessel Function Properties

Bessel functions have many useful properties [60]. Some of the more important common ones involve the even and odd nature of the modes. Listed in Table D-1 are some of these properties. These properties were used to develop SPM theory especially when solving the MFIE using the convolution property of the addition theorem.

Table D-1: Modes and Symmetry of Bessel Functions.

$J_{-n}(x) = (-1)^n J_n(x)$
$J_{-n}(x) = J_n(-x)$
$Y_{-n}(x) = (-1)^n Y_n(x)$
$Y_n\left(e^{\pm j\pi}x\right) = e^{\mp jn\pi}Y_n(x) \pm 2jcos(n\pi)J_n(x)$
$H_n^{(1,2)}(x) = (-1)^n H_{-n}^{(1,2)}(x)$
$H_n^{(1)}(x) = \left(H_n^{(2)}(x^*)\right)^*$
$H_n^{(2)}(x) = \left(H_n^{(1)}(x^*)\right)^*$

The * indicates the complex conjugate.

D.4 Bessel Function Derivatives

Two Bessel function derivatives are given in equations $(D-10)$ to $(D-13)$.

$$J_n'(k\rho') = \frac{J_{n-1}(k\rho') - J_{n+1}(k\rho')}{2} \qquad (D-10)$$

and

$$\frac{\partial J_0(k\rho)}{\partial k\rho} = -J_1(k\rho) = J_0'(k\rho) \qquad (D-11)$$

$$Y_n'^{(k\rho')} = \frac{Y_{n-1}(k\rho') - Y_{n+1}(k\rho')}{2} \qquad (D-12)$$

and

$$\frac{\partial Y_0(k\rho)}{\partial k\rho} = -Y_1(k\rho) = Y_0'(k\rho) \qquad (D-13)$$

The derivative term $H_n'(k\rho')$ is defined by equations $(D-14)$ and $(D-15)$.

$$H_n'(k\rho') = \frac{H_{n-1}(k\rho') - H_{n+1}(k\rho')}{2} \qquad (D-14)$$

$$\frac{\partial H_0(k\rho')}{\partial k\rho'} = -H_1(k\rho) = H_0'(k\rho') \qquad (D-15)$$

$$J_{n-1}(\rho') = \frac{nJ_n(\rho')}{\rho'} + J_n'(\rho') \qquad (D-16)$$

$$Y_n'(\rho') = \frac{nY_n(\rho')}{\rho'} - Y_{n-1}(\rho') \qquad (D-17)$$

$$H_n'(\rho') = \frac{nH_n(\rho')}{\rho'} - H_{n-1}(\rho') \qquad (D-18)$$

$$J_{n+1}(\rho') = \frac{nJ_n(\rho')}{\rho'} - J_n'(\rho') \qquad (D-19)$$

$$J_{n-1}(k\rho') + J_{n+1}(k\rho') = \frac{2nJ_n(k\rho')}{\rho'} \qquad (D-20)$$

$$Y_{n-1}(k\rho') + Y_{n+1}(k\rho') = \frac{2nY_n(k\rho')}{\rho'} \qquad (D-21)$$

$$H_{n-1}(k\rho') + H_{n+1}(k\rho') = \frac{2nH_n(k\rho')}{\rho'} \qquad (D-22)$$

D.5 Hankel and Bessel Function Asymptotic Properties

Hankel functions are important in characterizing the electromagnetic fields analyzed with the Spectral Projection Method as outgoing waves. Hankel functions are generally the Green's function in integral expressions describing electromagnetic fields. The asymptotic approximation of Hankel functions for large arguments is given in equation $(D-23)$. The Spectral Projection Model uses this approximation in order to characterize the **H**-spectral signature of electric and magnetic field plane waves.

$$H_n^{(2)}(\rho) = \sqrt{\frac{2}{\pi\rho}}\, e^{-j\left(\rho-\frac{\pi}{4}\right)} e^{-\frac{jn\pi}{2}} \qquad \rho \to \infty \qquad (D-23)$$

The asymptotic approximation of Bessel functions of the first and second kind for small arguments is given in equations $(D-24)$ through $(D-27)$.

$$J_0(\rho) = 1 \qquad \rho \to 0 \qquad (D-24)$$

$$J_n(\rho) = \frac{1}{n!}\left(\frac{\rho}{2}\right)^n \qquad \rho \to 0, n > 0 \qquad (D-25)$$

$$Y_0(\rho) = \frac{2}{\pi} ln\left(\frac{\gamma\rho}{2}\right) \qquad \rho \to 0, \gamma = 1.781 \qquad (D-26)$$

$$Y_n(\rho) = -\frac{(\rho-1)!}{\pi}\left(\frac{2}{\rho}\right)^n \qquad \rho \to 0, n > 0 \qquad (D-27)$$

The Bessel functions are most suitable for waves that require functions with a finite value of zero within the solution domain. From equations $(D-26)$ and $(D-27)$ it is evident that the Hankel functions are not suitable for this case. This is because of the singularity at zero from the imaginary part of the function, i.e. Weber's form of the Bessel function of the second kind $Y_n(\rho)$. The Hankel functions are more suitable for waves that are outward due to the fact they are complex valued and can be approximated asymptotically by

$$H_n^{(2)}(\rho) \sim e^{-\frac{jn\pi}{2}} \qquad (D-28)$$

at large values of ρ in the far-field.

Bessel functions are best suited for waves that decay to zero because their asymptotic approximations tend to zero at infinity. See equation $(D-29)$

$$J_n(\rho) = \sqrt{\frac{2}{\pi\rho}} cos\left(\rho - \frac{\pi}{4} - \frac{n\pi}{2}\right) \qquad \rho \to \infty \qquad (D-29)$$

Hankel functions are best for outward waves because their imaginary part equals the real part at infinity $(D-30)$, and becomes a complex sinusoidal function $(D-28)$.

$$Y(\rho)=\sqrt{\frac{2}{\pi\rho}}sin\left(\rho-\frac{\pi}{4}-\frac{n\pi}{2}\right) \qquad \rho\to\infty \qquad (D-30)$$

Most time harmonic electromagnetic analysis uses the complex term $e^{j(\boldsymbol{k}\cdot\boldsymbol{r}-\omega t)}$ to represent waves in free space.

Appendix E: Derivation of $J_n(z)$ in the Fast Multipole Method

E.1 Bessel's Definition of $J_n(z)$

This appendix details the mathematics used to derive equation $(3-12)$ for the Fast Multipole Method [27]. To begin, Bessel's definition of $J_n(z)$ in integral form according to Watson [59] is $(E-1)$,

$$J_n(z) = \frac{1}{2\pi}\int_0^{2\pi} cos(n\theta - zsin\theta)d\theta \qquad (E-1)$$

and

$$J_n(z) = \frac{1}{2\pi}\int_{\xi}^{2\pi+\xi} e^{j(n\theta - zsin\theta)}d\theta \qquad (E-2)$$

E.2 Simplification of the Integral for $J_n(z)$

Because the function $J_n(z)$ is periodic in 2π, we can use the trigonometric identities to expand equation $(E-2)$ into equation $(E-7)$.

$$cos(n\theta - zsin\theta) = cos(zsin\theta)cos(n\theta) + sin(zsin\theta)sin(n\theta) \qquad (E-3)$$

$$e^{-jn\theta}e^{jzsin\theta} = [\,cos(n\theta) - jsin(n\theta)][cos(zsin\theta) + jsin(zsin\theta)] \qquad (E-4)$$

$$e^{-jzsin\theta}e^{jn\theta} = [cos(zsin\theta)\,cos(n\theta) - jcos(zsin\theta)sin(n\theta) + jsin(zsin\theta)cos(n\theta) + \,sin(zsin\theta)sin(n\theta)]/4 \qquad (E-5)$$

$$e^{-jzsin\theta}e^{-jn\theta} = [cos(zsin\theta)\,cos(n\theta) - jcos(zsin\theta)sin(n\theta) - jsin(zsin\theta)cos(n\theta) - \,sin(zsin\theta)sin(n\theta)]/4 \qquad (E-6)$$

$$e^{-jzsin\theta}e^{-jn(\theta+\pi)} = [cos(zsin\theta)\,cos\big(n(\theta+\pi)\big) - jcos(zsin\theta)sin\big(n(\theta+\pi)\big) - jsin(zsin\theta)cos\big(n(\theta+\pi)\big) - \,sin(zsin\theta)sin\big(n(\theta+\pi)\big)]/4 \qquad (E-7)$$

Now making further substitutions with equations $(E-8)$ through $(E-11)$ into equation $(E-7)$,

$$sin(n(\theta+\pi)) = \sin(n\theta)\cos(n\pi) + \cos(n\theta)\sin(n\pi) \qquad (E-8)$$

$$sin(n(\theta+\pi)) = \sin(n\theta)\,e^{jn\pi} \qquad (E-9)$$

$$cos(n(\theta+\pi)) = \cos(n\theta)\cos(n\pi) - \sin(n\theta)\sin(n\pi) \qquad (E-10)$$

$$cos(n(\theta+\pi)) = \cos(n\theta)\,e^{jn\pi} \qquad (E-11)$$

equation $(E-11)$ results.

$$e^{-jzsin\theta}e^{-jn(\theta+\pi)} = [cos(zsin\theta)\,cos\big(n(\theta+\pi)\big) - jcos(zsin\theta)\sin(n\theta)\,e^{jn\pi} - jsin(zsin\theta)cos\big(n(\theta+\pi)\big) - sin(zsin\theta)\sin(n\theta)\,e^{jn\pi}]/4 \qquad (E-12)$$

Figure E-1 shows plots of products of functions given in equation $(E-12)$ to determine whether they are even or odd functions.

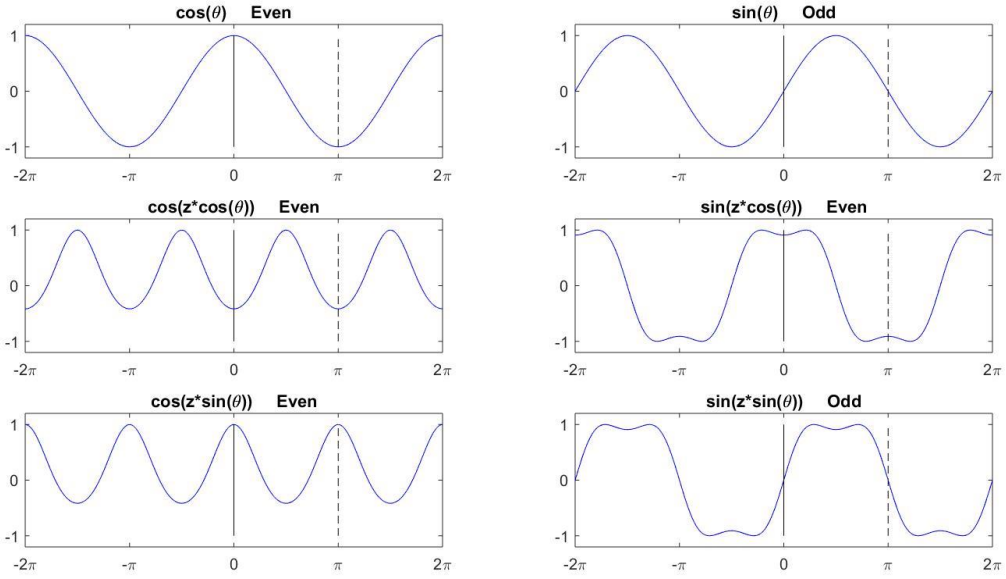

Figure E-1: Plot of products of trigonometric functions.

The plots in Figure E-1 are useful in performing the integrations in equations $(E-13)$ and $(E-14)$.

$$\int_0^{2\pi} cos(zsin\theta - n\theta)d\theta = \int_0^{2\pi} e^{-jzsin\theta}e^{jn\theta}d\theta \qquad (E-13)$$

$$\int_0^{2\pi} cos(zsin\theta - n\theta)d\theta = \int_0^{2\pi} e^{zsin\theta}e^{-jn\theta}d\theta \qquad (E-14)$$

The most common integral form of the Bessel function is given in equation $(E-15)$,

$$J_n(z) = \frac{1}{2\pi}\int_0^{2\pi} e^{-jzsin\theta}\,e^{jn\theta}d\theta \qquad (E-15)$$

The integral form of the Bessel function in equation $(E-16)$ may be found in Harrington [35], derived using equations $(E-17)$ through $(E-19)$ below.

$$J_n(z) = \frac{j^n}{2\pi}\int_0^{2\pi} e^{-jzcos\theta}\, e^{-jn\theta} d\theta \qquad (E-16)$$

$$j^n = e^{jn\frac{\pi}{2}} \qquad (E-17)$$

$$sin\left(\theta + \frac{\pi}{2}\right) = cos(\theta) \qquad (E-18)$$

$$cos\left(\theta - \frac{\pi}{2}\right) = sin(\theta) \qquad (E-19)$$

Equation $(E-20)$ is the precursor to the equation $(3-12)$ found in the Fast Multipole Method referenced by Jin [27].

$$J_n(z) = \frac{1}{2\pi}\int_0^{2\pi} e^{-jzcos\theta}\, e^{-jn\left(\theta-\frac{\pi}{2}\right)} d\theta \qquad (E-20)$$

E.3 Integral for $J_n(z)$ of the Fast Multipole Method

Substituting values given in equations $(E-21)$ and $(E-22)$ into $(E-20)$, after some algebra one arrives at the final expression in equation $(E-25)$. Equation $(E-25)$ is consistent with equation $(3-12)$.

$$z = k_0 d \qquad (E-21)$$

$$\theta = \alpha - \phi_d \qquad (E-22)$$

$$J_n(z) = \frac{1}{2\pi}\int_0^{2\pi} e^{-jk_0 dcos(\alpha-\phi_d)}\, e^{-jn\left(\alpha-\phi_d-\frac{\pi}{2}\right)} d\theta \qquad (E-23)$$

$$J_n(z)e^{-jn(\pi+\phi_d)} = \frac{1}{2\pi}\int_0^{2\pi} e^{-jk_0 dcos(\alpha-\phi_d)} e^{-jn\left(\alpha-\phi_d-\frac{\pi}{2}\right)}\, e^{-jn(\pi+\phi_d)} d\theta \qquad (E-24)$$

$$J_n(z)e^{-jn(\pi+\phi_d)} = \frac{1}{2\pi}\int_0^{2\pi} e^{-jk_0 dcos(\alpha-\phi_d)}\, e^{-jn\left(\alpha+\frac{\pi}{2}\right)} d\theta \qquad (E-25)$$

Appendix F: Two-Dimensional Cross-Sectional Patterns

F.1 Generating Different Geometries by Addition of Opposite Rotating Vectors

One powerful feature of the Spectral Projection Model and Direct SPM methods is that one can analyze many types of electromagnetic structures. This section describes how one can generate these structures by rotating the coordinates of two circles around the origin. It is possible to define different shapes as the sum of rotating vectors around circles of different radii by rotating the vectors at different angular rates.

F.1.1 Elliptical Surface Pattern

To calculate the sum of the two rotating vectors, assume there exists two sets of vectors, $\rho \in \left\{\rho_1 e^{-j\xi_1}, \rho_2 e^{-2j\xi_1}, \ \ldots, \rho_N e^{-Nj\xi_1}\right\}$ and $\rho' \in \left\{\rho_1{}' e^{j\xi_1{}'}, \rho_2{}' e^{2j\xi_1{}'}, \ \ldots, \rho_N{}' e^{Nj\xi_1{}'}\right\}$. For this first example, vector ρ rotates clockwise and vector ρ' rotates counterclockwise at the same angular rate. They each may have a different magnitude. If one sums each pair together such that $\rho_n'' = \rho_n'^{e^{j\xi_n}{}'} + \rho_n e^{-j\xi_n}$, then the set of vector sums becomes $\rho'' \in \{\rho_1'', \rho_2'', \ \ldots, \rho_N''\}$. The resultant column vector ρ'' which is the sum of the column vector ρ' and column vector ρ is given in equation $(F-1)$.

$$\begin{bmatrix} \rho_1'' \\ \vdots \\ \rho_n'' \\ \vdots \\ \rho_N'' \end{bmatrix} = \begin{bmatrix} \rho_1{}' \\ \vdots \\ \rho_n{}' \\ \vdots \\ \rho_N{}' \end{bmatrix} + \begin{bmatrix} \rho_1 \\ \vdots \\ \rho_n \\ \vdots \\ \rho_N \end{bmatrix} \qquad (F-1)$$

See Figures F-1a and F-1b for a plot of the circles generated by points ρ_n, ρ_n', and ρ_n''.

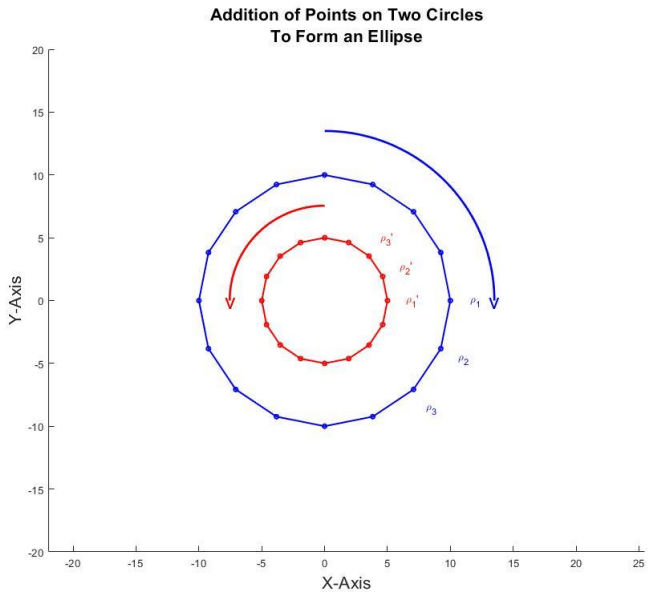

a)

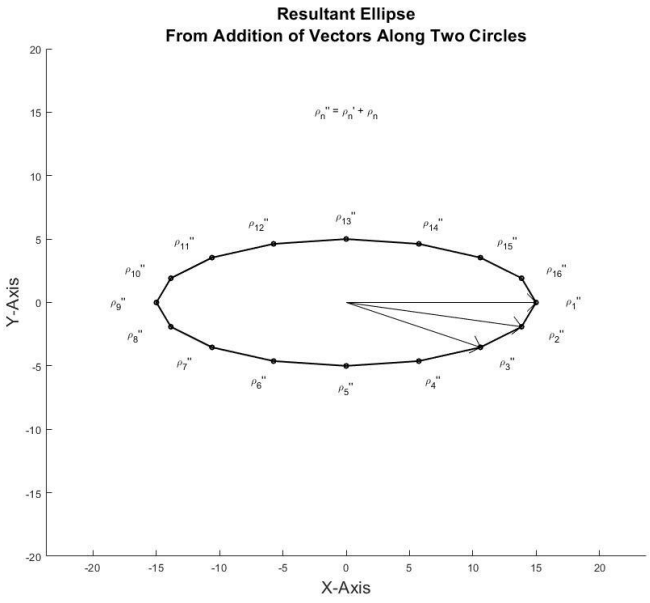

b)

Figure F-1: a) Generating surfaces for an ellipse with axial ratio 2:1. b) Resultant ellipse pattern.

F.1.2 Cardioid Surface Pattern

For the second example, vector ρ rotates counterclockwise at twice the angular rate that vector ρ' rotates. They each have a different magnitude. See Figure F-2a. If one sums each pair together such that $\rho_n'' = \rho_n' e^{j\xi_n} + \rho_n e^{2j\xi_n}$, the cardioid figure shown in Figure F-2b results.

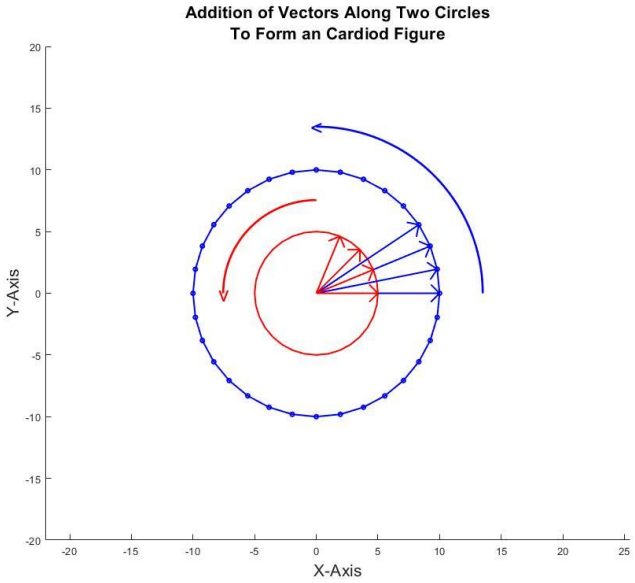

a)

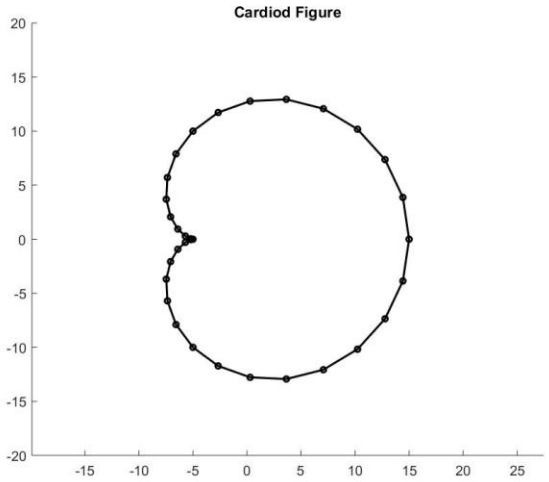

b)

Figure F-2: a) Generating surfaces for a cardioid. b) Resultant cardioid pattern.

F.1.3 Undulating Surface Pattern

For the third example, vector ρ rotates counterclockwise at eight times the angular rate that vector ρ' rotates. They each have a different magnitude. See Figure F-3a. If one sums each pair together such that $\rho_n'' = \rho_n' e^{j\xi_n} + \rho_n e^{8j\xi_n}$, the undulating surface shown in Figure F-3b results.

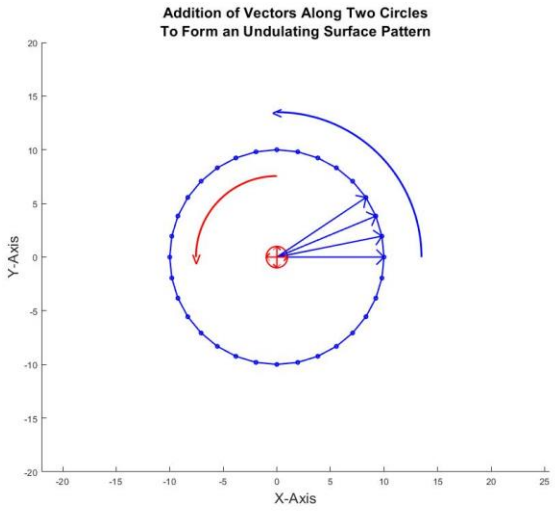

a)

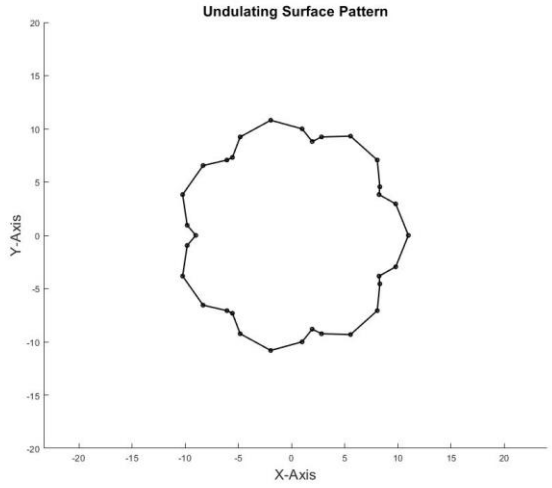

b)

Figure F-3: a) Generating surfaces for an undulating pattern. b) Resultant undulating pattern for the surface.

A variety of patterns can be generated using this technique. The Spectral Projection Model uses this method to analyze ellipses and randomly shaped objects. By adding more rotating vectors, one can add more degrees of freedom to the generating function, and a greater variety of geometries, including some that are not symmetrical.

Appendix G: Conjugate Gradient Method

G.1 Conjugate Gradient Introduction

As mentioned earlier, iterative techniques [74-81] have been developed that improved the speed and accuracy of solving very large systems of EM operator equations as more powerful computers were made. One popular iterative technique used to invert matrices is the conjugate gradient method.

The conjugate gradient method has been widely used as an alternative to Gaussian elimination to invert complex matrices. This section describes how the conjugate gradient method works with relevant illustrations. Research into the Spatial Frequency Technique was done to improve the develop high speed algorithms to solve 2D infinitely long cylinder problems. The speed of the algorithms was compared to the Method of Moment and the Conjugate Gradient Method. The algorithm of the Conjugate Gradient Method is given in this section as a comparison to the fast convergence algorithm in Chapter 4.

G.2 Quadratic Functions

The general formula for a quadratic function in one variable is written in equation $(G-1)$.

$$f(x) = ax^2 + bx + c \qquad (G-1)$$

This function $f(x)$ is a parabola, and the minimum value of the parabola can be determined by setting the derivative equal to 0. See Figure G-1.

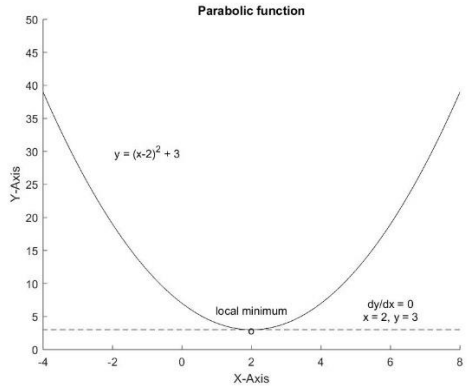

Figure G-1: Quadratic function with local minimum equal to two.

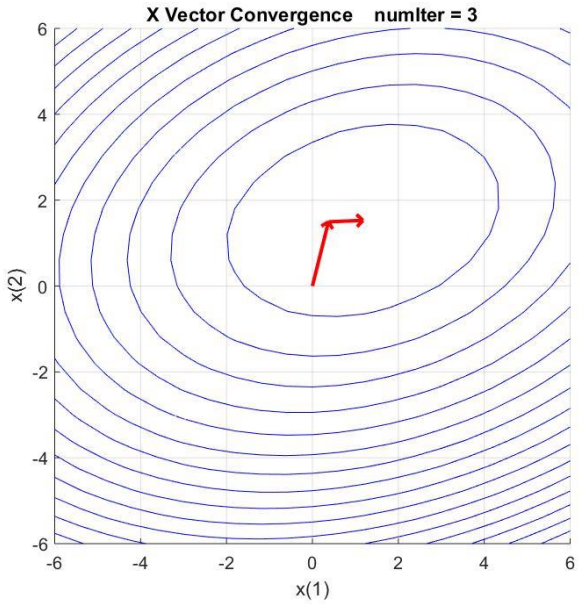

Figure G-2: Directional vectors pointing to the minimum of the quadratic surface.

An example of a multivariate function is $f(X)$, with its set of variables, $X = \{x_1, x_2, \dots, x_n\}$. The gradient of the function, ∇f, is shown in equation $(G-2)$.

$$\nabla f = \left[\frac{\partial f}{\partial x_1}\ \frac{\partial f}{\partial x_2} \dots \frac{\partial f}{\partial x_n}\right]^T = 0 \qquad (G-2)$$

A contour plot with lines of constant value is plotted in Figure G-2 for a multivariate function of two variables. The directional vectors illustrate the path taken to reach the surface minimum.

G.3 Positive Definite Matrices

The conjugate gradient method only works with matrices that are positive definite. To be positive definite, a matrix $A \in R^{n\times n}$ must satisfy the following condition,

$$\hat{x}^T A \hat{x} > 0 \qquad (G-3)$$

for all non-zero vectors $\hat{x}$ with real elements. An alternative definition is that matrix A is positive definite if it is symmetric and all its eigenvalues are positive.

G.4 Functionals

To understand the conjugate gradient method, one begins by defining a quadratic functional $f(\hat{x})$ with $\hat{x} \in V$, vector space V. A functional is a function that maps vector space V into a scalar. An example of a quadratic functional is $f(\hat{x})$ shown in equation $(G-4)$.

Matrix $A \in R^{n\times n}$, vector $\hat{x} \in R^{n\times 1}$, and vector $\hat{c} \in R^{1\times 1}$. Vector $\hat{c}$ may be regarded as a scalar.

$$f(\hat{x}) = \frac{1}{2}\hat{x}^T A\hat{x} - \hat{b}^T\hat{x} + \hat{c} \qquad (G-4)$$

To minimize the functional, the first step is to take gradient of $f(\hat{x})$

$$\nabla f(\hat{x}) = \frac{1}{2}\hat{x}^T A^T + \frac{1}{2}\hat{x}^T A - \hat{b}^T \qquad (G-5)$$

and because A is symmetrical, $A^T = A$. Thus, using matrix algebra,

$$\nabla f(\hat{x}) = \left(A\hat{x} - \hat{b}\right)^T \qquad (G-6)$$

The vector $\hat{x} = \hat{x}_{min}$ is when the gradient is zero, and $f(\hat{x}_{min})$ is the local minimum. So $\hat{x}$ is referred to as the global minimizer. See Figure G-3 for an example of a plot of a functional $f(\hat{x})$ and its gradient, $\nabla f(\hat{x})$.

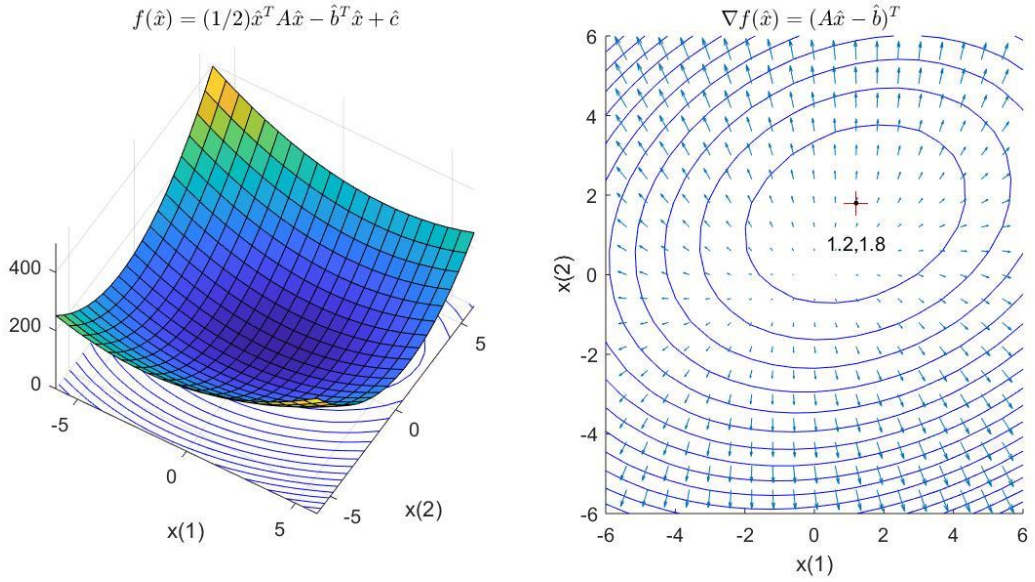

a) b)

Figure G-3: 3D plot of a) functional $f(\hat{x})$ and its b) gradient $\nabla f(\hat{x})$.

G.5 Iteration – Calculation of Step Size γ_m

Most iterative methods use a recursive relationship to calculate the next value of some variable. For the conjugate gradient method, a recursive sequence is used to calculate future values of vector $\hat{x}$ given an initial guess of $\hat{x}^{(0)}$.

$$\hat{x}^{(m+1)} = \hat{x}^{(m)} + \gamma_m \hat{d}^{(m)} \qquad (G-7)$$

The vector $\hat{d}^{(m)}$ is called the search direction, and scalar γ_m is called the step size. To calculate new values of the step size that minimizes $f(\hat{x})$ for $\hat{x} = \hat{x}^{(m)} + \gamma \hat{d}^{(m)}$ substitute into the functional,

$$\frac{\partial f\left(\hat{x}^{(m)} + \gamma_m \hat{d}^{(m)}\right)}{\partial \gamma} = 0 \qquad (G-8)$$

which yields

$$\gamma_m = \frac{\left(d^{(m)}\right)^T r^{(m)}}{(d^{(m)})^T A d^{(m)}} \qquad (G-9)$$

Ideally, the gradient of the functional would equal zero at the local minimum quickly. As calculated earlier, it equals the result in equation $(G-10)$.

$$\nabla f\left(\hat{x}^{(m)}\right) = A\hat{x}^{(m)} - \hat{b} \qquad (G-10)$$

And the remainder is defined as the residual $\hat{r}^{(m)}$.

$$\nabla f\left(\hat{x}^{(m)}\right) = \hat{r}^{(m)} \qquad (G-11)$$

G.6 Iteration – Calculation of Weighting Factor α_m

The reason the method is called the conjugate gradient is because the direction vector is chosen negative to the gradient, which is the residual. This is the direction of maximum decrease in the value of the function that points to the new value of $\hat{d}^{(m+1)}$ closer to the minimum.

$$\hat{d}^{(m+1)} = -\hat{r}^{(m+1)} + \alpha_m \hat{d}^{(m)} \qquad (G-12)$$

The initial value of the direction vector is set as $\hat{d}^{(0)} = -\hat{r}^{(0)}$.

The last step is to choose a value for α_m. If one defines an inner product of two vectors $\hat{u}$ and $\hat{w}$ using the positive definite matrix A as in equation $(G-13)$, one can write

$$\langle \hat{w}, A\hat{u} \rangle = \langle \hat{u}, A\hat{w} \rangle = \hat{w}^T A\hat{u} = \hat{u}^T A\hat{w} \qquad (G-13)$$

The vectors $\hat{u}$ and $\hat{w}$ are said to be A-conjugate (or A-orthogonal) when

$$\hat{u}^T A\hat{w} = 0 \qquad (G-14)$$

The conjugate gradient method uses a process that A-orthogonalizes the direction vectors $\hat{d}^{(m+1)}$ and $\hat{d}^{(m)}$ with respect to the inner product above, thus finding the minimum of the A-norm surface $\|\hat{d} - \hat{d}_m\|_A$ generated by the vectors $\hat{d}$ and $\hat{d}_m$ [55]. Now substitute for $\hat{u}$ and $\hat{w}$ using $\hat{d}^{(m)}$ and $\hat{d}^{(m+1)}$.

$$\hat{d}^{(m)^T} A\hat{d}^{(m+1)} = \hat{d}^{(m+1)^T} A\hat{d}^{(m)} = 0 \qquad (G-15)$$

After making the recursive substitution, $\hat{d}^{(m+1)} = -\hat{r}^{(m+1)} + \alpha_m \hat{d}^{(m)}$, the expression for α_m from equation $(G-11)$ becomes

$$\alpha_m = \frac{\hat{r}^{(m+1)^T} A\hat{d}^{(m)}}{\hat{d}^{(m)^T} A\hat{d}^{(m)}} \qquad (G-16)$$

A plot of the direction vectors, $\alpha_m \hat{d}^{(m)}$, for three iterations generated by the functional $f(\hat{x})$ is shown in Figure G- 4.

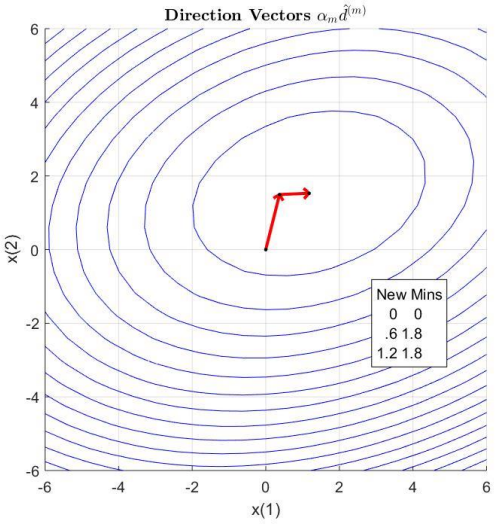

Figure G-4: Minimums and directional vectors to the minimum of a parabolic surface.

All the direction vectors are orthogonal and are conjugate gradient to the surface $\|\hat{x} - \hat{z}\|_A$ with $\hat{z} \in R^{n\times 1}$. In Figure G-5 the new minimums on the surfaces $\|\hat{x} - \hat{x}^{(m)}\|_A$ for the first three iterations are shown.

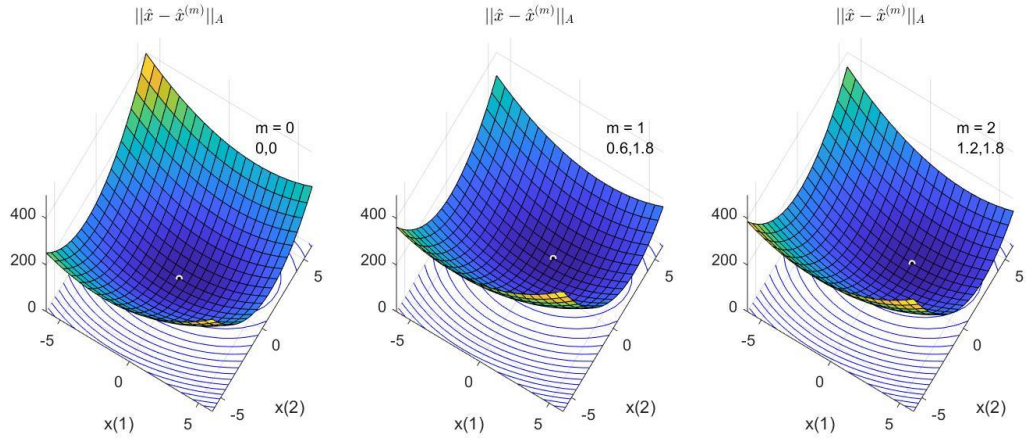

a) b) c)

Figure G-5: Surfaces and new minimums for first three iterations of the conjugate gradient algorithm at a) iteration m=0 b) iteration m=1 and c) iteration m=2.

The vector $\gamma_m \hat{d}^{(m)}$ moves the vector $\hat{x}^{(m)}$ to $\hat{x}^{(m+1)}$ along the surface of the parabola generated by the functional $f(\hat{x})$. This vector $\hat{x}^{(m+1)}$ is a new minimum along the surface of the A-norm. In other words, $f\left(\hat{x}^{(m+1)}\right)$ is a minimum on the line passing through points $\hat{x}^{(m+1)}$ and $\hat{x}^{(m)}$ in the direction $\hat{d}^{(m)}$. The final iteration at m = 3 yields convergence of the algorithm to a given tolerance [54,55].

G.7 Conjugate Gradient Algorithm

$$\hat{r}^{(0)} = A\hat{x}^{(0)} - \hat{b} \qquad (G-17)$$

$$\hat{d}^{(0)} = -\hat{r}^{(0)} \qquad (G-18)$$

$$\delta^{(0)} = \hat{r}^{(0)^T}\hat{r}^{(0)} \qquad (G-19)$$

$$for\ m = 0, 1, 2, \ldots \qquad (G-20)$$

$$u = A\hat{d}^{(m)} \qquad (G-21)$$

$$\gamma_m = \frac{\delta^{(m)}}{\hat{d}^{(m)^T}\hat{u}} \qquad (G-22)$$

$$\hat{x}^{(m+1)} = \hat{x}^{(m)} + \gamma_m \hat{d}^{(m)} \qquad (G-23)$$

$$\hat{r}^{(m+1)} = \hat{r}^{(m)} + \gamma_m \hat{u} \qquad (G-24)$$

$$\delta^{(m+1)} = \hat{r}^{(m+1)^T}\hat{r}^{(m+1)} \qquad (G-25)$$

$$if\ \sqrt{\delta^{(m+1)}} < tolerance, stop\ \ \hat{x}^{(m+1)} \qquad (G-26)$$

$$\alpha_m = \frac{\delta^{(m+1)}}{\delta^{(m)}} \qquad (G-27)$$

$$\hat{d}^{(m+1)} = -\hat{r}^{(m+1)} + \alpha_m \hat{d}^{(m)} \qquad (G-28)$$

$$end \qquad (G-29)$$

Appendix H: Linear Algebra, Inner Product, and Projection

H.1 Projection of Vectors onto Vectors and Subspaces

To understand the Spectral Projection Model, it is important to review the concept of projections. This next discussion defines projections with respect to vectors, subspaces, functions, and functional subspaces [82-89]. This section on linear algebra will act as a link between the concept of projection and the functional aspects of the Spectral Projection Model.

The projection of a vector onto another vector is a familiar tool used in physics. Figure H-1a is an illustration of a vector **v** projected onto a vector **b**. The projection is vector **p**. The projection vector **p** is collinear with **b**, and the vector orthogonal to the projection vector is **o**. The vector **o** represents the "error" between **v** and **b**.

$$\mathbf{p} = \frac{\mathbf{b^T v}}{\mathbf{b^T b}}\mathbf{v} \qquad (\mathrm{H}-1)$$

The expression $\mathbf{b^T v}$ is referred to as a dot product of **b** and **v**, written $\langle \mathbf{b}, \mathbf{v} \rangle = \mathbf{b^T v}$.

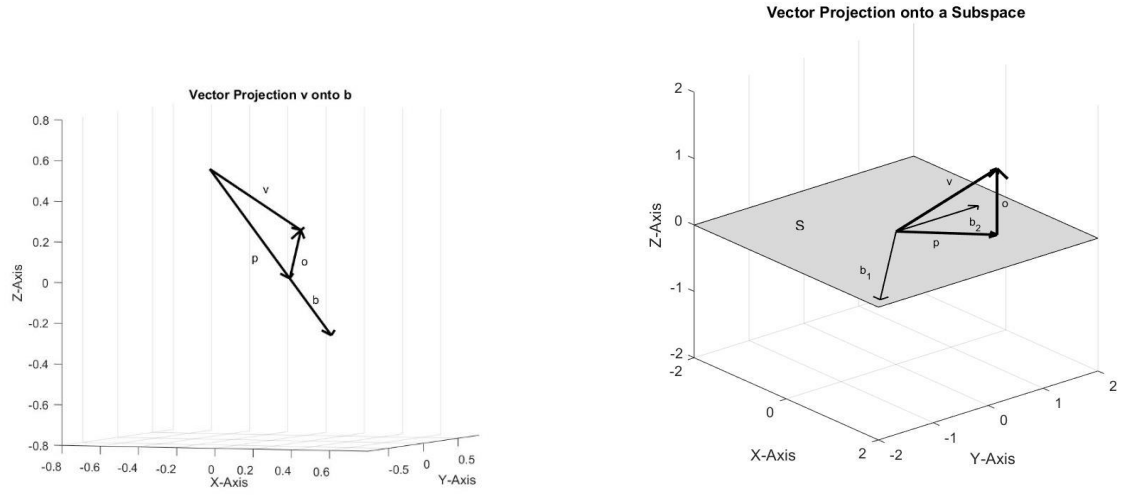

a) b)

Figure H-1: a) Vector projection **v** onto **b.** b) Vector projection **v** onto subspace *S.*

Shown in Figure H-1b is the vector **v** projected onto the subspace *S* defined by the plane at z = 0. Vectors $\mathbf{b_1}$ and $\mathbf{b_2}$ are independent vectors and make up a basis or column space for the subspace *S*. The vector **p** is the projection vector onto the subspace *S*, and vector **o** is orthogonal to vector **p,** and therefore orthogonal to the subspace *S*. This vector **o** represents the "error"

between the projection **p** onto subspace S and vector **v**. It may be viewed similar to the vector **o** in Figure H-1a.

Shown in Figure H-1b is an example of a projection of vector **v** onto the subspace *S* comprised of vectors $\mathbf{b_1}$, $\mathbf{b_2}$ and $\mathbf{b_3}$. The subspace *S* may be written in matrix form as seen in equation (H-2). Matrix M is made up of column vectors $\mathbf{b_1}$, $\mathbf{b_2}$ and $\mathbf{b_3}$. Note that vector $\mathbf{b_3}$ is a zero-column vector and is not independent of vectors $\mathbf{b_1}$ and $\mathbf{b_2}$. The vector **o** is called the vector representation of the null space of the matrix *M*.

$$\begin{matrix}\mathbf{b_1} & \mathbf{b_2} & \mathbf{b_3} & \mathbf{v} & \mathbf{p} & \mathbf{o}\end{matrix}$$
$$\begin{bmatrix} 1.8 & 0 & 0 \\ -1.8 & 1.5 & 0 \\ 0 & 0 & 0 \end{bmatrix}\begin{bmatrix}1\\1\\1\end{bmatrix} = \begin{bmatrix}1.8\\-.3\\0\end{bmatrix} \qquad \begin{bmatrix}0\\0\\1\end{bmatrix} \qquad (\mathrm{H}-2)$$

$$M = \begin{bmatrix} 1.8 & 0 & 0 \\ -1.8 & 1.5 & 0 \\ 0 & 0 & 0 \end{bmatrix} \qquad (\mathrm{H}-3)$$

H.2 Projection of Vectors and Inner Products of Functions

Because SPM deals with Bessel and Hankel functions used to solve from Maxwell's equations, this next section ties the concept of projection in linear algebra to the Hankel Addition theorem and Bessel functions used in the Spectral Projection Model.

The inner product of two functions $f(x)$ and $g(x)$ in L^2 space is often defined by the following notation shown in equation $(\mathrm{H}-4)$, and the integral product of functions shown in equation $(\mathrm{H}-5)$.

$$s = \langle f(x), g(x) \rangle \qquad (\mathrm{H}-4)$$

$$s = \int_L f(x)g(x)dx \qquad (\mathrm{H}-5)$$

In both equations *s* is a scalar. Take for example two sinusoidal functions. Figure H-2 shows two continuous functions, *f(x), g(x)* and *f(x)g(x)*. Figure H-3 shows the corresponding discrete sequences, *f(n), g(n)* and their product *f(n)g(n)*, which are sampled versions of the two continuous sinusoidal functions. The inner product integration is approximated by the summation of the product of *f(n)g(n)*.

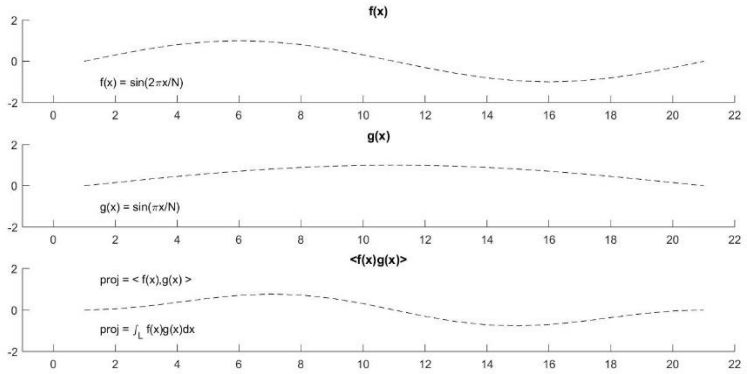

Figure H-2: Continuous functions *f(x)* and *g(x)* and the product *f(x)g(x)*. The product is integrated over a defined interval.

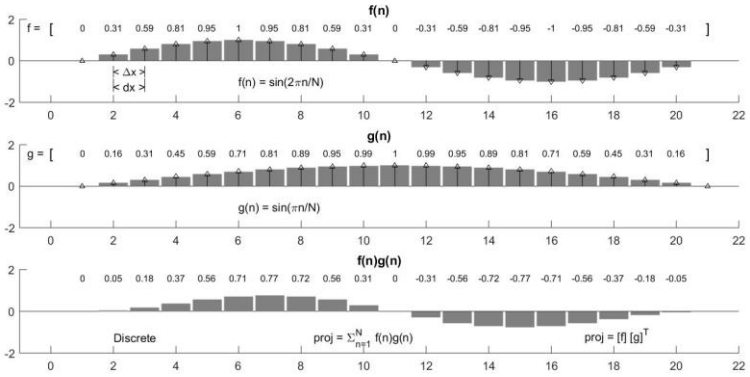

Figure H-3: Sampled continuous functions *f(x)* and *g(x)* and their discretized forms *f(n)* and *g(n)*.

When performing the integration for the inner product $\langle f(x), g(x)\rangle$ numerically, each function may be subdivided into N intervals and sampled at the midpoint of an interval of length Δx. The interval Δx approximates the infinitesimal interval dx. The two functions are then regarded as sequences that are multiplied and summed together.

$$\langle f(x), g(x)\rangle \cong \sum_{n=0}^{N-1} f(n)g(n)\,\Delta x \qquad (\mathrm{H}-6)$$

The sequences $f(n)$ and $g(n)$ may be considered as vectors because the projection $\langle \mathbf{b}, \mathbf{a}\rangle$ is calculated the same as the inner product $\langle f(n), g(n)\rangle$ with $\Delta x = \frac{1}{N}$.

$$Proj_{\mathbf{b},\mathbf{a}} = \langle \mathbf{b}, \mathbf{a} \rangle = \sum_{n=1}^{N} \boldsymbol{b_n a_n} \qquad (\mathrm{H}-7)$$

$$Proj_{f(n),g(n)} = \langle f(n), g(n) \rangle = \sum_{n=0}^{N-1} f(n) g(n) \Delta x \qquad (\mathrm{H}-8)$$

When using the Method of Moments and Spectral Projection Model, this value of varies between consecutive points along the contour being integrated depending on the geometry of the object.

In this dissertation the term inner product of two vectors is used interchangeably with projection of a function $f(x)$ onto a set of points at coordinates $X: x \in \{x_1, x_2, \dots, x_N\}$, and its corresponding sequence of points $f(n)$. Bessel and Hankel functions are widely used, and they are sampled at their midpoints over the intervals of interest. We refer to this technique as collocation or point matching. In this way we avoid the computational difficulty of integration, and optimize the speed of the code. As discussed earlier in Chapter 6, the speed of populating and inverting the DSPM matrix is faster than the MOM matrix, especially if MOM needs to implement basis functions over which the integrations are performed.

Appendix I: FMM and Addition Theorem Convolution

I.1 Fourier Transforms and Important Relations

This section derives the relationship between the Fast Multipole Method [27] and its link to the Spectral Projection Model and the spectral signature of currents discussed in this dissertation.

The Fourier transform for continuous objects is defined as equation $(I-1)$,

$$F[f(x)] = \int_{-\infty}^{\infty} f(x) e^{-j\omega x} dx \qquad (I-1)$$

and the frequency response of a discrete spatial system is given in equation $(I-2)$.

$$H\left(e^{j\omega}\right) = \sum_{n=-\infty}^{\infty} h(n)\, e^{-jn\omega} \qquad (I-2)$$

The next three trigonometric identities $(I-3)$ to $(I-5)$ will be used in this derivation.

$$cos(\phi) = sin\left(\phi + \frac{\pi}{2}\right) \qquad (I-3)$$

$$sin(\phi) = cos\left(\phi - \frac{\pi}{2}\right) \qquad (I-4)$$

$$j^{-n} = \left(\frac{1}{j}\right)^{n} = (-j)^{n} = e^{-j\frac{\pi}{2}n} \qquad (I-5)$$

I.2 Fourier Transform of Bessel Functions

The exponential function in the left of equation $(I-6)$ is equal to an infinite sum of phase shifted Bessel functions.

$$e^{-jk\rho cos(\phi)} = \sum_{n=-\infty}^{\infty} j^{-n} J_n(\beta\rho)\, e^{jn\phi} \qquad (I-6)$$

Using relations $(I-3)$ to $(I-5)$, one can write expression $(I-6)$ as $(I-8)$.

$$e^{-jk\rho sin(\phi)} = \sum_{n=-\infty}^{\infty} j^{-n} J_n(\beta\rho)\, e^{jn\left(\phi-\frac{\pi}{2}\right)} \qquad (I-7)$$

$$e^{-jk\rho sin(\phi)} = \sum_{n=-\infty}^{\infty} J_n(\beta\rho)\, e^{jn\phi} e^{-j\pi n} \qquad (I-8)$$

The spectral signature of uniform incident electric plane wave is defined in equation $(I-9)$,

$$E^i(\rho,\phi) = I_{\rho,\phi} = \sum_{n=-\infty}^{\infty} J_n(\beta\rho)\, e^{jn\phi} \qquad (I-9)$$

and using equation $(I-6)$,

$$e^{-jk\rho cos\left(\phi+\frac{\pi}{2}\right)} = \sum_{n=-\infty}^{\infty} J_n(\beta\rho)\, e^{jn\phi} \qquad (I-10)$$

I.3 Fourier Transform and FMM Terms

Looking at equation $(E-16)$ from the Fast Multipole Method, one can expand it to

$$e^{-jk\rho cos(\alpha_r-\phi)} = e^{-jk\rho[cos(\alpha_r)cos(\phi)+sin(\alpha_r)sin(\phi)]} \qquad (I-11)$$

Now one may define ρ_x and ρ_y in equation $(I-12)$,

$$\rho cos(\phi) = \rho_x \qquad \rho sin(\phi) = \rho_y \qquad (I-12)$$

Substituting one obtains $(I-13)$.

$$e^{-jk\rho cos(\alpha_r-\phi)} = e^{-jk\rho_x cos(\alpha_r)} e^{-jk\rho_y sin(\alpha_r)} \qquad (I-13)$$

Next, from equation $(I-13)$ the Fourier transforms $(I-14)$ through $(I-16)$ are defined.

$$F_{xy} = e^{-jk\rho cos(\alpha_r-\phi)} \qquad (I-14)$$

$$F_x = e^{-jk\rho_x cos(\alpha_r)} \qquad (I-15)$$

$$F_y = e^{-jk\rho_y sin(\alpha_r)} \qquad (I-16)$$

$$F_{xy} = F_x F_y \qquad (I-17)$$

One can conclude from equation $(I-17)$ using properties of the Fourier transform that the inverse Fourier transforms in equation $(I-18)$ to $(I-21)$ exist. The $\otimes$ symbol is for convolution.

$$F_{xy} = F\left[f_x[n] \otimes f_y[n]\right] \qquad (I-18)$$

$$f_x[n] = \sum_{n=-\infty}^{\infty} J_n(\beta\rho_x)\, e^{jn\alpha_r} e^{-jn\frac{\pi}{2}} \qquad (I-19)$$

$$f_y[n] = \sum_{n=-\infty}^{\infty} J_n(\beta\rho_y)\, e^{jn\alpha_r} e^{-jn\pi} \qquad (I-20)$$

$$f_x[n] \otimes f_y[n] = \sum_{n=-\infty}^{\infty} J_n(\beta\rho_x)\, e^{jn\alpha_r} e^{-jn\frac{\pi}{2}} \otimes \sum_{n=-\infty}^{\infty} J_n(\beta\rho_y)\, e^{jn\alpha_r} e^{-jn\pi} \qquad (I-21)$$

The convolution of sequences $f_x[n]$ and $f_y[n]$ is performed in equation $(I-21)$. Carrying out the convolution one gets the following expression $(I-22)$.

$$f_x[n] \otimes f_y[n] = \sum_{r=-\infty}^{\infty} f_x(r)\, f_y(n-r) \qquad (I-22)$$

For the computational purposes, the variable $r \to \infty$ is truncated to $|r| \to R$, and equation $(I-22)$ is rewritten as $(I-23)$ by substituting from equation $(I-8)$.

$$f_x[n] \otimes f_y[n] = \sum_{r=-R}^{R} J_r(\beta\rho_x)\, e^{jr\alpha_r} e^{-jr\frac{\pi}{2}}\, J_{n-r}(\beta\rho_y) e^{j(n-r)\alpha_r} e^{-j(n-r)\pi} \qquad (I-23)$$

with the following substitution $\pi = -\pi$.

$$f_x[n] \otimes f_y[n] = \sum_{r=-R}^{R} J_r(\beta\rho_x)\, J_{n-r}(\beta\rho_y) e^{j(n-r)(\pi)} e^{-jr\left(\frac{\pi}{2}\right)} \qquad (I-24)$$

As is clear from equation $(I-24)$, the addition theorem used in FMM is the convolution of two functions, i.e. $f_x[n] \otimes f_y[n]$.

Appendix J: Image Theory

J.1 Image Theory - PEC as the Ground Plane

This section gives a brief discussion of the relationship between image theory [36, 90-92] and the Spectral Projection Model. The Spectral Projection Model was initially called the Extended Image Theory, but later renamed because of its extensive use of projections.

To begin, a line charge source or line current source radiates electromagnetic energy to observation points in the near-field and the far-field. If the source is near a PEC object, electromagnetic will reflect off the object or diffract around the object. If the object is a PEC ground plane, the energy will be reflected off the ground plane. See Figure J-1.

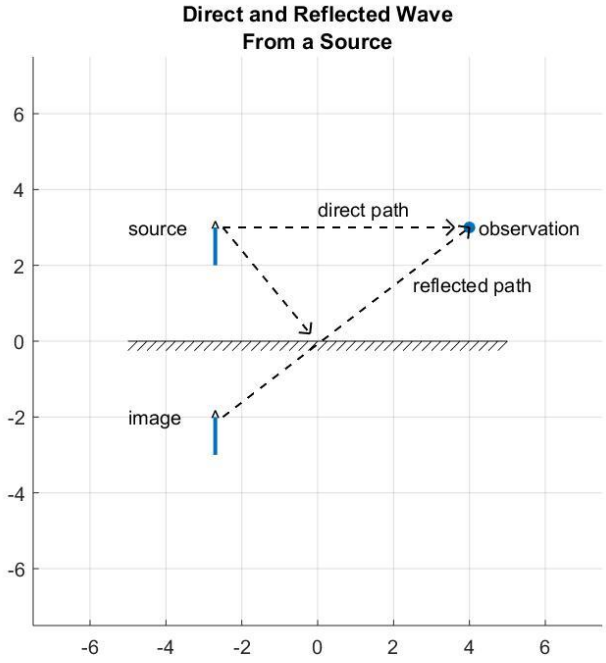

Figure J-1: Reflection of a vertically polarized electromagnetic wave off a ground plane.

Notice in Figure J-1 that the image current (which is virtual), lies on the opposite side of the conducting plane, equally distant from the surface.

J.2 Addition Theorem Conditions for the Spectral Projection Model

The Spectral Projection Model has its roots in image theory because when using the addition theorem, the condition $\rho > \rho'$ must be met.

$$H_m^{(2)}(\beta|\boldsymbol{\rho}-\boldsymbol{\rho}'|)e^{jm\phi''} = \sum_{n=-\infty}^{\infty} H_{m+n}^{(2)}(\beta|\boldsymbol{\rho}|)J_n(\beta|\boldsymbol{\rho}'|)e^{j[(m+n)\phi - n\phi']} \qquad (J-1)$$

In the case of image theory, ρ' source vectors extend from the origin to the line current sources and ρ vectors are from the origin to the observation points on the surface of the conductor. See Figure J-2.

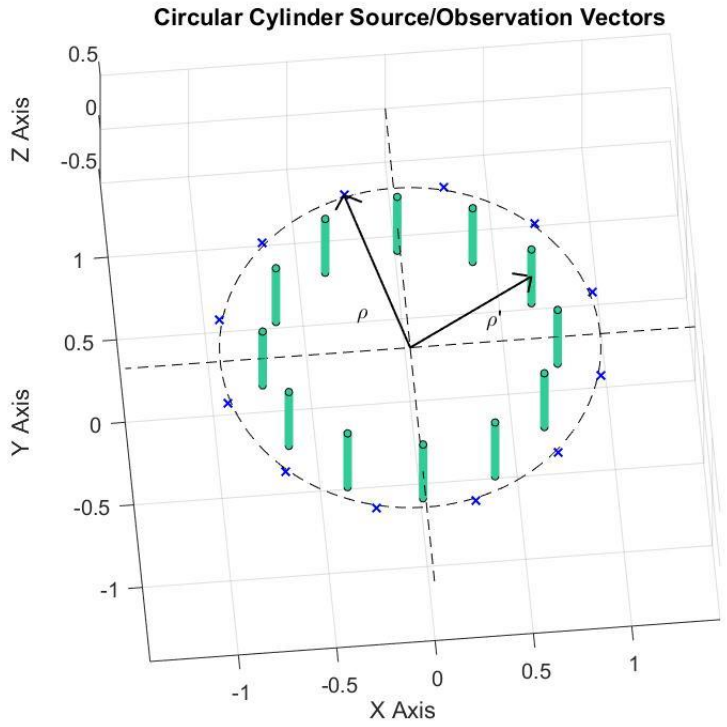

Figure J-2: Line sources in a circular conducting cylinder, and observation points on the surface.

The similarity between Figures J-1 and J-2 comes from following. For a source above an infinite ground plane, the image current lies beneath the ground plane where the electric field equals zero. For a conducting cylinder, an electric line source in the near or far field generates the incident electric field that excites the conducting cylinder. To satisfy the addition theorem the observation points must be on the conducting cylinder where the tangential electric field equals zero. Assume the radius of the circle is a. The observation points are on the surface at $\rho = a$. To

meet the addition theorem requirement for sources ρ', the relation $a < \rho'$ must be satisfied. The induced current source points and observation points are both on the cylinder surface.

J.3 Electric Line Charges near a Conducting Cylinder

For the electrostatic case, an infinitely long line charge outside a conducting ring must have an infinitely long image charge inside the ring to ensure the voltage potential on the ring equals zero. See Figure J-3.

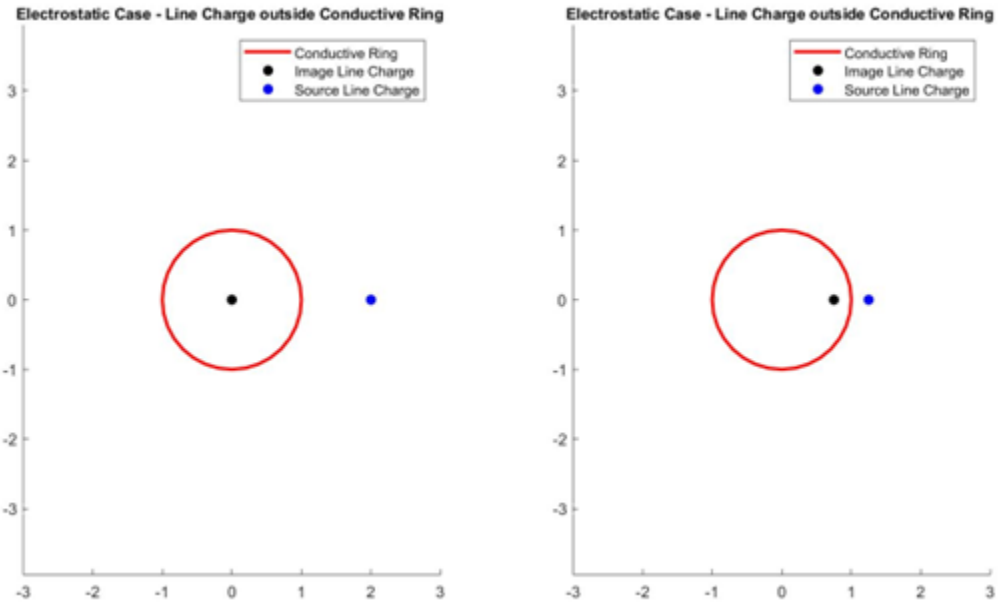

a) b)

Figure J-3: Single line charge outside an infinitely long PEC circular cylinder, and its image line charge inside the cylinder. a) Source charge is away from surface b) Source charge near surface.

For multiple infinitely long line charges outside the conducting ring spaced 60^o apart, there must be an equal number of infinitely long image line charges placed 60^o apart inside the circular cylinder. See Figure J-4. Each line charge produces an image charge on the inside of the cylinder to satisfy the boundary condition that the electric field on the conductor must equal zero.

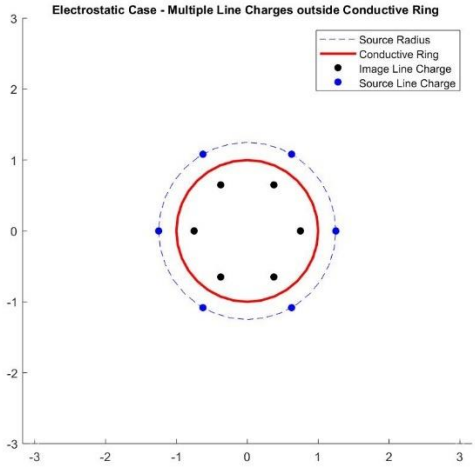

Figure J-4: Multiple line charges outside an infinitely long PEC circular cylinder and their image line charges inside the cylinder.

Similarly, each virtual current on the surface of a conductor must generate an equal and opposite induced current for the electric field boundary conditions to be satisfied. See Figure J-5. So, the electrostatic case is analogous to the time harmonic case for DSPM.

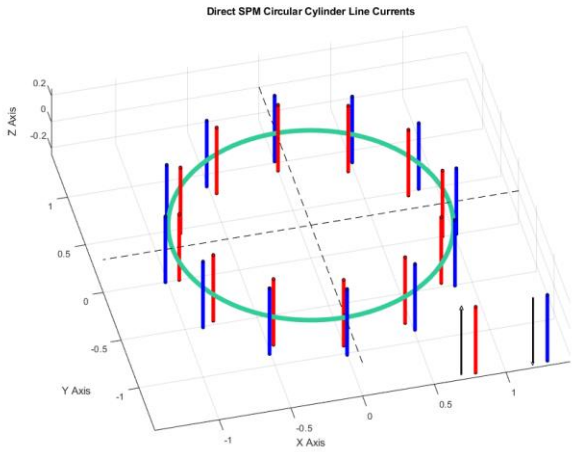

Figure J-5: Illustration of virtual current sources on an infinitely long circular cylinder in blue, and induced surface line currents in red. Surface and induced currents are in opposite directions. The cylinder is in green.

Appendix K: Fourier Series, Fourier Transform, DTFT, and DFT

K.1 Fourier Series and Transform in Time and Space

This section discusses the important relations of Fourier series and Fourier transforms used in the Spatial Frequency Technique and Spectral Projection Model [90-97]. In table K-1 the relationship between signals in the spatial domain versus the Fourier domain are listed. Discretization in one domain transforms the signal into a periodic signal in the other domain. If a signal is continuous in one domain, it is non-periodic in the alternate domain.

Table K-1: Signal Characteristics of Spatial Domain vs. Fourier Domain.

Spatial domain	Fourier domain
Continuous and non-periodic	Fourier transform
	Continuous and non-periodic
Continuous and periodic	Fourier series
	Discrete and non-periodic
Discrete and non-periodic	Discrete time (space) Fourier transform
	Continuous and periodic
Discrete and periodic	Discrete Fourier transform
	Discrete and periodic

K.2 Discrete Fourier Transform of a Function

The discrete Fourier series and discrete Fourier transform are the most effective ways of dealing with discrete waveforms. These transformations can be applied to discretized spatial waveforms analogous to the way the Fourier transform is applied to continuous waveforms in space. In the spatial frequency domain, these discretized waveforms can be thought of as frequency sampled discrete waveforms. Both the Spatial Frequency Technique and the Spectral Projection Model use the properties of the Discrete Fourier Transform and the Fourier Operator in their methodology.

The discrete Fourier transform for sequence $x[n]$ is defined in equations $(K-1)$ and $(K-2)$.

$$x[n] \overset{F}{\leftrightarrow} X(k) \qquad (K-1)$$

$$X[k] = \sum_{n=0}^{N-1} x[n] e^{-jkn\left(\frac{2\pi}{N}\right)} \qquad (K-2)$$

Shown in Figure K-1 is an example of a discretized object over one period, its discrete time (space) Fourier transform (DTFT), and five spatial periods of the discretized object, and five spatial frequency periods of its DFT.

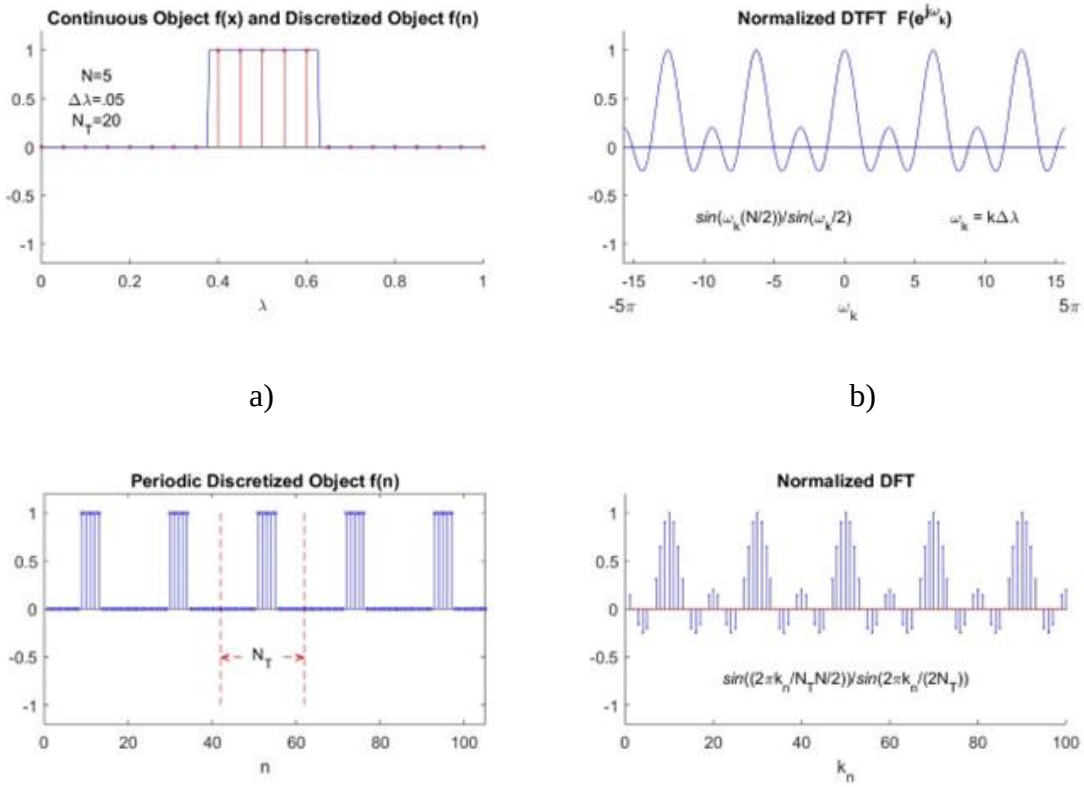

Figure K-1: a) Discretized pulse function. b) Normalized discrete time (space) Fourier transform of pulse function. c) Periodic discretized pulse function. d) Normalized discrete Fourier transform.

The two-dimensional discrete Fourier transform is written in equations $(K-3)$ and $(K-4)$.

$$x[n,m] \overset{F}{\leftrightarrow} X(k_1,k_2) \qquad (K-3)$$

$$X[k_1,k_2] = \sum_{n=0}^{N-1} \sum_{m=0}^{M-1} x[n,m] e^{-jk_1 n\left(\frac{2\pi}{N}\right)} e^{-jk_2 n\left(\frac{2\pi}{M}\right)} \qquad (K-4)$$

In order to use the DFT to analyze a PEC object like a finite length strip, one must assume that the structure is periodic in space. It is necessary to discretize the strip into sufficiently small segments so that its maximum spatial frequency is large enough to satisfy the Nyquist criterion.

The DFT is a linear transformation that maps a set of shifted delta functions at points $x_m, \in \{x_0, x_1, \ldots x_{M-1}\}$ located equally spaced on a grid, to a set of complex exponentials functions $e^{\frac{-j2\pi k_m}{M_x}}$. It also has the properties of the Fourier Transform, including the differentiation and convolution. The DFT mapping for one-dimensional and two-dimensional objects is illustrated in Figure K-2.

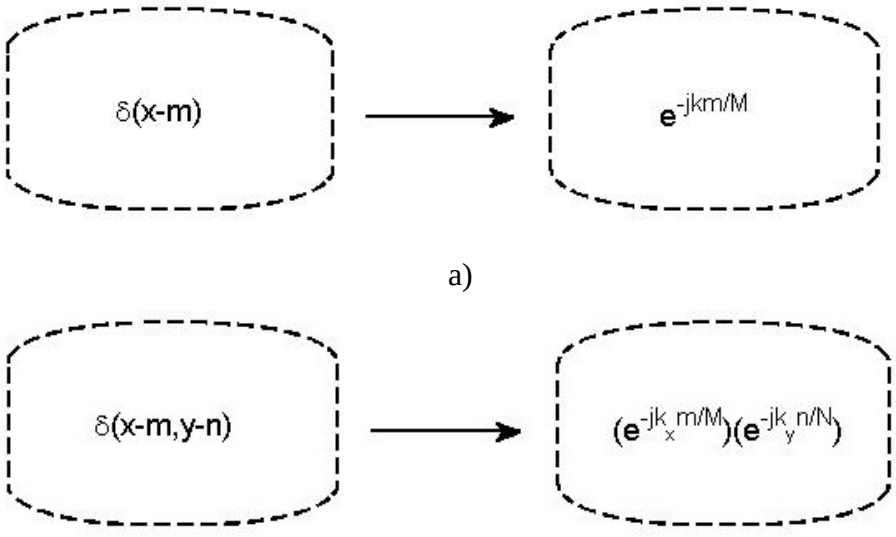

Figure K-2: Mapping from spatial domain to spatial frequency domain for a) one-dimensional DFT and b) two-dimensional DFT.

K.3 The Discrete Fourier Transform and the Roots of Unity

If one substitutes the term W_N from equation $(K-5)$ into equation $(K-2)$, equation $(K-6)$ results.

$$W_N = e^{j\left(\frac{2\pi}{N}\right)} \qquad (K-5)$$

$$X[k] = \sum_{n=0}^{N-1} x[n] W_N^{-kn} \qquad (K-6)$$

The terms $W_N^n \quad n \in \{0,1,\ldots N-1\}$ are called the *N* roots of unity. Illustrated in Figure K-3 are the roots of unity for a 4-point DFT and an 8-point DFT.

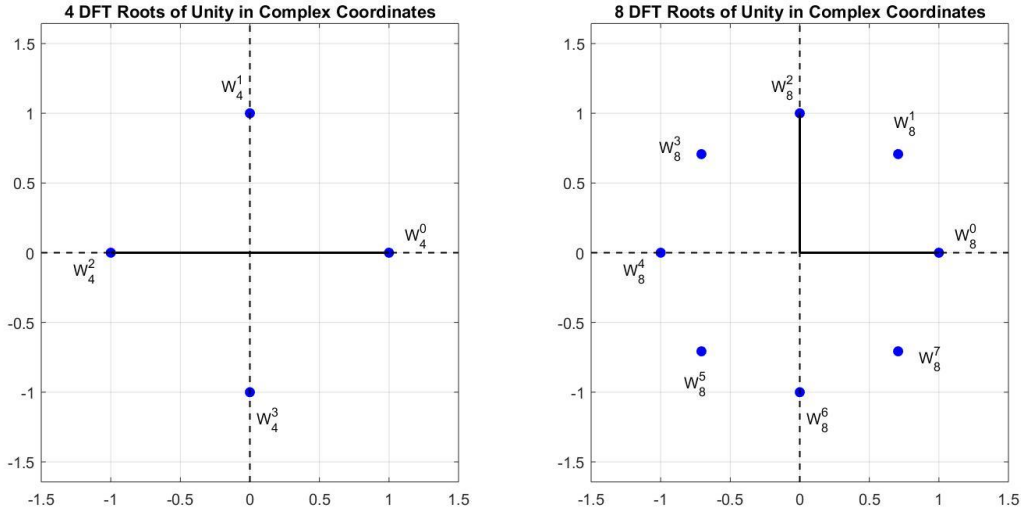

a) b)

Figure K-3: Roots of unity for a a) 4-point DFT and a b) 8-point DFT.

For a four-point DFT, the roots of unity calculated in equations $(K-7)$ through $(K-10)$.

$$W_0^4 = e^{j\left(\frac{2\pi}{4}\right)(0)} = 1 \qquad (K-7)$$

$$W_1^4 = e^{j\left(\frac{2\pi}{4}\right)(1)} = i \qquad (K-8)$$

$$W_2^4 = e^{j\left(\frac{2\pi}{4}\right)(2)} = -1 \qquad (K-9)$$

$$W_3^4 = e^{-j\left(\frac{2\pi}{4}\right)(3)} = -i \qquad (K-10)$$

These points given in equations $(K-7)$ to $(K-10)$ are plotted in Figure K-3.

K.4 Fourier Operator

In order to calculate the discrete Fourier transform of a vector containing points $x_m, \in \{x_0, x_1, \ldots x_{M-1} \quad\}$, one may project the vector $\hat{x}$ given in equation $(K-11)$

$$\hat{x} = \begin{bmatrix} x(0) \\ x(1) \\ x(2) \\ x(3) \end{bmatrix} \tag{K-11}$$

onto the Fourier operator given in equation $(K-12)$.

$$F = \begin{bmatrix} 1 & 1 & 1 & 1 \\ 1 & \left(e^{-j\frac{2\pi}{4}}\right)^1 & \left(e^{-j\frac{2\pi}{4}}\right)^2 & \left(e^{-j\frac{2\pi}{4}}\right)^3 \\ 1 & \left(e^{-j\frac{2\pi}{4}}\right)^2 & \left(e^{-j\frac{2\pi}{4}}\right)^4 & \left(e^{-j\frac{2\pi}{4}}\right)^6 \\ 1 & \left(e^{-j\frac{2\pi}{4}}\right)^3 & \left(e^{-j\frac{2\pi}{4}}\right)^6 & \left(e^{-j\frac{2\pi}{4}}\right)^9 \end{bmatrix} \tag{K-12}$$

The resulting discrete Fourier transform $\hat{X}$ of the vector $\hat{x}$ is shown in equation $(K-13)$.

$$\begin{bmatrix} 1 & 1 & 1 & 1 \\ 1 & \left(e^{-j\frac{2\pi}{4}}\right)^1 & \left(e^{-j\frac{2\pi}{4}}\right)^2 & \left(e^{-j\frac{2\pi}{4}}\right)^3 \\ 1 & \left(e^{-j\frac{2\pi}{4}}\right)^2 & \left(e^{-j\frac{2\pi}{4}}\right)^4 & \left(e^{-j\frac{2\pi}{4}}\right)^6 \\ 1 & \left(e^{-j\frac{2\pi}{4}}\right)^3 & \left(e^{-j\frac{2\pi}{4}}\right)^6 & \left(e^{-j\frac{2\pi}{4}}\right)^9 \end{bmatrix} \begin{bmatrix} x(0) \\ x(1) \\ x(2) \\ x(3) \end{bmatrix} = \begin{bmatrix} X(K_0) \\ X(K_1) \\ X(K_2) \\ X(K_3) \end{bmatrix} \tag{K-13}$$

One advantage to transforming calculations to the Fourier domain is the ability to use the FFT algorithm [98,99] to speed up calculations. This was used in formulating the SFT analysis, and used in the SPM and DSPM analysis in calculating Hadamard products.

K.5 Fourier Transform of Some Important Green's Functions

The Fourier transform of important Green's functions used in this dissertation are presented next. These Fourier transforms were used extensively in the development of the Spatial Frequency Technique for analyzing various one dimensional and two-dimension structures. For two dimensional problems, the Hankel function of the second kind and first kind are usually used. The Fourier transform of each is given below in equations $(K-14)$ through $(K-17)$.

$$F\left\{H_0^{(2)}\left(k_0\sqrt{x^2+y^2}\right)\right\}$$

$$= \int_{-\infty}^{\infty}\int_{-\infty}^{\infty} H_0^{(2)}\left(k_0\sqrt{x^2+y^2}\right)e^{jxk_x}e^{jyk_y}dxdy \qquad (K-14)$$

$$F\left\{H_0^{(2)}\left(k_0\sqrt{x^2+y^2}\right)\right\} = \frac{-1}{2\pi\left(k_0^2-k_x^2-k_y^2\right)} \qquad (K-15)$$

$$F\left\{\frac{j}{4}H_0^{(1)}\left(k_0\sqrt{x^2+y^2}\right)\right\}$$

$$= \frac{j}{4}\int_{-\infty}^{\infty}\int_{-\infty}^{\infty} H_0^{(1)}\left(k_0\sqrt{x^2+y^2}\right)e^{jxk_x}e^{jyk_y}dxdy \qquad (K-16)$$

$$F\left\{\frac{j}{4}H_0^{(1)}\left(k_0\sqrt{x^2+y^2}\right)\right\} = \frac{-1}{2\pi\left(k_0^2-k_x^2-k_y^2\right)} \qquad (K-17)$$

For three dimensional problems, the Hankel function of the second kind is used often also. The Fourier transform of this function is given below in equations $(K-18)$ to $(K-19)$.

$$F\left\{H_0^{(2)}\left(k_0\sqrt{x^2+y^2+z^2}\right)\right\}$$

$$= \int_{-\infty}^{\infty}\int_{-\infty}^{\infty} H_0^{(2)}\left(k_0\sqrt{x^2+y^2+z^2}\right)e^{jxk_x}e^{jyk_y}e^{jzk_z}dxdydz \qquad (\mathrm{K}-18)$$

$$F\left\{H_0^{(2)}\left(k_0\sqrt{x^2+y^2+z^2}\right)\right\} = \frac{-1}{2\pi\left(k_0^2-k_x^2-k_y^2-k_z^2\right)} \qquad (K-19)$$

For one dimensional problems with symmetry around the origin, the Hankel function $H_0^{(2)}(k_0|x|)$, is the correct choice of Green's function. The corresponding Fourier transform is given in equations $(K-20)$ and $(K-22)$.

$$F\left\{H_0^{(2)}(k_0|x|)\right\} = \int_{-\infty}^{\infty} H_0^{(2)}(k_0|x|)\,e^{-jkx}dx \qquad (K-20)$$

$$F\left\{H_0^{(2)}(k_0|x|)\right\} = \frac{2}{\sqrt{k_0^2-k^2}} \qquad k_0 > k \qquad (K-21)$$

$$F\left\{H_0^{(2)}(k_0|x|)\right\} = \frac{2}{\sqrt{k^2-k_0^2}} \qquad k_0 < k \qquad (K-22)$$

For two dimensional problems in which one integrates only the x variable, the Fourier transforms in equations $(K-23)$ to $(K-25)$ may be used.

$$F\left\{H_0^{(2)}\left(k_0\sqrt{x^2+y^2}\right)\right\}=\int_{-\infty}^{\infty}H_0^{(2)}\left(k_0\sqrt{x^2+y^2}\right)e^{-jkx}dx \qquad (K-23)$$

$$F\left\{H_0^{(2)}\left(k_0\sqrt{x^2+y^2}\right)\right\}=\frac{2e^{-j|y|\sqrt{k_0^2-k^2}}}{\sqrt{k_0^2-k^2}} \qquad k_0>k \qquad (K-24)$$

$$F\left\{H_0^{(2)}\left(k_0\sqrt{x^2+y^2}\right)\right\}=\frac{2je^{-j|y|\sqrt{k^2-k_0^2}}}{\sqrt{k^2-k_0^2}} \qquad k_0<k \qquad (K-25)$$

For three dimensional problems from point sources, the spherical Hankel function is important to use. Below in equations $(K-26)$ to $(K-28)$ is the Fourier transform taken with respect to only the x variable.

$$F\left\{h_0^{(2)}\left(k_0\sqrt{x^2+y^2}\right)\right\}=\int_{-\infty}^{\infty}h_0^{(2)}\left(k_0\sqrt{x^2+y^2}\right)e^{-jkx}dx \qquad (K-26)$$

$$F\left\{h_0^{(2)}\left(k_0\sqrt{x^2+y^2}\right)\right\}=\frac{2}{\sqrt{k_0}}\,H_0^{(2)}\left(|y|\sqrt{k_0^2-k^2}\right) \qquad k_0>k \qquad (K-27)$$

$$F\left\{h_0^{(2)}\left(k_0\sqrt{x^2+y^2}\right)\right\}=j\frac{4}{\pi\sqrt{k_0}}K_0\left(|y|\sqrt{k^2-k_0^2}\right) \qquad k_0<k \qquad (K-28)$$

For spherical Hankel functions integrated with respect to two variables, equations $(K-29)$ and $(K-30)$ are used.

$$F\left\{\int_{-\infty}^{\infty}\int_{-\infty}^{\infty}h_0^{(2)}\left(k_0\sqrt{x^2+y^2}\right)\right\}=\int_{-\infty}^{\infty}\int_{-\infty}^{\infty}h_0^{(2)}\left(k_0\sqrt{x^2+y^2}\right)e^{-jk_xx}e^{-jk_yy}dxdy \qquad (K-29)$$

$$F\left\{\int_{-\infty}^{\infty}\int_{-\infty}^{\infty}h_0^{(2)}\left(k_0\sqrt{x^2+y^2}\right)\right\}=\frac{4/\sqrt{k_0}}{\sqrt{k_0^2-k_x^2-k_y^2}} \qquad k_0>\sqrt{k_x^2+k_y^2} \qquad (K-30)$$

K.6 Discrete Fourier Transform for Non-Grid Objects

The following discrete Fourier transforms were used for objects which when discretized did not have uniform spacing, and non-uniform grids with $dx=\frac{L_1}{N}$ and $dy=\frac{L_2}{N}$ could be used.

$$G_{DFT}(k_x) = \frac{1}{N}\sum_{n=0}^{N-1} g(x[n])e^{-\frac{jk_x x[n]}{dx \cdot N}} \qquad (K-31)$$

$$G_{DFT}(k_x, k_y) = \frac{1}{NM}\sum_{n=0}^{N-1}\sum_{m=0}^{M-1} g(x[n], y[m])\left(e^{-\frac{jk_x x[n]}{dx \cdot N}}\right)\left(e^{-\frac{jk_y y[m]}{dy \cdot M}}\right) \qquad (K-32)$$

For discretization along an angle ψ from 0 to 2π with $d\psi = \frac{2\pi}{N}$,

$$G_{DFT}(k) = \frac{1}{N}\sum_{n=0}^{N-1} e^{-\frac{jk\psi[n]}{d\psi \cdot N}} \qquad (K-33)$$

Appendix L: Hadamard Product, Fourier Operators, and Convolution

L.1 Definition of a Hadamard Product

The Hadamard product ∘ is an element-by-element multiplication of two *M x N* matrices. The symbol ∘ will represent the multiplication operation. An example is given in equation $(L-1)$.

$$\begin{bmatrix} a & b \\ c & d \end{bmatrix} \circ \begin{bmatrix} e & f \\ g & h \end{bmatrix} = \begin{bmatrix} ae & bf \\ cg & dh \end{bmatrix} = A \qquad (L-1)$$

L.2 Hadamard Product Properties

The Hadamard product [100] has many properties which are stated below in equations $(L-2)$ through $(L-6)$.

$$C = A \circ B = B \circ A \qquad (L-2)$$

$$Cx = [A \circ B]x \qquad (L-3)$$

$$C \circ (A+B) = C \circ A + C \circ B \qquad (L-4)$$

$$\alpha(A \circ B) = (\alpha A) \circ B = A \circ (\alpha B) \qquad (L-5)$$

$$D(A \circ B)E = DAE \circ B = (DA) \circ (BE) \qquad (L-6)$$

L.3 Spectral Projection Model and the Hadamard Product

The **J**-spectral signature and **H**-spectral signature may be written as the Hadamard products shown below in equations $(L-7)$ to $(L-10)$.

$$\begin{bmatrix} \vdots & \vdots & \vdots \\ \vdots & J_k(\beta|\boldsymbol{\rho_n}|)e^{jk\phi_n} & \vdots \\ \vdots & \vdots & \vdots \end{bmatrix}$$

$$= \begin{bmatrix} J_{-K}(\beta|\boldsymbol{\rho_0}|)e^{-jK\phi_0} & \vdots & \vdots & \vdots & J_{-K}(\beta|\boldsymbol{\rho_{N-1}}|)e^{-jK\phi_{N-1}} \\ \vdots & \vdots & \vdots & \vdots & \vdots \\ \vdots & \vdots & J_k(\beta|\boldsymbol{\rho_n}|)e^{jk\phi_n} & \vdots & \vdots \\ \vdots & \vdots & \vdots & \vdots & \vdots \\ J_K(\beta|\boldsymbol{\rho_0}|)e^{jK\phi_0} & \vdots & \vdots & \vdots & J_K(\beta|\boldsymbol{\rho_{N-1}}|)e^{jK\phi_{N-1}} \end{bmatrix} \qquad (L-7)$$

$$\begin{bmatrix} \vdots & \vdots & \vdots \\ \vdots & J_k(\beta|\boldsymbol{\rho_n}|)e^{jk\phi_n} & \vdots \\ \vdots & \vdots & \vdots \end{bmatrix}$$

$$= \begin{bmatrix} J_{-K}(\beta|\boldsymbol{\rho_0}|) & \vdots & \vdots & \vdots & J_{-K}(\beta|\boldsymbol{\rho_{N-1}}|) \\ \vdots & \vdots & \vdots & \vdots & \vdots \\ \vdots & \vdots & J_k(\beta|\boldsymbol{\rho_n}|) & \vdots & \vdots \\ \vdots & \vdots & \vdots & \vdots & \vdots \\ J_K(\beta|\boldsymbol{\rho_0}|) & \vdots & \vdots & \vdots & J_K(\beta|\boldsymbol{\rho_{N-1}}|) \end{bmatrix} \circ \begin{bmatrix} e^{-jK\phi_0} & \vdots & \vdots & \vdots & e^{-jK\phi_{N-1}} \\ \vdots & \vdots & \vdots & \vdots & \vdots \\ \vdots & \vdots & e^{jk\phi_n} & \vdots & \vdots \\ \vdots & \vdots & \vdots & \vdots & \vdots \\ e^{jK\phi_0} & \vdots & \vdots & \vdots & e^{jK\phi_{N-1}} \end{bmatrix}$$

$$(L-8)$$

$$\begin{bmatrix} \vdots & \vdots & \vdots \\ \vdots & H_k^{(2)}(\beta|\boldsymbol{\rho_n}|)e^{jk\phi_n} & \vdots \\ \vdots & \vdots & \vdots \end{bmatrix}$$

$$= \begin{bmatrix} H_{-K}^{(2)}(\beta|\boldsymbol{\rho_0}|)e^{-jK\phi_0} & \vdots & \vdots & \vdots & H_{-K}^{(2)}\left(\beta\left|\boldsymbol{\rho_{N_0-1}}\right|\right)e^{-jK\phi_{N-1}} \\ \vdots & \vdots & \vdots & \vdots & \vdots \\ \vdots & \vdots & H_k^{(2)}(\beta|\boldsymbol{\rho_n}|)e^{jk\phi_n} & \vdots & \vdots \\ \vdots & \vdots & \vdots & \vdots & \vdots \\ H_K^{(2)}(\beta|\boldsymbol{\rho_0}|)e^{jK\phi_0} & \vdots & \vdots & \vdots & H_K^{(2)}\left(\beta\left|\boldsymbol{\rho_{N_0-1}}\right|\right)e^{jK\phi_{N-1}} \end{bmatrix} \qquad (L-9)$$

$$\begin{bmatrix} \vdots & \vdots & \vdots \\ \vdots & H_k^{(2)}(\beta|\boldsymbol{\rho_n}|)e^{jk\phi_n} & \vdots \\ \vdots & \vdots & \vdots \end{bmatrix}$$

$$= \begin{bmatrix} H_{-K}^{(2)}(\beta|\boldsymbol{\rho_0}|) & \vdots & \vdots & \vdots & H_{-K}^{(2)}(\beta|\boldsymbol{\rho_{N-1}}|) \\ \vdots & \vdots & \vdots & \vdots & \vdots \\ \vdots & \vdots & H_k^{(2)}(\beta|\boldsymbol{\rho_n}|) & \vdots & \vdots \\ \vdots & \vdots & \vdots & \vdots & \vdots \\ H_K^{(2)}(\beta|\boldsymbol{\rho}_0|) & \vdots & \vdots & \vdots & H_K^{(2)}(\beta|\boldsymbol{\rho_{N-1}}|) \end{bmatrix} \circ \begin{bmatrix} e^{-jK\phi_0} & \vdots & \vdots & \vdots & e^{-jK\phi_{N-1}} \\ \vdots & \vdots & \vdots & \vdots & \vdots \\ \vdots & \vdots & e^{jk\phi_n} & \vdots & \vdots \\ \vdots & \vdots & \vdots & \vdots & \vdots \\ e^{jK\phi_0} & \vdots & \vdots & \vdots & e^{jK\phi_{N-1}} \end{bmatrix}$$

$$(L-10)$$

$$\begin{bmatrix} e^{-jK\phi_0} & \vdots & \vdots & \vdots & e^{-jK\phi_{N-1}} \\ \vdots & \vdots & \vdots & \vdots & \vdots \\ \vdots & \vdots & e^{jk\phi_n} & \vdots & \vdots \\ \vdots & \vdots & \vdots & \vdots & \vdots \\ e^{jK\phi_0} & \vdots & \vdots & \vdots & e^{jK\phi_{N-1}} \end{bmatrix} = exp \begin{bmatrix} -jK\phi_0 & \vdots & \vdots & \vdots & -jK\phi_{N-1} \\ \vdots & \vdots & \vdots & \vdots & \vdots \\ \vdots & \vdots & jk\phi_n & \vdots & \vdots \\ \vdots & \vdots & \vdots & \vdots & \vdots \\ jK\phi_0 & \vdots & \vdots & \vdots & jK\phi_{N-1} \end{bmatrix} \qquad (L-11)$$

The shifted Fourier operator $\begin{bmatrix} \cdots & \cdots & \cdots \\ \cdots & \bar{\bar{F}} & \cdots \\ \cdots & \cdots & \cdots \end{bmatrix}$ is defined by equation $(L-12)$ for the angles $\phi_n \quad n \in \{0,1,\ldots N-1\}$ where $\phi_n = 2\pi n/N$.

$$\begin{bmatrix} \cdots & \cdots & \cdots \\ \cdots & \bar{F} & \cdots \\ \cdots & \cdots & \cdots \end{bmatrix} = \begin{bmatrix} e^{-jK\phi_0} & : & : & : & e^{-jK\phi_{N-1}} \\ : & : & : & : & : \\ : & : & e^{jk\phi_n} & : & : \\ : & : & : & : & : \\ e^{jK\phi_0} & : & : & : & e^{jK\phi_{N-1}} \end{bmatrix} \qquad (L-12)$$

L.4 SPM and Unitary Matrices

As mentioned earlier in this appendix, a unitary matrix U has the unique property $U^H = U^{-1}$. This leads to the fundamental property of unitary matrices: the inverse of U equals the conjugate transpose of U, or

$$UU^H = I \qquad (L-13)$$

The Fourier operator matrix $\begin{bmatrix} \cdots & \cdots & \cdots \\ \cdots & F & \cdots \\ \cdots & \cdots & \cdots \end{bmatrix}$ is unitary. For the *N* roots of unity defined in equation $(L-14)$,

$$W_N = e^{j(2\pi/N)} \qquad (L-14)$$

the Fourier operator matrix for $N = 4$ becomes equation $(L-15)$.

$$\begin{bmatrix} \cdots & \cdots & \cdots \\ \cdots & F & \cdots \\ \cdots & \cdots & \cdots \end{bmatrix} = \begin{bmatrix} 1 & 1 & 1 & 1 \\ 1 & {W_N}^{-1} & {W_N}^{-2} & {W_N}^{-3} \\ 1 & {W_N}^{-2} & {W_N}^{-4} & {W_N}^{-6} \\ 1 & {W_N}^{-3} & {W_N}^{-6} & {W_N}^{-9} \end{bmatrix} \qquad (L-15)$$

and the inverse Fourier operator matrix for $N = 4$ becomes equation $(L-16)$

$$\begin{bmatrix} \cdots & \cdots & \cdots \\ \cdots & F & \cdots \\ \cdots & \cdots & \cdots \end{bmatrix}^H = \begin{bmatrix} 1 & 1 & 1 & 1 \\ 1 & {W_N}^{1} & {W_N}^{2} & {W_N}^{3} \\ 1 & {W_N}^{2} & {W_N}^{4} & {W_N}^{6} \\ 1 & {W_N}^{3} & {W_N}^{6} & {W_N}^{9} \end{bmatrix} \qquad (L-16)$$

This matrix satisfies the following equation for unitary matrices,

$$\begin{bmatrix} \cdots & \cdots & \cdots \\ \cdots & F & \cdots \\ \cdots & \cdots & \cdots \end{bmatrix} \begin{bmatrix} \cdots & \cdots & \cdots \\ \cdots & F & \cdots \\ \cdots & \cdots & \cdots \end{bmatrix}^H = \begin{bmatrix} \cdots & \cdots & \cdots \\ \cdots & I & \cdots \\ \cdots & \cdots & \cdots \end{bmatrix} \qquad (L-17)$$

The unitary property of the Fourier Operator, $\begin{bmatrix} \cdots & \cdots & \cdots \\ \cdots & F & \cdots \\ \cdots & \cdots & \cdots \end{bmatrix}$, is shown graphically in Figure L-1.

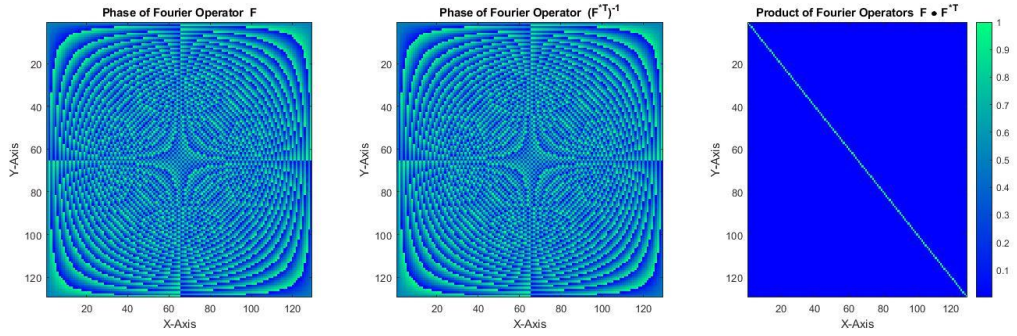

a) b) c)

Figure L-1: Fourier operator matrices. a) Fourier operator. b) Phase of the inverse conjugate transpose of Fourier operator. c) Magnitude product of the two matrices.

The shifted Fourier operator matrix $\begin{bmatrix} \cdots & \cdots & \cdots \\ \cdots & \bar{F} & \cdots \\ \cdots & \cdots & \cdots \end{bmatrix}$ described in equation $(L-18)$ is unitary, and satisfies the following equation,

$$\begin{bmatrix} \cdots & \cdots & \cdots \\ \cdots & \bar{F} & \cdots \\ \cdots & \cdots & \cdots \end{bmatrix}\begin{bmatrix} \cdots & \cdots & \cdots \\ \cdots & \bar{F} & \cdots \\ \cdots & \cdots & \cdots \end{bmatrix}^{H} = \begin{bmatrix} \cdots & \cdots & \cdots \\ \cdots & I & \cdots \\ \cdots & \cdots & \cdots \end{bmatrix} \qquad (L-18)$$

The matrix $\begin{bmatrix} \cdots & \cdots & \cdots \\ \cdots & \bar{F} & \cdots \\ \cdots & \cdots & \cdots \end{bmatrix}^{H}$ is a shifted version of the inverse Fourier operator. The matrix $\begin{bmatrix} \cdots & \cdots & \cdots \\ \cdots & S & \cdots \\ \cdots & \cdots & \cdots \end{bmatrix}$ shifts the rows of $\begin{bmatrix} \cdots & \cdots & \cdots \\ \cdots & F & \cdots \\ \cdots & \cdots & \cdots \end{bmatrix}^{H}$ downward by $K/2$.

$$\begin{bmatrix} \cdots & \cdots & \cdots \\ \cdots & \bar{F} & \cdots \\ \cdots & \cdots & \cdots \end{bmatrix}^{H} = \begin{bmatrix} \cdots & \cdots & \cdots \\ \cdots & S & \cdots \\ \cdots & \cdots & \cdots \end{bmatrix}\begin{bmatrix} \cdots & \cdots & \cdots \\ \cdots & F & \cdots \\ \cdots & \cdots & \cdots \end{bmatrix}^{H} \qquad (L-19)$$

An example of the shifted Fourier matrix is shown below. A shift matrix is defined in equation $(L-20)$,

$$\begin{bmatrix} \cdots & \cdots & \cdots \\ \cdots & S & \cdots \\ \cdots & \cdots & \cdots \end{bmatrix} = \begin{bmatrix} 0 & 0 & 0 & 1 & 0 \\ 0 & 0 & 0 & 0 & 1 \\ 1 & 0 & 0 & 0 & 0 \\ 0 & 1 & 0 & 0 & 0 \\ 0 & 0 & 1 & 0 & 0 \end{bmatrix} \qquad row\ shift\ down\ 2 \qquad (L-20)$$

and Fourier operator in equation $(L-21)$.

$$\begin{bmatrix} \cdots & \cdots & \cdots \\ \cdots & F & \cdots \\ \cdots & \cdots & \cdots \end{bmatrix}^H = \begin{bmatrix} 1 & 1 & 1 & 1 & 1 \\ 1 & {W_N}^1 & {W_N}^2 & {W_N}^3 & {W_N}^4 \\ 1 & {W_N}^2 & {W_N}^4 & {W_N}^6 & {W_N}^8 \\ 1 & {W_N}^3 & {W_N}^6 & {W_N}^9 & {W_N}^{12} \\ 1 & {W_N}^4 & {W_N}^8 & {W_N}^{12} & {W_N}^{16} \end{bmatrix} \qquad (L-21)$$

The shifted inverse Fourier operator is shown in equation $(L-21)$.

$$\begin{bmatrix} \cdots & \cdots & \cdots \\ \cdots & \bar{F} & \cdots \\ \cdots & \cdots & \cdots \end{bmatrix}^H = \begin{bmatrix} 1 & {W_N}^3 & {W_N}^6 & {W_N}^9 & {W_N}^{12} \\ 1 & {W_N}^4 & {W_N}^8 & {W_N}^{12} & {W_N}^{16} \\ 1 & {W_N}^0 & {W_N}^0 & {W_N}^0 & {W_N}^0 \\ 1 & {W_N}^1 & {W_N}^2 & {W_N}^3 & {W_N}^4 \\ 1 & {W_N}^2 & {W_N}^4 & {W_N}^6 & {W_N}^8 \end{bmatrix} \qquad (L-22)$$

Now multiply the first two rows of $\begin{bmatrix} \cdots & \cdots & \cdots \\ \cdots & \bar{F} & \cdots \\ \cdots & \cdots & \cdots \end{bmatrix}^H$ in equation $(L-21)$ by multiples of $n \cdot 2\pi/N$ with $N = 5$, and rewrite equation $(L-23)$.

$$\begin{bmatrix} \cdots & \cdots & \cdots \\ \cdots & \bar{F} & \cdots \\ \cdots & \cdots & \cdots \end{bmatrix}^H = \begin{bmatrix} 1 & {W_N}^{-2} & {W_N}^{-4} & {W_N}^{-6} & {W_N}^{-8} \\ 1 & {W_N}^{-1} & {W_N}^{-2} & {W_N}^{-3} & {W_N}^{-4} \\ 1 & {W_N}^0 & {W_N}^0 & {W_N}^0 & {W_N}^0 \\ 1 & {W_N}^1 & {W_N}^2 & {W_N}^3 & {W_N}^4 \\ 1 & {W_N}^2 & {W_N}^4 & {W_N}^6 & {W_N}^8 \end{bmatrix} \qquad (L-23)$$

After comparing the functions $exp\begin{bmatrix} \cdots & \cdots & \cdots \\ \cdots & \bar{F} & \cdots \\ \cdots & \cdots & \cdots \end{bmatrix}^H$ and equation $(L-11)$, the expressions are the same for both.

$$exp\begin{bmatrix} \cdots & \cdots & \cdots \\ \cdots & \bar{F} & \cdots \\ \cdots & \cdots & \cdots \end{bmatrix}^H = exp\left(j\begin{bmatrix} 0 & -2 & -4 & -6 & -8 \\ 0 & -1 & -2 & -3 & -4 \\ 0 & 0 & 0 & 0 & 0 \\ 0 & 1 & 2 & 3 & 4 \\ 0 & 2 & 4 & 6 & 8 \end{bmatrix}\frac{2\pi}{5} \right) \qquad (L-24)$$

It is clear that the shifted inverse Fourier operator in equation $(L-11)$ is the same as that in $(L-23)$ when $\phi_{n+1} - \phi_n = 2\pi/N$ and $\phi_0 = 0$. Depending upon whether the modes are ordered from $\{-K \ldots k \ldots K\}$ or $\{K \ldots k \ldots -K\}$ will determine whether the exponential matrix for the spectral signatures is the shifted Fourier operator or the shifted inverse Fourier operator.

The large argument approximation for a Hankel function with angle $\phi_0{}'$ is given in equation $(5-70)$.

$$H_k^{(2)}(\beta|\boldsymbol{\rho_0}'|)|_{\rho_0{}'\to\infty} \Rightarrow e^{jk\left(\phi_0{}'-\frac{\pi}{2}\right)} \tag{5-70}$$

The **H**-spectral signature matrix for large arguments is given in equation $(L-25)$.

$$\begin{bmatrix} \vdots & \vdots & \vdots \\ \vdots & H_k^{(2)}(\beta|\boldsymbol{\rho_n}|)|_{\rho_n\to\infty} & \vdots \\ \vdots & \vdots & \vdots \end{bmatrix} = \begin{bmatrix} e^{-jK\left(\phi_0-\frac{\pi}{2}\right)} & \vdots & \vdots & \vdots & e^{-jK\left(\phi_{N_S-1}-\frac{\pi}{2}\right)} \\ \vdots & \vdots & \vdots & \vdots & \vdots \\ \vdots & \vdots & \vdots & \vdots & \vdots \\ \vdots & \vdots & \vdots & \vdots & \vdots \\ e^{jK\left(\phi_0-\frac{\pi}{2}\right)} & \vdots & \vdots & \vdots & e^{jK\left(\phi_{N_S-1}-\frac{\pi}{2}\right)} \end{bmatrix} \tag{L-25}$$

If each column of the shifted inverse Fourier operator is multiplied by the phase shift $e^{-jk\frac{\pi}{2}}$, one obtains the far-field **H**-spectral signature matrix.

The far-field **H**-spectral signature matrix is equal to matrix product $\begin{bmatrix} \ddots & 0 & 0 \\ 0 & D_S & 0 \\ 0 & 0 & \ddots \end{bmatrix}\begin{bmatrix} \cdots & \cdots & \cdots \\ \cdots & \overline{F^H} & \cdots \\ \cdots & \cdots & \cdots \end{bmatrix}$ where the diagonal matrix $\begin{bmatrix} \ddots & 0 & 0 \\ 0 & D_S & 0 \\ 0 & 0 & \ddots \end{bmatrix}$ applies the $e^{-jk\frac{\pi}{2}}$ phase shift to each column.

$$\begin{bmatrix} \ddots & 0 & 0 & 0 & 0 \\ 0 & \ddots & 0 & 0 & 0 \\ 0 & 0 & D_S & 0 & 0 \\ 0 & 0 & 0 & \ddots & 0 \\ 0 & 0 & 0 & 0 & \ddots \end{bmatrix} = \begin{bmatrix} e^{jK\frac{\pi}{2}} & 0 & 0 & 0 & 0 \\ 0 & \ddots & 0 & 0 & 0 \\ 0 & 0 & e^{-jk\frac{\pi}{2}} & 0 & 0 \\ 0 & 0 & 0 & \ddots & 0 \\ 0 & 0 & 0 & 0 & e^{-jK\frac{\pi}{2}} \end{bmatrix} \tag{5-121}$$

Thus, the matrix equality between the far-field **H**-spectral signature matrix and the DFT Fourier operator exists as given in equation $(5-122)$ and $(5-123)$.

$$\begin{bmatrix} \cdots & \cdots & \cdots \\ \cdots & H_k^{(2)}(\beta(\rho\to\infty) & \cdots \\ \cdots & \cdots & \cdots \end{bmatrix} = \begin{bmatrix} \ddots & 0 & 0 \\ 0 & D_S & 0 \\ 0 & 0 & \ddots \end{bmatrix}\begin{bmatrix} \cdots & \cdots & \cdots \\ \cdots & \overline{F^H} & \cdots \\ \cdots & \cdots & \cdots \end{bmatrix} \tag{5-122}$$

L.5 Hadamard Product and Convolution

Two important properties used in SPM and DSPM is that the addition theorem is a form of convolution. Define a matrix $\begin{bmatrix} \cdots & \cdots & \cdots \\ \cdots & H_{ob} & \cdots \\ \cdots & \cdots & \cdots \end{bmatrix}$ which is the convolution $*$ of the matrices $\begin{bmatrix} \cdots & \cdots & \cdots \\ \cdots & H & \cdots \\ \cdots & \cdots & \cdots \end{bmatrix}$ and $\begin{bmatrix} \cdots & \cdots & \cdots \\ \cdots & J & \cdots \\ \cdots & \cdots & \cdots \end{bmatrix}$.

$$\begin{bmatrix} \cdots & \cdots & \cdots \\ \cdots & H_{ob} & \cdots \\ \cdots & \cdots & \cdots \end{bmatrix} = \begin{bmatrix} \cdots & \cdots & \cdots \\ \cdots & H & \cdots \\ \cdots & \cdots & \cdots \end{bmatrix} \otimes \begin{bmatrix} \cdots & \cdots & \cdots \\ \cdots & J & \cdots \\ \cdots & \cdots & \cdots \end{bmatrix} \qquad (L-26)$$

If one converts these to the Fourier domain, one can write the convolution as a Hadamard product,

$$\begin{bmatrix} \cdots & \cdots & \cdots \\ \cdots & F & \cdots \\ \cdots & \cdots & \cdots \end{bmatrix} \begin{bmatrix} \cdots & \cdots & \cdots \\ \cdots & H_{ob} & \cdots \\ \cdots & \cdots & \cdots \end{bmatrix} = \begin{bmatrix} \cdots & \cdots & \cdots \\ \cdots & F & \cdots \\ \cdots & \cdots & \cdots \end{bmatrix} \begin{bmatrix} \cdots & \cdots & \cdots \\ \cdots & H & \cdots \\ \cdots & \cdots & \cdots \end{bmatrix} \odot \begin{bmatrix} \cdots & \cdots & \cdots \\ \cdots & F & \cdots \\ \cdots & \cdots & \cdots \end{bmatrix} \begin{bmatrix} \cdots & \cdots & \cdots \\ \cdots & J & \cdots \\ \cdots & \cdots & \cdots \end{bmatrix} \qquad (L-27)$$

and calculate the product by equation $(\mathrm{L}-28)$.

$$\begin{bmatrix} \cdots & \cdots & \cdots \\ \cdots & H_{ob} & \cdots \\ \cdots & \cdots & \cdots \end{bmatrix} = \begin{bmatrix} \cdots & \cdots & \cdots \\ \cdots & F & \cdots \\ \cdots & \cdots & \cdots \end{bmatrix}^{H} \left(\begin{bmatrix} \cdots & \cdots & \cdots \\ \cdots & F & \cdots \\ \cdots & \cdots & \cdots \end{bmatrix} \begin{bmatrix} \cdots & \cdots & \cdots \\ \cdots & H & \cdots \\ \cdots & \cdots & \cdots \end{bmatrix} \odot \begin{bmatrix} \cdots & \cdots & \cdots \\ \cdots & F & \cdots \\ \cdots & \cdots & \cdots \end{bmatrix} \begin{bmatrix} \cdots & \cdots & \cdots \\ \cdots & J & \cdots \\ \cdots & \cdots & \cdots \end{bmatrix} \right) \qquad (L-28)$$

Appendix M: Enforcement of Boundary Conditions for DSPM Equations

M.1 Incident and Scattered Fields for the DSPM Model

For an infinitely long cylinder, when an external line source is moved close to the surface of a conducting cylinder, each induced current source can be represented as a delta function. These excitation sources at the surface act as virtual sources, and so can be thought of as eigensources.

External line sources and incident electric fields outside the cylinder may be decomposed into a collection of virtual currents or eigensources. The basis of the Direct Spectral Projection Model is that the **H**-spectral signature of any external line source or incident electric field can be expressed as the weighted sum of the **H**-spectral signatures of a set of virtual sources. The induced currents are the output function. Because each induced current source is a scaled version of an equal and opposite eigensource, by finding the weights of the virtual currents one can calculate the induced currents on the surface of the cylinder.

Unlike the Spectral Projection Model, it is not necessary to write the full addition theorem to characterize the incident and scattered electric fields at the surface of the conducting body. Boundary conditions are implicit in the formulation of the Direct Spectral Projection Method because virtual and induced currents produce equal and opposite electric fields at every observation point on the surface. This is illustrated in Figure M-1.

M.2 Enforcing Boundary Conditions with DSPM

To meet the electric field boundary conditions on the surface of the PEC cylinder, the following equation must be satisfied between the incident and scattered fields at points $n \in \{1, 2, \dots, N\}$.

$$\begin{bmatrix} E_{inc,1} \\ E_{inc,n} \\ E_{inc,N} \end{bmatrix} = - \begin{bmatrix} E_{scat,1} \\ E_{scat,n} \\ E_{scat,N} \end{bmatrix} \qquad (M-1)$$

.

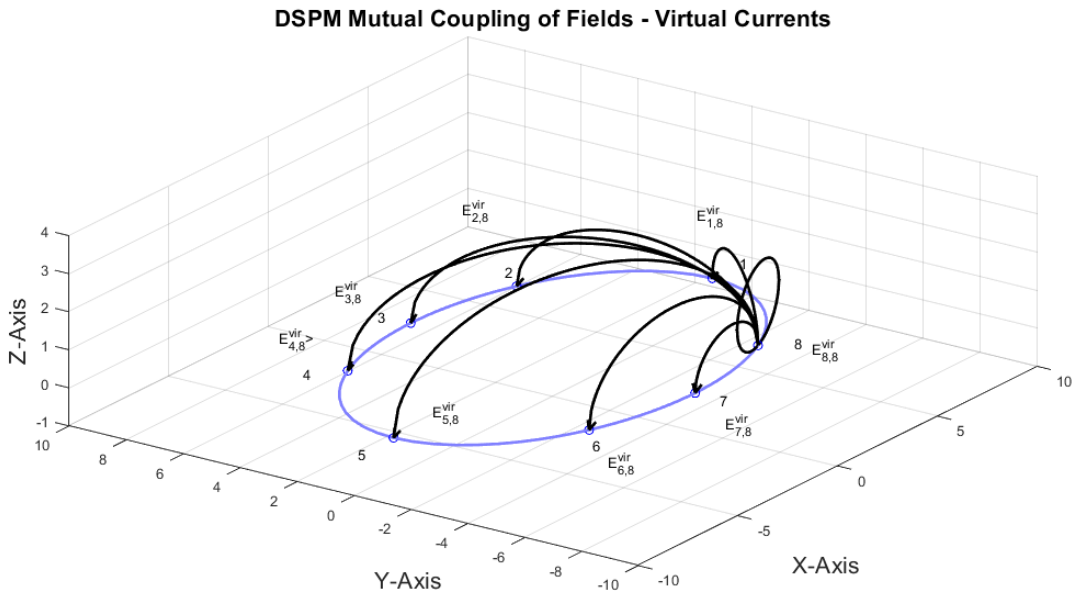

a)

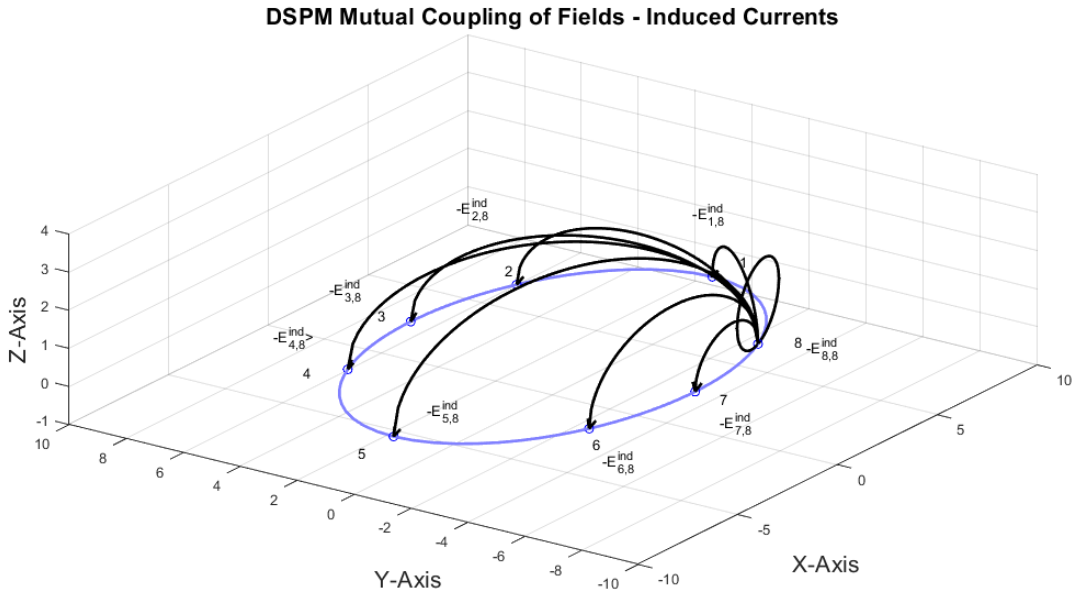

b)

Figure M-1: Contributions to electric field from a virtual source on an infinitely long cylinder. b) Contributions to electric field from a virtual source on an infinitely long cylinder.

In the case of DSPM, the incident fields are represented by virtual sources that generate an electric field equivalent to that of the external sources. Scattered fields are produced by induced currents. So, boundary conditions in equation $(M-1)$ can be written as $(M-2)$.

$$\begin{bmatrix} E_{vir,1} \\ E_{vir,n} \\ E_{vir,N} \end{bmatrix} = -\begin{bmatrix} E_{ind,1} \\ E_{ind,n} \\ E_{ind,N} \end{bmatrix} \qquad (M-2)$$

The electric fields produced by the virtual sources $\begin{bmatrix} \vdots \\ \vdots \\ E_{vir,n} \\ \vdots \\ \vdots \end{bmatrix}$ are equivalent to the electric fields produced by the incident sources $\begin{bmatrix} E_{inc,1} \\ E_{inc,n} \\ E_{inc,N} \end{bmatrix}$. To calculate the equivalent electric field from the virtual sources, one must project the collective **H**-spectral signature of the virtual sources $(M-3)$ onto the **J** $^{\mathbf{T}}$-spectral signature of the observation points $(M-4)$ at the surface. The incident field at the boundary is equal to the weighted sum of the **H**-spectral signature of the incident sources projected onto the **J** $^{\mathbf{T}}$-spectral signature of the same observation points at the surface. Because the same **J** $^{\mathbf{T}}$-spectral signature matrix is used in this equality, it does not appear in the final DSPM equation. But its importance must be emphasized because it is responsible for the convergence of the solution in the DSPM equation.

$$\begin{bmatrix} : & : & : \\ : & H_k^{(2)}(\beta|\boldsymbol{\rho_n}|)e^{jk\phi_n} & : \\ : & : & : \end{bmatrix}$$

$$= \begin{bmatrix} H_{-K}^{(2)}(\beta|\boldsymbol{\rho_0}|)e^{-jK\phi_0} & : & : & : & H_{-K}^{(2)}\left(\beta\left|\boldsymbol{\rho_{N_O-1}}\right|\right)e^{-jK\phi_{N-1}} \\ : & : & : & : & : \\ : & : & H_k^{(2)}(\beta|\boldsymbol{\rho_n}|)e^{jk\phi_n} & : & : \\ : & : & : & : & : \\ H_K^{(2)}(\beta|\boldsymbol{\rho_0}|)e^{jK\phi_0} & : & : & : & H_K^{(2)}\left(\beta\left|\boldsymbol{\rho_{N_O-1}}\right|\right)e^{jK\phi_{N-1}} \end{bmatrix} \qquad (M-3)$$

$$\begin{bmatrix} \vdots & \vdots & \vdots \\ \vdots & J_k(\beta|\boldsymbol{\rho_n}|)e^{jk\phi_n} & \vdots \\ \vdots & \vdots & \vdots \end{bmatrix}^T$$

$$= \begin{bmatrix} J_{-K}(\beta|\boldsymbol{\rho_0}|)e^{-jK\phi_0} & \vdots & \vdots & \vdots & J_{-K}(\beta|\boldsymbol{\rho_{N-1}}|)e^{-jK\phi_{N-1}} \\ \vdots & \vdots & \vdots & \vdots & \vdots \\ \vdots & \vdots & J_k(\beta|\boldsymbol{\rho_n}|)e^{jk\phi_n} & \vdots & \vdots \\ \vdots & \vdots & \vdots & \vdots & \vdots \\ J_K(\beta|\boldsymbol{\rho_0}|)e^{jK\phi_0} & \vdots & \vdots & \vdots & J_K(\beta|\boldsymbol{\rho_{N-1}}|)e^{jK\phi_{N-1}} \end{bmatrix}^T \qquad (M-4)$$

The spectral signature of an incident plane wave from direction ϕ_0 can be represented by an infinitely long vector in $C^{1\times\infty}$ space, and the **H**-spectral signature subspace of the *M+1* observation points on the surface is also made up of infinite dimensional columns $k \to \infty$. The magnitude of the **H**-spectral signature grows larger $\left|\hat{h}_{ss,M,-K}\right| \to \infty$ for $K \to \infty$. This is shown in matrix equation $(M-5)$ below.

$$\begin{bmatrix} \left|\hat{h}_{ss,0,-K}\right| \to \infty & \cdots & \left|\hat{h}_{ss,m,-K}\right| \to \infty & \cdots & \left|\hat{h}_{ss,M,-K}\right| \to \infty \\ \vdots & \vdots & \vdots & \vdots & \vdots \\ \hat{h}_{ss,0,k} & \vdots & \hat{h}_{ss,m,k} & \vdots & \hat{h}_{ss,M,k} \\ \vdots & \vdots & \vdots & \vdots & \vdots \\ \left|\hat{h}_{ss,0,K}\right| \to \infty & \cdots & \left|\hat{h}_{ss,m,K}\right| \to \infty & \cdots & \left|\hat{h}_{ss,M,K}\right| \to \infty \end{bmatrix} \begin{bmatrix} a_0 \\ \vdots \\ a_m \\ \vdots \\ a_{M-1} \end{bmatrix} = \begin{bmatrix} \left|e^{jk\phi_0}\right| = 1 \quad k \to -\infty \\ e^{jk\phi_{-K}} \\ \vdots \\ e^{jk\phi_0} \\ \vdots \\ e^{jk\phi_K} \\ \left|e^{jk\phi_0}\right| = 1 \quad k \to \infty \end{bmatrix}$$

$$(M-5)$$

Similarly, the **J** $^{\mathbf{T}}$-spectral signature subspace of the *M+1* observation points on the surface is made up of infinite dimensional rows. The magnitude of the **J**-spectral signature in this case grows smaller $\left|\hat{J}_{ss,0,K}\right| \to 0$ for $K \to \infty$. This is shown in matrix equation $(M-6)$ below.

$$\begin{bmatrix} \left|\hat{J}_{ss,0,-K}\right| \to 0 & \cdots & \left|\hat{J}_{ss,0,k}\right| \to 0 & \cdots & \left|\hat{J}_{ss,0,K}\right| \to 0 \\ \vdots & \vdots & \vdots & \vdots & \vdots \\ \hat{J}_{ss,m,-K} & \vdots & \hat{J}_{ss,m,k} & \vdots & \hat{J}_{ss,m,K} \\ \vdots & \vdots & \vdots & \vdots & \vdots \\ \left|\hat{J}_{ss,M,-K}\right| \to 0 & \cdots & \left|\hat{J}_{ss,M,k}\right| \to 0 & \cdots & \left|\hat{J}_{ss,M,K}\right| \to 0 \end{bmatrix}^{\boldsymbol{T}} \qquad (M-6)$$

The magnitude plot of the Hankel functions vs. modes is shown in both matrix form and graphically in Figure M-2. The magnitude of the **H**-spectral signature increases as the mode number increases.

$$\begin{bmatrix} \left|\hat{h}_{ss,0,-K}\right| \to \infty & \cdots & \left|\hat{h}_{ss,m,-K}\right| \to \infty & \cdots & \left|\hat{h}_{ss,M,-K}\right| \to \infty \\ \vdots & \vdots & \vdots & \vdots & \vdots \\ \hat{h}_{ss,0,k} & \vdots & \hat{h}_{ss,m,k} & \vdots & \hat{h}_{ss,M,k} \\ \vdots & \vdots & \vdots & \vdots & \vdots \\ \left|\hat{h}_{ss,0,K}\right| \to \infty & \cdots & \left|\hat{h}_{ss,m,K}\right| \to \infty & \cdots & \left|\hat{h}_{ss,M,K}\right| \to \infty \end{bmatrix}$$

a)

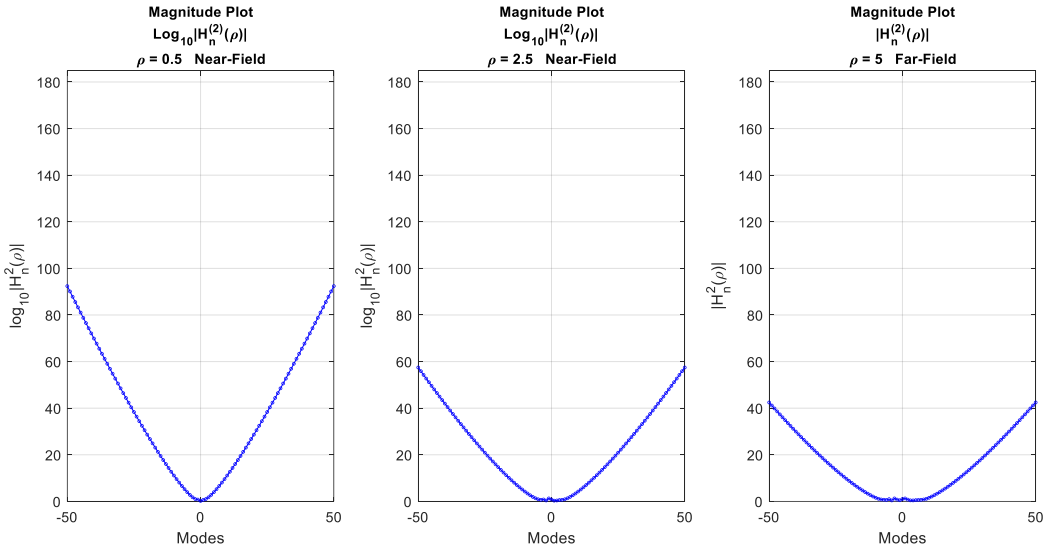

b) c) d)

Figure M-2: Magnitude plot of **H**-spectral signature modes for different axial lengths $\rho = .5, \rho = 2.5, \rho = 5$. a) Matrix representation. b, c, d) Modes vs. magnitude.

The plot of modes -*K* to *K* vs. magnitude of Bessel functions is shown below in Figure M-3. The matrix is shown as the **J** $^{\mathbf{T}}$-spectral signatures of the observation points.

$$\begin{bmatrix} \left|\hat{J}_{ss,0,-K}\right| \to 0 & \cdots & \left|\hat{J}_{ss,0,k}\right| \to 0 & \cdots & \left|\hat{J}_{ss,0,K}\right| \to 0 \\ \vdots & \vdots & \vdots & \vdots & \vdots \\ \hat{J}_{ss,m,-K} & \vdots & \hat{J}_{ss,m,k} & \vdots & \hat{J}_{ss,m,K} \\ \vdots & \vdots & \vdots & \vdots & \vdots \\ \left|\hat{J}_{ss,M,-K}\right| \to 0 & \cdots & \left|\hat{J}_{ss,M,k}\right| \to 0 & \cdots & \left|\hat{J}_{ss,M,K}\right| \to 0 \end{bmatrix}^{\boldsymbol{T}}$$

a)

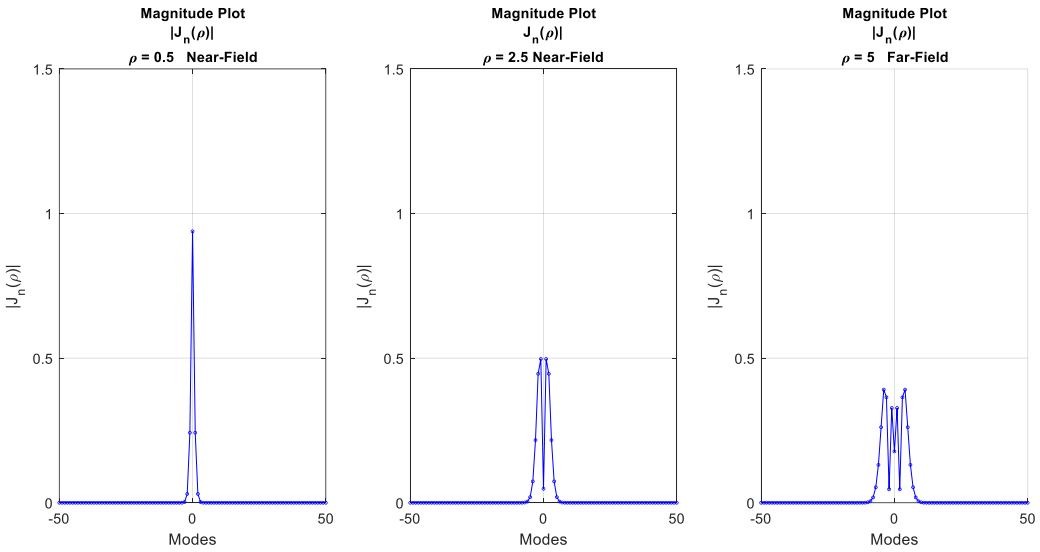

b) c) d)

Figure M-3: Magnitude plot of $\mathbf{J}^{\mathbf{T}}$-spectral signature modes for different axial lengths $\rho = .5, \rho = 2.5, \rho = 5$. a) Matrix representation. b, c, d) Modes vs. magnitude.

In the magnitude plot of the $\mathbf{J}^{\mathbf{T}}$-spectral signatures, the value of the bessel function approaches zero for the higher order modes. This means that this matrix acts as a low-pass filter, and multiplying the **H**-spectral signature vector by this matrix drives this product to zero and thus provides for the convergence of the addition theorem. The electric field boundary conditions are enforced by projecting the **H**-spectral signatures onto the $\mathbf{J}^{\mathbf{T}}$-spectral signatures at the surface over a defined number of modes. This is similar to the way higher order sinusoidal harmonics are filtered out by the basis functions when implementing the Method of Moments and the Spatial Frequency Technique. See Figure M-4 below.

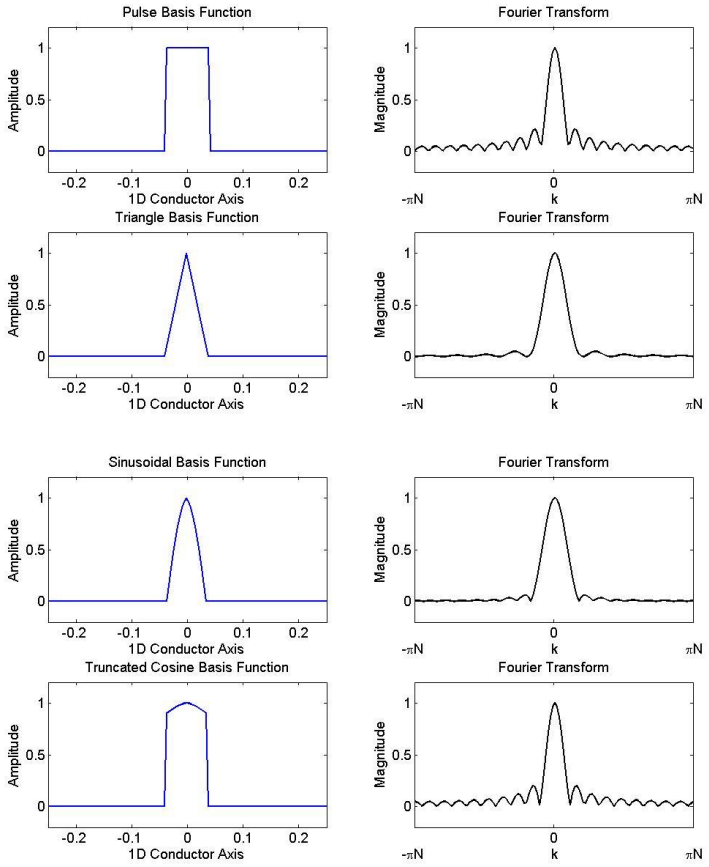

Figure M-4: Fourier transforms of different basis functions: rectangular pulse waveform, triangular waveform, sinusoidal wave, and truncated cosine waveform.

When both sides of the DSPM equation are multiplied by the $\mathbf{J}^{\mathbf{T}}$-spectral signatures the boundary conditions are enforced. On the left side of the equation, the matrix product becomes $(M-7)$.

$$\begin{bmatrix} |\hat{J}_{ss,0,-K}| \to 0 & \cdots & |\hat{J}_{ss,0,k}| \to 0 & \cdots & |\hat{J}_{ss,0,K}| \to 0 \\ \vdots & & \vdots & & \vdots \\ \hat{J}_{ss,m,-K} & \vdots & \hat{J}_{ss,m,k} & \vdots & \hat{J}_{ss,m,K} \\ \vdots & & \vdots & & \vdots \\ |\hat{J}_{ss,M,-K}| \to 0 & \cdots & |\hat{J}_{ss,M,k}| \to 0 & \cdots & |\hat{J}_{ss,M,K}| \to 0 \end{bmatrix}^{T} \begin{bmatrix} |\hat{h}_{ss,0,-K}| \to \infty & \cdots & |\hat{h}_{ss,m,-K}| \to \infty & \cdots & |\hat{h}_{ss,M,-K}| \to \infty \\ \vdots & & \vdots & & \vdots \\ \hat{h}_{ss,0,k} & \vdots & \hat{h}_{ss,m,k} & \vdots & \hat{h}_{ss,M,k} \\ \vdots & & \vdots & & \vdots \\ |\hat{h}_{ss,0,K}| \to \infty & \cdots & |\hat{h}_{ss,m,K}| \to \infty & \cdots & |\hat{h}_{ss,M,K}| \to \infty \end{bmatrix}$$

$$(M-7)$$

Figure M-5 illustrates how the outer modes of the **J** $^{\mathbf{T}}$-spectral filter the higher order modes of the **H**-spectral signature to zero, and ensure convergence of the matrix product.

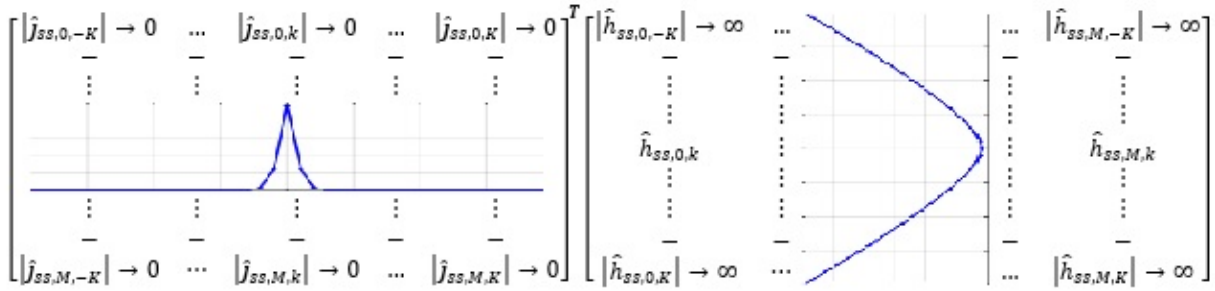

Figure M-5: Filtering of the outer modes of the product of the **J** $^{\mathbf{T}}$-spectral subspace and **H**-spectral signature subspaces.

The spectral signature of the incident field from a current source at (ρ_0, ϕ_0) was given earlier and written again in equation $(M-8)$.

$$\begin{bmatrix} \cdots \\ \hat{\imath}_{ss,inc,Ie} \\ \cdots \end{bmatrix} = -\frac{\beta^2 I_e}{4\omega\varepsilon} \begin{bmatrix} H_{-K}^{(2)}(\beta|\boldsymbol{\rho_0}|)e^{-jK\phi_0} \\ \vdots \\ H_{k}^{(2)}(\beta|\boldsymbol{\rho_0}|)e^{jk\phi_0} \\ \vdots \\ H_{K-1}^{(2)}(\beta|\boldsymbol{\rho_0}|)e^{jK\phi_0} \end{bmatrix} \qquad (M-8)$$

In order to represent a plane wave incident from an angle $\phi_0{}'$, the matrix expression in equation $(M-9)$ is shown.

$$\begin{bmatrix} \vdots \\ i_{ss,inc,Ie}^{ff} \\ \vdots \end{bmatrix} = E_0 \begin{bmatrix} e^{-jK\left(\phi_0\prime - \frac{\pi}{2}\right)} \\ \vdots \\ e^{jk\left(\phi_0\prime - \frac{\pi}{2}\right)} \\ \vdots \\ e^{jK\left(\phi_0\prime - \frac{\pi}{2}\right)} \end{bmatrix} \qquad (M-9)$$

The actual magnitude of the incident field is defined by the infinite vector on the right-hand side of the matrix equation, and is a constant value of one.

$$\left| \begin{bmatrix} \vdots \\ - - - - - - \\ e^{-jK\phi_0} \\ \vdots \\ e^{jk\phi_0} \\ \vdots \\ e^{jK\phi_0} \\ - - - - - - \\ \vdots \end{bmatrix} \right| = \begin{bmatrix} \vdots \\ - - - - - - \\ \vdots \\ \vdots \\ 1 \\ \vdots \\ \vdots \\ - - - - - - \\ \vdots \end{bmatrix} \qquad (M-10)$$

The spectral signatures of each observation point *m* is defined by an infinitely long spectral signature column vector $\hat{h}_{ss,m,k}$. The spectral signature s_k for $s_k \in \{-K, \ldots k, \ldots K\}$ represents the region in which the boundary conditions are applied. As the length of the column vectors gets larger (for greater *K* modes), the magnitude of the **H**-spectral signatures goes to infinity $|s_k| \to \infty$, as shown in Figure M-5. By multiplying both sides by **J** $^{\mathbf{T}}$-spectral signature subspace, the electric field boundary conditions are met through the low-pass filter effect. For large axial ratios, the number of modes in the spectral signature of an object increases. This limits application of the DSPM by the larger axial dimension, unless translation is performed to mitigate its effects.

This procedure forces the vectors representing the **H**-spectral signatures of the induced currents on the left-hand side of the equation to be equal to the vectors representing the **H**-spectral signatures of the incident currents on the right-hand side of the equation. Moreover, it can be used to force any two vectors representing the **H**-spectral signature of the induced and incident currents to satisfy the boundary conditions at the surface of the conductor.